

http://researchcommons.waikato.ac.nz/

Research Commons at the University of Waikato

Copyright Statement:

The digital copy of this thesis is protected by the Copyright Act 1994 (New Zealand).

The thesis may be consulted by you, provided you comply with the provisions of the Act and the following conditions of use:

- Any use you make of these documents or images must be for research or private study purposes only, and you may not make them available to any other person.
- Authors control the copyright of their thesis. You will recognise the author's right to be identified as the author of the thesis, and due acknowledgement will be made to the author where appropriate.
- You will obtain the author's permission before publishing any material from the thesis.

Simulation, measurement, and design of multi-electrode spinal cord stimulation Leads with a focus on MRI safeness and stimuli induced artefacts

A thesis

submitted in partial fulfilment

of the requirements for the degree

of

Doctor of Philosophy in Engineering

at

The University of Waikato

by

Dirk Hartung



THE UNIVERSITY OF
WAIKATO
Te Whare Wānanga o Waikato

September 2019

Abstract

The electromagnetic (EM) and thermodynamic (TD) models for a Spinal Cord Stimulator (SCS) presented in this work, permit on one hand to analyse the impact of electrical stimuli patterns on artefacts and on the other hand to analyse the impact of RF exposure during MRI scans on tissue heating. Historically, many models have focused on single electrode Leads whereas this work focuses on multi-electrode Leads.

Testing of Leads and IPGs for Magnetic Resonance Imaging (MRI) compliance is a tedious, time-consuming and expensive process. A table-top RF test bed has been conceived and calibrated to systematically investigate MRI compliance for various RF exposure scenarios. In addition, a table-top test bed has been conceived to determine the propagation constant of electromagnetic (EM) waves along Leads embedded in electrolytes.

A thin low permittivity layer around the multi-lumen conduct (MLC) has been added to the EM model to solve the discrepancy between measured and initially calculated propagation constants.

Further, several new measures to minimise tissue heating caused by Leads during MRI scans are presented.

The work compares EM and TD simulation results obtained from finite element method (FEM) solvers with measurement results obtained from various test beds that have been conceived or adapted. Despite some discrepancies between simulated and measured results the EM and

thermodynamic models permit to investigate the impact of stimuli patterns on artefacts and the impact of RF exposure on tissue heating.

The results show that worst case tissue heating does not necessarily occur at the distal end electrode in multi-electrode Leads and that RF exposure scenarios have an impact on locations where RF power is dissipated at the distal end.

Simulations and measurements show that Lead wire routing anomalies, i.e. changes in RF coupling between Lead wires along a multi-lumen conduct, have a significant impact on locations where RF power is dissipated at the distal end.

The measures proposed to minimise tissue heating have proved their effectiveness in both the table-top RF test bed and in a 3 Tesla MRI scanner.

Finally, artefacts captured by recording electrodes in multi-electrode Leads can be significantly reduced if the input impedance of the recording amplifier is low during stimuli on therapeutic electrodes.

Blank Page

Contents

I. Statement vi
II. Sponsors vi
III. Software vi
IV. Computing resources vi
V. Acknowledgements vii
VI. Objectives vii
VII. Symbols viii
VIII. Subscripts xiv
IX. Constants xv
X. Operators xvi
XI. Notations xvi
XII. Conventions xvii
XIII. Abbreviations and Terminology xix
XIV. Tables xxi
XV. Figures xxiii

1. Introduction 1
2. Background 4
2.1 Overview 4
2.2 Origins of pain 4
2.3 Spinal Cord Stimulation 5
2.4 Magnetic Resonance Imaging 10
2.4.1 Principles 10
2.4.2 RF induced heating 11
2.4.3 Misconceptions 17
2.4.4 Safety criteria for RF induced heating 19
2.5 Electromagnetic waves 21
2.6 Electromagnetic wave propagation 22
2.7 Electrolytes 25
2.8 Electrode potentials and current densities 27
2.9 Interface dynamics 32
2.10 Heat transfer 36
3. Configurations 38
3.1 Overview 38
3.2 Simulated and/or tested configurations 42
4. Methods 48
4.1 Electromagnetic modelling 48
4.1.1 Overview 48
4.1.2 Electromagnetic design flow 48
4.1.3 Models and setup for harmonic stimulus 52
4.1.3.1 Spinal Cord Stimulator 52
4.1.3.2 MRI RF coils and phantom torso 54
4.1.4 EM exposure scenarios for harmonic stimulus 56
4.1.4.1 Full plane wave excitation 57
4.1.4.2 Partial plane wave excitation 57
4.1.5 Models and setup for transient stimulus 62
4.1.6 Mesh parameter for IPG and Leads 64
4.2 Thermodynamic modelling 67
4.2.1 Overview 67

4.2.2 Thermodynamic design flow 67
4.2.3 Models and setup for heat dissipation 70
4.2.4 Mesh parameter for distal end 71
4.3 Test and measurement setups 73
4.3.1 Overview 73
4.3.2 Voltages, currents and resistances 74
4.3.3 Step function 75
4.3.4 Time Domain Reflectometry 76
4.3.5 Permittivity and conductivity 76
4.3.6 RF transfer function 78
4.3.7 RF heating 83
4.3.7.1 Overview 83
4.3.7.2 Test bed components 87
4.3.7.3 Temperature calibration 94
4.3.7.4 Local electric fields and local deposited power 97
4.3.7.5 Fields and power deposition in phantom torso 101
4.3.7.6 Conclusion 109
4.3.8 Pulse pattern and artefacts 110
5. Results 115
5.1 MRI safeness 115
5.1.1 Overview 115
5.1.2 Surface currents on platinum electrodes 116
5.1.3 Permittivity and conductivity of electrolytes 119
5.1.4 Viscosity estimations of gelled saline solution 121
5.1.5 Isolated coaxial filars 123
5.1.6 EM waves along MLC 128
5.1.6.1 Overview 128
5.1.6.2 Planar wave excitation 129
5.1.6.3 Coaxial wave excitation 139
5.1.6.4 RF transfer function 147
5.1.6.5 Inconsistencies in attenuation and phase slopes 153
5.1.6.6 Inconsistencies in reflections at distal end 156
5.1.6.7 Auxiliary electrodes along MLC 162
5.1.7 EM waves along Lead 169
5.1.8 Influence of material parameters 175
5.1.8.1 Conductance of Lead wires 175
5.1.8.2 Surface roughness of Lead wires 178
5.1.8.3 Permittivity of MLC 182

5.1.8.4 Loss factor of MLC 184
5.1.8.5 Conclusion 186
5.1.9 Influence of design variations 187
5.1.9.1 Base cases 187
5.1.9.2 Helical electrodes 189
5.1.9.3 Coupled auxiliary filars 191
5.1.9.4 Coupled interleaved auxiliary electrodes 192
5.1.9.5 Number of electrodes 193
5.1.9.6 Angular position of wires and electrodes 199
5.1.9.7 Auxiliary electrodes at proximity end 203
5.1.9.8 Distal end extension and auxiliary electrodes at PE 204
5.1.9.9 Distal end extension and RC network at PE 206
5.1.10 Frequency dependence 209
5.1.11 RF test bed - RF induced temperature rise 211
5.1.11.1 Overview 211
5.1.11.2 Position of IPG and Leads in PT 212
5.1.11.3 Therapeutic electrodes without Lead wires 213
5.1.11.4 Therapeutic electrodes (base cases) 215
5.1.11.5 Therapeutic and interleaved auxiliary electrodes 230
5.1.11.6 Therapeutic and auxiliary electrodes at PE 238
5.1.11.7 Therapeutic electrodes, resistors, DE extension 256
5.1.12 3T MRI scanner - RF induced temperature rise 264
5.1.13 Simplified analytic models 268
5.1.13.1 Simple electrodynamic model 268
5.1.13.2 Simple thermodynamic model 271
5.2 Artefacts 275
5.2.1 Overview 275
5.2.2 Voltages, currents and resistances 275
5.2.3 Step function and transient response 279
5.2.4 Electric and magnetic fields 281
5.2.5 Monophasic positive pulse patterns 283
5.2.6 Monophasic negative pulse pattern 284
5.2.7 Bi-phasic pulse pattern 287
5.2.8 Summary 290
6. Conclusions and outlook 291
References 293
R.1 Books 293

R.2 Publications 296
R.3 Specifications and standards 317
R.4 Software 318
R.5 Databases 318
R.6 Internet 319
Appendices 320
A Properties of matter 320
A.1 Human tissue 320
A.2 Platinum 321
A.3 Pellethane 323
A.4 Saline solution 324
A.5 Gelled saline solution 324
B MRI scanner parameter 326
B.1 MRI scanner - GE - 3.0 T 326
B.2 MRI gradient pulse pattern parameter 327
B.3 MRI RF pulse pattern parameter 327
C Electromagnetic modelling 329
C.1. Surface currents on electrodes 329
C.2. RF permittivity and conductivity extraction 331
C.3. EM wave excitation scenarios 336
D Thermodynamic modelling 344
D.1 Heat dissipation in perfused tissue 344

I. Statement

I hereby declare that this document contains my own work. The work presented here is based on my unpublished treatise about "Spinal Cord Stimulation - Model Based Approach for MRI Safeness, Stimuli, and Artefacts" drafted in March 2019. Any contribution made by third parties is referenced in this document.

II. Sponsors

This project has been co-sponsored, among others, by Saluda Medical (Sydney, Australia) and the University of Waikato (Hamilton, New Zealand). MRI measurements have been made possible by Midland MRI (Hamilton, New Zealand).

III. Software

For electromagnetic simulations the ANSYS Electromagnetics Design Suites (Release 18.2.0) and for thermodynamic simulations the ANSYS Fluent Design Suites (Release 18.2.0) have been used. Algorithms for EM and thermal analysis have been programmed in Matlab and Excel.

IV. Computing resources

All simulations have been carried out using a DELL Precision Tower 5810 with 16 GB (32 GB) RAM and 256 GB (512 GB) hard disk.

V. Acknowledgements

I am grateful to all who have provided their support and I respect all those who haven't.

VI. Objectives

Spinal Cord Stimulators (SCS) should efficiently stimulate predefined sets of nerve fibres in the dorsal column of the spinal cord without affecting neighbouring nerve fibres. The first objective is to obtain an electro-dynamic model for the operating mode allowing the analysis of stimuli sequences and artefacts. The non-operating mode is chosen for medical examinations, surgical interventions or firmware upgrades. A wide range of medical analysis relies on results obtained from Magnetic Resonance Imaging (MRI) scans. The second objective is to obtain an electro-dynamic and thermodynamic model allowing the prediction of RF induced heating of implanted SCS caused by exposure to pulsed RF sequences encountered in MRI scanners. The third objective is to conceive RF test beds that permit to characterise wave propagation along isolated Lead wires and to measure RF induced temperature rise at electrodes and Implanted Pulse Generators (IPGs). The fourth objective is to identify measures reducing human tissue heating caused by SCS during MRI scans and verifying the effectiveness of the measures in RF test beds and MRI scanners. Further, the models should be applicable to other electrode shapes and configurations and wire routing scenarios between electrodes and IPGs. The research focus is on SCS but research results should be applicable to other types of stimulators, such as deep brain stimulators, vagus nerve stimulators, implantable cardioverter-defibrillators, cochlear implants or pacemakers.

VII. Symbols

Latin symbols

Symbol	***Designation***	***Unit***
A	*Area*	m^2
B	*Magnetic flux density* *Magnetic displacement*	$T = \frac{V \cdot s}{m^2}$
B_0	*Magnetic flux density (static)* *Magnetic displacement (static)*	$\frac{V \cdot s}{m^2}$
B_1	*Magnetic flux density (dynamic)* *Magnetic displacement (dynamic)*	$\frac{V \cdot s}{m^2}$
C	*Capacitance*	$F = \frac{A \cdot s}{V}$
C'	*Capacitance per meter*	$\frac{F}{m} = \frac{A \cdot s}{V \cdot m}$
c_{mass}	*Thermal capacity (mass specific)*	$\frac{J}{kg \cdot K}$
$C_{p,i}$	*Plasma constant*	$\frac{A}{m \cdot V \cdot s}$
D	*Diffusion coefficient*	$\frac{m^2}{s}$
D	*Electric flux density* *Electric displacement*	$\frac{A \cdot s}{m^2}$
D_{em}	*Electro-dynamic diffusion coefficient*	$\frac{m^2}{s}$
D_{th}	*Thermal diffusion constant*	$\frac{m^2}{s}$
E	*Electric field*	$\frac{V}{m}$
E	*Energy*	$J = W \cdot s$ $J = V \cdot A \cdot s$
F	*Force*	$N = \frac{kg \cdot m}{s^2}$
f	*Factor*	1
f	*Flow constant*	$\frac{W}{m^3 \cdot K}$
f	*Frequency*	$\frac{1}{s}$

continued on next page

Symbol	*Designation*	*Unit*
G	*Conductance*	$S = \frac{A}{V}$
G	*Gradient field of magnetic flux density*	$\frac{V \cdot s}{m^3}$
G'	*Conductance per meter*	$\frac{S}{m} = \frac{A}{V \cdot m}$
H	*Magnetic field*	$\frac{V}{m^2}$
I	*Current*	A
I	*Quantity*	1
J	*Angular momentum (total)*	$J \cdot s = \frac{kg \cdot m^2}{s}$
J	*Electric current density*	$\frac{A}{m^2}$
K	*Correction factor for rough surfaces*	1
$\tilde{k} = k_{Re} + j \cdot k_{Im}$	*Complex wave propagation constant*	$\frac{1}{m}$
k_{Im}	*Imaginary part of complex wave propagation constant (attenuation constant)*	$\frac{1}{m}$
k_{Re}	*Real part of complex wave propagation constant (phase constant)*	$\frac{rad}{m}$
k_{th}	*Thermal conductivity*	$\frac{\mathrm{W}}{m \cdot K} = \frac{\mathrm{V} \cdot \mathrm{A}}{m \cdot K}$
L	*Angular momentum (orbital)*	$J \cdot s = \frac{kg \cdot m^2}{s}$
L	*Inductance*	$H = \frac{V \cdot s}{A}$
L	*Length and/or width of selected slice in MRI scan*	m
L	*Number of sampled data points*	1
L'	*Inductance per meter*	$\frac{H}{m} = \frac{V \cdot s}{A \cdot m}$
l	*Length*	m
l_c	*Characteristic diffusion length*	m
M	*Gradient field (number of applied gradients)*	1
M	*Magnetic current density*	$\frac{V}{m^2}$
M	*Magnetisation*	$\frac{A}{m}$

continued on next page

Symbol	*Designation*	*Unit*
m	*Magnetic dipole moment*	$A \cdot m^2$
m	*Mass*	kg
N	*Number of samples* *Number of species* *Number of electrons*	1
n	*Index of refraction* *Normal vector* *Integer number*	1
n_e	*Electron density*	$\frac{electrons}{m^3}$
P	*Polarisation*	$\frac{A \cdot s}{V \cdot m}$
$P_{eddy,loss}$	*Dissipated power due to eddy currents*	$W = V \cdot A$
$P_{em,loss}$	*Dissipated power due to electromagnetic fields*	W
p	*Dissipated power density*	$\frac{W}{m^3} = \frac{V \cdot A}{m^3}$
p	*Impulse*	$kg \cdot \frac{m}{s}$
Q, q	*Charge*	$\mathrm{C} = \mathrm{A} \cdot \mathrm{s}$
q	*Rate of heat generation*	$\frac{W}{m^3}$
R	*Resistance*	$\Omega = \frac{V}{A}$
R'	*Resistance per meter*	$\frac{\Omega}{m} = \frac{V}{A \cdot m}$
r	*Location of field point* *Radius*	m
r	*Reflection coefficient*	1
r'	*Location of source point*	m
S	*Angular momentum (spin)*	$J \cdot s = \frac{kg \cdot m^2}{s}$
S	*Surface*	m^2
s	*Spin quantum number*	1
s	*Stretch, line segment*	m
SAR	*Specific Absorption Rate*	$\frac{\mathrm{W}}{kg} = \frac{\mathrm{V} \cdot \mathrm{A}}{kg}$
T	*Period*	s
T	*Temperature*	K

continued on next page

Symbol	*Designation*	*Unit*
t	*Time*	s
t	*Transmission coefficient*	1
t_c	*Characteristic diffusion time*	s
$tan(\delta_{diel})$	*Dielectric loss tangent*	1
$tan(\delta_e)$	*Electric loss tangent*	1
$tan(\delta_m)$	*Magnetic loss tangent*	1
u	*Cartesian coordinate in frequency domain (normalised)*	1
V	*Voltage*	V
V	*Volume*	m^3
$\tilde{v}$	*Complex propagation velocity*	$\frac{m}{s}$
v	*Cartesian coordinate in frequency domain (normalised)*	1
W_{em}	*Power (dissipated)*	$\mathrm{W} = \mathrm{V} \cdot \mathrm{A}$
w	*Width*	m
w_{em}	*Power density (dissipated)*	$\frac{\mathrm{W}}{m^3} = \frac{\mathrm{V} \cdot \mathrm{A}}{m^3}$
x	*Cartesian coordinate (x-component)*	m
y	*Cartesian coordinate (y-component)*	m
Z_c	*Impedance (characteristic)*	$\Omega = \frac{V}{A}$
Z_w	*Impedance (wave)*	$\Omega = \frac{V}{A}$
z	*Cartesian coordinate (z-component)*	m
z	*Number of free electrons per atom*	$\frac{electrons}{atom}$

Table P-1 Latin symbols

Greek symbols

Symbol	***Designation***	***Unit***
α	*Angle*	$^\circ \ or \ rad$
$\alpha, \alpha(\omega)$	*Attenuation constant*	$\frac{1}{m}$
$\alpha(\omega)$	*Dielectric polarizability function*	$\frac{A \cdot s}{V \cdot m}$
α	*Thermal expansion coefficient*	$\frac{1}{K}$
β	*Angle*	$^\circ \ or \ rad$
$\beta, \beta(\omega)$	*Phase constant* *Propagation constant*	$\frac{rad}{m}$
$\beta(\omega)$	*Dielectric dampening function*	$\frac{A \cdot s}{V \cdot m}$
γ	*Gyromagnetic ratio*	$\frac{A \cdot s}{kg} = \frac{rad}{s \cdot T}$
$\gamma = \alpha + j \cdot \beta$	*Complex characteristic propagation constant*	$\frac{1}{m}$
δ	*Skin depth*	m
$\tilde{\varepsilon} = \varepsilon' + j \cdot \varepsilon''$ $\tilde{\varepsilon} = \varepsilon_0 \cdot (\varepsilon_s + j \cdot \varepsilon_l)$	*Complex permittivity*	$\frac{A \cdot s}{V \cdot m}$
ε_l	*Dielectric loss factor*	1
$\varepsilon_s, \varepsilon_r$	*Relative permittivity*	1
$\zeta_{b,i}$	*damping constant of bound electron in state i*	$\frac{1}{s}$
$\zeta_{f,i}$	*damping constant of free electron in state i*	$\frac{1}{s}$
η	*Potential*	V
η	*Viscosity*	$\frac{J \cdot s}{m^3}$
ϑ	*Angle*	$^\circ \ or \ rad$
λ	*Wavelength in matter*	m
λ_0	*Wavelength in free space*	m
μ	*Mobility of charge carriers*	$\frac{m^2}{V \cdot s}$
$\tilde{\mu} = \mu' + j \cdot \mu''$ $\tilde{\mu} = \mu_0 \cdot (\mu_s + j \cdot \mu_l)$	*Complex permeability*	$\frac{V \cdot s}{A \cdot m}$

continued on next page

Symbol	*Designation*	*Unit*
μ_l	*Magnetic loss factor*	1
$\mu_{m,a}$	*Mass (atomic)*	$\frac{kg}{mol}$
μ_s	*Relative permeability*	1
ρ	*Charge density*	$\frac{A \cdot s}{m^3}$
ρ	*Mass density*	$\frac{kg}{m^3}$
$\tilde{\varrho} = \varrho' + j \cdot \varrho''$	*Complex magnetic conductivity*	$\frac{V}{A \cdot m}$
$\tilde{\varrho} = \varrho' + j \cdot \varrho''$	*Complex resistivity*	$\Omega \cdot \mathrm{m} = \frac{V \cdot m}{A}$
$\tilde{\sigma} = \sigma' + j \cdot \sigma''$	*Complex electric conductivity*	$\frac{A}{V \cdot m}$
τ	*Relaxation time constant*	s
$\tau_{e,2c}$	*Mean free flight time of electron between two collisions*	s
$\tau_{chronaxie}$	*time necessary for a stimulus current twice the rheobase current that triggers an action potential or muscle contraction*	s
Φ	*Magnetic flux*	$Wb = V \cdot s$
Φ, φ	*Potential*	V
φ	*Angle*	$^\circ \ or \ rad$
ω	*Angular frequency*	$\frac{rad}{s}$
ω	*Frequency (angular)*	$\frac{rad}{s}$
$\omega_{0,i}$	*Frequency (angular) of bound electron in state i*	$\frac{rad}{s}$
$\omega_{p,i}$	*Frequency (angular) of plasma in state i*	$\frac{rad}{s}$

Table P-2 Greek symbols

VIII. Subscripts

Symbol	*Designation*	*Unit*
c	*Characteristic*	N/A
Im	*Imaginary part*	N/A
i	*Incident component*	N/A
$\parallel$	*Parallel*	N/A
pp	*Peak to peak*	N/A
$\perp$	*Perpendicular*	N/A
p	*Point (Location)*	N/A
Re	*Real part*	N/A
r	*Reflected component*	N/A
rms	*Root mean square*	N/A
t	*Transmitted component* *Tangential component*	N/A
w	*Wave*	N/A

Table P-3 Subscripts

IX. Constants

Symbol	*Designation*	*Value*	*Unit*
N_A	*Avogadro constant*	$6.02214085774 \cdot 10^{23}$	$\frac{molecules}{mol}$
μ_B	*Bohr magneton*	$-9274.009994(57) \cdot 10^{-27}$	$\frac{J}{T}$
k	*Boltzmann constant*	$1.380622 \cdot 10^{-23}$	$\frac{J}{K}$
e^-	*Electron charge*	$-1.602176620898 \cdot 10^{-19}$	$A \cdot s$
F	*Faraday constant*	96486.7	$\frac{A \cdot s}{mol}$
μ_N	*Nuclear magneton*	$5.050783699(31) \cdot 10^{-27}$	$\frac{J}{T}$
μ_0	*Permeability (vacuum)*	$1.256637061 \cdot 10^{-6}$	$\frac{V \cdot s}{A \cdot m}$
ε_0	*Permittivity (vacuum)*	$8.854185 \cdot 10^{-12}$	$\frac{A \cdot s}{V \cdot m}$
h	*Planck's constant*	$6.626196 \cdot 10^{-34}$	$J \cdot s$
e^+	*Proton charge*	$+1.602176620898 \cdot 10^{-19}$	$A \cdot s$
m_e	*Rest mass of electron*	$9.1093835611 \cdot 10^{-31}$	kg
m_p	*Rest mass of proton*	$1.67262189821 \cdot 10^{-27}$	kg
c_0	*Velocity of electromagnetic waves in vacuum*	$2.99792500 \cdot 10^{8}$	$\frac{m}{s}$

Table P-4 Constants

X. Operators

Symbol	*Designation*	*Unit*
j	*Imaginary unit*	N/A
$\times$	*Vector (cross) product*	N/A
$\cdot$	*Scalar (dot) product*	N/A
$*$	*Convolution*	N/A
$grad$ ∇	*Gradient operator*	$\frac{1}{m}$
div $\nabla\cdot$	*Divergence operator*	$\frac{1}{m}$
rot $\nabla\times$	*Rotation (curl) operator*	$\frac{1}{m}$
Δ	*Laplace operator*	$\frac{1}{m^2}$
Δ	*Difference operator*	N/A

Table P-5 Operators

XI. Notations

Symbol	*Designation*	*Unit*
$\vec{}$	*Vector*	*N/A*
$\hat{}$	*Unit vector*	*N/A*
$\langle\ \rangle$	*Average value*	*N/A*
$\tilde{}$	*Complex scalar*	*N/A*
$\vec{\tilde{}}$	*Complex vector*	*N/A*
$\underline{\ }$	*Tensor*	*N/A*
$\underline{\tilde{}}$	*Complex tensor*	*N/A*
$\lvert\ \rvert$	*Magnitude*	*N/A*
$\lVert\ \rVert$	*Norm*	*N/A*
$\angle$	*Angle*	*N/A*
$^\circ$	*Angle in degrees*	$^\circ$
rad	*Angle in radians*	rad
[ ]	*SI units (usually after equations)*	*N/A*

Table P-6 Notations

XII. Conventions

It is assumed that a wave $\overrightarrow{W}(\vec{r},t)$ propagating into positive coordinate directions is represented by following exponential in the frequency domain:

$$\overrightarrow{W}(\vec{r},t) = \left|\overrightarrow{W_0}(\vec{r}_0,t_0)\right| \cdot e^{j\cdot\varphi_{W,0}(\vec{r}_0,t_0)} \cdot e^{+j\cdot\left(\tilde{k}\cdot\vec{r}(t)-\omega\cdot t\right)} \tag{P-1}$$

This convention leads to following sign conventions in the frequency domain for permittivity, permeability, and conductivity, respectively:

$$\tilde{\varepsilon} = \varepsilon' + j\cdot\varepsilon''$$
$$\tilde{\mu} = \mu' + j\cdot\mu''$$
$$\tilde{\sigma} = \sigma' + j\cdot\sigma'' \tag{P-2}$$

It is further assumed that, if not otherwise stated, all (complex) vector fields and all (complex) field components are total fields, i.e. the superposition of incident and scattered fields.

$$\vec{\tilde{F}}_{total} = \vec{\tilde{F}}_{incident} + \vec{\tilde{F}}_{scatterd} \tag{P-3}$$

Finally, all scalar and vector field magnitudes, if not otherwise stated, are peak field magnitudes. For harmonic sinusoidal signals the peak and rms field magnitudes are related as follows

$$\left|\vec{\tilde{F}}_{rms}\right| = \frac{\left|\vec{\tilde{F}}_{peak}\right|}{\sqrt{2}} \tag{P-4}$$

The magnitude of field quantities is derived as follows:

- Calculation of field components F_x, F_y, F_z at a given location (mesh point) and for a given phase of the harmonic source function.
- Averaging of field components F_x, F_y, F_z over neighbouring mesh points at a given phase.
- Smoothing of averaged field components F_x, F_y, F_z over neighbouring mesh points at a given phase.

Averaging and smoothing are background processes to interpolate field points that are not located on mesh points using weighted averages ([SW1] - [SW4]). The averaging and smoothing algorithms are not explicitly disclosed. In most cases, weighted averages are determined using angles and distances between field points on a line or plane in space and surrounding mesh points.

The magnitude of local fields is either colour coded or equivalent to the length of corresponding arrows.

If not otherwise stated, field quantities have following units:

Electric field distribution in $\left[\frac{V}{m}\right]$

Surface current densities in $\left[\frac{A}{m}\right]$

Volume current densities in $\left[\frac{A}{m^2}\right]$

Volume loss density in $\left[\frac{Watt}{m^3}\right]$

Specific Absorption Rate in $\left[\frac{Watt}{kg}\right]$

XIII. Abbreviations and Terminology

Designation	Description
af	artefact
AP	Action Potential
AWG	Arbitrary Waveform Generator
BL	Boundary Layer around MLC
BSRE	Bulk Saline Reference Electrode
Case	Platinum case of IPG containing electronic circuitry
CC	Coaxial Cavity
CCW	Counter Clockwise orientation
Contact(s)	Cylindrical cuff(s) at proximity end of Lead inside the Header
CP	Circular Polarisation
CSF	Cerebrospinal Fluid
CW	Continuous (Harmonic) Wave Form
CW	Clockwise orientation
DC	Dorsal Column Direct Current
DE	Distal End: location along Lead or multi-lumen conduct that is opposite to the location where an IPG or a signal source is connected (proximity end)
DL	Double Layer around electrodes
DLC	Dorsolateral Column
DVXX	Design Variation of SCS, where XX denotes an index number
DW	Distilled Water
ECAP	Evoked Cumulated Action Potential
EM	Electromagnetic Wave (often interchangeable with RF Wave)
ERT	Evoked Response Telemetry
Electrode(s)	Cylindrical cuff(s) at distal end of Lead in contact with human tissue (electrolyte)
FD	Frequency Domain
Header	Interface between the IPG and the proximity end of the Lead
ID	Image Domain
IMD	Implanted Medical Device
IPG	Implanted Pulse Generator consisting of two major parts, the Case and the Header
Lead	Multi-lumen conduct equipped with twelve wires and twelve electrodes at one end (called the distal end of the Lead) and twelve contacts at the other end of the Lead (called the proximity end of the Lead)

continued on next page

Designation	Description
Lead wire	Single or stranded wire connecting electrodes at the DE and contacts at the PE, usually routed through one of the multi-lumen conducts
LP	Linear Polarisation
MLC	Multi-lumen conduct: cylindrical extruded thermoplastic polyurethane elastomer with (twelve) conducts containing one Lead wire each and a centre conduct for insertion of a surgical tool
MSC	Multi-Channel System; customised test and measurement system for SCS
MRI	Magnetic Resonance Imaging
NMR	Nuclear Magnetic Resonance
NP	Negative Pulse
OSC	Oscilloscope
PE	Proximity End: Location along a Lead or multi-lumen conduct where an IPG or a signal source is connected
PAA	Poly-Acrylic Acid (gelling agent for phantom torso)
PEC	Perfect Electric Conductor
PML	Perfect Matched Layer
PP	Positive Pulse
Probe	Electric or magnetic field detector or temperature sensor
PS	Pulse Sequence
PT	Phantom Torso: acrylic container filled with gelled saline solution (650 mm x 420 mm x 160 mm)
RF	Radio Frequency Waves in the frequency range from 8 MHz to 512 MHz (often interchangeable with EM Wave)
RMS, rms	Root Mean Square
SAR	Specific Absorption Rate
SC	Spinal Cord
SCS	Spinal Cord Stimulator including IPG and Lead
SG	Signal Generator
SGG	Signal Generator Ground
st	stimulus
TD	Thermodynamic (model)
TD	Time Domain (analysis)
TL	Transmission Line
TS	Test Setup
UMXX	Unmodified (standard) SCS, where XX denotes an index number
VNA	Vector Network Analyser

Table P-7 Abbreviations and Terminology

XIV. Tables

Table P-1 Latin symbols xi
Table P-2 Greek symbols xiii
Table P-3 Subscripts xiv
Table P-4 Constants xv
Table P-5 Operators xvi
Table P-6 Notations xvi
Table P-7 Abbreviations and Terminology xx

Table 2-1 RF magnetic flux density parameter 13
Table 2-2 Gradient magnetic flux density parameter 13
Table 2-3 Comparison between gradient and RF parameter 14
Table 3-1 Base configurations 43
Table 3-2 Design variations - coiled electrodes 43
Table 3-3 Design variations - auxiliary filars 44
Table 3-4 Design variations - angular position of Lead wires 44
Table 3-5 Design variations - number of Lead wires and electrodes 44
Table 3-6 Design variations - interleaved therapeutic and auxiliary electrodes 45
Table 3-7 Design variations - auxiliary electrodes integrated into IPG header 45
Table 3-8 Design variations - resistor matrix integrated into IPG header 46
Table 3-9 Design variations - distal end extension 46
Table 3-10 Design variations - distal end extension and resistor matrix 46
Table 3-11 Design variations - distal end extension, resistor matrix and aux. electrodes 47
Table 3-12 Design variation tested in 3T MRI scanner 47
Table 4-1 Electromagnetics - initial mesh settings 51
Table 4-2 EM model - evolutions 52
Table 4-3 Analysis settings - harmonic stimulus 54
Table 4-4 Double layer parameter 64
Table 4-5 Analysis settings - transient stimulus 64
Table 4-6 Typical initial mesh settings 64
Table 4-7 Typical mesh refinements 65
Table 4-8 Maximum number of tetrahedra for EM model 65
Table 4-9 Thermodynamics - initial mesh settings 69
Table 4-10 Typical number of tetrahedra for thermodynamic model 71
Table 4-11 Test and measurement equipment for voltages and currents 74
Table 4-12 Test and measurement equipment for step function 75
Table 4-13 Test and measurement equipment for TDR 76

Table 4-14 Test and measurement equipment for permittivity and conductivity 77
Table 4-15 Test and measurement equipment for RF transfer function test bed 78
Table 4-16 Test and measurement equipment for RF induced temperature increase measurements 84
Table 4-17 Relationship between input power, local deposited power and local electric field strength 101
Table 4-18 Test and measurement equipment 110
Table 5-1 Saline solutions 119
Table 5-2 Relative permittivity and conductivity at 64 MHz 119
Table 5-3 Relative permittivity and conductivity at 128 MHz 119
Table 5-4 Coaxial cable characteristics 123
Table 5-5 TDR measurement results for guided wave front 124
Table 5-6 TDR measurement results for common wave front 127
Table 5-7 Dimensions - planar wave excitation 130
Table 5-8 Dimensions - coaxial wave excitation 140
Table 5-9 Power deposition in saline volume for electrodes without Lead wires 214
Table 5-10 MRI scanner and test and measurement equipment 265
Table 5-11 Comparison of electric field magnitudes at Electrode E01 for a normalised incident electric field according to Figure 4-93 270
Table 5-12 Comparison of temperature increases after 300 seconds ... 274

Table A-1 Electrical characteristics for selected human tissues at 128 MHz [P154] 320
Table A-2 Constituent chemical species of CSF [P152] 320
Table A-3 Thermodynamic parameter of CSF [DB1] 321
Table A-4 Typical characteristics of platinum Lead wires and electrodes [B19] 321
Table A-5 Characteristics of electromagnetic waves in platinum 322
Table A-6 Comparison of wave and particle (electron) velocities in platinum 322
Table A-7 Characteristics of Pellethane [B19] 323
Table A-8 Characteristics of electromagnetic waves in Pellethane 323
Table A-9 Characteristics of saline solution 324
Table A-10 Characteristics of gelled saline at 20 °C 324
Table A-11 Characteristics of electromagnetic waves in saline 325

Table B-1 MRI parameter 326
Table B-2 Typical gradient pulse parameter for MRI scanner - GE - 3.0 T 327
Table B-3 Typical RF pulse parameter for MRI scanner - GE - 3.0 T 327
Table B-4 Typical pulse widths and pulse periods MRI scanner - GE - 3.0 T 328

XV. Figures

Figure 2-1 Outline of wire 15
Figure 2-2 Temperature increase at distal, un-isolated end of wire (adapted from [P105]) 15
Figure 2-3 Outline of multiple wires 16
Figure 2-4 Temperature increase at distal, un-isolated ends of wire (adapted from [P105]) 16
Figure 2-5 Outline with two coupled wires 16
Figure 2-6 Temperature increase at distal, un-isolated end of wire E01 (adapted from [P105]) 16
Figure 2-7 Electric field strength envelope superimposed on typical electric field distribution along a Lead with twelve electrodes for an incident axiolateral plane wave with an incident electric field strength of 1 Vm at 128 MHz. The Lead length varies from 200 mm to 1200 mm. 20
Figure 3-1 Electrode numbering 38
Figure 3-2 Cylinder electrode 38
Figure 3-3 MLC 39
Figure 3-4 Wire positions 39
Figure 3-5 Dimensions of MLC in [mm] 39
Figure 3-6 Single Lead wire 39
Figure 3-7 Implanted Pulse Generator (IPG) 40
Figure 3-8 Lead wires grounded to IPG case 40
Figure 3-9 Lead wires open ended in IPG header 40
Figure 3-10 Helical electrodes 40
Figure 3-11 Coupling to auxiliary wires 41
Figure 3-12 Coupling to Lead wires or interconnect layers 41
Figure 3-13 Lead wires capacitive coupled to auxiliary electrodes in IPG 41
Figure 3-14 Lead wires capacitive coupled to resistor ring in IPG 41
Figure 3-15 Auxiliary electrode 42
Figure 3-16 Lead wire extension 42
Figure 4-1 Electromagnetics - design parameter 49
Figure 4-2 Electromagnetics - design flow (adapted from [SW1]) 50
Figure 4-3 Model - Electromagnetics - IPG and Lead 52
Figure 4-4 Model - Electromagnetic - Distal End and Electrode numbering 53
Figure 4-5 Model - Electromagnetics - MLC with boundary layer 53
Figure 4-6 Model - Electromagnetics - Electrode at distal end 53
Figure 4-7 Model - Electromagnetics - Double layer around electrode 53
Figure 4-8 Field sources $\varphi = 0$, phantom torso and location of Path EDS 55

Figure 4-9 Displacement of phantom torso in MRI bore 55
Figure 4-10 Full plane wave excitation scenario 57
Figure 4-11 Distal end excitation Locations of sources 58
Figure 4-12 Centre excitation Locations of sources 58
Figure 4-13 Proximity end excitation Locations of sources 58
Figure 4-14 Distal end excitation - reflections of waves 59
Figure 4-15 Centre excitation - reflections of waves 60
Figure 4-16 Proximity end excitation - reflections of waves 60
Figure 4-17 Equivalent wave port array 61
Figure 4-18 Equivalent dipole array 61
Figure 4-19 Magnitude of incident tangential electric field along Lead for a time-harmonic electric field of 1 V/m (peak) 61
Figure 4-20 Phase of incident tangential electric field along Lead for a time-harmonic electric field of 1 V/m (peak) 61
Figure 4-21 Electrodes with double layers at distal end 62
Figure 4-22 Transmit and Receive Wires 62
Figure 4-23 Transmit wires feeding Electrodes E01 and E02 62
Figure 4-24 Receive Wires from Electrodes E04 and E07 62
Figure 4-25 Transmit voltage of +1.0 Volt applied between E01 and E02 63
Figure 4-26 Transmit voltage of -1.0 Volt applied between E01 and E02 63
Figure 4-27 Transmit voltage of +1.0 / - 1.0 Volt applied between E01 and E02 63
Figure 4-28 Transmit voltage of -1.0 / + 1.0 Volt applied between E01 and E02 63
Figure 4-29 Surface mesh for saline 65
Figure 4-30 Volume mesh for saline 65
Figure 4-31 Surface mesh for saline around distal end 66
Figure 4-32 Volume mesh for saline around distal end 66
Figure 4-33 Volume mesh for electrodes 66
Figure 4-34 Volume mesh for wires 66
Figure 4-35 Surface mesh for isolator 66
Figure 4-36 Volume mesh for isolator 66
Figure 4-37 Thermodynamics - design parameter 67
Figure 4-38 Thermodynamics - design flow (adapted from [SW2] and [SW3]) 69
Figure 4-39 Volume with distal end and boundary conditions 70
Figure 4-40 Location of temperature sensors 70
Figure 4-41 Section view of typical mesh for thermodynamic simulations 72
Figure 4-42 Test and measurement setup for voltages and currents 74
Figure 4-43 Test and measurement setup for step function 75
Figure 4-44 Test and measurement setup for TDR 76
Figure 4-45 VNA with test fixture 77
Figure 4-46 Test fixture 77
Figure 4-47 S-parameter simulation setup 77

Figure 4-48 Outline of RF transfer function test bed with RF wave launcher and H-Probe(s) 79
Figure 4-49 RF transfer function test bed with VNA and H-Probe(s) 79
Figure 4-50 RF transfer function test bed with VNA, Spectrum Analyser and H-Probe(s) 79
Figure 4-51 Probe orientation for TEM Mode 80
Figure 4-52 Probe orientation for H Mode 80
Figure 4-53 Surface currents on detector probe for transfer function test bed without wave launcher; the detector probe captures RF signals from the surrounding air about 50 dB above the weakest RF signal at the distal end of the the MLC. 80
Figure 4-54 Transfer function test bed without RF wave launcher showing significant radiation into the surrounding air and a strong surface wave 81
Figure 4-55 RF wave launcher in phantom torso 81
Figure 4-56 Source probe in RF wave launcher 81
Figure 4-57 Transfer function test bed with RF wave launcher showing a significant reduction of radiation into the surrounding air and concentration of the propagating wave around the MLC 82
Figure 4-58 RF test bed connected to power amplification chain 83
Figure 4-59 Centre line between dipole rows 83
Figure 4-60 TS-1 - Dipole array verification 84
Figure 4-61 TS-2 - Amplitude and phase measurements along centre line between dipole rows 85
Figure 4-62 TS-3 - Power transfer measurements along centre line between dipole rows 85
Figure 4-63 TS-4 - Power deposition and temperature measurements (calibration) 86
Figure 4-64 TS-5 - Power deposition and temperature measurements (along Lead) 86
Figure 4-65 Single Dipole 87
Figure 4-66 Return loss of single dipole 88
Figure 4-67 Input impedance of single dipole 88
Figure 4-68 Dipole array with Lead placed along centre line 88
Figure 4-69 Co-linear dipole array in phantom torso 89
Figure 4-70 Return loss of dipole array 89
Figure 4-71 Input impedance of dipole array 89
Figure 4-72 4-way power splitter 90
Figure 4-73 Return loss of 4-way power divider 90
Figure 4-74 Insertion loss of 4-way power divider 90
Figure 4-75 Directional coupler 91
Figure 4-76 Return loss of directional coupler 91
Figure 4-77 Insertion loss of directional coupler 91
Figure 4-78 Probes and sensors 92
Figure 4-79 Temperature sensors at distal end of Lead 92

Figure 4-80 Test bed feed point power as function of signal generator output power 92
Figure 4-81 RF heating test bed 93
Figure 4-82 Dummy Lead with dummy electrodes 94
Figure 4-83 Dummy Lead location in RF test bed 94
Figure 4-84 Calibration Simulation - Temp. Transient 95
Figure 4-85 Calibration Simulation - Temp. Transient after 300 s 95
Figure 4-86 Calibration Measurement - Temp. Transient 96
Figure 4-87 Calibration Measurement - Temp. Transient after 300 s 96
Figure 4-88 Calibration Differences - Temp. Transient after 300 s 96
Figure 4-89 Outline of RF test bed with dipoles and E-probe 97
Figure 4-90 Total electric field and total tangential electric field 97
Figure 4-91 Magnitude of calculated total tangential electric field (red) and total electric field (blue) along centre line for 50 Watt input power per dipole 98
Figure 4-92 Total electric field and temperature increase along centre line between dipole rows for 50 Watt input power per dipole 98
Figure 4-93 Magnitude of measured and calculated tangential electric field 99
Figure 4-94 Phase of measured and calculated tangential electric field 100
Figure 4-95 Measured and calculated detected power along centre line for 1 Watt input power per dipole 100
Figure 4-96 Incident electric vector field of Source S1 for $Es, 1 = 1\,Vm \cdot ej0$ in plane yz 102
Figure 4-97 Incident electric vector field of Source S1 for $Es, 1 = 1\,Vm \cdot ej0$ - plane xz 102
Figure 4-98 Incident electric vector field of Source S2 for $Es, 2 = 1\,Vm \cdot ej0$ in plane yz 102
Figure 4-99 Incident electric vector field of Source S2 for $Es, 2 = 1\,Vm \cdot ej0$ in plane xz 102
Figure 4-100 Incident electric vector field of Source S1 for $Es, 1 = 1\,Vm \cdot ej0$ on phantom torso surface 103
Figure 4-101 Incident electric vector field of Source S2 for $Es, 2 = 1\,Vm \cdot ej0$ on phantom torso surface 103
Figure 4-102 Total electric field on horizontal top plane of phantom torso for $\varphi = 0$ 104
Figure 4-103 Total electric field on horizontal centre plane of phantom torso for $\varphi = 0$ 104
Figure 4-104 Total electric field on horizontal bottom plane of phantom torso for $\varphi = 0$ 104
Figure 4-105 Total electric field on vertical front plane of phantom torso for $\varphi = 0$ 104
Figure 4-106 Total electric field on vertical centre plane of phantom torso for $\varphi = 0$ 104
Figure 4-107 Total electric field on vertical back plane of phantom torso for $\varphi = 0$ 105

Figure 4-108 Peak total tangential electric field at centre of Path EDS Parameter y: vertical displacement of Path EDS from centre line in PT....106
Figure 4-109 Peak total tangential electric field at centre of Path EDS Parameter x: horizontal displacement of Path EDS from centre line in PT....106
Figure 4-110 Electric field in PT at iso-centre in horizontal x-z plane for $2.0\,Wkg$ A) Peak magnitude B) Vector plot....107
Figure 4-111 Electric field in PT at iso-centre in vertical x-y plane for $2.0\,Wkg$ A) Peak magnitude B) Vector plot....107
Figure 4-112 Electric field in PT at iso-centre in vertical y-z plane for $2.0\,Wkg$ A) Peak magnitude B) Vector plot....108
Figure 4-113 Electric field in PT in vertical y-z plane at 150 mm offset from iso-centre for $2.0\,Wkg$ A) Peak magnitude B) Vector plot....108
Figure 4-114 Test Setup #1 - E01 - E02 (st) and E04 - E07 (af)....111
Figure 4-115 Agilent Waveform Generator....112
Figure 4-116 Tektronix Oscilloscope....112
Figure 4-117 Oscilloscope Probes....112
Figure 4-118 CLS/eCLS Lead termination box (indicative only)....112
Figure 4-119 Pulse into resistive loads R = 50 Ω R $\rightarrow\ \infty$ (Open) R = 100 kΩ....113
Figure 4-120 Rise time (RT) and Fall Time (FT) for pulse into resistive load R $\rightarrow\ \infty$ (Open)....113
Figure 4-121 Rise time (RT) and Fall Time (FT) for pulse into E01 and E02 (R ~ 100 kΩ)....114
Figure 4-122 Compression point of ERT amplifier....114
Figure 4-123 Gain of ERT amplifier....114
Figure 4-124 Phase of ERT amplifier....114
Figure 4-125 Voltage drop with respect to BSRE....115
Figure 4-126 Voltage drop with respect to floating SGG....115
Figure 5-1 Surface current on platinum electrode....117
Figure 5-2 Cumulated surface current on platinum electrode for $Ex, z = 0 = 1Vm$....117
Figure 5-3 Cumulated phase shift of surface current on platinum electrode for $Ex, z = 0 = 1Vm$....117
Figure 5-4 Deionised water A) Relative permittivity B) Conductivity....120
Figure 5-5 Deionised water plus sodium chloride A) Relative permittivity B) Conductivity....120
Figure 5-6 Deionised water plus sodium chloride plus polyacrylic acid A) Relative permittivity B) Conductivity....120
Figure 5-7 Electrodes floating in layer of saline solution surrounded by gelled saline clots....121
Figure 5-8 Particle velocities in water and gelled saline solution (HEC)....122
Figure 5-9 Coaxial cable and dismantling lengths of outer conductor at distal end....123
Figure 5-10 TDR measurements results....124

Figure 5-11 Coaxial cable with dismantled distal end in gelled saline (the wave front travelling to the left via the outer conductor of the coaxial cable has been neglected) 126
Figure 5-12 Twelve wire MLC in saline and planar wave excitation 129
Figure 5-13 Offset from Wire W01 into saline 130
Figure 5-14 Cross-section of twelve wire MLC without BL 131
Figure 5-15 Cross-section of Wire W01 to Electrode E01 and path designation 131
Figure 5-16 Total transversal electric and magnetic field components for a MLC length of 600 mm; MLC without BL 133
Figure 5-17 Magnitude of total electric (red) and magnetic (blue) field for φ=0° along MLC; MLC without BL 134
Figure 5-18 Magnitude of total radial electric field between conductor surface and MLC surface at z = 220 mm; MLC without BL 135
Figure 5-19 Magnitude of total radial electric field from MLC surface into saline at z = 220 mm; MLC without BL 135
Figure 5-20 Magnitude of total angular magnetic field from MLC surface into saline at z = 300 mm; Parameter: distance from wire surface; MLC without BL 136
Figure 5-21 Magnitude of total surface current along MLC along conductor-isolator (red) and isolator-saline (blue) surface; MLC without BL 137
Figure 5-22 Magnitude of total surface current on Wire 01 around circumference along Lead; Parameter: location on wire perimeter; MLC without BL 138
Figure 5-23 Twelve wire MLC in saline and coaxial excitation 139
Figure 5-24 Coaxial wave ports and MLC 140
Figure 5-25 Reflection loss at Wave Port 1 as function of MLC length (no boundary layer) 141
Figure 5-26 Insertion loss between Wave Ports 1 and 2 as function of MLC length (no boundary layer) 141
Figure 5-27 Transversal electric and magnetic field components for MLC length of 600 mm (no boundary layer) 142
Figure 5-28 Magnitude of total electric and magnetic field for φ=0° along MLC (no boundary layer) 143
Figure 5-29 Magnitude of radial electric field between conductor surface and MLC surface at z = 300 mm 143
Figure 5-30 Magnitude of radial electric field from MLC surface into saline at z = 300 mm 144
Figure 5-31 Magnitude of total angular magnetic field from MLC surface into saline at z = 300 mm; Parameter: distance from wire surface; MLC without BL 145
Figure 5-32 Magnitude of total surface current along MLC on conductor-isolator (red) and isolator-saline (blue) surface; MLC without BL 145

Figure 5-33 Magnitude of total surface current on Wire 01 around circumference along MLC; Parameter: location on wire perimeter; MLC without BL 146
Figure 5-34 Attenuation for TEM Mode along 955 mm twelve wire MLC; Lead wires open ended and isolated from saline at distal end 148
Figure 5-35 Insertion phase for TEM Mode along 955 mm twelve wire MLC; Lead wires open ended and isolated from saline at distal end 148
Figure 5-36 Attenuation for H Mode along 955 mm twelve wire MLC; Lead wires open ended and isolated from saline at distal end 149
Figure 5-37 Insertion phase for H Mode along 955 mm twelve wire MLC; Lead wires open ended and isolated from saline at distal end 149
Figure 5-38 Attenuation for TEM Mode along 950 mm twelve wire MLC; Lead wires shorted in star point and immersed in gelled saline at distal 150
Figure 5-39 Insertion phase for TEM Mode along 950 mm twelve wire MLC; Lead wires shorted in star point and immersed in gelled saline at distal 150
Figure 5-40 Attenuation for H Mode along 950 mm twelve wire MLC; Lead wires shorted in star point and immersed in gelled saline at distal 151
Figure 5-41 Insertion phase for H Mode along 950 mm twelve wire MLC; Lead wires shorted in star point and immersed in gelled saline at distal 151
Figure 5-42 Calculated IL difference $\Delta IL = ILwith\ BL - ILwithout\ BL$ between Wave Ports 1 and 2 as function of MLC length 153
Figure 5-43 Magnitude of total electric and magnetic fields along 1200 mm long MLC for φ=0° predicted with EM Model #1 (without BL) 154
Figure 5-44 Magnitude of total electric and magnetic fields along 1200 mm long MLC for φ=0° predicted with EM Model #2 (with BL $(\varepsilon r{\sim}2.5; t{\sim}150\ \mu m)$) 154
Figure 5-45 Reflection loss at Wave Port 1 as function of Lead length including a boundary layer $(\varepsilon r{\sim}2.5; t{\sim}150\ \mu m)$ 155
Figure 5-46 Insertion loss between Wave Ports 1 and 2 as function of Lead length including a boundary layer $(\varepsilon r{\sim}2.5; t{\sim}150\ \mu m)$ 155
Figure 5-47 Single wave reflection at distal end $(r \approx 0.97 \cdot e + j34\pi)$ .. 156
Figure 5-48 Source probe in proximity to MLC 157
Figure 5-49 MLC embedded in electrolyte (saline) 157
Figure 5-50 Lorentz' law - sign conventions and vector fields 158
Figure 5-51 Motion of positive ions due to electric field at φ=130° on longitudinal cross-section at distal end 159

Figure 5-52 Motion of positive ions due to electric field at φ=310° on longitudinal cross-section at distal end 159
Figure 5-53 Motion of negative ions due to electric field at φ=130° on longitudinal cross-section at distal end 159
Figure 5-54 Motion of negative ions due to electric field at φ=310° on longitudinal cross-section at distal end 159
Figure 5-55 Motion of positive ions due to electric and magnetic fields at φ=90° on longitudinal cross-section at distal end 160
Figure 5-56 Motion of positive ions due to electric and magnetic field at φ=270° on longitudinal cross-section at distal end 160
Figure 5-57 Motion of negative ions due to electric and magnetic fields at φ=90° on longitudinal cross-section at distal end 160
Figure 5-58 Motion of negative ions due to electric and magnetic field at φ=270° on longitudinal cross-section at distal end 160
Figure 5-59 Constructive superposition of ionic dipole moments (purple arrows) due to circular motion of ions caused by electric and magnetic fields at φ=90° on transversal cross-section at distal end 161
Figure 5-60 Destructive superposition of ionic dipole moments (purple arrows) due to circular motion of ions caused by electric and magnetic fields at φ=90° on transversal cross-section at distal end 161
Figure 5-61 Twelve wire MLC with auxiliary electrode in gelled saline cube (including BL) for coaxial port excitation 163
Figure 5-62 Twelve wire MLC with auxiliary electrode in gelled saline cube (including BL) for planar wave excitation ... 163
Figure 5-63 Position and length of auxiliary electrode 163
Figure 5-64 Insertion loss difference between Wave Ports 1 and 2 as function of MLC length and a 3 mm long auxiliary electrode Case 1: C =100 pF and Case 2: C < 0.3 pF... 164
Figure 5-65 Insertion loss difference between Wave Ports 1 and 2 as function of auxiliary electrode length for a MLC length of 600 mm Case 1: $\sim 33\ pFmm$ and Case 2: $\sim 0.1\ pFmm$ 165
Figure 5-66 Return loss at Wave Port 1 as function of auxiliary electrode length for a MLC length of 600 mm Case 2: $\sim 0.1\ pFmm$ 166
Figure 5-67 Insertion loss between Wave Ports 1 and 2 as function of auxiliary electrode length for a MLC length of 600 mm Case 2: $\sim 0.1\ pFmm$ 167
Figure 5-68 Complex magnitude of electric field strength along Wire 01 as function of auxiliary electrode length for a MLC length of 600 mm Parameter: auxiliary electrode length 168

Figure 5-69 Complex magnitude of magnetic field strength along Wire 01 as function of auxiliary electrode length for a MLC length of 600 mm Parameter: auxiliary electrode length 168
Figure 5-70 Twelve wire MLC in saline with integration paths 169
Figure 5-71 UM03 - Transversal electric field components for Lead length of 600 mm 172
Figure 5-72 UM03 - Equivalent differential electric field strength between Lead wires at 128 MHz for a Lead length of 600 mm 173
Figure 5-73 UM03 - magnitude of total radial electric field at 128 MHz for a Lead length of 600 mm Red curve: from centre of Electrode E01 into gelled saline Blue curve: from centre between Electrodes E01 and E02 into gelled saline 174
Figure 5-74 Conductivity: $0\ Sm$ 176
Figure 5-75 Conductivity: $0\ Sm$ 176
Figure 5-76 Conductivity: $1\ Sm$ 176
Figure 5-77 Conductivity: $10\ Sm$ 176
Figure 5-78 Conductivity: $100\ Sm$ 176
Figure 5-79 Conductivity: $1\prime 000\ Sm$ 176
Figure 5-80 Conductivity: $10\prime 000\ Sm$ 176
Figure 5-81 Conductivity: $100\prime 000\ Sm$ 176
Figure 5-82 Conductivity: $1\prime 000\prime 000\ Sm$ 177
Figure 5-83 Conductivity: $10\prime 000\prime 000\ Sm$ 177
Figure 5-84 Maximum electric field strength at distal end electrode E01 as function of Lead wire conductivity 177
Figure 5-85 Surface roughness correction factors as function of $\Delta rms\delta$ 179
Figure 5-86 RMS surface roughness Δrms at 128 MHz as function of square cannonball surface roughness correction factor 179
Figure 5-87 Insertion loss of micro-coaxial transmission line at 128 MHz Parameter: cannonball surface roughness correction factor 180
Figure 5-88 Relative permittivity: 1 182
Figure 5-89 Relative permittivity: 3.16 182
Figure 5-90 Relative permittivity: 10 182
Figure 5-91 Relative permittivity: 31.6 182
Figure 5-92 Relative permittivity: 100 182
Figure 5-93 Relative permittivity: 316 182
Figure 5-94 Relative permittivity: 1000 183
Figure 5-95 Maximum electric field strength at distal end electrode E01 as function of relative permittivity of the MLC 183
Figure 5-96 Loss factor: 0.0001 184
Figure 5-97 Loss factor: 0.001 184
Figure 5-98 Loss factor: 0.01 184

Figure 5-99 Loss factor: 0.1 184
Figure 5-100 Loss factor: 1.0 184
Figure 5-101 Loss factor: 10.0 184
Figure 5-102 Loss factor: 100 185
Figure 5-103 Loss factor: 1000 185
Figure 5-104 Maximum electric field strength at distal end electrode E01 as function of MLC loss factor 185
Figure 5-105 UM01 (wires open ended in IPG header) - electric fields for solid electrodes 188
Figure 5-106 UM02 (wires shorted to IPG in header) - electric fields for solid electrodes 188
Figure 5-107 Helical electrode 189
Figure 5-108 DV00 (wires open ended in IPG header) - electric fields for coiled electrodes 190
Figure 5-109 DV0A (wires connected to IPG case) - electric fields for coiled electrodes 190
Figure 5-110 Coupling to auxiliary wires 191
Figure 5-111 DV11 - electric field for twelve additional auxiliary wires 191
Figure 5-112 DV08 - Auxiliary electrode 192
Figure 5-113 DV08 - Auxiliary electrodes interleaved with therapeutic electrodes 192
Figure 5-114 DV08 - Lead wires grounded at IPG 192
Figure 5-115 DV08 - Magnitude of electric field 193
Figure 5-116 Multi-lumen cross-section and wire routing (looking from distal towards proximity end) 194
Figure 5-117 Cross-section of Wire W01 to Electrode E01 and path designation for surface currents (looking from proximity towards distal end) 194
Figure 5-118 DV07B - electric field distribution for twelve therapeutic electrodes 195
Figure 5-119 DV07B - electric field distribution for eight therapeutic electrodes 195
Figure 5-120 DV07B - electric field distribution for four therapeutic electrodes 195
Figure 5-121 DV07B - electric field distribution for two therapeutic electrodes 196
Figure 5-122 DV07B - electric field distribution for one therapeutic electrode 196
Figure 5-123 UM01 - electric field distribution for one therapeutic electrode but without auxiliary electrodes (for comparison) 196
Figure 5-124 DV07B - surface currents on Wire 01 for eight therapeutic electrodes and nine auxiliary electrodes 198
Figure 5-125 DV07B - surface currents on Wire 01 for one therapeutic electrode and two auxiliary electrodes 198
Figure 5-126 Detected anomalies in multi-lumen sections 199
Figure 5-127 Wire positions A) UM02 B) DV16 C) DV17 200

Figure 5-128 UM02 - electric fields along Lead - (CW 1 2 3 4 5 6 7 8 9 10 11 12) 201
Figure 5-129 DV16 - electric fields along Lead - (CW 1 11 8 3 7 9 2 10 5 4 6 12) 202
Figure 5-130 DV17 - electric fields along Lead - (CW 1 2 4 6 8 10 12 11 9 7 5 3) 202
Figure 5-131 Capacitive coupled auxiliary electrodes at proximity end A) DV08C1 - long auxiliary electrodes B) DV08C2 - short auxiliary electrodes 203
Figure 5-132 DV08H1 A) Short capacitive coupled auxiliary electrodes at proximity end B) Distal end extension 204
Figure 5-133 DV08C0 - electric field at distal end for Lead length of 600 mm without Lead extension (for comparison)..... 205
Figure 5-134 DV08H1 - electric field at distal end for Lead length of 600 mm and Lead extensions between 10 mm and 50 mm 205
Figure 5-135 DV08H2 and DV08H3 A) Lead wires capacitive coupled to ring of resistors at proximity end B) Distal end extension with $L = 10\,mm$ 206
Figure 5-136 Electric field at distal end for a Lead length of 600 mm A) DV08H2 (100 Ohm resistors) B) DV08H3 (30 Ohm resistors)..... 207
Figure 5-137 Differential voltage between Lead wires A) UM03 (wires grounded to IPG case) B) DV08H2 (100 Ohm resistors) C) DV08H3 (30 Ohm resistors)..... 208
Figure 5-138 DV07A - Therapeutic and auxiliary electrodes..... 209
Figure 5-139 DV07A - Auxiliary electrode 209
Figure 5-140 DV07A - Lead wires open ended in IPG header..... 209
Figure 5-141 DV07A - frequency dependence of maximum electric field at distal end electrode E01 for Lead length of 200 mm 210
Figure 5-142 Lead (200 mm) and IPG position in RF test bed..... 212
Figure 5-143 Lead (600 mm) and IPG position in RF test bed for distal end RF exposure..... 212
Figure 5-144 Lead (600 mm) and IPG position in RF test bed for centred RF exposure 212
Figure 5-145 Lead (600 mm) and IPG position in RF test bed for proximity end RF exposure..... 212
Figure 5-146 UM01 - IPG and Lead without Lead wires..... 213
Figure 5-147 Therapeutic electrodes without Lead wires..... 213
Figure 5-148 Magnitude of electric field along Lead (200 mm) without Lead wires..... 213
Figure 5-149 Steady state temperature increase for electrodes without Lead wires..... 214
Figure 5-150 UM03 - wires shorted to IPG case..... 216
Figure 5-151 UM03 - electrode numbering 216
Figure 5-152 UM03 - 200 mm - short - complex magnitude of electric field at distal end..... 216

Figure 5-153 UM03 - 200 mm - short Simulation - Temp. Transient....217
Figure 5-154 UM03 - 200 mm - short Simulation - Temp. after 300 s..217
Figure 5-155 UM03 - 200 mm - short Measurement - Temp. Transient....217
Figure 5-156 UM03 - 200 mm - short Measurement - Temp. after 300 s....217
Figure 5-157 UM03 - 200 mm - short Difference - Temp. after 300 s..218
Figure 5-158 UM03 - wires shorted to IPG case....219
Figure 5-159 UM03 - electrode numbering....219
Figure 5-160 UM03 - 600 mm - short - complex magnitude of electric field at distal end....219
Figure 5-161 UM03 - 600 mm - short Simulation - Temp. Transient....220
Figure 5-162 UM03 - 600 mm - short Simulation - Temp. after 300 s..220
Figure 5-163 UM03 - 600 mm - short Measurement - Temp. Transient....220
Figure 5-164 UM03 - 600 mm - short Measurement - Temp. after 300 s....220
Figure 5-165 UM03 - 600 mm - short Difference - Temp. after 300 s..220
Figure 5-166 UM04 - wires open-ended in IPG case....222
Figure 5-167 UM04 - electrode numbering....222
Figure 5-168 UM04 - 200 mm - open - complex magnitude of electric field at distal end....222
Figure 5-169 UM04 - 200 mm - open Simulation - Temp. Transient....223
Figure 5-170 UM04 - 200 mm - open Simulation - Temp. after 300 s..223
Figure 5-171 UM04 - 200 mm - open Measurement - Temp. Transient....223
Figure 5-172 UM04 - 200 mm - open Measurement - Temp. after 300 s....223
Figure 5-173 UM04 - 200 mm - open Difference - Temp. after 300 s..223
Figure 5-174 UM04 - wires open-ended in IPG case....225
Figure 5-175 UM04 - electrode numbering....225
Figure 5-176 UM04 - 600 mm - open - complex magnitude of electric field at distal end....225
Figure 5-177 UM04 - 600 mm - open Simulation - Temp. Transient....226
Figure 5-178 UM04 - 600 mm - open Simulation - Temp. after 300 s..226
Figure 5-179 UM04 - 600 mm - open Measurement - Temp. Transient....226
Figure 5-180 UM04 - 600 mm - open Measurement - Temp. after 300 s....226
Figure 5-181 UM04 - 600 mm - open Difference - Temp. after 300 s..226
Figure 5-182 Comparison of measured temperature patterns for investigated configurations....228
Figure 5-183 Comparison of simulation data....229
Figure 5-184 DV08B - wires shorted to IPG case....230
Figure 5-185 DV08B - outline - distal end....230
Figure 5-186 DV08B - Lead at distal end....230
Figure 5-187 DV08B - 200 mm - short - complex magnitude of el. field at distal end....231

Figure 5-188 DV08B - 200 mm - short Simulation - Temp. Transient ..231
Figure 5-189 DV08B - 200 mm - short Simulation - Temp. after 300 s 231
Figure 5-190 DV08B - 200 mm - short Measurement - Temp. Transient..... 231
Figure 5-191 DV08B - 200 mm - short Measurement - Temp. after 300 s 231
Figure 5-192 DV08B - 200 mm - short Difference - Temp. after 300 s 232
Figure 5-193 Comparison between measured temperature increases after after 300 s A) UM03 for 200 mm (without auxiliary electrodes) B) DV08B for 200 mm (with auxiliary electrodes) 232
Figure 5-194 DV08B - 600 mm - short - complex magnitude of el. field at distal end 233
Figure 5-195 DV08B - 600 mm - short Simulation - Temp. Transient ..233
Figure 5-196 DV08B - 600 mm - short Simulation - Temp. after 300 s 233
Figure 5-197 DV08B - 600 mm - short Measurement - Temp. Transient..... 234
Figure 5-198 DV08B - 600 mm - short Measurement - Temp. after 300 s 234
Figure 5-199 DV08B - 600 mm - short Difference - Temp. after 300 s 234
Figure 5-200 Comparison between difference patterns after 300 s A) UM03 for 600 mm (without auxiliary electrodes) B) DV08B for 600 mm (with auxiliary electrodes) 235
Figure 5-201 Comparison between measured temperature increases after 300 s A) UM03 for 600 mm (without auxiliary electrodes) B) DV08B for 600 mm (with auxiliary electrodes) 235
Figure 5-202 DV08B - comparison between measurement and simulation data 237
Figure 5-203 DV08C1 - auxiliary electrodes capacitive coupled to saline at proximity end 239
Figure 5-204 DV08C1 - outline - distal end 239
Figure 5-205 DV08C1 - 600 mm - complex magnitude of el. field at distal end 240
Figure 5-206 DV08C1 - 600 mm Simulation - Temp. Transient 240
Figure 5-207 DV08C1 - 600 mm Simulation - Temp. after 300 s 240
Figure 5-208 DV08C1 - 600 mm Measurement - Temp. Transient..... 240
Figure 5-209 DV08C1 - 600 mm Measurement - Temp. after 300 s..... 240
Figure 5-210 DV08C1 - 600 mm Difference - Temp. after 300 s 241
Figure 5-211 Comparison between measured temperature increases after 300 s A) DV08B for 600 mm (without auxiliary electrodes at proximity end) B) DV08C1 for 600 mm (with auxiliary electrodes at proximity end) 241

Figure 5-212 Comparison between difference patterns after 300 s A) DV08B for 600 mm (without auxiliary electrodes at proximity end) B) DV08C1 for 600 mm (with auxiliary electrodes at proximity end) 242
Figure 5-213 DV08C2 - auxiliary electrodes capacitive coupled to saline at proximity end 243
Figure 5-214 DV08C2 - outline - distal end 243
Figure 5-215 DV08C2 - 600 mm - complex magnitude of el. field at distal end 244
Figure 5-216 DV08C2 - 600 mm Simulation - Temp. Transient 244
Figure 5-217 DV08C2 - 600 mm Simulation - Temp. after 300 s 244
Figure 5-218 DV08C2 - 600 mm Measurement - Temp. Transient 244
Figure 5-219 DV08C2 - 600 mm Measurement - Temp. after 300 s 244
Figure 5-220 DV08C2 - 600 mm Difference - Temp. after 300 s 245
Figure 5-221 Comparison between measured temperature increases after 300 s A) DV08C1 for 600 mm (with 5.0 mm aux. electrodes at proximity end) B) DV08C2 for 600 mm (with 2.5 mm aux. electrodes at proximity end) 245
Figure 5-222 Comparison between difference patterns after 300 s A) DV08C1 for 600 mm (with 5.0 mm aux. electrodes at proximity end) B) DV08C2 for 600 mm (with 2.5 mm aux. electrodes at proximity end) 246
Figure 5-223 DV08C3 - Lead wires capacitive coupled to ring of resistors at proximity end 247
Figure 5-224 DV08C3 - outline - distal end 247
Figure 5-225 DV08C3 - 600 mm - complex magnitude of el. field at distal end 248
Figure 5-226 DV08C3 - 600 mm Simulation - Temp. Transient 248
Figure 5-227 DV08C3 - 600 mm Simulation - Temp. after 300 s 248
Figure 5-228 DV0C3 - 600 mm Measurement - Temp. Transient 248
Figure 5-229 DV0C3 - 600 mm Measurement - Temp. after 300 s 248
Figure 5-230 DV08C3 - 600 mm Difference - Temp. after 300 s 249
Figure 5-231 Comparison between measured temperature increases after 300 s A) DV08C2 for 600 mm (with 2.5 mm aux. electrodes at proximity end) B) DV08C3 for 600 mm (with 100 Ohm resistor ring at proximity end) 249
Figure 5-232 DV08D1 - Lead wires capacitive coupled to ring of resistors at IPG case 250
Figure 5-233 DV08D1 - outline - distal end 250
Figure 5-234 DV08D1 - Lead at distal end 250
Figure 5-235 DV08D1 - 600 mm - complex magnitude of el. field at distal end 251
Figure 5-236 DV08D1 - 600 mm Simulation - Temp. Transient 251
Figure 5-237 DV08D1 - 600 mm Simulation - Temp. after 300 s 251
Figure 5-238 DV0D1 - 600 mm Measurement - Temp. Transient Therapeutic electrodes 251
Figure 5-239 DV0D1 - 600 mm Measurement - Temp. Therapeutic Electrodes after 300 s 251

Figure 5-240 DV0D1 - 600 mm Measurement - Temp. Transient Auxiliary electrodes 252
Figure 5-241 DV0D1 - 600 mm Measurement - Temp. Auxiliary Electrodes after 300 s 252
Figure 5-242 DV08D1 - 600 mm Difference - Temp. after 300 s 252
Figure 5-243 Comparison between measured temperature increases after 300 s A) DV08C3 for 600 mm (100 Ohm) B) DV08D1 for 600 mm (100 Ohm; 12 additional aux. electrodes) 253
Figure 5-244 Comparison of measured temperature increases after 300 s A) DV08C1 for 600 mm (with 5.0 mm aux. electrodes at proximity end) B) DV08C2 for 600 mm (with 2.5 mm aux. electrodes at proximity end) C) DV08C3 for 600 mm (with 100 Ohm resistor ring at proximity end) D) DV08D1 for 600 mm (100 Ohm; 12 additional aux. electrodes) 254
Figure 5-245 Comparison of simulated temperature increases after 300 s A) DV08C1 for 600 mm (with 5.0 mm aux. electrodes at proximity end) B) DV08C2 for 600 mm (with 2.5 mm aux. electrodes at proximity end) C) DV08C3 for 600 mm (with 100 Ohm resistor ring at proximity end) D) DV08D1 for 600 mm (100 Ohm; 12 additional aux. electrodes) 255
Figure 5-246 DV08LX - Outline - IPG and Lead 258
Figure 5-247 DV08LX - Lead wires capacitive coupled to ring of resistors in IPG header 259
Figure 5-248 DV08LX - outline - distal end 259
Figure 5-249 DV08LX - outline - length extension 259
Figure 5-250 DV08LX - outline - auxiliary electrodes 259
Figure 5-251 DV08LX - outline - auxiliary electrode numbering 259
Figure 5-252 DV08L3_10_DEE - 600 mm - complex magnitude of el. field along Lead 260
Figure 5-253 DV08L3_10_DEE - 600 mm Simulation - Temp. Transient 260
Figure 5-254 DV08L3_10_DEE - 600 mm Simulation - Temp. after 300 s 260
Figure 5-255 DV08L3_10_DEE Measurement - Temp. Transient 260
Figure 5-256 DV08L3_10_DEE Measurement - Temp. after 300 s 260
Figure 5-257 DV08L3_10_DEE Difference - Temp. after 300 s 261
Figure 5-258 Comparison of measured temperature increases after 300 s A) DV08L3_50_DEE (50 mm Lead extension) B) DV08L3_30_DEE (30 mm Lead extension) C) DV08L3_10_DEE (10 mm Lead extension) 262
Figure 5-259 Comparison of measured temperature increases after 300 s A) DV08L3_10_DEE (distal end excitation) B) DV08L3_10_CEE (centre excitation) C) DV08L3_10_PEE (proximity end excitation) 263
Figure 5-260 General Electric 3 Tesla Horizontal Field Scanner 264

Figure 5-261 Phantom torso with IPG, Lead and temperature sensors 264
Figure 5-262 Position of temperature sensors on electrodes E01 and E02 264
Figure 5-263 Position of IPG and Leads in PT and 3T MRI scanner 265
Figure 5-264 DV08L3_10_XXX - envelope of maximum recorded temperature increase 266
Figure 5-265 DV08L3_10_XXX - temperature increase after 900 s for all electrodes 266
Figure 5-266 Superposition of IPG and Lead on Hugo Human Body Model at $f = 128\ MHz$ and $BRF, rms = 2.1\ \mu T$; colour coding of the electric field is for rms electric field strengths 267
Figure 5-267 Electric field distribution at 128 MHz along a 200 mm MLC terminated with Electrode E01 for a normalised incident electric field according to Figure 4-93 (magnetic dipole; $\pm\ 100\ mm$) 269
Figure 5-268 Electric field distribution at 128 MHz along a 600 mm MLC terminated with Electrode E01 for a normalised incident electric field according to Figure 4-93 (magnetic dipole; $+\ 100\ mm - 200\ mm$) 269
Figure 5-269 Total electric field along line radially pointing from the centre of the distal end electrode surface into saline solution for an incident axio-lateral electric field of $1\ Vm$ 271
Figure 5-270 Perfusion rate in gelled saline as function of EM wave intensity 273
Figure 5-271 Calculated temperature rise at Electrode E01 for four base cases 273
Figure 5-272 Current vs. voltage after 8 seconds 276
Figure 5-273 DC resistance after 8 seconds 276
Figure 5-274 Small signal RF resistance after 8 seconds 277
Figure 5-275 Current vs. time for constant voltage 278
Figure 5-276 Simplified equivalent circuit diagram with three time constants 279
Figure 5-277 Voltage drop over resistance $RV1 = 7.2\ Ohm$ caused by step function of $+4V$ into Electrode E02 with return path via Electrode E01 280
Figure 5-278 Electric field magnitude for bipolar stimulus of 4 VDC between E01 and E02 281
Figure 5-279 Magnetic field magnitude for bipolar stimulus of 4 VDC between E01 and E02 281
Figure 5-280 Decrease of electric field magnitude into gelled saline at E01 for bipolar stimulus of 4 VDC between E01 and E02 282
Figure 5-281 Decrease of magnetic field magnitude into gelled saline at E01 (red curve) and half way between E01

and E02 (blue curve) for bipolar stimulus of 4 VDC between E01 and E02 282
Figure 5-282 Monophasic positive pulse pattern for $\tau = 5\ ms$ and $T = 10\ ms$ 283
Figure 5-283 Measured artefacts between Electrodes E04 and E07 as function of resistance RV2 caused by a positive bipolar monophasic input pulse between Electrodes E01 and E02 (see Figure 4-114)..... 283
Figure 5-284 Calculated artefacts between Electrodes E04 and E07 as function of resistance RV2 caused by a positive bipolar monophasic input pulse between Electrodes E01 and E02 (see Figure 4-23 and Figure 4-24); Parameter: $Rdl = 10.1\ k\Omega\ and\ Cdl = 2.5\ \mu F$ 284
Figure 5-285 Monophasic negative pulse pattern for $\tau = 250\ \mu s$ and $T = 1\ ms$ 285
Figure 5-286 Artefacts between Electrodes E04 and E07 as function of resistance RV2 caused by a negative bipolar monophasic input pulse of 1 V between Electrodes E01 and E02 A) Full pulse B) Zoom into tail of pulse 285
Figure 5-287 Calculated artefacts between Electrodes E04 and E07 as function of resistance RV2 caused by a negative bipolar monophasic input pulse of 1 V between Electrodes E01 and E02 (see Figure 4-23 and Figure 4-24); Parameter: $Rdl = 10.1\ k\Omega\ and\ Cdl = 2.5\ \mu F$ A) Full pulse B) Zoom into tail of pulse 286
Figure 5-288 Biphasic pulse pattern for $\tau = 250\ \mu s$ and $T = 4\ ms$ 287
Figure 5-289 Currents caused by a bipolar biphasic pulse pattern of ± 2 V between Electrodes E01 and E02 A) Measured current through resistance $RV1 = 5\ Ohm$ B) Calculated current through Wires W01 and W02; Parameter: $Rdl = 105\ \Omega\ and\ Cdl = 2.5\ \mu F$ 288
Figure 5-290 Artefacts between Electrodes E04 and E07 caused by a bipolar biphasic pulse pattern of ± 2 V between Electrodes E01 and E02 A) Measured B) Calculated; Parameter: $Rdl = 105\ \Omega\ and\ Cdl = 2.5\ \mu F$ 289
Figure 5-291 Zoom into artefacts between Electrodes E04 and E07 caused by a bipolar biphasic pulse pattern of ± 2 V between Electrodes E01 and E02 A) Measured B) Calculated; Parameter: $Rdl = 105\ \Omega\ and\ Cdl = 2.5\ \mu F$ .. 290

Figure A-1 Normalised dampened field magnitude (platinum)..... 322
Figure A-2 Normalised un-dampened field magnitude (platinum)..... 322
Figure A-3 Normalised field magnitude (Pellethane, period not to scale)..... 323
Figure A-4 Normalised field magnitude (gelled saline)..... 325
Figure A-5 Normalised un-dampened field magnitude (gelled saline) .. 325

Figure C-1 Coordinate system 329
Figure C-2 Field components 329
Figure C-3 Schematic of coaxial test fixture 331
Figure C-4 Dimensions of coaxial cavity 331
Figure C-5 Equivalent transmission line circuit of coaxial test fixture ... 331
Figure C-6 Transmission line with reflections at both ends 336

Figure D-1 Outline of solution domain 345

All thoughts have already been thought and all ideas have already been explored but putting thoughts and ideas into action are a truly difficult thing.

Inspired by Johann Wolfgang von Goethe

1. Introduction

This work uses electromagnetic and thermodynamic modelling to investigate two aspects of implanted Spinal Cord Stimulators (SCS); safeness of stimulators during Magnetic Resonance Imaging (MRI) scans and the impact of electrical stimuli pattern on artefacts that inhibit the recording of neural responses during and after stimulus.

Previous work in this field has focused primarily on single electrode stimulators. The first aim of this work is to conceive an electromagnetic and thermodynamic model that characterises a multi-electrode Lead, composed of a multi-lumen conduct (MLC) and embedded Lead wires, and an Implanted Pulse Generator (IPG). The second aim is to use this model to analyse new concepts to minimise tissue heating during MRI scans and to analyse concepts to minimise artefacts on recording electrodes. The third aim is to build three RF test beds; an RF test bed that generates RF fields equivalent to the RF fields generated in 3 Tesla MRI scanners, an RF test bed that allows to measure EM wave propagation along Leads, and an RF test bed that allows to extract material properties of electrolytes. The test beds serve to compare simulation results with measurement results. The fourth aim is to refine the models by comparing measurement results with simulation results.

The work relies on and crosses several domains of expertise; such as electromagnetics, thermodynamics and interface dynamics. In addition to normal operating conditions inside a human body, SCS are exposed to strong electromagnetic fields during MRI scans. The state of the art in the domains that are relevant to this work are summarised in Chapter 2. Readers who are familiar with those domains can skip this chapter.

The test specimen in this work is a spinal cord stimulator, composed of Lead and IPG, provided by Saluda Medical. Parts of the original spinal cord stimulator have been modified throughout this work to verify the impact of design modifications on MRI safeness.

Chapter 3 describes and characterises the base cases, i.e. the original spinal cord stimulator configurations, and design variations, i.e. modifications applied to the original spinal cord stimulator. Base cases and design variations have been been modelled and measured.

A large part of the analysis has been conducted using Finite Element Methods (FEM) to solve the system of governing differential equations describing electromagnetic and thermodynamic effects. Simulation results have been benchmarked against measurements. For this purpose, a table-top RF test bed for RF induced heating, a test bed to determine propagation constants along Leads, and a test fixture to determine material properties of electrolytes have been conceived and realised. Other test beds have been adapted for specific measurement purposes, such as DC, transient, Time Domain Reflectometry (TDR), pulse pattern and artefact measurements.

Chapter 4 describes the modelling approach for time-harmonic and transient stimuli (Section 4.1), the modelling approach for heat transfer (Section 4.2), and the test beds (Section 4.3).

The bulk of simulation and measurement results are presented in Chapter 5. This chapter is divided into two main sections. Section 5.1 presents the results for MRI safeness. This includes surface currents on platinum electrodes, permittivities and conductivities of electrolytes, propagation velocities along isolated coaxial filars, EM wave propagation along multi-lumen conducts and Leads, impact of Lead material

parameters and design variations on electric field distributions at distal end electrodes, and the impact of design variations on temperature increase at distal end electrodes. Section 5.2 summarises the results for electric stimuli induced artefacts. This includes measurements of voltages, currents and resistances between adjacent electrodes, transient responses of electrodes immersed in electrolytes, and artefacts generated by electrodes immersed in electrolytes.

Chapter 6 consolidates results and provides an outlook for further research work.

The appendices summarise information about properties of matter, MRI scanner parameters, set of equations derived for electromagnetic and thermodynamic modelling, and source codes.

2. Background

2.1 Overview

This work relies on several domains. The following sections provide an overview. In Section 2.2 the origins of pain are briefly addressed and Section 2.3 summarises spinal cord stimulation (SCS) techniques and adverse effects of neural stimulation. Section 2.4 reviews the fundamentals of Magnetic Resonance Imaging (MRI), the causes of tissue heating, summarises misconceptions, and outlines criteria for MRI safeness assessment of Implanted Medical Devices (IMDs). Section 2.5 recapitulates the fundamentals of electromagnetic wave theory and Section 2.6 outlines electromagnetic wave propagation along Leads. Characteristics of electrolytes are described in Section 2.7 and electrode potentials and current densities through electrode surfaces are highlighted in Section 2.8. Interface dynamics between Implanted Medical Devices (IMDs) and tissue are addressed in Section 2.9. Finally, heat transfer mechanisms in human tissue are outlined in Section 2.10. Readers who are familiar with these domains can proceed with Chapter 3.

2.2 Origins of pain

Pain manifests in different guises and causes of pain have been analysed and synthesised in theoretical frameworks for centuries. A working definition of pain has been postulated by the International Association for the Study of Pain (IASP) in 1986 as follows [P152]:

"... an unpleasant sensory and emotional experience associated with actual or potential tissue damage, or described in terms of tissue damage, or both ..."

Depending on the location and causes of pain several types of pain can be distinguished. A short overview is presented in Reference [IN1]. Electrical neuromodulation such as deep brain and spinal cord stimulation tries to mediate the effects of neuropathic pain. The origins of pain, the mechanisms of pain transmission, and appropriate measures for pain relief are still an area of controversial debate and ongoing intensive research. Melzack and Wall [P151] laid out pain perception mechanisms in their seminal paper about gate control theory in 1965. Gate control theory developed out of inconsistencies discovered in specificity theory, intensity theory and pattern theory [P151]. Dominant pain pathways and endogenous pain inhibition mechanisms are summarised in Reference [B7].

2.3 Spinal Cord Stimulation

Spinal Cord Stimulation (SCS) is a technique used to reduce pain sensations of patients with chronic pain by means of electric stimuli. Pain signals originate either from lesions of sensory neurons or from permanent stimulus of "pain sensors" distributed throughout the human body. Following Melzack's and Wall's hypotheses [P151], Wall and Sweet applied electrical stimulus via needle electrodes to eight patients who reported pain relief during and after electric stimulus [P130]. Shortly after, Shealy reported results obtained from electrically stimulating dorsal column segments in cats [P127] and later on results from electrically stimulating the dorsal column of a patient with chronic pain [P128]. In all cases, significant pain relief has been observed. These promising results have initiated the systematic analysis of spinal cord stimulation techniques. Today, spinal cord stimulation (SCS) is frequently applied to relief patients from pain caused by chronic diseases or injuries, such as Cancer Pain (CP), Complex Regional Pain Syndrome (CRPS), Critical Limb Ischaemic (CLI), Failed Back Surgery Syndrome (FBSS), Headache (HA),

Ischaemic Pain Conditions (IPC), Painful Diabetic Neuropathy (PDA), Peripheral Arterial Disease (PAD), Phantom Limb Pain (PLP), Refractory Angina Pectoris (RAP), and Visceral Pain (VP).

Spinal Cord Stimulation (SCS) techniques interact with neurons to suppress pain signals transmitted from pain sensors via sensory nerve fibres towards the brain. Neurons are the cells that receive, process, and transmit information. Neuron types are described in Reference [B8]. Stimulation techniques are described in References [B4] and [B5] and safe protocols are summarised in References [P56] and [P59]. However, the exact mechanism of how electrical stimulation of spinal cord segments works is not fully understood, today. The following explanations try to shed light onto the mechanisms; (1) during axonal stimulation electrical potentials and/or currents around stimulating electrodes activate or block the propagation of action potentials along axons, (2) during presynaptic stimulation electrical potentials and/or currents around electrodes inhibit or excite the release of neurotransmitters, and (3) during postsynaptic stimulation electrical potentials and/or currents around electrodes inhibit or excite action potentials either by (a) facilitating or impeding the attachment of neurotransmitters to receptors and therefore influencing the opening or closing of ion channels or (b) depolarising or hyperpolarising axon hillocks and therefore initiating or inhibiting the launch of action potentials.

Axons (or nerve fibres) are central and peripheral processes emerging from cell bodies and are the signal transmission lines in the human central and peripheral nervous system carrying information in form of propagating electrical signals [B8]. These signals are called Action Potentials (AP). Electrical signals propagating along several co-located axons are called Evoked Compound Action Potentials (ECAP). An action potential (AP) is a change in membrane resting potential caused by an inflow of ions into the cell or an outflow of ions out of the cell due to an external stimulus ([B5],

[P3], [P4]). Models for excitable cells are found in Reference [P105]. The duration of an AP, i.e. the time span from a change in nominal cell potential back to nominal cell potential is different for different cell types and described in [B2]. The role of gated ion channels during cell depolarisation is outlined in Reference [B2]. The duration between depolarisation peaks and hyperpolarisation troughs of APs in neural cells differ depending on the type of neuron and is presented in Reference [P125]. Maximum repetition rates (or repetition frequencies) for APs in neural networks can vary depending on neuron types. Repetition rates are described in Reference [P126]. However, average neural firing rates (or firing frequencies) on neural networks are much lower and conservative estimates range from 0.1 Hz to 100 Hz [P126]. Waveform shapes of action potentials are monostable, bistable or oscillating. Propagation of action potentials along sections of unmyelinated axons is called continuous propagation whereas propagation of action potentials along sections of myelinated (i.e. partially shielded or insulated) axons is called saltatory propagation. Both, continuous and saltatory propagation can mathematically be described by nonlinear parabolic differential reaction-diffusion equations ([B19], [P26], [P33]).

Most SCS operate on the assumption that electric stimulation of first order touch and proprioception neurons in the DC (Aα and Aβ fibres) generates antidromic APs that inhibit the generation of APs on second order nociception neurons in the dorsal horn of the corresponding spinal cord segment (Aδ and C fibres) ([B4]).

Leads are implanted in the epidural space of the spinal cord under epidural anaesthesia ([P169]) and fluoroscopic guidance. For Leads with small cylindrical electrodes a minimally invasive percutaneous needle technique and for Leads with paddle electrodes open surgical exposure techniques (laminotomy or laminectomy) are applied. The battery powered pulse generator (IPG) is implanted in the buttock or abdominal

wall. A handheld controller that communicates over a short distance wireless link allows patients to control stimulus patterns generated by the IPG.

Electrodes for neural stimulation of dorsomedial and dorsolateral spinal cord nerve fibres are located in the epidural space, too. The epidural space is the area between the dura mater and the vertebral wall, containing lymphatics, spinal nerve roots, lose connective tissue, fatty tissue, small arteries and vertebral venous plexuses ([P168]). The epidural space is located outside the dural sac which is filled with cerebrospinal fluid (CSF). The human tissue surrounding distal end electrodes has strong electrolytic characteristics and has been systematically analysed and described in Reference [P101]. Tissue parameters relevant to electromagnetic and thermodynamic modelling are summarised in Appendix A.1. Morphometrics of the spinal vertebra and spinal cord are given in References [P120], [P170], [P171], and [P174]. Electrode configuration and size determine together with applied potentials and injected current densities the domain of influence of stimuli, i.e. the dorsolateral spreading and depth of penetration into subarachnoid space and superficial dorsal column ([P121], [P122]). Excessive pressure caused by electrodes next to nerve fibres can cause local paraesthesia or permanent nerve fibre lesions [P119]. Transmission and reception schemes for electrode arrays are outlined in Reference [B4]. Stimulation pulse patterns are described in References [P124] and [P132]. The rheobase is the minimum stimulus current (perception threshold) that is applied over a long time (~milliseconds) and triggers an action potential or muscle contraction. A simple relationship between stimulus duration and stimulus current is outlined in Reference [P123]. According to a quantitative study of electrical stimulation of central myelinated fibres in the dorsal columns of anesthetized and paralyzed cats [P115] the chronaxie of large spinal myelinated nerve fibres is in the range between 60 μs and 90 μs and the rheobase recorded with microelectrodes at about

300 μm offset from nerve fibres is between 25 μA and 50 μA. According to findings in [P121] nerve fibres are primarily excited at the location of the cathode. The stimulus current that generates discomfort sensations or initiates motoric responses in a dermatome is approximately 40 % above the perception threshold [P170]. Current density distributions in spinal cord segments caused by dorsomedial electrodes are shown in Reference [P132].

Knowledge of spinal nerve fibre types, sizes and distributions in the superficial dorsal column (DC) and dorsolateral column (DLC) of the spinal cord (SC) is essential for efficient spinal cord stimulation (SCS). References [P120], [P121], [P122], [P131] and [P170] consolidate the results. The mean diameter of nerve fibres in spinal nerve roots is presented in Reference [P172].

Artefacts are decaying electrical waveforms caused by relaxation of accumulated charges in human tissue and at interfaces between human tissue and electrodes after removal of electrical stimuli. Causes of artefacts and investigations for artefact reduction have been studied, among others, in publications [P115], [P116], [P117], [P118], [P129], and [P133]. Artefacts are not resulting from electrical signals propagating along nerve fibres. They can be mono-phasic or bi-phasic and the magnitude can be much higher than the electrical response of nerve fibres. Hence, artefacts can mask neural responses. Artefacts appear on two different time scales depending on surrounding human tissue; (1) artefacts occurring immediately after stimulation and for up to 4 ms and (2) artefacts occurring after 4 milliseconds.

Undesirable chemical reactions at electrode surfaces in contact with human tissue are described in References [B12] and [P56]. Most studies have been carried out using platinum electrodes immersed in saline solution ([P42], [P43], [P44], [P55]). The authors in Reference [P43] have

reported a linear relationship between the aggregated charge injected per phase and the dissolution of platinum electrodes in inorganic phosphate buffered saline (I-PBS) using UV spectrophotometric methods. Oxidation and electrochemical behaviour of chloride ions on platinum electrodes is descried in References [P57] and [P58].

2.4 Magnetic Resonance Imaging

2.4.1 Principles

Magnetic Resonance Imaging (MRI) scanners use the effect of Nuclear Magnetic Resonance (NMR) to produce detailed 2D and 3D maps of body parts for medical analysis. Hereby, isotopes with an odd number of protons and/or neutrons have a non-zero spin magnetic moment (([B1], [B27], [B28], [P86])). The magnetic dipoles are aligned with the z-axis due to the strong static magnetic flux densities $\vec{B}_{0,eff}$ and are tipped into the x-y plane if the impinging RF signal's frequency is the same as the Larmor frequency of the precessing magnetic moments $\vec{m}$ ([P135]). The set of macroscopic, phenomenological equations introduced by Felix Bloch in 1946 describes the motion of nuclear magnetization $\vec{m}(t)$ for given relaxation time constants T_1 and T_2. Gyromagnetic ratios and Larmor frequencies for $\alpha = 90°$ are given in Reference [B26]. Spin relaxation types and times are described in References [B26], [B28], [B29], [P136], and [P137].

Many different algorithms have been developed in order to transform data from the time domain (TD) into the frequency domain (FD) and then into the image domains (ID). Most algorithms are based on Fast Fourier Transform (FTT) algorithms using symmetries and redundancies in data matrices. Several types of MRI scanning techniques exist and are described in References [B1], [B27], and [B28]. Images produced from

MRI scans need interpretation since local magnetic flux density is used to extract image points and there are a number of factors that influence the local magnetic flux density. Pitfalls in MRI image interpretation are summarised in Reference [B29].

2.4.2 RF induced heating

The discovery of RF induced heating of human tissue dates back to Nikola Tesla and his publication of "Massage With Currents of High Frequency" in 1891. In the context of MRI scanning, damage in human tissue predominantly results from thermal exposure and depends on both, temperature and time. Studies conducted by Goldstein et al. [P106] and van Rhoon et al. [P114] show that the rate of cell death in human tissue significantly increases at local temperatures above 43°C. Therefore, thermal exposure times are often referenced to cumulative equivalent minutes at 43°C (CEM43°C). As a rule of thumb, the exposure time has to be decreased by a factor of two for every degree of temperature increase above 43°C and can be increased by a factor of two for every degree of temperature decrease below 43°C for the same level of cell death. A major area of debate is still the maximum body core temperature and the maximum local temperature rise and exposure time for different parts of the human body without any long-term adverse effects for human metabolism and human tissue.

Adverse effects during MRI scans are caused by induced surface currents on Lead wires and electrodes resulting from strong time-varying electromagnetic fields and their continuation as volume currents into human tissue. Eventually, the volume currents can heat and burn surrounding human tissue leading to irreversible tissue damage. Known adverse effects are described in Reference [P112].

Safety during MRI scanning is a major concern. Risks associated with MRI scanning are summarised in References [SPE1], [SPE2], and [SPE3] and MRI safety limits are tabulated in Reference [SPE4]. The focus in this work is on risks associated with temperature increase due to exposure to time-varying electro-magnetic fields. However, the consensus limits for temperature increase using total mass average SAR values lead to significant underestimations of local temperature increases around IMDs and Leads. For tissue with a density of approximately $1000\ \frac{kg}{m^3}$ ...

- local SAR values represent an infinitesimal volume element
- $1\ g$ averaged SAR values represent a volume element of $10\ mm\ x\ 10\ mm\ x\ 10\ mm$, equivalent to up to two electrodes in one volume element
- $10\ g$ averaged SAR values represent a volume element of $21\ mm\ x\ 21\ mm\ x\ 21\ mm$, equivalent to up to three electrodes in one volume element

A $1\ g$ volume element can contain perfused and un-perfused tissue changing heat transport mechanism across the volume element. In case of perfused tissue the local temperature increase can be lower whereas in un-perfused tissue the local temperature increase can be higher. Temperature gradients in un-perfused tissue are as high as 3 K per mm. In un-perfused tissue, averaged SAR values would lead to a significant underestimation of local temperature increase. In most cases, SAR values are higher in surface layers around the human body and lower at the core. In addition, averaged whole body SAR values depend on MRI scanning techniques and applied averaging algorithms. Therefore, whole-body SAR values provide only a rough indication of expected RF exposure of medical devices and resulting temperature increases ([P107]).

During MRI scans, two major causes for heating of human tissue have been identified; heating due to time-harmonic RF fields and heating due to

switching of gradient fields. RF fields transmitted by RF coils induce circular currents (eddy currents) inside the human body. Simulations by [P134] show that eddy currents in human tissue decay with half-life times in the order of nanoseconds and in most MRI scan scenarios fully decay before application of pulsed RF signals. Table 2-1 and Table 2-2 summarise worst case RF and gradient magnetic flux density parameter for a typical 3 Tesla MRI scanner (see Appendices B.1, B.2, and B.3 for details of pulse patterns).

Summary of typical RF magnetic flux density parameter			
Maximum RF magnetic flux density at isocentre	$B_{RF,max}$	30.00	µT
Pulse width of RF signal	T_P	500.00	µs
Frequency of RF signal	f_{RF}	128.00	MHz
Period of RF signal	T_{RF}	7.81	ns
Rate of change of RF magnetic flux density	dB_{RF}/dt	15'360	T/s

Table 2-1 RF magnetic flux density parameter

Summary of typical gradient magnetic flux density parameter			
Maximum gradient magnetic flux density at isocentre	$B_{G,max}$	20.00	µT
Dwell time	t_d	0.00	ms
Rise/fall time peak - peak	t_f	0.20	ms
Period of gradient magnetic flux density	T_G	0.40	ms
Equivalent pulse frequency	f_G	2'500	Hz
Rate of change of gradient magnetic flux density	dB_G/dt	0.2	T/s

Table 2-2 Gradient magnetic flux density parameter

The number of RF signal periods in one gradient pulse width and the factor between RF rate of change and gradient rate of change are given in Table 2-3. The comparison shows that the impact of RF induced heating is approximately $51'200\,x\,76'800 \approx 3.9 \cdot 10^9$ more important than the impact of gradient induced heating.

Number of RF signal periods in one gradient pulse width	$N_{RF,G}$	51'200
Factor between RF rate of change and gradient rate of change	$(dB_{RF}/dt) / (dB_G/dt)$	76'800

Table 2-3 Comparison between gradient and RF parameter

RF exposure of Leads and IPGs is not homogeneous. Factors influencing the level of RF exposure are (1) the exact position of the human body with respect to the RF coils of the MRI machine, (2) the routing scheme and position of IPG and Lead within the human body, (3) the physiology of the human body (sometimes expressed by a Body Mass Index (BMI)), and (4) the tissue properties surrounding Leads and IPG (e.g. conductivity, permittivity, dielectric loss tangent, viscosity, perfusion rate)

RF induced heating at Leads and IMDs predominantly occurs at distal or proximity end electrodes connected to insulated wires which are in contact with human tissue. Assuming that RF energy is accumulated by Leads and IMDs during exposure to RF signals, first principles lead to the measures listed below in order to minimise temperature increase at electrodes:

- increasing RF resistivity of Lead wires, e.g. due to lower wire conductivity, surface roughening, or resistive surface coating
- increasing wire RF impedance using coiled wires
- creating passive coupling between therapeutic and non-therapeutic (auxiliary) Lead wires
- using capacitive coupled floating, decoy, or auxiliary electrodes
- using braids to shield Lead wires
- using in-line inductance and parallel capacitance to create low-pass or band-stop RF filters
- resistively loading wires to adsorb RF energy at the distal or proximity end of Lead wires
- reactive loading of Lead wires to change positions of voltage and current minima and maxima along Lead wires

Typical temperature increases at distal end electrodes for varying Lead lengths have been reported in the literature ([P103], [P104], [P108], [P109], [P110], [P111], [P112], [P113]).

Figure 2-2, Figure 2-4, and Figure 2-6 show results obtained from temperature measurements of electrical copper wires in gelled saline solution exposed to RF fields from a 3 Tesla MRI scanner that generates an average SAR of $1\ \frac{W}{kg}$ for five minutes [P108].

A typical curve for temperature increase around the distal, un-insulated end of a copper wire in contact with saline solution as function of wire length is shown in Figure 2-2.

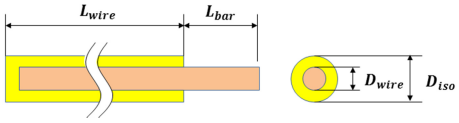

Figure 2-1 Outline of wire

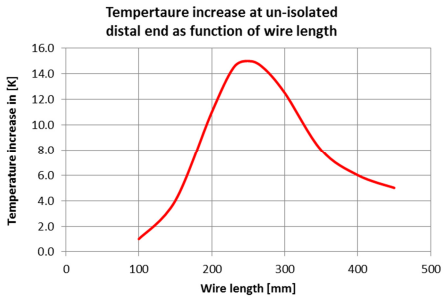

Figure 2-2 Temperature increase at distal, un-isolated end of wire (adapted from [P108])

Further, the temperature increase at the distal end in multiple isolated wires seems to be lower compared with the temperature increase at the distal end for the single wire scenario as shown in Figure 2-4.

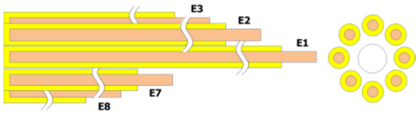

Figure 2-3 Outline of multiple wires

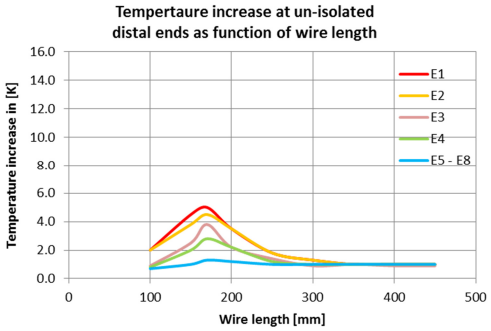

Figure 2-4 Temperature increase at distal, un-isolated ends of wire (adapted from [P108])

Finally, the temperature increase at the distal ends in multiple isolated wires seems to be further reduced by coupled bare wires in contact with the gelled saline solution (see Figure 2-6).

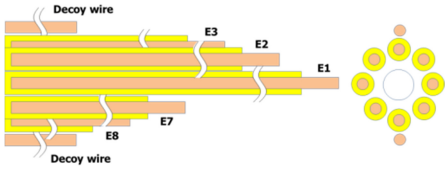

Figure 2-5 Outline with two coupled wires

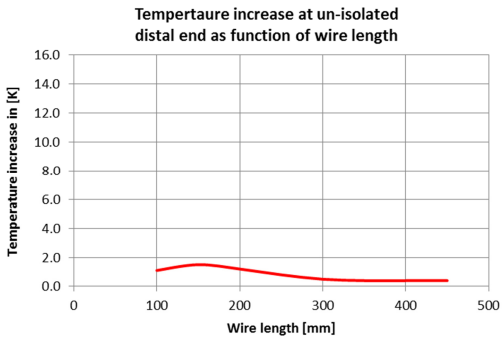

Figure 2-6 Temperature increase at distal, un-isolated end of wire E01 (adapted from [P108])

Some authors normalise worst case Lead wire lengths to wavelength. However, there are some ambiguities with this representation:

- Wavelength is associated with a single dominant propagating wave mode along the Lead but several propagating wave modes can be simultaneously present depending on excitation schemes and Lead lengths.

- Loading scenarios at the distal and proximity end (e.g., short, open, capacitive, inductive and resistive loading) and/or reactive capacitive or inductive coupling along the Lead change magnitude and location of voltage and current minima and maxima and therefore change worst case wire lengths.

2.4.3 Misconceptions

In the following a few misconceptions are presented first and then evidence is provided.

1. Embedded SCS are excited at a single location along the Lead and there is a single electrode responsible for worst case tissue heating.
2. In multi-electrode Leads, the most significant temperature increase occurs at the electrode located at the distal end.
3. Loading of Lead wires at the proximity end (IPG) has negligible impact on temperature increase at electrodes located at the distal end.
4. Temperature increases at electrodes depend mainly on Lead length, i.e. longer Lead lengths result in lower temperature increases.
5. A single (resonant) electromagnetic mode carrying almost all energy is the cause of tissue heating at electrodes located at the distal end.
6. Electrode temperature increases linearly with RF exposure time.

With respect to misconception 1, embedded SCS are exposed to RF fields that change in amplitude and phase along the Lead. Further, several electrodes at the distal end contribute to tissue heating. This misconception has led to proposals of various distributed RF filter topologies that lead to temperature decreases in a particular RF exposure scenario but may result in temperature increases in other RF exposure scenarios.

With respect to misconceptions 2, 3, and 4, the locations of electrodes that exhibit the highest temperature increase depend on several factors; the distribution of RF sources along the Lead, Lead length, wire routing in MLCs, coupling between wires and electrodes at the distal end, coupling between wires in MLCs, coupling between wires of MLCs and human tissue and loading scenarios at both, the proximity and distal end. These misconceptions have led to proposals using capacitive coupled auxiliary wires (partially) in contact with human tissue neglecting that this only changes locations of maxima and minima of electric field (voltage) and magnetic field (current) nodes along the Lead and shifting the maximum temperature increase at the distal end from one electrode to another electrode. In addition, capacitive coupling using auxiliary wires reduces the insertion loss experienced by wavelets travelling along the Lead resulting in higher magnitudes of electric and magnetic fields at proximity and distal ends. The reduction in insertion loss results from replacing lossy tissue with highly conductive auxiliary wires. The wavelets traveling towards the distal end can either be primary wavelets caused by an incident electric field or secondary wavelets from reflections at the proximity end (IPG) or distal end. In worst case scenarios, the distal end sections of auxiliary wires can show temperatures increases far beyond temperature increases at electrodes.

With respect to misconception 5, the electromagnetic energy transported in and around MLCs embedded in human tissue is carried between two dominant common modes and up to (x-1) dominant differential modes where x represents the number of wires in the MLC. The energy distribution between the modes depends on the magnitude and phase and angle of incidence of the exciting RF field. This misconception has led to proposals where resistive and reactive circuitry is placed in various configurations between single Lead wires and human tissue. A star type short circuit between Lead wires at the proximity end leads to full

reflection of all differential modes. Resistive and reactive loading of star points to human tissue has negligible effects on absorption and reflection of common modes since wave energy is contained in a large cross-sectional area around the MLC. Further, reactive circuits at reflection points merely shift temperature maxima at the distal end from one electrode to another. Any effective solution has to take into account energy absorption for all modes.

With respect to misconception 6, a quasi-steady state temperature is in most cases achieved after 90 seconds CW RF exposure or after 450 seconds pulsed wave RF exposure assuming a duty cycle of 20%. Thermal equilibrium is caused by heat advection, convection and conduction in human tissue and in gelled saline.

2.4.4 Safety criteria for RF induced heating

MRI safety of IMDs with respect to RF induced heating can be assessed in many different ways. From my perspective and in decreasing order of accuracy, following criteria can be applied to analyse RF induced temperature increase in the vicinity of metal to human tissue boundaries for Leads and IPGs:

- Measured temperature increase at electrodes and cases in vivo
- Measured temperature increase at electrodes and cases in vitro (phantom torso)
- Calculated temperature increases caused by volume loss densities (deposited power per volume element) taking into account thermal capacities, thermal conductivities, heat advection, heat conduction, and heat convection per constituent part of human tissue and using appropriate thermal boundary conditions
- Calculated volume loss densities and local specific adsorption rates

- Calculated electric field distributions along IMDs and Leads for different RF exposure scenarios

Temperature increase at electrodes results primarily from ionic volume currents caused by strong electric and magnetic fields penetrating human tissue ([P112]). Although at the bottom end of assessment methods, electric field strength distributions provide valuable information about areas that are prone to high temperature increases. Therefore, normalised electric field strength envelopes of the total complex electric field along IPG and Lead provide a first level of analysis whether a Lead and IPG comply with a given maximum temperature increase. Here, the normalisation is applied with respect to $1\ \frac{V}{m}$ incident tangential electric field. The normalised electric field strength envelope on the surface of an IMD that causes a maximum temperature increase of about 2°C above background temperature increase for a whole body average SAR value of $2\ \frac{W}{kg}$ is approximately $10\ \frac{V}{m}$. In Figure 2-7, the envelope is superimposed on a typical calculated electric field strength distribution along a Lead.

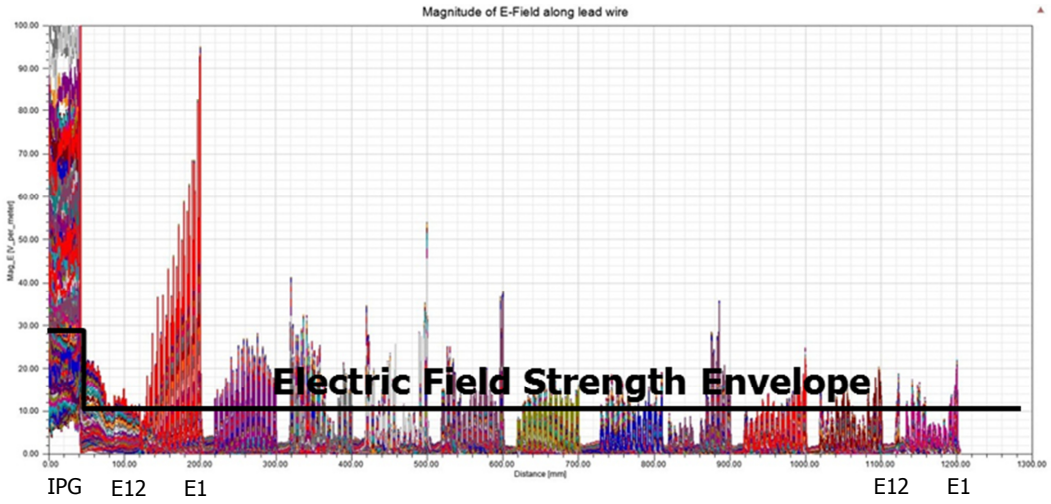

Figure 2-7 Electric field strength envelope superimposed on typical electric field distribution along a Lead with twelve electrodes for an incident axiolateral plane wave with an incident electric field strength of $1\ \frac{V}{m}$ at 128 MHz. The Lead length varies from 200 mm to 1200 mm.

2.5 Electromagnetic waves

The foundations for electromagnetics (EM) are outlined in References [B13] to [B19]. Electromagnetic fields interact with matter causing displacement of free and bound charges. In response, the displaced free and bound charges create scattered electromagnetic fields. Both fields superpose and create a total measurable electromagnetic field. The interaction between electric and magnetic fields and matter is described by three constitutional equations. The first constitutional equation relates electric fields and free (unbound) charges, the second constitutional equation relates electric fields and bound charges and the third constitutional equation relates magnetic fields and orientation of magnetic dipoles by a quantity called magnetic displacement or magnetic flux density. The complex dielectric function combines bound and free (unbound) signed charges into one equation ([P7], [P97], [P98], [P154]). Complex dielectric functions of solvents and solutions can be determined using terahertz transmission spectroscopy ([P67]) or VNA based RF and microwave measurement techniques ([P68]). The dielectric decrement is a reduction in the effective permittivity of a solution caused by free ions. The reduction in effective permittivity results from (1) volume effects, i.e. the higher the concentration of free ions the lower the permittivity in the solution, (2) irrotational bonding, i.e. the attachment of molecules of the solution to an ion through electrostatic forces resulting in a reduction of the dipole moment, (3) kinetic depolarisation, i.e. an external electric field aligns the dipole moment of the solvent and solute molecules. Kinetic depolarisation results from the movement of an ion (solute molecule) into the opposite direction of the aligned solvent dipoles resulting in a decrease of the mobility of ions due to frictional forces. Volume effects and irrotational bonding are static equilibrium effects whereas kinetic depolarisation is a dynamic effect.

The cause-effect relationship between stationary and time-varying magnetic flux density $\vec{M}$ and $\frac{\delta \vec{B}}{\delta t}$, respectively and induced electric fields $\vec{E}$ is described by the law of induction and the cause-effect relationship between continuous and time-varying motion of free and bound electric charge densities $\vec{J}$ and $\frac{\delta \vec{D}}{\delta t}$, respectively and induced magnetic fields $\vec{H}$ is described by the law of magnetic flux. Finally, two conservation laws describe that electric and magnetic charges are conserved. The set of equations and laws above is referred to as Maxwell's equations although Heavyside has put them into the mathematical form known today. For time-harmonic electromagnetic fields in source free regions Helmholtz has derived three second order partial differential equations for electric and magnetic fields and electric current densities. The partial differential equations together with initial conditions, electromagnetic sources, material properties, and boundary conditions describe the wave propagation and diffusion process and form the basis of all electromagnetic simulators. For numerical treatment the partial differential equations are transformed into difference equations and constituent geometrical objects are replaced by three dimensional meshes.

2.6 Electromagnetic wave propagation

Transmission lines

Leads and nerve fibres (axons) carry electromagnetic power when excited by RF signals or potential gradients, respectively and act similar to transmission lines. A general waveguide circuit theory for linear, isotropic, lossy materials is presented in Reference [P24]. Here, three transmission line types are of interest; axonal transmission lines representative for action potential propagation along axons, and single wire and coaxial transmission lines representative for Leads embedded in lossy matter. A

model for action potential propagation along unmyelinated and myelinated axons is described in References [P21] and [P25], respectively. The coupling between therapeutic electrodes located in the epidural space of the spinal canal and axons in dorsomedial and dorsolateral columns of the spinal cord as well as the excitation and propagation of action potentials will be presented in due course. Signal propagation along low loss single wire transmission lines have been analysed at the beginning of the 20th century ([P23], [P31]), reviewed in References [P29] and [P30], and equivalent circuits have been proposed at the turn of the 21st century ([P28]). EM propagation along circular waveguides with multiple concentric lossy dielectrics has been investigated in Reference [P32]. Mode designations and parameter for coaxial transmission lines are outlined in Reference [B16]. In this work, fundamental TEM modes and H-modes are considered.

Surface waves

Electromagnetic (EM) surface waves can be excited along Leads embedded in electrolytes (or human tissue). EM surface wave types have been reviewed in Reference [P27]. Surface waves exhibit cut-off frequencies, propagate along the interface of two media with different material properties, have quasi-exponentially decay of electric and magnetic field components perpendicular to interfaces (both directions, i.e. into both media) and show energy transport predominately along interfaces. Further, surface waves can only be excited under specific conditions such as coupling of incident waves from high permittivity regions onto low permittivity regions (critical angle of incidence and total reflection), coupling via prisms or gratings into boundary regions, or coupling via slab waveguides. In addition, surface wave propagation require either (1) different permittivity, permeability, or conductivity tensors between two media, (2) permittivity, permeability, and/or conductivity gradients inside a single media, or (3) different crystal

structures (tensors) between two media. Finally, surface waves can be classified according to their predominant field patterns. Transverse magnetic waves (TM) propagate due to different permittivities and/or conductivities resulting in surface impedances with an inductive reactive part, transverse electric waves (TE) propagate due to different permeabilities resulting in surface impedances with a capacitive reactive part, and hybrid forms between TE and TM waves, due to different permittivities, conductivities and permeabilities, where EH waves have a dominant transversal electric field component and HE waves have a dominant transversal magnetic field component. The excitable surface wave types that can propagate along Leads embedded in electrolytes are transverse Scholte waves where particle (ion) movement is confined and perpendicular to the surface layer and perpendicular to the wave's propagation direction. The perpendicular (radial) particle (ion) movement results from perpendicular (radial) electric fields and transversal (radial) viscosity gradients observed in double layers. Love waves are transverse waves where particle (ion) movement is confined and parallel to the surface layer and perpendicular to the wave's propagation direction. The longitudinal particle (ion) movement results from longitudinal electric fields and transversal (radial) viscosity gradients observed in double layers. The magnitude of particle (ion) motions decreases exponentially from the surface for both, Scholte and Love waves. A third surface wave type is the superposition of Scholte and Love waves, called Rayleigh wave. Rayleigh waves show both, longitudinal and transversal motion of surface particles (ions). Longitudinal and transversal waves can show a phase difference. Magnitudes of particle motion decrease exponentially from the surface.

2.7 Electrolytes

All matter containing free moving ions is called an electrolyte and human tissue has strong electrolytic character ([B3]). Electrical current in electrolytes is characterised by the flow of ions ([B12]). Ions can be positively or negatively charged and if both ion types are present they move in opposite directions for a given potential difference. Further, the higher the concentration of ions in the electrolyte the higher the current for a given potential difference ([P20]). Alkaline water electrolytes are composed of potassium hydroxide (KOH) or sodium hydroxide (NaOH) dissolved in water. The hydroxide ions (OH^-) transport the charge from one electrode to the other ([P14]). Acidic water electrolytes are composed of chemical species capable of donating hydrogen ions (H^+), e.g. hydrogen chloride (HCl) donates its hydrogen ion to form a hydronium ion H_3O^+ that transports the charge from one electrode to the other ([P14]). Free ions are ions with molecules of surrounding solution attached to their outer shells ([P2]). Free ions do not have a proper dipole moment but orient neighbouring molecules of the solution. If an external electric field is applied to the solution, the dipole moments of the molecules in the solution next to free ions are only partly aligned with the external field and therefore reduce the effective permittivity of the solution. The dipole moment of liquid water and NaCl solutions has been derived in References [P160] and [P166], respectively. In aqueous solutions, water molecules bond to positive metal ions (cations) through dative covalent bonds where oxygen atoms donate both electrons to the bond. The first layer of water molecules around the metal ion is called the first hydration shell or first coordination sphere. A second layer of water molecules can bond to the first layer of water molecules through hydrogen bonds. The second layer of water molecules around the metal ion is called the second hydration shell or second coordination sphere. Within the first solvation shell, the bond strength increases with the metal ion's electrical charge and

decreases with increasing distance from the metal ion's surface. The average time a water molecule is bonded to a metal ion can range from 100 ps to several years. In addition, water molecules from the first and second hydration shell can frequently change position. Water clusters are described in Reference [P1]. Using hydration free energies as measure for the degree of solvation, it can be demonstrated that negative ions are solvated more strongly than positive ions ([P5]). The structure of hydrated shells in aqueous NaCl solutions using molecular dynamics simulations is analysed in Reference [P6]. Dielectric properties of aqueous NaCl solutions in the frequency range between 20 MHz and 40 GHz have been analysed in Reference [P13] and dielectric relaxation time constants are presented in Reference [P99]. For NaCl concentrations of $1.0\,\frac{mol}{l}$ at $25°C$ the relaxation time of the solvent is approximately $\sim 7.5\,ps$. Conductivity of human tissue is heterogeneous and anisotropic and depends on frequency due to its molecular and structural building blocks [P134]. At frequencies below 100 MHz mobile ions hit cell membranes and therefore cell membrane structure mainly determines AC conductivity. At frequencies above 100 MHz, mobile ions jiggle around their resting position and therefore ion concentrations inside and outside of cells mainly determine AC conductivity.

2.8 Electrode potentials and current densities

Electro-chemical potentials in electrolytes cannot exceed a few Volts (e.g. water ~1.23 V, aqueous NaCl ~2.19 V) due to the onset of decomposition of the electrolyte ([P15], [P57], [P58]). Potential differences between 0.1 V and 1.0 V result in field strengths between $10^8 \frac{V}{m}$ and $10^{10} \frac{V}{m}$. These field strengths are in general above dielectric breakdown voltages for many materials (e.g. water $\sim 7 \cdot 10^7 \frac{V}{m}$ [B6]; glass $\sim 1.0 \cdot 10^7 \frac{V}{m}$ [B6]).

The Poisson Boltzmann equation describes the steady state electric potential $\varphi(\vec{r})$ in electrolytes from a distribution of fixed charges $\rho_{fix}(\vec{r})$ and a distribution of mobile charges $\rho_{mob}(\vec{r})$. The fixed charges are located on solid surfaces immersed in or in contact with the electrolyte whereas the mobile charges (ions) are located inside the electrolyte. The steady state electric potential $\varphi(\vec{r})$ is the superposition of a mean potential resulting from fixed charges and the potential resulting from the mobile charges once they have achieved their final positions.

The surface potential is the potential difference between the electrode surface and the bulk electrolyte. The surface potential is often estimated from Grahame's equation where the surface charge of solids immersed in electrolytes is equal to the amount of charge inside the electrolyte within a layer of 1 Debye length above the solid's surface.

What follows are a few relevant definitions of potentials at electrode / electrolyte interfaces. The Helmholtz potential is the potential difference between the electrode surface and the Inner Helmholtz Boundary (IHB). The Stern potential is the electric potential difference between the layer of ions directly in contact with the electrode and the bulk electrolyte. The zeta potential is the electric potential difference between the outermost

ionic layer still attached to the electrode and the bulk electrolyte in the fluid. Outermost ionic layers with high positive or negative zeta potential are stable while layers with low zeta potentials tend to disintegrate. A streaming potential difference $\Delta\varphi_{stream}$ results from an electrolyte moving along a charged surface due to a pressure difference across that surface. The streaming potential difference between two points on the surface is positive when the electric potential on the high pressure side is more positive. Slip processes and their impact on surface conductivity and permittivity are analysed in Reference [P40]. The decomposition potential is the minimum potential difference between anode and cathode of an electrolytic cell to initiate electrolysis. The decomposition potential is the minimum potential difference between anode and cathode of an electrolytic cell to initiate electrolysis. The equilibrium potential is defined for a single ion species. At the equilibrium potential the cathodic current density across the electrode / electrolyte interface is equal to the anodic current density resulting in zero electrolysis. The over-potential $\Delta\varphi$ is the potential difference between the electrode potential and the electrode to electrolyte equilibrium potential. The activation over-potential is the potential difference above the equilibrium value required to produce a net current (net electron transfer) in a redox reaction. The reaction over-potential is the potential difference above the equilibrium value preceding a net current (net electron transfer) in a redox reaction and is closely linked to the activation energy. Concentration over-potential refers to the potential to annihilate the depletion of charges at the electrode surface when the (fast) electrochemical reaction rate at the electrode lowers the electrode's surface charge concentration below the charge concentration of the bulk solution and hence reduces the ability of the charges to reach the electrode surface. Bubble over-potential refers to the depletion of charge-carriers due to the formation of physical bubbles. Bubbles can reduce the effective electrode area and increase local current densities. The diffusion over-potential refers to the over-potential to start diffusion of chemical species. The polarisation over-potential refers to the over-

potential when the maximum diffusion rate of chemical species is achieved.

Current densities in electrolytes are expressed by Faraday's law, stating that (1) the mass m of a given chemical species released or deposited at an electrode is proportional to the charge passed through the solution, (2) the mass m of a given chemical species released or deposited at an electrode is proportional to the molar mass of the species in the solution, and (3) the mass m of a given chemical species released or deposited at an electrode is inversely proportional to the signed number of the fundamental charge of the species in the solution.

The exchange current density (or Faradaic current density) J_{ex} is expressed by the Butler Volmer equation. The exchange current density is the electrical current density through the surface of an electrode that is in contact with a fluid without causing any intermediate reactions at the surface (e.g. specific adsorption). The exchange current density $J_{ex,0}$ is the electric current density at zero over-potential $\Delta\varphi$, i.e. the cathodic current density is equal to the anodic current density resulting in zero electrolysis at the surface. A high exchange current density $J_{ex,0}$ results in low changes of the over-potential $\Delta\varphi$ due to charge transfer and a low exchange current density $J_{ex,0}$ results in high changes of the overpotential $\Delta\varphi$ due to charge transfer. Cathodic and anodic reactions can occur on the surface depending on the voltage difference between the electrode and the fluid. Cathodic reactions occur when the electrode potential is lower (negative) than the equilibrium potential. Anodic reactions occur when the electrode potential is higher (positive) than the equilibrium potential. The exchange current density J_{ex} depends on; (1) redox reactions, (2) electrode type and surface, (3) ratio of concentrations for oxidised and reduced species, and (4) temperature. The net electric current density through the electrode surface is proportional to the net reaction rate on the electrode surface. The net reaction rate itself, i.e. the difference

between the oxidation and reduction reaction rate, depends on the potential difference between the electrode and the bulk electrolyte. In addition, the potential difference defines the coverage of reactants and intermediate and final products on the electrode surface. The exchange current density through conductor - electrolyte interfaces is approximated by the Butler–Volmer equation. Exchange current densities in aqueous systems are summarised in Reference [P50]. The surface charge transfer resistance R_{ct} in $\Omega \cdot m^2$ can by estimated from the exchange current density (J_{ex}) versus over-voltage relationship $(\Delta\varphi \; or \; \eta)$ expressed by the Butler Volmer equation using a linear approximation of e-functions for low over-voltages η.

In a Faradaic Process the charge is transferred from the electrode across the Helmholtz Double Layer into the bulk electrolyte, or vice versa, resulting in anodic and cathodic processes. In a Non-Faradaic Process charge is not transferred from the electrode across the Helmholtz Double Layer into the bulk electrolyte, or vice versa, but the structure of the Helmholtz Double Layer can change. At over-potentials close to the equilibrium potential (potential where no net current flows), the reaction rate is not limited by the rate at which reactants in the electrolyte arrive at the electrode surface (i.e. limitation of electron transfer speed at the interface). At over-potentials further away from the equilibrium potential (potentials where still no net current flows across the double layer), the reaction rate is limited by the rate at which reactants in the electrolyte arrive at the electrode surface (i.e. limitation of mass transport speed of reactants towards the interface). If the electron transfer speed is much larger than the mass transport speed the Faradaic Process is reversible. Small over-potentials result in large current densities near the surface. In this case, the products are not quickly transported away from the electrode surface and hence the charge transferred to those products is stored next to the surface for a certain amount of time. If the over-potential is reversed before a significant amount of products (or charge)

can be transported (diffused) away from the electrode surface, products formed from reactants can be converted back to reactants. If the electron transfer speed is much lower than the mass transport speed the Faradaic Process is not reversible. Large over-potentials are required to induce sensible current densities near the surface. In this case, the products are quickly transported away from the electrode surface and hence charges transferred to those products are moved away before any products can be converted back to their reactants. There is no charge storage near the electrode surface. If the over-potential is reversed after a significant amount of products (or charge) has been transported (diffused) away from the electrode surface, products formed from reactants cannot be converted back to reactants. Reaction products and net charge is transferred into the electrolyte resulting in a permanent change of the electrolyte's constitution, e.g. precipitation or evolution as gas. Irreversible Faradaic Processes should be avoided in stimulation of human tissue.

Ionic current density due to concentration gradients of charge carriers, potential gradients across charge carriers and motion of charge carriers is described by the Nernst Planck equation.

The reaction rate determines the time scale of a chemical reaction, i.e. whether it is a quick or slow reaction. Expression for hydrogen electrode reaction rates are presented in Reference [P19].

The Arrhenius equation (Arrhenius Factor) describes the temperature dependence of reaction rates r. To trigger a transformation (reaction) a minimum amount of energy, called the activation energy E_a, is necessary. The number of reactants that have kinetic energy greater than the activation energy E_a at temperature T can be derived from the Boltzmann distribution. The Tafel equation relates over-potential and exchange current density. A detailed analysis of Tafel slopes and corresponding reaction rates is given in Reference [P16].

Next, equilibrium conditions for electrode / electrolyte interfaces are shortly summarised. (1) The divergence of electric flux density through the electrolyte-metal boundary and through the (fictitious) bulk to double layer boundary has to be equal to the corresponding volume charge density where the electric field along a line segment starting at the electrode surface and ending in the electrolyte is characterised by the gradient of the electrical potential and the electric flux density and electric field are linked via the permittivity. (2) The momentum of ions moving into the double layer is equal to the momentum of ions moving out of the double layer. (3) The mass of ions moving into the double layer is equal to the mass of ions moving out of the double layer. (4) The internal energy in the double layer is constant. (5) In thermodynamic equilibrium the Gibb's free energy is a minimum.

2.9 Interface dynamics

Implanted Medical Devices (IMDs) are in direct contact with human tissue. The interface layers between IMDs and tissue influence operating conditions and have a significant impact on RF wave propagation along Leads during MRI scans and therefore determine field distributions around distal end electrodes and their role in tissue heating. Interface processes determine macroscopic material properties such as permeability, permittivity, conductivity, and viscosity in interface regions between bulk materials with different material properties ([B20], [B21], [P38] - [P41], [P46] - [P54], [P60] - [P65][P62]) and therefore have a major impact on (1) wave propagation along MLCs embedded in electrolytes, (2) reversible charge storage and release at electrodes, (3) irreversible charge transfer at electrodes, and (4) heat transfer at electrodes. In interface regions isotropic bulk materials can exhibit strong anisotropic behaviour. For example, (charged) chemical species can align their electric and/or magnetic dipole moments or encounter changes in their mobility for

different spatial directions. Fundamentals of electrochemical deposition processes are described in Reference [B12]. In addition, charge transfer and charge redistribution processes can occur at the interface between two different materials, such as metal-insulator ([B21], [P45], [P47], [P51], [P52], [P54], [P64], [P65]), metal-electrolyte ([P9], [P10], [P41], [P46], [P48], [P49], [P53], [P60]), or insulator-electrolyte interfaces ([P61], [P62], [P63]). These processes lead to (1) changes of electron densities in transition regions, (2) adsorption and desorption of species on/from interfaces, (3) charge transfer across the interface, (4) charge transport towards and away from the interface due to electric potential differences (migration) in half spaces, (5) charge transport along the interface plane due to electric potential differences (migration) along the interface plane, (6) charge transport towards and away from the interface due to concentration differences (diffusion) in half spaces, (7) charge transport along the interface plane due to concentration differences (diffusion) along the interface plane, (8) charge transport towards and away from the interface due to pressure differences (convection) in half spaces, (9) charge transport along the interface plane due to pressure differences (convection) along the interface plane, (10) charge transport towards and away from the interface due to temperature differences (convection) in half spaces, (11) charge transport along the interface due to temperature differences (convection) along the interface plane, and (12) generation and recombination of species on both sides of the interface. The interface regions that affect wave propagation along Leads are; (1) metal-insulator interfaces; e.g. insulated Lead wires, (2) insulator-electrolyte interfaces; e.g. MLCs embedded in human tissue, (3) metal insulator electrolyte interfaces; e.g. MLCs with Lead wires embedded in human tissue, (4) metal electrolyte interface; e.g. transition regions between electrode and human tissue, and (5) metal - conductive polymer - electrolyte interface, e.g. conductive polymers for impedance matching that are sandwiched between electrodes and human tissue. Measurable effects of underlying interface dynamics are changes in wave propagation

characteristics along embedded waveguides such as attenuation, wavelength, and phase shift. In electromagnetic models they are taken into account using conductivity, permittivity and permeability tensors. Unfortunately, tensor matrices used in electromagnetic field simulations are prone to numerical instabilities leading to significant jumps in field values between mesh nodes, faces, and volume elements ([P138]).

Determining the dynamics of constituent species at interfaces requires advanced test and measurement equipment. Electrochemical Impedance Spectroscopy (EIS) is applied to generate impedance versus frequency plots for small harmonic signals injected into test specimens (often superimposed on larger constant DC signals) to extract discrete equivalent circuit models. General EIS techniques are described in References [B10] and [B11], and an EIS theory for heterogeneous electrodes is outlined in Reference [P70]. Further insight into interface layer structures has been reported in [P72] using X-ray photoelectron spectroscopy. Scanning probe microscope techniques are commonly used to generate images from surfaces and to provide insight into molecular dynamics at the surface. A probe is moved either in direct contact or contactless over the surface. The distance between the probe and the surface is controlled by feedback loops steering three-axis piezoelectric motors with very high spatial resolution. Here, only scanning techniques that provide insight into the surface topology and the electro-chemical interface dynamics are shortly described. In absorption and fluorescence spectroscopy solid, liquid or gaseous samples are illuminated with a spectrum of electromagnetic waves (photons) [P87]. In absorption spectroscopy wave energy is absorbed, reflected or transmitted from the sample. The absorbed wavelength can be correlated with types of chemical elements. In fluorescence spectroscopy wave energy can move electrons of chemical elements into higher orbits resulting in a release of photons. The wavelength of photons can be correlated with types of chemical elements.

Both methods can provide inside into the relative coverage of adsorbed species at interfaces.

X-Ray Photoelectron Spectroscopy (XPS) is a spectroscopic method intended to measure the constitutive elements of thin surface layers up to 10 nm deep into material samples. The sample is embedded into a vacuum chamber and exposed to a high voltage x-ray (photon) beam that excites the surface atoms [B25]. The surface atoms emit electrons. The electrons are counted and classified according to their kinetic energy to determine elements types, occurrence, and electronic and chemical states. This technique is used, among others, to identify dissolved platinum from platinum electrodes in human tissue.

In Scanning Electrochemical Atomic Force Microscopy (SECM-AFM) the surface of a (conductive) solid-electrolyte boundary region is scanned using a cantilever that is moved in the electrolyte either in contact with or contactless over the surface of the solid (AFM). Integrated into the cantilever is an isolated working electrode for detection of electrochemical processes occurring at the surface. The main advantage of this method is that surface mapping and electrochemical measurements are decoupled. Further insight into the operating principles are outlined in references [P66], [P74], [P78], [P79], [P80], [P81], [P82], [P83], [P88], and [P96].

In Scanning Ion Conductance Microscopy (SICM) the surface of a solid-electrolyte boundary region is scanned using a micropipette filled with an electrolyte. Immersed into the electrolyte is an electrode. The ionic current through the tip of the micropipette is used to control the vertical distance between the micropipette and the surface. If the micropipette approaches the surface the gap between the tip of the micropipette and the surface narrows and hence the conductance between the working electrode and the counter electrode decreases. Principles of operation are found in references [P77] and [P94].

In a combined Scanning Electrochemical and Ion Conductance Microscopy (SECM-SICM) the surface of a conductor-electrolyte boundary region is scanned using a nanopipette for ion conductance measurements and a colocated annular electrode on the outside of the nanopipette for faradaic current measurements. The ionic current through the tip of the micropipette is used to control the vertical distance between the nanopipette and the surface. References [P69], [P84], [P90], and [P91] further explore and highlight the possibilities of SECM-SICM measurements.

Surface energy measurement techniques for solids and liquids provide valuable insight into surface bonding types and reaction mechanisms. For surface tension measurements (contact angle) models and methodologies have been developed to extract the total surface energy and the fractions attributable to polar, non-polar and hydrogen bonding ([P95], [P85], [P73], [P93]).

2.10 Heat transfer

If free (mobile) electrons on metal surfaces and free (mobile) ions in human tissue are exposed to electromagnetic fields, surface and volume currents are induced, respectively. Both, surface and volume currents generate heat, whereas the contribution of volume currents in human tissue is in most cases higher than the contribution of surface currents on conductive surfaces. Reference [B9] provides an overview over mass and heat transfer in fluid systems. Heat is volatile energy and is correlated to temperature and to kinetic energy of colliding micro-particles in objects whereas an object can be any type of volume filled with matter. The kinetic energy and the collision rate of micro-particles in an object can be influenced by many mechanisms; (1) electromagnetic exposure (e.g. light, RF), (2) friction (e.g. current, pressure), (3) chemical reactions (e.g.

metabolism, reactor, fire). Objects tend to minimise their volatile energy through a process called heat transfer. The heat transfer can occur in three different forms; (1) radiation from an object's surface into the surrounding environment, (2) convection from an object's surface to a medium in motion (e.g. gas or fluid), or (3) conduction from an object's surface to a medium at rest (e.g. solid). All three heat transfer mechanisms can occur simultaneously although in many cases one or two mechanisms are dominant. The local temperature of an object depends on heat transfer rates (heat transfer per time) per unit area. Several parameters have an impact on heat transfer rates; (1) temperature differences between objects, (2) thermal properties of objects, such as specific heat capacities and thermal conductivities, (3) flow velocities of micro-particles, (4) flow patterns of micro-particles determined by viscosities and mass densities, (5) surface areas, and (6) natural convection determined by heat expansion coefficients and gravity. In the context of this work, the focus lies on local heating around electrodes embedded in human tissue (or gelled saline solution as replacement for human tissue). The tissue around electrodes is heated due to exposure to electromagnetic fields. Heat transfer in tissue involves predominantly thermal conduction and thermal convection (perfusion) where human tissue and body liquids (e.g. blood) act as heat transport carriers. In 1948, Pennes [P186] established a second order partial differential equation describing heat transfer through homogenous tissue from heat sources located on or inside the tissue. Depending on the types of heat sources numerous adaptations have been applied to Pennes' heat equation. Non-equilibrium thermodynamics are treated in Reference [B35].

3. Configurations

3.1 Overview

This chapter summarises the terminology used in subsequent chapters to describe and distinguish base cases and design variations of Leads and IPGs.

Therapeutic (E) and auxiliary (A) electrodes are numbered from the distal end of the Lead towards the proximity end where the IPG is located (Figure 3-1). An electrode is a cylindrical platinum cuff connected to a (Lead) wire (Figure 3-2). The inner diameter of electrodes is ~1.3 mm and the outer diameter is ~1.4 mm. The therapeutic electrode length is 3 mm and the edge to edge spacing between two electrodes is 4 mm. Lead wires are running in small longitudinal conducts of the MLC. The larger centre conduct is used to accommodate a stylet wire for guidance of the Lead during the surgical procedure. At the distal end of the centre conduct a stylet plug is located (not shown). The MLC is a thermoplastic polyurethane elastomer (Figure 3-3). The material properties are described in Appendix A.3 and the dimensions are given in Figure 3-5. Lead wires (W) in the MLC are numbered clockwise from 1 to 12 starting at the nine o'clock position when locking into the multi-lumen-conduct from the proximity towards the distal end. Wire 1 is connected to Electrode 1 (Figure 3-4).

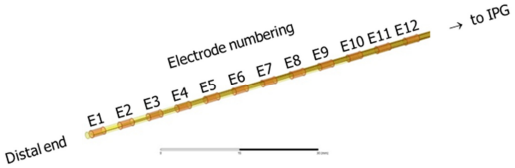

Figure 3-1 Electrode numbering

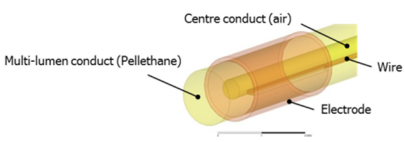

Figure 3-2 Cylinder electrode

A single Lead wire has a diameter of 95 μm and is made of 19 platinum strands each having a diameter of 19 μm. The single Lead wire is coated with a thin ETFE coating resulting in an overall diameter of 120 μm (Figure Figure 3-6).

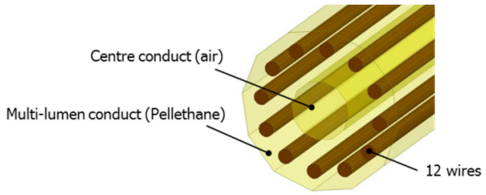

Figure 3-3 MLC

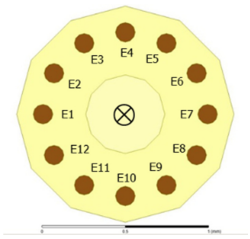

Figure 3-4 Wire positions

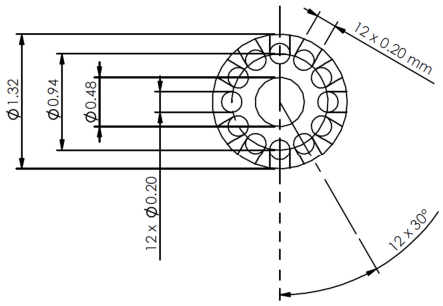

Figure 3-5 Dimensions of MLC in [mm]

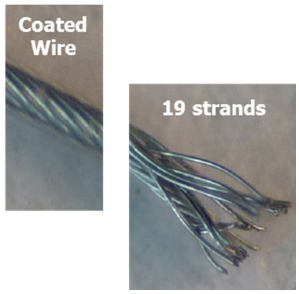

Figure 3-6 Single Lead wire

The Implanted Pulse Generator (IPG) is shown in Figure 3-7. The constituent parts relevant for EM simulations are the platinum case (bottom part) and the header (top part). The header accommodates the interface between Lead wires and electronics inside the platinum case. Two termination scenarios for Lead wires inside the header are considered. In a first scenario the Lead wires are shorted (grounded) to the platinum case (Figure 3-8) and in a second scenario the Lead wires are open ended (Figure 3-9). Other termination scenarios are investigated later on.

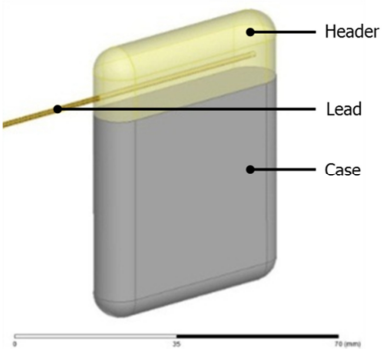

Figure 3-7 Implanted Pulse Generator (IPG)

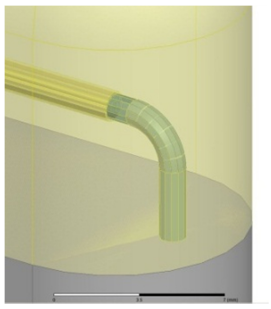

Figure 3-8 Lead wires grounded to IPG case

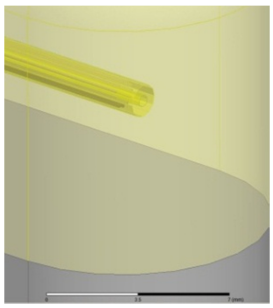

Figure 3-9 Lead wires open ended in IPG header

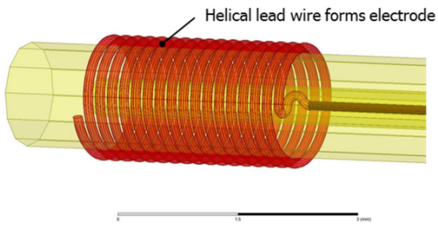

Figure 3-10 Helical electrodes

In view of MRI safeness several design variations have been investigated. Terminology and outlines are shortly presented. Apart from cylindrical electrodes shown in Figure 3-2 helical electrodes might be an alternative (Figure 3-10). This idea is further explored in Section 5.1.9.2. Building on previously developed ideas from [P108] a ring of auxiliary wires around the perimeter of the multi-lumen-conduct might be envisaged (Figure 3-11) despite the disadvantages indicated in Section 2.4. Results are presented in Section 5.1.9.3. To maximise the electrode surface and to minimise the deposited power per electrode area auxiliary electrodes can be coupled to Lead wires or interconnect layers and interleaved with therapeutic electrodes. These ideas are explored in Section 5.1.9.4.

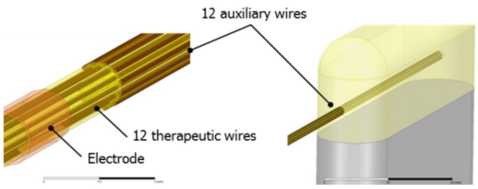

Figure 3-11 Coupling to auxiliary wires

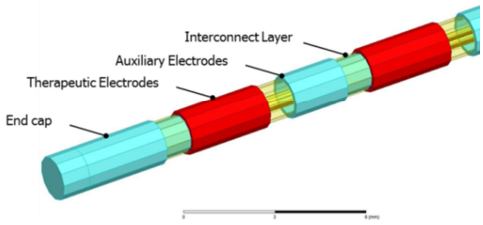

Figure 3-12 Coupling to Lead wires or interconnect layers

Further, Lead wires can be capacitive coupled to auxiliary electrodes at the IPG header increasing the number of electrodes and hence the surface area where electromagnetic energy can be drained into human tissue (Figure 3-13). This idea is investigated in Section 5.1.9.7.

Rings of capacitive coupled resistors or resistor matrices linking individual Lead wires can be integrated into the MLC to dissipate electromagnetic energy propagating along the Lead wires (Figure 3-14). The resistor matrices can be placed at the distal or proximity end or at any location in between.

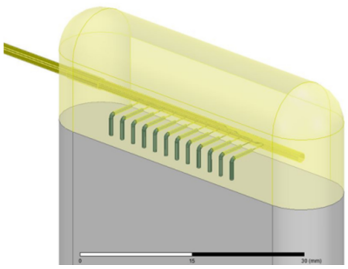

Figure 3-13 Lead wires capacitive coupled to auxiliary electrodes in IPG

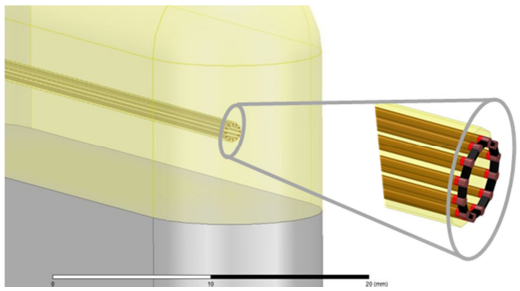

Figure 3-14 Lead wires capacitive coupled to resistor ring in IPG

Instead of interleaving auxiliary electrodes with therapeutic electrodes auxiliary electrodes can be placed along the MLC (Figure 3-15). The idea is analysed in Section 5.1.6.7.

Using a short distal end extension (Figure 3-16) and routing all wires up to the distal end instead of terminating them at the respective electrodes is analysed in Section 5.1.9.8.

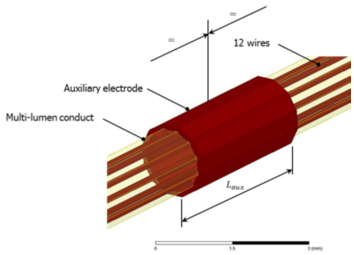

Figure 3-15 Auxiliary electrode

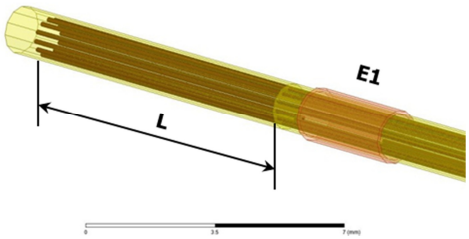

Figure 3-16 Lead wire extension

3.2 Simulated and/or tested configurations

The base cases and design variations have been numbered and those presented in this document are summarised in the following tables for future reference. Specific configurations refer to both, changes in constituent parts of the spinal cord stimulator (IPG and Lead) and changes applied to the EM model. Simulation and measurement results are presented in Chapter 5.

Base configuration

The base configuration (base case) refers to a Saluda Medical IPG case and header and a Lead with 12 electrodes that has not been modified apart from the termination of Lead wires at the proximity end and the length of the MLC.

Common configuration:

- IPG
- 12 Lead wires
- 12 therapeutic electrodes

Ref. number	Specific configuration
UM01	• Wires open ended in IPG header • No double layer around electrodes • No boundary layer around MLC
UM02	• Wires grounded to IPG case • No double layer around electrodes • No boundary layer around MLC
UM03	• Wires grounded to IPG case • Double layer around electrodes • Boundary layer around MLC
UM04	• Wires open ended in IPG header • Double layer around electrodes • Boundary layer around MLC

Table 3-1 Base configurations

Design variations

Single or multiple design variations outlined in the previous section have been applied to the base case. The configurations are synthesised below.

Coiled Electrodes

Common configuration:

- IPG
- 12 Lead wires
- 12 coiled therapeutic electrodes

Ref. number	Specific configuration
DV00	• Wires open ended in IPG header
DV0A	• Wires grounded to IPG case

Table 3-2 Design variations - coiled electrodes

Auxiliary filars

Ref. number	Configuration
DV11	• IPG • 12 Lead wires • 12 therapeutic electrodes • 12 open ended auxiliary wires along MLC • Wires open ended in IPG header

Table 3-3 Design variations - auxiliary filars

Angular position of Lead wires in MLC

Common configuration:

- IPG
- 12 Lead wires
- 12 therapeutic electrodes
- Wires grounded to IPG case

Ref. number	Specific configuration
DV16	• Angular orientations of therapeutic electrodes and wires CW 1 11 8 3 7 9 2 10 5 4 6 12
DV17	• Angular orientations of therapeutic electrodes and wires CW 1 2 4 6 8 10 12 11 9 7 5 3

Table 3-4 Design variations - angular position of Lead wires

Number of Lead wires and therapeutic and auxiliary electrodes

Ref. number	Configuration
DV07B	• IPG • 12 ... 1 Lead wires • 12 ... 1 therapeutic electrodes capacitive coupled to shield layer • 13 ... 2 interleaved auxiliary electrodes connected to shield layer at distal end • Continuous interconnect shield layer at distal end • Wires open ended in IPG header

Table 3-5 Design variations - number of Lead wires and electrodes

Interleaved therapeutic & auxiliary electrodes

Common configuration:

- IPG
- 12 Lead wires

Ref. number	Specific configuration
DV07A	• 12 therapeutic electrodes capacitive coupled to shield layer • 13 interleaved auxiliary electrodes connected to shield layer at distal end • Separate shield layers for therapeutic / auxiliary electrode pairs • Wires open ended in IPG header
DV08	• 12 therapeutic electrodes capacitive coupled to shield layer • 13 interleaved auxiliary electrodes connected to shield layer at distal end • Separate shield layers for therapeutic / auxiliary electrode pairs • Wires grounded to IPG case
DV08B	• 12 therapeutic electrodes • 12 interleaved auxiliary electrodes capacitive coupled to Lead wires • Wires grounded to IPG case

Table 3-6 Design variations - interleaved therapeutic and auxiliary electrodes

Auxiliary electrodes integrated into IPG header

Common configuration:

- IPG
- 12 Lead wires (600 mm)
- 12 therapeutic electrodes

Ref. number	Specific configuration
DV08C0	• Lead wires capacitive-coupled (C=330 pF) to 2.5 mm long wires in IPG header
DV08C1	• 12 interleaved auxiliary electrodes capacitive coupled to Lead wires • Lead wires capacitive-coupled (C=330 pF) to 5 mm long wires in IPG header
DV08C2	• 12 interleaved auxiliary electrodes capacitive coupled to Lead wires • Lead wires capacitive-coupled (C=330 pF) to 2.5 mm long wires in IPG header

Table 3-7 Design variations - auxiliary electrodes integrated into IPG header

Resistor matrix integrated into IPG header

Common configuration:

- IPG
- 12 Lead wires (600 mm)
- 12 therapeutic electrodes
- 12 interleaved auxiliary electrodes capacitive coupled to Lead wires

Ref. number	Specific configuration
DV08C3	• Lead wires capacitive-coupled (C=330 pF) to isolated ring of 100 Ohm resistors in IPG header
DV08D1	• 12 additional auxiliary electrodes capacitive coupled to Lead wires (C=100 pF; length: 2 mm; spacing: 7 mm) • Lead wires capacitive-coupled (C=330 pF) to isolated ring of 100 Ohm resistors in IPG header

Table 3-8 Design variations - resistor matrix integrated into IPG header

MLC extension at distal end

Ref. number	Configuration
DV08H1	• IPG • 12 Lead wires (600 mm) • 12 therapeutic electrodes • 12 wire extensions at distal end open ended in Pellethane (10, 20, 30, 40, 50 mm) • Lead wires capacitive-coupled (C=330 pF) to 2.5 mm long wires in IPG header

Table 3-9 Design variations - distal end extension

MLC extension at distal end and resistor matrix

Common configuration:

- IPG
- 12 Lead wires (600 mm)
- 12 therapeutic electrodes
- 12 wire extensions at distal end
  open ended in Pellethane (10 mm)
- Plane wave excitation

Ref. number	Specific configuration
DV08H2	• Lead wires capacitive-coupled (C=330 pF) to isolated ring of 100 Ohm resistors in IPG header
DV08H3	• Lead wires capacitive-coupled (C=330 pF) to isolated ring of 30 Ohm resistors in IPG header

Table 3-10 Design variations - distal end extension and resistor matrix

MLC extension, resistor matrix, auxiliary electrodes

Common configuration:

- IPG
- 12 Lead wires (600 mm)
- 12 therapeutic electrodes
- 2 additional auxiliary electrode at 250 mm and 350 mm
  12 wires capacitive coupled to auxiliary electrodes
  C=100 pF; L=2 mm
- Lead wires capacitive-coupled (C=330 pF) to isolated ring of 100 Ohm resistors in IPG header
- Length 600 mm

Ref. number	Specific configuration
DV08L1_50_DEE	• 12 wire extensions at distal end open ended in Pellethane (50 mm) • Distal End Excitation
DV08L2_30_DEE	• 12 wire extensions at distal end open ended in Pellethane (30 mm) • Distal End Excitation
DV08L3_10_DEE	• 12 wire extensions at distal end open ended in Pellethane (10 mm) • Distal End Excitation
DV08L3_10_CEE	• 12 wire extensions at distal end open ended in Pellethane (10 mm) • Centre Excitation
DV08L3_10_PEE	• 12 wire extensions at distal end open ended in Pellethane (10 mm) • Proximity End Excitation

Table 3-11 Design variations - distal end extension, resistor matrix and aux. electrodes

Configuration tested in 3T MRI scanner

Ref. number	Configuration
DV08L3_10_MRI_3T_01	• IPG • 12 Lead wires (600 mm) • 12 therapeutic electrodes • 12 wire extensions at distal end open ended in Pellethane (10 mm) • 2 additional auxiliary electrode at 250 mm and 350 mm 12 wires capacitive coupled to auxiliary electrodes C=100 pF; L=2 mm • Lead wires capacitive-coupled (C=330 pF) to isolated ring of 100 Ohm resistors in IPG header • Length 600 mm • 37 MRI, Phantom Torso, centre line, height 45 mm, 2 W/kg

Table 3-12 Design variation tested in 3T MRI scanner

4. Methods

4.1 Electromagnetic modelling

4.1.1 Overview

This chapter outlines the EM design flow, and describes the EM models for harmonic and transient stimulus. The design flow for solving the set of equations that describe wave propagation and diffusion is presented in Section 4.1.2. The models and setup for harmonic stimulus, i.e. models for RF induced heating, are outlined in Section 4.1.3. Section 4.1.4 describes the RF sources used to illuminate the problem domain. In Section 4.1.5 models and setup for transient stimulus, i.e. models for stimulus induced artefacts, are presented. This chapter concludes with Section 4.1.6 showing typical mesh parameters and mesh sizes.

4.1.2 Electromagnetic design flow

Electromagnetic simulations have been carried out with the software package referenced in Section III Software. The design parameter for electromagnetic problems are summarised in Figure 4-1. The solution type determines whether steady state or transient solutions are calculated and the type of quantity that is determined: modal or terminal s-parameter, resonance frequencies, resonance currents and voltages, terminal voltages and currents, and /or field quantities. The geometric model includes geometrical dimensions and material assignments of the object whereas geometric non-model objects include lines, faces and volumes for post

processing, e.g. field quantities along lines or on surfaces, loss densities and stored energy in volumes, or power transfer through surfaces.

Meshing is the process of creating a discrete representative model of the object. The boundary conditions determine how waves impinging on the encapsulating surface of the analysis domain are treated.

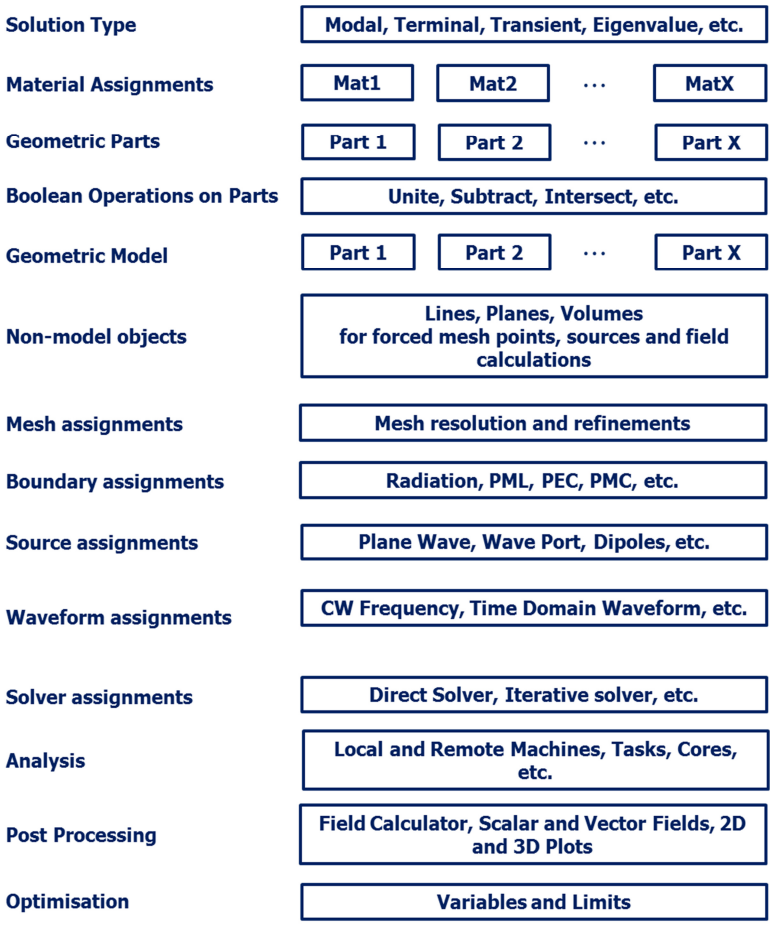

Figure 4-1 Electromagnetics - design parameter

For example, waves can be (partially) reflected or absorbed. Sources launch a wave or signal into the analysis domain. Source types are planar waves, arbitrarily shaped wave ports, or electric or magnetic dipoles. The waveform can be assigned in the frequency or time domain. The type of matrix solver determines memory requirements. A general guideline is that a direct solver requires more memory and is faster compared with an iterative solver that requires less memory and more time. The analysis can

be carried out on a single machine or on a cluster of machines. The design flow is outlined in Figure 4-2.

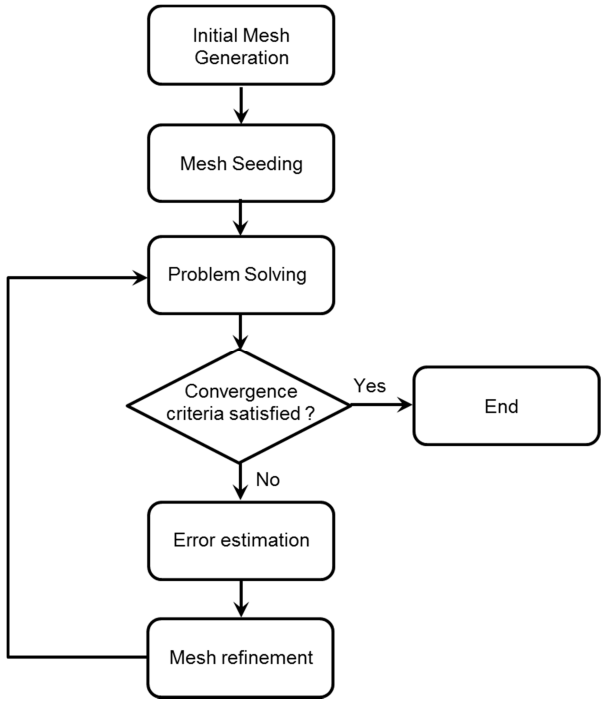

Figure 4-2 Electromagnetics - design flow (adapted from [SW1])

The initial mesh is generated using a Delaunay independent patch conforming tetrahedral assembly mesher with advancing-front point insertion technique used for mesh refinement. The underlying meshing algorithm is outlined in Reference [P142]. The initial mesh settings are summarised in Table 4-1. The initial mesh (Reference [SW4]) is refined using length, surface and volume constraints (mesh seeding). Model resolutions for electrodes and double layers have been manually adjusted. Length and surface based mesh vertices have been added for electrodes, Lead wires and the MLC and volume based mesh vertices have been added for the saline solution. In addition, forced mesh points along the MLC and Lead wires have been introduced using non-model objects.

Mesh Control	**Parameter**
Relevance Center	Medium
Smoothing	Medium
Transition	Fast
Span Angle	Coarse
Transition ratio	0.272
Inflation algorithm	O-grid based
Collision avoidance	Stair stepping
Shape checking	Based on element volume, face warping, and face angle

Table 4-1 Electromagnetics - initial mesh settings

The Galerkin method ([B23], [B30], [B31], [P144]) is used to transform Maxwell's differential equations for a tetrahedral unit cell into an element matrix and the Finite Element Method ([B32], [B33]) is used to assemble all tetrahedral unit cells into a global matrix. The global matrix is solved using one of the following solvers (algorithms):

- for plane wave and modal steady state analysis
    - Direct Matrix Solver (DMS) using Gaussian Elimination Algorithms (GEA) based on LU matrix decomposition as described in Reference [P147]
    - Iterative Matrix Solver (IMS) as described in References [P140] and [P150]
- for transient analysis
    - Transient Implicit Solver (TIS) using the finite element time domain (FETD) method with implicit time stepping as described in Reference [B33]. The TIS is unconditional stable.

Depending on convergence criteria (see Table 4-3 and Table 4-5) and error estimations, mesh sizes are refined and orders of basis functions are adapted until the solution converges.

4.1.3 Models and setup for harmonic stimulus

The electromagnetic model (EM model) has evolved over time. The evolution steps are summarised in Table 4-2. The Standard Model includes material parameter for MLC, Lead wires, electrodes, IPG case and header, and gelled saline as outlined in Appendices A.2, A.3 and A.5. A Boundary Layer (BL) around the MLC and a Double Layer (DL) around electrodes has been added later on. Finally, a conductivity tensor has been added for gelled saline.

	Standard Model	Boundary Layer	Double Layer	Conductivity Tensor
EM Model #1	X			
EM Model #2	X	X	X	
EM Model #3	X	X	X	X

Table 4-2 EM model - evolutions

4.1.3.1 Spinal Cord Stimulator

The models created for harmonic stimulus focus on the responses of Spinal Cord Stimulators (SCS) exposed to electromagnetic waves encountered in 3T MRI scanners (128 MHz). The geometrical model is shown in Figure 4-3 and is composed of the IPG, the MLC with Lead wires and the distal end (DE) electrodes.

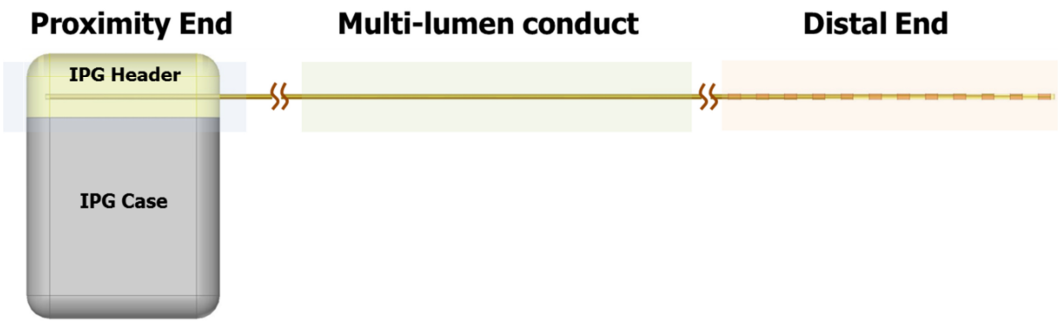

Figure 4-3 Model - Electromagnetics - IPG and Lead

The distal end section with electrode numbering is shown in Figure 4-4.



Figure 4-4 Model - Electromagnetic - Distal End and Electrode numbering

Included in EM models #2 and #3 are IPG case and IPG header (Figure 4-3), MLC including boundary layer (Figure 4-5), centre and Lead wire conducts and stylet plug (Figure 4-6), Lead wires, and electrodes including a double layer (Figure 4-7).

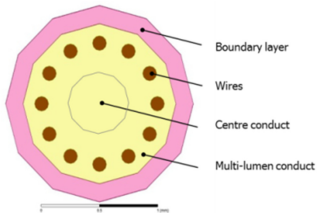

Figure 4-5 Model - Electromagnetics - MLC with boundary layer

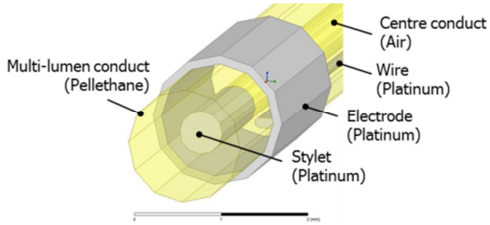

Figure 4-6 Model - Electromagnetics - Electrode at distal end

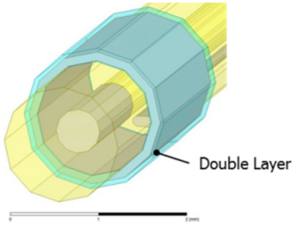

Figure 4-7 Model - Electromagnetics - Double layer around electrode

The analysis settings for harmonic stimulus are summarised in Table 4-3. The convergence criteria for the matrix solver have been set to 2% for maximum s-parameter variations and/or maximum energy variations between two iteration steps. Depending on the analysis scenario different types of EM sources have been used. Boundary conditions have been adapted to optimise simulation speed and accuracy. A linear interpolation has been chosen to determine field values from calculated nodal values.

Parameter	Setting
Solution Type	Incident wave or modal
Sources	Plane wave, magnetic or electric dipole, or wave port
Convergence criteria	Max. delta S < 0.02 or max. delta E < 0.02
Boundaries	PEC, PML, and/or radiation
Basis Function	First order
Solver	Direct or Iterative Solver

Table 4-3 Analysis settings - harmonic stimulus

If not otherwise stated simulation results for harmonic stimulus are given for ...

- a sinusoidal linear polarised incident electric field of 1 $\frac{V}{m}$ at 128 MHz
- the total electromagnetic field, i.e. the superposition of incident and scattered electromagnetic fields
- field quantities along the multi-lumen to saline and the electrode to saline boundary

4.1.3.2 MRI RF coils and phantom torso

The objective is to determine local electric field strengths along a given path inside a phantom torso filled with gelled saline caused by a 3T MRI scanner. The fields from the RF coils should result in an average SAR of $2.0\ \frac{W}{kg}$ within the phantom torso. The path of interest follows the path of the epidural space in humans. The location of the epidural space can be estimated from the body surface area [P71] and statistical data [P173]. For a person with Body Mass Index (BMI) of 20 $\frac{kg}{m^2}$ the location of the epidural space is approximately 38 mm inside the human body measured from the dorsomedial side.

For the analysis in subsequent chapters the location of Path EDS is 45 mm above the bottom of the phantom torso. The simulation settings are shown in Figure 4-8 and are equivalent to a 3T MRI scanner with a bore

diameter of 600 mm. The centre of the phantom torso is located 70 mm below the iso-centre of the bore (Figure 4-9).

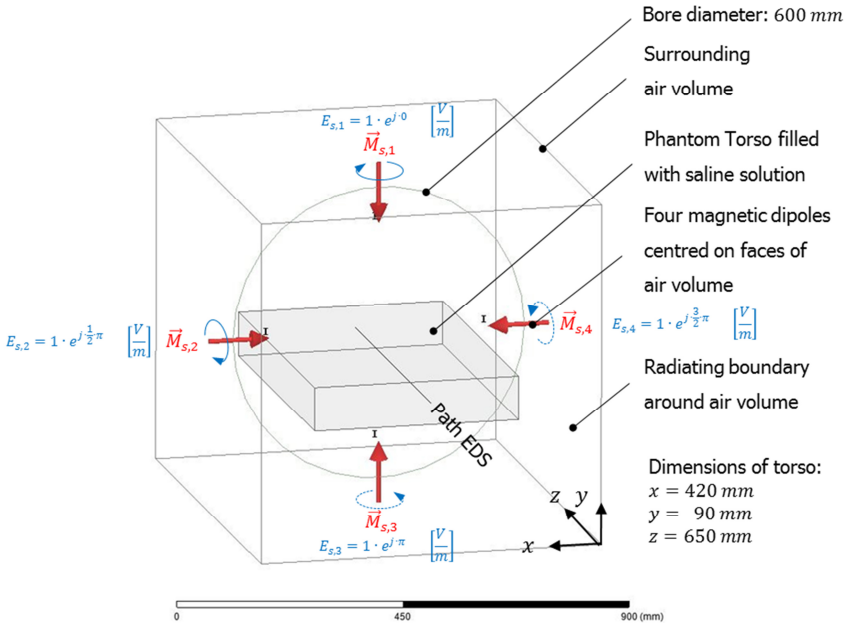

Figure 4-8 Field sources ($\varphi = 0$), phantom torso and location of Path EDS

Sources are magnetic dipoles with magnetic polarisation vector $\vec{M}_{s,x}$ located 350 mm offset from the centre of the torso. The tangential field strength of the magnetic dipole is set to $E_{s,x} = E_{s,mag} \cdot e^{j(\varphi+\varphi_x)}$ per source where $E_{s,mag}$ and φ_x are magnitude and phase offset, respectively.

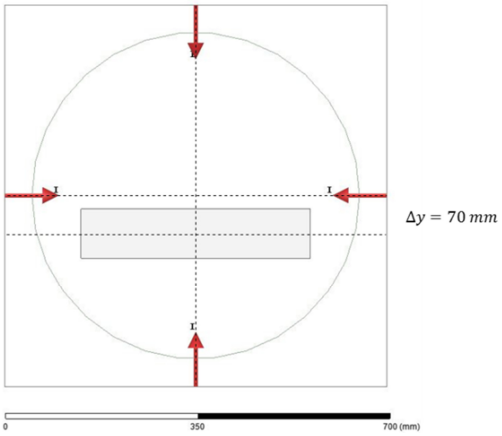

Figure 4-9 Displacement of phantom torso in MRI bore

There are four sources having indices $x = 1,2,3,4$. Further, the tangential source field strength is constant over a radius of 450 mm perpendicular to each magnetic polarisation vector.

For a circular rotating polarisation the source excitations $(\varphi = 0)$ are defined as follows ...

$$S1 \rightarrow E_{s,1} = 1\,\frac{V}{m} \cdot e^{j(0)};\; S2 \rightarrow E_{s,2} = 1\,\frac{V}{m} \cdot e^{j \cdot \frac{1}{2}\pi};$$
$$S3 \rightarrow E_{s,3} = 1\,\frac{V}{m} \cdot e^{j \cdot \pi};\; S4 \rightarrow E_{s,4} = 1\,\frac{V}{m} \cdot e^{j \cdot \frac{3}{2}\pi} \qquad (4\text{–}1)$$

The simulation results are presented in Section 5.1.10.

4.1.4 EM exposure scenarios for harmonic stimulus

Different exposure scenarios of IPG and Lead have been applied during simulation runs. First simulation runs have been carried out using a full plane wave excitation described in Section 4.1.4.1. Later on, simulation runs have been carried out using partial plane wave excitations at the distal and proximity end and half way between the distal and proximity end (Section 4.1.4.2). These excitation scenarios are similar to the excitation scenarios used in the table top RF heating test bed described in Section 4.3.7. The distal end RF excitation scenario is representative for typical RF excitation scenarios encountered in MRI scanners where the distal end is more exposed than the proximity end.

4.1.4.1 Full plane wave excitation

The saline is illuminated with a linear polarised time-harmonic electric field of 1 V/m (peak) that is constant throughout the volume of the saline as shown in Figure 4-10.

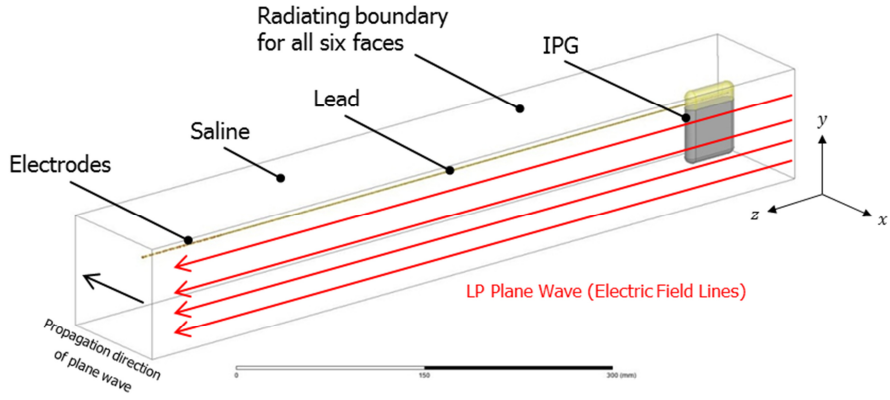

Figure 4-10 Full plane wave excitation scenario

The incident field generates a scattered field on the IPG surface, along the MLC and around the electrodes. Both, incident and scattered fields superimpose and create the total field. The total field generates surface and volume currents whereas the volume currents provoke local temperature increases in human tissue (gelled saline).

4.1.4.2 Partial plane wave excitation

Here, the saline is illuminated with four sources that create amplitude and phase distributions equivalent to the dipole array conceived for the RF heating test bed. The location of IPG, MLC and electrodes with respect to the sources is indicated in Figure 4-11, Figure 4-12, and Figure 4-13 for distal end, centre, and proximity end excitation, respectively.

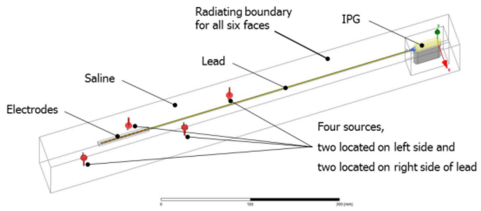

Figure 4-11 Distal end excitation
Locations of sources

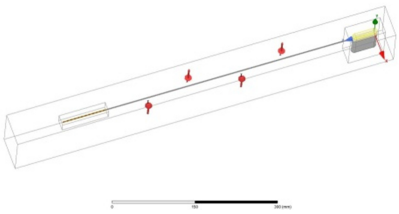

Figure 4-12 Centre excitation
Locations of sources

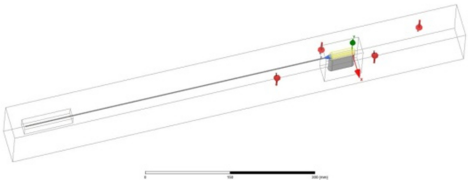

Figure 4-13 Proximity end excitation
Locations of sources

Electromagnetic waves are travelling along the MLC towards the distal and proximity end and are reflected. Two common mode waves and 12 differential mode waves have to be distinguished.

The two common mode waves propagate simultaneously in two thin annular layers, one layer is located between the ring of Lead wires and the perimeter of the MLC and the other layer is located in a boundary layer formed around the MLC. The dominant common mode is a quasi-coaxial TEM mode with transversal radial electric field components and transversal angular magnetic field components. The second common mode is an E-Mode with a longitudinal electric field in the boundary layer and surrounding tissue (saline). The common modes are explored in Section 5.1.6.4.

The differential modes are excited and propagate between wires of the MLC in case of unequal wire lengths or unequal terminations of wires at the distal and proximity end. The differential modes are explored in Section 5.1.7.

Common modes face significant attenuation compared with differential modes. The common modes are attenuated due to the conductive tissue (saline) surrounding the MLC whereas the differential modes are predominately attenuated due to the dielectric loss of the MLC.

The induced scattered field distributions around the electrodes are quite different for distal end, central, and proximity end excitation. The three scenarios are shown Figure 4-14, Figure 4-15, and Figure 4-16.

For distal end excitation the electrodes capture most of the incident electromagnetic wave energy and waves are propagating from the distal end towards the proximity end where they are reflected.

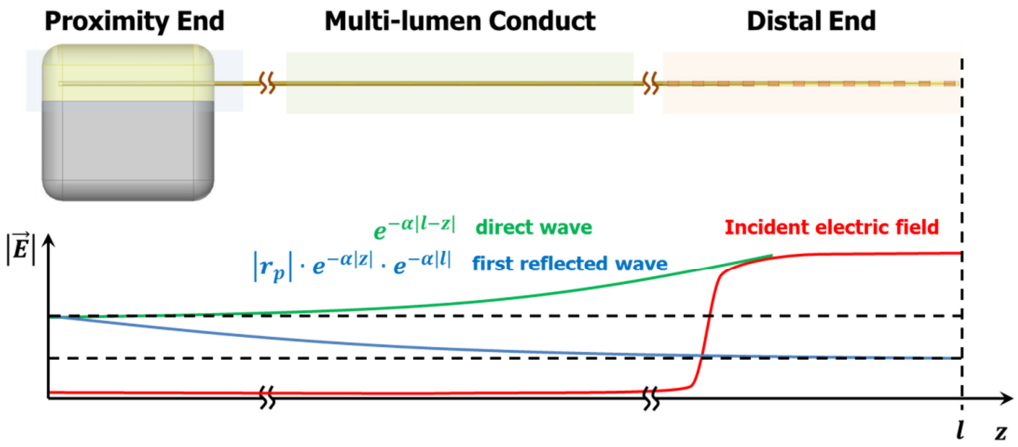

Figure 4-14 Distal end excitation - reflections of waves

For centre excitation waves travel towards the distal and proximity end where they are reflected. The electrodes are not directly exposed.

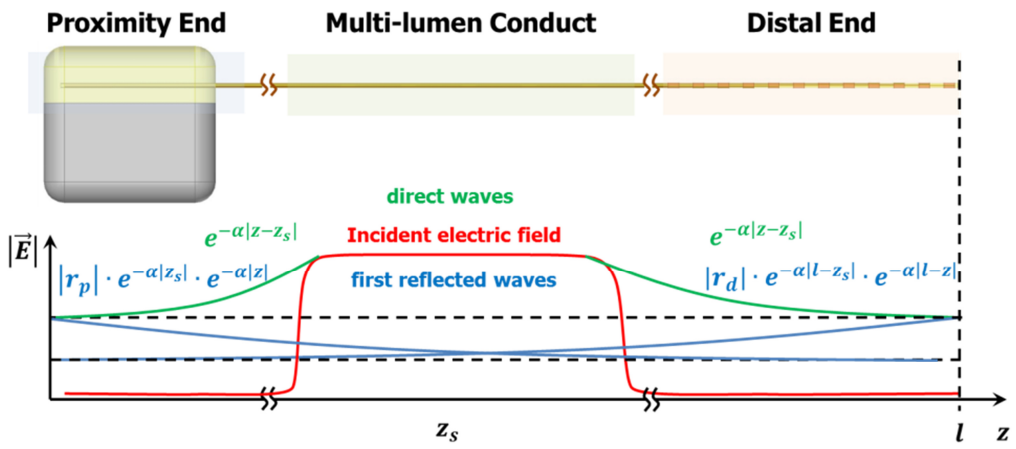

Figure 4-15 Centre excitation - reflections of waves

And finally, for proximity end excitation the waves travel towards the distal end where they are reflected. Electrodes are not directly exposed to the incident field but standing waves form over a short section at the distal end.

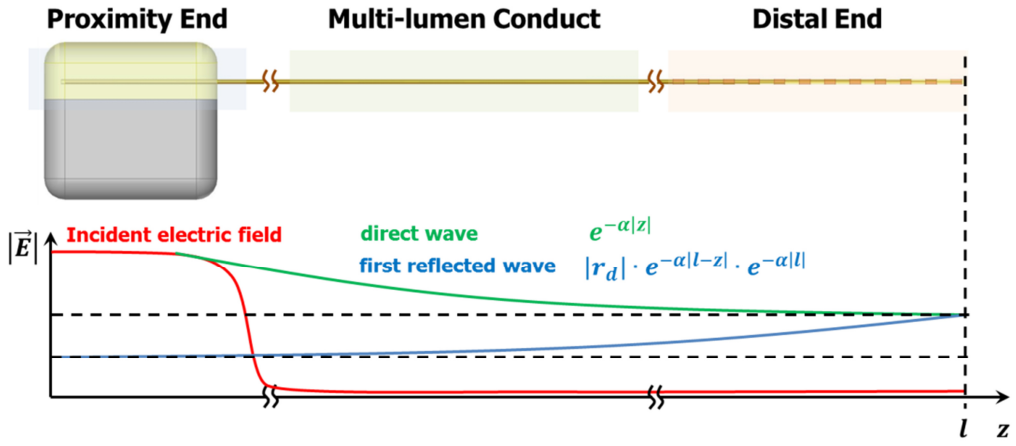

Figure 4-16 Proximity end excitation - reflections of waves

Several equivalent sources have been used to partially excite the Lead, primarily to cope with limited computing resources. Apart from a magnetic dipole array, a wave port array and a dipole array have been used. Equivalence is with respect to driving electric and magnetic field magnitudes and phases and power deposition inside a volume element around the distal end.

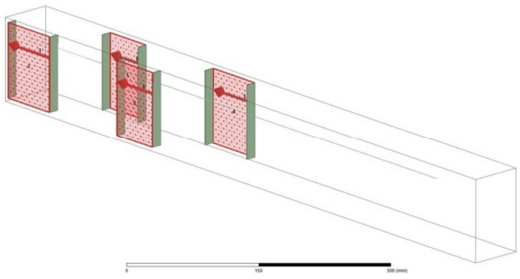

Figure 4-17 Equivalent wave port array

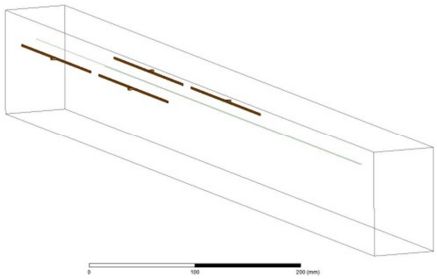

Figure 4-18 Equivalent dipole array

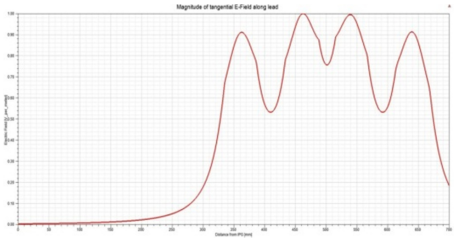

Figure 4-19 Magnitude of incident tangential electric field along Lead for a time-harmonic electric field of 1 V/m (peak)

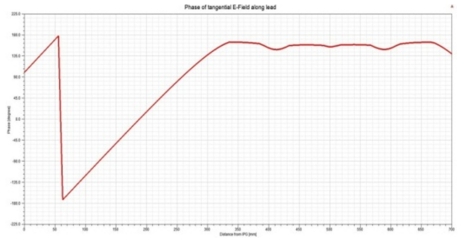

Figure 4-20 Phase of incident tangential electric field along Lead for a time-harmonic electric field of 1 V/m (peak)

4.1.5 Models and setup for transient stimulus

For transient simulations, i.e. for stimulus induced artefact predictions, only the distal end with therapeutic electrodes and their double layers and the boundary layer around the MLC has been taken into account (Figure 4-21). Two transmit and two receive wires have been selected from the bundle of 12 wires in the MLC (Figure 4-22). The pulse pattern has been injected through a wave port into Electrodes E01 and E02 (Figure 4-23). Source wire resistors of 1 Ohm each have been added to Wire W01 and W02. The polarity of the transmit voltage is defined from W01 to W02 and the currents are injected into the wave port. Artefacts are detected between Electrodes E04 and E07. The polarity of the receive voltage is from W04 to W07 and receive currents are defined as shown in Figure 4-24. The receive wires W04 and W07 are terminated in a variable differential resistance and the remaining (idle) wires are shorted together close to the wave port.

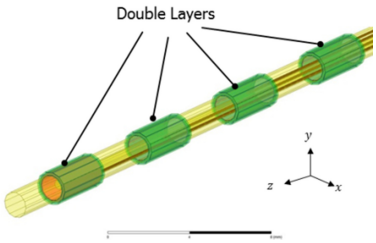

Figure 4-21 Electrodes with double layers at distal end

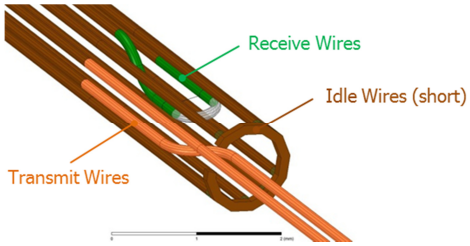

Figure 4-22 Transmit and Receive Wires

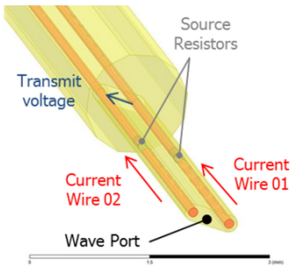

Figure 4-23 Transmit wires feeding Electrodes E01 and E02

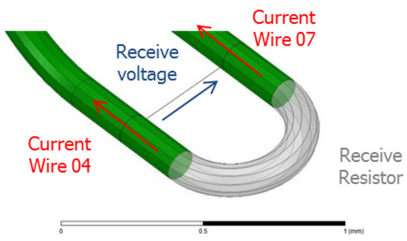

Figure 4-24 Receive Wires from Electrodes E04 and E07

Several pulse patterns have been applied. Monophasic pulse patterns are shown in Figure 4-25 and Figure 4-26 and biphasic pulse patterns are shown in Figure 4-27 and Figure 4-28.

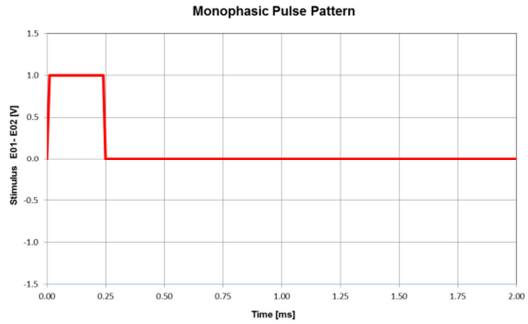

Figure 4-25 Transmit voltage of +1.0 Volt applied between E01 and E02

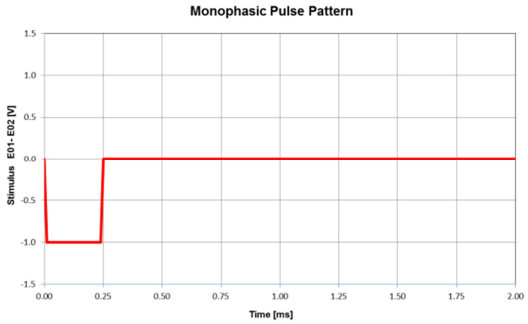

Figure 4-26 Transmit voltage of -1.0 Volt applied between E01 and E02

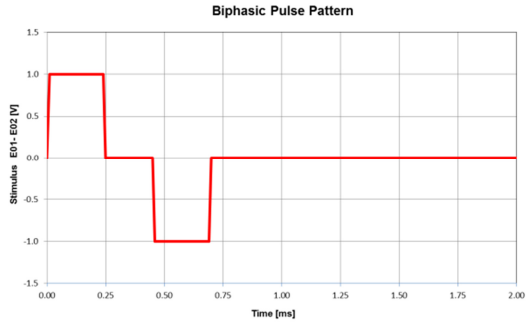

Figure 4-27 Transmit voltage of +1.0 / - 1.0 Volt applied between E01 and E02

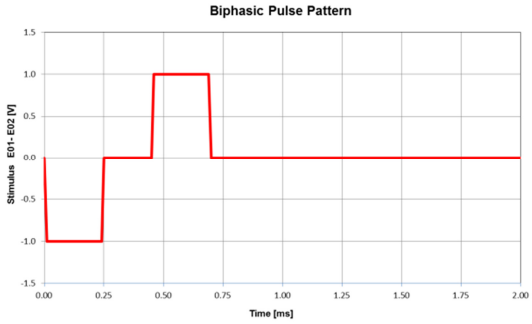

Figure 4-28 Transmit voltage of -1.0 / + 1.0 Volt applied between E01 and E02

The parameters applied for the double layer around electrodes in transient simulations are given in Table 4-4. For pulse voltages of $\pm 2\,V$ the resistances have been extracted from DC voltage and current measurements (Section 5.2.2) and for pulse voltages of $\pm 4\,V$ from transient responses (Section 5.2.3). The capacitances have been extracted from calculations and measurements carried out in Reference [P18].

Maximum Pulse Voltage $[V]$	Double Layer Resistance $[Ohm]$	Double Layer Capacitance $[\mu F]$
$\pm 2\ V$	$10'100$	2.50
$\pm 4\ V$	105	2.50

Table 4-4 Double layer parameter

The analysis settings for transient stimulus are summarised in Table 4-5.

Parameter	**Setting**
Solution Type	Transient
Sources	Wave Port
Convergence criteria	Max. delta S < 0.02 or max. delta E < 0.02
Boundaries	Perfect E and/or Radiation
Basis Function	First order
Solver	Implicit Solver

Table 4-5 Analysis settings - transient stimulus

The EM transient model does not take into account diffusion of charged chemical species away from or towards electrodes. Therefore, calculated slopes of field quantities will exhibit an exponential decay which is slightly steeper than a decay including diffusion of chemical species.

4.1.6 Mesh parameter for IPG and Leads

The initial mesh settings for both harmonic and transient stimulus are given in Table 4-6.

Parameter	**Setting**
Mesh method	Classic
Maximum surface deviation from curved surfaces	1 mm
Maximum normal deviation from curved surfaces	30 degrees
Maximum aspect ratio of mesh triangles	10

Table 4-6 Typical initial mesh settings

The mesh density has been refined in critical areas to increase resolution and analysis accuracy. The mesh refinements are summarised in Table 4-7.

Location	**Refinement**
Saline around distal end	max. mesh length: 2 mm
Electrodes	max. mesh length: 0.5 mm
MLC between IPG and distal end	max. mesh length: 20 mm
MLC at distal end	max. mesh length: 2 mm

Table 4-7 Typical mesh refinements

Table 4-8 summarises the maximum number of tetrahedra for constituent parts of the EM model. The total number of tetrahedra is approximately 850'000. In most cases the number of tetrahedra had to be reduced due to limitations in computational resources. Many EM simulations had to be run with less than 400'000 tetrahedra.

Part	**Number of tetrahedra**
MLC	458240
Wires	245156
Saline	96370
Centre conduct	28498
Electrodes	5438
IPG	4919

Table 4-8 Maximum number of tetrahedra for EM model

Typical surface and volume meshes for different regions are presented in the following figures.

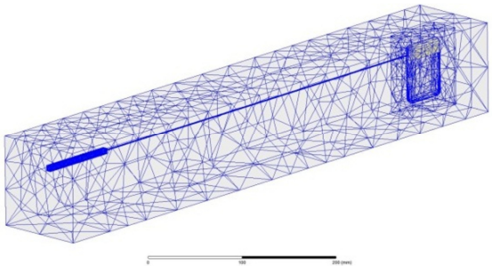

Figure 4-29 Surface mesh for saline

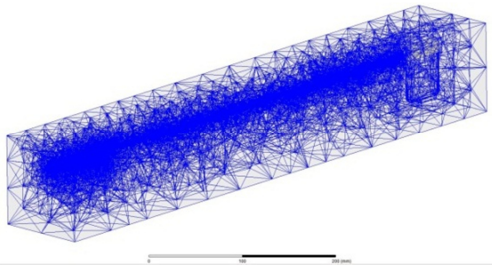

Figure 4-30 Volume mesh for saline

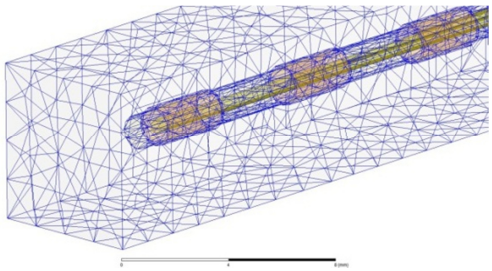

Figure 4-31 Surface mesh for saline around distal end

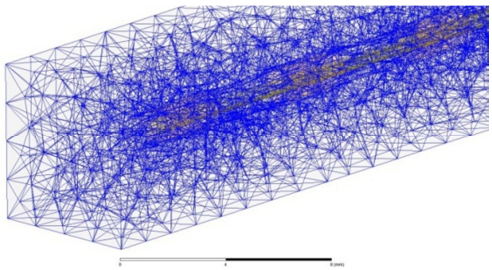

Figure 4-32 Volume mesh for saline around distal end

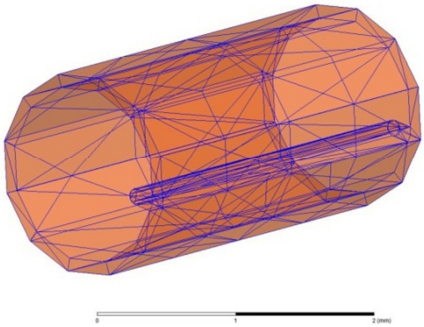

Figure 4-33 Volume mesh for electrodes

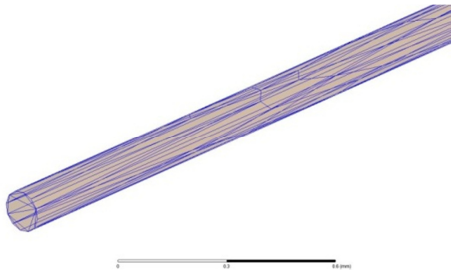

Figure 4-34 Volume mesh for wires

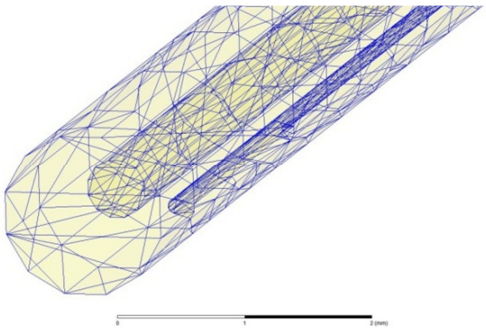

Figure 4-35 Surface mesh for isolator

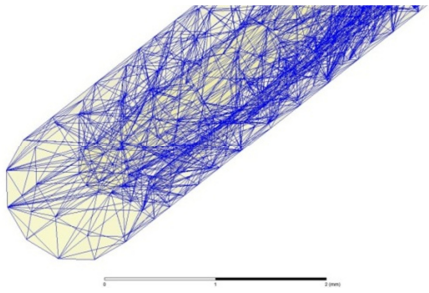

Figure 4-36 Volume mesh for isolator

4.2 Thermodynamic modelling

4.2.1 Overview

The following sections describe the thermodynamic design flow applied in this work (Section 4.2.2), models and setups for thermal analysis (Section 4.2.3), and typical mesh parameter and mesh sizes (Section 4.2.4).

4.2.2 Thermodynamic design flow

Thermodynamic simulations have been carried out with the software package referenced in Section III Software. The thermodynamic design parameter are summarised in Figure 4-37.

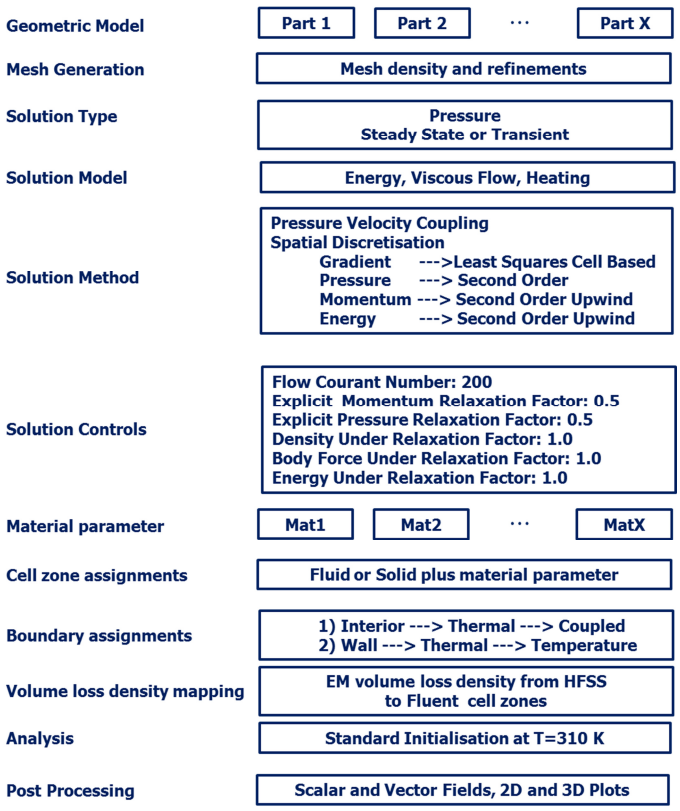

Figure 4-37 Thermodynamics - design parameter

Starting from a simplified geometric model that only includes geometries relevant to the thermal simulation a mesh is generated (see Reference [SW4]). In general, the mesh density for similar parts is higher for thermodynamic simulations compared with the mesh density for electromagnetic simulations. In low frequency electromagnetic problems the mesh density is predominately determined by the propagation constant and hence a fraction of the wavelength. For heat transfer the mesh density is determined by a fraction of the characteristic diffusion length. The wavelength in low frequency electromagnetic problems is much longer than the characteristic diffusion length for heat transfer. Hence, the mesh density is higher in heat transfer simulations. In addition, during coupled electromagnetic and thermodynamic analysis the volume loss density in voxels obtained from the electromagnetic analysis is mapped into voxels for the thermodynamic analysis. This mapping is done once at the beginning of the thermodynamic analysis. The mesh is fixed throughout the thermodynamic analysis and must be fine enough to allow for convergence over the full analysis time span.

Material properties for fluids (gelled saline) and solids (platinum, Pellethane) are assigned and linked to cell zones. Further, boundaries between cell zones as well as global boundaries are specified. In a next step, solution types, models, methods and controls are defined as well as sensor locations for temperature recordings. Finally, the volume loss density from EM simulations is mapped into volume cells of the thermodynamic model.

The mesh is generated using a Delaunay independent patch conforming tetrahedral assembly mesher ([P138], [P140], [P146], [P148]), similar to the mesher used for electromagnetic problems. But, the mesh size is fixed during the problem solving process. The mesh settings are summarised in Table 4-9. The maximum edge length for electrodes and MLC is 0.5 mm

and the maximum edge length for the surrounding saline solution is 2.0 mm.

Mesh Control	**Parameter**
Relevance Center	Medium
Smoothing	Medium
Transition	Slow
Span Angle	Fine
Transition ratio	0.272
Inflation algorithm	O-grid based
Collision avoidance	Layer compression
Shape checking	Based on orthogonal quality

Table 4-9 Thermodynamics - initial mesh settings

The thermodynamic design flow is outlined in Figure 4-38. After mapping of the EM volume loss density the problem solving process is initiated. First, the coupled system of momentum and pressure-based continuity equations is solved using a finite difference method in space and time [P143].

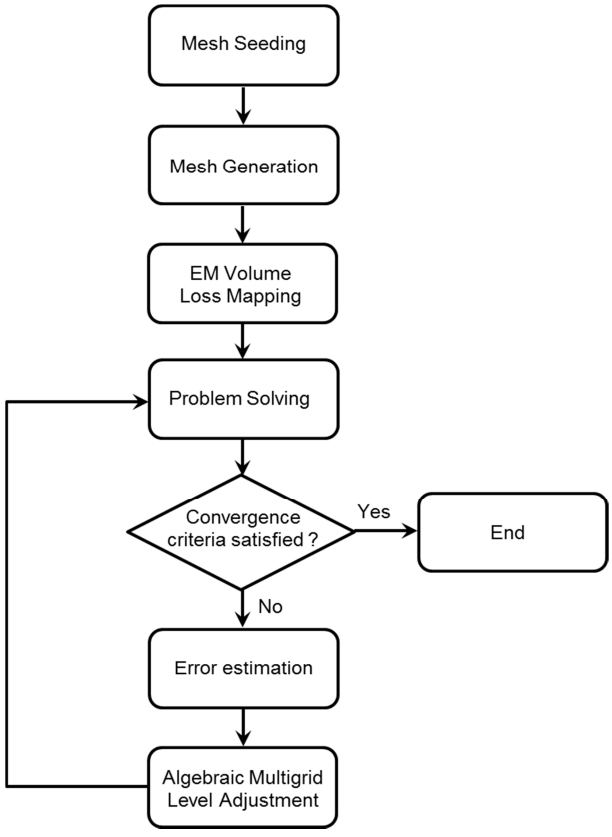

Figure 4-38 Thermodynamics - design flow (adapted from [SW2] and [SW3])

Then, mass fluxes through faces and pressure and velocity fields are determined. Next, the heat and energy equations are solved using an Incomplete Lower Upper (ILU) decomposition technique [P149]. Finally, the convergence is checked and the multigrid level will be adjusted until convergence is achieved [P145]. In this work the convergence criteria for the energy equation is 10^{-6} and for all other equations the convergence criteria is 10^{-3}.

4.2.3 Models and setup for heat dissipation

The thermodynamic model has been simplified as shown in Figure 4-39. The model includes a 20 mm x 20 mm x 89 mm gelled saline volume, a MLC and electrodes.

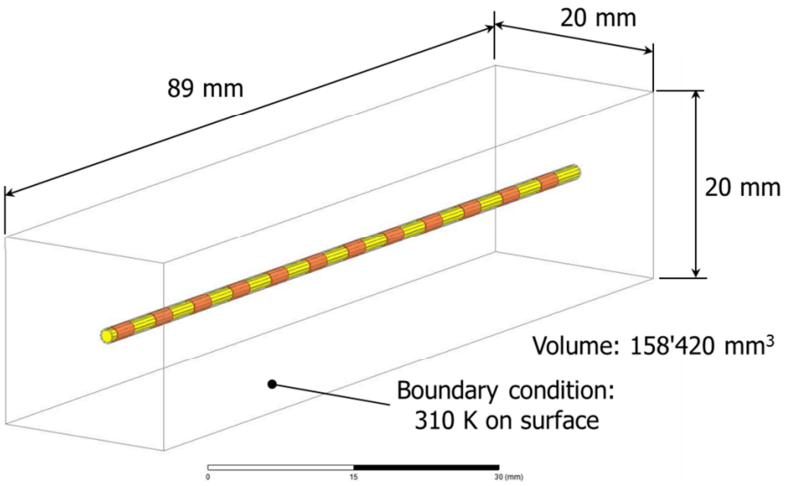

Figure 4-39 Volume with distal end and boundary conditions

The temperature sensors have been placed mid-way between the distal ends of electrodes (Figure 4-40).

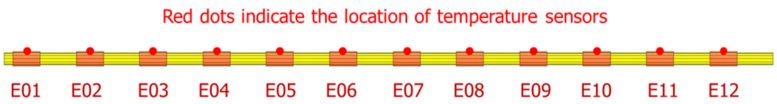

Figure 4-40 Location of temperature sensors

To account for natural convection caused by volume heat sources, the Boussinesq approximation has been applied [B34]. The approximations assume that (1) the fluid is incompressible, (2) the fluid mass is conserved, (3) the fluid mass density $\rho_0(\vec{r})$ is treated as constant apart from the buoyancy term in the momentum equation where fluid mass density is approximated by a constant term and a term that is proportional to the temperature rise, (3) small temperature changes cause small fluid density changes, (4) small fluid density changes have no (little) effect on inertial terms but strong effects on gravitational terms of the momentum equation, (5) the initial mass density $\rho_0(\vec{r})$ is isotropic, (6) the gravity $g_0(\vec{r})$ is constant, (7) the thermal expansion coefficient α_T is constant, (8) single phase, single component liquids, and (9) constant mass transport. The viscosity of gelled saline applied in the Boussinesq model is derived in Section 5.1.4. A viscosity measurement technique using miniature balls is described in Reference [P92].

4.2.4 Mesh parameter for distal end

The number of nodes and tetrahedra for the distal end volume, MLC and electrodes is given in Table 4-10. Figure 4-41 shows a section view of the mesh at the distal end. The mesh density is higher at the electrodes and slightly decreases towards the global boundary.

Part	**Number of tetrahedra**
Nodes	146'131
Elements	621'760

Table 4-10 Typical number of tetrahedra for thermodynamic model

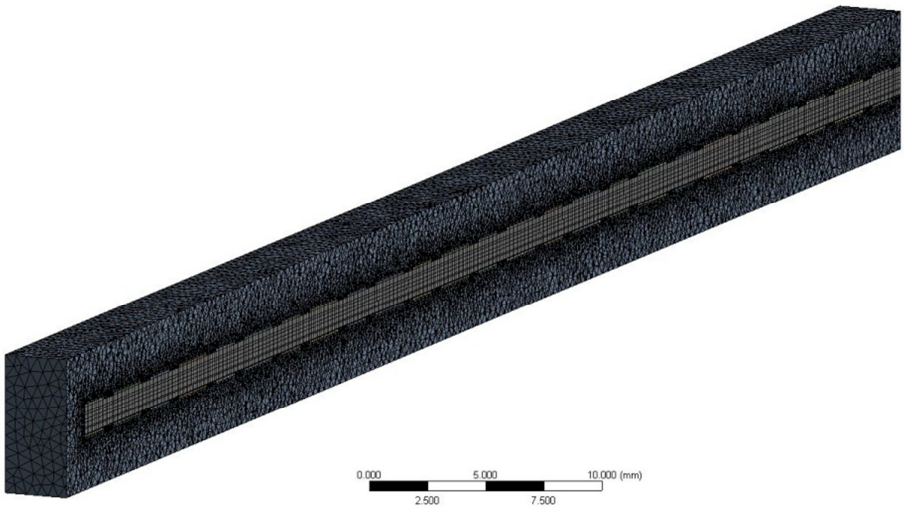

Figure 4-41 Section view of typical mesh for thermodynamic simulations

4.3 Test and measurement setups

4.3.1 Overview

This chapter describes test setups, test fixtures and test beds for model parameter extractions and benchmarking of EM and thermodynamic simulation results.

- Test setup for DC voltages, DC currents, and DC resistances of electrodes immersed in (gelled) saline solution (Section 4.3.2)
- Test setup for step responses of electrodes immersed in (gelled) saline solution (Section 4.3.3)
- Test setup for transient responses of isolated coaxial filars immersed in (gelled) saline solution (Section 4.3.4)
- Test fixture for RF permittivity and conductivity measurements of electrolytes (Section 4.3.5)
- Test bed for RF transfer function measurements along MLCs (Section 4.3.6)
- Test bed for RF induced heating of Spinal Cord Stimulators (Section 4.3.7)
- Test setup for artefact measurements caused by pulses injected into electrodes immersed in (buffered) saline solution (Section 4.3.8)

Each test bed is shortly described in subsequent sections. Measurement results obtained with these test beds are presented in Chapter 5.

4.3.2 Voltages, currents and resistances

The test and measurement equipment is summarised in Table 4-11 and the setup is outlined in Figure 4-42. A Lead with 12 electrodes is immersed in a bucket of saline solution and DC voltages and currents between electrodes are measured to determine DC resistances, sweet spots in characteristic IV curves and onset of electrolysis [B3]. The results are summarised in Section 5.2.2.

Type	Manufacturer	Model
Triple channel DC Power Supply	Tektronix	2231A-30-3
Voltage - 6.5 Digit Multimeter	Agilent	34401A
Current - 6.5 Digit Multimeter	Agilent	34401A
Resistor wheel	N/A	N/A
Saline solution $\left(\sigma = 0.188\ \frac{S}{m}\right)$	N/A	N/A
12 electrode Lead (900 mm)	Saluda Medical	N/A
Interface board	N/A	N/A

Table 4-11 Test and measurement equipment for voltages and currents

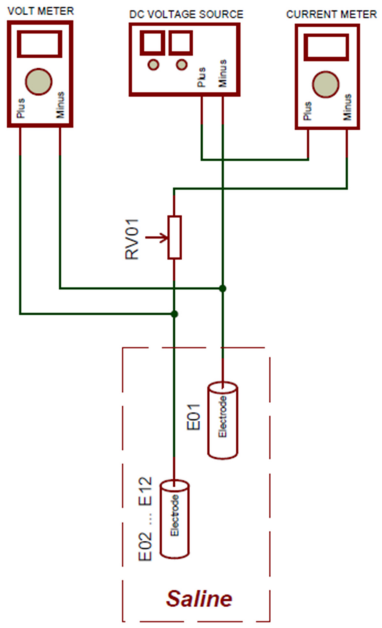

Figure 4-42 Test and measurement setup for voltages and currents

4.3.3 Step function

The test and measurement equipment is summarised in Table 4-12 and the setup is outlined in Figure 4-43. A Lead with 12 electrodes is immersed in a bucket of saline solution and the step response over resistor RV1 is measured to determine electrode double layer resistances. The results are summarised in Section 5.2.3.

Type	Manufacturer	Model
Arbitrary Function Generator with floating outputs	Tektronix	AFG3102
Oscilloscope	Tektronix	TDS2014C
Resistor wheel	N/A	N/A
Switch	N/A	N/A
Saline solution $\left(\sigma = 0.188\ \frac{S}{m}\right)$	N/A	N/A
12 electrode Lead (900 mm)	Saluda Medical	N/A
Interface board	N/A	N/A

Table 4-12 Test and measurement equipment for step function

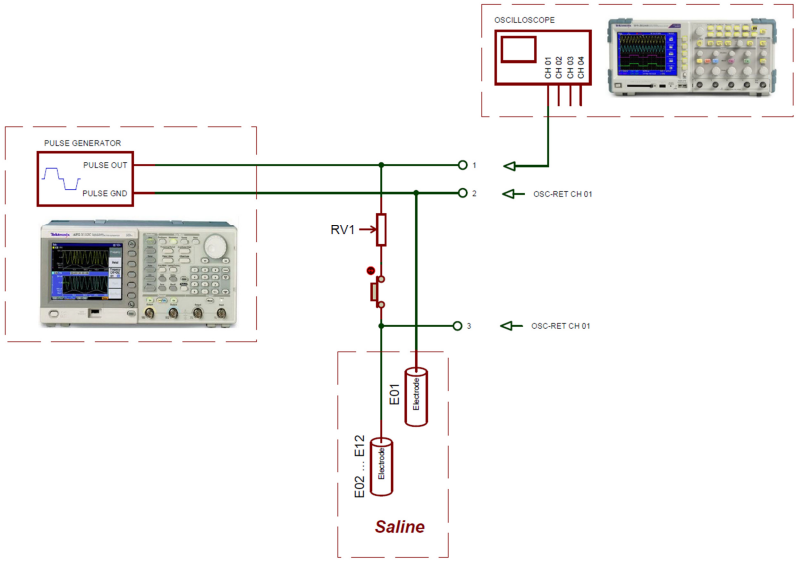

Figure 4-43 Test and measurement setup for step function

4.3.4 Time Domain Reflectometry

The test and measurement equipment is summarised in Table 4-13 and the setup is outlined in Figure 4-44. The distal end section of a connectorised coaxial cable with dismantled outer conductor is immersed in a bucket of gelled saline solution and the time domain response is measured to determine propagation velocity and distal end reflection behaviour. The results are summarised in Section 5.1.5.

Type	Manufacturer	Model
Digital Communication Analyser	Agilent	86100C
Differential TDR Module DC - 18 GHz	Agilent	54754A

Table 4-13 Test and measurement equipment for TDR

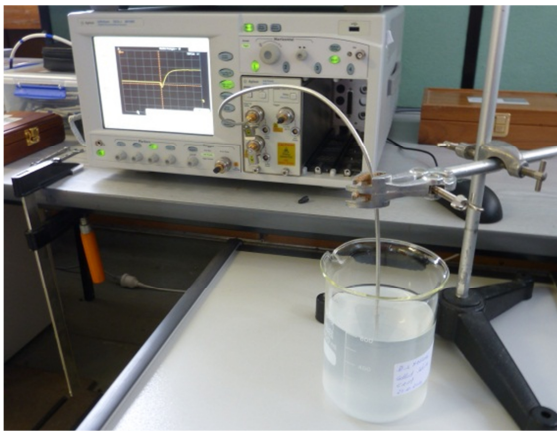

Figure 4-44 Test and measurement setup for TDR

4.3.5 Permittivity and conductivity

The test and measurement equipment is summarised in Table 4-14 and the setup is outlined in Figure 4-45, Figure 4-46, and Figure 4-47. Electrolytes are filled into a coaxial cavity of a transmission line to determine their RF permittivity and conductivity. The results are summarised in Section 5.1.3.

Type	Manufacturer	Model
Vector Network Analyser 300 kHz - 9 GHz	Agilent	E8358A
Calibration Kit Type N	Agilent	85032F
Adapters N-SMA	Pasternack	PE9081
Transmission line test fixture	Custom made	N/A

Table 4-14 Test and measurement equipment for permittivity and conductivity

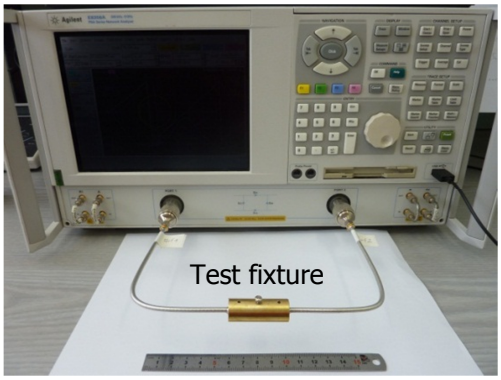

Figure 4-45 VNA with test fixture

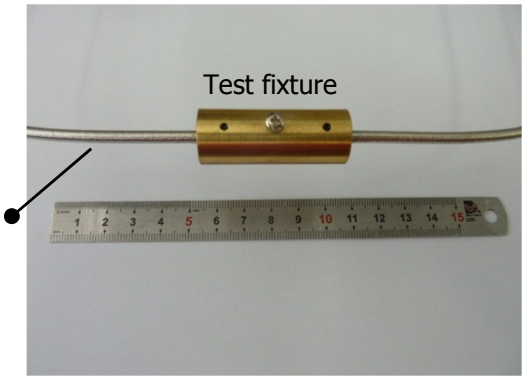

Figure 4-46 Test fixture

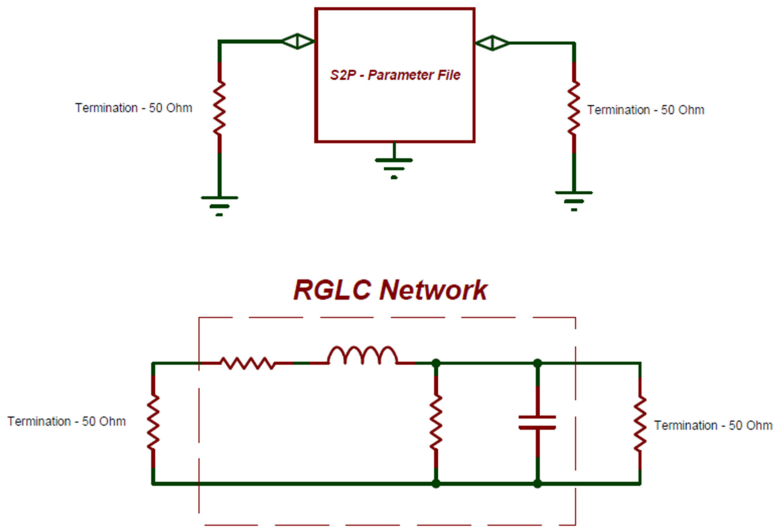

Figure 4-47 S-parameter simulation setup

The calibration has been carried out using N type calibration standards and the reference plane has been moved into the test fixture. The N to SMA adapters have a return loss of better 40 dB between 20 MHz and 200 MHz and introduce a slight calibration error. The approach applied for RF permittivity and conductivity extraction is summarised in Appendix C.2. The results are presented in Section 5.1.3.

4.3.6 RF transfer function

A table top test bed for RF transfer function measurements has been conceived. RF transfer function measurements provide insight into attenuation and phase constants of waves travelling along transmission lines. The test and measurement equipment is summarised in Table 4-15 and the test setups are outlined in Figure 4-48, Figure 4-49, and Figure 4-50. The configuration in Figure 4-49 has been used for RF amplitude and phase measurements whereas the configuration in Figure 4-50 has been used for RF amplitude measurements at the distal end (higher sensitivity of spectrum analyser).

Type	Manufacturer	Model
Vector Network Analyser 300 kHz - 9 GHz	Agilent	E8358A
Calibration Kit for VNA Type N	Agilent	85032F
Spectrum Analyser 9 kHz - 3 GHz	Agilent	E4403B
Test bed • 1 x phantom torso • 1 x wave launcher	Custom made	N/A
H-field probes	Custom made	N/A
E-field probes	Custom made	N/A
RF jumper cables (N connectors)	N/A	N/A
RF jumper cables (SMA connectors)	Mini-Circuits	N/A

Table 4-15 Test and measurement equipment for RF transfer function test bed

A MLC with 12 platinum Lead wires is centred in the phantom torso. A matched source probe injects a wave at the proximity end into the MLC and a matched detector probe senses the RF signal (amplitude and phase) along the MLC. The return loss for both probes is better than -11 dB at 128 MHz. The platinum wires are open ended and isolated from the gelled saline at the proximity end. The wires at the distal end are either open ended or shorted to the gelled saline.

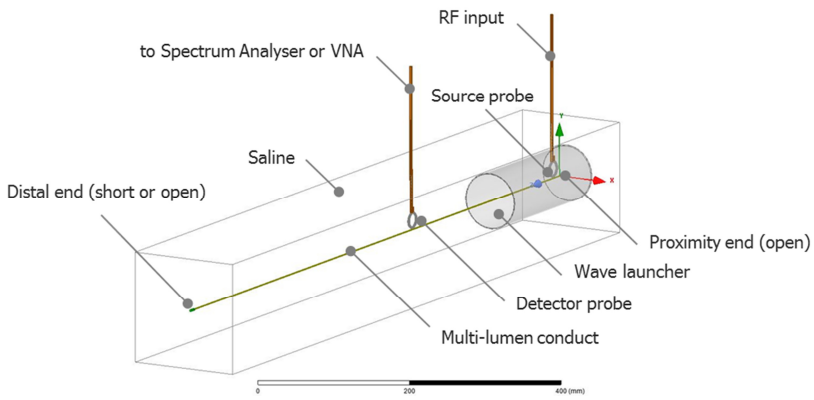

Figure 4-48 Outline of RF transfer function test bed with RF wave launcher and H-Probe(s)

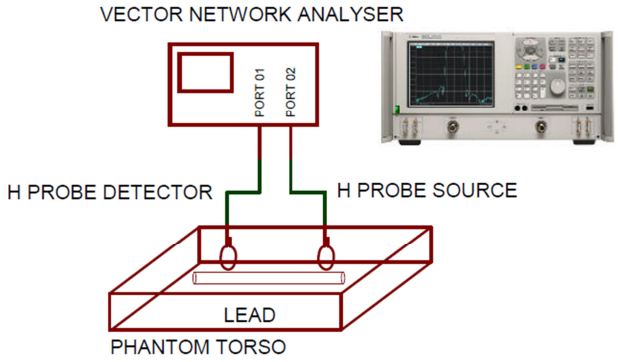

Figure 4-49 RF transfer function test bed with VNA and H-Probe(s)

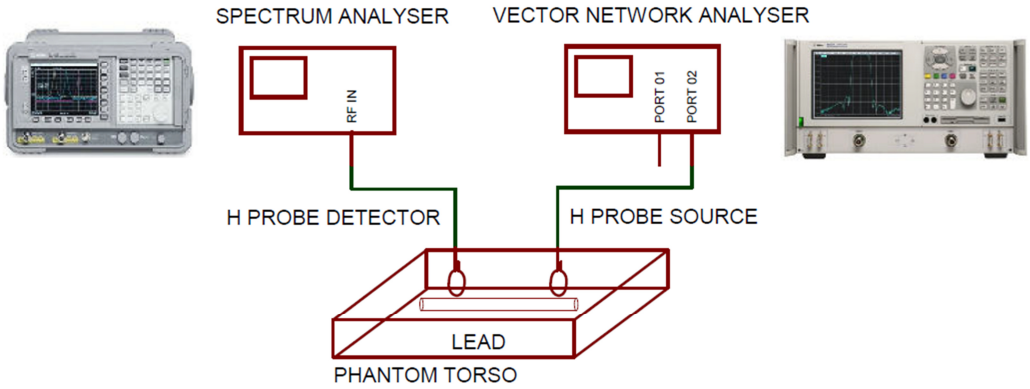

Figure 4-50 RF transfer function test bed with VNA, Spectrum Analyser and H-Probe(s)

Two types of H-Probes have been used. The first type (Figure 4-51) has been used to inject the RF signal into the MLC and to detect the TEM Mode (transversal angular H-field component) along the MLC. The loop is oriented in longitudinal direction. The second type (Figure 4-52) has been

used to detect the H-Mode (longitudinal H-field component). The loop is oriented in transversal direction. The measurement results are summarised in Section 5.1.6.4.

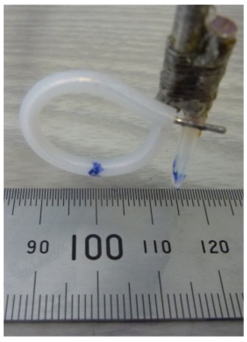

Figure 4-51 Probe orientation for TEM Mode

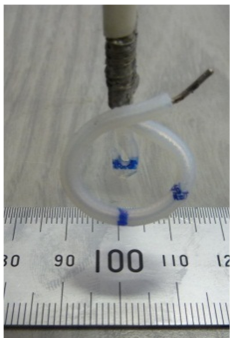

Figure 4-52 Probe orientation for H Mode

A particular problem was that the signal injected into the immersed source probe created surface currents on the outer conductor of the coaxial feed cable. The surface currents propagated along the coaxial cable and radiated from the coaxial cable into the laboratory environment. In addition, a surface wave was propagating along the gelled saline to air interface of the phantom torso. For an injected RF power of 10 dBm into the source probe the detected RF level in the lab environment above the phantom torso was about -40 dBm. The immersed matched detector probe still captured an RF signal of - 50 dBm (Figure 4-53).

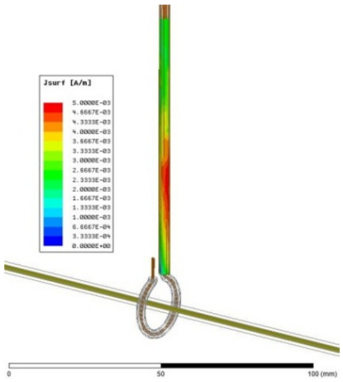

Figure 4-53 Surface currents on detector probe for transfer function test bed without wave launcher; the detector probe captures RF signals from the surrounding air about 50 dB above the weakest RF signal at the distal end of the the MLC.

The RF level of the wave propagating along the MLC is in the range between -50 dBm close to the proximity end and -100 dBm close to the distal end. In the worst case the interfering RF level is 50 dB above the desired RF level. Figure 4-54 shows a test bed simulation with source and detector probes. The surface currents on the source probe's coaxial feed cable radiate into the surrounding environment and create a strong surface wave that is propagating along the saline to air interface. The surface wave energy is captured by the detector probe leading to a strong interference signal.

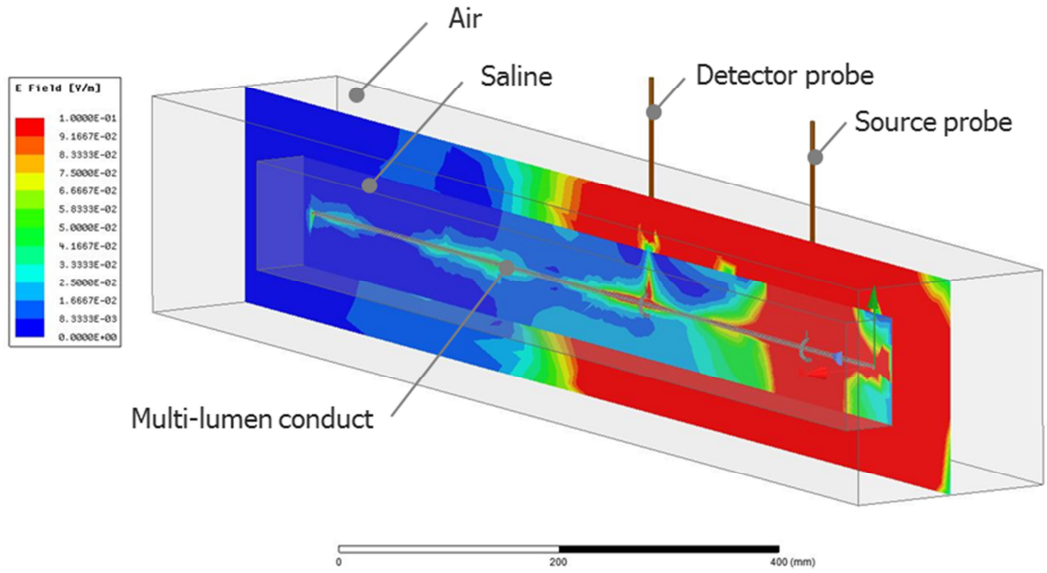

Figure 4-54 Transfer function test bed without RF wave launcher showing significant radiation into the surrounding air and a strong surface wave

A cylindrical RF wave launcher has been conceived to confine the injected RF signal inside the saline (Figure 4-55 and Figure 4-56).

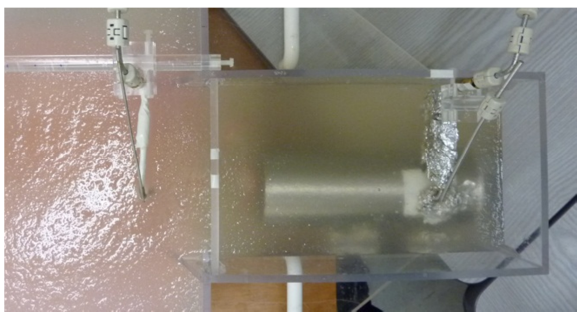

Figure 4-55 RF wave launcher in phantom torso



Figure 4-56 Source probe in RF wave launcher

Figure 4-57 shows a test bed simulation with RF wave launcher. The surface wave has been significantly suppressed and the wave launched from the source probe is confined around the MLC. The detected RF level originating from the source probe above the saline surface reduced to -95 dBm and the RF level detected along the MLC inside the phantom torso was at least 15 dB above any interfering RF level from the environment.

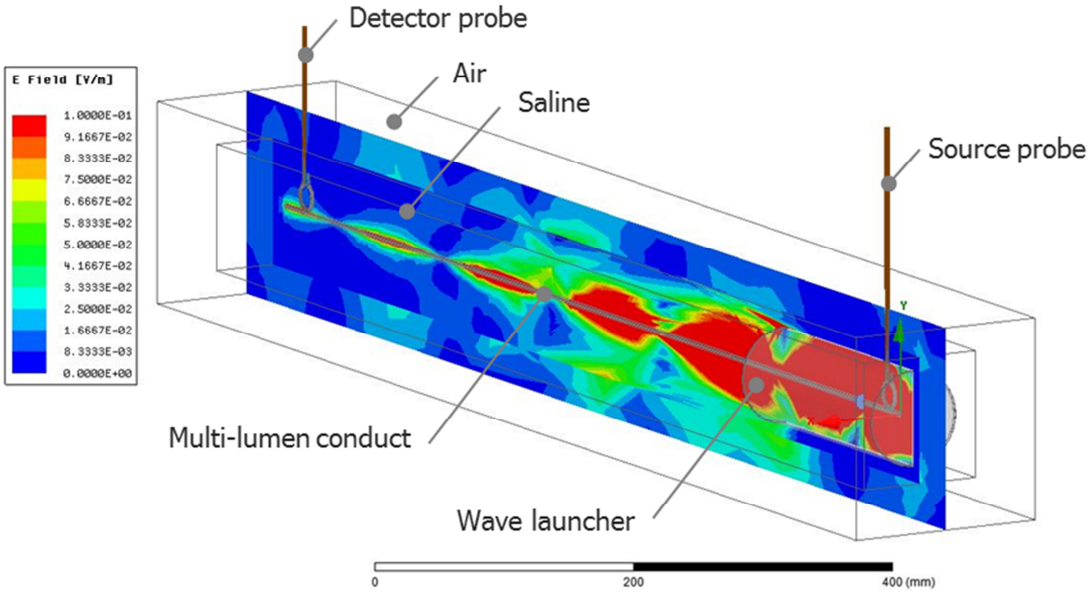

Figure 4-57 Transfer function test bed with RF wave launcher showing a significant reduction of radiation into the surrounding air and concentration of the propagating wave around the MLC

The RF transfer function test bed can be further improved using four axis step motors for positioning of detector probes along test specimens. The first axis steers the detector probe vertically, the second and third axis positions the detector probe horizontally and the fourth axis changes the orientation of the detector probe with respect to the test specimen. Further, data acquisition and detector probe positioning can be automated.

4.3.7 RF heating

4.3.7.1 Overview

A table top test bed for RF induced heating at 128 MHz has been conceived to emulate RF heating caused by typical 3T MRI scanners. The basic RF heating test bed consists of a signal generator, a power amplification chain, a dipole array immersed into a phantom torso with gelled saline and a pair of fibre-optic temperature sensors (Figure 4-58). The test specimen (IPG, Lead) is placed inside the phantom torso along the centre line between two dipole rows (Figure 4-59).

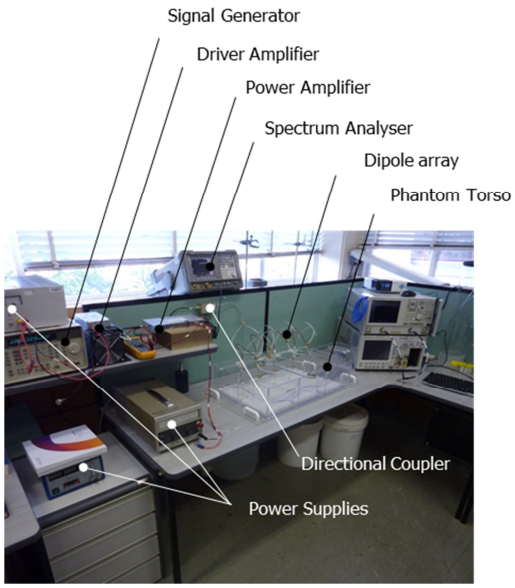

Figure 4-58 RF test bed connected to power amplification chain

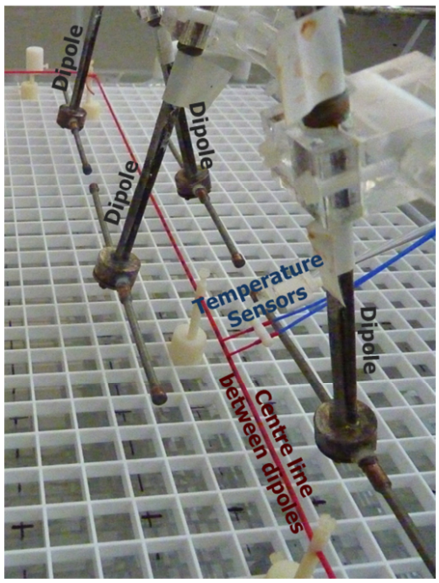

Figure 4-59 Centre line between dipole rows

Five different test setups have been used for verification of test bed components, measurement of field strengths and deposited power, and RF induced temperature increase. The test and measurement equipment is summarised in Table 4-16 and the test setups are outlined in Figure 4-60 to Figure 4-64.

Type	Manufacturer	Model
Vector Network Analyser 300 kHz - 9 GHz	Agilent	E8358A
Calibration Kit for VNA Type N	Agilent	85032F
Spectrum Analyser 9 kHz - 3 GHz	Agilent	E4403B
Signal Generator 9 kHz - 2000 MHz	Agilent	8648B
Fibre-Optic Thermometer	OPTOCON	FOTEMP2
Fibre-Optic Temperature Probes	OPTOCON	TS2/10
Test bed • 1 x phantom torso • 4 x dipoles • 4 x matching transformers • 1 x 4-way power splitter	Custom made Dimensions of phantom torso: L = 650 mm W = 420 mm H = 160 mm	N/A
H-field probes	Custom made	N/A
E-field probes	Custom made	N/A
Power Amplifier 270 Watt CW	Silicon Valley Power Amplifiers	PAB250-100-500-25-A0
Power Amplifier 1 Watt CW	Bruker	BLMH0.5
Power Supply 28 VDC / 30 A	Trio	PD35-20
Power Supply 12 VDC / 3 A	BK Precision	1670A
Power Supply 24 VDC / 10 A	Topward Electric Instruments	TPS2000
Directional Coupler	Pulsar Microwave	C50-108-4814N
Attenuators 20 dB	Mini-Circuits	N/A
Adapters N-SMA	Pasternack	PE9081
RF power load 100 Watt DC - 3 GHz	Mini-Circuits	N/A
RF jumper cables (N connectors)	N/A	N/A
RF jumper cables (SMA connectors)	Mini-Circuits	N/A
Fans	N/A	N/A
Multimeters	Fluke	N/A

Table 4-16 Test and measurement equipment for RF induced temperature increase measurements

The test setup in Figure 4-60 (TS-1) was utilized to verify return loss of individual dipoles and the dipole array.

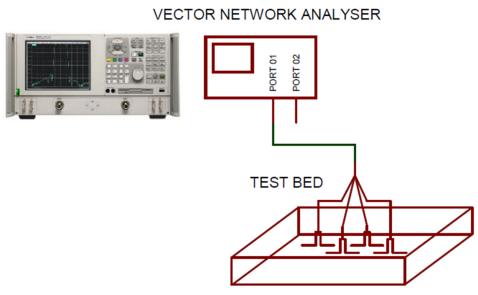

Figure 4-60 TS-1 - Dipole array verification

Amplitude and phase measurements along the centre line between two dipole rows were carried out with the test setup (TS-2) outlined in Figure 4-61.

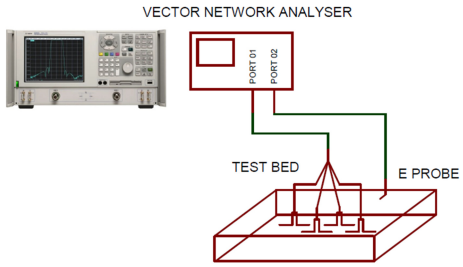

Figure 4-61 TS-2 - Amplitude and phase measurements along centre line between dipole rows

The power deposited from the dipoles along the centre line between two dipole rows was determined with the test setup (TS-3) shown in Figure 4-62.

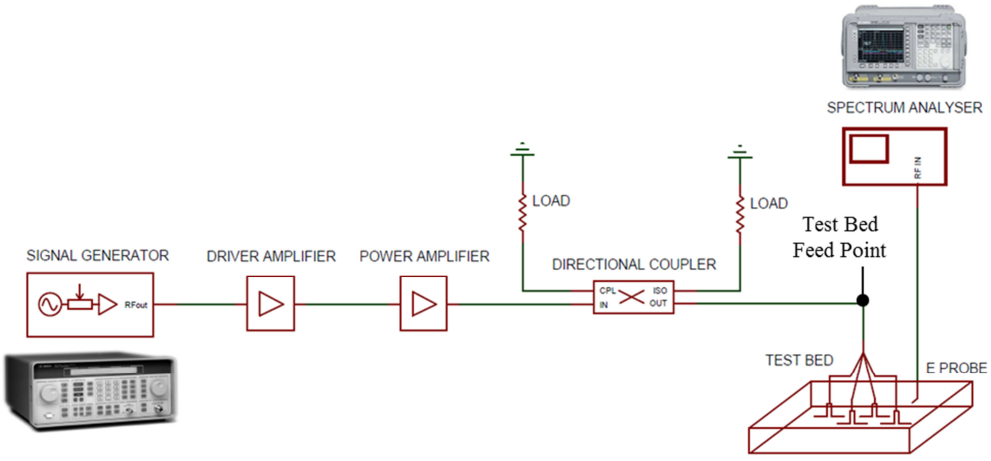

Figure 4-62 TS-3 - Power transfer measurements along centre line between dipole rows

RF induced temperature increase recordings along the centre line between two dipoles without and with test specimen were achieved using the test setups (TS-4 and TS-5) shown in Figure 4-63 and Figure 4-64, respectively.

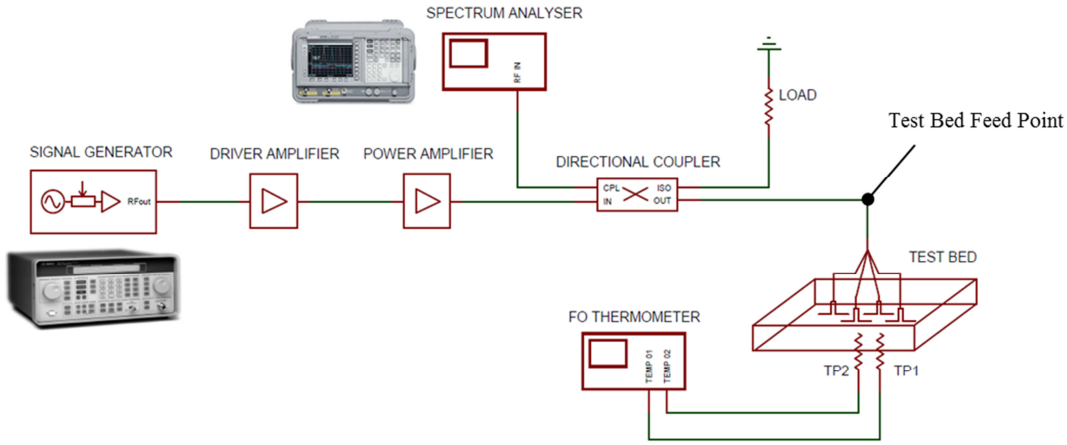

Figure 4-63 TS-4 - Power deposition and temperature measurements (calibration)

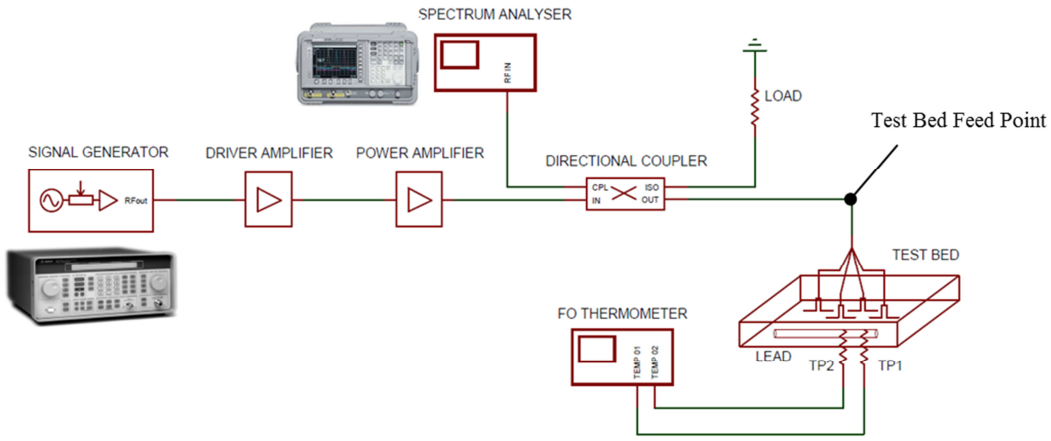

Figure 4-64 TS-5 - Power deposition and temperature measurements (along Lead)

4.3.7.2 Test bed components

The constituent components of the test bed are briefly described below.

Dipoles

Figure 4-65 shows a single dipole. The dipole length is 160 mm and the input impedance at the dipole feed point between the dipole branches is 17.2 + j2.2 Ohm. The wavelength for a planar wave in gelled saline is about 227 mm. Therefore, the dipole length is about 0.7 times the wavelength in gelled saline. A compromise had to be made between dipole length and input impedance. The input impedance of 17 Ohm has been transformed into 50 Ohm using two parallel quarter wavelength coaxial cable sections of 75 Ohm and 30 Ohm. In addition, a quarter wavelength coaxial cable balun has been added to the feed point.

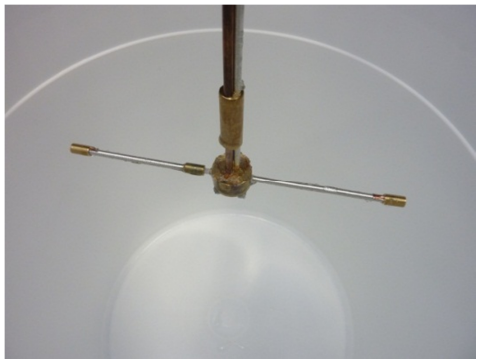

Figure 4-65 Single Dipole

Measured return loss and input impedance for the dipole immersed into gelled saline are shown in Figure 4-66 and Figure 4-67, respectively. The return loss is better 27 dB at 128 MHz and the -14 dB return loss bandwidth is approximately 60%.

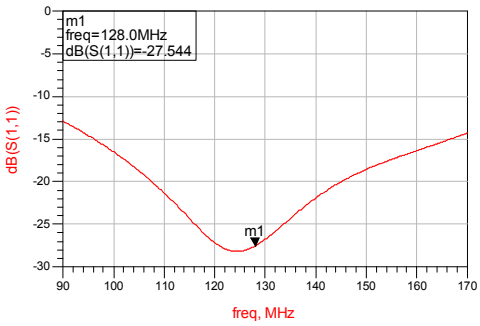

Figure 4-66 Return loss of single dipole

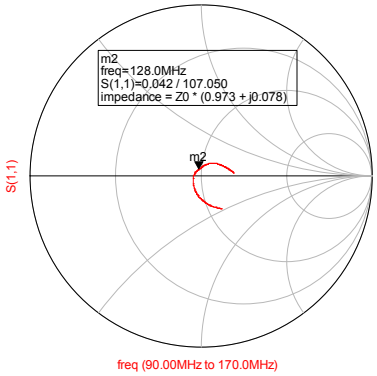

Figure 4-67 Input impedance of single dipole

Dipole array

The dipole array used in all subsequent measurements consists of four dipoles in two rows with two dipoles per row (Figure 4-68). The spacing between dipoles in E-Plane and H-Plane is 180 mm and 60 mm, respectively. The dipole centres of the first row are shifted by 100 mm in the E-Plane with respect to the dipole centres of the second row. Figure 4-69 shows a co-linear dipole array configuration with its constituent components.

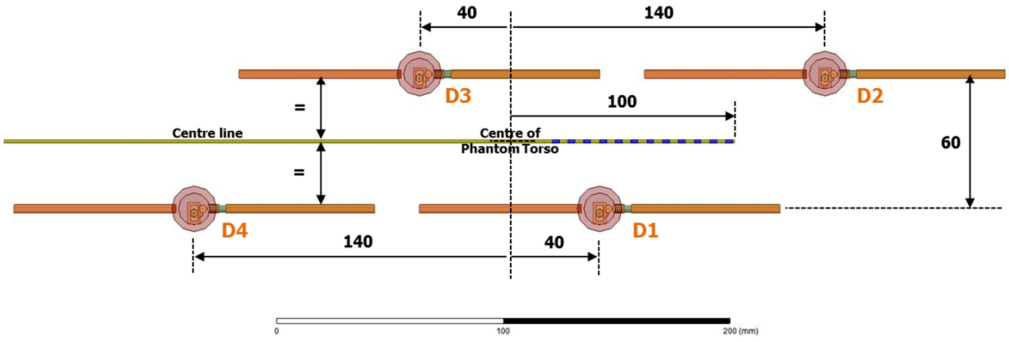

Figure 4-68 Dipole array with Lead placed along centre line

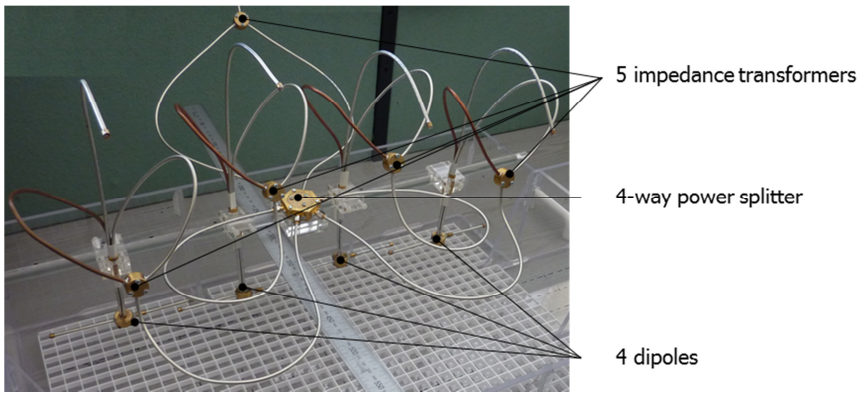

Figure 4-69 Co-linear dipole array in phantom torso

The return loss measured into the 4-way power splitter is better -18 dB when the dipole array is immersed into gelled saline. The reduction in return loss (compared with the single dipole) results from proximity coupling between dipoles in both, E-planes and H-planes. The results are shown in Figure 4-70 and Figure 4-71, respectively.

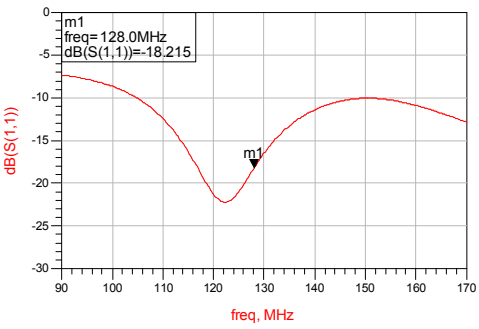

Figure 4-70 Return loss of dipole array

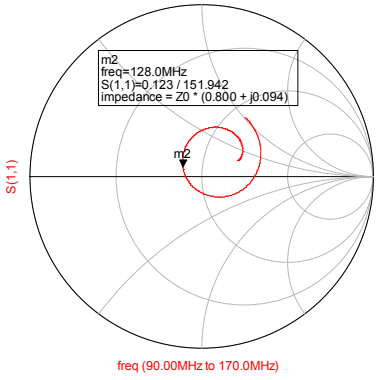

Figure 4-71 Input impedance of dipole array

4-way power splitter

A low insertion loss 4-way reactive power splitter for 128 MHz capable of handling 500 Watt CW power has been designed and realised (Figure 4-72).

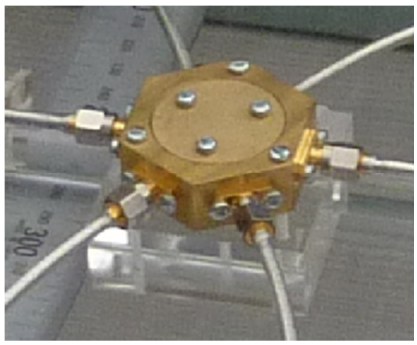

Figure 4-72 4-way power splitter

Return and insertion loss are shown in Figure 4-73 and Figure 4-74. At 128 MHz the return loss is better than -28 dB and the insertion loss above splitting loss 0.15 dB.

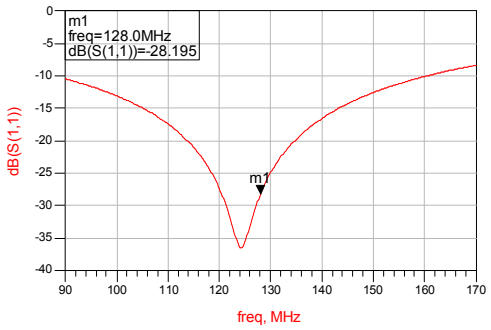

Figure 4-73 Return loss of 4-way power divider

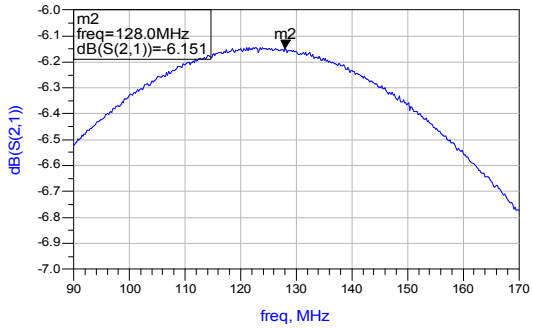

Figure 4-74 Insertion loss of 4-way power divider

Directional Coupler

A directional coupler (Figure 4-75) has been used either to measure the reflected power from the dipole array or to measure the transferred power into the dipole array. The performance of the directional coupler is summarised in Figure 4-76 and Figure 4-77. The return loss at 128 MHz is better 30 dB and the coupling loss approximately -50.3 dB.

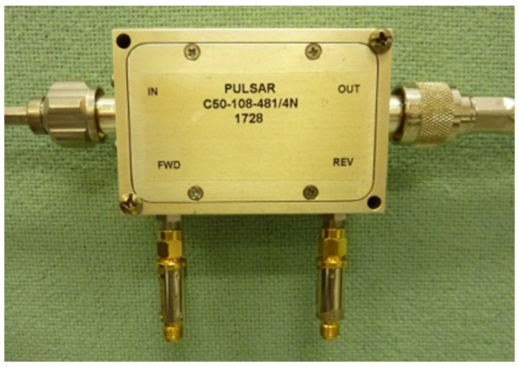

Figure 4-75 Directional coupler

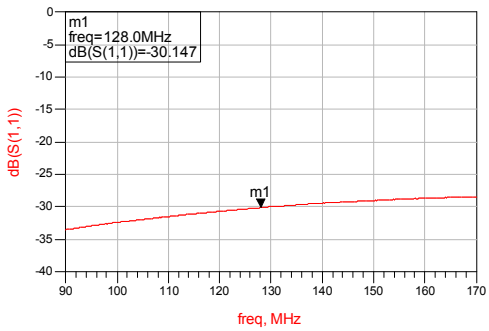

Figure 4-76 Return loss of directional coupler

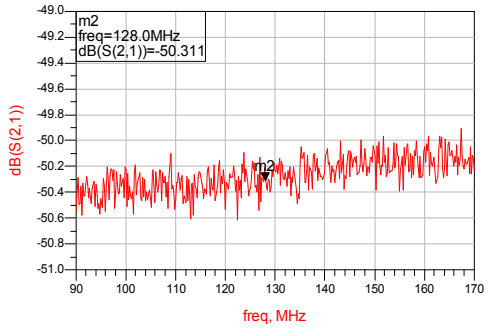

Figure 4-77 Insertion loss of directional coupler

Probes and sensors

Two types of RF probes and one type of temperature probe have been used. Both, H-field and E-field probes were used to detect field components in gelled saline in order to validate the EM model conceived for the RF test bed. The GaAs temperature sensors were used to record local temperature increases during RF test bed calibration and during evaluations of base cases and design variations. The probes are shown in Figure 4-78 and Figure 4-79.

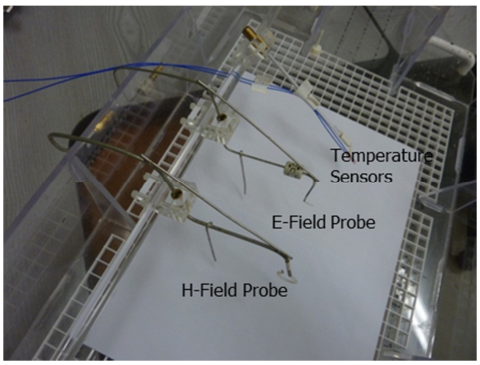

Figure 4-78 Probes and sensors

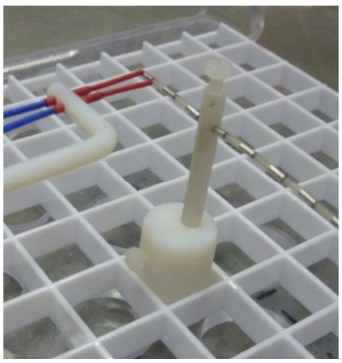

Figure 4-79 Temperature sensors at distal end of Lead

Power amplification chain

The RF power fed into the test bed feed point indicated in Figure 4-63 and Figure 4-64 as function of signal generator output power is given in Figure 4-80. The CW RF power injected into the dipole array for RF induced temperature measurements was between 210 and 220 Watt. A 10 Watt power drop was observed over a 5 minute test sequence due to heating of the power amplifier's base plate from 20°C to 45°C.

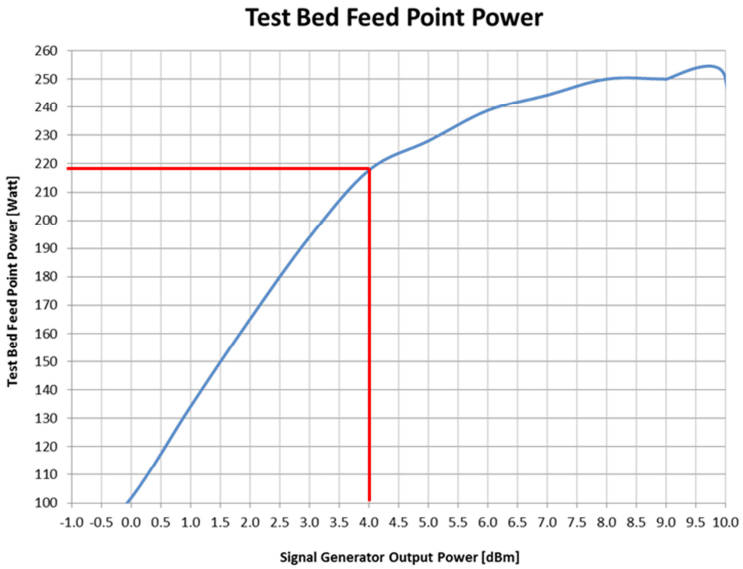

Figure 4-80 Test bed feed point power as function of signal generator output power

RF heating test bed

Figure 4-81 shows the phantom torso filled with gelled saline. The filling height is approximately 90 mm. The two row dipole array is fixed on an acrylic bar centred on top of the phantom torso. The location of the dipoles is 45 mm beneath the surface of the gelled saline. An acrylic sliding bar is used for the temperature sensors.

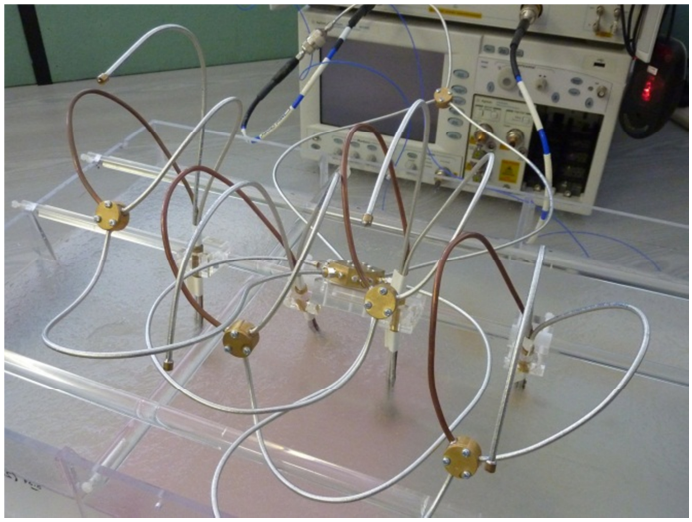

Figure 4-81 RF heating test bed

4.3.7.3 Temperature calibration

In a first step, the RF induced temperature increase, caused by the dipole array, at electrode locations has to be determined. A non-conductive "dummy" Lead with non-conductive "dummy" electrodes has been assembled (Figure 4-82) and located along the centre line shown in Figure 4-68 and Figure 4-83.

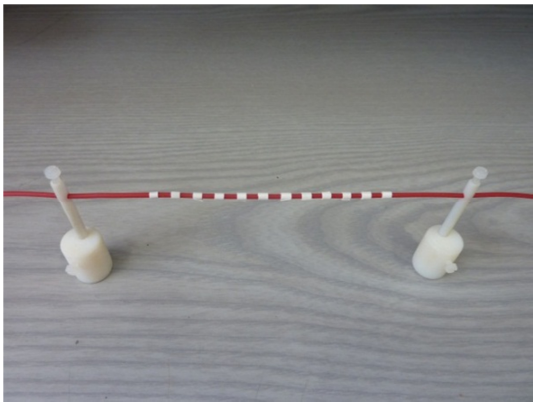

Figure 4-82 Dummy Lead with dummy electrodes

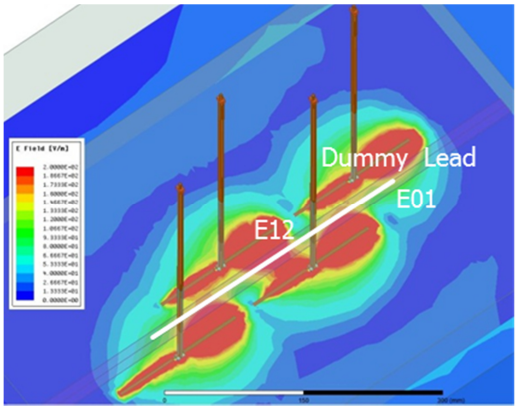

Figure 4-83 Dummy Lead location in RF test bed

The expected temperature increase from thermal conduction for an input power of 50 Watt per dipole over 300 seconds has been simulated and is shown in Figure 4-84 and Figure 4-85. The simulation settings have been summarised in Sections 4.2.3 and 4.2.4. For comparison, the measured temperature increase for the same input power level and period of time is given in Figure 4-86 and Figure 4-87 and the difference between measured and simulated temperature increase is extracted in Figure 4-88. The difference of up to 1.3°C has two causes. A small fraction of the difference is attributed to the onset of thermal convection from the dipoles towards the centre line. The temperature rise at the dipoles' feed points after 300 seconds is approximately 40°C. The larger part of the difference is attributed to the thermal simulation settings. The volume around the Lead shown in Figure 4-39 is extracted from the total volume and a

constant temperature is assumed on the boundary. The power deposited in this volume drives the temperature increase over time. However, the temperature on the boundary for the same volume element inside the RF test bed is not constant but increases over time. Therefore, the measured temperature increase is higher than the simulated temperature increase. Further, in simulations this leads to thermal equilibrium after about 300 seconds whereas in measurements a constant temperature increase per time unit is still visible after 300 seconds.

Limitations in available computing resources did not allow increasing the simulation volume, to include the impact of heat transfer from the dipole array, and/or to include thermal convection terms.

Despite these restrictions, the simulation settings permit to extract changes in temperature increase caused by "real" Leads with respect to the calibration scenario with "dummy" Leads.

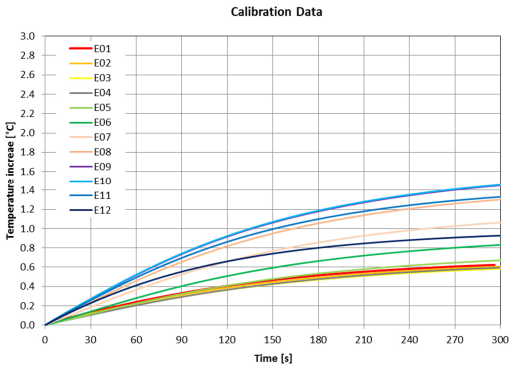

Figure 4-84 Calibration Simulation - Temp. Transient

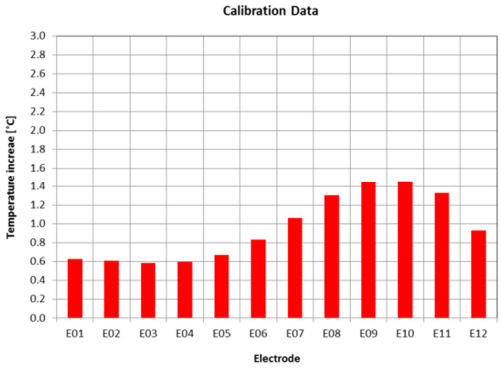

Figure 4-85 Calibration Simulation - Temp. Transient after 300 s

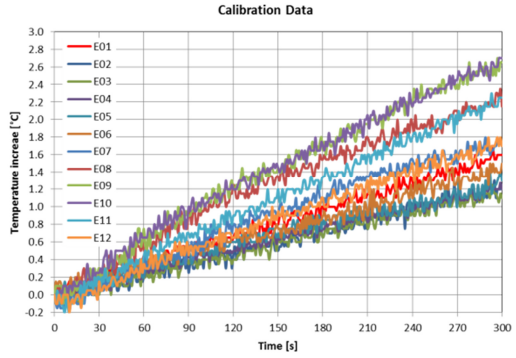

Figure 4-86 Calibration Measurement - Temp. Transient

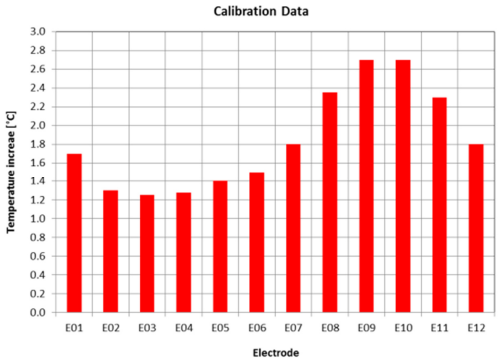

Figure 4-87 Calibration Measurement - Temp. Transient after 300 s

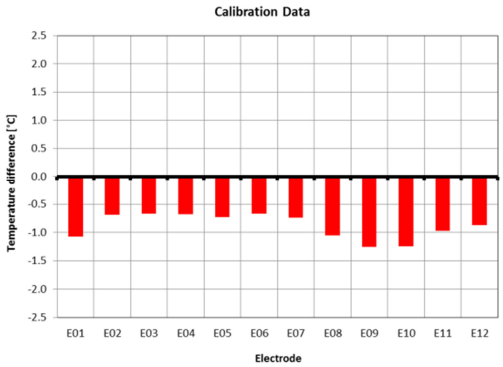

Figure 4-88 Calibration Differences - Temp. Transient after 300 s

Simulated and measured temperature rises for each electrode location have been stored in separate calibration files. The calibration data has been subtracted from subsequent simulated and measured temperature rises. Therefore, temperature increases caused by "real" Leads in subsequent sections refer to temperature increases above temperature increases caused by the "dummy" Lead.

4.3.7.4 Local electric fields and local deposited power

In a second step, the magnitude and phase of the local total tangential electric field along the centre line has been determined using a sliding E-Probe. The test configuration is shown in Figure 4-61 and Figure 4-89.

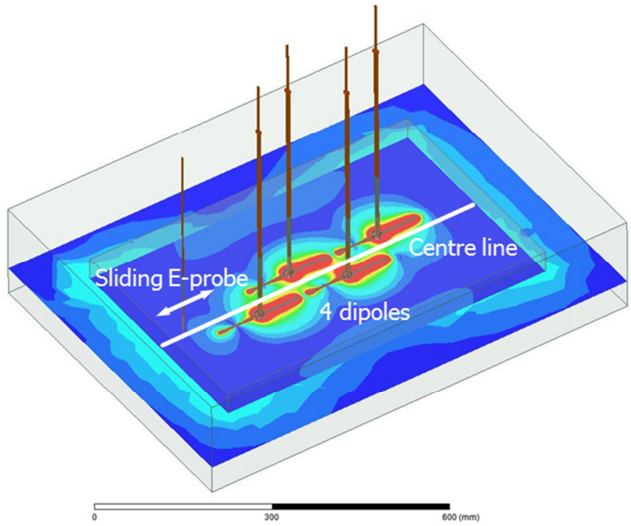

Figure 4-89 Outline of RF test bed with dipoles and E-probe

Since the centre line is located in-between the two dipole rows within the transition region from the reactive to the radiating near field the local electric field is not tangential to the centre line. The predominant field component for the local temperature increase is the total electric field whereas the total tangential electric field influences the surface currents induced along Leads. The difference is sketched in Figure 4-90.

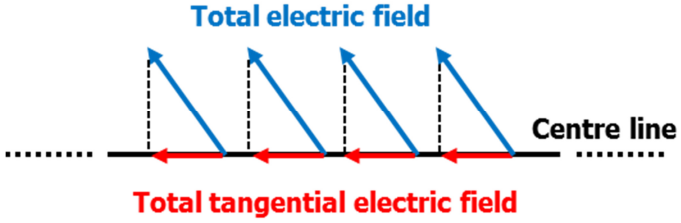

Figure 4-90 Total electric field and total tangential electric field

Figure 4-91 shows the calculated total tangential electric field and the total electric field along the centre line between the dipole rows and Figure 4-92 shows that measured temperature increase correlates well with the magnitude of the total electric field.

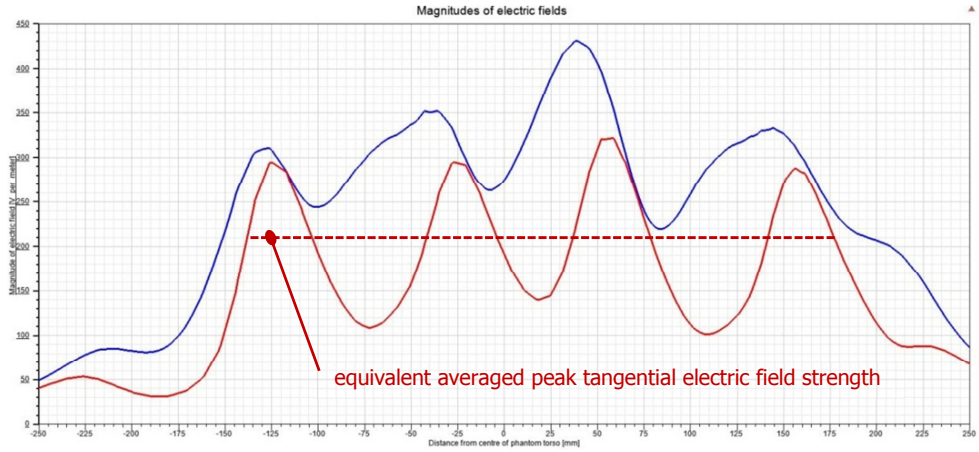

Figure 4-91 Magnitude of calculated total tangential electric field (red) and total electric field (blue) along centre line for 50 Watt input power per dipole

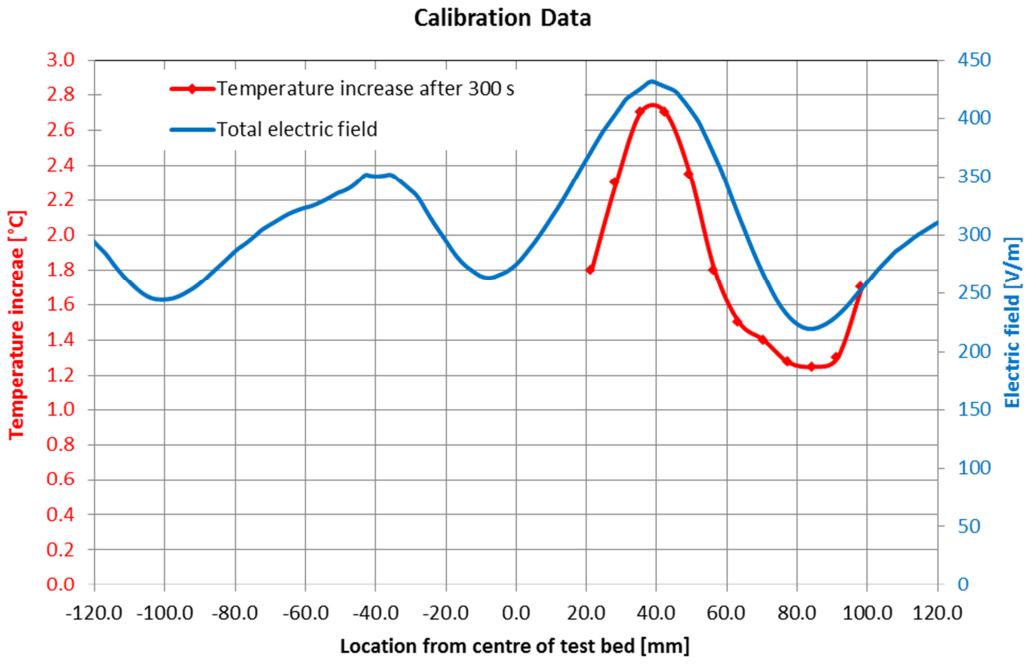

Figure 4-92 Total electric field and temperature increase along centre line between dipole rows for 50 Watt input power per dipole

Figure 4-93 shows measured and calculated normalised total tangential electric fields along the centre line. The normalisation is with respect to corresponding electric field strength maxima. The measured and calculated phase progression along the centre line is shown in Figure 4-94 shows. The line segment between -60 mm and -90 mm along the centre line was not accessible with the sliding temperature sensor. The calculated total tangential electric field for an equivalent magnetic dipole array and a wave port array has been added to Figure 4-93. These two antenna arrays, in addition to a third simplified dipole array, have been used to replace the actual dipole array in electromagnetic simulations later on. Combining dipole antenna array together with IPG and Lead into a single EM and thermodynamic model was not possible due to limitations in available computing resources.

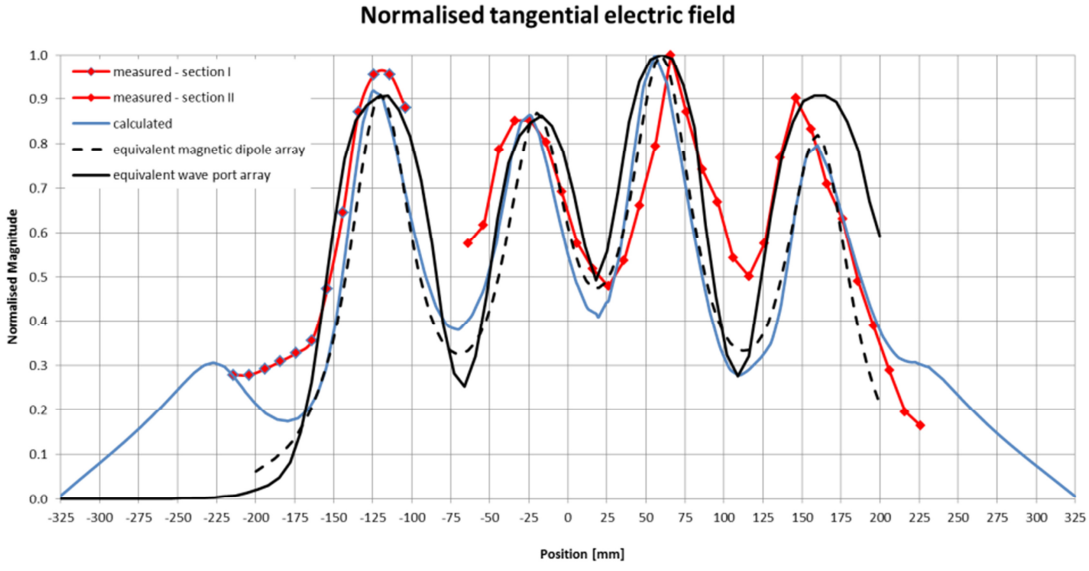

Figure 4-93 Magnitude of measured and calculated tangential electric field

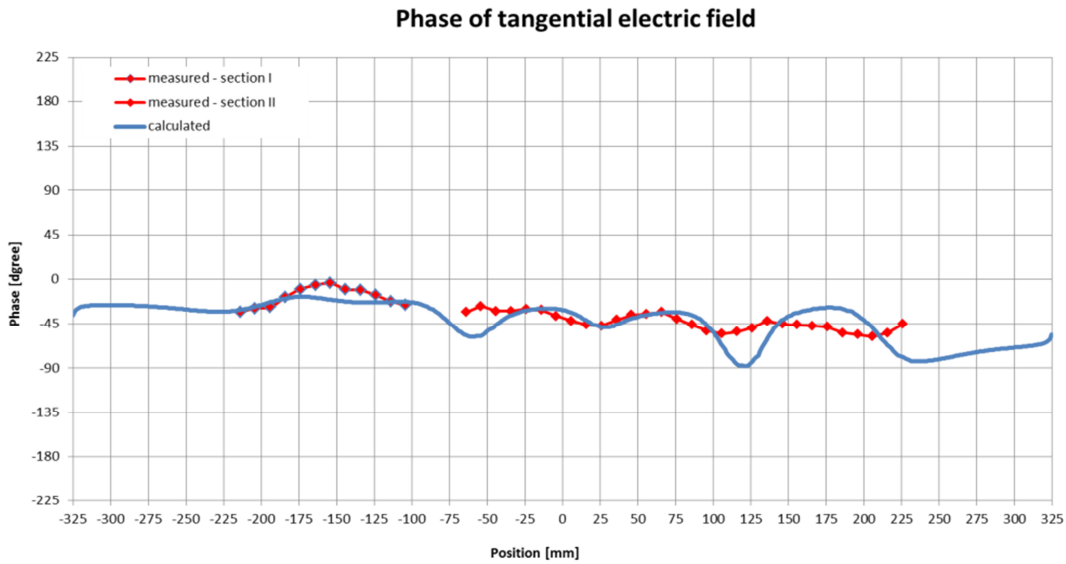

Figure 4-94 Phase of measured and calculated tangential electric field

The power transfer from the dipole array towards the E-Probe has been calculated and measured for 1 Watt input power per dipole using the test setup outlined in Figure 4-62. Calculated and measured results are presented in Figure 4-95.

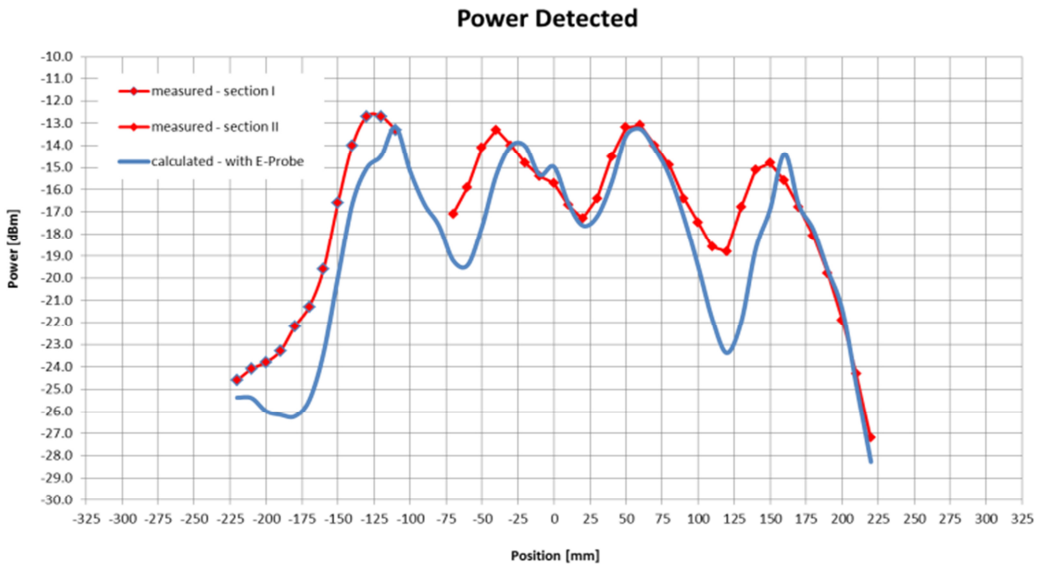

Figure 4-95 Measured and calculated detected power along centre line for 1 Watt input power per dipole

Table 4-17 summarises the relationships between input power and local electric field strength. The local electric field strength is proportional to the square root of the input power into the dipole array.

Input power per dipole [dBm]	Maximum measured power along centre line [dBm]	Maximum calculated power along centre line [dBm]	Maximum calculated total tangential electric field along centre line [V/m]	Maximum calculated total electric field along centre line [V/m]
30.0	-12.7	-13.2	45.5	60.9
47.0	X	X	321.8	430.9

Table 4-17 Relationship between input power, local deposited power and local electric field strength

4.3.7.5 Fields and power deposition in phantom torso

Before concluding this chapter, the electric field strength generated with the RF heating test bed is benchmarked against the electric field strength encountered in a phantom torso positioned in a typical 3T MRI scanner. The objective is to determine the magnitude of the tangential electric field strength along Path EDS sketched in Figure 4-8 for a given average SAR in the phantom torso and to compare this magnitude with the magnitude along the centre line between dipoles of the RF heating test bed (Figure 4-68).

The simulation settings have been outlined in Section 4.1.3.2. Here, the results are presented.

4.3.7.5.1 Fields from magnetic dipoles

In a first step, the electric and magnetic fields generated from magnetic dipoles have been analysed to ensure that they are representative for fields generated by typical RF coils in MRI scanners. The field patterns are shown in Figure 4-96 and Figure 4-97 for two orthogonal planes of Source 1, and in Figure 4-98 and Figure 4-99 for Source 2. Sources 3 and 4 have similar patterns.

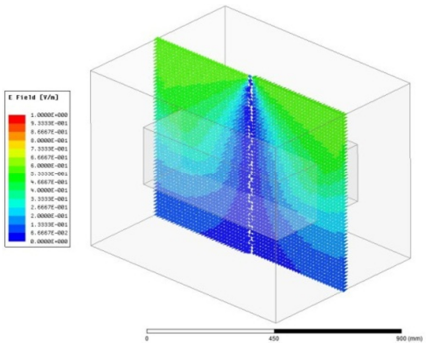

Figure 4-96 Incident electric vector field of Source S1 for $E_{s,1} = 1\,\frac{V}{m} \cdot e^{j(0)}$ in plane yz

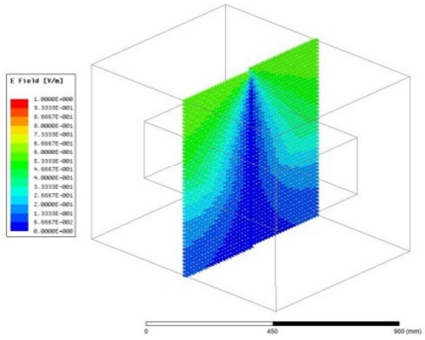

Figure 4-97 Incident electric vector field of Source S1 for $E_{s,1} = 1\,\frac{V}{m} \cdot e^{j(0)}$ - plane xz

In Figure 4-100 and Figure 4-101 the incident field patterns from Source 1 and Source 2 are projected onto the phantom torso surface.

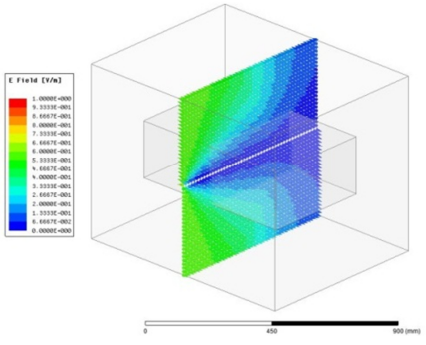

Figure 4-98 Incident electric vector field of Source S2 for $E_{s,2} = 1\,\frac{V}{m} \cdot e^{j(0)}$ in plane yz

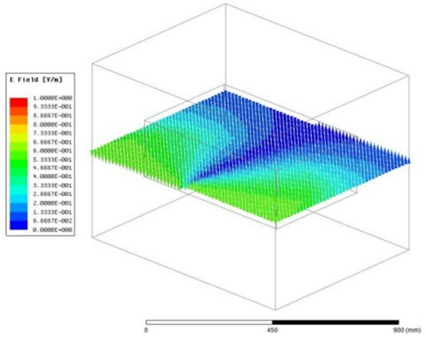

Figure 4-99 Incident electric vector field of Source S2 for $E_{s,2} = 1\,\frac{V}{m} \cdot e^{j(0)}$ in plane xz

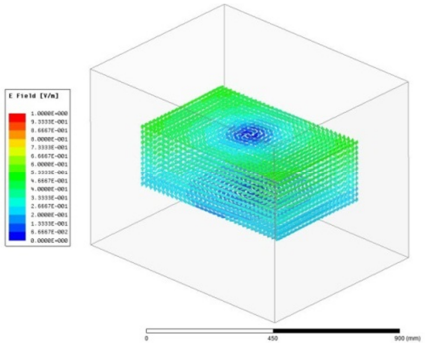

Figure 4-100 Incident electric vector field of Source S1 for $E_{s,1} = 1\ \frac{V}{m} \cdot e^{j(0)}$ on phantom torso surface

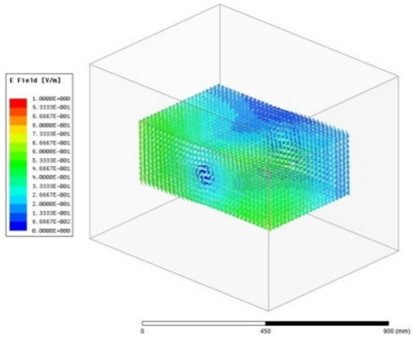

Figure 4-101 Incident electric vector field of Source S2 for $E_{s,2} = 1\ \frac{V}{m} \cdot e^{j(0)}$ on phantom torso surface

Summing up, the source field patterns are representative for field patterns generated by typical RF coils.

In a second step, the incident field patterns for circular rotational polarisation have been analysed. The phase progression for the four sources is ...

$$S1 \rightarrow E_{s,1} = E_{s,mag} \cdot e^{j(0)};\ S2 \rightarrow E_{s,2} = E_{s,mag} \cdot e^{j\cdot\frac{1}{2}\cdot\pi}$$
$$S3 \rightarrow E_{s,3} = E_{s,mag} \cdot e^{j\cdot\pi};\ S4 \rightarrow E_{s,4} = E_{s,mag} \cdot e^{j\cdot\frac{3}{2}\cdot\pi} \quad (4\text{–}2)$$

The field patterns have been projected onto three horizontal and three vertical surfaces. The horizontal surfaces (y-z plane) are the top, centre and bottom plane (Figure 4-102 to Figure 4-104) of the phantom torso and the vertical surfaces (x-z plane) are the front, centre and back plane (Figure 4-105 to Figure 4-107).

Horizontal Planes

A linear oriented electric field is observed on both, top and bottom plane whereas the field orientation is in opposite directions. The centre plane shows a curl pattern with zero electric field strength at the centre.

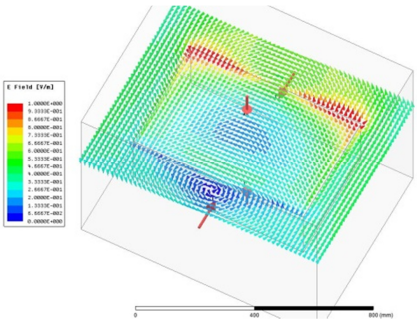

Figure 4-102 Total electric field on horizontal top plane of phantom torso for $\varphi = 0$

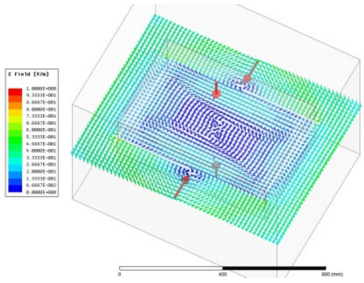

Figure 4-103 Total electric field on horizontal centre plane of phantom torso for $\varphi = 0$

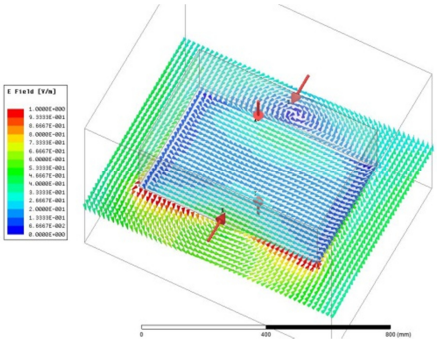

Figure 4-104 Total electric field on horizontal bottom plane of phantom torso for $\varphi = 0$

Vertical Planes

A counter-clockwise curl pattern is observed on all three vertical planes with zero electric field strength at the centre.

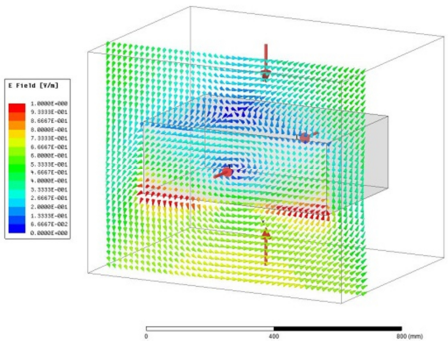

Figure 4-105 Total electric field on vertical front plane of phantom torso for $\varphi = 0$

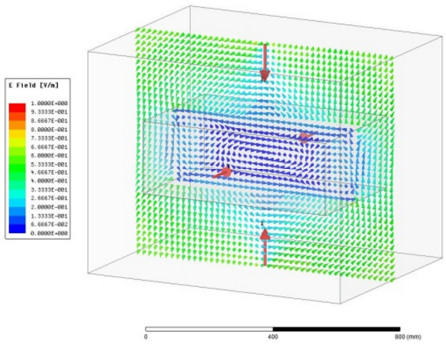

Figure 4-106 Total electric field on vertical centre plane of phantom torso for $\varphi = 0$

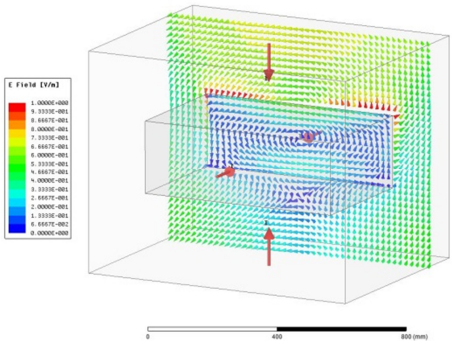

Figure 4-107 Total electric field on vertical back plane of phantom torso for $\varphi = 0$

No anomalies in the incident field patterns have been detected for circular rotational polarisation. Looking into the positive z-direction, the field pattern revolves clockwise around the phantom torso in the x-y plane (Figure 4-8).

4.3.7.5.2 Total tangential electric field along Path EDS

The resulting peak total tangential electric field strength at the centre of Path EDS (Figure 4-8) caused by the revolving incident electric field is shown in Figure 4-108 for vertical and in Figure 4-109 for horizontal displacements of Path EDS. In both displacement directions the total tangential electric field increases with increasing distance from the centre line. The total tangential electric field strength is proportional to the square root of the average SAR inside the PT. Not shown in the figures, but important to note is that the total tangential electric field strength is not constant along Path EDS but drops parabolically from its maximum at the centre towards zero at the transition between the PT and the surrounding air volume.

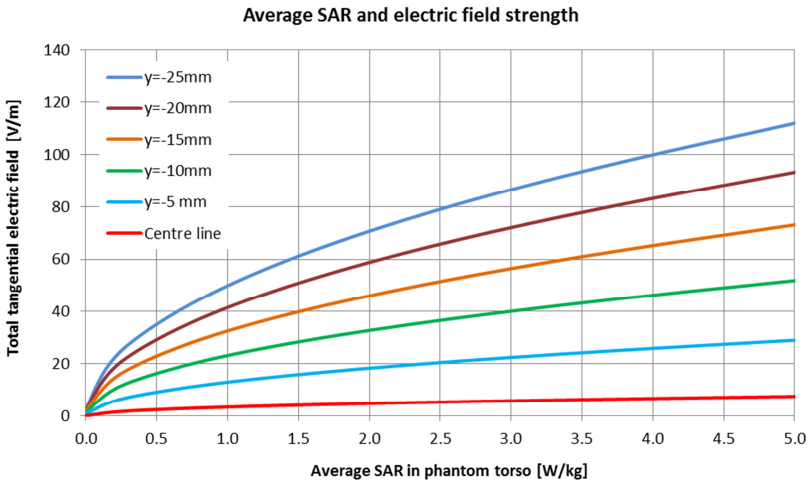

Figure 4-108 Peak total tangential electric field at centre of Path EDS
Parameter y: vertical displacement of Path EDS from centre line in PT

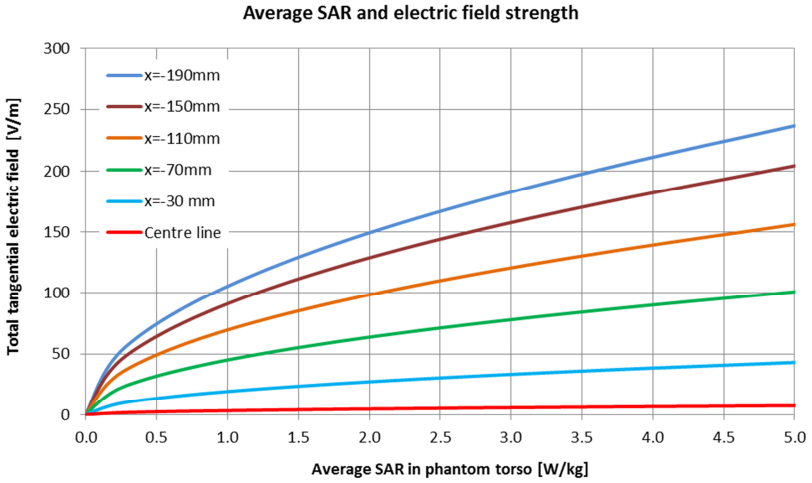

Figure 4-109 Peak total tangential electric field at centre of Path EDS
Parameter x: horizontal displacement of Path EDS from centre line in PT

Figure 4-110 to Figure 4-112 show magnitude and vector plots in three orthogonal planes through the iso-centre of the PT for an average SAR of $2.0\ \frac{W}{kg}$. Electric field strengths concentrate at the boundary between the PT and the surrounding air volume. The electric field at the iso-centre is zero.

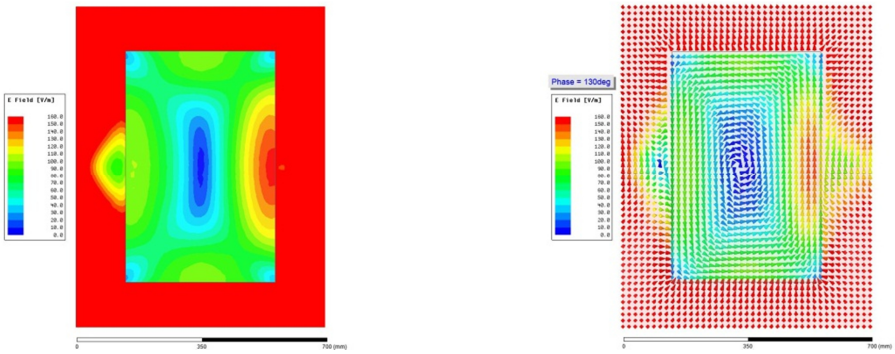

A) B)

Figure 4-110 Electric field in PT at iso-centre in horizontal x-z plane for $2.0\ \frac{W}{kg}$
A) Peak magnitude
B) Vector plot

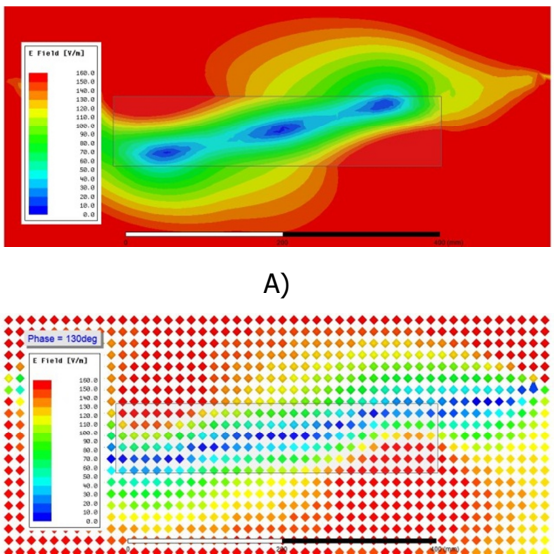

A)

B)

Figure 4-111 Electric field in PT at iso-centre in vertical x-y plane for $2.0\ \frac{W}{kg}$
A) Peak magnitude
B) Vector plot

Figure 4-111 shows the formation of three electric field nodes along the first diagonal from the bottom left to the top right corner and two electric field maxima along the second diagonal from the top left to the bottom right corner. Routing Leads through minima during RF induced temperature testing will lead to overoptimistic results.

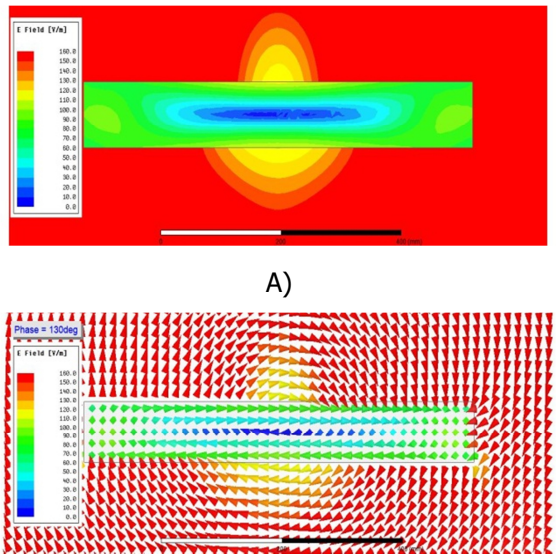

A)

B)

Figure 4-112 Electric field in PT at iso-centre in vertical y-z plane for $2.0\ \frac{W}{kg}$
A) Peak magnitude
B) Vector plot

The peak electric field distribution on a vertical plane 150 mm offset from the iso-centre of the PT is shown in Figure 4-113. The region with low peak electric field strength is clearly visible.

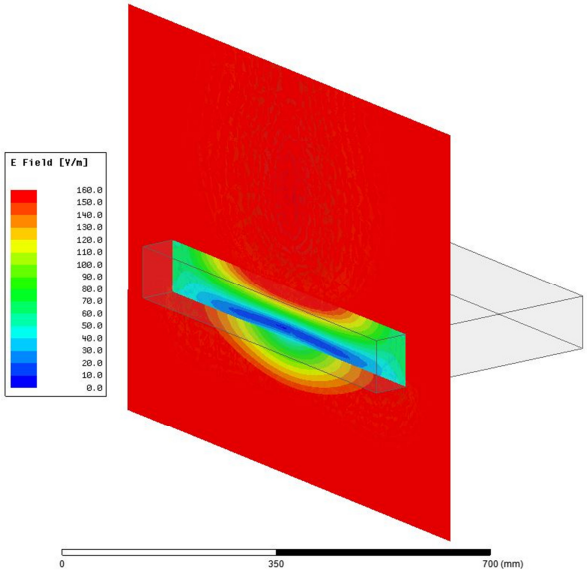

Figure 4-113 Electric field in PT in vertical y-z plane at 150 mm offset from iso-centre for $2.0\ \frac{W}{kg}$
A) Peak magnitude
B) Vector plot

Location of minima and maxima inside the PT depend on MRI frequency, PT size, filling liquid and filling height, and location within the MRI scanner. Therefore, appropriate Lead routing for RF induced temperature increase measurements with PTs in MRI scanners should take into account locations of local field strength minima and maxima inside the PT.

4.3.7.6 Conclusion

The results above show that EM and thermodynamic models provide reasonable results in order to proceed with the analysis of RF induced heating caused by Leads and IPGs. A peak tangential electric field of $300\ \frac{V}{m}$ has been applied in subsequent EM and thermal simulations to determine temperature rises along test specimen (base cases and design variations of Leads and IPGs). Further, peak tangential electric field strengths of 300 V/m generated by the RF test bed are representative for peak electric field strengths encountered in phantom torsos exposed to RF fields generated by 3T MRI scanners for an average SAR of $2.0\ \frac{W}{kg}$.

The RF heating test bed can be further improved. To minimise thermal convection from dipoles towards the centre line, the phantom torso can be divided by thin Mylar or acrylic walls separating dipoles from test specimens. Further, increasing the number of dipoles per row and interleaving the dipoles in each row reduces the difference between tangential electric field minima and maxima along the centre line. In addition, more dipoles per row permit the generation of amplitude and phase progressions along the centre line to emulate various RF exposure scenarios. Next, the near field radiation patterns of individual dipoles show an asymmetry. This asymmetry can be minimised using thin layers of dielectric coating on dipole branches. Finally, using three axis step motors

for temperature probe positioning, data acquisition and probe positioning can be automated.

4.3.8 Pulse pattern and artefacts

The test bed described in this section has been used for pulse pattern and artefact measurements for Leads immersed in (phosphate buffered) saline solution. The test and measurement equipment is summarised in Table 4-18, the properties of the saline solution are given in Appendix A.4, and the test setup is shown in Figure 4-114.

Type	**Manufacturer / Design House**	**Model**
Multimeter	Fluke	N/A
20 MHz Function / Arbitrary Waveform Generator	Agilent	33220A
Four Channel Digital Storage Oscilloscope 100 MHz / 1 GS/s	Tektronix	TPS-2014B
Battery Powered ERT Amplifier	NICTA / Saluda Medical	v2r3
Oscilloscope test probes 10 MΩ / 12 pF / 100 MHz	Tektronix	TPP0101
Lead- RJ45 Interface Box	Saluda Medical	N/A
MCS RJ45 Breakout Board	Saluda Medical	v1r2
CLS/eCLS Lead termination box	Saluda Medical	100428 Rev1
RJ45 patch cables	N/A	N/A
RJ45 pigtail cables	N/A	N/A
Single wire clamp cables	N/A	N/A
BNC to double wire patch cable	N/A	N/A
Resistor wheels	N/A	N/A
Platinum reference electrode	N/A	N/A

Table 4-18 Test and measurement equipment

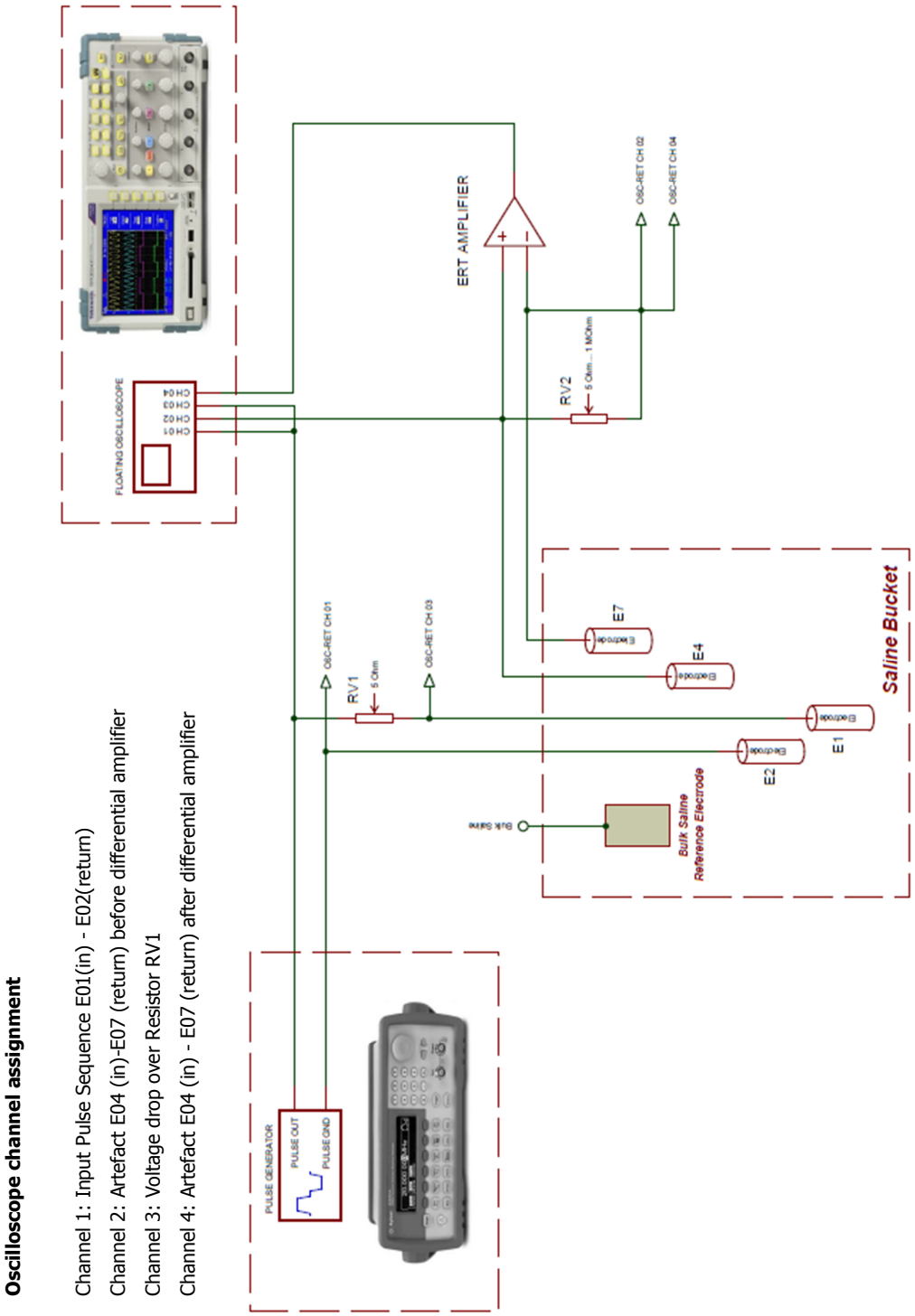

Oscilloscope channel assignment

Channel 1: Input Pulse Sequence E01(in) - E02(return)
Channel 2: Artefact E04 (in)-E07 (return) before differential amplifier
Channel 3: Voltage drop over Resistor RV1
Channel 4: Artefact E04 (in) - E07 (return) after differential amplifier

Figure 4-114 Test Setup #1 - E01 - E02 (st) and E04 - E07 (af)

Signal generator output and oscilloscope inputs are floating as shown in Figure 4-115 and Figure 4-116. A schematic overview of the oscilloscope probes is given in Figure 4-117 and a typical Lead termination box for verification measurements is sketched in Figure 4-118.

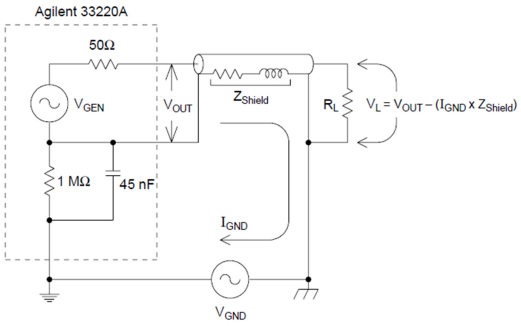

Figure 4-115 Agilent Waveform Generator

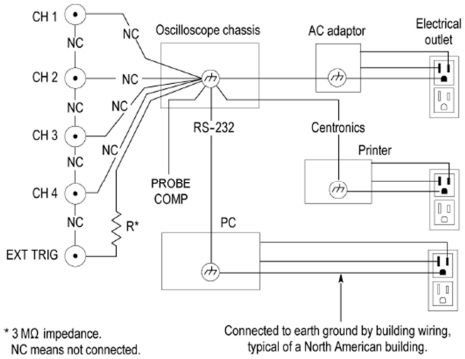

Figure 4-116 Tektronix Oscilloscope

$R_1 = 10\ M\Omega$

$C_V = 15\ \ldots 25\ pF$

$C_{Probe} \leq 12\ pF$

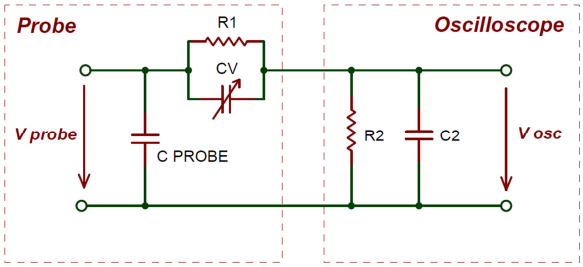

$$V_{osc} = \frac{R_2}{R_1 + R_2} V_{probe}$$

$R_2 = 1\ M\Omega$

$C_2 = 20\ pF$

Figure 4-117 Oscilloscope Probes

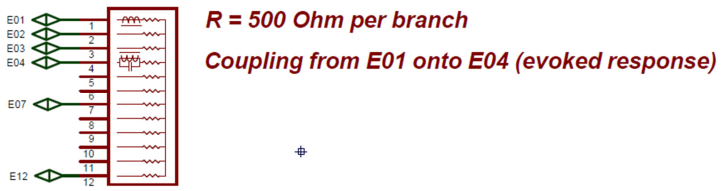

Figure 4-118 CLS/eCLS Lead termination box (indicative only)

A few verification measurements have been carried out. These measurements are summarised below.

Figure 4-119 shows a positive pulse of 1 V injected into three different resistive terminations. For R $\rightarrow \infty$ (open) and R = 100 kOhm the voltage pulse is reflected, resulting in a measured voltage twice the injected voltage due to the high termination resistance compared with the low characteristic impedance of the the coaxial wave port of the signal generator (50 Ohm). For R = 50 Ohm the measured voltage is 1 V and no reflections are observed.

Figure 4-120 and Figure 4-121 show rise and fall times from the signal generator measured for a termination with R $\rightarrow \infty$ (open) and for Electrodes E01 and E02 immersed into saline solution. The rise and fall times for R $\rightarrow \infty$ are approximately 10 ns and for Electrodes E01 and E02 immersed into saline solution approximately 100 ns.

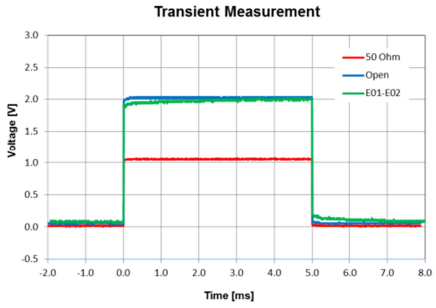

Figure 4-119 Pulse into resistive loads
R = 50 Ω
R $\rightarrow \infty$ (Open)
R = 100 kΩ

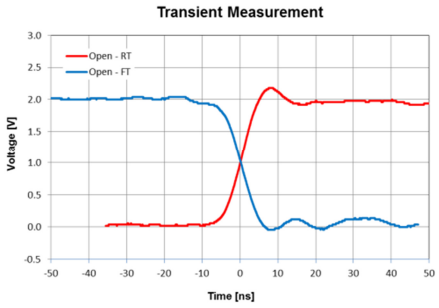

Figure 4-120 Rise time (RT) and Fall Time (FT) for pulse into resistive load
R $\rightarrow \infty$ (Open)

The compression point and transfer gain and phase of the Evoked Response Telemetry (ERT) amplifier have been verified (Figure 4-122, Figure 4-123, and Figure 4-124). A linear response is observed for input voltages below ±100 mV and for frequencies below 1000 Hz.

This limits the maximum slew rate to 1 ms and only slow varying input signals can be resolved.

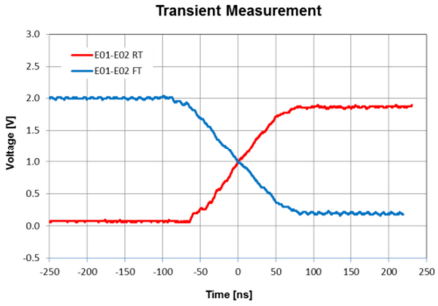

Figure 4-121 Rise time (RT) and Fall Time (FT) for pulse into E01 and E02 (R ~ 100 kΩ)

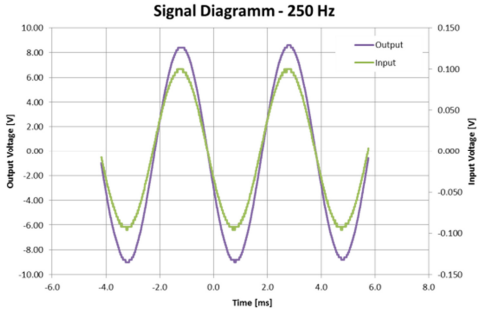

Figure 4-122 Compression point of ERT amplifier

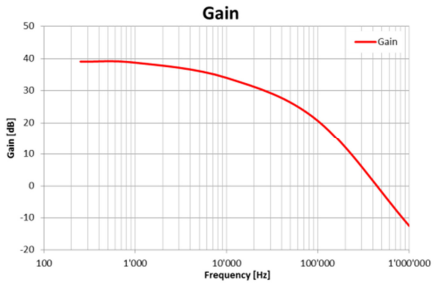

Figure 4-123 Gain of ERT amplifier

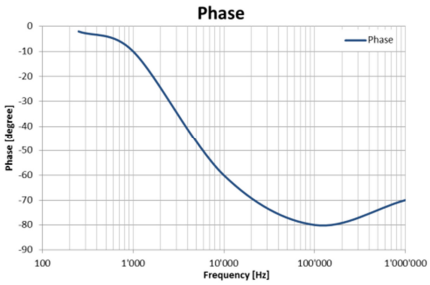

Figure 4-124 Phase of ERT amplifier

Figure 4-125 shows a pulse pattern with ±2 Volt peak voltage injected from the signal generator into Electrodes E01 and E02. The measured voltage is ±4 Volt peak due to the high resistance of the saline solution (1000 Ohm) compared with the low resistance of the coaxial wave port impedance (50 Ohm). The voltage drop from E01 and E02 with respect to the Bulk Saline Reference Electrode (BSRE) is ±2 Volt and the voltage difference between E01 and E02 is ±4 Volt. Figure 4-126 shows the measured voltage drop from E01 and E02 with respect to the floating Signal Generator Ground (SGG). The voltage difference between between E01 and E02 is ±4 Volt but with Electrode E02 clamped to the floating SGG.

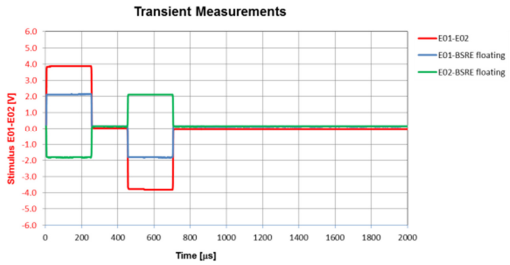

Figure 4-125 Voltage drop with respect to BSRE

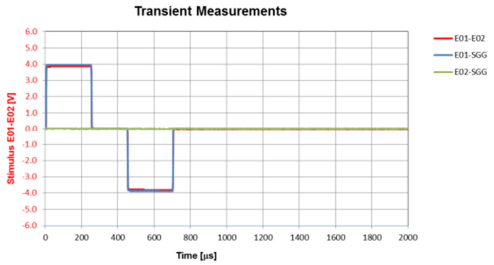

Figure 4-126 Voltage drop with respect to floating SGG

If not otherwise stated, all subsequent pulse and artefact measurements have been made with respect to the floating SGG.

5. Results

5.1 MRI safeness

5.1.1 Overview

This chapter presents simulation and measurement results with a focus on factors influencing heat generation in human tissue from spinal cord stimulators exposed to typical RF pulse sequences encountered in 3 Tesla MRI scanners. In addition, the suitability of the EM models to predict artefacts has been analysed and simulation results are benchmarked against measurements.

An overview of results presented in subsequent sections is given below:

- Analysis of surface currents on platinum electrodes (Section 5.1.2)
- Determination of permittivities and conductivities of electrolytes used in test and measurements and simulations (Section 5.1.3)

- Estimation of the average viscosity of gelled saline for thermodynamic simulations (Section 5.1.4)
- Determination of the propagation velocity along isolated coaxial filars in gelled saline using Time Domain Reflectometry (Section 5.1.5).
- Analysis of EM wave propagation along twelve wire MLC (Section 5.1.6)
- Analysis of EM wave propagation along Lead with twelve electrodes (Section 5.1.7)
- Influence of Lead material parameter on distal end electric fields (Section 5.1.8)
- Influence of base cases and design variations on distal end electric fields (Section 5.1.9)
- Impact of MRI scanner RF frequency on distal end electric fields (Section 5.1.10)
- RF induced temperature rise generated with the RF test bed for selected design variations including benchmarking of measured and predicted results (Section 5.1.11)
- RF induced temperature rise generated with a 3T MRI scanner for final design variation (Section 5.1.12)
- A simplified analytical model to estimate distal end temperature increase (Section 5.1.13)

5.1.2 Surface currents on platinum electrodes

Longitudinal surface currents on cylindrical electrodes in contact with human tissue are a major cause for high electric fringe fields at electrodes' distal ends (Figure 5-1). The electric fringe fields induce volume currents penetrating into the human tissue and therefore contribute to RF induced heating. Magnitudes of electric fringe fields can be up to 50% higher than magnitudes of radial electric fields encountered at the centre between distal ends of electrodes (examples are shown in Figure 5-152 and Figure

5-160). The approach used to determine surface currents is described in Appendix C.1. Magnitude and phase of the longitudinal cumulated surface current for a cylindrical platinum electrode with an outer radius of $725\ \mu m$ and an inner radius of $660\ \mu m$ at $128\ MHz$, driven by a total peak electric field of $E_{x,z=0} = 1\frac{V}{m}$ parallel to the electrode surface, are shown in Figure 5-2 and Figure 5-3, respectively. The penetration depth of surface currents on platinum electrodes is $\sim 60\ \mu m$ and the skin depth is $\sim 14.5\ \mu m$.

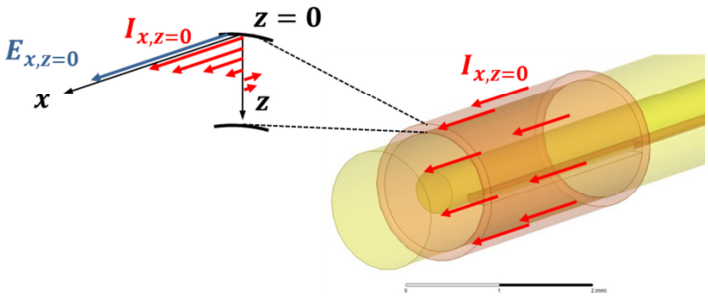

Figure 5-1 Surface current on platinum electrode

For an incident parallel electric field of $E_{inc,x,z=0} = 1\frac{V}{m}$ the resulting parallel electric field on the electrode surface is $E_{x,z=0} = 108 \cdot 10^{-6}\frac{V}{m}$. Assuming an incident parallel electric field of $300\frac{V}{m}$, as generated by the RF heating test bed described in Section 4.3.7, the longitudinal surface current on the electrode is $\sim 15.2\ mA$.

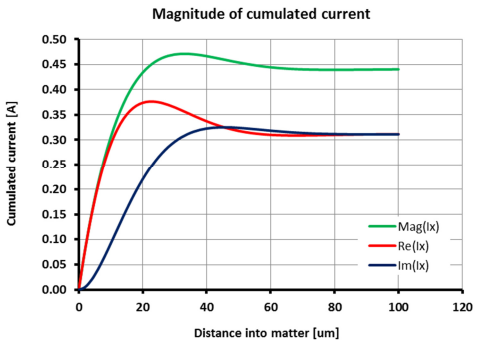

Figure 5-2 Cumulated surface current on platinum electrode for $E_{x,z=0} = 1\frac{V}{m}$

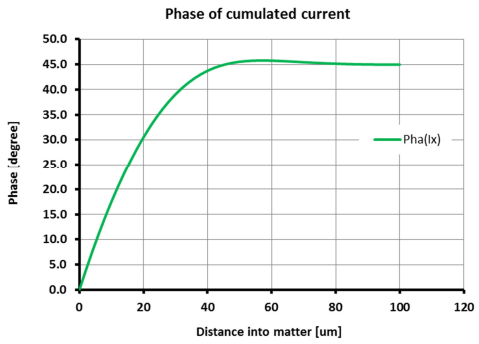

Figure 5-3 Cumulated phase shift of surface current on platinum electrode for $E_{x,z=0} = 1\frac{V}{m}$

Reducing longitudinal surface currents on electrode surfaces reduces electric fringe fields at distal ends leading to lower volume currents and hence less local RF induced heating.

Several approaches can be envisaged to minimise longitudinal surface currents. Doping of platinum electrodes can lead to anisotropic surface conductivities with high conductivity perpendicular to the surface and low conductivity parallel to the surface. Further, electrodes can be coated with anisotropic conducting polymer-hydrogels similar to those presented in References [P155], [P159] and [P163]. Finally, distal ends of electrodes can be coated with dielectric layers in order to minimise electric fringe fields. The results are not presented in this document.

5.1.3 Permittivity and conductivity of electrolytes

This section summarises the results of measured relative permittivities and conductivities of electrolytes used in transient, RF induced heating and transfer function measurements at 128 MHz. The material parameters have been extracted from s-parameter measurements using a coaxial cavity (CC) test fixture described in Section 4.3.5. The algorithm applied to extract material parameters is summarised in Appendix C.2. Two different electrolytes have been used; deionised water (DW) with sodium chloride (NaCl), and deionised water with sodium chloride and polyacrylic acid (PAA). The last electrolyte is referred to as gelled saline. The mass concentrations are summarised in Table 5-1 and the results are presented in Table 5-2 and Table 5-3 for 64 MHz and 128 MHz, respectively. The frequency dependence of relative permittivities and conductivities between 20 MHz and 200 MHz is shown in Figure 5-4 to Figure 5-6.

Type	**Designation**
DW - NaCl	Deionised water with 0.8 g/litre NaCl
DW - NaCl - PAA	Deionised water with 1.4 g/litre NaCl and 9.0 g/litre poly-acrylic acid

Table 5-1 Saline solutions

Electrolyte	**Permittivity**	**Conductivity** $\left[\frac{S}{m}\right]$
Deionised Water (DW)	78.5	$1.1 \cdot 10^{-3}$
Deionised Water with NaCl (DW + NaCl)	78.3	0.15
Deionised Water with NaCl and PAA (DW + NaCl + PAA)	86.7	0.45

Table 5-2 Relative permittivity and conductivity at 64 MHz

Electrolyte	**Permittivity**	**Conductivity** $\left[\frac{S}{m}\right]$
Deionised Water (DW)	82.6	$5.6 \cdot 10^{-3}$
Deionised Water with NaCl (DW + NaCl)	82.0	0.17
Deionised Water with NaCl and PAA (DW + NaCl + PAA)	87.2	0.51

Table 5-3 Relative permittivity and conductivity at 128 MHz

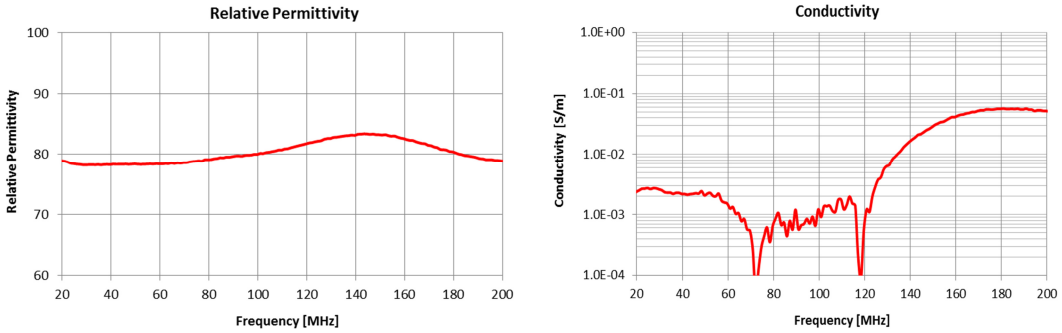

A) B)

Figure 5-4 Deionised water
A) Relative permittivity
B) Conductivity

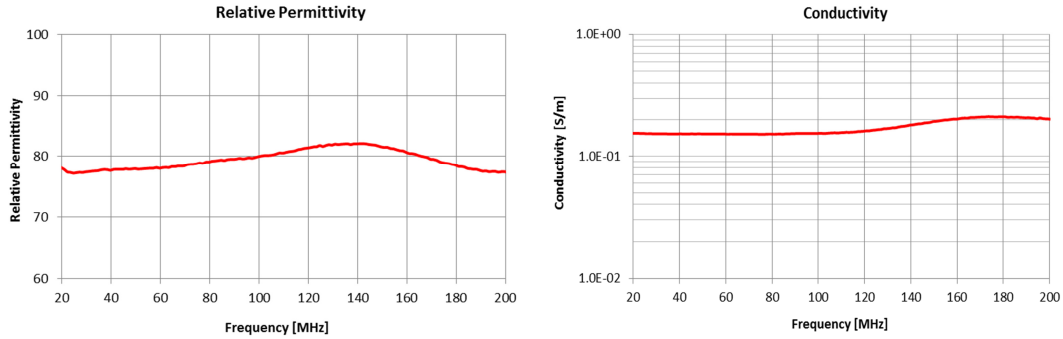

A) B)

Figure 5-5 Deionised water plus sodium chloride
A) Relative permittivity
B) Conductivity

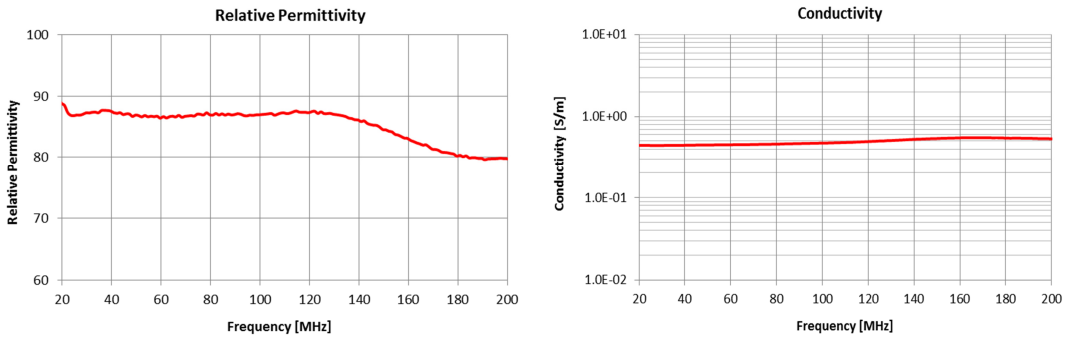

A) B)

Figure 5-6 Deionised water plus sodium chloride plus polyacrylic acid
A) Relative permittivity
B) Conductivity

The measurement repeatability for conductivities is $\pm 0.01\ \frac{S}{m}$ and for relative permittivities $\pm 1\ \%$. For the two electrolytes, extracted RF conductivties at 64 MHz and 128 MHz are within $\pm 15\%$ of measured DC conductivties. The measured RF conductivity of deionised water drops at 70 MHz and 120 MHz. The cause has not been explored. Adding polyacrylic acid to saline increases the relative permittivity by $\sim 10\%$ in the frequency range between 20 MHz and 140 MHz.

5.1.4 Viscosity estimations of gelled saline solution

Figure 5-7 shows cylindrical electrodes immersed in a typical gelled saline solution. Electrodes and MLC are surrounded by a thin layer of saline solution and floating gelled saline clots. The average radius of the multifaceted saline clots varies between 0.5 mm and 4.0 mm. The thin layer of saline solution ranges from 50 μm to 300 μm.

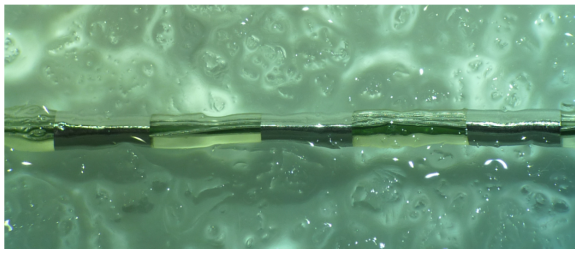

Figure 5-7 Electrodes floating in layer of saline solution surrounded by gelled saline clots

The gelled saline clots inhibit advective heat transfer but due to layers of surrounding saline solution do not inhibit diffusive heat transfer. Depending on the size and location of surrounding gelled saline clots the diffusive heat transfer can reach the same order of magnitude as the conductive heat transfer ([P185]). Therefore, the impact of gelled saline remains a major uncertainty factor in calculating local temperature increase from calculated RF induced volume loss densities.

The average viscosity has been determined from data in Reference [P185]. Figure 5-8 shows the relationship between tracer particle velocities and temperature differences. The particle velocity in gelled saline is approximately 100 times lower than the particle velocity in water for temperature differences up to 20 K.

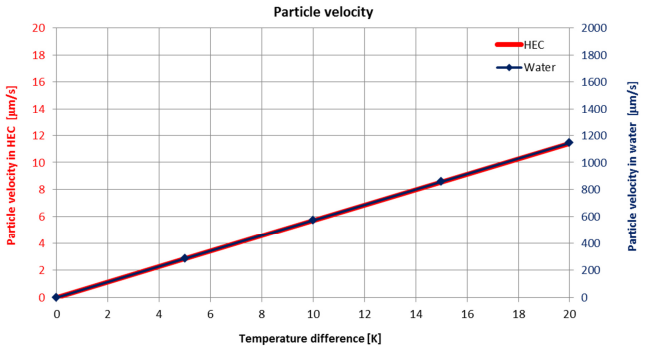

Figure 5-8 Particle velocities in water and gelled saline solution (HEC)

Using the relationship for micro-particle mobility ...

$$\mu_p = \frac{1}{6 \cdot \pi \cdot \eta_f \cdot r} \qquad \left[\frac{m^2}{N \cdot s} \cdot \frac{1}{m} = \frac{m^2}{J \cdot s} = \frac{s}{kg}\right] \tag{5–1}$$

... and the relationship between micro-particle velocity $\vec{v}_p$ and driving force ...

$$\vec{v}_p = \mu_p \cdot \vec{F}_p \qquad \left[\frac{m}{s}\right] \tag{5–2}$$

... results in an average viscosity of diffusing micro-particles in gelled saline of ...

$$\eta_{f,gs} \approx \eta_{f,w} \cdot \frac{\left|\vec{v}_{p,w}\right|}{\left|\vec{v}_{p,gs}\right|} \cdot \frac{r_w}{r_s} \approx 891\ \mu Pa \cdot s\ \cdot\ 10 \cdot 1 \approx 89\ mPa \cdot s \tag{5–3}$$

Here, it is assumed that the average radius r_s of micro-particles diffusing in gelled saline solution is equal to the radius r_w of micro-particles diffusing in pure water. Thermochemical radii of complex ions are given in Reference [P17] and the structure of PAA in electrolyte solutions (gelled saline) is analysed in References [P153] and [P157]. The impact of gelling

agents on temperature rises near electrodes has been measured in Reference [P162].

5.1.5 Isolated coaxial filars

Here, the aim is to determine the propagation velocity and distal end reflection behaviour of a short isolated coaxial filar immersed in gelled saline. The measurement object is a hand-formable, connectorised coaxial cable where the outer conductor is removed at one end. The characteristics of the coaxial cable are given in Table 5-4, the test setup is described in Section 4.3.4 and an outline of the distal end section is shown in Figure 5-9.

Designation	Value	Unit
Cable type: Hand-formable semi-rigid 141 coaxial cable with tinned copper braid outer conductor, silver-plated inner conductor, PTFE insulation	N/A	
Connector type	SMA male	
Cable length including SMA male connector(mechanical length)	580.0	mm
Cable length (effective electrical length)	577.4	mm
Characteristic impedance	50	Ohm
Outer conductor diameter	2.97	mm
Inner conductor diameter	0.91	mm
Phase velocity with respect to vacuum phase velocity	69.5	%

Table 5-4 Coaxial cable characteristics

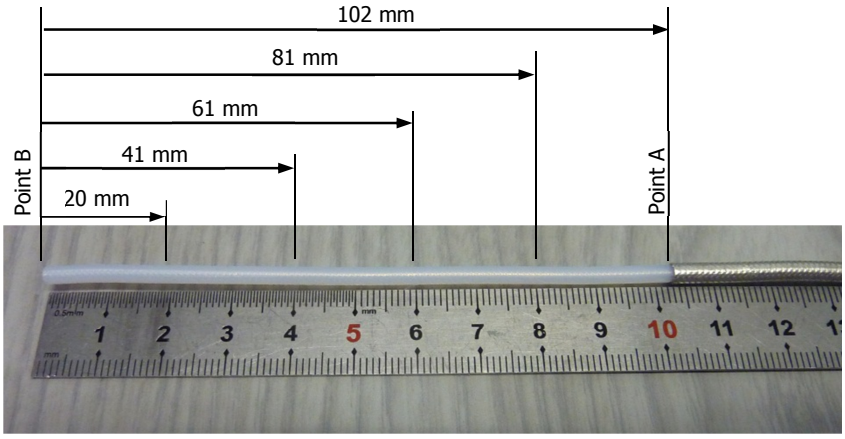

Figure 5-9 Coaxial cable and dismantling lengths of outer conductor at distal end

The inner conductor of the coaxial cable has been isolated from the gelled saline and the outer conductor has been gradually stripped off from 20 mm to 100 mm in steps of 20 mm. The stepped TDR responses have been superimposed and are shown in Figure 5-10. Time t_2 represents the time delay between the isolated distal end (Point B) and the reference plane and time t_1 the time delay between the transition region (Point A) and the reference plane.

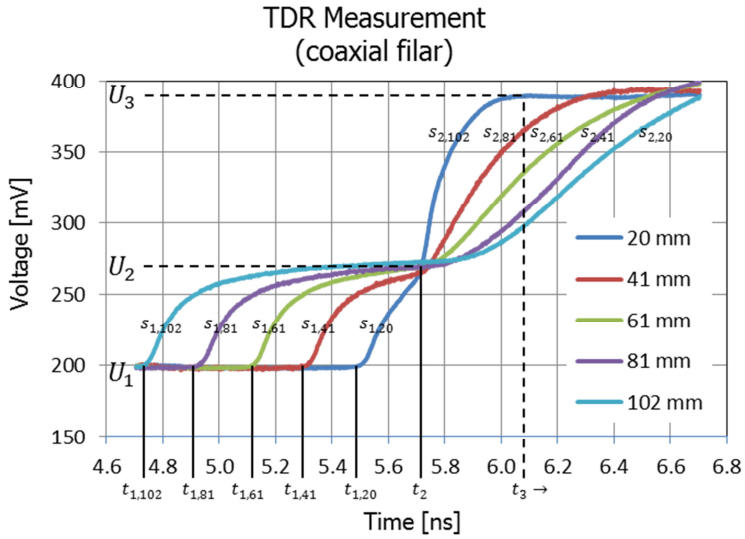

Figure 5-10 TDR measurements results

The propagation velocity along the short isolated coaxial filar section as function of dismantling length Δl is given in Table 5-5. The propagation velocity is close to the propagation velocity inside the coaxial cable. The positive slopes s_1 are all similar and indicate constant dispersion along dismantled sections.

Δl [mm]	Δl [m]	t1 [ns]	t2 [ns]	Δt [ns]	Δt [s]	v_p [m/s]	v_p/c_0	ε_r
20.000	0.020	5.492	5.707	0.215	2.150E-10	1.860E+08	0.621	2.597
41.000	0.041	5.296	5.707	0.411	4.110E-10	1.995E+08	0.666	2.258
61.000	0.061	5.107	5.707	0.600	6.000E-10	2.033E+08	0.678	2.174
81.000	0.081	4.910	5.707	0.797	7.970E-10	2.033E+08	0.678	2.175
102.000	0.102	4.716	5.707	0.991	9.910E-10	2.059E+08	0.687	2.121

Table 5-5 TDR measurement results for guided wave front

The characteristic impedance Z_{is} of the immersed dismantled section can be estimated from the reflection coefficient.

$$r = \frac{Z_{is} - Z_0}{Z_{is} + Z_0} = \frac{U_{reflected}}{U_{incident}} \approx \frac{270\ mV - 200\ mV}{200\ mV} \approx\ 0.35 \tag{5–4}$$

$$Z_{is} = Z_0 \cdot \frac{1 + r}{1 - r} \approx 50\ Ohm \cdot \frac{1 + 0.35}{1 - 0.35} \approx 104\ Ohm \tag{5–5}$$

Since the distal end termination did not change, the reflection at Point B should not vary as function of dismantled length and hence all slopes s_2 should superimpose. But slopes s_2 vary significantly. The slope profiles vary from an exponential profile for very short isolated filars towards a diffusion profile for longer isolated filars. The rate of change of slopes s_2 decreases and approachs zero for long dismantling lengths. The distal end shows serial resistance capacitance (RC) behaviour where the resistance dominates the initial TDR response at t_2 and the capacitance the TDR response for $t \to \infty$. In-between t_2 and $t \to \infty$ resistance as well as capacitance seem to increase as function of dismantling length. Above a certain dismantling length the rate of change of the TDR slope approaches zero, i.e. the TDR slope is constant. The question is what does change the reflection behaviour at the distal end as function of dismantling length?

What follows is an attempt to explain the observed behaviour. The distal end of the dismantled coaxial cable is immersed into gelled saline (Figure 5-11) until the immersion length L has no influence on the TDR measurement. The solid blue arrows indicate the electric field vectors of the forward travelling wave front from the TDR port towards the distal end. The dashed blue arrows indicate the backward (reflected) wave front travelling from the distal end towards the TDR port superimposed on the forward travelling wave. The solid and dashed red arrows designate the

surface currents on the coaxial inner conductor and the ionic volume currents above the isolator, respectively. The solid green lines represent wavefronts inside the isolator and gelled saline. Paths P_1 … P_m … P_∞ show the infinite number of ionic current return paths. Point A presents the transition from the coaxial cable section to the coaxial filar section and points B_{XX} reflection points according to the dismantling length. From Point A towards the distal end the forward travelling transversal (radial) electric and (angular) magnetic fields start to penetrate into the gelled saline building a conic section. At the (isolated) distal end the electric field magnitude increases and the surface current on the coaxial filar section reverses leading to a reversal of the transversal angular magnetic field. The TDR responses for $t < t_2$ in Figure 5-10 are caused by ionic current return paths P_1 … P_m close to the isolator surface and hence are synonymous with wave fronts propagation predominantly inside or close to the isolator.

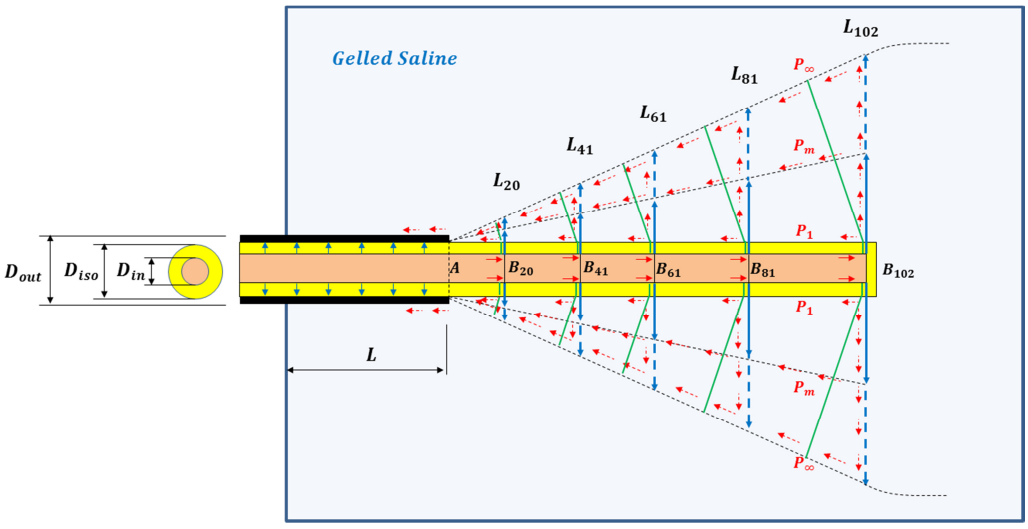

Figure 5-11 Coaxial cable with dismantled distal end in gelled saline (the wave front travelling to the left via the outer conductor of the coaxial cable has been neglected)

On the contrary, for $t > t_2$ the TDR responses are dominated increasingly by volume currents with return paths P_m … P_∞ caused by an increase of the radial electric field at the reflection point and an increase in time delay associated with increasing path lengths P_1 … P_m … P_∞. The radial ionic volume currents are bended back to the isolator due to the electric field

gradient which decreases from the distal end towards Point A. For short dismantling lengths L_{XX} the time delay caused by paths through gelled saline is short and hence the transition time from U_2 to U_3 is short, too. For longer dismantling lengths L_{XX} the transition time between U_2 and U_3 increases until changes in dismantling lengths L_{XX} have only a marginal impact on the time delay $t_3 - t_2$. With increasing dismantling length the transition region at Point B blurs and a clear separation between the reflected guided wave front inside the isolator and the reflected surface wave front in gelled saline is difficult. For long dismantling lengths, guided and surface wavefronts approach each other and build a common wavefront that propagates with constant propagation velocity. To estimate the characteristic propagation velocity for a particular filar in gelled saline (or any other electrolyte) the rates of change of the TDR slopes between t_2 and t_3 have to approach zero. The time delay between t_1 and t_3 and the corresponding dismantling length L_{XX} allow the calculation of the characteristic propagation velocity. For this particular case the propagation velocity is $\sim 0.268\ c_0$ (Table 5-6).

Δl [mm]	Δl [m]	t1 [ns]	t3 [ns]	Δt [ns]	Δt [s]	v_p [m/s]	v_p/c_0	ε_r
152.000	0.152	4.210	8.000	3.790	3.790E-09	8.021E+07	0.268	13.969

Table 5-6 TDR measurement results for common wave front

For comparison, the propagation velocity of a plane wave in gelled saline is $\sim 0.097\ c_0$.

5.1.6 EM waves along MLC

5.1.6.1 Overview

In this section, the wave propagation along a MLC with 12 platinum Lead wires is analysed. The MLC is embedded in gelled saline. Material characteristics of the platinum Lead wires, MLC, and gelled saline are outlined in Appendices A.2, A.3, and A.5, respectively.

The objective is to determine attenuation and phase constants, electric and magnetic field distributions, surface currents and penetration depths of field components into gelled saline. For the analysis, both ends of the MLC are terminated in their characteristic impedances to minimise distal end reflections. Two scenarios are investigated. The first scenario considers a plane wave excitation, similar to the exposure in an MRI scanner, and the second scenario considers a wave excitation from a coaxial wave port. Further, calculated parameters are benchmarked against transfer function measurements and inconsistencies are highlighted.

Finally, the addition of auxiliary electrodes is explored to increase the insertion loss between distal and proximity ends of the MLC.

5.1.6.2 Planar wave excitation

Electric and magnetic vector fields along the MLC and surface currents on a single wire are presented for a planar incident linear polarised sinusoidal electromagnetic wave with electric field strength of $1.0\ \frac{V}{m}$. If not otherwise stated the calculated field components are given for the total electromagnetic field in following units:

- electric field strengths in $\left[\frac{V}{m}\right]$
- magnetic field strengths in $\left[\frac{A}{m}\right]$
- surface currents in $\left[\frac{A}{m}\right]$.

5.1.6.2.1 Simulation settings

Figure 5-12 shows how the MLC is embedded into a gelled saline cube. The gelled saline cube is embedded into a radiating boundary. Simulations with Uniaxial Perfect Matched Layer (UPML) boundaries provide similar results due to the high attenuation of the gelled saline and hence the quick decay of scattered waves. EM Model #1 (Table 4-2) has been applied for the following analysis.

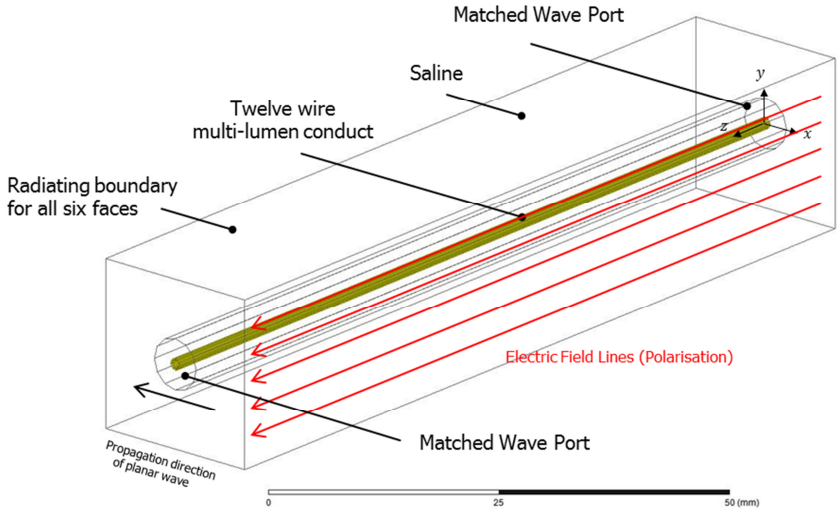

Figure 5-12 Twelve wire MLC in saline and planar wave excitation

Both ends are terminated in wave ports with characteristic impedance equivalent to the characteristic impedance of the MLC:

- Common mode characteristic impedance:
  $Z_{o,c} \approx (28 + j7)\ Ohm$
- Differential mode characteristic impedance between two Lead wires:
  $Z_{o,d} \approx (34 - j2)\ Ohm$

An unattenuated planar wave is incident from one side onto the MLC. Table 5-7 summarises model dimensions.

Part	**Dimensions and parameters**
Wave Port	Diameter: 20 mm
Wires	Diameter: 120 µm Embedded in MLC and not in contact with saline
MLC	Length: 600 mm Diameter: 1.32 mm
Saline	Length (z-dimension): 600 mm Width (x-dimension): 20 mm Height (y-dimension): 20 mm

Table 5-7 Dimensions - planar wave excitation

Radial dimensions are measured from the surface of Lead wires, crossing the thin isolation of the MLC and penetrating into the gelled saline solution (Figure 5-14).

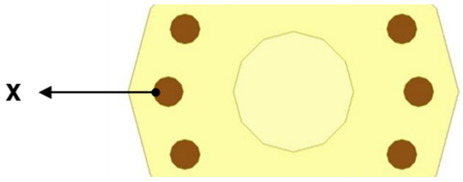

Figure 5-13 Offset from Wire W01 into saline

Figure 5-15 shows a cross-section of the MLC with wire numbering scheme. Wires are numbered clockwise starting at the left side. The distal end is located perpendicular into the paper and the proximity end is located perpendicular out of the paper.

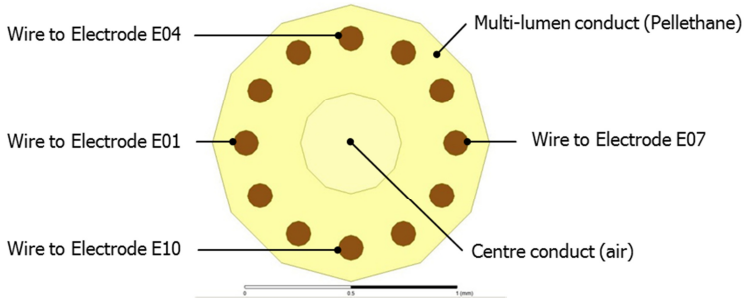

Figure 5-14 Cross-section of twelve wire MLC without BL

For surface currents along Lead wires the orientation scheme indicated in Figure 5-15 is applied. The 0° path faces the gelled saline solution and the 180° path faces the centre of the MLC.

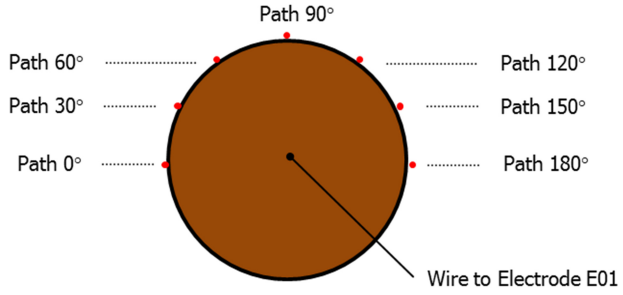

Figure 5-15 Cross-section of Wire W01 to Electrode E01 and path designation

5.1.6.2.2 Electric and magnetic vector fields

Figure 5-16 shows calculated transversal electric and magnetic vector fields along the MLC in steps of 50 mm starting from the matched wave port at z = 0 mm towards the centre of the MLC at z = 300 mm. The phase angle φ = 130° refers to the phase of the incident planar wave with maxima of transversal electric fields at both wave ports. The slight asymmetry of some field plots is attributed to asymmetric meshes in any given transversal plane. The field patterns lead to following conclusions. First, the interior of the MLC shows no significant electric and magnetic field magnitudes, i.e. the interior is nearly free of electric and magnetic fields. Second, the mode pattern looks similar to a TEM mode excited in a

coaxial waveguide with lossy outer conductor (gelled saline). Third, the transversal electric and magnetic mode patterns do not significantly change along the MLC.

Vector plot of electric field on transversal plane at φ=130°

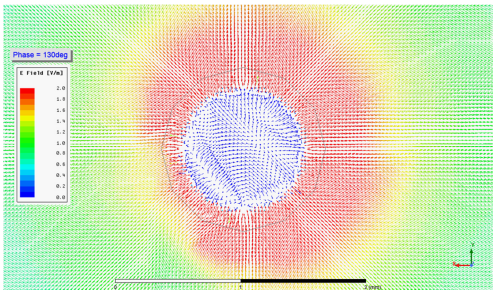

z=0 mm

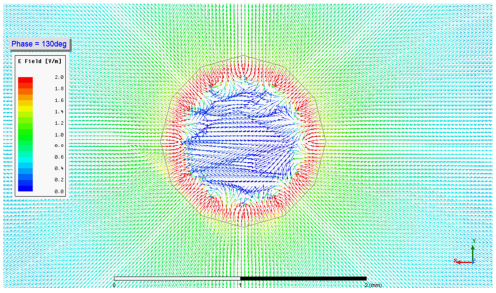

z=50 mm

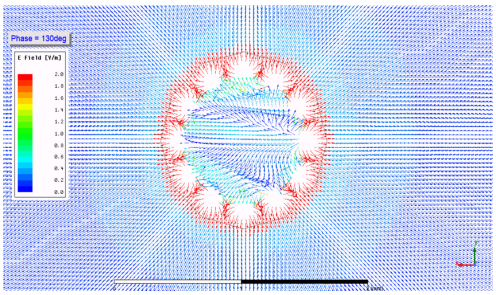

z=100 mm

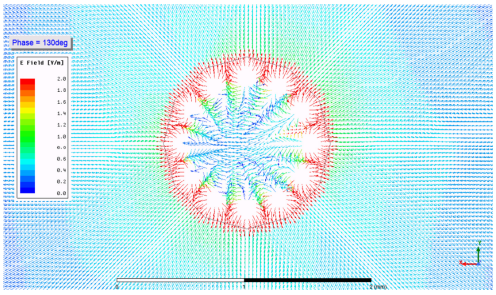

z=150 mm

Vector plot of magnetic field on transversal plane at φ=130°

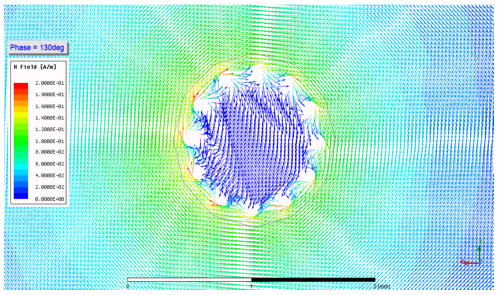

z=0 mm

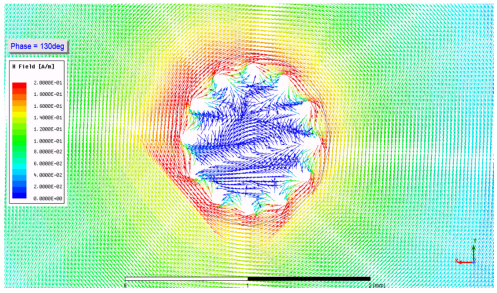

z=50 mm

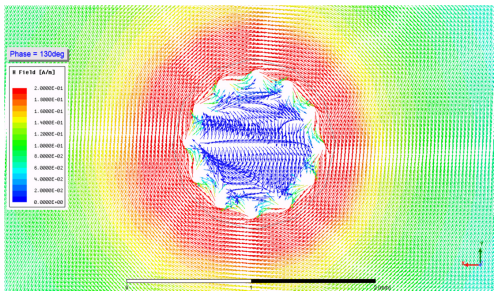

z=100 mm

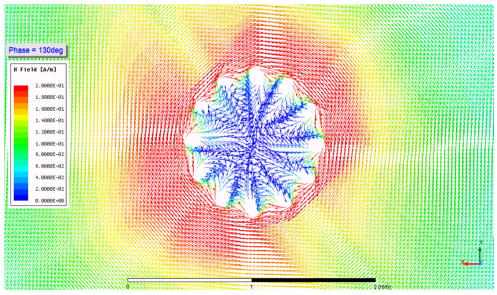

z=150 mm

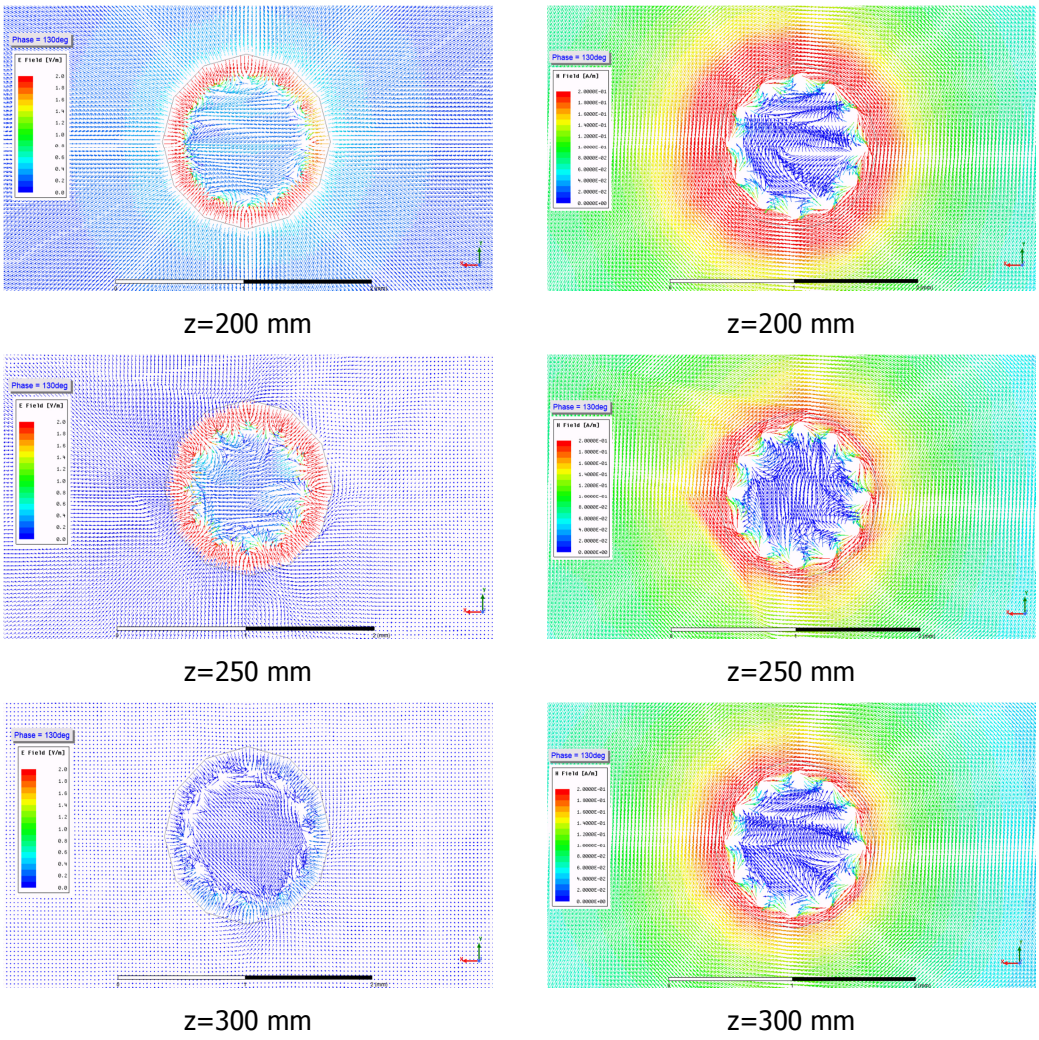

Figure 5-16 Total transversal electric and magnetic field components for a MLC length of 600 mm; MLC without BL

5.1.6.2.3 Magnitude of vector fields

Figure 5-17 shows (radial) electric and (angular) magnetic field magnitudes along Lead wire W01 (Path 0°), along the MLC to saline interface, and along a path 1 mm inside the gelled saline solution (measured from the MLC surface).

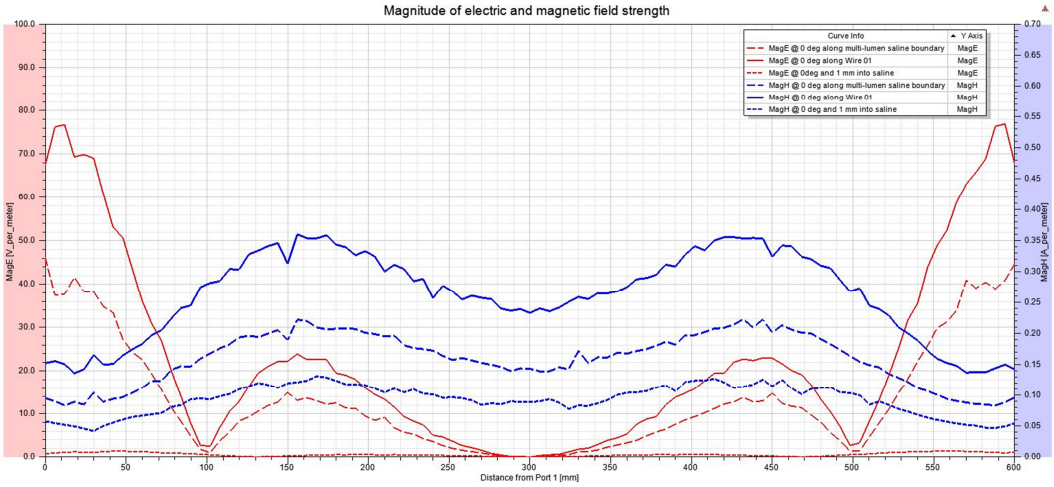

Figure 5-17 Magnitude of total electric (red) and magnetic (blue) field for φ=0° along MLC; MLC without BL

The magnitude of the electric field drops sharply at the MLC surface whereas the magnitude of the magnetic field decays slowly into the saline. The decrease in electric and magnetic field strength is reported in the next section. The wavelength at 128 MHz is approximately 300 mm.

5.1.6.2.4 Magnitude of radial electric field

The radial electric field drops over two sections. The first section (Figure 5-18) lies between the wire surface and the MLC surface and the second section (Figure 5-19) lies above the MLC surface and extends into the gelled saline.

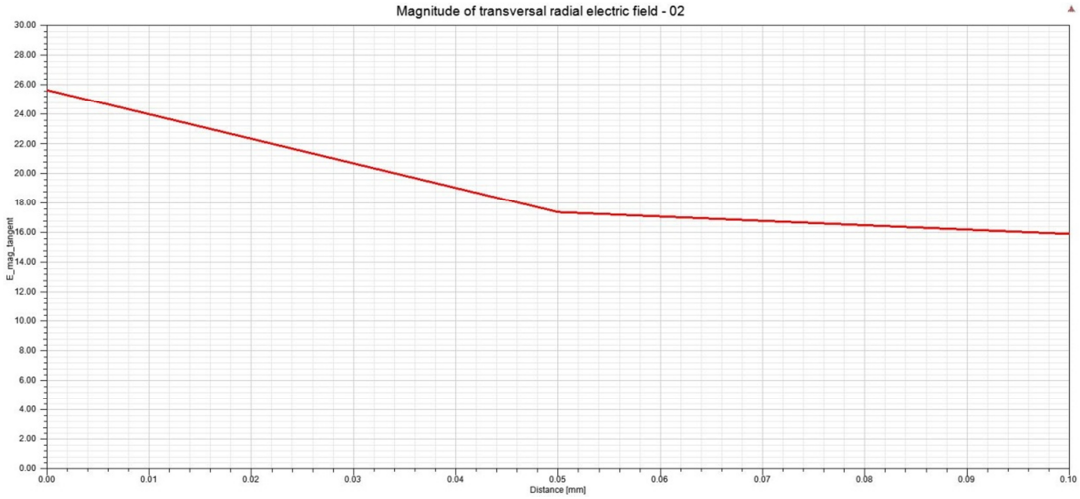

Figure 5-18 Magnitude of total radial electric field between conductor surface and MLC surface at z = 220 mm; MLC without BL

The magnitude of the transversal radial electric field drops by about 61% between the conductor surface and the MLC surface (Figure 5-18). From the MLC surface, the magnitude decays exponentially into the saline and at about 3 mm into the saline the magnitude decreased to 1% of its value at the MLC surface (Figure 5-19). Therefore, 99 % of the electric field is concentrated in a circular cross section with radius $r_e \cong 3.7$ mm around the centre of the MLC.

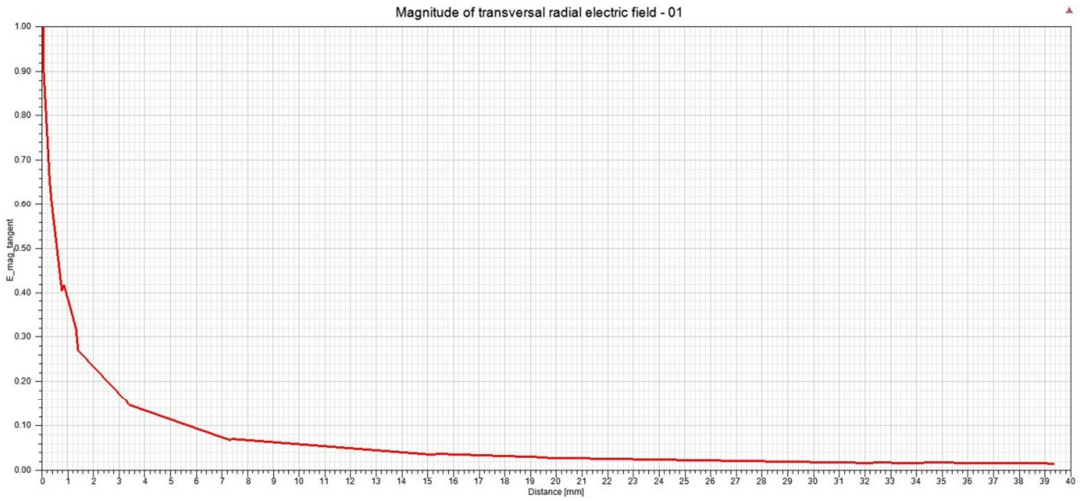

Figure 5-19 Magnitude of total radial electric field from MLC surface into saline at z = 220 mm; MLC without BL

5.1.6.2.5 Magnitude of angular magnetic field

The concentric angular magnetic field is shown in Figure 5-20 for varying distances from the Lead wire surface (Figure 5-13). The magnitude of the transversal angular magnetic field drops by about 57% between the conductor surface and the MLC surface and then decays exponentially into the gelled saline. At about 16 mm into the gelled saline the magnitude decreased to 10% of its value at the MLC surface. The angular magnetic field component extends more than 5 times further into the saline than the radial electric field component and more than 90 % of the magnetic field is concentrated in a circular cross section with radius $r_h \cong 16.7$ mm around the centre of the MLC.

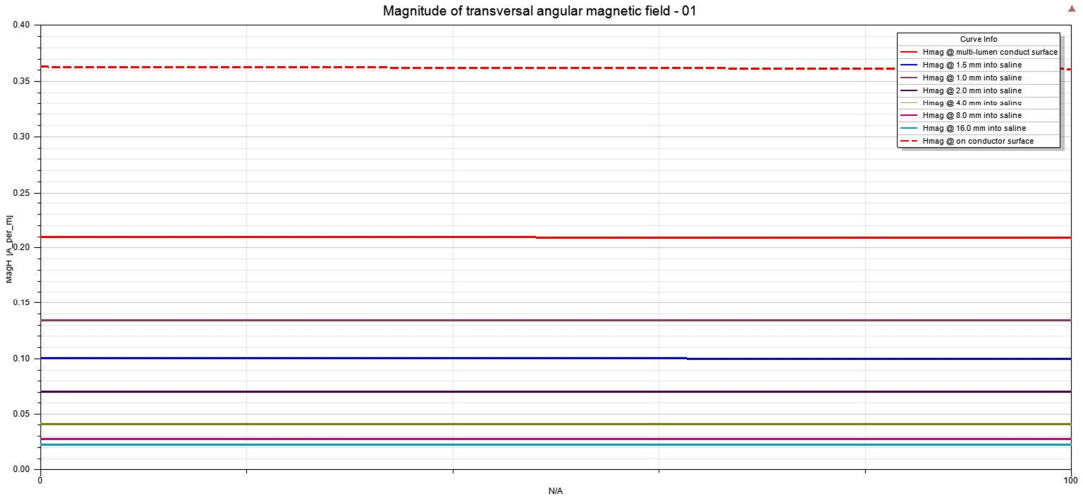

Figure 5-20 Magnitude of total angular magnetic field from MLC surface into saline at z = 300 mm; Parameter: distance from wire surface; MLC without BL

5.1.6.2.6 Magnitude of surface currents

Figure 5-21 shows a five point interpolation of surface current magnitudes along the MLC. The red curve represents the surface current on the Lead wire surface and the blue curve represents the surface current on the multi-lumen to gelled saline boundary. The two surface currents point in opposite directions and the surface current on the conductor surface is approximately ten times stronger than the surface current on the multi-lumen to gelled saline boundary.

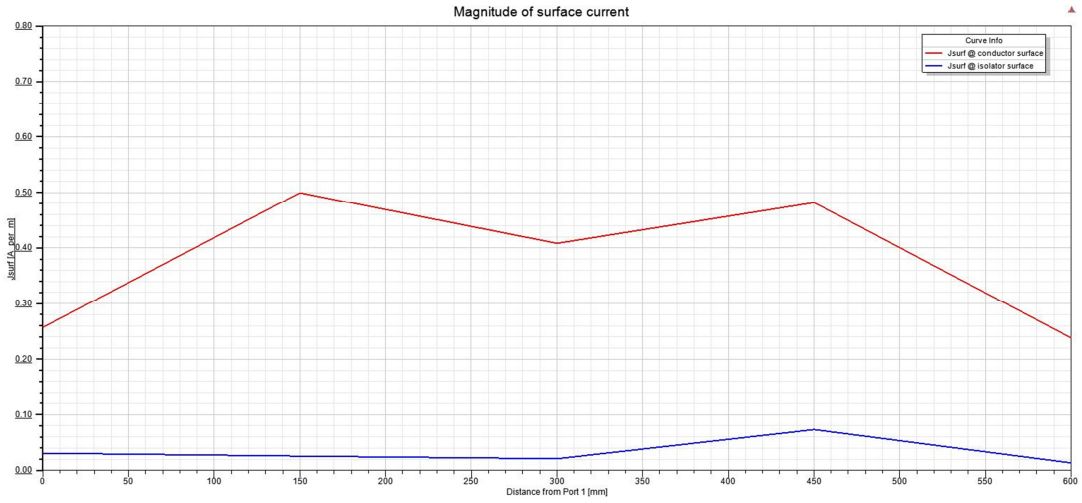

Figure 5-21 Magnitude of total surface current along MLC along conductor-isolator (red) and isolator-saline (blue) surface; MLC without BL

Further, Figure 5-22 shows a five point interpolation of surface current magnitudes around a single Lead wire. The magnitude varies around the perimeter of the wire and has a maximum on the face pointing towards the multi-lumen to gelled saline boundary (Path 0°) and a minimum on the face pointing towards the centre of the MLC (Path 180°). The ratio between maximum and minimum surface current on a single wire for a given position along the Lead is greater than 100.

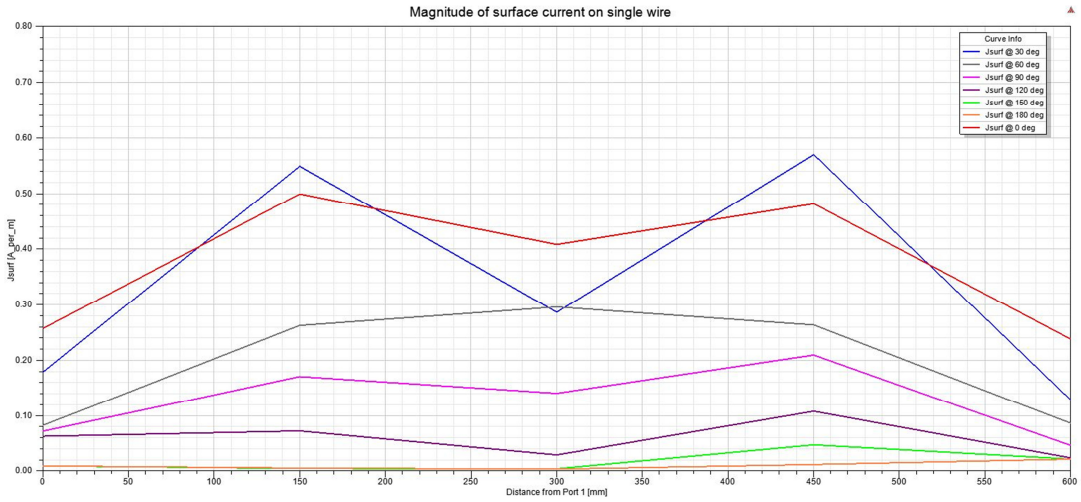

Figure 5-22 Magnitude of total surface current on Wire 01 around circumference along Lead; Parameter: location on wire perimeter; MLC without BL

5.1.6.3 Coaxial wave excitation

The following simulation results are presented for a coaxial wave excitation at one end of the MLC:

- Reflection loss and insertion loss
- Electric and magnetic vector fields and vector field components
- Surface currents

If not otherwise stated the fields are shown for...

- a sinusoidal coaxial TEM mode of 1 µW injected into Wave Port 1
- the total electromagnetic field
- electric field strengths in $\left[\frac{V}{m}\right]$
- magnetic field strengths in $\left[\frac{A}{m}\right]$
- surface currents in $\left[\frac{A}{m}\right]$.

5.1.6.3.1 Simulation settings

Figure 5-23 depicts the MLC embedded into the gelled saline cube with two wave ports at the distal ends. A coaxial TEM wave is injected into the right wave port. The left wave port is terminated. Both wave ports are matched with their characteristic impedances. EM Model #1 (Table 4-2) has been applied for the following analysis.

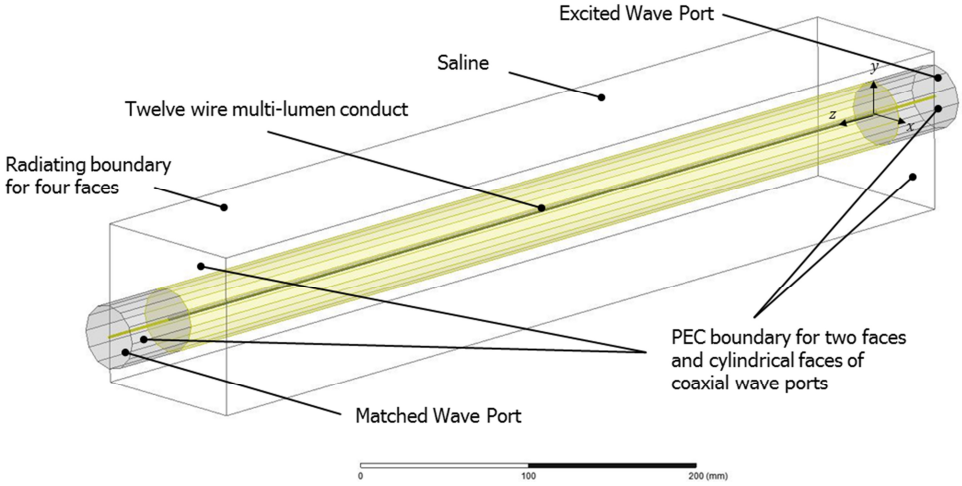

Figure 5-23 Twelve wire MLC in saline and coaxial excitation

The two wave ports consist of conductive hollow cylindrical sections embedded inside the MLC extensions (Figure 5-24). The cylindrical sections interface with the ring of 12 Lead wires of the MLC. One wave port is excited between the cylindrical section and the boundary between MLC and gelled saline (Integration Line).

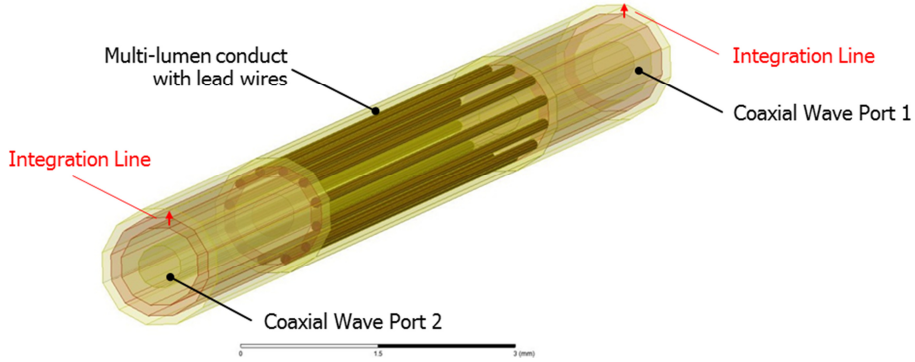

Figure 5-24 Coaxial wave ports and MLC

The model dimensions are summarised in Table 5-8.

Part	**Dimensions**
Wave Port	Diameter: 40 mm Length: 50 mm
Wires	Diameter: 120 µm Embedded in MLC and not in contact with saline
MLC	Diameter: 1.32 mm Length: 600 mm
Saline	Length (z-dimension): depending on length of MLC Width (x-dimension): 20 mm Height (y-dimension): 20 mm

Table 5-8 Dimensions - coaxial wave excitation

5.1.6.3.2 Reflection and insertion loss

The wave ports are matched having a return loss better than 20 dB for MLC lengths between 100 mm and 1200 mm (Figure 5-25) indicating that field pattern distortions from wave port reflections can be neglected.

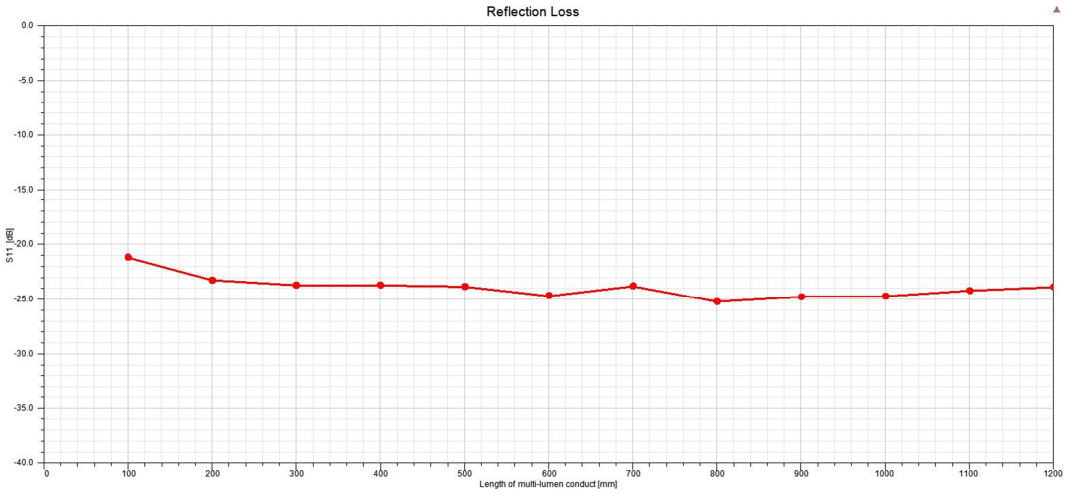

Figure 5-25 Reflection loss at Wave Port 1 as function of MLC length (no boundary layer)

The insertion loss shows a steep slope with approximately 6 dB per 100 mm (Figure 5-26).

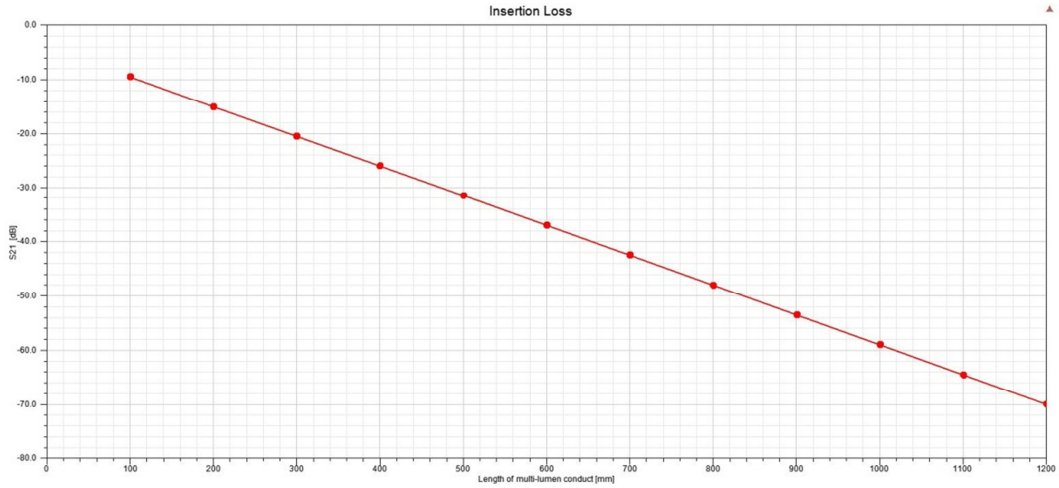

Figure 5-26 Insertion loss between Wave Ports 1 and 2 as function of MLC length (no boundary layer)

5.1.6.3.3 Electric and magnetic vector fields

The electric and magnetic field patterns on a transversal cross-section for coaxial mode excitation (Figure 5-27) and planar wave excitation (Figure 5-16) are very similar. Therefore, attenuation and phase constants can be deduced from a coaxial TEM wave excitation scheme.

Vector plot of electric field on transversal plane at φ=50°

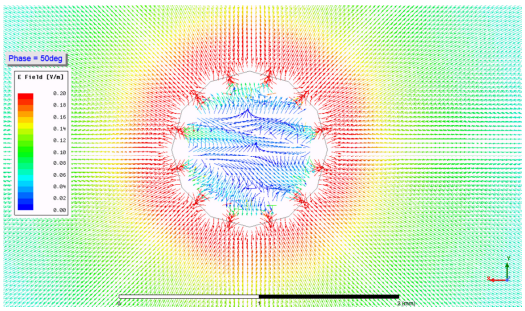

z=300 mm

Vector plot of magnetic field on transversal plane at φ=50°

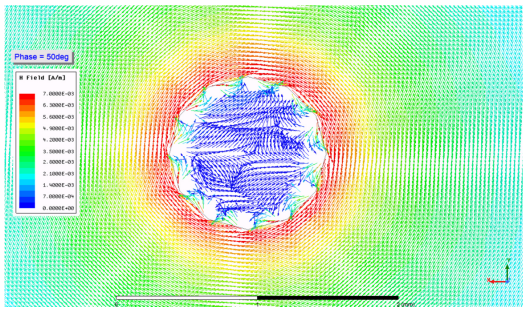

z=300 mm

Figure 5-27 Transversal electric and magnetic field components for MLC length of 600 mm (no boundary layer)

5.1.6.3.4 Magnitude of vector fields

Figure 5-28 shows (radial) electric and (angular) magnetic field magnitudes along the Lead wire W01 (Path 0°), along the MLC to saline interface, and along a path 1 mm inside the gelled saline solution (measured from the MLC surface). Similar to the planar wave excitation the magnitude of the electric field drops sharply at the MLC surface whereas the magnitude of the magnetic field decays slowly into the saline. The decrease in electric and magnetic field strength is reported in the next section. The wavelength is approximately 300 mm.

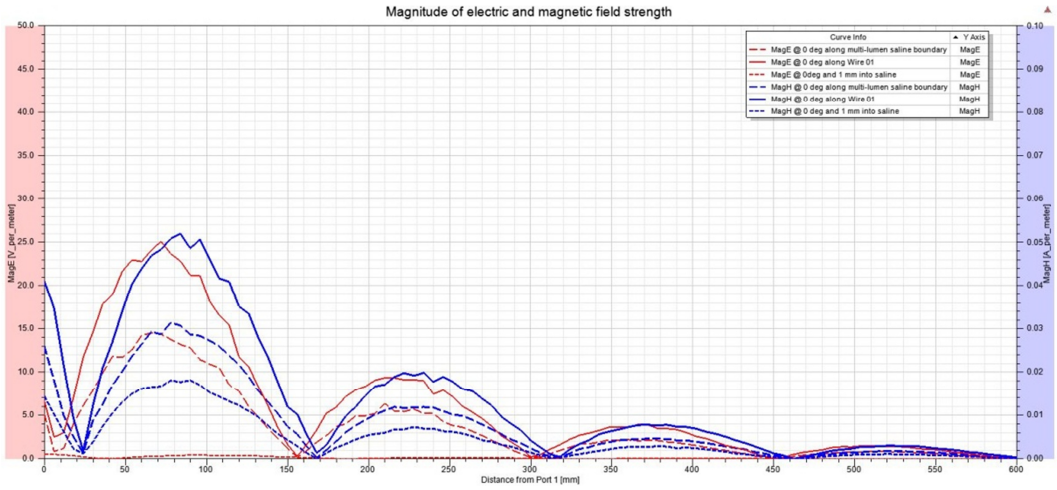

Figure 5-28 Magnitude of total electric and magnetic field for φ=0° along MLC (no boundary layer)

5.1.6.3.5 Magnitude of radial electric field

Similar to the planar wave excitation, the radial electric field drops over two sections. The first section (Figure 5-29) is between the wire surface and the MLC surface and the second section (Figure 5-30) lies above the MLC surface and extends into the gelled saline.

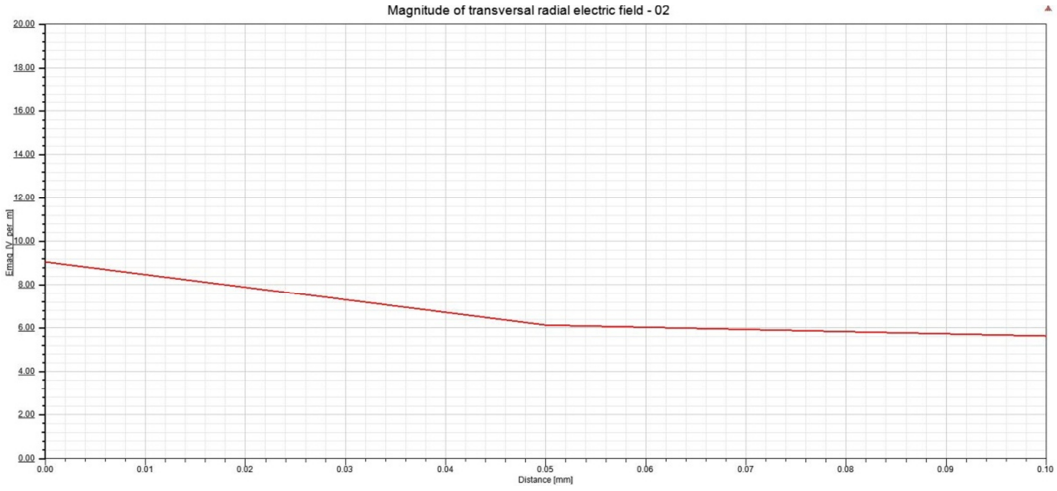

Figure 5-29 Magnitude of radial electric field between conductor surface and MLC surface at z = 300 mm

The transversal radial electric field decay behaves the same way as outlined for the planar wave excitation scenario in section 5.1.6.2.4.

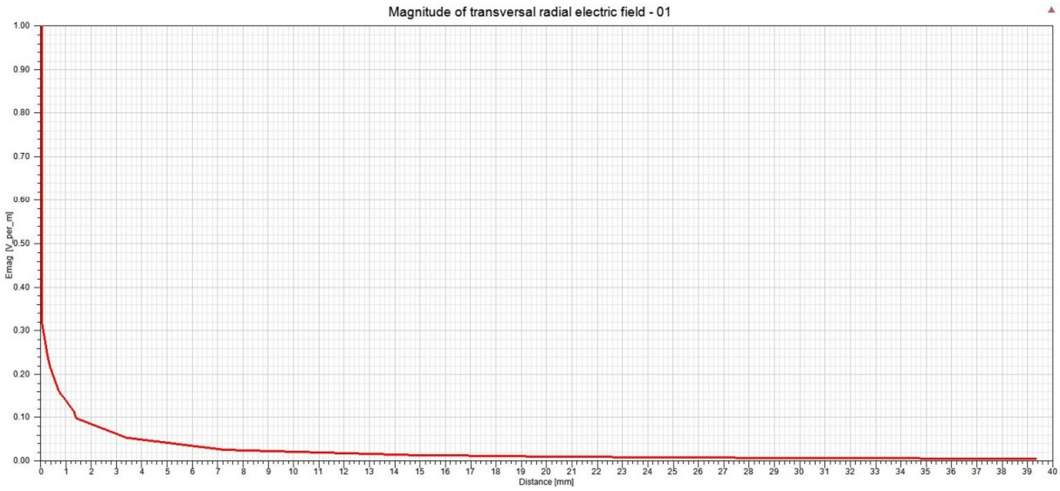

Figure 5-30 Magnitude of radial electric field from MLC surface into saline at z = 300 mm

5.1.6.3.6 Magnitude of angular magnetic field

The concentric angular magnetic field is shown in Figure 5-31 for varying distances off the Lead wire surface. At 16 mm into the saline the magnitude of the transversal angular magnetic field decreases to 3% of its value at the MLC surface. The magnetic field extends more than 5 times further into the gelled saline than the electric field. The magnetic field is more confined around the MLC for coaxial wave excitation compared with planar wave excitation whereas the electric field penetration into saline is comparable with planar wave excitation.

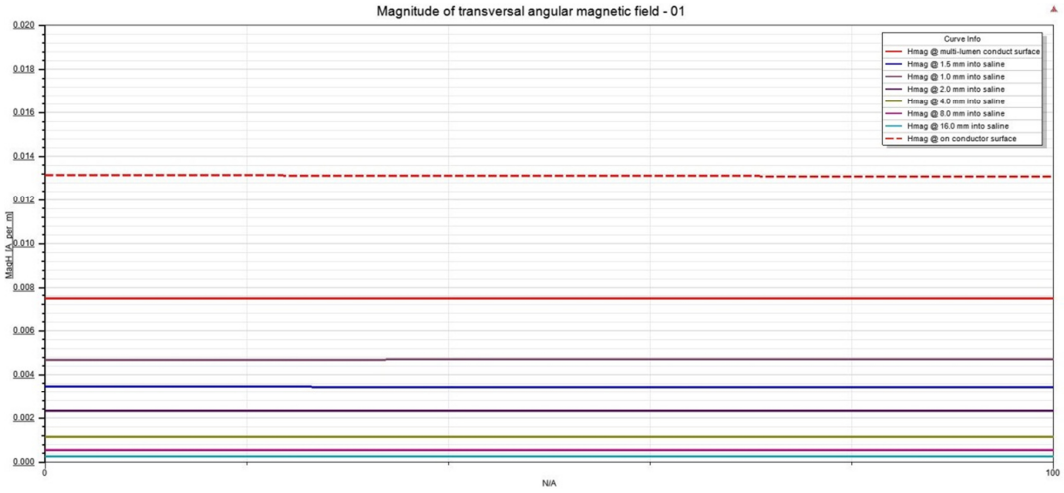

Figure 5-31 Magnitude of total angular magnetic field from MLC surface into saline at z = 300 mm; Parameter: distance from wire surface; MLC without BL

5.1.6.3.7 Magnitude of surface currents

Figure 5-32 shows a seven point interpolation of surface current magnitudes along the MLC. The red curve represents the surface current on the Lead wire surface and the blue curve represents the surface current on the multi-lumen to gelled saline boundary. The two surface currents point in opposite directions and the surface current on the conductor surface is approximately ten times stronger than the surface current on the multi-lumen to gelled saline boundary. The ratio is equivalent to the ratio stated for the planar wave excitation scenario.

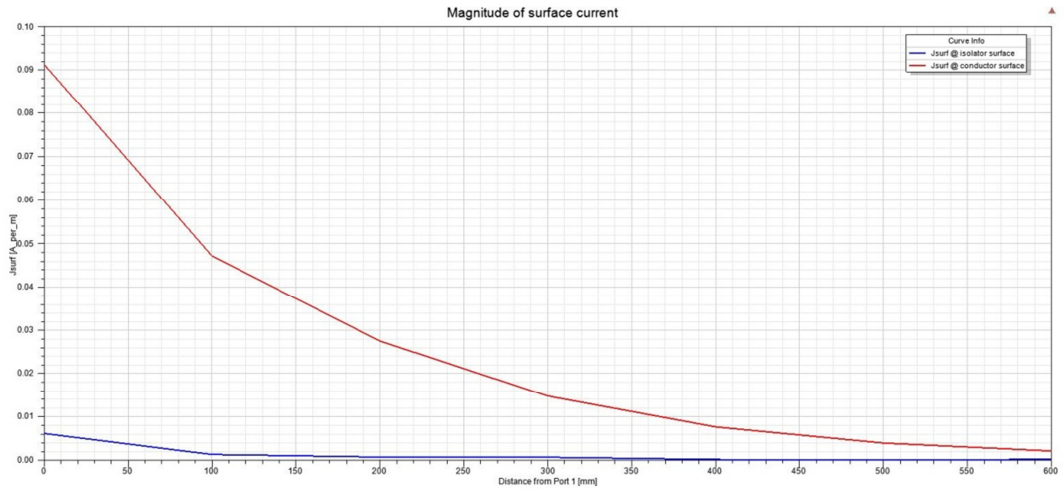

Figure 5-32 Magnitude of total surface current along MLC on conductor-isolator (red) and isolator-saline (blue) surface; MLC without BL

Figure 5-33 shows a seven point interpolation of surface current magnitudes around a single Lead wire. As for the planar excitation scenario, the magnitude varies around the perimeter of a single wire. The magnitude has a maximum on the face pointing towards the multi-lumen to gelled saline boundary (Path 0°) and a minimum on the face pointing towards the centre of the MLC (Path 180°). The ratio between maximum and minimum surface current on a single wire for a given position along the Lead is greater than 10. This ratio is ten times less than the equivalent ratio for planar wave excitation.

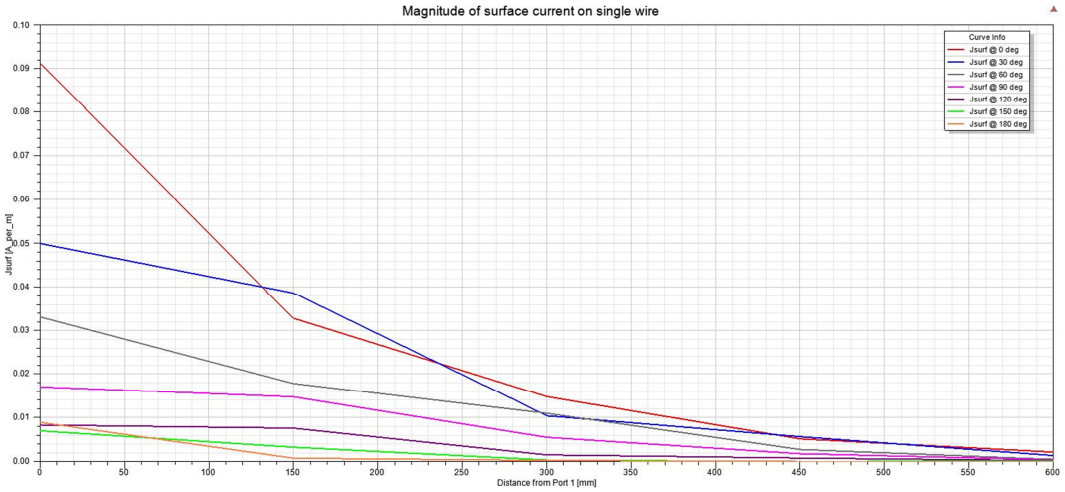

Figure 5-33 Magnitude of total surface current on Wire 01 around circumference along MLC; Parameter: location on wire perimeter; MLC without BL

5.1.6.4 RF transfer function

5.1.6.4.1 Overview

The RF transfer function has been measured at 128 MHz using the test bed described in Section 4.3.6. Four measurement series have been recorded:

- For TEM Mode and H Mode: all Lead wires isolated and open ended at the distal end of the MLC.
- For TEM Mode and H Mode: all Lead wires shorted in a star point at the distal end of the MLC. The star point is immersed in gelled saline.

5.1.6.4.2 TEM Mode - open at distal end

Figure 5-34 and Figure 5-35 show measured and calculated attenuation and insertion phase for the TEM Mode along the open ended MLC. In addition, a linear curve fitting of measured and calculated attenuation for data points between 200 mm and 560 mm is added. To match the attenuation and phase slopes a low permittivity Boundary Layer (BL) $(\varepsilon_r \sim 2.5; t \sim 150\ \mu m)$ shown in Figure 4-7 has been added to the EM model of the the MLC. Section 5.1.6.5 provides further explanations. A major inconsistency between measured and calculated transfer function is visible at the distal end. The measured attenuation shows a deep null about 20 mm from the distal end and the measured phase starts to deviate at about 200 mm from the distal end. The reflection coefficient at the distal end is approximately $r \approx 0.97 \cdot e^{+j\frac{3}{4}\pi}$. Any geometrical modifications of the MLC EM model within reasonable dimensional and material parameter limits have not resulted in a match between measured and calculated

attenuation and insertion phase at the distal end. Varying measurement probe sizes and varying positions of the distal end of the MLC in the phantom torso have resulted in similar results. It seems that the gelled saline shows strong anisotropic behaviour, especially visible around significant discontinuities where local standing waves build up. Adding to the EM model a thin disk with high permeability perpendicular to the MLC axis at the distal end, results in calculated attenuation and insertion phases, that approach measured attenuation and insertion phases. Section 5.1.6.6 tries to provide further insight.

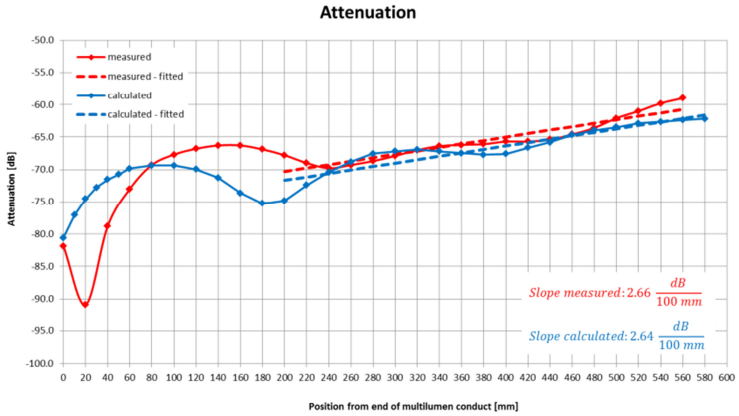

Figure 5-34 Attenuation for TEM Mode along 955 mm twelve wire MLC; Lead wires open ended and isolated from saline at distal end

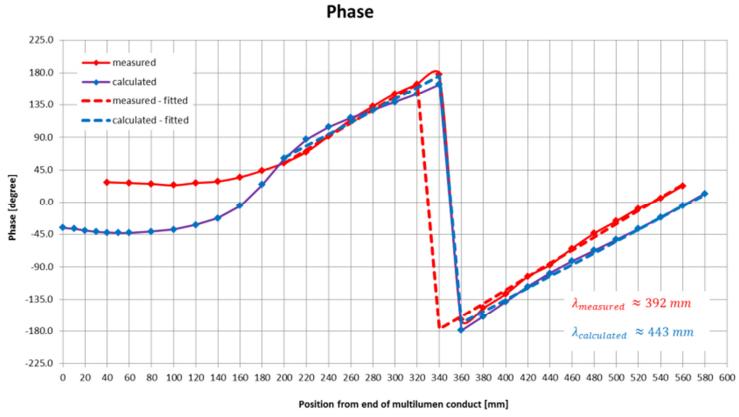

Figure 5-35 Insertion phase for TEM Mode along 955 mm twelve wire MLC; Lead wires open ended and isolated from saline at distal end

5.1.6.4.3 H Mode - open at distal end

Figure 5-36 and Figure 5-37 show measured and calculated attenuation and insertion phase for the H Mode along the open ended MLC. The H Mode magnitude is between 10 dB and 15 dB below the TEM Mode magnitude and the phase of the H Mode lags the phase of the TEM Mode by about 45°. Attenuation and phase slopes of the H Mode are similar to the TEM Mode. The inconsistencies for the H Mode at the distal end are similar to those reported for the TEM Mode. The insertion phase could not be recorded up to the distal end due to limitations of the VNA's dynamic range.

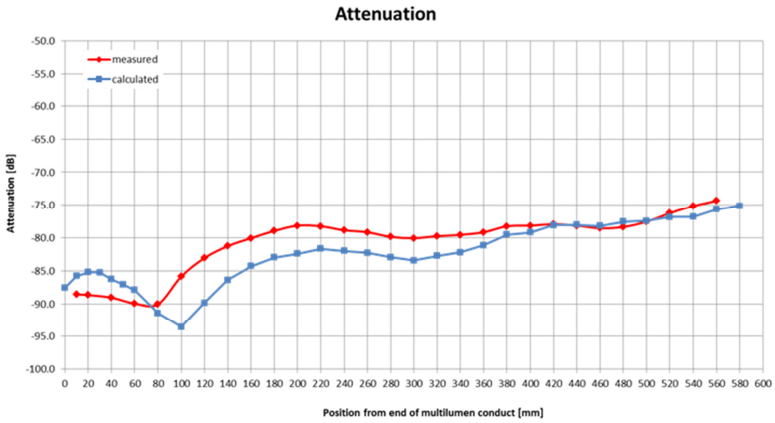

Figure 5-36 Attenuation for H Mode along 955 mm twelve wire MLC; Lead wires open ended and isolated from saline at distal end

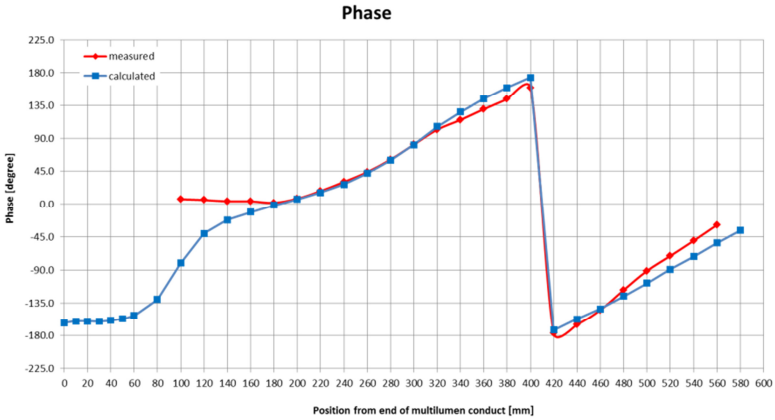

Figure 5-37 Insertion phase for H Mode along 955 mm twelve wire MLC; Lead wires open ended and isolated from saline at distal end

5.1.6.4.4 TEM Mode - short at distal end

Figure 5-36 and Figure 5-37 show measured and calculated attenuation and insertion phase for the TEM Mode along the MLC with shorted wires at the distal end. A shift of 30 mm towards the proximity end is observed for measured attenuation compared with calculated attenuation. Minima and maxima of measured attenuation are further apart compared with calculated attenuation. However, the averaged attenuation and phase slopes are similar and match the attenuation and phase slopes for the case with open ended Lead wires.

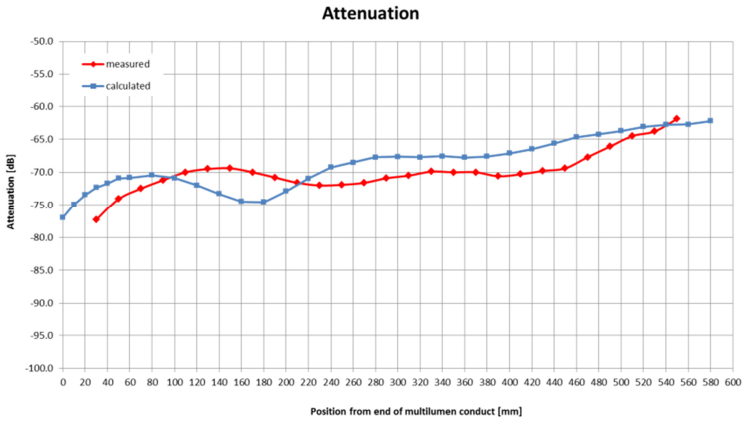

Figure 5-38 Attenuation for TEM Mode along 950 mm twelve wire MLC; Lead wires shorted in star point and immersed in gelled saline at distal

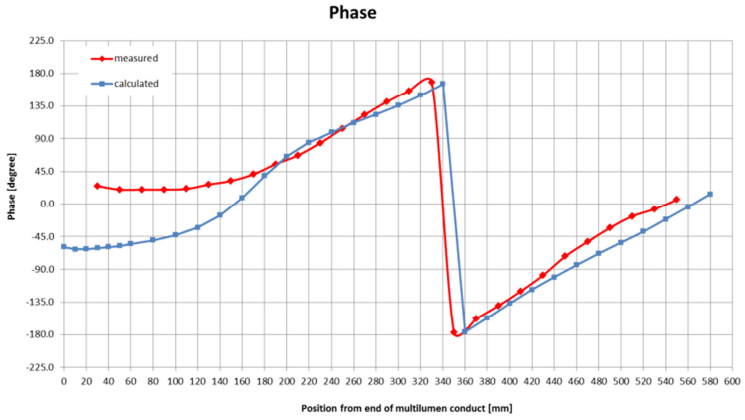

Figure 5-39 Insertion phase for TEM Mode along 950 mm twelve wire MLC; Lead wires shorted in star point and immersed in gelled saline at distal

5.1.6.4.5 H Mode - short at distal end

Figure 5-40 and Figure 5-41 show measured and calculated attenuation and insertion phase for the H Mode along the MLC with shorted wires at the distal end. Despite some deviations in the measured and calculated attenuation between 360 mm and 500 mm the averaged attenuation slopes are similar. The measured and calculated phase slopes differ between 440 mm and 540 mm but the average phase slopes still match. The cause of the attenuation difference at the distal end could not be resolved. Limitations of the VNA's dynamic range did not allow recording the insertion phase up to the distal end.

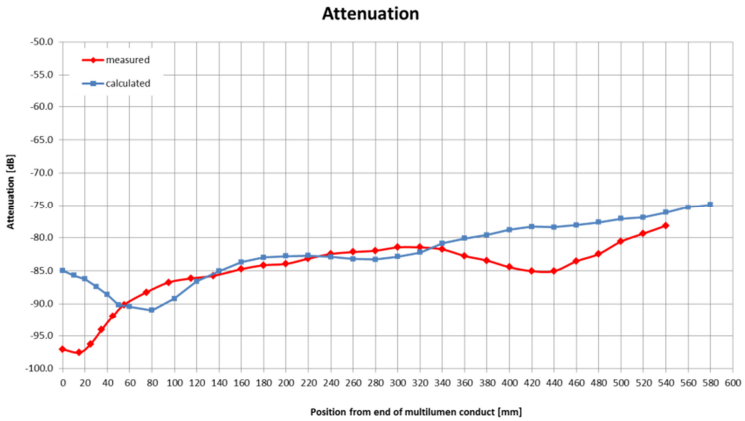

Figure 5-40 Attenuation for H Mode along 950 mm twelve wire MLC; Lead wires shorted in star point and immersed in gelled saline at distal

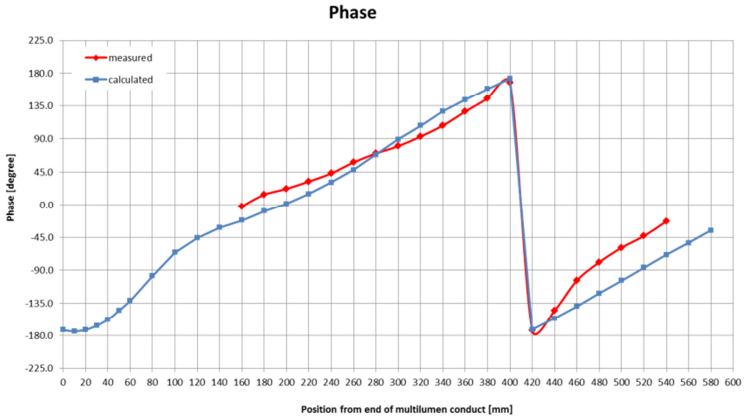

Figure 5-41 Insertion phase for H Mode along 950 mm twelve wire MLC; Lead wires shorted in star point and immersed in gelled saline at distal

5.1.6.4.6 Summary

Attenuation constants, phase slopes and wavelengths for the dominant TEM and H Mode travelling along the MLC have between deduced from transfer functions measurements. The standard EM model for the MLC has been adjusted using a low permittivity boundary layer to match measured and calculated attenuations, phase slopes and wavelengths. Inconsistencies in the measured and calculated attenuation and phase slopes at the distal end have been identified but could not be fully resolved. Explanations are given in Sections 5.1.6.5 and 5.1.6.6.

5.1.6.5 Inconsistencies in attenuation and phase slopes

While measuring the transfer function along a twelve wire MLC discrepancies between calculated and measured wavelength and attenuation have been identified. The calculated wavelengths of about 300 mm is about 25 % shorter than the measured wavelength of about 400 mm and the calculated attenuation of approximately 70 dB is significantly higher than the measured attenuation of approximately 25 dB. A very thin low permittivity Boundary Layer (BL) $(\varepsilon_r \sim 2.5; t \sim 150\ \mu m)$ has been added to EM Model #1 (see Section 4.1.3) to match attenuation and phase slopes. Figure 5-42 shows the calculated difference in attenuation for a MLC with and without BL.

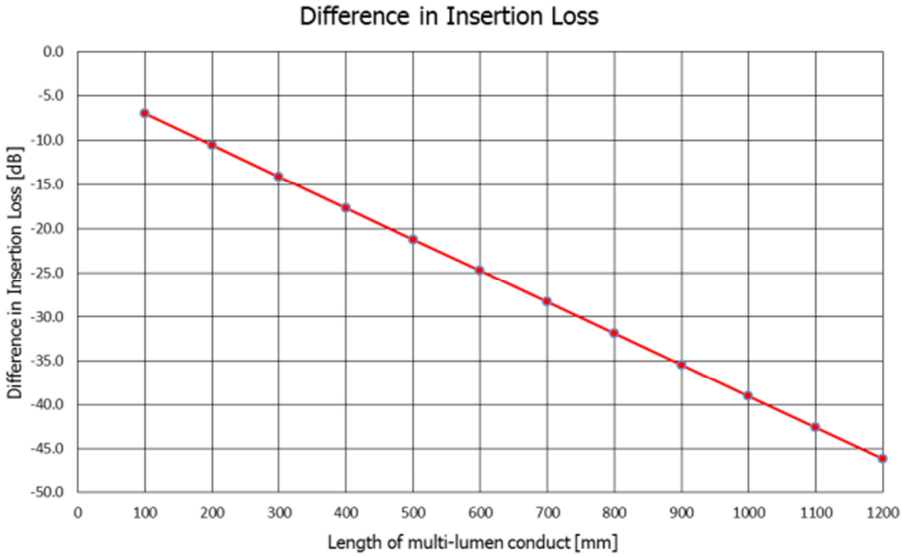

Figure 5-42 Calculated IL difference ($\Delta IL = IL_{with\ BL} - IL_{without\ BL}$) between Wave Ports 1 and 2 as function of MLC length

The boundary layer has been included in electromagnetic simulations later on (EM Model #2 and EM Model #3). The calculated wavelength and attenuation for a 1200 mm long twelve wire MLC that is excited by a coaxial wave port are outlined in Figure 5-43 (without BL) and Figure 5-44 (with BL), respectively.

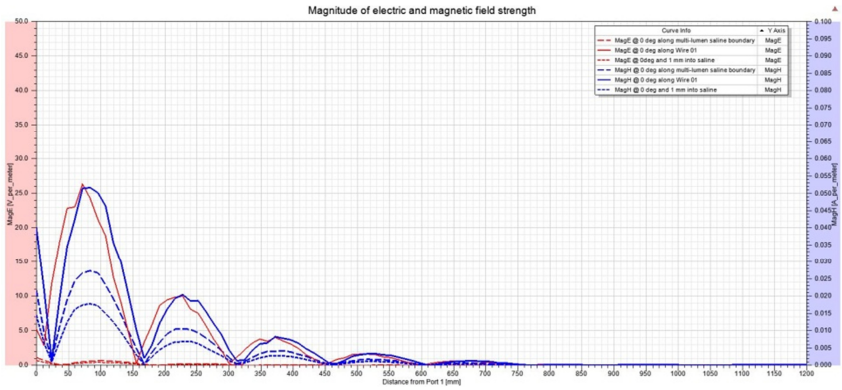

Figure 5-43 Magnitude of total electric and magnetic fields along 1200 mm long MLC for φ=0° predicted with EM Model #1 (without BL)

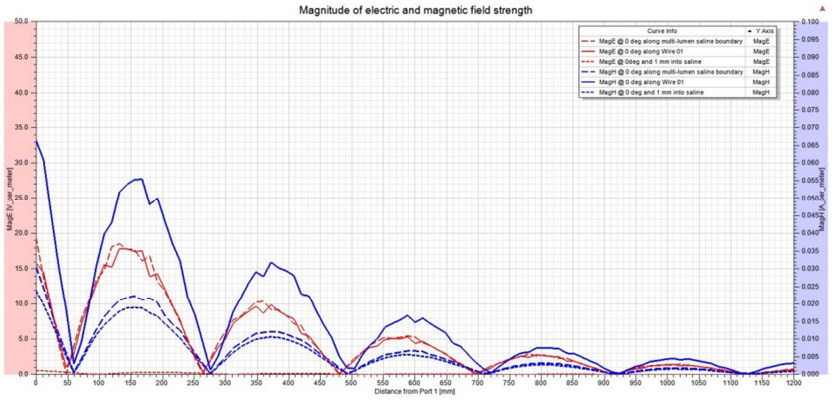

Figure 5-44 Magnitude of total electric and magnetic fields along 1200 mm long MLC for φ=0° predicted with EM Model #2 (with BL ($\varepsilon_r \sim 2.5; t \sim 150\ \mu m$))

Wave port reflection loss and insertion loss for the case with boundary layer are shown in Figure 5-45 and Figure 5-46. For all MLC lengths the calculated reflection loss is better -20 dB and has negligible influence on the insertion loss.

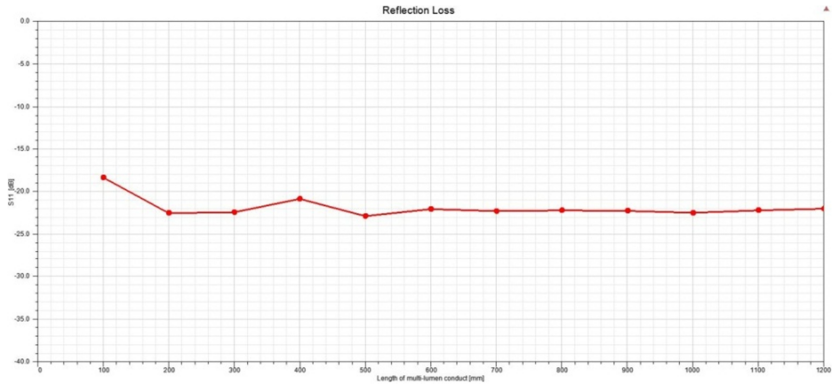

Figure 5-45 Reflection loss at Wave Port 1 as function of Lead length including a boundary layer $(\varepsilon_r{\sim}2.5; t{\sim}150\ \mu m)$

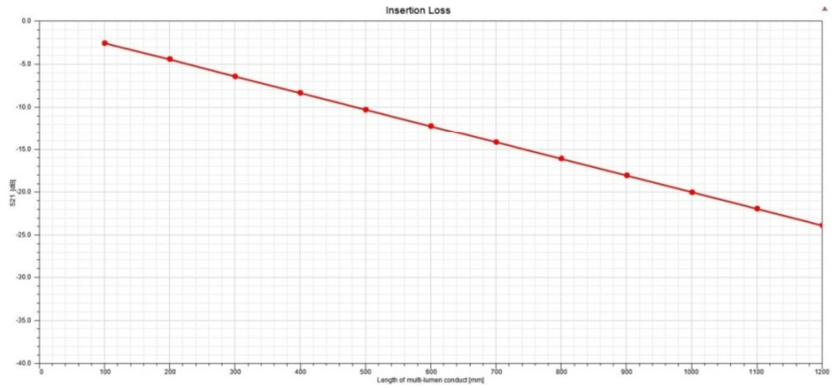

Figure 5-46 Insertion loss between Wave Ports 1 and 2 as function of Lead length including a boundary layer $(\varepsilon_r{\sim}2.5; t{\sim}150\ \mu m)$

Calculated phase slopes and attenuations including the BL are consistent with transfer function measurements presented in Section 5.1.6.4 and metrics presented in Section 5.1.4. The relative permittivity of the BL has been increased to $\varepsilon_r{\sim}3.5$ later on to better match the phase slope. It is supposed, that the BL results from a change in state of Na^+ and Cl^- ions (with their respective hydration shells) adsorbed on the surface of the MLC leading to a significant decrease of the effective permittivity. The influence of the state of water on electric permittivity has been analysed in References [P164], [P165], and [P167] and the impact of hydrophobic and hydrophilic surfaces on local permittivity and viscosity profiles has been reported in References [P38] and [P39].

5.1.6.6 Inconsistencies in reflections at distal end

The measured transfer function for the TEM Mode along the open ended MLC shows a deep null about 20 mm from the distal end. This reflection point resembles a termination with a reflection coefficient of $r \approx 0.97 \cdot e^{+j\frac{3}{4}\pi}$. Incident, reflected and superposed waves for a single reflection are shown in Figure 5-47.

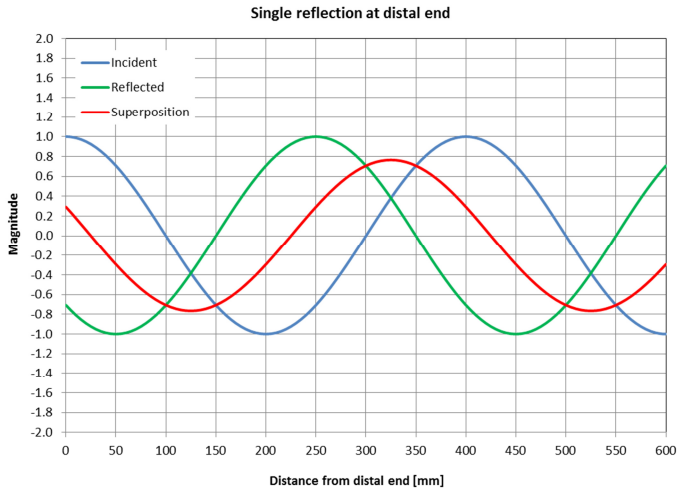

Figure 5-47 Single wave reflection at distal end ($r \approx 0.97 \cdot e^{+j\frac{3}{4}\pi}$)

The open ended MLC induces a phase shift of $\varphi = \frac{\pi}{4}$ for the reflected TEM Mode. This phase shift represents an equivalent MLC length extension of 50 mm at 128 MHz. Since the measured electric and magnetic fields drop immediately after the distal end the phase shift cannot result from a MLC length extension. Therefore, the phase shift of the reflected wave has to result from changes in material properties at the distal end. A relaxation process that causes a time delay of $980\,ps$, equivalent to a phase shift of $\varphi = \frac{\pi}{4}$, might be one cause for the observed shift. But, according to reference [P99] the relaxation time of water for NaCl concentrations of $1.0\,\frac{mol}{l}$ at $25°C$ is approximately $\sim 7.5\,ps$. The relaxation time of the solvent is two orders of magnitude lower than the relaxation time attributable to the equivalent length extension.

Another cause that might explain the phase shift is that a thin high permeability layer oriented perpendicular to the axis of the Lead forms at the distal end. EM simulations have shown that such a layer creates a deep null in the RF transfer function about 20 mm from the distal end.

In addition to the two causes indicated above a third cause is presented below, linked to the motion of charge carriers (ions) in gelled saline surrounding the MLC. The motion of ions in solution under the influence of stationary electric fields is explored in Reference [P20] and the motion of ions in solution under the influence of stationary electric and magnetic fields is analysed in References [P11] and [P12]. Here, the focus is on the motion of ions under the influence of time-harmonic electromagnetic fields next to the MLC. A quasi TEM wave is induced by a source probe at the proximity end as outlined in Figure 5-48 and the distal end is open-ended, i.e. the wires are isolated from the surrounding electrolyte.

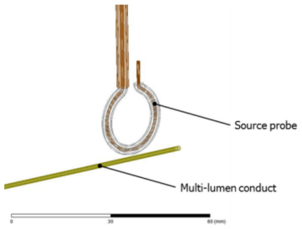

Figure 5-48 Source probe in proximity to MLC

The wave energy propagating along the MLC is concentrated within an effective cross section (volume) shown in Figure 5-49.

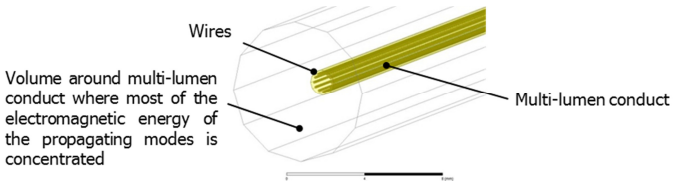

Figure 5-49 MLC embedded in electrolyte (saline)

The Lorentz law describes the superposition of forces and fields at field point P resulting from charges at rest and in motion at source point S (Figure 5-50).

From Coulomb's law follows ...

$$\vec{F}_{P,C} = \frac{1}{4\pi R^2} \cdot Q_S \cdot \frac{1}{\varepsilon_0} \cdot Q_P \cdot \hat{r}_{21} = \frac{1}{4\pi} \cdot \frac{1}{\varepsilon_0} \cdot Q_S \cdot Q_P \cdot \frac{\vec{r}_P - \vec{r}_S}{|\vec{r}_P - \vec{r}_S|^3} \tag{5–6}$$

From Ampere's law follows ...

$$\vec{F}_{P,A} = \frac{1}{4\pi|\vec{r}_P - \vec{r}_S|^2} \cdot \mu_0 \cdot \left[(I_P \cdot \vec{l}_P) \times \left((I_S \cdot \vec{l}_S) \times \hat{r}_{21}\right)\right] = (I_P \cdot \vec{l}_P) \times \vec{B}_S = (\vec{v}_P \cdot Q_P) \times \vec{B}_S \tag{5–7}$$

From the contributions of Coulomb's and Ampere's law follows ...

$$\vec{F}_{P,L} = \vec{F}_{P,C} + \vec{F}_{P,A} \tag{5–8}$$

$$\vec{F}_{P,L} = \frac{1}{4\pi} \cdot \frac{1}{|\vec{r}_P - \vec{r}_S|^3} \cdot Q_S \cdot Q_P \cdot \left[\frac{1}{\varepsilon_0} \cdot (\vec{r}_P - \vec{r}_S) + \mu_0 \cdot \left[(\vec{v}_P) \times \left((\vec{v}_S) \times (\vec{r}_P - \vec{r}_S)\right)\right]\right] \tag{5–9}$$

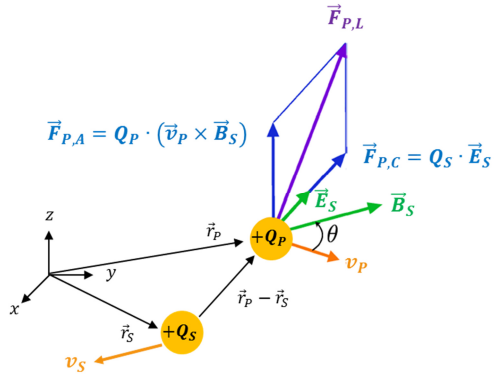

Figure 5-50 Lorentz' law - sign conventions and vector fields

Figure 5-51 to Figure 5-54 show positive and negative charged ions superimposed on typical electric field distributions for 128 MHz at the distal end of the MLC. Figure 5-55 to Figure 5-58 show show positive and negative charged ions superimposed on typical magnetic field distributions.

The left and right columns in the figures below indicate electric fields pointing radially away from and radially towards the MLC, respectively. Field orientations and resulting migration directions of ions are indicated as follows:

- blue arrows — instantaneous direction of electric vector field at the location of the charged particle
- read arrows — instantaneous direction of magnetic vector field at the location of the charged particle
- green arrows — direction of migration of charged particle due to instantaneous magnetic vector fields at the location of the charged particle

The resulting instantaneous ionic migration direction lies in the plane spanned by blue and green arrows and is indicated by dotted black lines with arrow heads in Figure 5-55 to Figure 5-58.

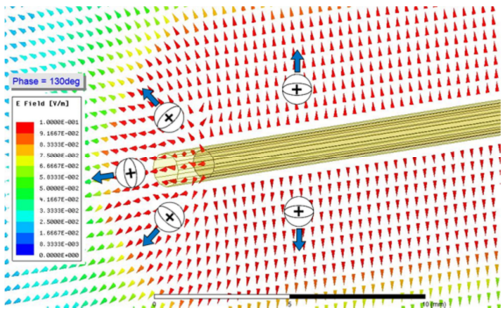

Figure 5-51 Motion of positive ions due to electric field at φ=130° on longitudinal cross-section at distal end

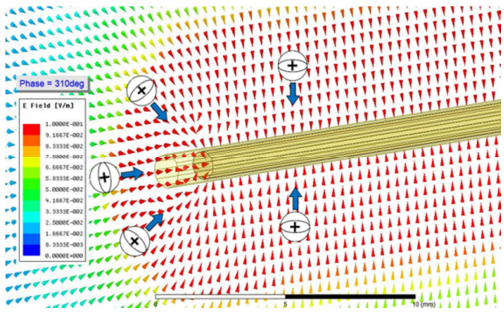

Figure 5-52 Motion of positive ions due to electric field at φ=310° on longitudinal cross-section at distal end

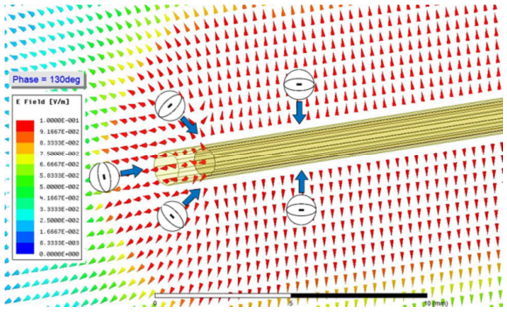

Figure 5-53 Motion of negative ions due to electric field at φ=130° on longitudinal cross-section at distal end

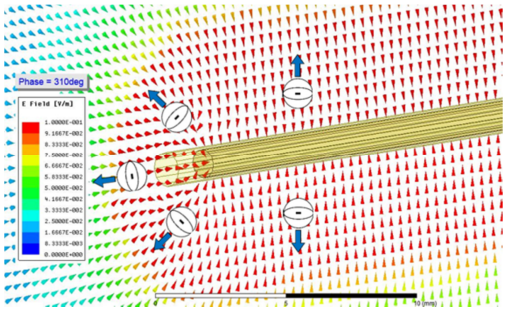

Figure 5-54 Motion of negative ions due to electric field at φ=310° on longitudinal cross-section at distal end

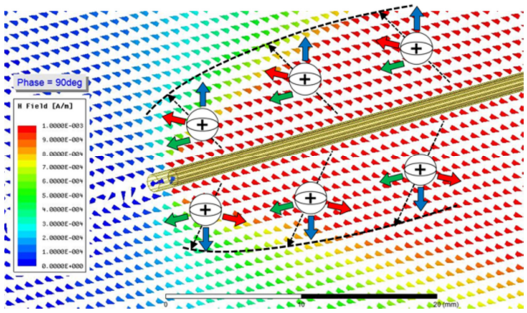

Figure 5-55 Motion of positive ions due to electric and magnetic fields at φ=90° on longitudinal cross-section at distal end

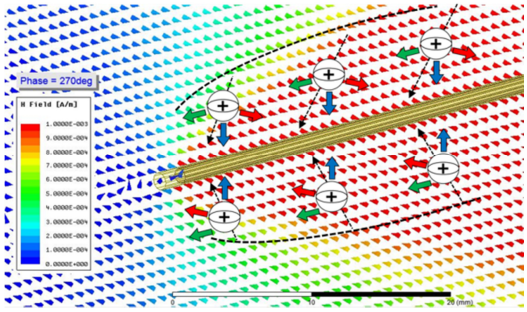

Figure 5-56 Motion of positive ions due to electric and magnetic field at φ=270° on longitudinal cross-section at distal end

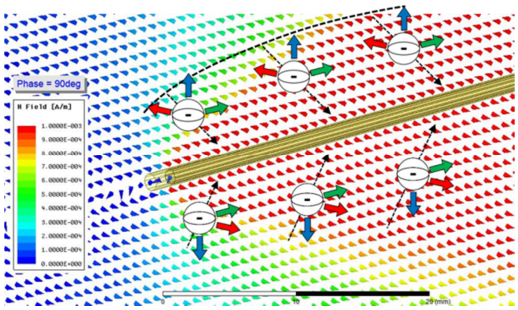

Figure 5-57 Motion of negative ions due to electric and magnetic fields at φ=90° on longitudinal cross-section at distal end

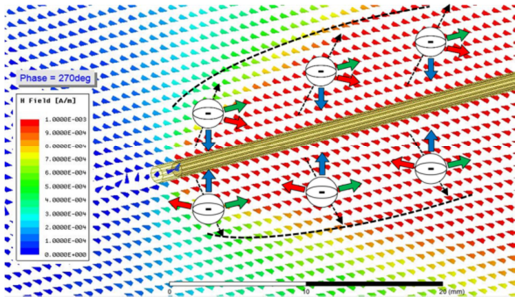

Figure 5-58 Motion of negative ions due to electric and magnetic field at φ=270° on longitudinal cross-section at distal end

Following conclusions can be drawn from the EM forces acting on the ions. For a given position along the MLC maxima of driving electric fields lag maxima of magnetic fields by ~40° resulting in stored energy inside the volume indicated in Figure 5-49. Ions move (migrate) away or towards the MLC depending on the orientation of electric and magnetic fields and the ion's net charge. Positive ions tend to migrate into the direction of wave propagation and negative ions tend to migrate into the opposite direction. The migration is counterbalanced by electrostatic forces between the ions. Further, the centres of mass of positive and negative ions describe closed loops during one full cycle of the exciting electromagnetic wave. This is indicated in Figure 5-59 and Figure 5-60 for constructive and destructive superposition of the induced magnetic dipole moments and the magnetic field component of the electromagnetic wave. It is supposed that

destructive superposition prevails during the steady state, but both constructive and destructive superposition exists during transitions between steady states.

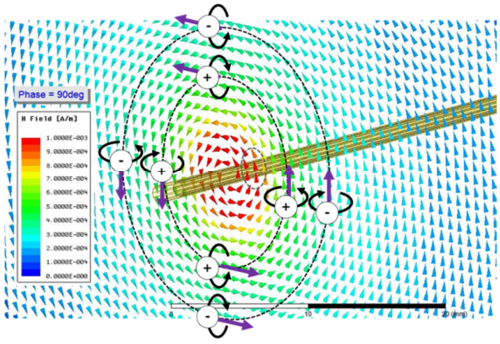

Figure 5-59 Constructive superposition of ionic dipole moments (purple arrows) due to circular motion of ions caused by electric and magnetic fields at φ=90° on transversal cross-section at distal end

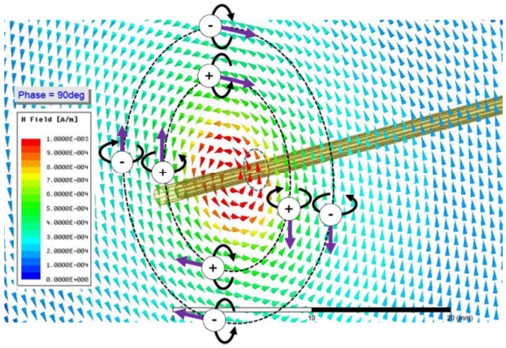

Figure 5-60 Destructive superposition of ionic dipole moments (purple arrows) due to circular motion of ions caused by electric and magnetic fields at φ=90° on transversal cross-section at distal end

The circular movement of ions can be decomposed into two linear orthogonal oscillations, one in radial and the other in longitudinal direction. The longitudinal oscillation of charged particles represents an additional volume current along the axis of the MLC and the radial oscillation of charged particles represents an additional volume current perpendicular to the axis of the MLC. These volume currents can be integrated into EM models using cross-coupling terms for the conductivity tensor matrix.

$$\vec{J}_{vol} = \underline{\tilde{\sigma}} \cdot \vec{E} \tag{5–10}$$

with

$$\underline{\tilde{\sigma}} = \begin{bmatrix} \tilde{\sigma}_{11} & -\tilde{\sigma}_{12} & -\tilde{\sigma}_{13} \\ \tilde{\sigma}_{21} & \tilde{\sigma}_{22} & -\tilde{\sigma}_{23} \\ \tilde{\sigma}_{31} & \tilde{\sigma}_{32} & \tilde{\sigma}_{33} \end{bmatrix} \qquad \left[\frac{A}{V \cdot m}\right] \tag{5–11}$$

However, the cross-coupling terms lead to significant numerical instabilities. A value of $-0.25\ \frac{S}{m}$ for off-diagonal coefficient of the conductivity tensor matrix was applied in EM Model #3. This value best matched calculated and measured temperature rise patterns at the distal end of Leads, where particular attention was paid to minimise Lead wire routing anomalies described in Section 5.1.9.6. Summing up, only molecular dynamic measurement techniques briefly described in Section 2.9 can provide further insight into the underlying causes.

5.1.6.7 Auxiliary electrodes along MLC

This section summarises and compares simulation runs for a twelve wire dielectric MLC with and without a single capacitive-coupled auxiliary electrode placed in saline solution and excited by a matched coaxial wave port. The main objective for introducing auxiliary electrodes is to increase the attenuation for the (common) TEM mode propagating along the MLC. As outlined in Section 4.1.3.2 waves are reflected at both, the distal and proximity end and can either result in constructive or destructive interference depending on the location along the MLC. Constructive interference at distal end electrodes results in higher deposited power in the surrounding gelled saline (human tissue) and hence leads to higher temperature increases.

5.1.6.7.1 Simulation settings

The simulation settings for insertion and reflection loss simulations are outlined in Figure 5-61 and the simulation settings for field quantities are outlined in Figure 5-62.

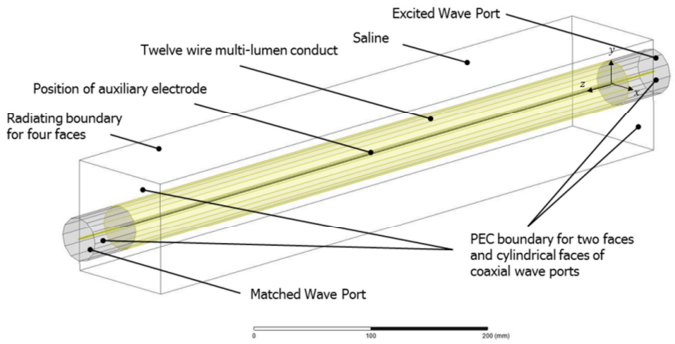

Figure 5-61 Twelve wire MLC with auxiliary electrode in gelled saline cube (including BL) for coaxial port excitation

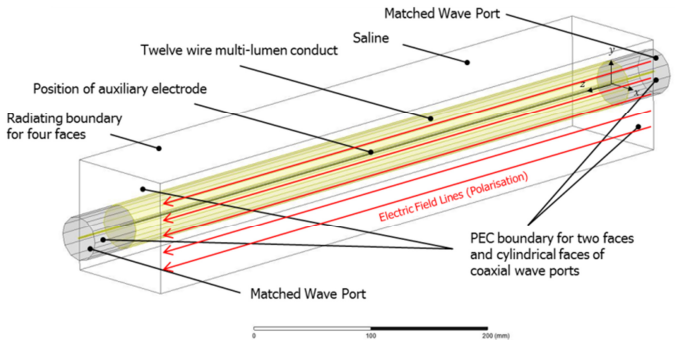

Figure 5-62 Twelve wire MLC with auxiliary electrode in gelled saline cube (including BL) for planar wave excitation

The auxiliary electrode (Figure 5-63) is centred between the two wave ports. Two cases are considered. In the first case, each Lead wire is capacitive coupled to the auxiliary electrode with $\sim 33\ \frac{pF}{mm}$. In the second case, each Lead wire is capacitive coupled through the thin 50 µm isolating layer ($\sim 0.1\ \frac{pF}{mm}$) of the MLC. The reflection loss at both wave ports is less than $-20\ dB$ for all investigated scenarios.

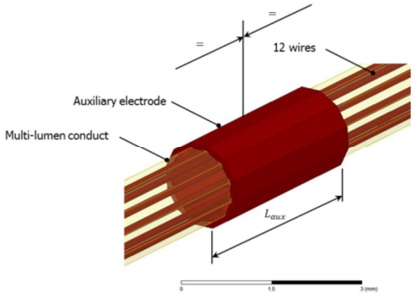

Figure 5-63 Position and length of auxiliary electrode

5.1.6.7.2 Influence of MLC length

Figure 5-64 shows the influence of the MLC length on the insertion loss difference between a MLC with and without auxiliary electrode. The auxiliary electrode is 3 mm long and placed half way between the distal and proximity end of the MLC. The insertion loss difference is defined as follows:

$$IL_{diff} = IL_{with\ aux.\ electrode} - IL_{without\ aux.\ electrode} \tag{5–12}$$

The multi-lumen-conduct length has a negligible influence on the insertion loss difference. For strong capacitive coupling (Case 1: 100 pF per Lead wire) the insertion loss difference is approximately 2 dB and for weak capacitive coupling (Case 2: 0.3 pF per Lead wire) the insertion loss difference is approximately 0.5 dB.

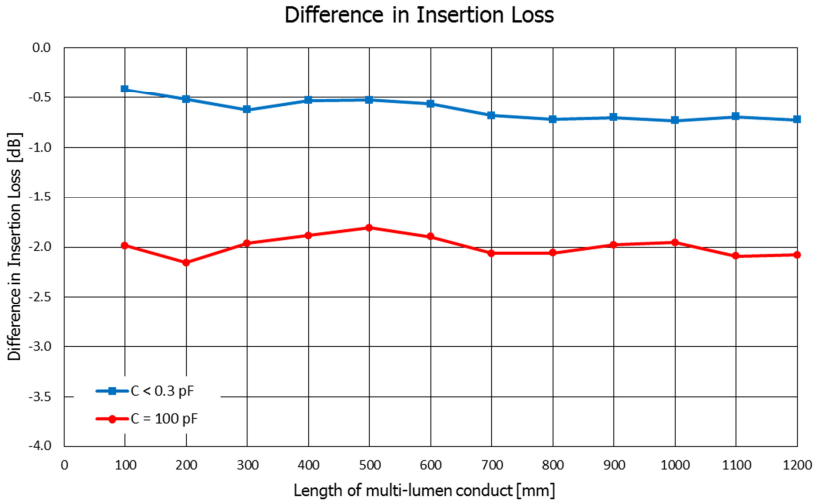

Figure 5-64 Insertion loss difference between Wave Ports 1 and 2 as function of MLC length and a 3 mm long auxiliary electrode
Case 1: C =100 pF and Case 2: C < 0.3 pF

For a 3T (128 MHz) MRI scanner a single strong capacitive coupled auxiliary electrode can be replaced by four weak capacitive coupled

auxiliary electrodes each separated by a distance of about $\frac{\lambda_{TEM}}{16} \approx \frac{400\ mm}{16} \approx 25\ mm$.

5.1.6.7.3 Influence of auxiliary electrode length - Part 1

Figure 5-65 indicates the influence of the length of a single auxiliary electrode placed half way between the proximity and distal end of a MLC with 12 Lead wires. Each wire is capacitive coupled to the auxiliary electrode. The coupling capacitance per wire increases with auxiliary electrode length. The capacitive coupling for Case 1 is $\sim 33\ \frac{pF}{mm}$ and for Case 2 $\sim 0.1\ \frac{pF}{mm}$.

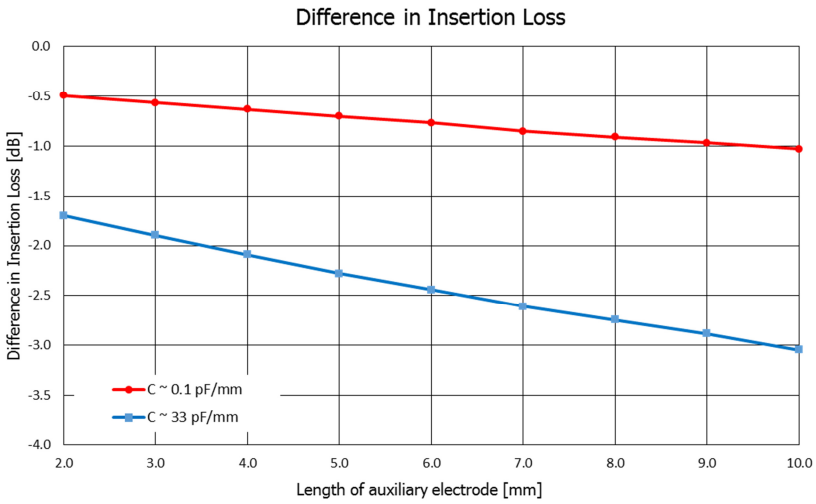

Figure 5-65 Insertion loss difference between Wave Ports 1 and 2 as function of auxiliary electrode length for a MLC length of 600 mm
Case 1: $\sim 33\ \frac{pF}{mm}$ and Case 2: $\sim 0.1\ \frac{pF}{mm}$

The slope for Case 1 is approximately $-0.13\ \frac{dB}{mm}$ and for Case 2 $-0.05\ \frac{dB}{mm}$.

5.1.6.7.4 Influence of auxiliary electrode length - Part 2

In this section only Case 2 is considered, i.e. weak capacitive coupling between Lead wires and a single (long) auxiliary electrode. For long lengths, the auxiliary electrode acts like a shield around Lead wires. Figure 5-66 shows the reflection loss at Wave Port 1 as function of auxiliary electrode length. With increasing electrode length the reflection loss increases since the discontinuity presented by the auxiliary electrode increases. At long electrode lengths the reflection loss starts to slightly decrease due to destructive superposition from reflections at the proximity and distal end of the auxiliary electrode.

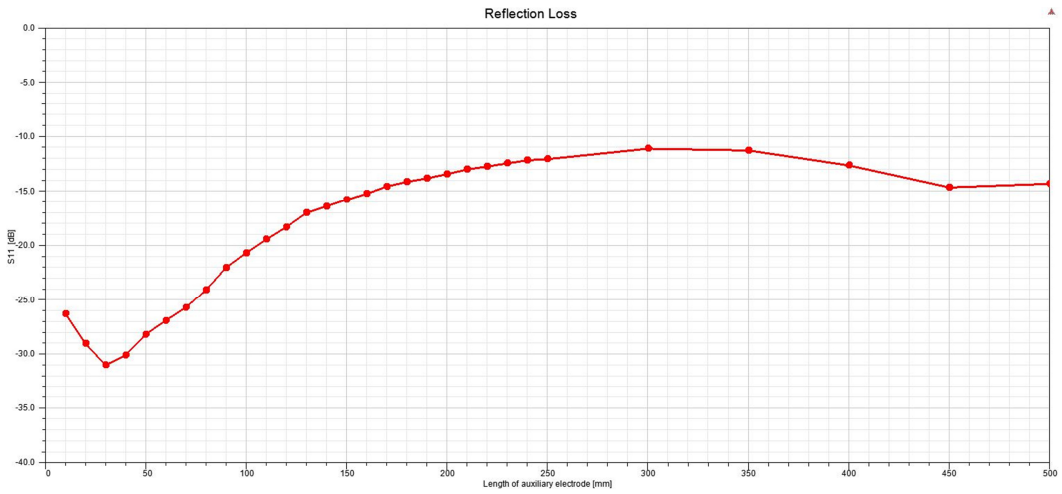

Figure 5-66 Return loss at Wave Port 1 as function of auxiliary electrode length for a MLC length of 600 mm
Case 2: $\sim 0.1\ \frac{pF}{mm}$

Figure 5-67 presents the insertion loss between Wave Ports 1 and 2 as function of auxiliary electrode length. A wave travelling along the MLC divides into two parts at the proximity end of the auxiliary electrode and recombines at the distal end of the auxiliary electrode. In the section between the proximity and distal end of the auxiliary electrode, one part of the wave is travelling as quasi coaxial TEM mode between the ring of Lead wires and the inner surface of the auxiliary electrode and the other part of the wave is travelling as quasi coaxial surface wave above the

outer surface of the auxiliary electrode. The propagation constants (attenuation and phase) for quasi TEM and quasi surface wave are different. For an auxiliary electrode length of 180 mm both waves cancel at the distal end of the auxiliary electrode leading to strong attenuation and decoupling of the wave ports. Above 180 mm the insertion loss decreases again. The quasi coaxial TEM wave has a lower propagation loss compared with the quasi coaxial surface wave and hence insertion loss is dominated by the insertion loss of the quasi coaxial TEM wave.

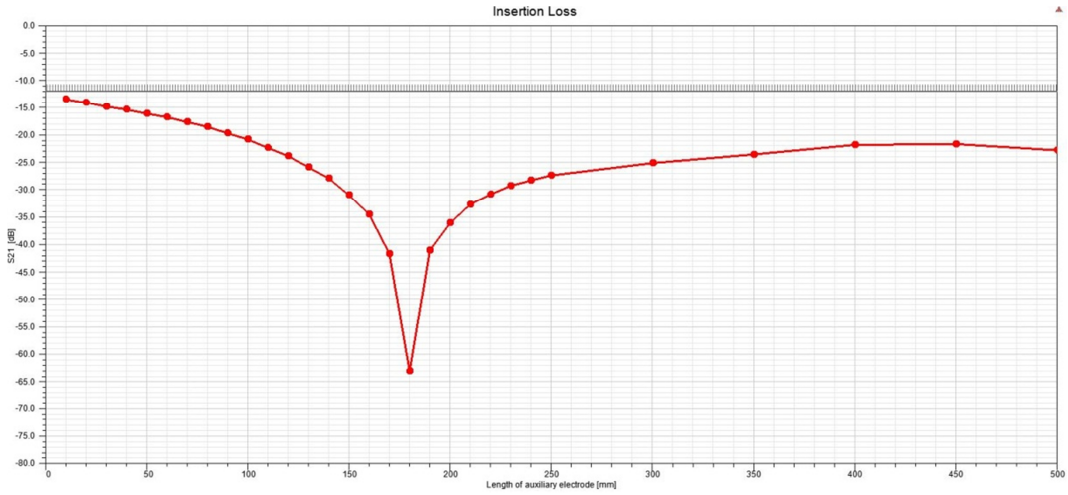

Figure 5-67 Insertion loss between Wave Ports 1 and 2 as function of auxiliary electrode length for a MLC length of 600 mm
Case 2: $\sim 0.1\ \frac{pF}{mm}$

To verify the impact of a long auxiliary electrode (shield) on transversal, radial electric field magnitudes and transversal angular magnetic field magnitudes at the distal ends of the MLC both, auxiliary electrode and MLC have been exposed to a planar wave as shown in Figure 5-62. The complex electric and magnetic field magnitudes (transversal radial electric and transversal angular magnetic fields) around the ring of 12 Lead wires as function of auxiliary electrode length is shown in Figure 5-68 and Figure 5-69.

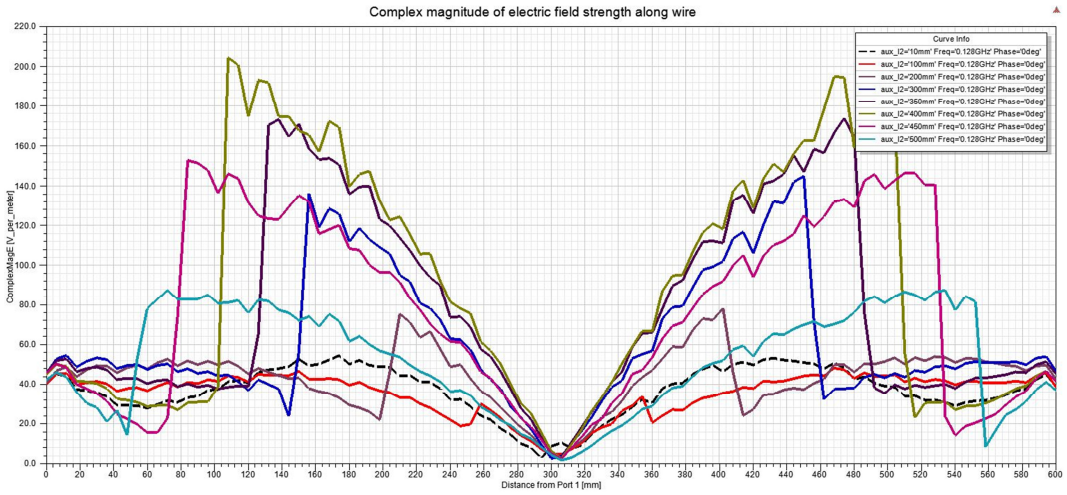

Figure 5-68 Complex magnitude of electric field strength along Wire 01 as function of auxiliary electrode length for a MLC length of 600 mm
Parameter: auxiliary electrode length

It can be seen that the auxiliary electrode has only a minor effect on the electric and magnetic field magnitude at distal ends (z = 0 mm and z = 600 mm).

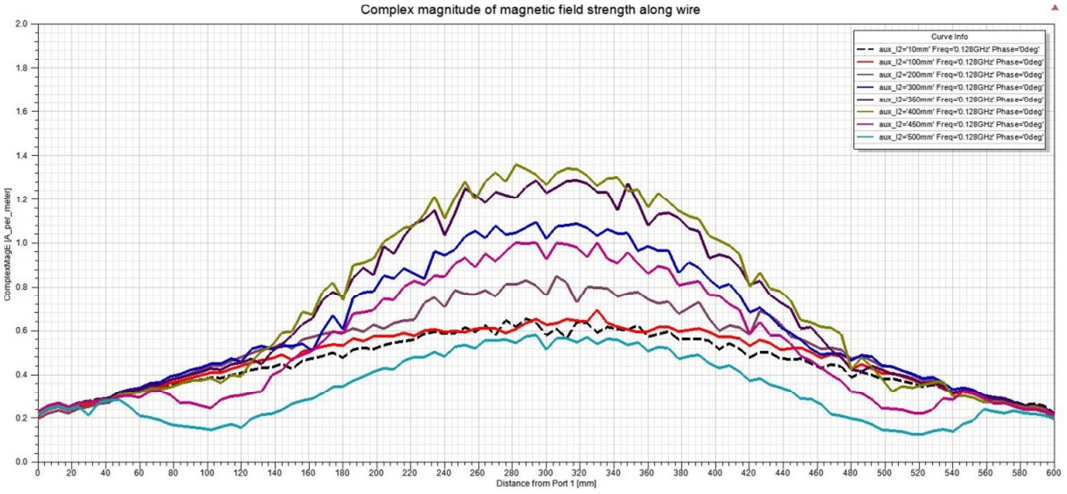

Figure 5-69 Complex magnitude of magnetic field strength along Wire 01 as function of auxiliary electrode length for a MLC length of 600 mm
Parameter: auxiliary electrode length

5.1.7 EM waves along Lead

In this section the evolution of transversal field patterns in longitudinal direction for Base Case UM03 and a Lead length of 600 mm is presented. Lead and IPG have been illuminated with a plane wave as outlined in Section 4.1.4.1. EM Model #2 (Table 4-2) has been applied. The permittivity of the isotropic boundary layer is 3.5 and the double layers of electrodes have the same characteristics as the bulk (gelled) saline. The wire numbering scheme and integration paths for differential voltages between wires and field components along the Lead are given in Figure 5-70. Wire W01 is routed to Electrode E01. Magnitude and vector plots for electric fields are shown for an incident electric field at $\varphi = 0°$ (Figure 5-71).

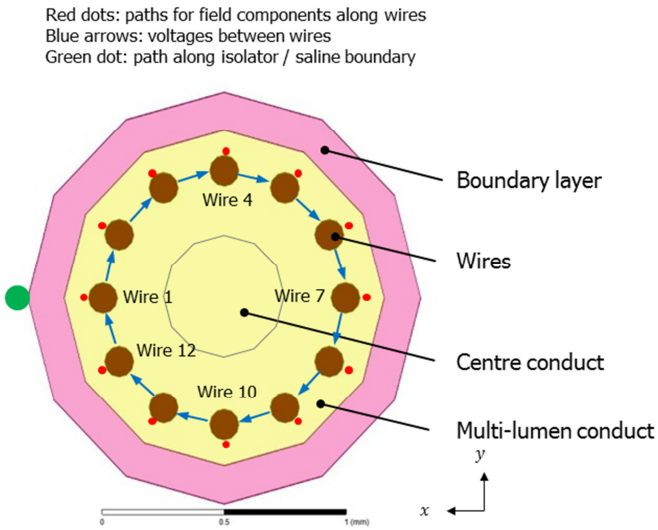

Figure 5-70 Twelve wire MLC in saline with integration paths

The location $z = 0\,mm$ is at the proximity end inside the IPG header. The evolution of the transversal electric fields is shown towards the distal end. The last plot at $z = 500\,mm$ shows field quantities just before the first distal electrode (E12).

Magnitude of transversal electric field	Vector plot of transversal electric field
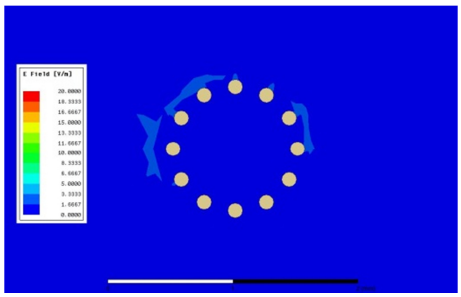	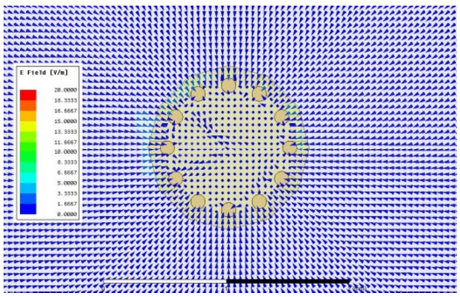
z=0 mm	z=0 mm
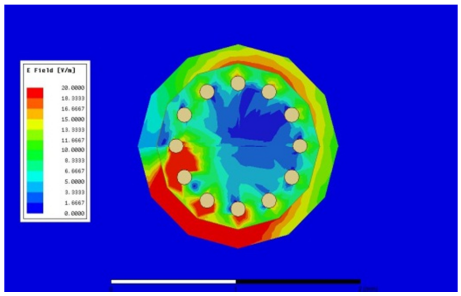	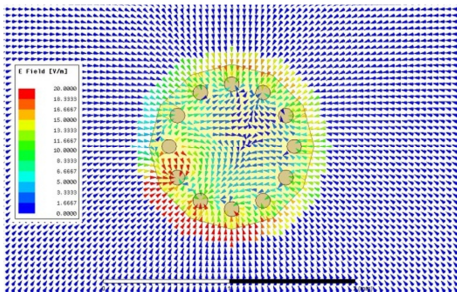
z=50 mm	z=50 mm
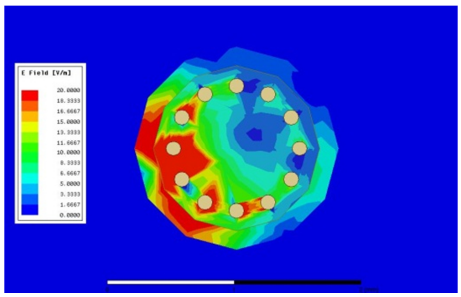	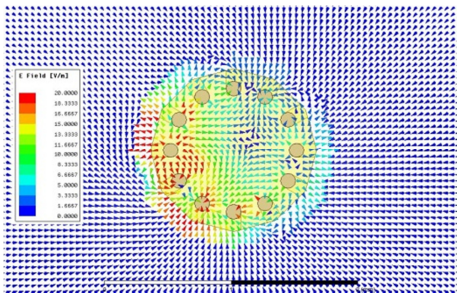
z=100 mm	z=100 mm
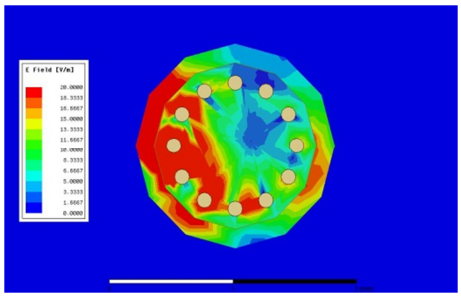	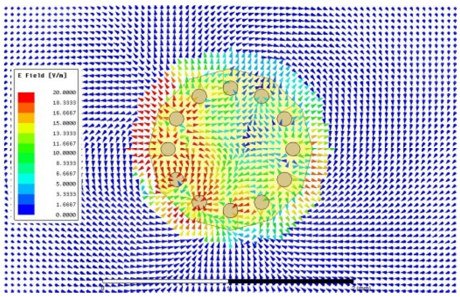
z=150 mm	z=150 mm

continued on next page

Magnitude of transversal electric field	Vector plot of transversal electric field
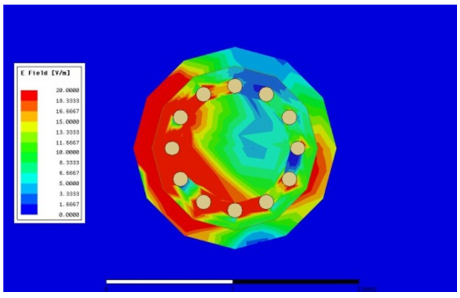	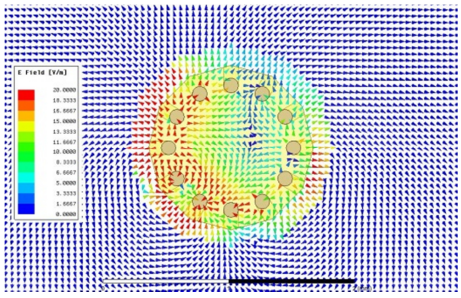
z=200 mm	z=200 mm
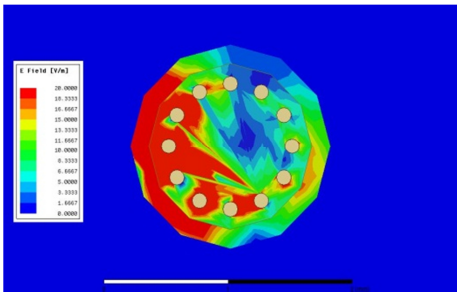	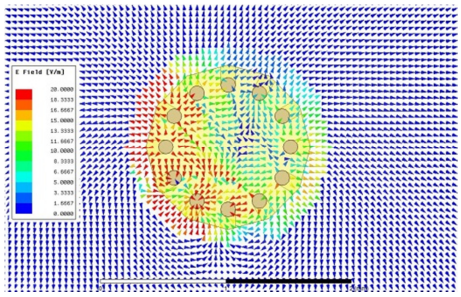
z=250 mm	z=250 mm
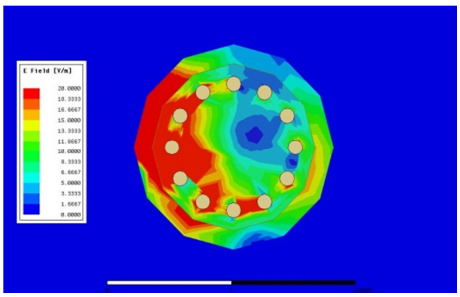	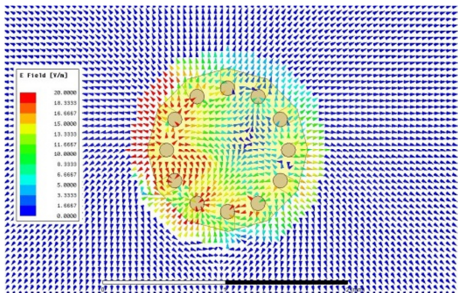
z=300 mm	z=300 mm
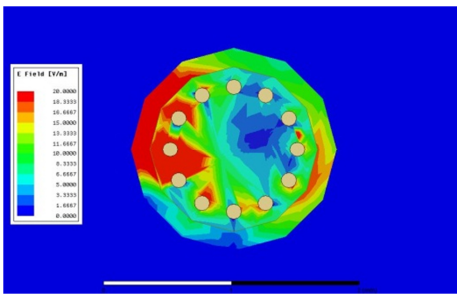	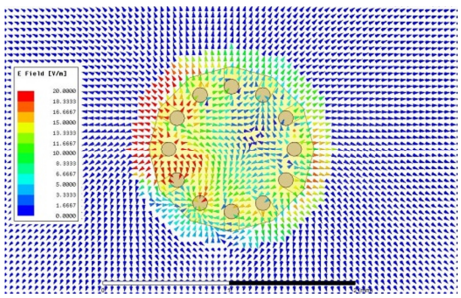
z=350 mm	z=350 mm

continued on next page

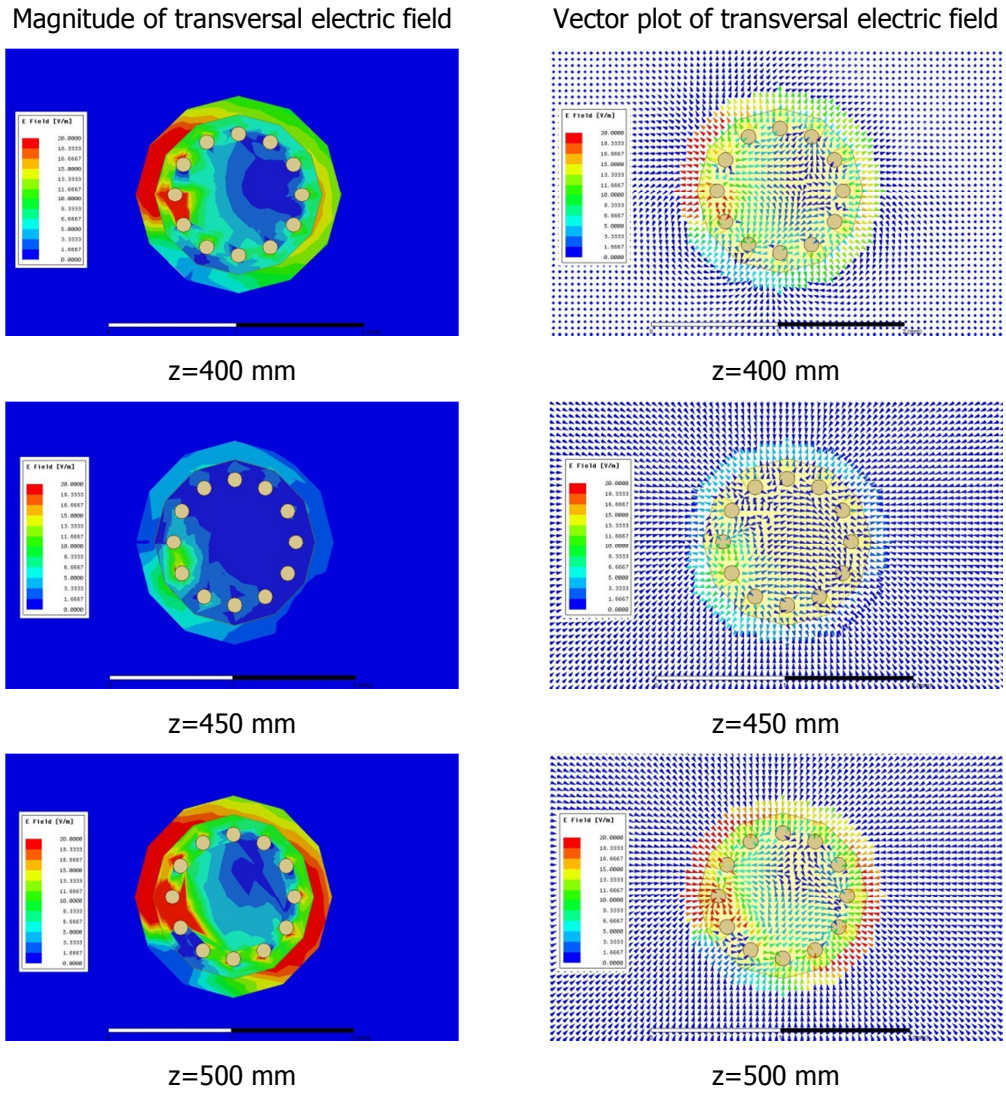

Figure 5-71 UM03 - Transversal electric field components for Lead length of 600 mm

The evolution of the transversal electric field along the Lead has one main cause that results in two distinct effects. The main cause is the unequal length of Lead wires running from the proximity end through the MLC towards the distal end. The Wire W01 to Electrode E01 is approximately 590 mm long and the Wire W12 to Electrode E12 is approximately 491 mm to long. The wire lengths in-between are shortened by 9 mm from E02 to E11. The first effect is that the unequal length of Lead wires introduces 12 reflection points for the common quasi TEM mode at the distal end separated by 7 mm and 12 reflection points at the proximity end separated by 2 mm. In addition, the difference between the reflection

points at the distal end approaches a quarter wavelength of the propagating quasi TEM mode. The second effect is that differential modes propagate between Lead wires resulting in standing wave patterns along the Lead. The dominant differential modes are between adjacent Lead wires (Figure 5-72).

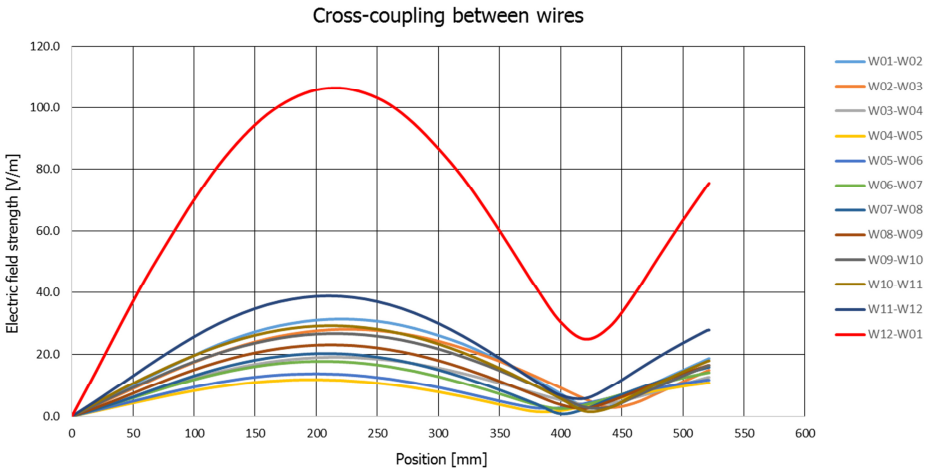

Figure 5-72 UM03 - Equivalent differential electric field strength between Lead wires at 128 MHz for a Lead length of 600 mm

The strongest standing wave builds up between Wire W12 and Wire W01. The maxima in the centre section are all co-located at $z = 220\,mm$ since a single reflection point for all Lead wires at the proximity end at $z = 0\,mm$ has been assumed for EM simulations. The wavelength of the differential modes is approximately $\lambda_d \approx 840\,mm$. This is rougly twice the wavelength observed for the common quasi TEM mode $(\lambda_c \approx 400\,mm)$. At the distal end the differential electric field strength between Wires W12 and W01 is approximately $75\,\frac{V}{m}$. For comparison, the radial electric field strength at the centre of Electrode E01 is approximately $9.0\,\frac{V}{m}$ (Figure 5-73), i.e. the differential electric field strength between Wire W12 and Wire W01 is about 8 times higher than the radial electric field strength at Electrode E01. But more important is the differential electric field strength between adjacent electrodes E01-E02, E02-E03, E03-E04, etc. The electric field magnitude between these electrode pairs varies between $10.0\,\frac{V}{m}$ and

$25.0\ \frac{V}{m}$ and has the same order of magnitude as the electric field strength pointing radially from the electrodes into the bulk electrolyte. Reducing the differential electric field between adjacent electrodes will therefore reduce the radial electric field and hence the electric field contribution to RF-induced heating.

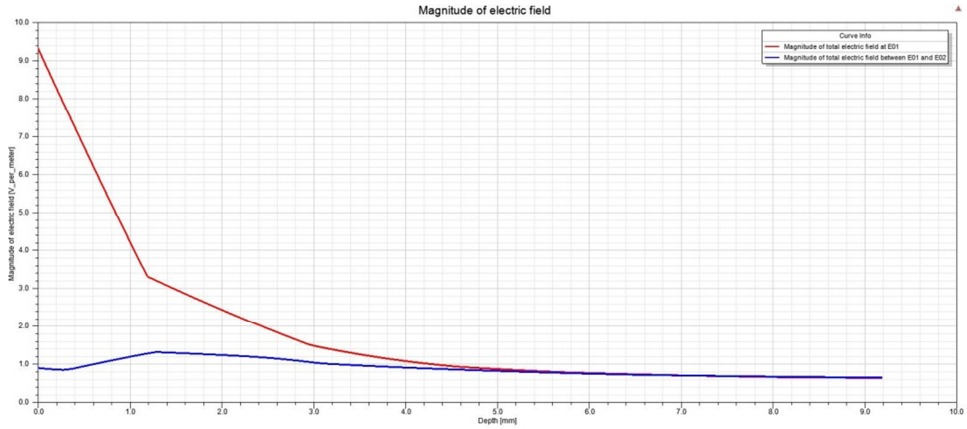

Figure 5-73 UM03 - magnitude of total radial electric field at 128 MHz for a Lead length of 600 mm
Red curve: from centre of Electrode E01 into gelled saline
Blue curve: from centre between Electrodes E01 and E02 into gelled saline

Ideas to minimise differential electric fields in multi-electrode Leads are explored in Section 5.1.9.8.

5.1.8 Influence of material parameters

In this section the influence of four Lead material parameters on wave attenuation and hence distal end electric fields at 128 MHz is investigated; conductance of Lead wires, surface roughness of Lead wires, and permittivity and loss factor of MLCs. High attenuation minimises the accumulation of RF energy at distal end electrodes and hence reduces the risk of RF induced temperature increase.

The results are presented for Base Case UM02 and a Lead length of 200 mm. EM Model #1 (Table 4-2) has been applied. Lead and IPG are described in Section 4.1.3.1 and have been illuminated with a plane wave as outlined in Section 4.1.4.1.

5.1.8.1 Conductance of Lead wires

The conductance for all twelve Lead wires with diameter $120\ \mu m$ has been simultaneously varied from $0\ \frac{S}{m}$ to $10'000'000\ \frac{S}{m}$ where the case of $0\ \frac{S}{m}$ represents electrodes without Lead wires. The evolution of the magnitude of the complex electric field is shown in Figure 5-74 to Figure 5-83. The scale of the ordinate (electric field) for a conductance of $0\ \frac{S}{m}$ is $10\ \frac{V}{m}$ and the scale of the ordinate for all other conductances is $100\ \frac{V}{m}$. The electric field at distal end electrodes increases with increasing conductance up to $10'000\ \frac{S}{m}$. With conductances above $10'000\ \frac{S}{m}$ the electric field magnitude at the more distal end electrodes increases faster. The high electric field strength at the IPG is confined within the IPG header and does not contribute to RF induced heating. But, high electric field strengths inside the IPG header might damage sensitive electronics inside the IPG case.

< IPG > E12 E01 < IPG > E12 E01

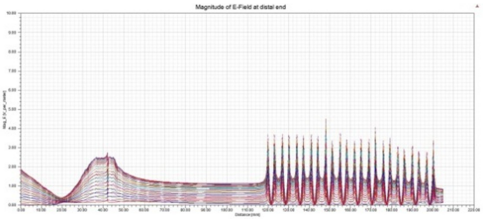

Figure 5-74 Conductivity: $0\ \frac{S}{m}$

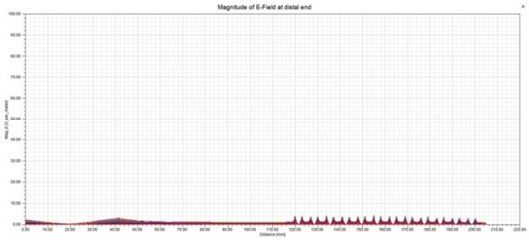

Figure 5-75 Conductivity: $0\ \frac{S}{m}$

< IPG > E12 E01

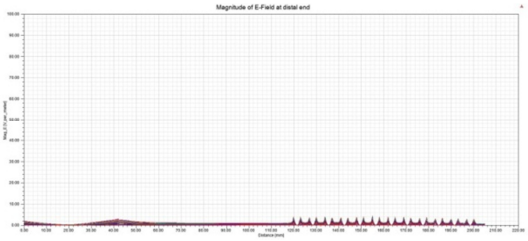

Figure 5-76 Conductivity: $1\ \frac{S}{m}$

< IPG > E12 E01

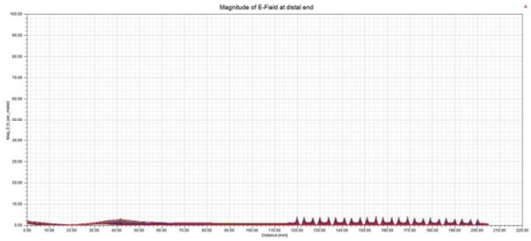

Figure 5-77 Conductivity: $10\ \frac{S}{m}$

< IPG > E12 E01

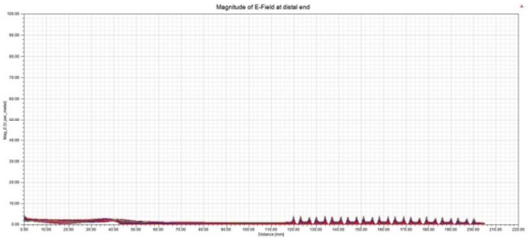

Figure 5-78 Conductivity: $100\ \frac{S}{m}$

< IPG > E12 E01

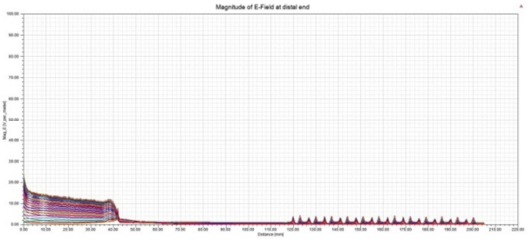

Figure 5-79 Conductivity: $1'000\ \frac{S}{m}$

< IPG > E12 E01

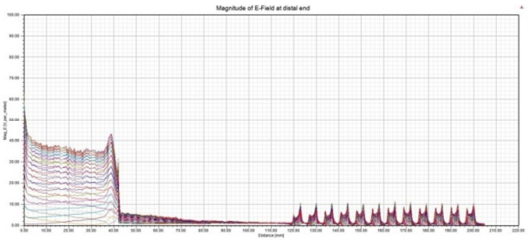

Figure 5-80 Conductivity: $10'000\ \frac{S}{m}$

< IPG > E12 E01

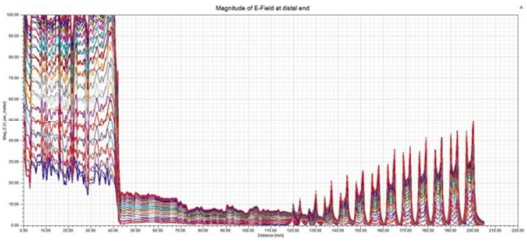

Figure 5-81 Conductivity: $100'000\ \frac{S}{m}$

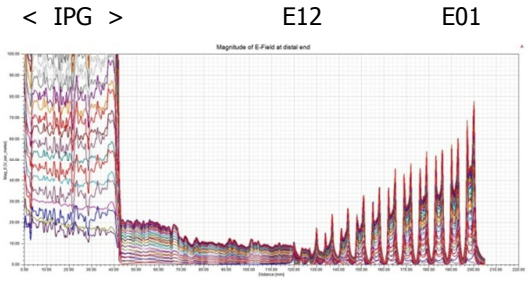

Figure 5-82 Conductivity: $1'000'000\ \frac{S}{m}$

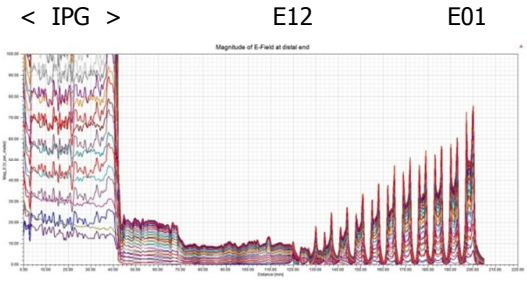

Figure 5-83 Conductivity: $10'000'000\ \frac{S}{m}$

The evolution of the electric field strength at the distal end Electrode E01 is shown in Figure 5-84. Below wire conductances of $1'000\ \frac{S}{m}$ the electric field strengths does not vary. In the transition region between $4'000\ \frac{S}{m}$ and $100'000\ \frac{S}{m}$, the electric field linearly increases on a log-log scale, rolls off at $350'000\ \frac{S}{m}$ and remains constant at $76\ \frac{V}{m}$ above $350'000\ \frac{S}{m}$.

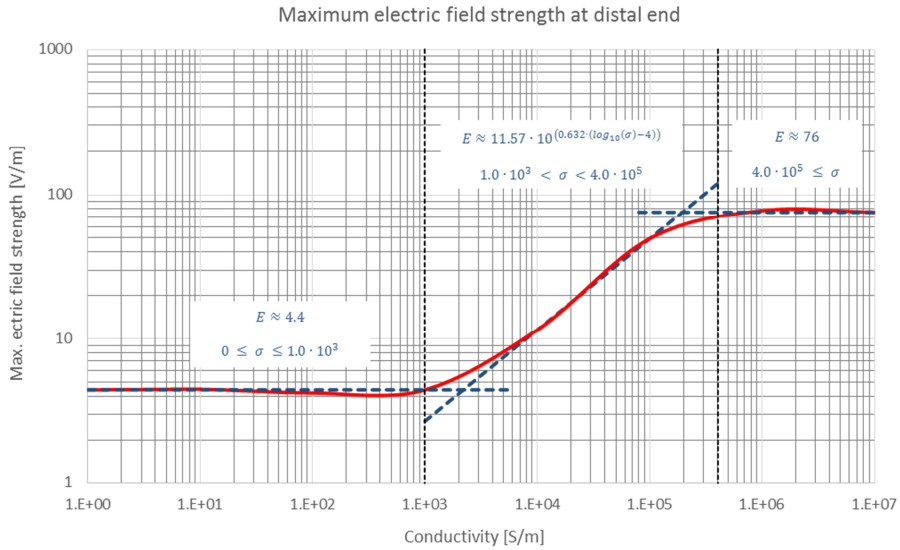

Figure 5-84 Maximum electric field strength at distal end electrode E01 as function of Lead wire conductivity

To decrease the deposited power at the distal end electrode by 50% the electric field has to be reduced by 71%. This means that the conductance of platinum wires has to drop from $\sim 9.4 \cdot 10^6\ \frac{S}{m}$ to $\sim 1 \cdot 10^5\ \frac{S}{m}$ or a factor of 94.

5.1.8.2 Surface roughness of Lead wires

Electromagnetic waves diffuse into highly conductive surfaces and magnitudes of field quantities decay quickly. Several models have been developed to take into account the impact of rough surfaces on surface resistance and excess power loss. Morgan [P179] investigated the power dissipation caused by infinitely long grooves of various sizes and shapes that are transverse or parallel to the flow of induced eddy currents. He concluded that transverse grooves with equal depths and widths can increase the power dissipation up to 100 % for transverse grooves and up to 36 % for parallel grooves. The increase depends on the ratio of the root mean square surface roughness to the skin depth. For transverse grooves with dimensions (widths and depths) of about one skin depth the power dissipation is about 60 % higher compared with the power dissipation of a smooth surface. The geometry of the grooves (square or triangular) does not have a significant impact on the power dissipation increase. He further investigated deep cracks where the width of the crack is about one skin depth and the depth is up to several skin depths. He concluded that the increase in power dissipation (compared with a smooth surface) is proportional to the area added by the walls of the crack. He further concluded that cracks with widths much smaller than the skin depth will have much less impact on the power dissipation increase due to the adverse effect of the shunt capacitance between the walls of the crack. Hammerstad and Jensen [P176] fitted Morgan's results for transverse grooves to an arctangent function as shown below. The factor K_{RF} is determined experimentally and allows $K_{surf,HJ}$ exceeding values of 2. Huray et al. [P177] have chosen a new approach to determine power loss. The surface is represented as stacked spheres (called snowballs) of varying sizes that reflect and absorb power. The reflected and absorbed power per sphere is expressed as power series of the ratio $\frac{\delta}{r_{sphere}}$, derived

from an electromagnetic field analysis. Since sphere radii can only be determined using Scanning Electron Microscopy (SEM) or Atomic Force Microscopy (AFM) the initial snowball model with different sizes of spheres has been simplified using single size spheres in order to synthesize the surface geometry. The simplified model is called cannonball model. The approach has been outlined by Simonovich [P182]. Other models are referenced below.

- Finite Element Model (Trefftz [P181])
- Hemispherical Model (Hall [P175])
- Small Perturbation Model (Sanderson [P180])
- Periodic Structure Model (Lukic [P178])
- Stochastic Model (Tsang [P183])
- Equivalent Boundary Conditions Model (Holloway [P102])

Figure 5-85 shows surface roughness correction factors as function of the ratio of rms surface roughness and skin depth $\left(\frac{\Delta_{rms}}{\delta}\right)$ for Hammerstad as well as square and hexagonal cannonball models. Figure 5-86 shows the root mean square surface roughness Δ_{rms} as function of the square cannonball surface roughness correction factor $K_{surf,i}$ for platinum at 128 MHz.

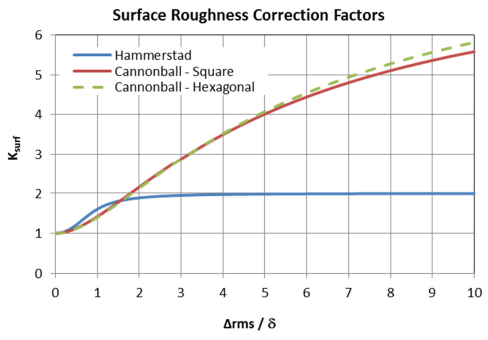

Figure 5-85 Surface roughness correction factors as function of $\frac{\Delta_{rms}}{\delta}$

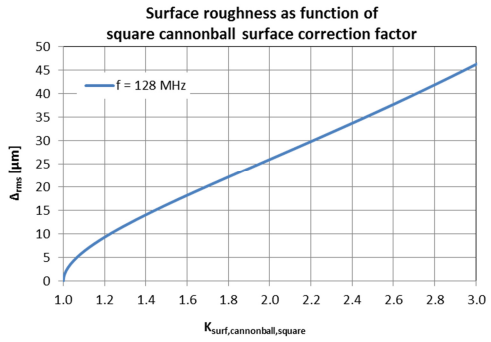

Figure 5-86 RMS surface roughness Δ_{rms} at 128 MHz as function of square cannonball surface roughness correction factor

A coaxial RGLC model has been applied for the following analysis. The simulated insertion loss at 128 MHz for a micro-coaxial transmission line with propagation characteristics equivalent to a MLC with 12 Lead wires is presented in Figure 5-87. The surface roughness for the inner conductor has been increased from a smooth surface with $K_{surf,i} = 1.0$ $(\Delta_{rms} = 0\ \mu m)$ to a rough surface with $K_{surf,i} = 3.0$ $(\Delta_{rms} \approx 45\ \mu m)$. The parameters of the micro-coaxial cable are given below.

$l = 600\ mm$ $\quad$ $\varepsilon_l = 0$

$r_i = 0.066\ mm$ $\quad$ $\sigma_i = 9.4 \cdot 10^6 \frac{S}{m}$ $(platinum)$

$r_o = 16.0\ mm$

$\varepsilon_r = 30$ $\quad$ $\sigma_o = 0.47 \frac{S}{m}$ $(gelled\ saline)$

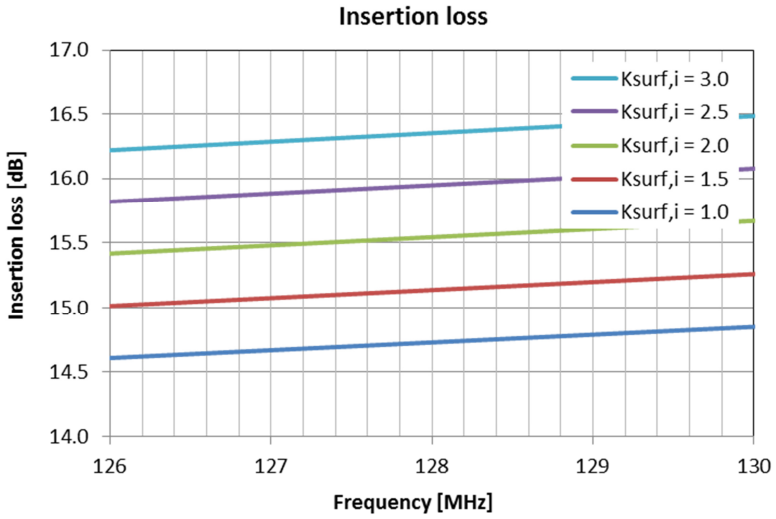

Figure 5-87 Insertion loss of micro-coaxial transmission line at 128 MHz
Parameter: cannonball surface roughness correction factor

The insertion loss for the micro-coaxial cable at 128 MHz varies between 14.7 dB (smooth surface) and 16.4 dB $(\Delta_{rms} = 45\ \mu m)$. Moderate surface roughness $(\Delta_{rms} \approx \delta \approx 14\ \mu m)$ applied to the inner conductor does not significantly alter the insertion loss $(\Delta_{IL} = 0.5\ dB)$. In addition, several factors limit the maximum surface roughness: They are summarised below.

- compliance with minimum diameter of conductor cross-sections ...
    - to comply with maximum DC resistances
    - to comply with requirements of mechanical strength during bending and torsion and to avoid creation and propagation of micro-cracks
- avoidance of corona effects in micro-gaps of roughened surfaces leading to fusion of surface regions during high electromagnetic field exposure
- adhesion of dust, bacteria or viruses

Lead wires in medical devices are made of stranded platinum wires (Figure 3-6). Strand diameters are about 19 μm. Applying surface roughening to those thin wires would severely compromise the mechanical strength. Therefore surface roughening is not an option to increase surface resistance.

5.1.8.3 Permittivity of MLC

In this section, the influence of MLC permittivity on distal end electric fields is analysed. The relative permittivity has been gradually increased from 1 to 1000 and the results are shown in Figure 5-88 to Figure 5-94. The scale of the ordinate (electric field) is $100\ \frac{V}{m}$. As indicated in Section 5.1.8.1, the high electric field strength at the IPG is confined within the IPG header and does not contribute to RF induced heating.

< IPG > E12 E01

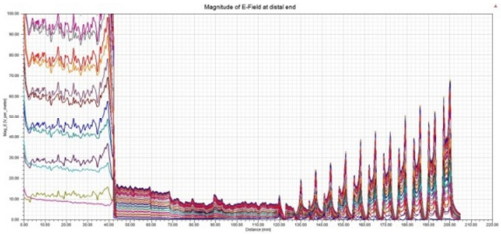

Figure 5-88 Relative permittivity: 1

< IPG > E12 E01

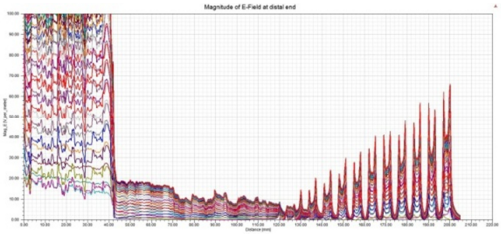

Figure 5-89 Relative permittivity: 3.16

< IPG > E12 E01

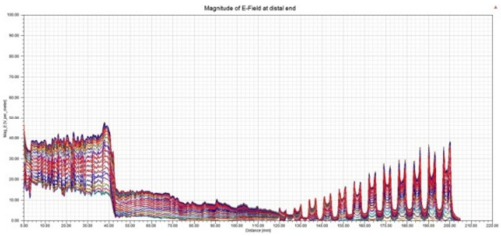

Figure 5-90 Relative permittivity: 10

< IPG > E12 E01

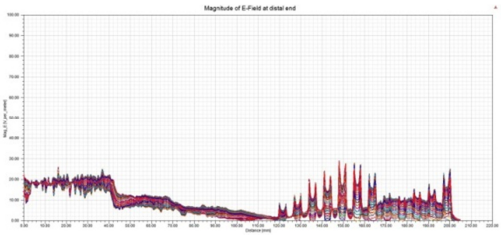

Figure 5-91 Relative permittivity: 31.6

< IPG > E12 E01

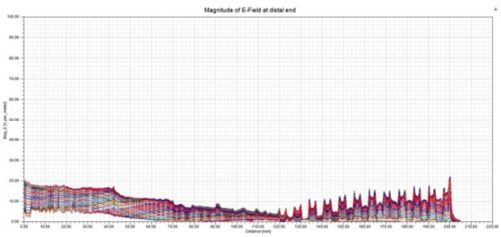

Figure 5-92 Relative permittivity: 100

< IPG > E12 E01

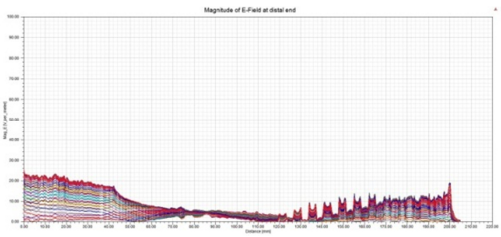

Figure 5-93 Relative permittivity: 316

< IPG > E12 E01

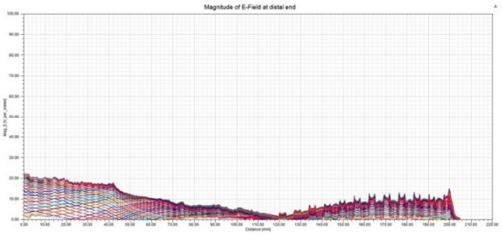

Figure 5-94 Relative permittivity: 1000

With increasing permittivity the electric fields are more confined within the MLC and do not significantly penetrate into the surrounding electrolyte (human tissue). The electric field at the distal end electrode E01 as function of relative permittivity is graphed in Figure 5-95. The maximum electric field strength at the distal end section is constant for relative permittivities below 3.0 and decreases linearly in a log/log chart for relative permittivities between 3.0 and 1000. At relative permittivities around 30 the electric field at distal end electrodes E01 to E06 decreases faster than the electric field at distal end electrodes E07 to E12. Summing up, moderate relative permittivity increases of MLCs can significantly reduce electric fields at distal end electrodes.

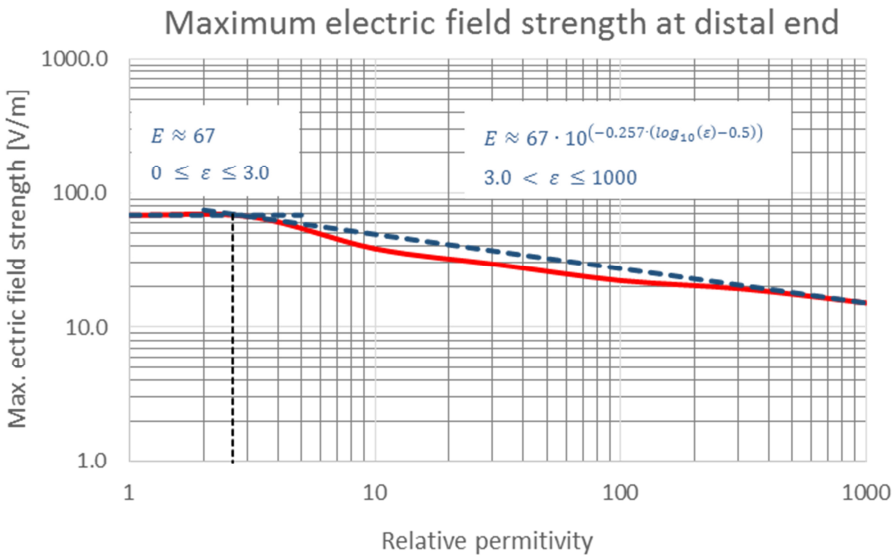

Figure 5-95 Maximum electric field strength at distal end electrode E01 as function of relative permittivity of the MLC

5.1.8.4 Loss factor of MLC

The impact of dielectric loss of the MLC on distal end electric fields is investigated in this section. The dielectric loss tangent has been gradually increased from 0.0001 to 1000 and the results are shown in Figure 5-96 to Figure 5-103. The scale of the ordinate (electric field) is $100\ \frac{V}{m}$.

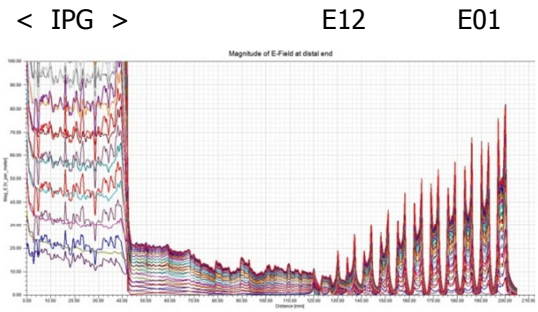

Figure 5-96 Loss factor: 0.0001

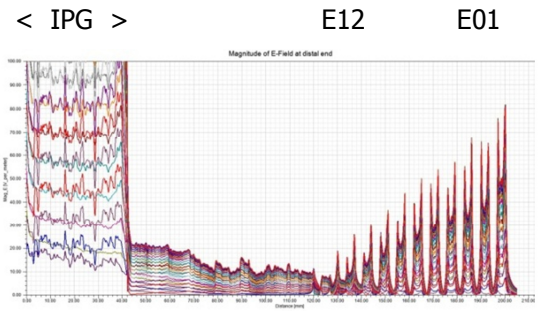

Figure 5-97 Loss factor: 0.001

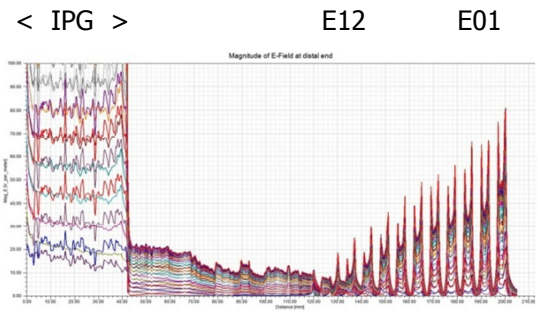

Figure 5-98 Loss factor: 0.01

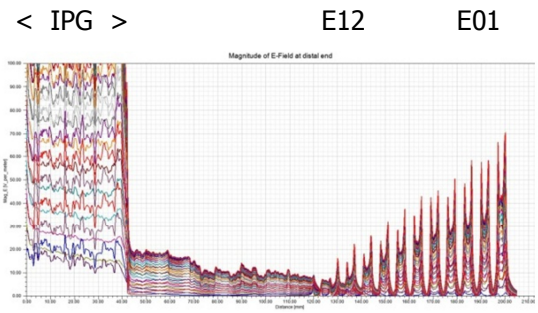

Figure 5-99 Loss factor: 0.1

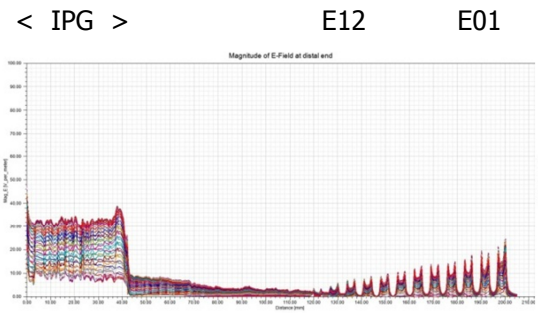

Figure 5-100 Loss factor: 1.0

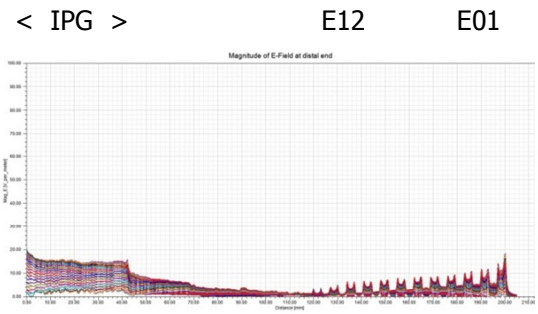

Figure 5-101 Loss factor: 10.0

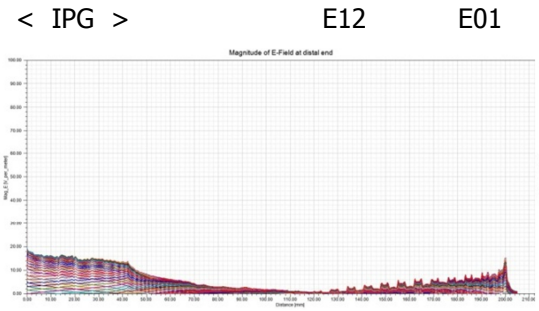

Figure 5-102 Loss factor: 100

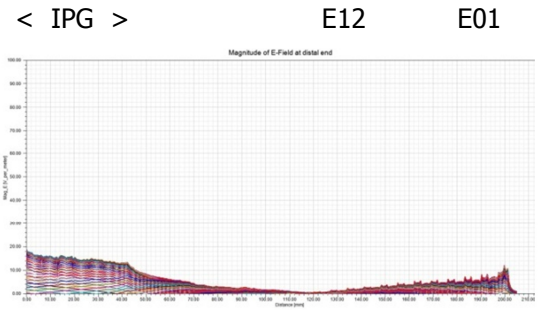

Figure 5-103 Loss factor: 1000

The maximum electric field strength at the distal end section decreases with increasing dielectric loss factor due to increasing attenuation of the propagating wave. The maximum electric field strength at the distal end section is constant for loss factors below 0.1 and then decreases linearly in a log/log chart for loss factors between 0.1 and 1.0. For loss factors above 1.0 the slope changes. The results are presented in Figure 5-104.

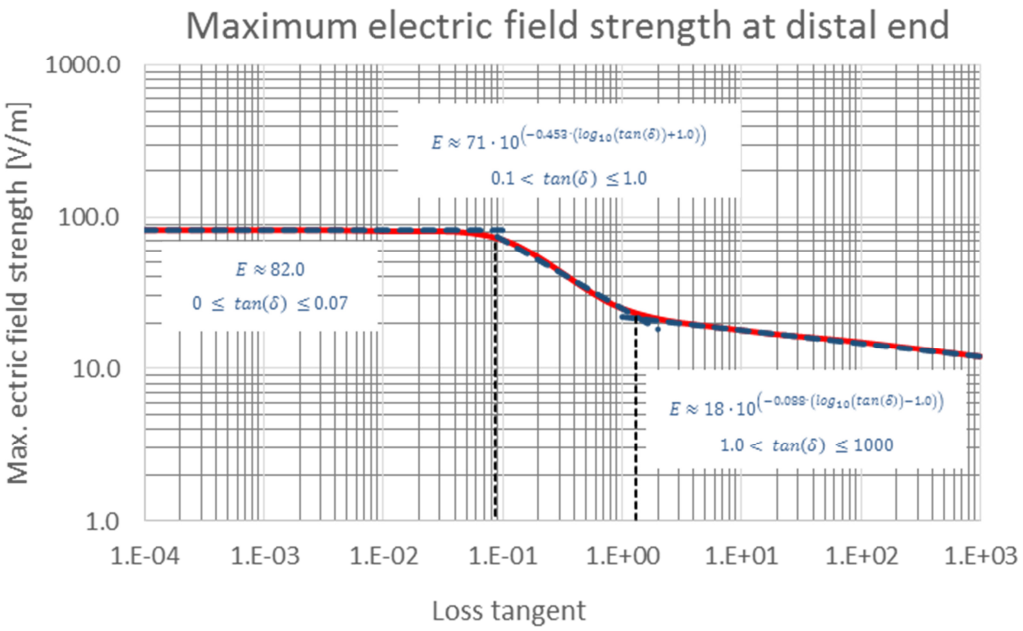

Figure 5-104 Maximum electric field strength at distal end electrode E01 as function of MLC loss factor

5.1.8.5 Conclusion

The simulation results confirm that high dielectric MLC materials paired with high dielectric loss factors can significantly reduce electric fields at distal ends and therefore RF induced heating. Extruded medical grade MLC profiles with relative permittivities between 20 and 50 and loss factors between 1 and 2 can be realised, today. For a relative permittivity of 30 and a loss factor of 1 the combined reduction factor for electric fields at the distal end is ~6. This would reduce the deposited power by a factor of ~36. On the contrary, increasing RF surface resistance using surface roughening techniques would not lead to significant electric field reductions at distal ends. In addition, roughening techniques severely impact the mechanical strength of platinum microwires.

5.1.9 Influence of design variations

Design variations are changes to geometrical aspects of MLC, Lead wires, electrodes, IPG case and IPG header. In addition, terminations impedances of Lead wires are considered. This section provides a general overview over investigated design variations and their impact on electric field distributions along Leads. The base cases and design variations have been shortly described in Chapter 3. A comparison between simulated and measured base cases and design variations is presented in Section 5.1.11.

If not otherwise stated, EM Model #1 (Table 4-2) has been applied for the initial analysis. Lead and IPG are described in Section 4.1.3.1 and have been illuminated with a plane wave as outlined in Section 4.1.4.1.

5.1.9.1 Base cases

Figure 5-105 (UM01) and Figure 5-106 (UM02) present superimposed simulation results for Lead lengths between 200 mm and 1200 mm. For comparison, an envelope curve at $10\frac{V}{m}$ has been added. A first analysis shows that open ended Lead wires at the IPG header have a detrimental effect on electric fields for short Lead lengths. For Lead lengths above 200 mm either open ended or shorted Lead wires show more favourable field distributions around distal end electrodes leaving the question open what the best termination at the proximity end is. The electric field distribution within the IPG header does not directly contribute to RF induced heating but high electric field strengths might cause voltages at capacitive coupled feed-throughs that are above dielectric breakdown voltages.

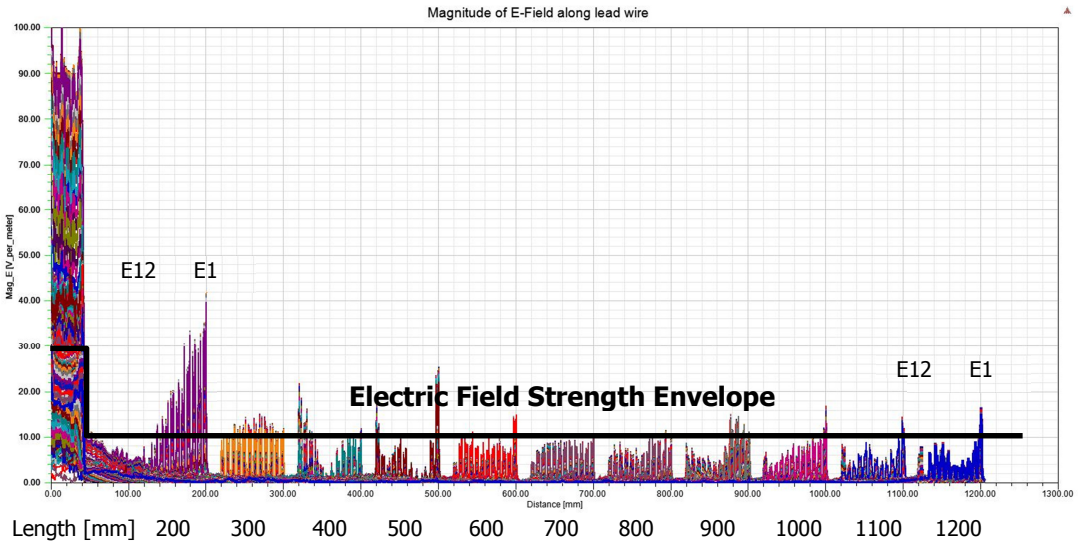

Figure 5-105 UM01 (wires open ended in IPG header) - electric fields for solid electrodes

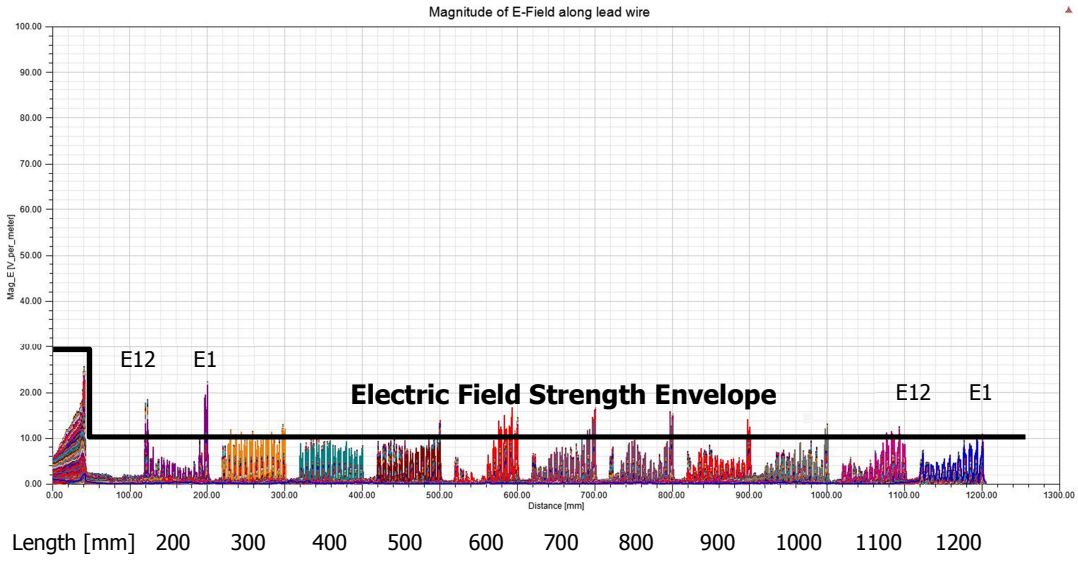

Figure 5-106 UM02 (wires shorted to IPG in header) - electric fields for solid electrodes

5.1.9.2 Helical electrodes

This section summarises the results from simulation runs for design variations DV00 and DV0A where solid cylindrical electrodes are replaced with coiled electrodes. Coiled electrodes provide an inductive termination to Lead wires increasing the magnetic and decreasing the electric field energy at the distal end. Since the magnetic field energy contribution to deposited power in electrolytes is lower than the electric field energy contribution, coiled electrodes should exhibit lower total deposited power.

The coiled electrodes are each 3 mm long and consist of approximately 17 wire turns per electrode (Figure 5-107). The wire diameter is 120 µm and the pitch between turns is 0.17 mm. The spacing between adjacent coiled electrodes is 4 mm.

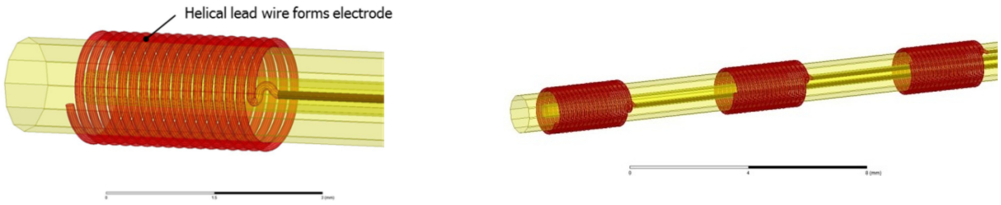

Figure 5-107 Helical electrode

Two scenarios have been investigated. The first scenario considers open-ended Lead wires at the IPG header and the second scenario considers shorted Lead wires to the IPG case. Figure 5-108 (DV00) and Figure 5-109 (DV0A) present superimposed simulation results for Lead lengths between 200 mm and 1000 mm. The simulation results show that the maximum electric field strength at the distal end of electrodes is on average 20 % lower for helical electrodes than the maximum electric field strength for equivalent solid cylindrical electrodes.

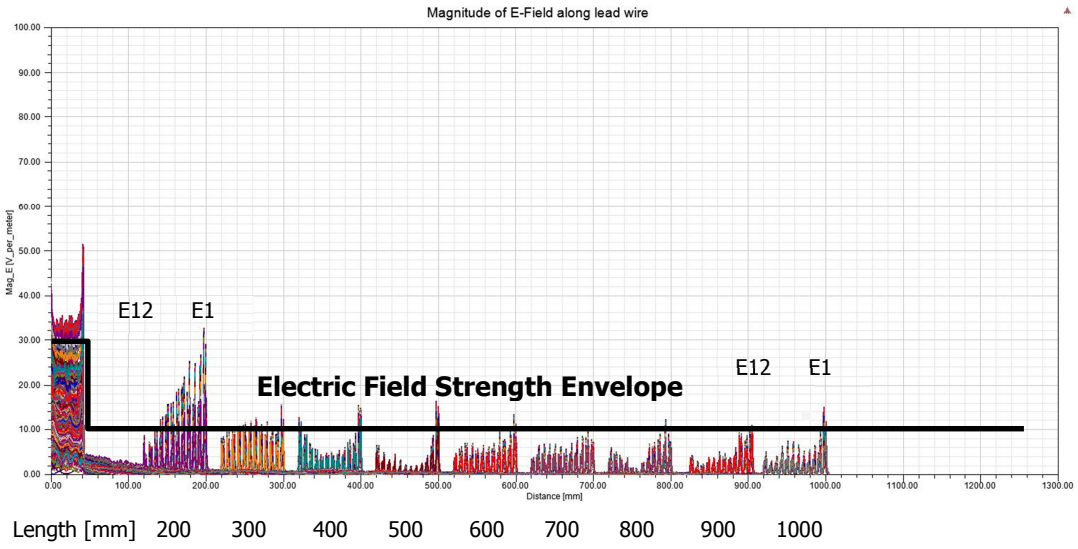

Figure 5-108 DV00 (wires open ended in IPG header) - electric fields for coiled electrodes

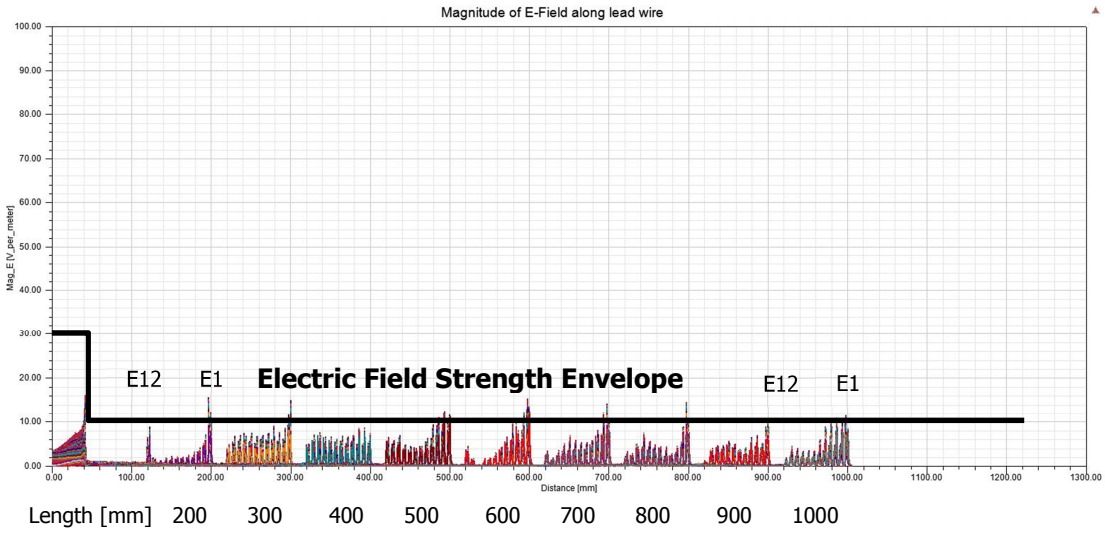

Figure 5-109 DV0A (wires connected to IPG case) - electric fields for coiled electrodes

Using coiled electrodes with centre feed points, i.e. feed points half way between the electrode's distal ends, and/or bifilar coiling can further reduce electric field exposure. In view of MRI safety, helical electrodes can lead to significant improvements over solid cylindrical electrodes without detrimental effects in their therapeutic use.

5.1.9.3 Coupled auxiliary filars

Auxiliary filars running along the outside of the MLC provide an RF shield for Lead wires running inside the MLC (Figure 5-110). On the other hand, auxiliary filars increase the average conductivity along the MLC surface and therefore reduce the attenuation for quasi coaxial TEM waves propagating between the ring of Lead wires and the perimeter of the MLC.

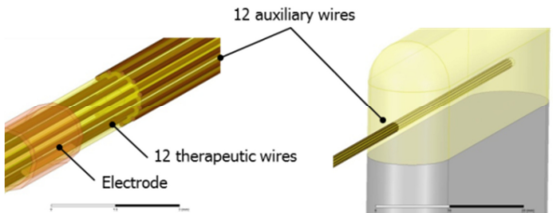

Figure 5-110 Coupling to auxiliary wires

Figure 5-111 (DV11) shows superimposed simulation results for Lead lengths between 200 mm and 1200 mm.

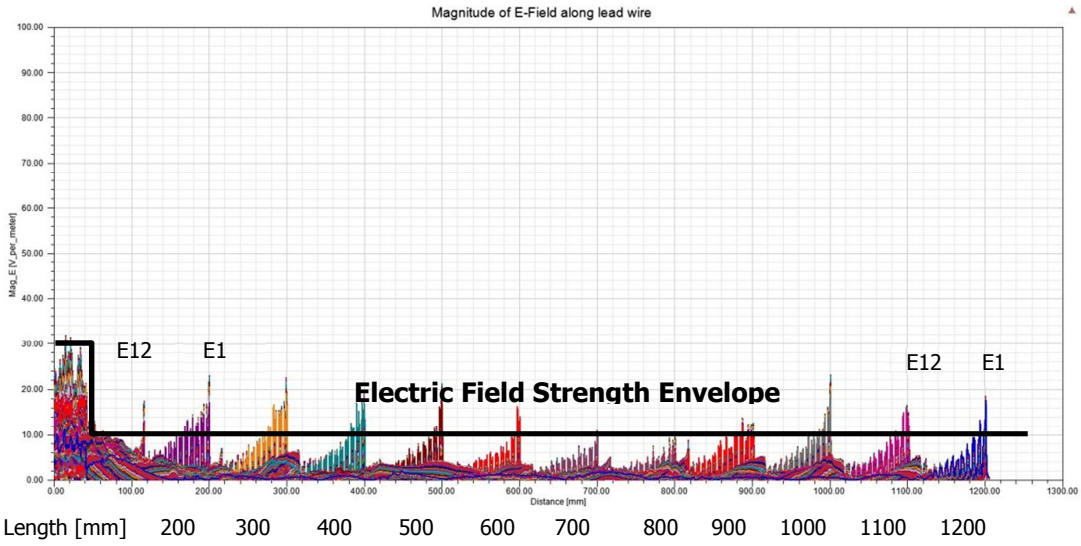

Figure 5-111 DV11 - electric field for twelve additional auxiliary wires

Apart from a significant reduction of electric fields inside the IPG header and for a Lead length of 200 mm there are no significant reductions for Lead lengths between 300 mm and 1200 mm.

5.1.9.4 Coupled interleaved auxiliary electrodes

Interleaving capacitive coupled auxiliary electrodes with therapeutic electrodes at the distal end increases the effective surface area of electrodes during RF exposure and hence reduces the power density per surface area. The design modifications that have been applied to the base case are shown below (Figure 5-112 to Figure 5-114). The coupling capacitance between the auxiliary electrode and the interconnect layer is ~100 pF using a thin layer of TiO_2 with relative permittivity of 100. Thin TiO_2 layers have break down voltages above operating voltages of IMDs and above voltages induced during MRI scans [P161].

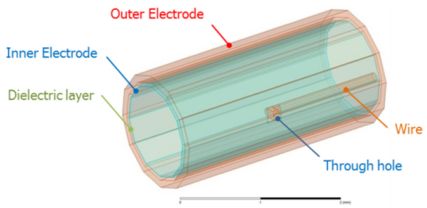

Figure 5-112 DV08 - Auxiliary electrode

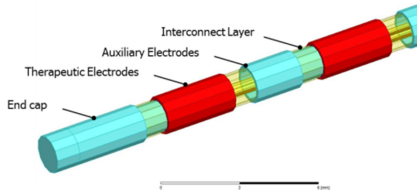

Figure 5-113 DV08 - Auxiliary electrodes interleaved with therapeutic electrodes

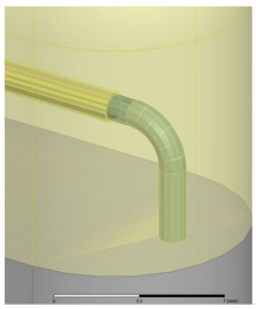

Figure 5-114 DV08 - Lead wires grounded at IPG

Figure 5-111 (DV08) shows superimposed simulation results for Lead lengths between 200 mm and 1200 mm.

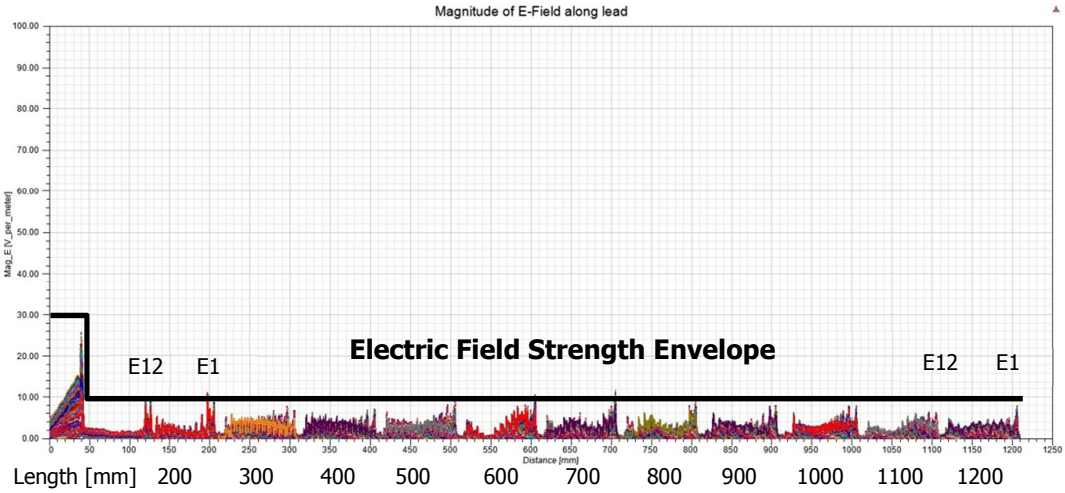

Figure 5-115 DV08 - Magnitude of electric field

For all Lead lengths a significant reduction of the electric field strength at distal end electrodes is observed. Measurement results for Lead lengths of 200 mm and 600 mm are presented in Section 5.1.11.5.

5.1.9.5 Number of electrodes

Leads with many electrodes seem to show lower worst case temperature increases at distal end electrodes during MRI scans than Leads with few electrodes. This section summarises results from simulation runs for design variation DV07B and a Lead length of 200 mm. The configuration at the distal end is the same as for design variation DV08 described in the previous section but the Lead wires are open ended in the IPG header. The number of therapeutic electrodes and Lead wires has been decreased from 12 to 1 and the number of auxiliary electrodes from 13 to 2 to see the impact of electric field distributions along distal end electrodes and to investigate the surface current distribution around the perimeter of a single Lead wire.

Figure 5-116 and Figure 5-117 show the wire routing inside the MLC and the path designations for surface currents on Wire W01, respectively.

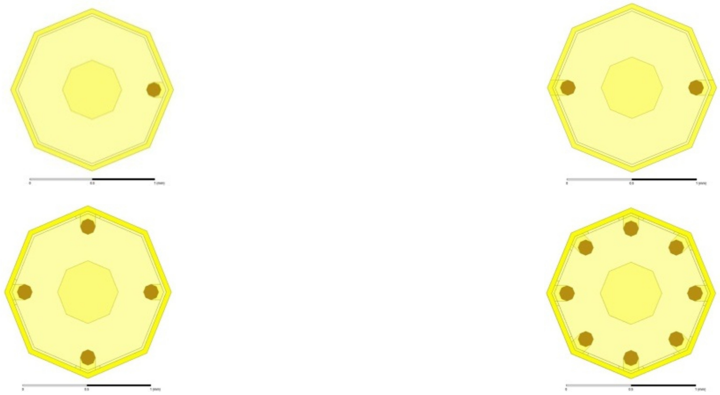

Figure 5-116 Multi-lumen cross-section and wire routing (looking from distal towards proximity end)

Path 0° is facing the surface and Path 180° is facing the centre of the MLC.

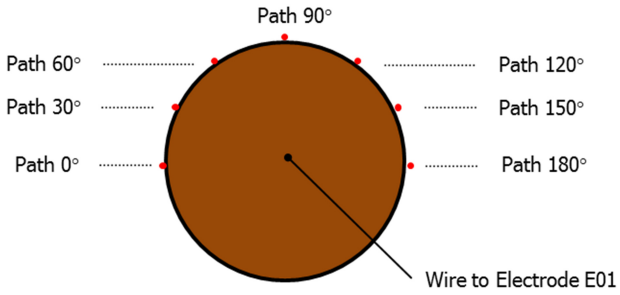

Figure 5-117 Cross-section of Wire W01 to Electrode E01 and path designation for surface currents (looking from proximity towards distal end)

Figure 5-118 to Figure 5-122 show the magnitude of the electric field strength at the distal end for 12, 8, 4, 2, and 1 therapeutic electrode(s). For comparison, Figure 5-123 shows the magnitude of the electric field strength for 1 therapeutic electrode but without adjacent auxiliary electrodes.

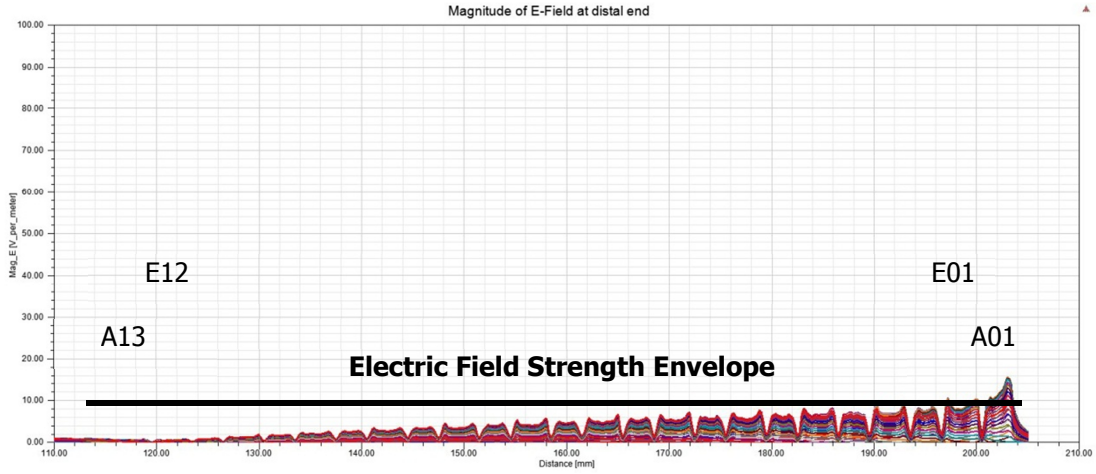

Figure 5-118 DV07B - electric field distribution for twelve therapeutic electrodes

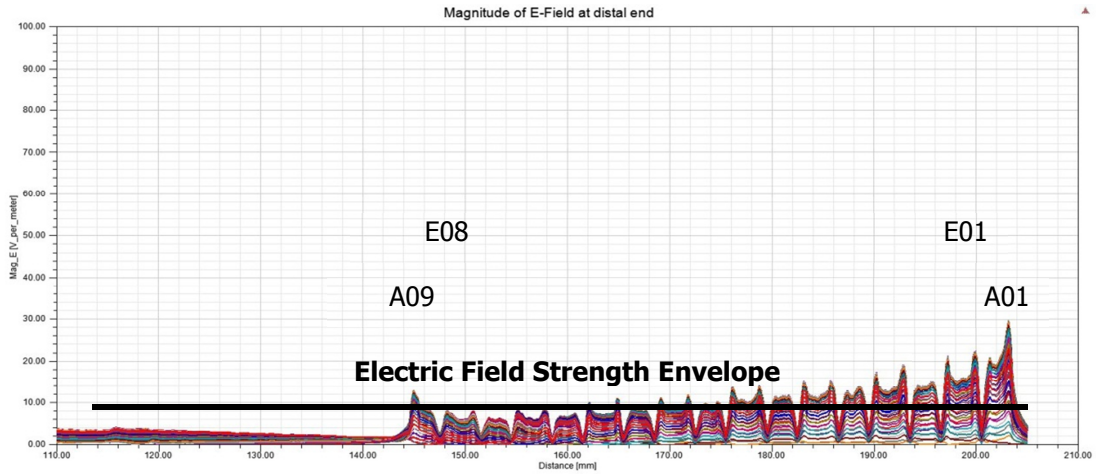

Figure 5-119 DV07B - electric field distribution for eight therapeutic electrodes

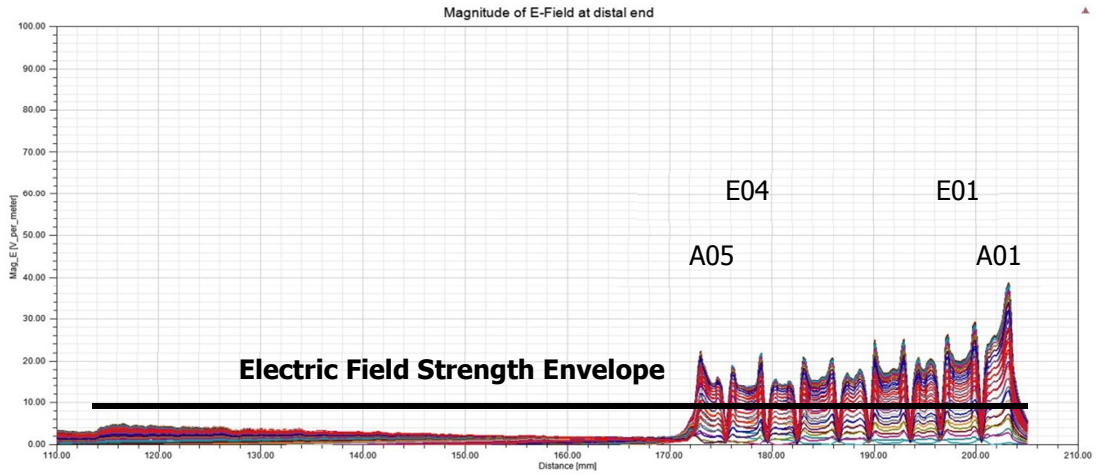

Figure 5-120 DV07B - electric field distribution for four therapeutic electrodes

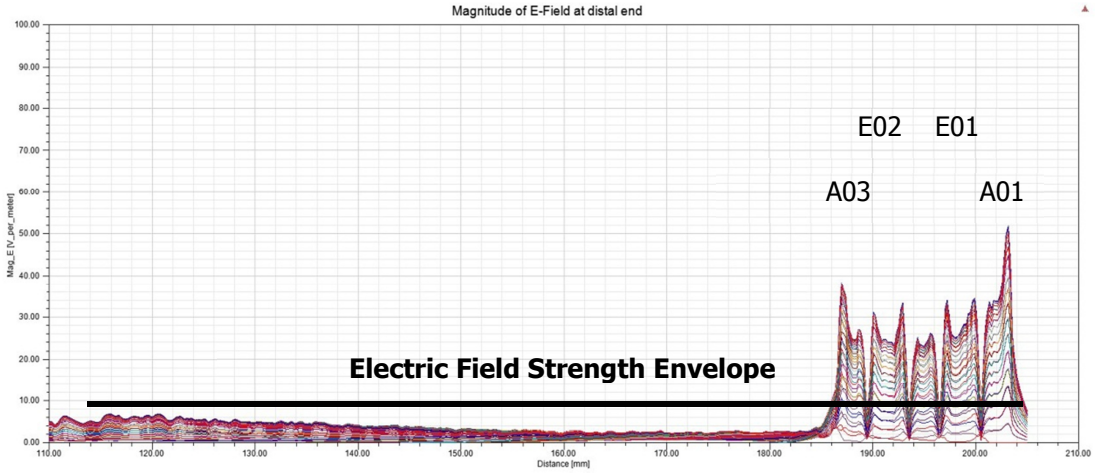

Figure 5-121 DV07B - electric field distribution for two therapeutic electrodes

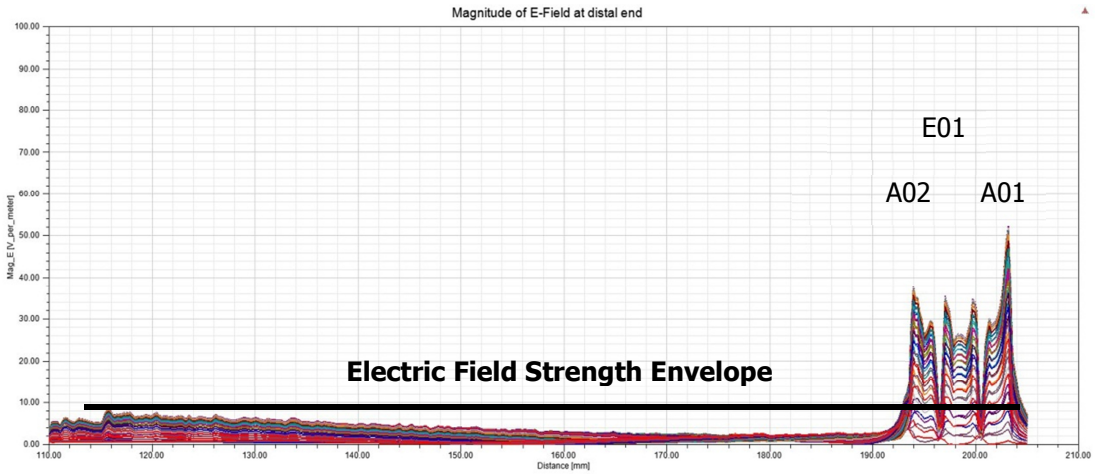

Figure 5-122 DV07B - electric field distribution for one therapeutic electrode

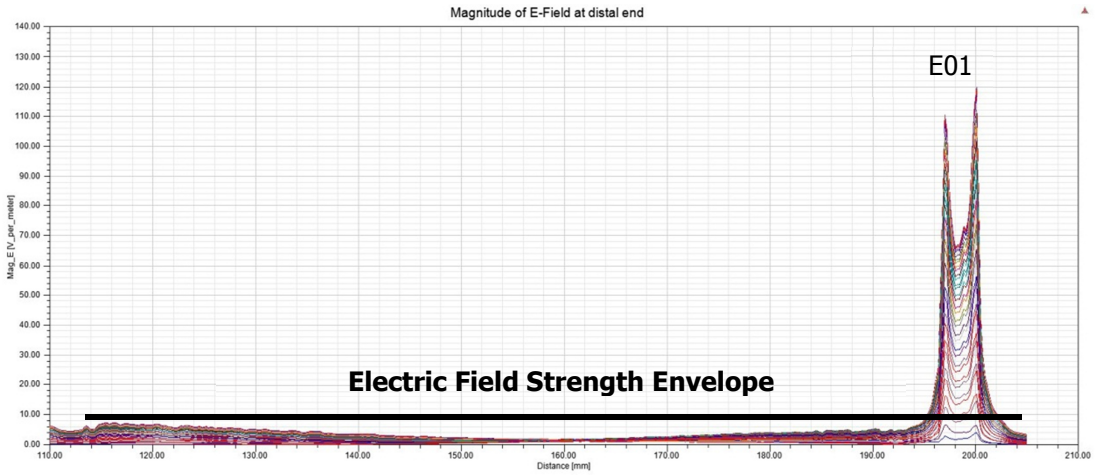

Figure 5-123 UM01 - electric field distribution for one therapeutic electrode but without auxiliary electrodes (for comparison)

With decreasing number of electrodes the peak electric field at distal end electrodes increases from $15\ \frac{V}{m}$ for 12 therapeutic and 13 auxiliary electrodes to $50\ \frac{V}{m}$ for 1 therapeutic and 2 auxiliary electrodes. For comparison, the electric field for 1 therapeutic electrode without auxiliary electrodes increases to $120\ \frac{V}{m}$.

For decreasing number of electrodes the electromagnetic energy captured by the Lead is dissipated over a decreasing electrode surface area and hence the deposited power per surface area increases resulting in higher local temperature increases. Further, for decreasing number of Lead wires the electric field is more concentrated inside the MLC resulting in less attenuation for waves propagating in longitudinal direction and hence increasing standing wave voltage and current peaks on remaining Lead wires.

Figure 5-124 and Figure 5-125 show surface current distributions on Wire 01 for eight and one therapeutic electrode(s), respectively. For eight therapeutic electrodes the magnitude of the surface current decreases around the perimeter of Wire 01 with a maximum along Path 0° and a minimum along Path 180°. The ratio between maximum and minimum surface current is ~5.8. For one therapeutic electrode the magnitude decreases around the perimeter but the ratio between maximum and minimum surface current is only ~1.4. In addition, the maximum magnitude of the surface current for eight and one therapeutic electrode(s) is $2.3\ \frac{A}{m}$ and $3.9\ \frac{A}{m}$, respectively. Therefore, the current density on a single wire in the eight electrode scenario is significantly lower than the current density on the single wire in the single electrode scenario.

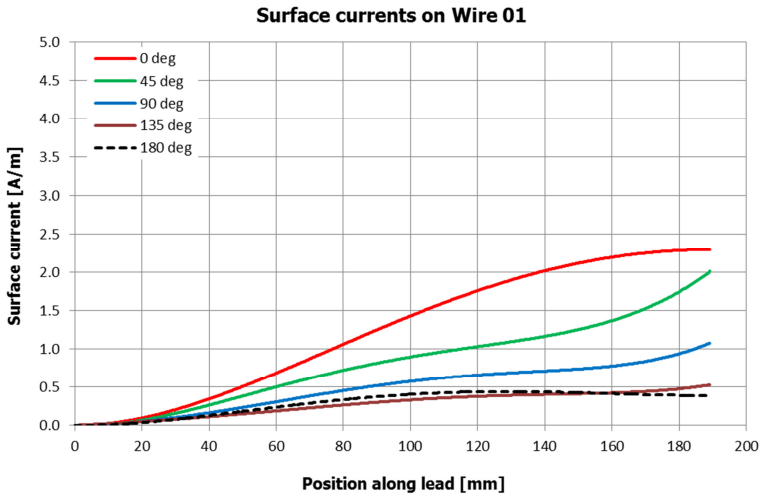

Figure 5-124 DV07B - surface currents on Wire 01 for eight therapeutic electrodes and nine auxiliary electrodes

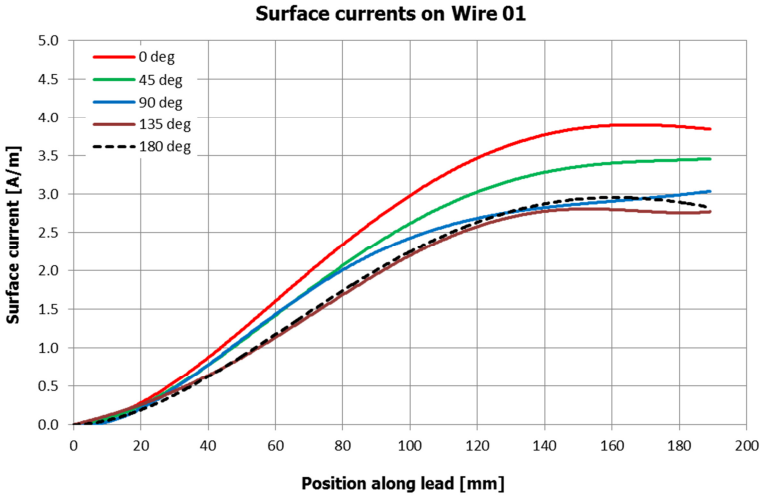

Figure 5-125 DV07B - surface currents on Wire 01 for one therapeutic electrode and two auxiliary electrodes

Summing up, multi-wire (multi-electrode) Leads are less susceptible to RF induced temperature increase than single wire (single electrode) Leads. Therefore, spare conducts in MLCs can be equipped with wires to form resistively loaded loops to absorb energy from impinging electromagnetic fields and to minimise surface currents on wires connected to therapeutic electrodes.

5.1.9.6 Angular position of wires and electrodes

Several Leads had one or more wire routing anomalies as indicated in Figure 5-126. Here, a Lead wire routing anomaly is a deviation from a straight path or a change in Lead wire spacing along the MLC. Although short circuits between Lead wires have not been observed RF coupling between wires is significantly affected by those anomalies. Anomaly Type 1 shows wires deviating from straight paths through the MLC. Anomaly Type 2 shows two or three wires clustering on one side of the MLC and Anomaly Type 3 shows more than three wires clustering together. Further, seams between electrodes and thermoplastic sleeves at the distal end showed cracks that led to saline solution entering into the central conduct. Finally, some thermoplastic sleeves squeezed all wires together reducing the average distance between wires.

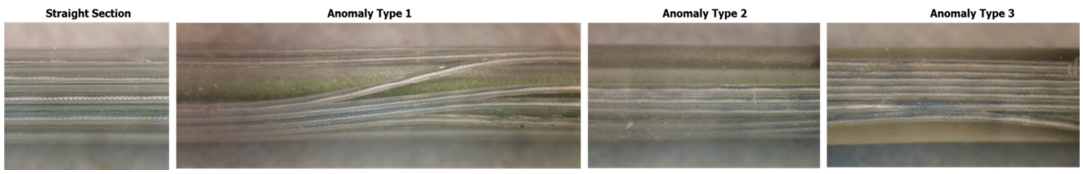

Figure 5-126 Detected anomalies in multi-lumen sections

A detailed analysis of the impact of each anomaly has not been carried out but particular care was applied to minimise wire routing anomalies and to seal the junction between electrodes and MLC in subsequent design variations.

This section explores whether angular positions of Lead wires in MLCs have an impact on electric field distributions along electrodes at the distal end. Various wire routing schemes have been analysed. The electrode numbering scheme has not been changed. Electrode E01 is the most distal electrode and Electrode E12 is the least distal electrode. The angular

positions of Lead wires for base case UM02 and design variations DV16 and DV17 are outlined in Figure 5-127 and listed below:

- UM02 - base case with Lead wires connected to IPG case. (Clockwise count starting at Electrode 1: CW 1 2 3 4 5 6 7 8 9 10 11 12.
- DV16 - same as UM02 but different angular position of wires in MLC. Clockwise count starting at Electrode 1: CW 1 11 8 3 7 9 2 10 5 4 6 12.
- DV17 - same as UM02 but different angular position of wires in MLC. Clockwise count starting at Electrode 1: CW 1 2 4 6 8 10 12 11 9 7 5 3.

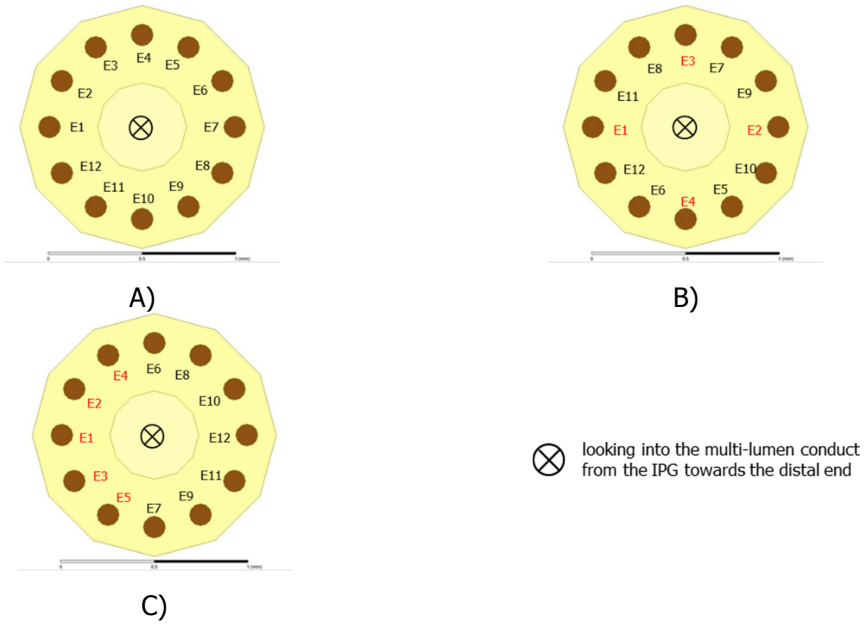

Figure 5-127 Wire positions
A) UM02
B) DV16
C) DV17

In routing scheme B) of Figure 5-127 Lead wires to the four distal end electrodes are not adjacent and maximally spaced apart, i.e. they exhibit the lowest RF coupling. In routing scheme C) of Figure 5-127 Lead wires to the distal end electrodes have the strongest RF coupling with similar Lead wire lengths (the difference in Lead wire length is equal to one or two electrode spacing). In addition, the distance between the shortest Lead wire (E12) and the longest Lead wire (E01) is maximised, i.e. these Lead wires exhibit the lowest RF coupling.

Electric field distributions are compared for Lead lengths between 200 mm and 1200 mm and are shown in Figure 5-128 to Figure 5-130.

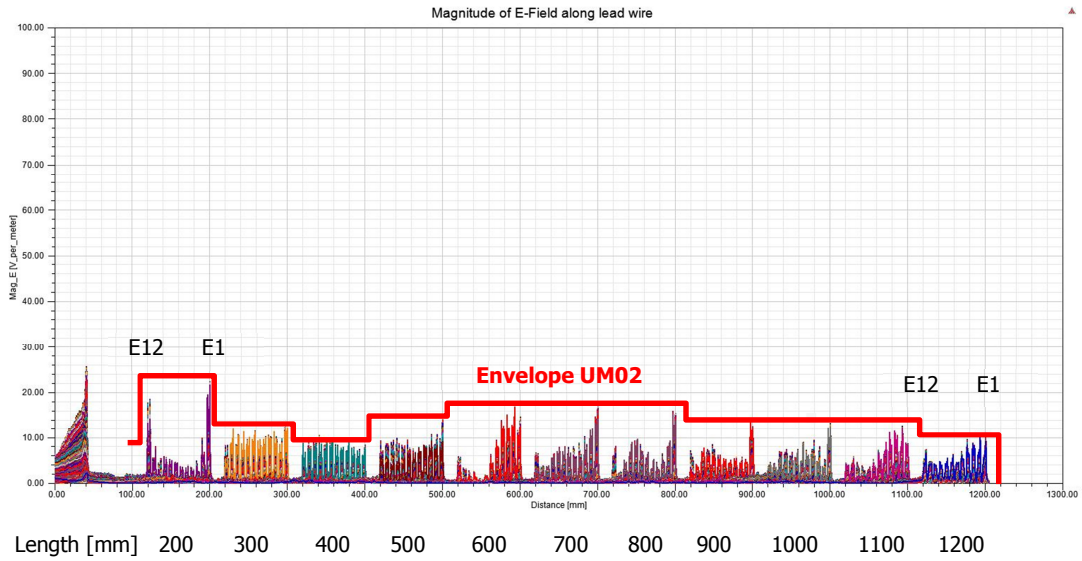

Figure 5-128 UM02 - electric fields along Lead - (CW 1 2 3 4 5 6 7 8 9 10 11 12)

Some angular positions reduce and some angular positions increase the electric field distribution for a given Lead length. Each individual wire shows a distinctive surface current (H-field) and voltage (E-field) distribution along its length that is influenced by all other wires through capacitive coupling (charge density distributions on wires) and inductive coupling (surface currents along wires) whereby adjacent wires have the strongest impact.

Some routing schemes create voltage (E-field) nodes, i.e. areas with low electric field strength, at the distal end. Design variation DV17 reduces the magnitude of the electric field strength at distal end electrodes for the majority of Lead lengths between 200 mm and 1200 mm. Optimising the routing scheme for a given Lead length can reduce the maximum electric field strength along distal end electrodes by 50%.

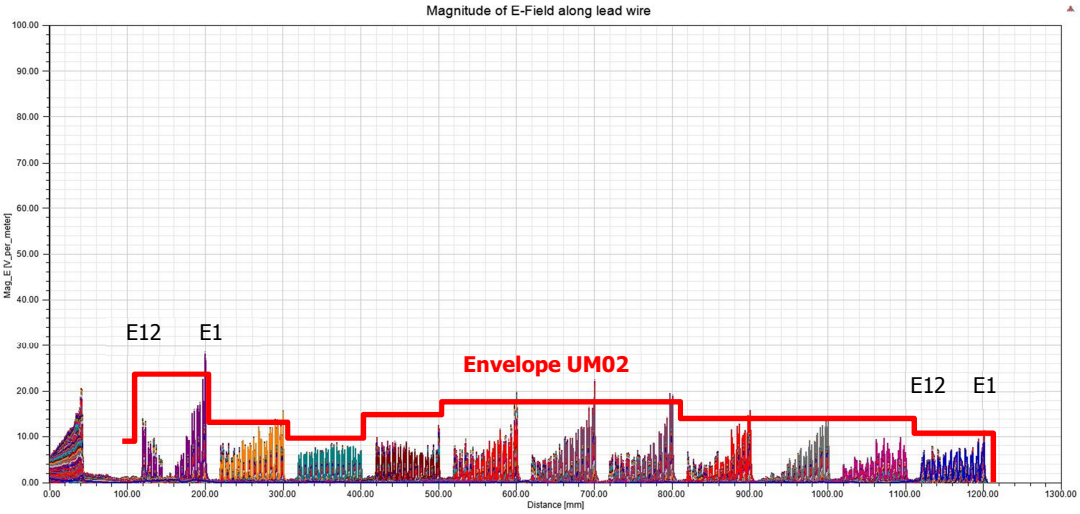

Figure 5-129 DV16 - electric fields along Lead - (CW 1 11 8 3 7 9 2 10 5 4 6 12)

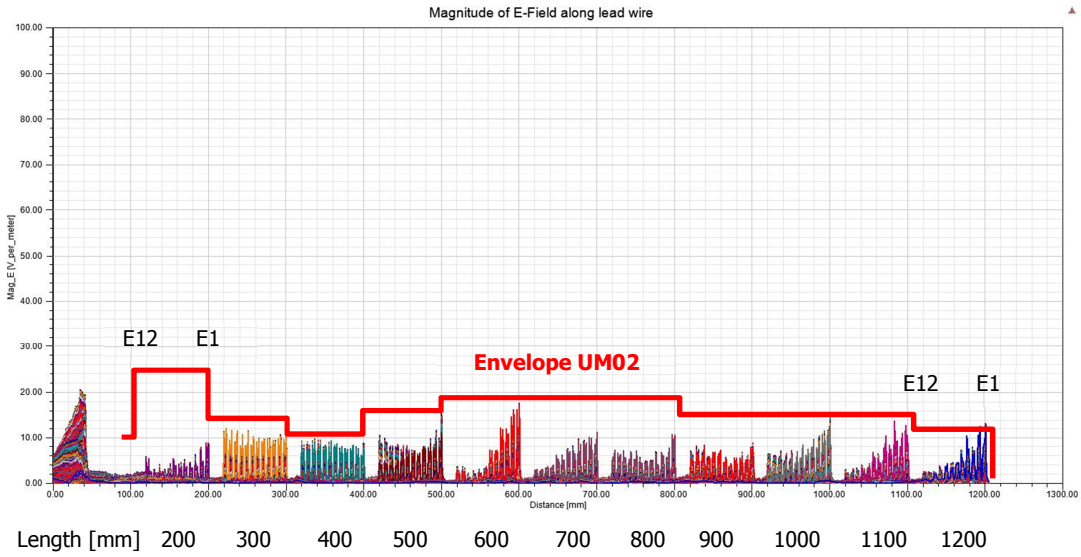

Figure 5-130 DV17 - electric fields along Lead - (CW 1 2 4 6 8 10 12 11 9 7 5 3)

In addition, following conclusions can be drawn. The first is that wire position within the MLC has an influence on electric field distributions at distal end electrodes and hence on power deposition at distal end electrodes. The second conclusion is that the field distribution at distal end electrodes depends on MLC length. The third conclusion is that wire routing anomalies and hence changes in RF coupling between wires can

significantly influence the field distribution at distal ends and hence wire routing anomalies should be minimised.

5.1.9.7 Auxiliary electrodes at proximity end

In Section 5.1.9.4 capacitive coupled auxiliary electrodes have been interleaved with therapeutic electrodes at the distal end. Here, capacitive coupled auxiliary electrodes are added at the proximity end (PE) to absorb energy from electromagnetic waves travelling from the distal towards the proximity end. The decoupling capacitances have 330 pF and present a low resistance at 128 MHz. Two configurations have been investigated; the first configuration considers long auxiliary electrodes, i.e. electrodes with large surface area, and the second configuration considers short electrodes, i.e. electrodes with smaller surface area. Surface area and electrode spacing determine terminal resistances for common and differential modes. Both configurations are outlined in Figure 5-131.

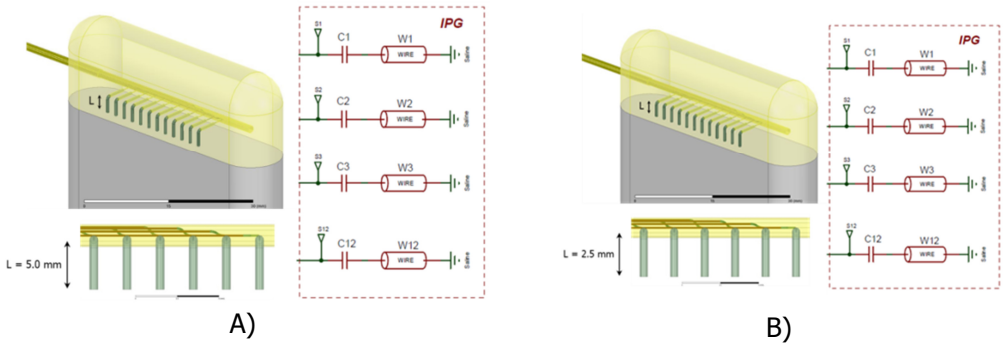

A) B)

Figure 5-131 Capacitive coupled auxiliary electrodes at proximity end
A) DV08C1 - long auxiliary electrodes
B) DV08C2 - short auxiliary electrodes

The configurations have been realised and simulated and measured results are presented in Sections 5.1.11.6.1 and 5.1.11.6.2.

5.1.9.8 Distal end extension and auxiliary electrodes at PE

In Section 5.1.6.4 the RF transfer function has been measured and inconsistencies between measured and simulated results have been further explored in Section 5.1.6.6. The amplitude of the measured RF transfer function shows a steep decrease 20 mm before the distal end. A significant fraction of RF power is deposited into electrolytes (human tissue) over distal end electrodes in standard Leads where wires are terminated at corresponding electrodes. Creating a voltage node over distal end electrodes would inherently decrease the power deposition. In addition, differential voltages between wires are generated if the wires have different lengths and/or if they are terminated at different locations along the Lead. This has been analysed in Section 5.1.7. Combining both findings, i.e. extending and equalising wire lengths beyond the distal end could lead to both, a voltage node and a reduction of differential voltages at the distal end (Figure 5-132). For the subsequent EM analysis EM Model #2 (Table 4-2) has been applied and Lead and IPG have been excited at the distal end as outlined in Figure 4-11.

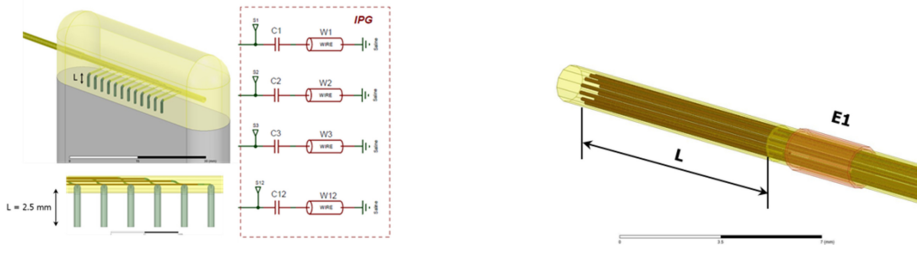

A) B)

Figure 5-132 DV08H1
A) Short capacitive coupled auxiliary electrodes at proximity end
B) Distal end extension

Electric field distributions are compared for a Lead length of 600 mm without Lead extension (DV08C0, Figure 5-133) and with Lead extensions from 10 mm to 50 mm in steps of 10 mm (DV08H1, Figure 5-134).

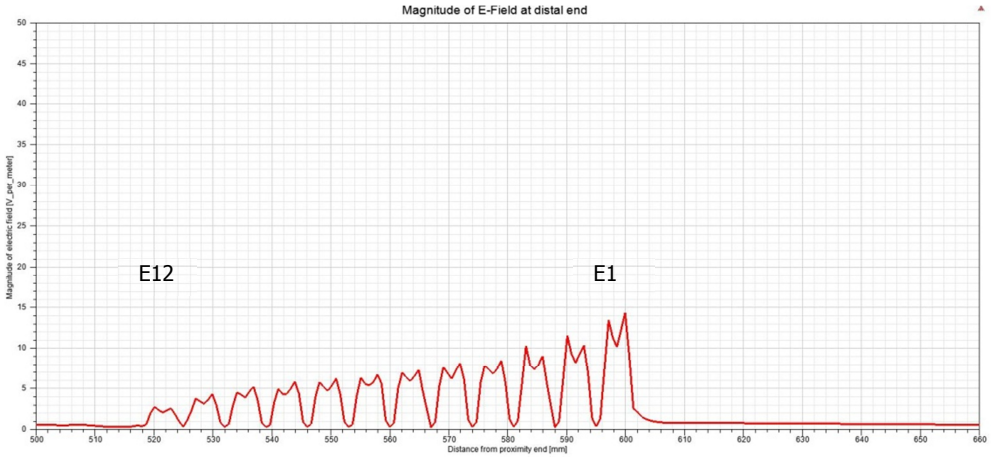

Figure 5-133 DV08C0 - electric field at distal end for Lead length of 600 mm without Lead extension (for comparison)

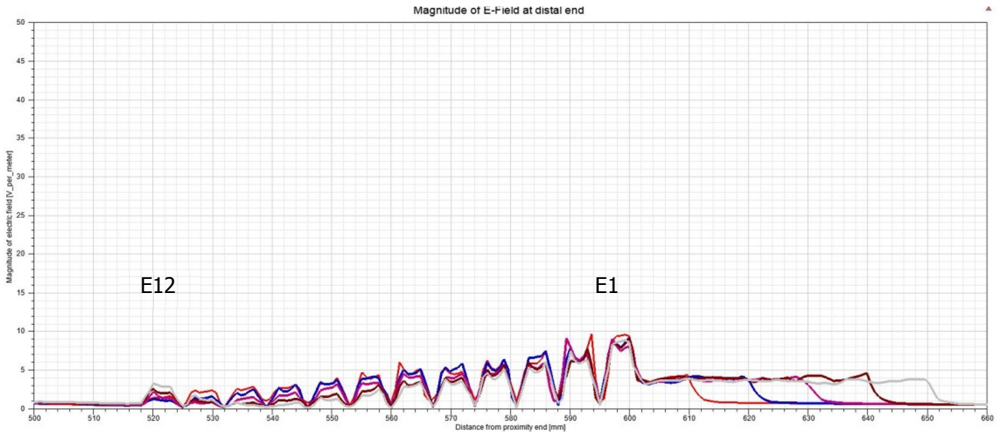

Figure 5-134 DV08H1 - electric field at distal end for Lead length of 600 mm and Lead extensions between 10 mm and 50 mm

Equal wire lengths at the distal end reduce the maximum electric field by 33 %. The length of the distal end extension has a minor effect in simulations but will probably have an impact during measurements since the distal end effect from RF transfer function measurements has not been integrated into EM model #2.

5.1.9.9 Distal end extension and RC network at PE

Capacitive coupled auxiliary electrodes at the proximity end have been replaced by equivalent capacitive coupled resistor matrices. This idea is presented in Figure 5-135. DC-decoupled resistors connect adjacent wires of the MLC. The decoupling capacitances have 330 pF and present a low resistance at 128 MHz. To maximise absorption of wave energy propagating from the distal towards the proximity end the resistance should match the characteristic impedance of an equivalent two wire transmission line embedded in an insulator. But, to create voltage minima at distal end electrodes the wire termination impedance can differ from the characteristic impedance.

The distal end extension with capacitive coupled auxiliary electrodes at the proximity end has shown a 33% reduction of electric fields at the distal end (see Section 5.1.9.8). Here, the impact of the resistor network has been analysed for two resistance values; 100 Ohm and 30 Ohm. The Lead extension is $L = 10\,mm$.

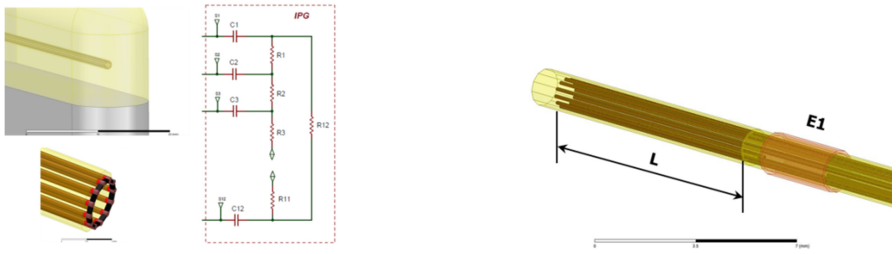

A) B)

Figure 5-135 DV08H2 and DV08H3
A) Lead wires capacitive coupled to ring of resistors at proximity end
B) Distal end extension with $L = 10\,mm$

The electric field distributions for both resistor networks are presented for a Lead length of 600 mm in Figure 5-136. They show no significant differences and the field magnitudes are similar to the field magnitudes for design variation DV08H1 presented in the previous section. In addition,

the differential voltages between Lead wires have been calculated and compared with base case UM03 (wires grounded to IPG case). The results are presented in Figure 5-137. Comparing base case UM03 with design variations DV08H2 and DV08H3, both resistor networks reduce the maximum differential voltage by approximately 50% and the differential voltages at the distal end by approximately 40%.

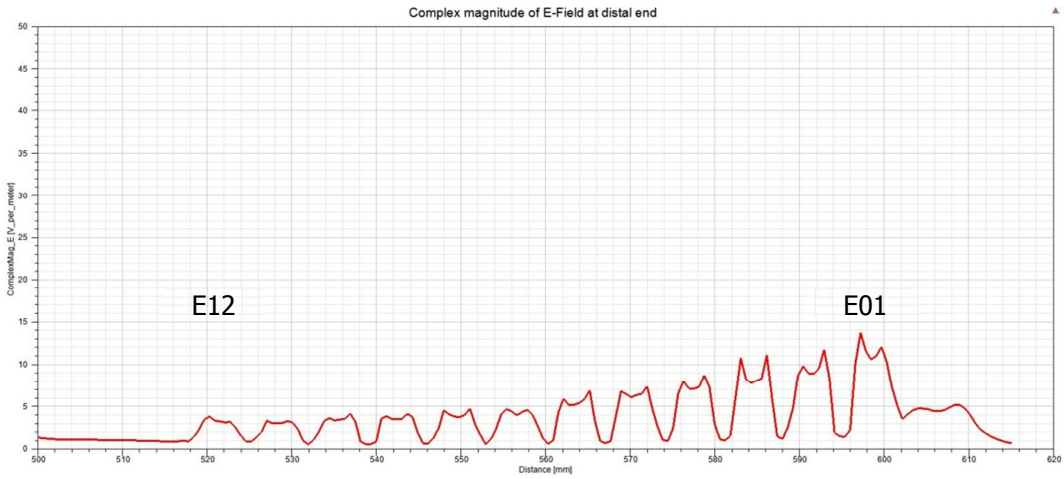

A)

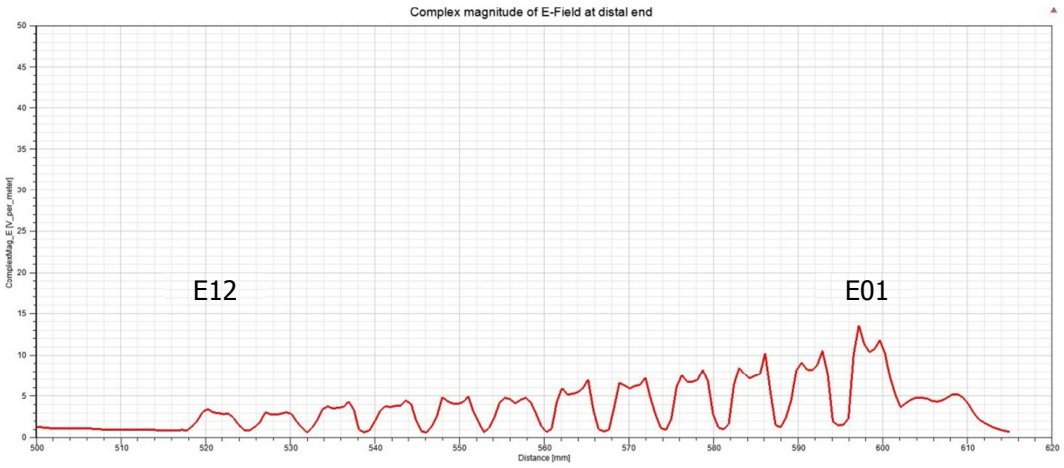

B)

Figure 5-136 Electric field at distal end for a Lead length of 600 mm
A) DV08H2 (100 Ohm resistors)
B) DV08H3 (30 Ohm resistors)

Comparing design variations DV08H2 and DV08H3, the termination resistance shifts voltage minima and maxima along the Lead. The optimum resistance value creates a voltage node at the distal end. The 100 Ohm resistor network is very close to this optimum value.

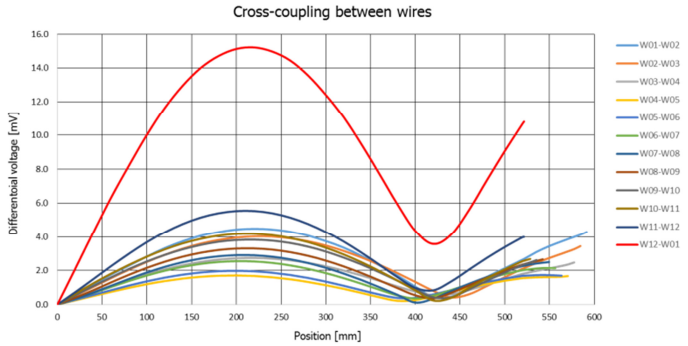

A)

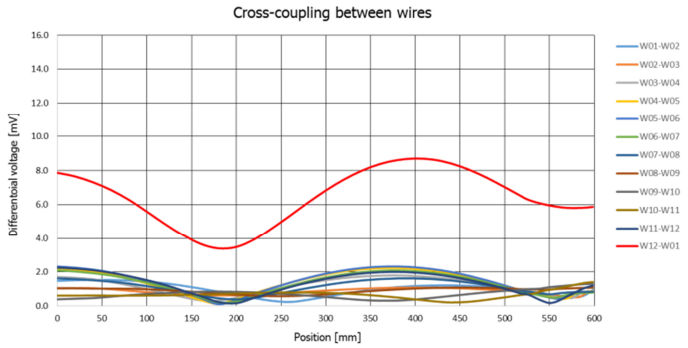

B)

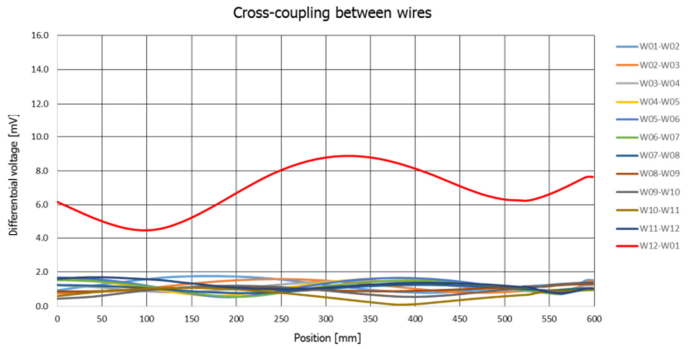

C)

Figure 5-137 Differential voltage between Lead wires
A) UM03 (wires grounded to IPG case)
B) DV08H2 (100 Ohm resistors)
C) DV08H3 (30 Ohm resistors)

5.1.10 Frequency dependence

In this section, the frequency dependence of the maximum electric field strength at the distal end is explored. The frequency has been swept from 4 MHz to 512 MHz covering the range from 0.1 Tesla to 12 Tesla NMR and MRI scanners.

If not otherwise stated, EM Model #1 (Table 4-2) has been applied for the analysis. Lead and IPG are described in Section 4.1.3.1 and have been illuminated with a plane wave as outlined in Section 4.1.4.1. The test specimen is a 200 mm long Lead with therapeutic and capacitive coupled auxiliary electrodes at the distal end and Lead wires open ended inside the IPG header. The coupling capacitance between the auxiliary electrode and the interconnect layer is ~100 pF using a thin layer of TiO_2 with relative permittivity of 100. The design variation is outlined in Figure 5-138 to Figure 5-140.

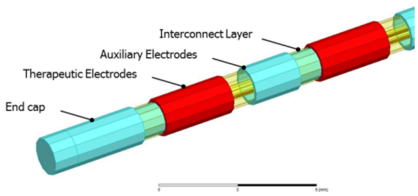

Figure 5-138 DV07A - Therapeutic and auxiliary electrodes

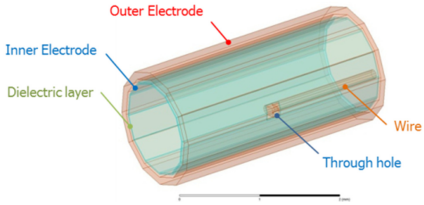

Figure 5-139 DV07A - Auxiliary electrode

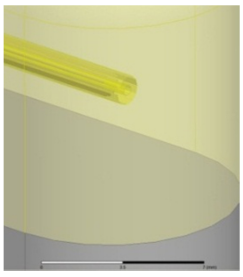

Figure 5-140 DV07A - Lead wires open ended in IPG header

The maximum electric field at the distal end electrode E01 for a Lead length of 200 mm is presented in Figure 5-141.

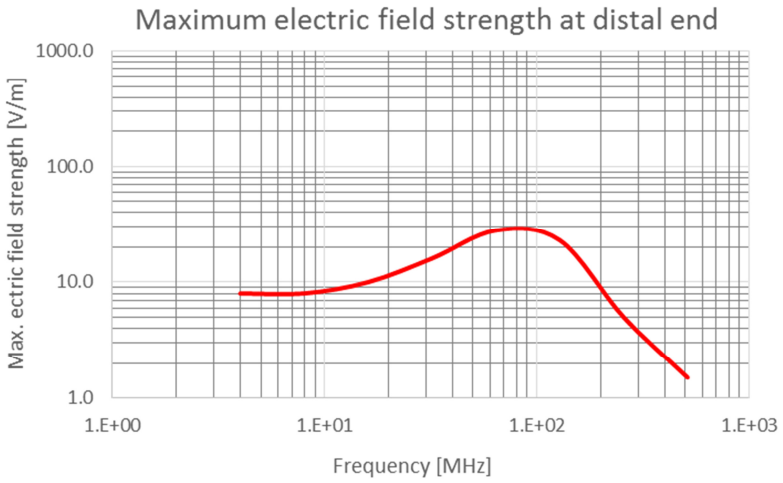

Figure 5-141 DV07A - frequency dependence of maximum electric field at distal end electrode E01 for Lead length of 200 mm

With increasing frequency the maximum field strength at the distal end increases, reaches a maximum at about 100 MHz and then decreases monotonically. The maximum value is 30 V/m at 100 MHz. Similar low pass frequency behaviour is observed for all unshielded design variations where the coupling capacitance between Lead wires and electrolyte (gelled saline) determines the corner frequency. For shielded Lead wires the corner frequency shifts to higher frequencies and for thinner insulation between Lead wires and electrolyte the corner frequency shifts to lower frequencies. The increase of the electric field around the corner frequency is due to a dampened resonance on the Lead. The resonance frequency depends on the termination resistance at the proximity end. For high termination impedances the resonant lengths is $l \approx n \cdot \frac{\lambda_e}{2}$ with $n = 1,2,3, \ldots$ and for low termination impedances the resonant lengths is $l \approx n \cdot \frac{\lambda_e}{4}$ with $n = 1,3,5, \ldots$ where λ_e is the wavelength of the dominant mode along the Lead.

5.1.11 RF test bed - RF induced temperature rise

5.1.11.1 Overview

This section summarises some of the temperature simulations and measurements for Leads and IPGs immersed into a phantom torso (PT) filled with gelled saline. The RF heating test bed has been described in Section 4.3.7 and the base cases and design variations have been summarised in Chapter 3. Measured and calculated temperature increase presented here is the difference between the temperature increase with test specimen, i.e. with IPG and Lead, and the background temperature increase without test specimen, i.e. the temperature increase without IPG and Lead. The temperature difference between measured and calculated (simulated) temperature increase is defined as follows:

$$\Delta T = \Delta T_{calculated} - \Delta T_{measured} \tag{5–13}$$

The routing schemes for distal, centre and proximity excitation for Lead lengths of 200 mm and 600 mm are presented in Section 5.1.11.2. The analysed configurations are shortly described below:

- Section 5.1.11.3: Therapeutic electrodes without Lead wires in order to determine the minimum theoretical temperature increase.
- Section 5.1.11.4: Base cases UM03 and UM04 for Lead lengths of 200 mm and 600 mm
- Section 5.1.11.5: Therapeutic and interleaved auxiliary electrodes at distal end (DV08B) for Lead lengths of 200 mm and 600 mm
- Section 5.1.11.6: Therapeutic and interleaved auxiliary electrodes with modifications of the proximity end (DV08C1, DV08C2, DV08C3, DV08D1) for a Lead length of 600 mm

- Section 5.1.11.7: Therapeutic electrodes with modified proximity end and two auxiliary electrodes (DV08LX_YY_ZEE) for a Lead length of 600 mm

Between two test runs the gelled saline was stirred to remove any temperature differences.

5.1.11.2 Position of IPG and Leads in PT

The position of the distal end inside the RF test bed for distal end excitation and all Lead lengths is shown in Figure 4-68. The position of the distal end for proximity and centre excitation has been changed. The positions are shown in Figure 5-142 to Figure 5-145.

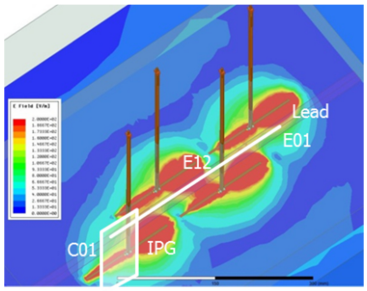

Figure 5-142 Lead (200 mm) and IPG position in RF test bed

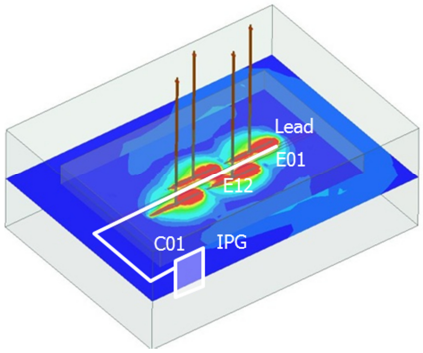

Figure 5-143 Lead (600 mm) and IPG position in RF test bed for distal end RF exposure

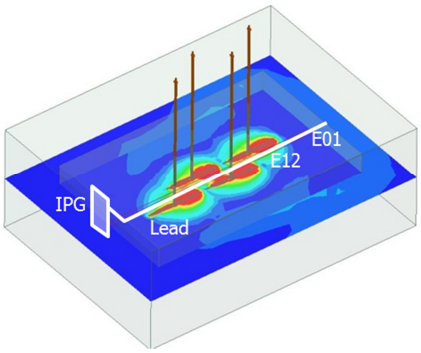

Figure 5-144 Lead (600 mm) and IPG position in RF test bed for centred RF exposure

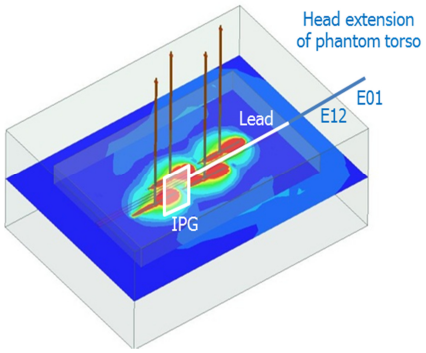

Figure 5-145 Lead (600 mm) and IPG position in RF test bed for proximity end RF exposure

5.1.11.3 Therapeutic electrodes without Lead wires

The purpose of this initial simulation is to determine a theoretical minimum temperature increase of therapeutic electrodes at the distal end for a 200 mm long MLC linking the distal end and the IPG. The Lead wires have been removed from the MLC. The simulation settings are given in Section 4.1.3.1 and Section 4.1.4.1 and the configuration is outlined in Figure 5-146 and Figure 5-147.

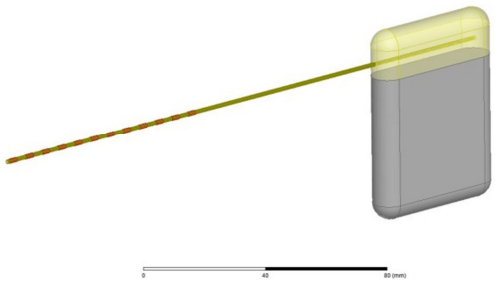

Figure 5-146 UM01 - IPG and Lead without Lead wires

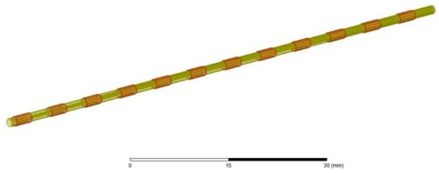

Figure 5-147 Therapeutic electrodes without Lead wires

The total electric field distribution along the MLC and electrode surface for an incident electric field of $1\ \frac{V}{m}$ is shown in Figure 5-148. The resulting peak electric field strength is $\sim 4\ \frac{V}{m}$.

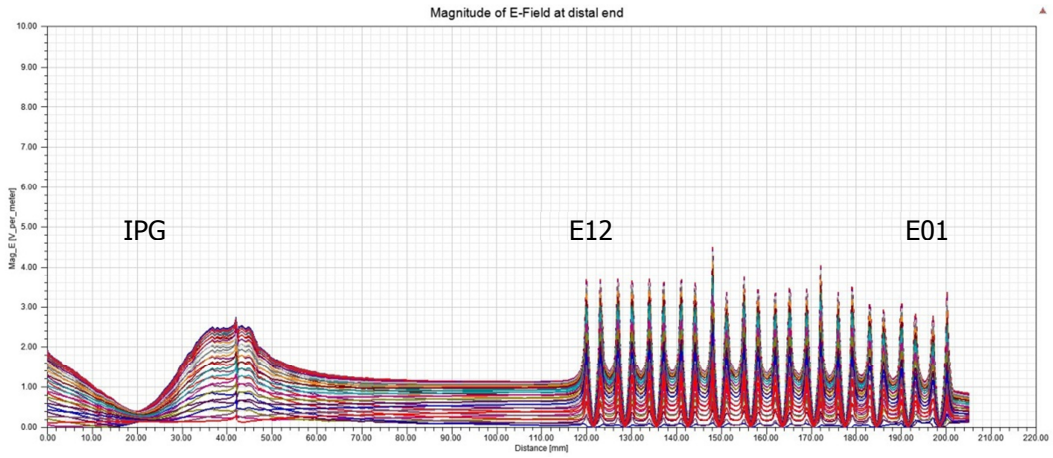

Figure 5-148 Magnitude of electric field along Lead (200 mm) without Lead wires

The power deposited inside a saline volume of 6 mm x 6 mm x 94 mm around the distal end as function of the incident electric field strength is given in Table 5-9.

Incident electric field strength $\left[\frac{\mathrm{V}}{\mathrm{m}}\right]$	Power deposited in saline volume	Steady state temperature increase $[\mathrm{K}]$
1	515 µW	~ 0
100	5.15 mW	0.01
500	128.8 mW	0.21
750	289.8 mW	0.47
1000	515.0 mW	0.83

Table 5-9 Power deposition in saline volume for electrodes without Lead wires

The power deposited leads to a local temperature increase. For the steady state case ($t \to \infty$) the temperature increase is graphed in Figure 5-149.

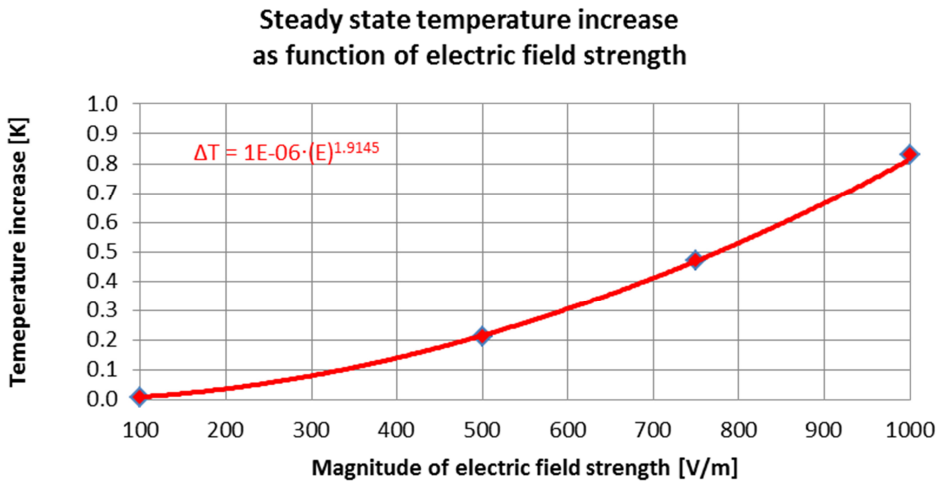

Figure 5-149 Steady state temperature increase for electrodes without Lead wires

Summing up, the temperature increase around the electrodes is less than $0.1\,K$ for an incident electric field of $300\,\frac{V}{m}$. For comparison, the peak tangential electric field generated by the RF heating test bed along the centre line for an input power of 200 Watt into the dipole array is $300\,\frac{V}{m}$.

5.1.11.4 Therapeutic electrodes (base cases)

In the following sub-sections four configurations are benchmarked in order to determine the impact of Lead length and the impact of shorted or open-ended Lead wires at the proximity end on temperature increase at the distal end. The four configurations are ...

- Lead 200 mm with Lead wires shorted to IPG case
- Lead 600 mm with Lead wires shorted to IPG case
- Lead 200 mm with open ended Lead wires in IPG header
- Lead 600 mm with open ended Lead wires in IPG header

In subsequent sections following simulation settings have been applied:

- EM model #3 (Table 4-2). The boundary layer has an isotropic permittivity of 3.5 and the double layer around the electrodes has the same characteristics as gelled saline. The off-diagonal coefficients of the conductivity tensor matrix (Equation (5–11)) have been set to $-0.25\ \frac{S}{m}$ for gelled saline.
- Electromagnetic simulation setups are shown in Figure 4-11 and Figure 4-18.
- The peak electric field strength along the centre line of the dipole array is $300\ \frac{V}{m}$.

5.1.11.4.1 UM03 - Lead 200 mm with wires shorted to IPG case

A 200 mm long Lead with 12 electrodes and Lead wires shorted in a star point to the IPG case is analysed. The configuration is shown in Figure 5-150 and Figure 5-151.

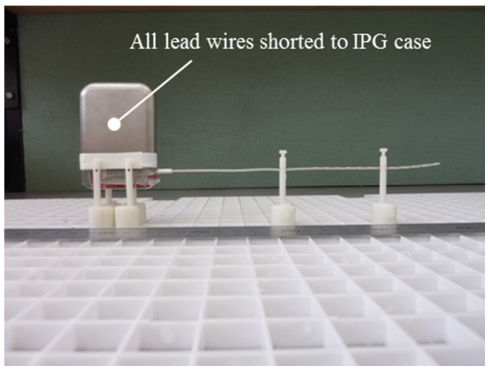

Figure 5-150 UM03 - wires shorted to IPG case

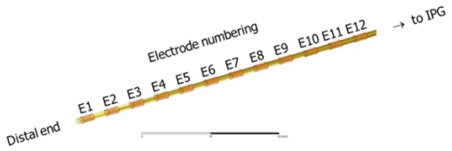

Figure 5-151 UM03 - electrode numbering

In a first step, the total electric field at the distal end has been simulated. The result is shown in Figure 5-152.

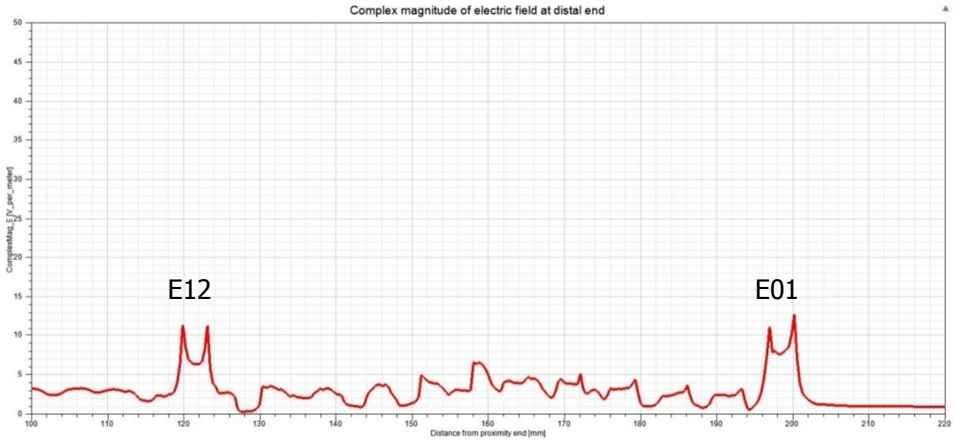

Figure 5-152 UM03 - 200 mm - short - complex magnitude of electric field at distal end

In a second step, the temperature increase around the distal end electrodes has been determined using the thermal simulation setup described in Section 4.2.3 for an exposure time of 300 seconds. The results of the transient simulations are shown in Figure 5-153 and Figure 5-154.

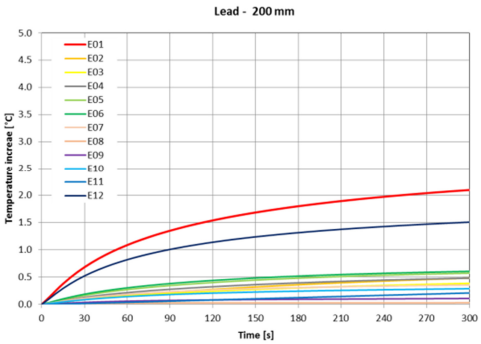

Figure 5-153 UM03 - 200 mm - short Simulation - Temp. Transient

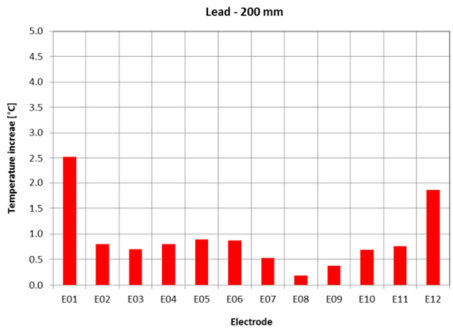

Figure 5-154 UM03 - 200 mm - short Simulation - Temp. after 300 s

In a third step, the temperature increase has been measured using the RF test bed described in Section 4.3.7 for an exposure time of 300 seconds and 200 Watt input power into the dipole array. The results are shown in Figure 5-155 and Figure 5-156.

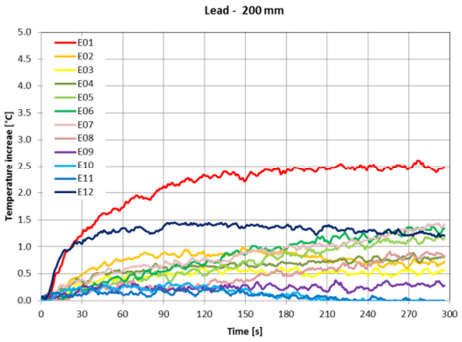

Figure 5-155 UM03 - 200 mm - short Measurement - Temp. Transient

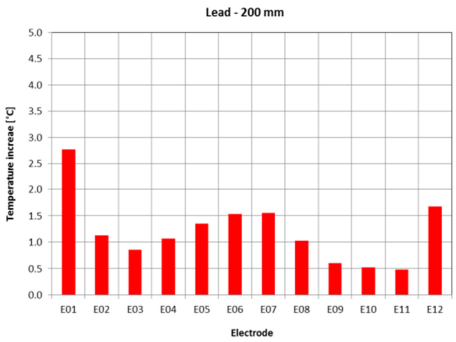

Figure 5-156 UM03 - 200 mm - short Measurement - Temp. after 300 s

In a final step, measured and calculated temperature increase after 300 seconds exposure time has been compared. The result is presented in Figure 5-157.

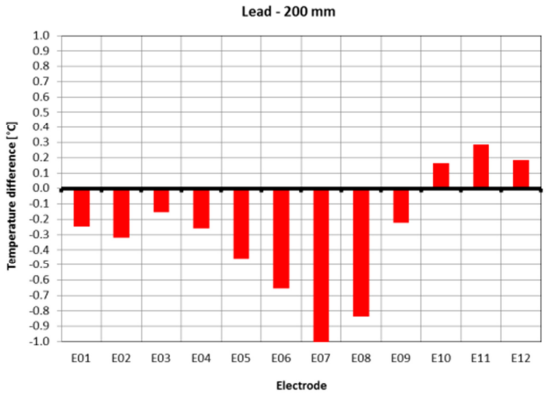

Figure 5-157 UM03 - 200 mm - short
Difference - Temp.
after 300 s

Simulated and measured temperature profiles after 300 seconds exposure time have the same shape (Figure 5-154 and Figure 5-156). A difference between measured and simulated results is apparent from a comparison of Figure 5-153 and Figure 5-155. Electrodes 10, 11 and 12 show a decrease in temperature after 90 seconds exposure time, and Electrodes 5, 6 and 7 show a linear increase in temperature. The temperature decrease can be explained by the onset of moderate convection around gelled saline clots whereas the linear temperature increase indicates that the electrodes are thermally isolated by gelled saline clots (see Section 5.1.4). The Lead wire routing in sections of the MLC is distorted and leads to strong cross-coupling between Lead wires. The wire routing anomalies have been outlined in Section 5.1.9.6.

The four analysis steps presented here have been applied in all subsequent sections.

5.1.11.4.2 UM03 - Lead 600 mm with wires shorted to IPG case

A 600 mm long Lead with 12 electrodes and Lead wires shorted in a star point to the IPG case is analysed. The configuration is shown in Figure 5-158 and Figure 5-159.

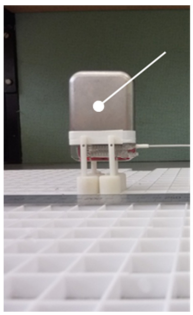

Figure 5-158 UM03 - wires shorted to IPG case

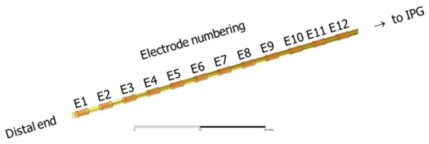

Figure 5-159 UM03 - electrode numbering

The total peak electric field at the distal end is shown in Figure 5-160 and the simulated transient responses in Figure 5-161 and Figure 5-162. Measured results are given in Figure 5-163 and Figure 5-164 and a comparison between simulated and measured results is shown in Figure 5-165.

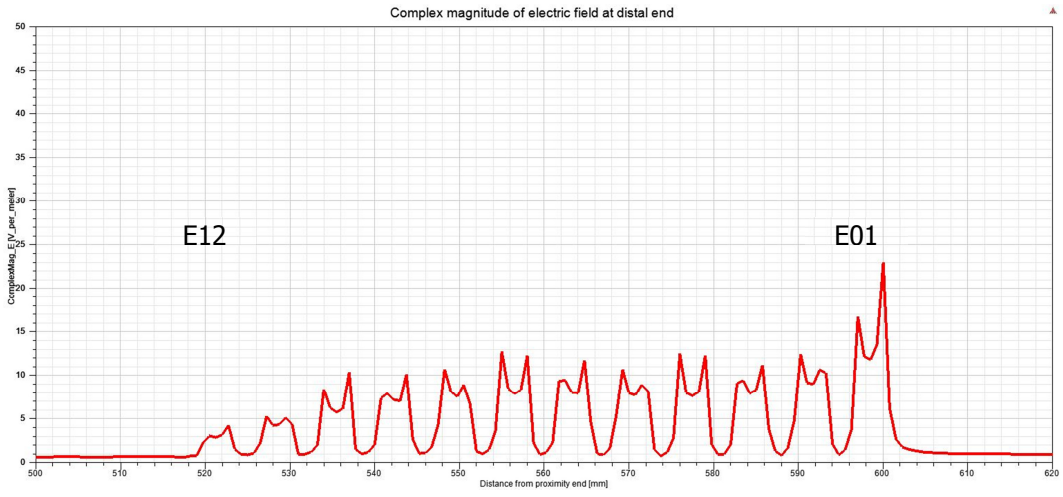

Figure 5-160 UM03 - 600 mm - short - complex magnitude of electric field at distal end

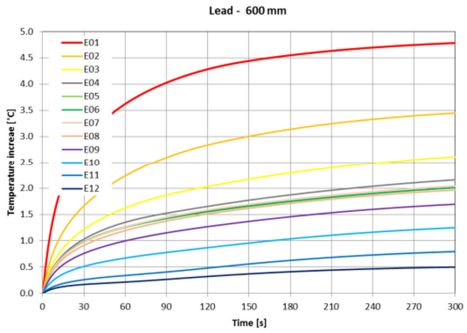

Figure 5-161 UM03 - 600 mm - short Simulation - Temp. Transient

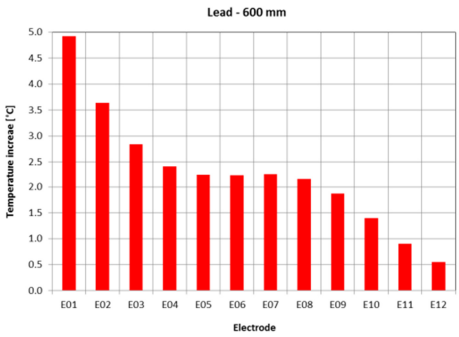

Figure 5-162 UM03 - 600 mm - short Simulation - Temp. after 300 s

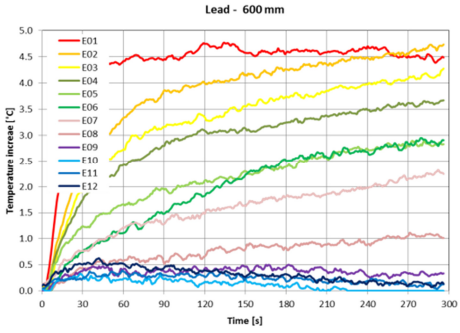

Figure 5-163 UM03 - 600 mm - short Measurement - Temp. Transient

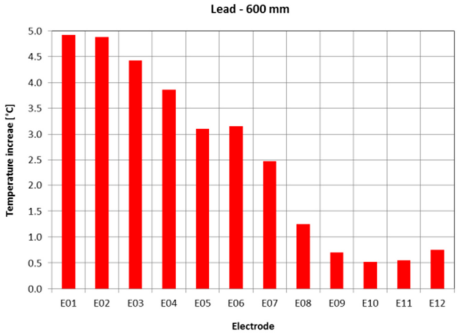

Figure 5-164 UM03 - 600 mm - short Measurement - Temp. after 300 s

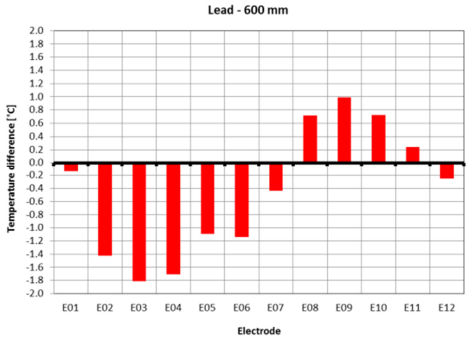

Figure 5-165 UM03 - 600 mm - short Difference - Temp. after 300 s

The average induced electric field strength at Electrode 1 has increased from $\sim 8 \frac{V}{m}$ for a Lead length of 200 mm (Figure 5-152) to $12 \frac{V}{m}$ for a Lead length of 600 mm (Figure 5-160) and the temperature increased from 2.7 K to 4.9 K at the distal end. Without convection the expected temperature increase is:

$$\frac{{E_1}^2}{{E_2}^2} \sim \frac{T_1}{T_2} \quad \rightarrow \quad T_2 = T_1 \cdot \frac{{E_2}^2}{{E_1}^2} = 2.7\ K \cdot \frac{\left(12\ \frac{V}{m}\right)^2}{\left(8\ \frac{V}{m}\right)^2} = \ 6.1\ K$$

(5–14)

With convection the exponent determining the temperature increase is:

$$\frac{{E_1}^n}{{E_2}^n} \sim \frac{T_1}{T_2} \quad \rightarrow \quad n = \frac{ln\left(\frac{T_1}{T_2}\right)}{ln\left(\frac{E_1}{E_2}\right)} = 1.5$$

(5–15)

Simulated and measured temperature profiles after 300 seconds exposure time are similar in shape and maximum measured and predicted temperature match well but a wave like difference pattern emerges in Figure 5-165. Electrodes 10, 11 and 12 show a decrease in temperature after 45 seconds exposure time and Electrodes 5, 6 and 7 show a steeper temperature increase. The temperature slope for Electrode 6 varies significantly from the slopes of all other electrodes.

The temperature decrease can be explained by the onset of moderate convection around gelled saline clots as outlined in Section 5.1.4 and the cause of higher measured temperatures around the centre electrodes can be attributed to thermal isolation from clusters of gelled saline clots.

5.1.11.4.3 UM04 - Lead 200 mm with open-ended wires in IPG

A 200 mm long Lead with 12 electrodes and Lead wires open ended at the proximity end (IPG case) is analysed. The configuration is shown in Figure 5-158 and Figure 5-159.

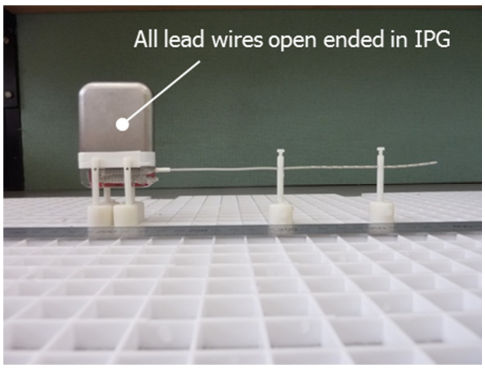

Figure 5-166 UM04 - wires open-ended in IPG case

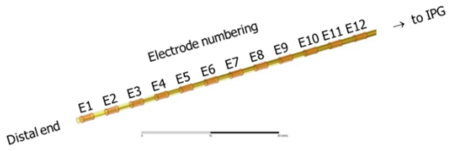

Figure 5-167 UM04 - electrode numbering

The total peak electric field at the distal end is shown in Figure 5-168 and the simulated transient responses in Figure 5-169 and Figure 5-170. Measured results are given in Figure 5-171 and Figure 5-172 and a comparison between simulated and measured results is shown in Figure 5-173.

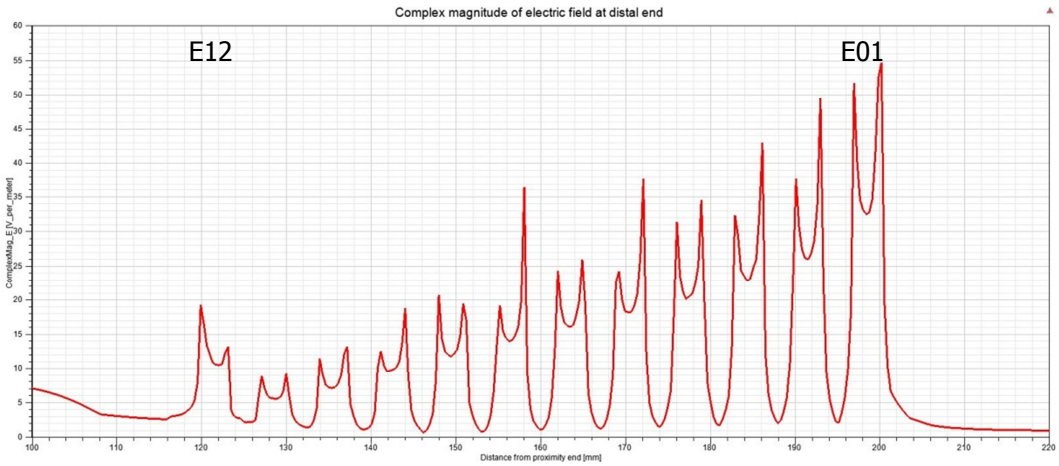

Figure 5-168 UM04 - 200 mm - open - complex magnitude of electric field at distal end

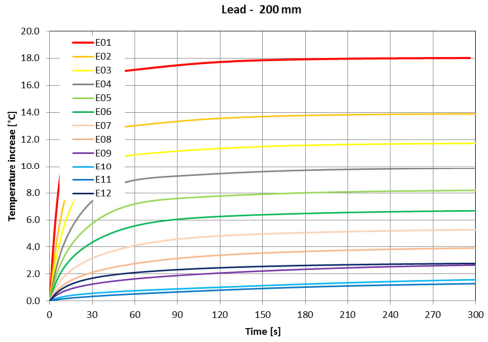

Figure 5-169 UM04 - 200 mm - open Simulation - Temp. Transient

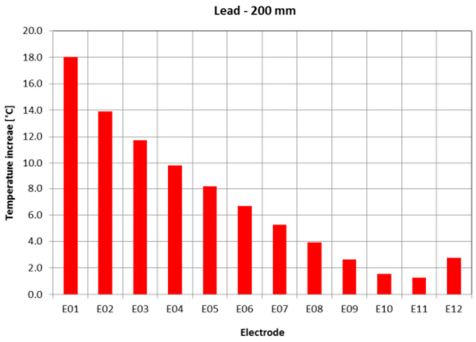

Figure 5-170 UM04 - 200 mm - open Simulation - Temp. after 300 s

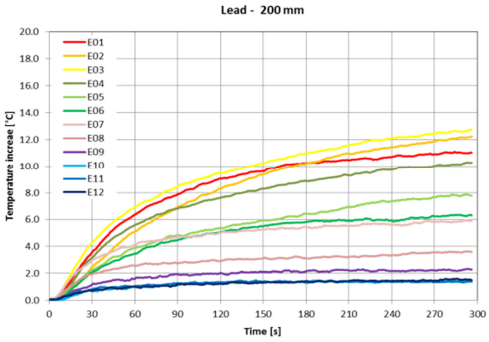

Figure 5-171 UM04 - 200 mm - open Measurement - Temp. Transient

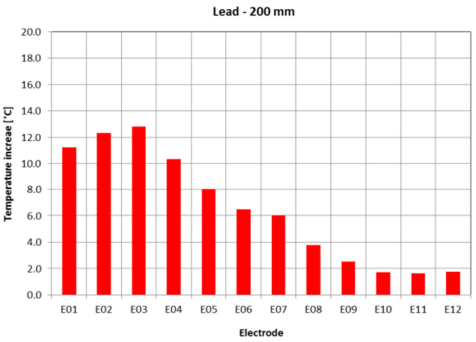

Figure 5-172 UM04 - 200 mm - open Measurement - Temp. after 300 s

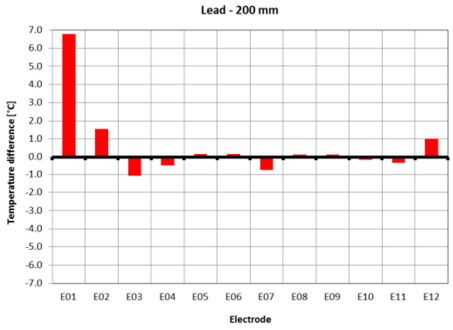

Figure 5-173 UM04 - 200 mm - open Difference - Temp. after 300 s

Simulated and measured temperature profiles after 300 seconds exposure time are similar in shape apart from Electrode E01 where significant differences are observed (Figure 5-173). Both, simulations and measurements confirm the impact of Lead wire termination at the proximity end on temperature increase at the distal end. In order to minimise the temperature increase at the distal end, low impedance at the proximity end seems to be more favourable than high impedance. The average induced electric field strength at Electrode E01 has increased from $\sim 8 \frac{V}{m}$ for a Lead length of 200 mm with shorted proximity end (Figure 5-152) to $32 \frac{V}{m}$ for a Lead length of 200 mm with open ended proximity end (Figure 5-168) and the temperature increased from 2.7 K to 11 K. Without convection $(n = 2)$ the expected temperature increase is ...

$$T_2 = T_1 \cdot \frac{{E_2}^2}{{E_1}^2} = 2.7\ K \cdot \frac{\left(32\ \frac{V}{m}\right)^2}{\left(8\ \frac{V}{m}\right)^2} = \ 43.2\ K \tag{5–16}$$

... and with convection, assuming an exponential coefficient of $n = 1.5$ determined with Equation (5–14), the temperature increase would be ...

$$T_2 = T_1 \cdot \frac{{E_2}^{1.5}}{{E_1}^{1.5}} = 2.7\ K \cdot \frac{\left(32\ \frac{V}{m}\right)^{1.5}}{\left(8\ \frac{V}{m}\right)^{1.5}} = \ 21.6\ K \tag{5–17}$$

For comparison, the calculated temperature increase for Electrode E01 is 18.0 K. It seems that thermal convection increases with increasing local field strength and hence local temperature differences. To match the measured temperature increase of about 12 K at the distal end electrodes the exponential coefficient is $n = 1.08$. Measured temperature slopes do not show anomalies. Therefore, a cautious preliminary conclusion is that gelled saline clot sizes around the MLC and electrodes might have an influence on measured temperature increases.

5.1.11.4.4 UM04 - Lead 600 mm with open-ended wires in IPG

A 600 mm long Lead with 12 electrodes and Lead wires open ended at the proximity end (IPG case) is analysed. The configuration is shown in Figure 5-174 and Figure 5-175.

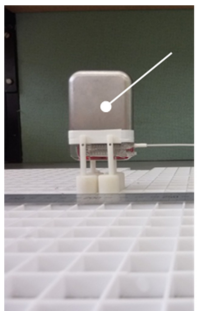

Figure 5-174 UM04 - wires open-ended in IPG case

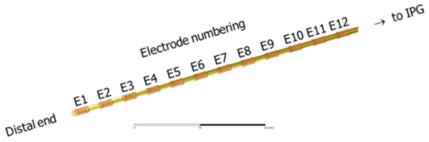

Figure 5-175 UM04 - electrode numbering

The total peak electric field at the distal end is shown in Figure 5-176 and the simulated transient responses in Figure 5-177 and Figure 5-178. Measured results are given in Figure 5-179 and Figure 5-180 and a comparison between simulated and measured results is shown in Figure 5-181.

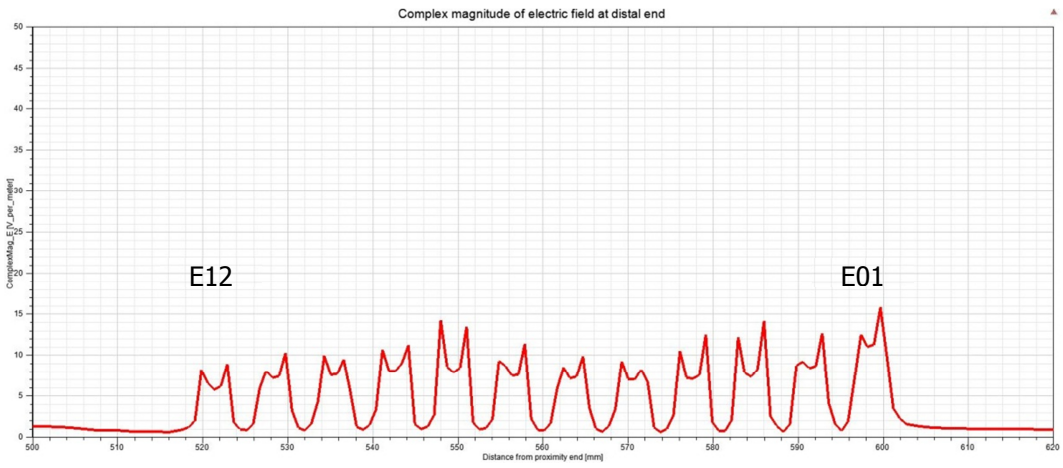

Figure 5-176 UM04 - 600 mm - open - complex magnitude of electric field at distal end

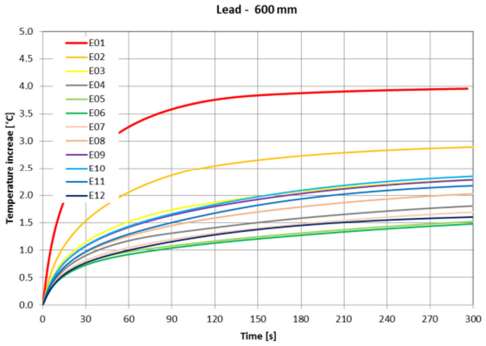

Figure 5-177 UM04 - 600 mm - open Simulation - Temp. Transient

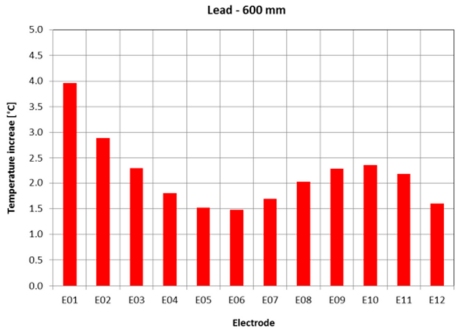

Figure 5-178 UM04 - 600 mm - open Simulation - Temp. after 300 s

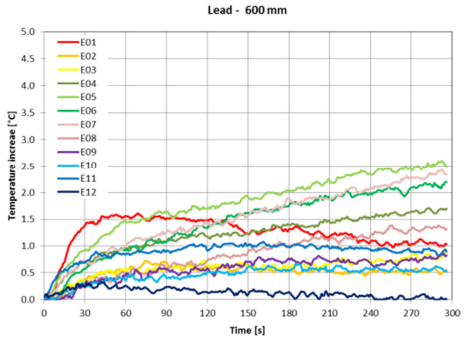

Figure 5-179 UM04 - 600 mm - open Measurement - Temp. Transient

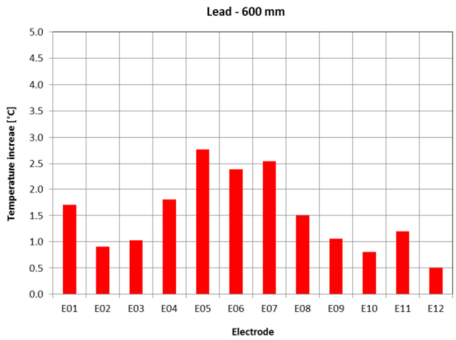

Figure 5-180 UM04 - 600 mm - open Measurement - Temp. after 300 s

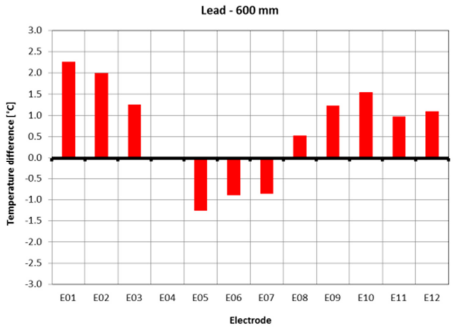

Figure 5-181 UM04 - 600 mm - open Difference - Temp. after 300 s

Simulated and measured temperature profiles after 300 seconds exposure time show significant differences (Figure 5-178 and Figure 5-180). Electrodes E01, E10 and E12 show temperature decreases after 45, 60 and 150 seconds exposure time. Electrodes E05, E06 and E07 show a linear temperature increase after 45 seconds.

Both, simulations and measurements show that open ended Lead wires at the proximity end show less temperature increase at the distal end than shorted Lead wires at the proximity end. At first sight this result is counterintuitive. An attenuation of about $2\ \frac{dB}{100\ mm}$ for the common TEM mode suggests that the TEM mode attenuation along a 600 mm long Lead is about $12\ dB$ and hence the reflection at the proximity end should have a marginal impact on the total electric field strength around electrodes at the distal end. But this is not the case. This supports the hypothesis that energy propagates along the Lead in more than one dominant electromagnetic mode. The reasoning has been summarised in Section 5.1.7.

The average induced electric field strength at Electrode E01 has increased from $\sim 8\frac{V}{m}$ for a Lead length of 200 mm with shorted proximity end (Figure 5-152) to $11\frac{V}{m}$ for a Lead length of 600 mm with open ended proximity end (Figure 5-178) but the measured temperature decreased from 2.7 K to 1.7 K. Without convection $(n = 2)$ the expected temperature increase is ...

$$T_2 = T_1 \cdot \frac{{E_2}^2}{{E_1}^2} = 2.7\ K \cdot \frac{\left(11\ \frac{V}{m}\right)^2}{\left(8\ \frac{V}{m}\right)^2} = 5.1\ K \tag{5–18}$$

... and with convection, assuming an exponential coefficient of $n = 1.5$ determined with Equation (5–14), the temperature increase would be ...

$$T_2 = T_1 \cdot \frac{{E_2}^{1.5}}{{E_1}^{1.5}} = 2.7\ K \cdot \frac{\left(11\ \frac{V}{m}\right)^{1.5}}{\left(8\ \frac{V}{m}\right)^{1.5}} = 4.4\ K$$

(5–19)

For comparison, the calculated temperature increase for Electrode E01 is 4.0 K. As reported in previous sections it seems that thermal convection increases with increasing local field strength and that gelled saline clot sizes around MLC and electrodes can significantly influence the local temperature increase.

5.1.11.4.5 Comparison of results for base cases

Measured and calculated temperature increase after 300 seconds RF exposure at distal end electrodes for the four investigated base cases is summarised in Figure 5-182 and Figure 5-183, respectively.

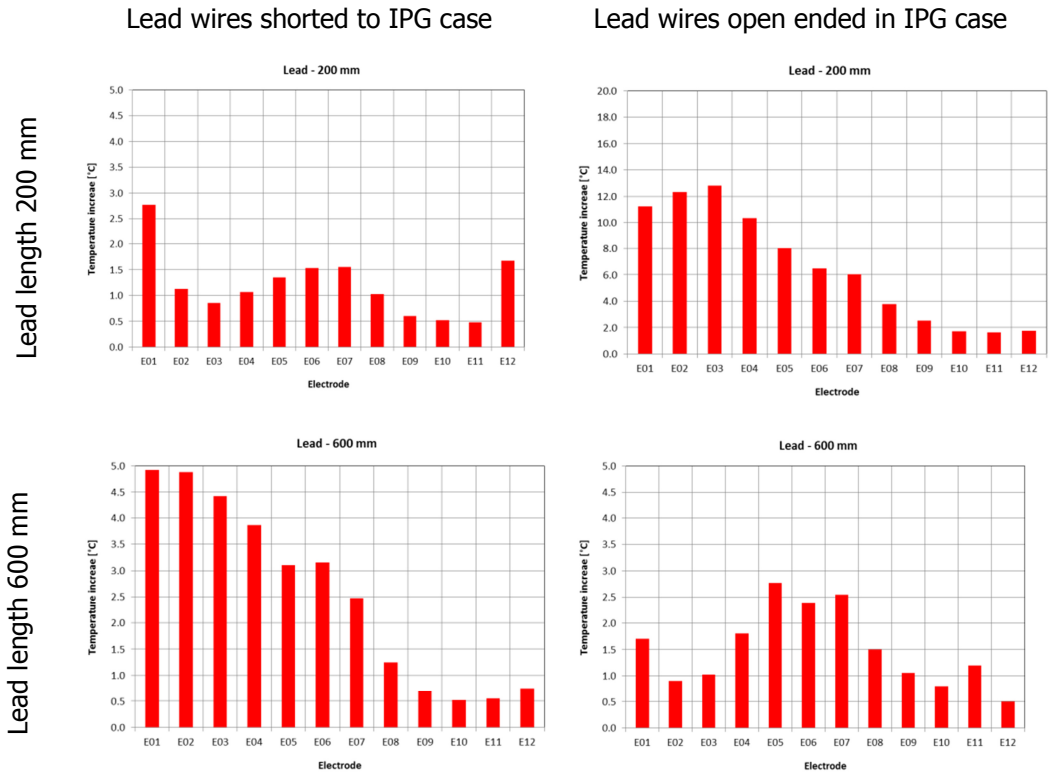

Figure 5-182 Comparison of measured temperature patterns for investigated configurations

For short Lead lengths the wire termination impedances at the proximity end have a major influence on the temperature rise at the distal end. For longer Lead lengths the influence of Lead termination impedances is less distinctive and a reversal in the impact of the two extreme cases, open-end and short, on temperature rise has been observed. The constructive and destructive superposition of a strongly attenuated common mode TEM wave and weakly attenuated differential wave modes between wires, in addition to energy cross-coupling between these two modes, are made responsible for the observed temperature increase patterns. Both measured and simulated temperature increases show similar evolutions with respect to Lead length variations and terminal impedances at the proximity end. However, some electrodes show abnormal temperature rise behaviour. The reasons for the differences are assumed to lie in the gelled saline structure described in Section 5.1.4 and in the wire routing anomalies outlined in Section 5.1.9.6.

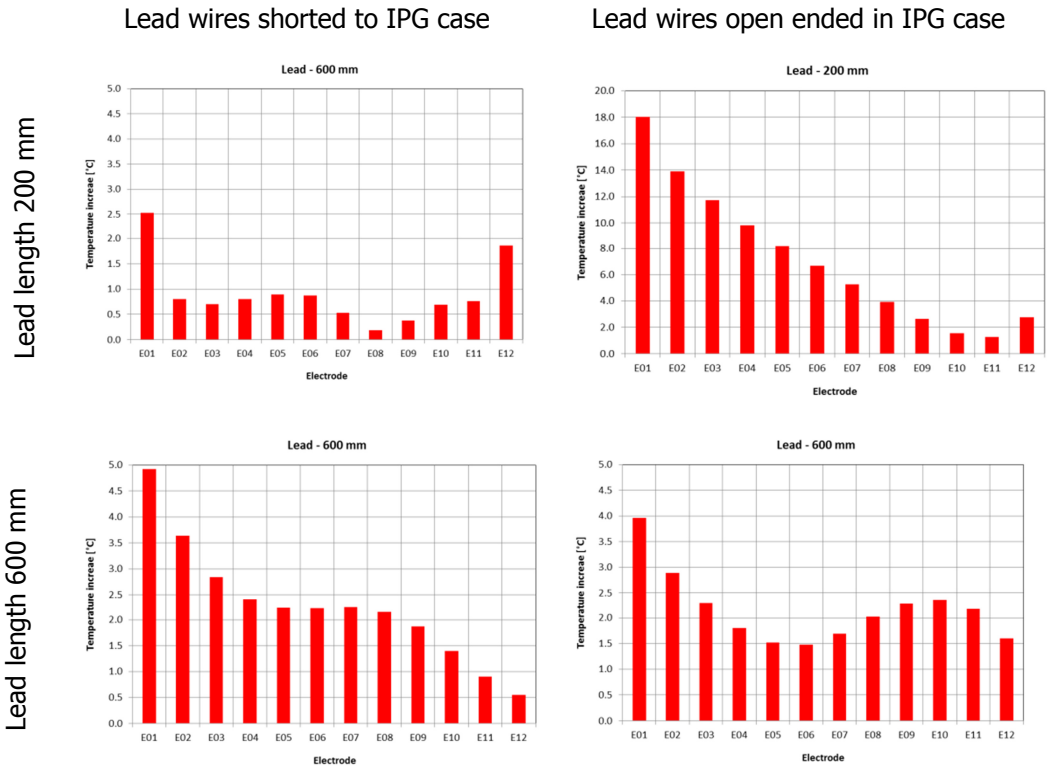

Figure 5-183 Comparison of simulation data

5.1.11.5 Therapeutic and interleaved auxiliary electrodes

The motivation for this simulation and test sequence is to determine the impact of twelve capacitive coupled auxiliary electrodes (A01-A12) interleaved with twelve therapeutic electrodes (E01-E12) on temperature rise at the distal end. The Lead wires at the proximity end are shorted to the IPG case (Figure 5-184). The auxiliary electrodes are 2 mm long and centred between therapeutic electrodes (Figure 5-185). Figure 5-186 shows the distal end of the assembled Lead. Results are presented for Lead lengths of 200 mm and 600 mm. The temperature has been recorded on therapeutic electrodes.

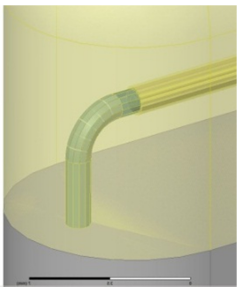

Figure 5-184 DV08B - wires shorted to IPG case

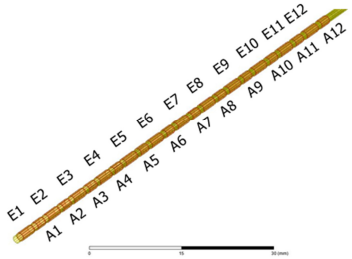

Figure 5-185 DV08B - outline - distal end

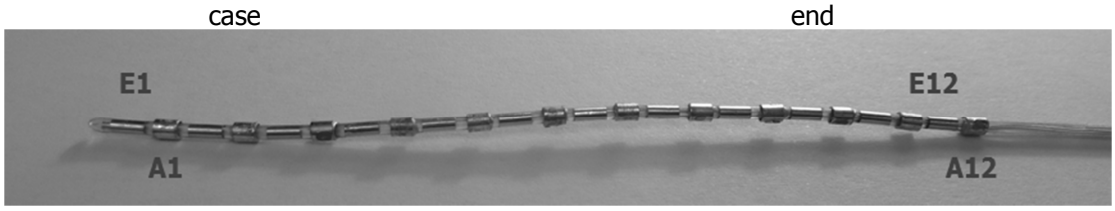

Figure 5-186 DV08B - Lead at distal end

5.1.11.5.1 DV08B - Lead 200 mm with wires shorted to IPG case

The total peak electric field at the distal end is shown in Figure 5-187 and the simulated transient responses in Figure 5-188 and Figure 5-189. Measured results are given in Figure 5-190 and Figure 5-191 and a comparison between simulated and measured results is shown in Figure 5-192.

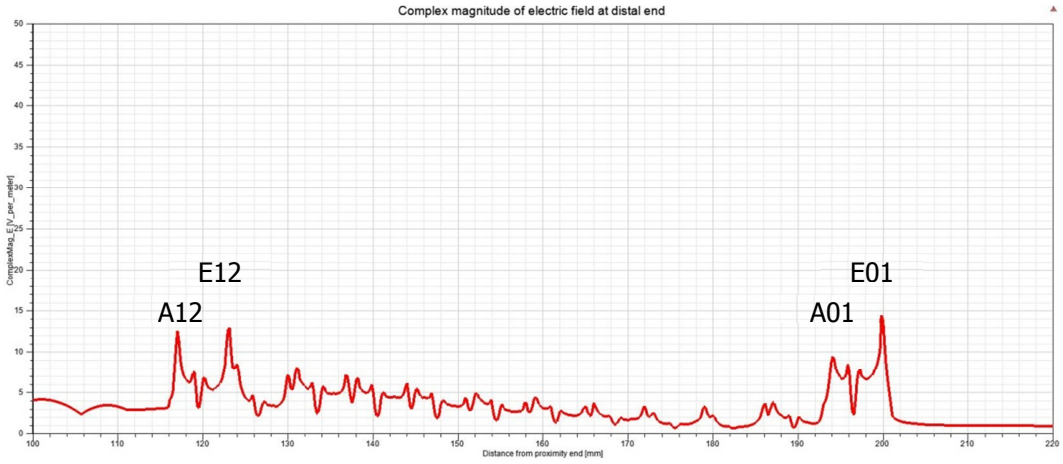

Figure 5-187 DV08B - 200 mm - short - complex magnitude of el. field at distal end

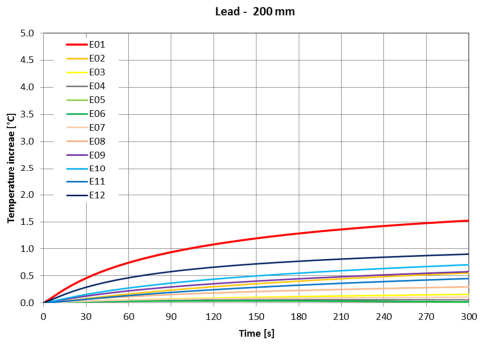

Figure 5-188 DV08B - 200 mm - short Simulation - Temp. Transient

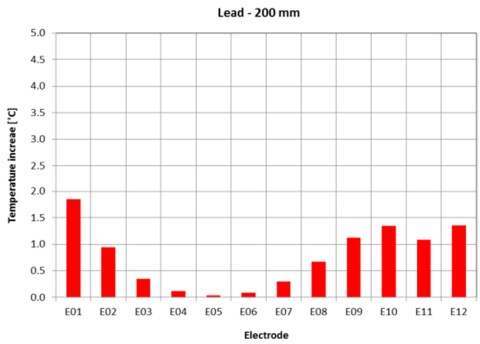

Figure 5-189 DV08B - 200 mm - short Simulation - Temp. after 300 s

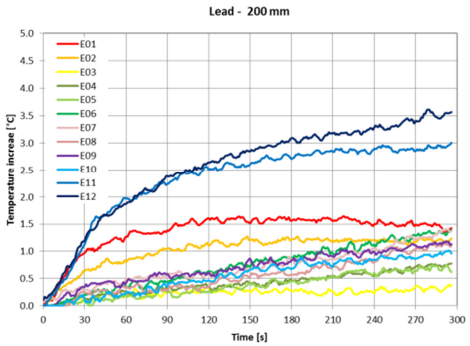

Figure 5-190 DV08B - 200 mm - short Measurement - Temp. Transient

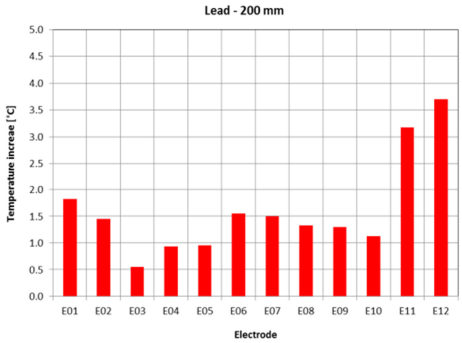

Figure 5-191 DV08B - 200 mm - short Measurement - Temp. after 300 s

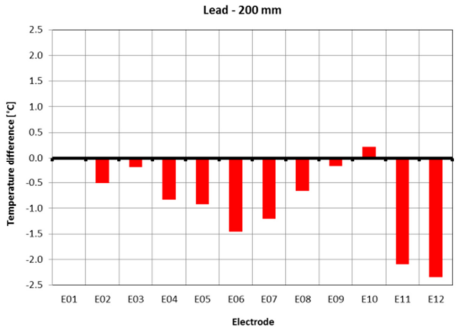

Figure 5-192 DV08B - 200 mm - short Difference - Temp. after 300 s

Simulated and measured temperature profiles after 300 seconds exposure time show similar patterns apart from electrodes E11 and E12. (Figure 5-189 and Figure 5-191). Electrode E01 shows a slight temperature decrease at the end of the 300 seconds exposure period and the centre electrodes show a linear increase in temperature. Reasons for these deviations have been discussed in previous sections. Figure 5-193 compares the case with and without auxiliary electrodes. The temperature increase at Electrode E01 has been decreased from 2.7 K to 1.7 K. The temperature profile for the centre electrodes has not been altered significantly. The discrepancy for Electrodes E11 and E12 could not be resolved. The Lead has been altered in the meantime for subsequent test sequences.

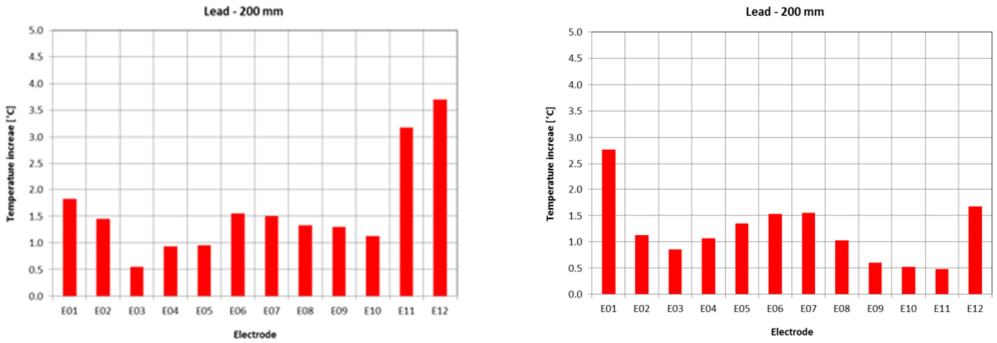

Figure 5-193 Comparison between measured temperature increases after after 300 s
A) UM03 for 200 mm (without auxiliary electrodes)
B) DV08B for 200 mm (with auxiliary electrodes)

5.1.11.5.2 DV08B - Lead 600 mm with wires shorted to IPG case

The total peak electric field at the distal end is shown in Figure 5-194 and the simulated transient responses in Figure 5-195 and Figure 5-196. Measured results are given in Figure 5-197 and Figure 5-198 and a comparison between simulated and measured results is shown in Figure 5-199.

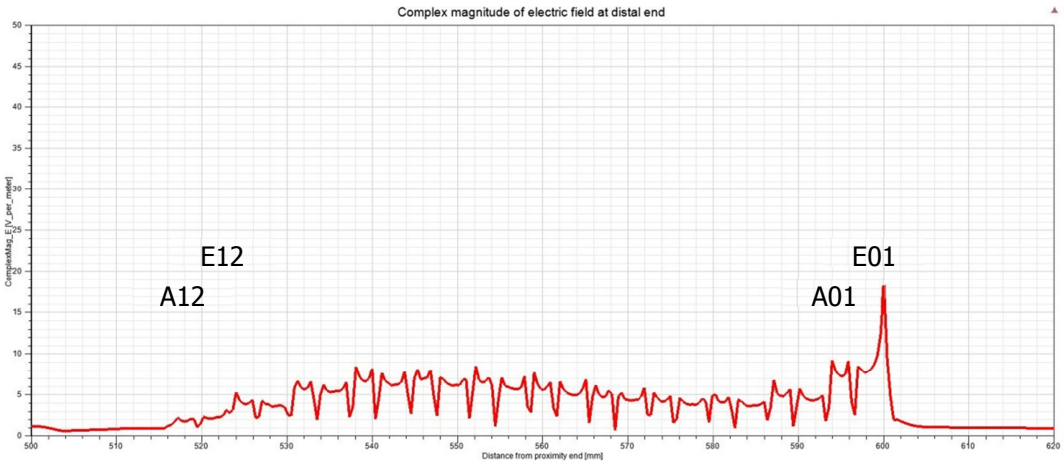

Figure 5-194 DV08B - 600 mm - short - complex magnitude of el. field at distal end

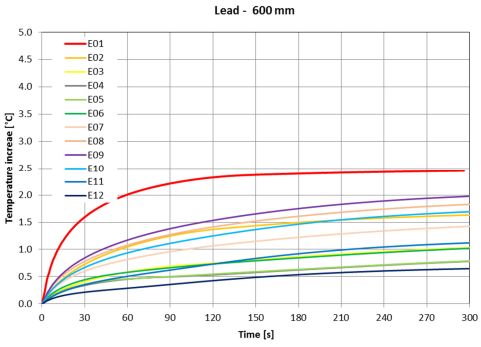

Figure 5-195 DV08B - 600 mm - short Simulation - Temp. Transient

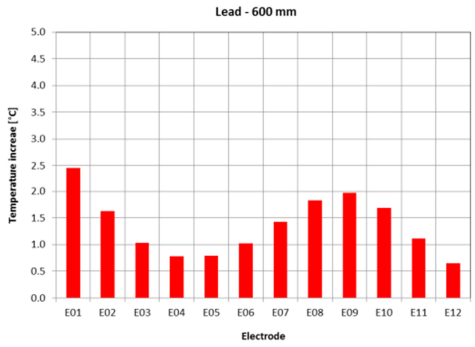

Figure 5-196 DV08B - 600 mm - short Simulation - Temp. after 300 s

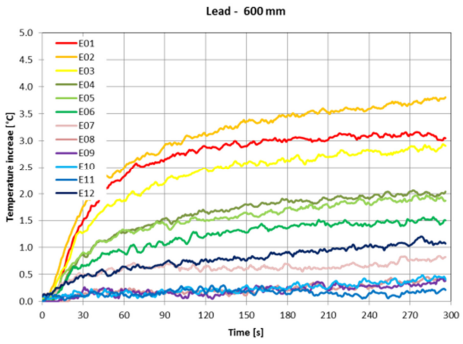

Figure 5-197 DV08B - 600 mm - short Measurement - Temp. Transient

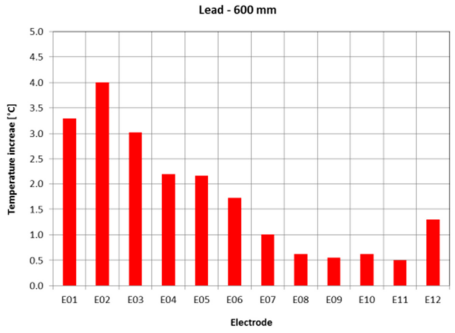

Figure 5-198 DV08B - 600 mm - short Measurement - Temp. after 300 s

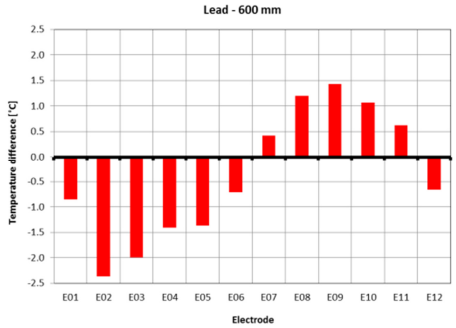

Figure 5-199 DV08B - 600 mm - short Difference - Temp. after 300 s

Simulated and measured temperature profiles after 300 seconds exposure time show dissimilar patterns and the maximum measured temperature increase is 4 K whereas the maximum calculated temperature increase is 2.5 K. A similar difference pattern has been observed for a Lead without auxiliary electrodes. A side-by-side comparison of the difference patterns is shown in Figure 5-200. It appears that, in addition to the lateral and longitudinal volume currents, taken into account by off-diagonal elements of the conductivity tensor matrix for gelled saline, other causes shift the minima and maxima at the distal end. Investigations using cross-coupling elements in permittivity and permeability tensor matrices to address reorientations in electric and magnetic dipole moments have not led to concluding results. Further, changes in material parameter of the gelled

saline volume surrounding the distal end, including double layer and boundary layer around electrodes and MLC, did not significantly alter the simulated electric field distribution along the distal end. A physical explanation for this observation is pending. Molecular dynamic measurement techniques described briefly in Section 2.9 can provide further insights.

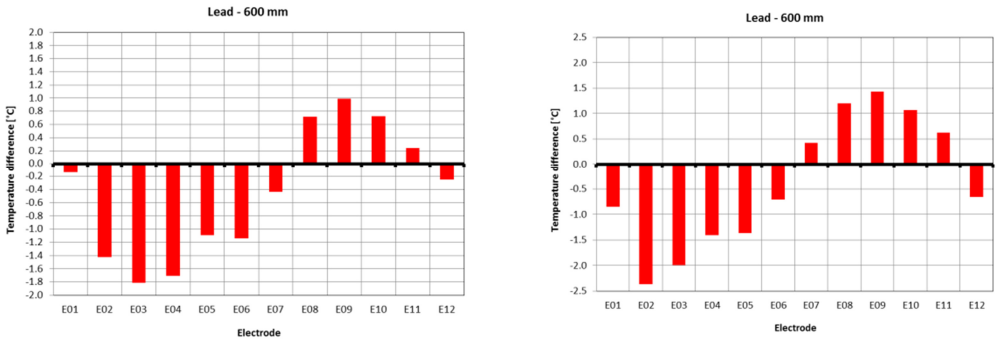

A) B)

Figure 5-200 Comparison between difference patterns after 300 s
A) UM03 for 600 mm (without auxiliary electrodes)
B) DV08B for 600 mm (with auxiliary electrodes)

The measured temperature increases for a 600 mm long Lead reveal that the maximum temperature increase at the distal end can be decreased by about 1 K using capacitive coupled auxiliary electrodes interleaved with therapeutic electrodes (Figure 5-201). A similar temperature decrease was observed at the distal end of a 200 mm long Lead.

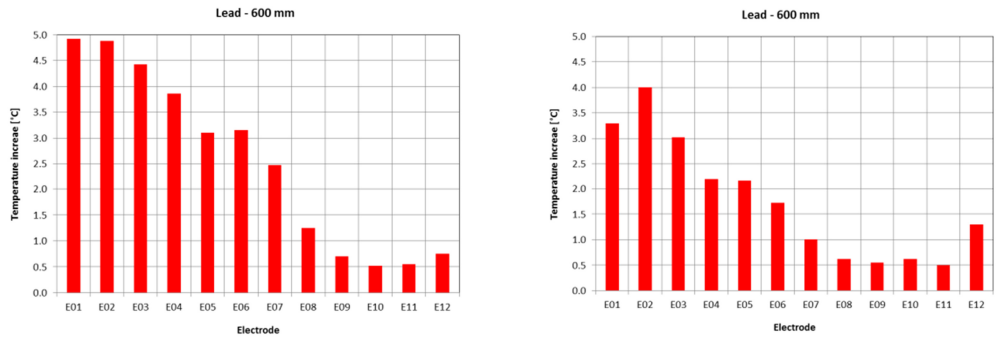

A) B)

Figure 5-201 Comparison between measured temperature increases after 300 s
A) UM03 for 600 mm (without auxiliary electrodes)
B) DV08B for 600 mm (with auxiliary electrodes)

The additional surface area of the auxiliary electrodes decreases the power density per electrode surface and hence the deposited power per volume element. But due to thermal conduction and convection between volume elements linking therapeutic and auxiliary electrodes, the temperature decrease is not proportional to the (added) surface area.

5.1.11.5.3 Comparison of results for DV08B

The electric field distribution around an electrode predominantly determines its temperature increase. Therefore, discrepancies in measured and calculated temperature increase patterns (profiles) arise from EM model limitations whereas discrepancies in absolute values have their origin in EM and thermodynamic model limitations. The origin of many of the discrepancies outlined in previous sections are supposed to be rooted in Lead wire routing anomalies, field strength dependent changes in convection, anisotropic behaviour of gelled saline at micro scales and reflection behaviour at the distal end for Lead lengths above 400 mm. Another source of uncertainty is the equivalent dipole array used in simulations due to limitations in computing resources. The calculated near field magnetic and electric field distributions along the centre line for the actual and the equivalent dipole array are very similar and therefore this source of discrepancy is considered marginal. Despite all the differences, simulations and measurements confirm that an increase of electrode surface area at the distal end leads to temperature reductions. To close this chapter, measured and calculated temperature increases for design variation DV08B are shown in Figure 5-202. The measurements show that the distal end electrode is not necessarily the one that causes the highest temperature increase in multi-electrode Leads embedded in gelled saline. The same observation has been made for base cases. The simulations show a tendency that centre and proximity electrodes are exposed to high electric field strengths, too.

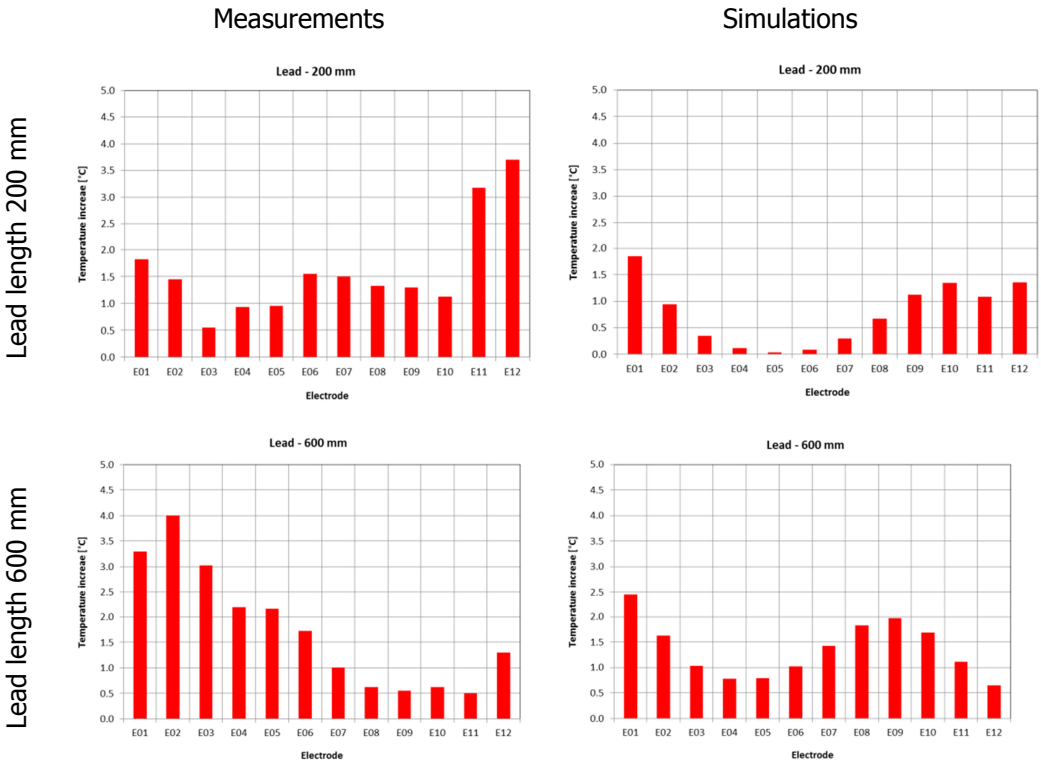

Figure 5-202 DV08B - comparison between measurement and simulation data

5.1.11.6 Therapeutic and auxiliary electrodes at PE

Developing the idea of auxiliary electrodes and increased surface area to minimise local temperature increases around electrodes, one might be inclined to explore the possibility of adding auxiliary electrodes at the proximity end and/or between distal and proximity end. These ideas are analysed in the following sections. Capacitive coupled auxiliary electrodes were added at the proximity end and have been replaced by resistors later on. In addition, the impact of auxiliary electrodes located along the MLC before therapeutic electrodes has been explored. The 600 mm Lead prepared for design variation DV08B has been adapted for the following analysis. Here, four configurations are presented ...

- Lead with capacitive coupled 5 mm long auxiliary electrodes at the proximity end
- Lead with capacitive coupled 2.5 mm long auxiliary electrodes at the proximity end
- Lead with capacitive coupled 100 Ohm resistor ring at the proximity end
- Lead with capacitive coupled 100 Ohm resistor ring at the proximity end and additional 12 auxiliary electrodes placed before the therapeutic electrodes

In subsequent sections following simulation settings have been applied:

- EM model #2 (Table 4-2). The boundary layer has an isotropic permittivity of 3.5 and the double layer around the electrodes has the same characteristics as gelled saline.
- Electromagnetic simulation setups are shown in Figure 4-11 and Figure 4-17.

- The peak electric field strength along the centre line of the dipole array is $300\ \frac{V}{m}$.

5.1.11.6.1 DV08C1 - Lead 600 mm

A 600 mm long Lead with twelve therapeutic and twelve interleaved auxiliary electrodes at the distal end and twelve 5 mm long auxiliary electrodes at the proximity end is analysed. The configuration is shown in Figure 5-203 and Figure 5-204.

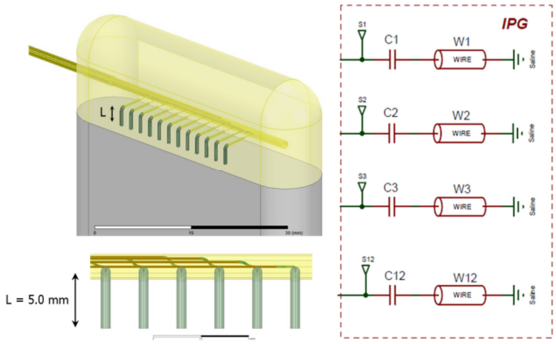

Figure 5-203 DV08C1 - auxiliary electrodes capacitive coupled to saline at proximity end

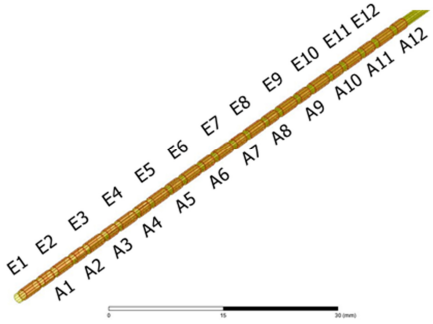

Figure 5-204 DV08C1 - outline - distal end

As in previous sections the same data presentation methodology is applied. The total peak electric field at the distal end is shown in Figure 5-205 and the simulated transient responses in Figure 5-206 and Figure 5-207. Measured results are given in Figure 5-208 and Figure 5-209 and a comparison between simulated and measured results is shown in Figure 5-210.

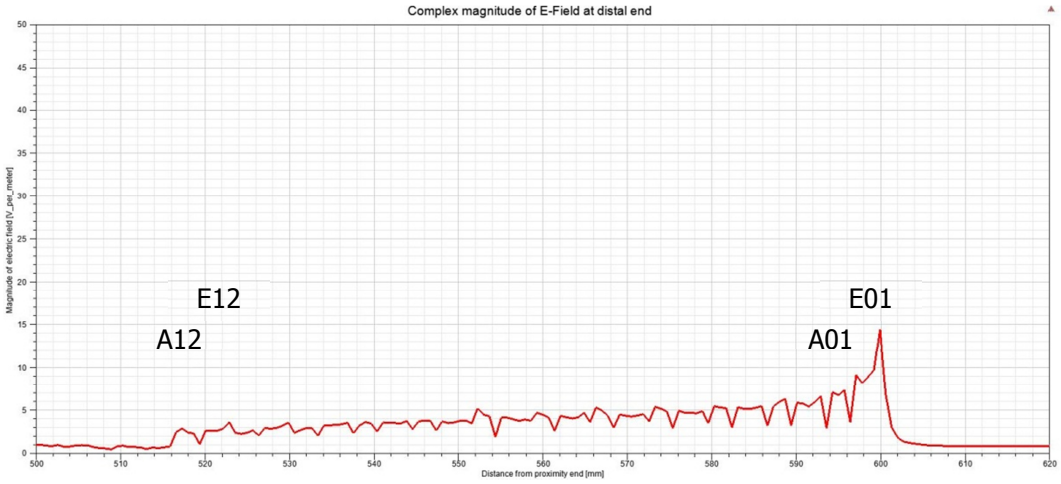

Figure 5-205 DV08C1 - 600 mm - complex magnitude of el. field at distal end

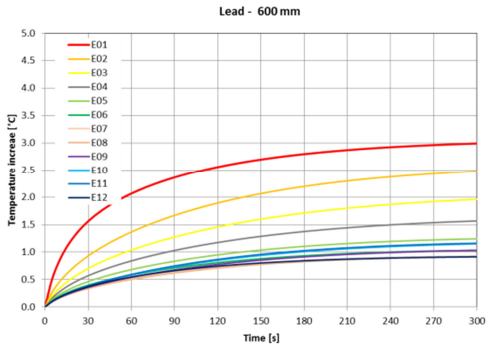

Figure 5-206 DV08C1 - 600 mm Simulation - Temp. Transient

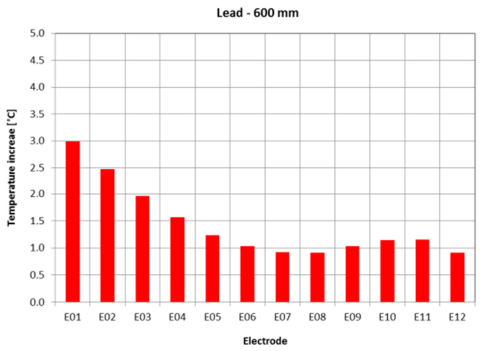

Figure 5-207 DV08C1 - 600 mm Simulation - Temp. after 300 s

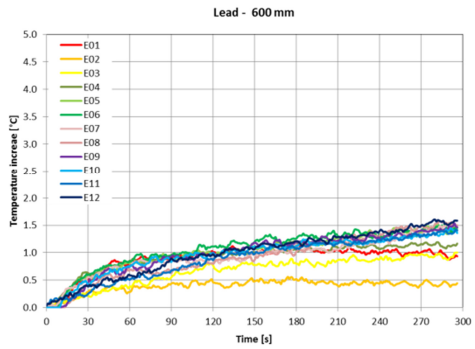

Figure 5-208 DV08C1 - 600 mm Measurement - Temp. Transient

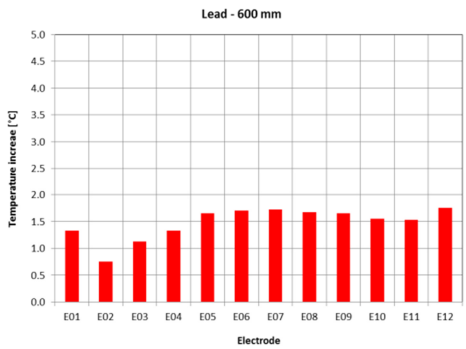

Figure 5-209 DV08C1 - 600 mm Measurement - Temp. after 300 s

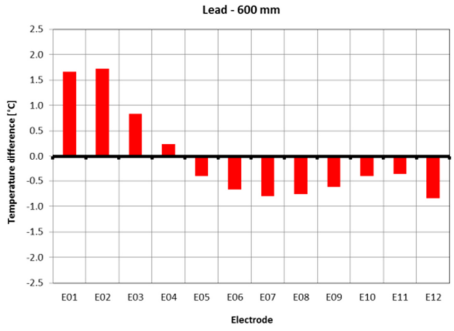

Figure 5-210 DV08C1 - 600 mm
Difference - Temp.
after 300 s

The differences between simulation and measurement results have been extensively discussed in previous sections. Here, the focus is on the impact of proximity end electrodes on distal end temperature increase. A comparison between DV08B and DV08C1 is shown in Figure 5-211. The maximum temperature increase is about 2.3 K less for the case with proximity end electrodes and the temperature rise profile is flat. The proximity electrodes present impedance matching for the common mode wave and simultaneously impedance matching for all differential modes. The common mode matching impedance is formed by the row of electrodes immersed in gelled saline equivalent to a resistive waveguide sink.

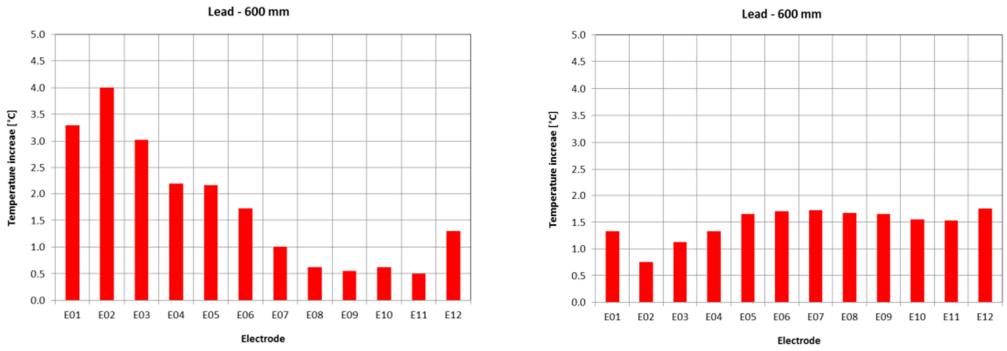

Figure 5-211 Comparison between measured temperature increases after 300 s
A) DV08B for 600 mm (without auxiliary electrodes at proximity end)
B) DV08C1 for 600 mm (with auxiliary electrodes at proximity end)

The differential mode matching impedance is formed by the gelled saline slabs sandwiched between adjacent electrodes. The temperature decrease at the distal end is another indication that differential modes carry energy.

Comparing design variations DV08B and DV08C1 a difference between calculated and measured temperature profiles at the distal end is observed. Although both difference profiles have a wave like shape calculated values are lower than measured values at the distal end for DV08B. For DV08C1 calculated values are higher than measured values at the distal end. It seems that under harmonic RF exposure gelled saline properties along the distal end change depending on magnitude and phase of differential voltages between electrodes.

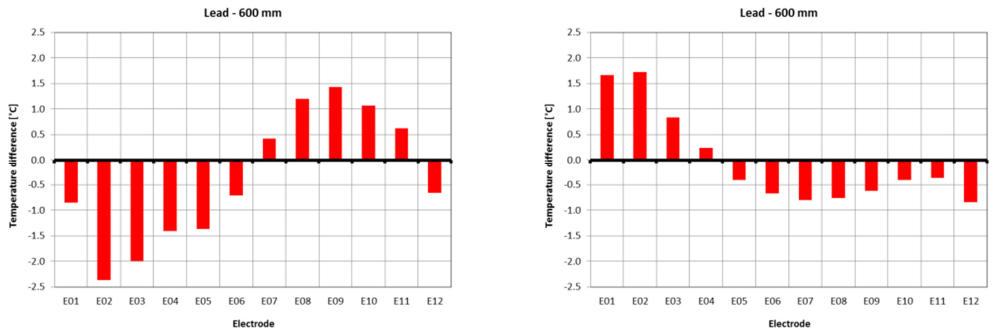

A) B)

Figure 5-212 Comparison between difference patterns after 300 s
A) DV08B for 600 mm (without auxiliary electrodes at proximity end)
B) DV08C1 for 600 mm (with auxiliary electrodes at proximity end)

Expanding the reasoning presented in Section 5.1.6.6, where discrepancies between simulated and measured transfer functions at the distal end of the MLC have been reported, voltage dependent relaxation processes in gelled saline might be responsible for the differences between simulated and measured temperature rises.

5.1.11.6.2 DV08C2 - Lead 600 mm

The impact of common and differential mode termination impedances at the proximity end on temperature rise and temperature rise profile at the distal end is further explored in this section by changing the length of the auxiliary electrodes from 5.0 mm to 2.5 mm at the proximity end. The Lead length is 600 mm. The configuration is shown in Figure 5-213 and Figure 5-214.

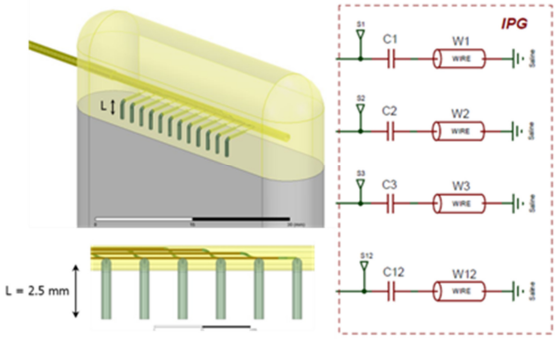

Figure 5-213 DV08C2 - auxiliary electrodes capacitive coupled to saline at proximity end

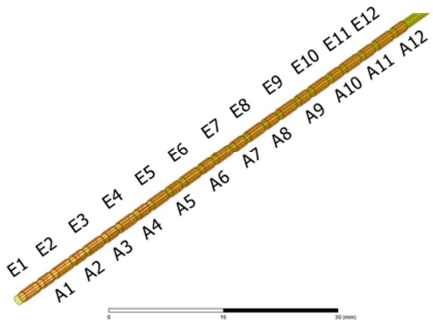

Figure 5-214 DV08C2 - outline - distal end

The total peak electric field at the distal end is shown in Figure 5-215 and the simulated transient responses in Figure 5-216 and Figure 5-217. Measured results are given in Figure 5-218 and Figure 5-219 and a comparison between simulated and measured results is shown in Figure 5-220.

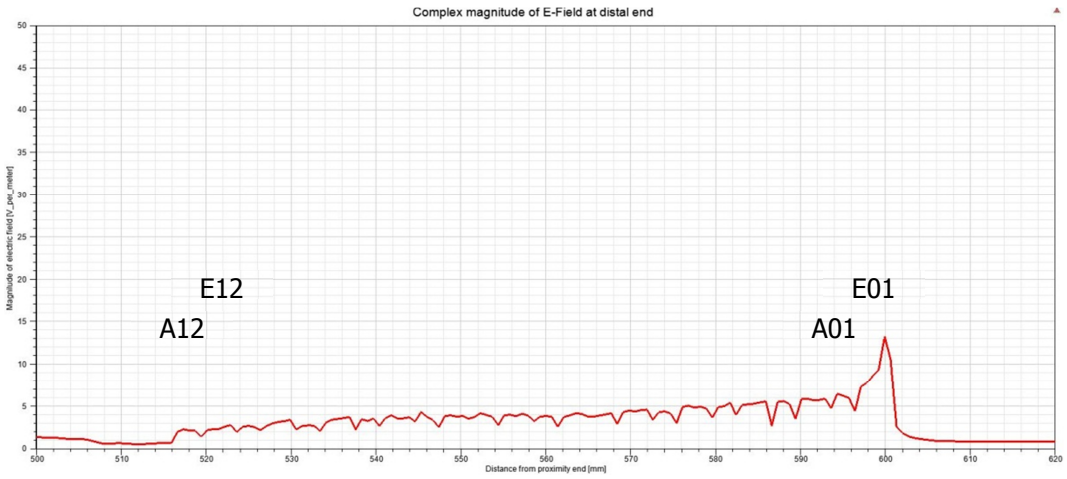

Figure 5-215 DV08C2 - 600 mm - complex magnitude of el. field at distal end

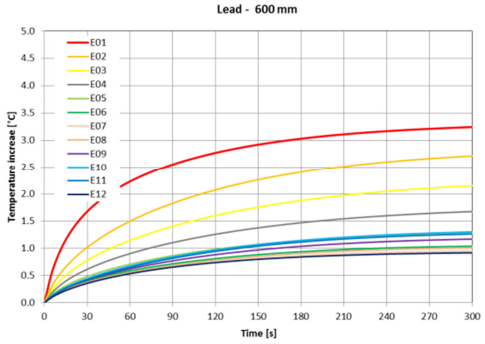

Figure 5-216 DV08C2 - 600 mm Simulation - Temp. Transient

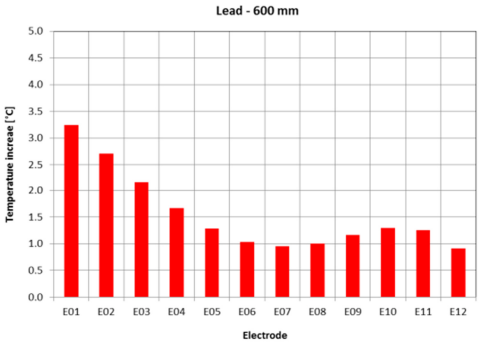

Figure 5-217 DV08C2 - 600 mm Simulation - Temp. after 300 s

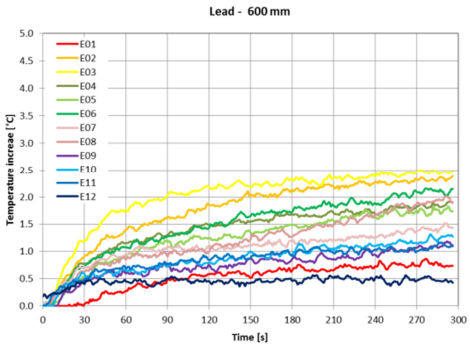

Figure 5-218 DV08C2 - 600 mm Measurement - Temp. Transient

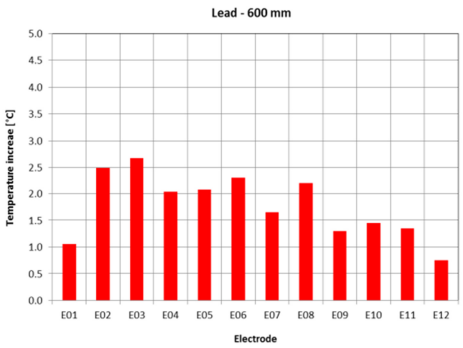

Figure 5-219 DV08C2 - 600 mm Measurement - Temp. after 300 s

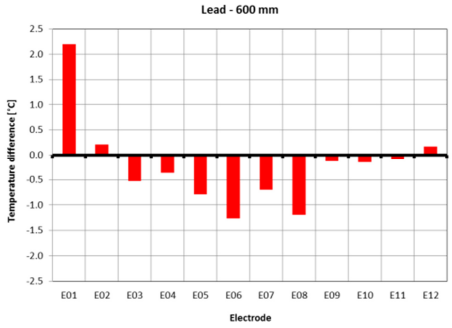

Figure 5-220 DV08C2 - 600 mm
Difference - Temp.
after 300 s

The comparison between design variations DV08C1 and DV08C2 shows that increasing common and differential mode resistances at the proximity end lead to a change in the temperature increase pattern and to higher worst case temperature increases at the distal end (Figure 5-221). Therefore, the common and differential mode terminal impedances at the proximity end are crucial for the resulting temperature increase at the distal end.

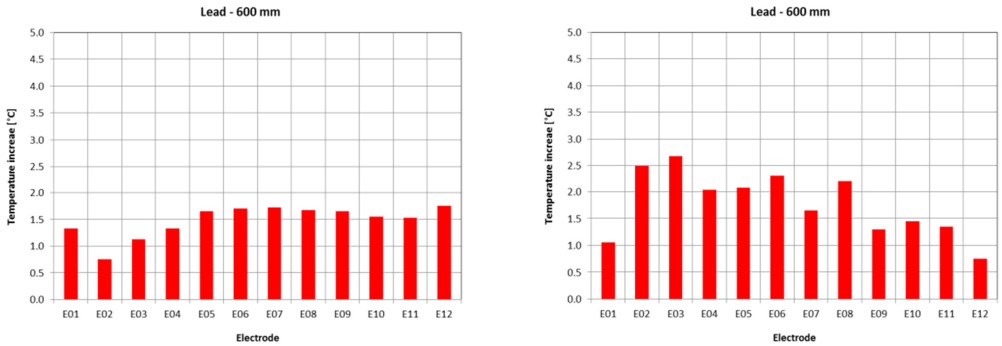

A) B)

Figure 5-221 Comparison between measured temperature increases after 300 s
A) DV08C1 for 600 mm (with 5.0 mm aux. electrodes at proximity end)
B) DV08C2 for 600 mm (with 2.5 mm aux. electrodes at proximity end)

The difference patterns between measured and calculated temperatures for design variations DV08C1 and DV08C2 have similar shapes (Figure 5-222).

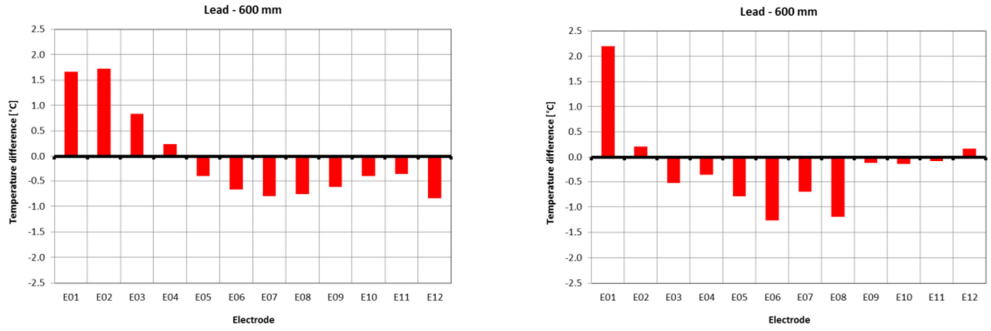

A) B)

Figure 5-222 Comparison between difference patterns after 300 s
A) DV08C1 for 600 mm (with 5.0 mm aux. electrodes at proximity end)
B) DV08C2 for 600 mm (with 2.5 mm aux. electrodes at proximity end)

5.1.11.6.3 DV08C3 - Lead 600 mm

The previous two sections explored the impact of the combined effect of common and differential mode termination impedances at the proximity end on distal end temperature profiles. In this section, Lead wires at the proximity end are open-ended inside the IPG header, i.e. not capacitive coupled to surrounding gelled saline, and therefore present high common mode impedance. The differential mode impedance at the proximity end is realised using a ring of floating capacitive coupled 100 Ohm resistors connecting adjacent Lead wires (Figure 5-223). The distal end has not been modified (Figure 5-224).

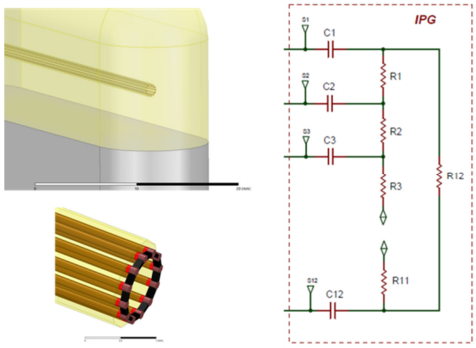

Figure 5-223 DV08C3 - Lead wires capacitive coupled to ring of resistors at proximity end

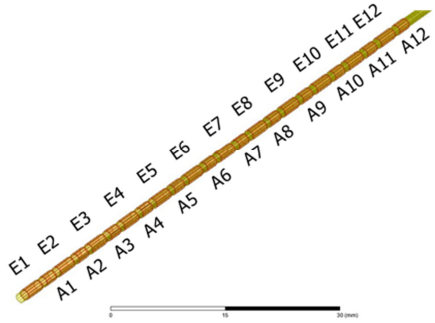

Figure 5-224 DV08C3 - outline - distal end

The total peak electric field at the distal end is shown in Figure 5-225 and the simulated transient responses in Figure 5-226 and Figure 5-227. Measured results are given in Figure 5-228 and Figure 5-229 and a comparison between simulated and measured results is shown in Figure 5-230.

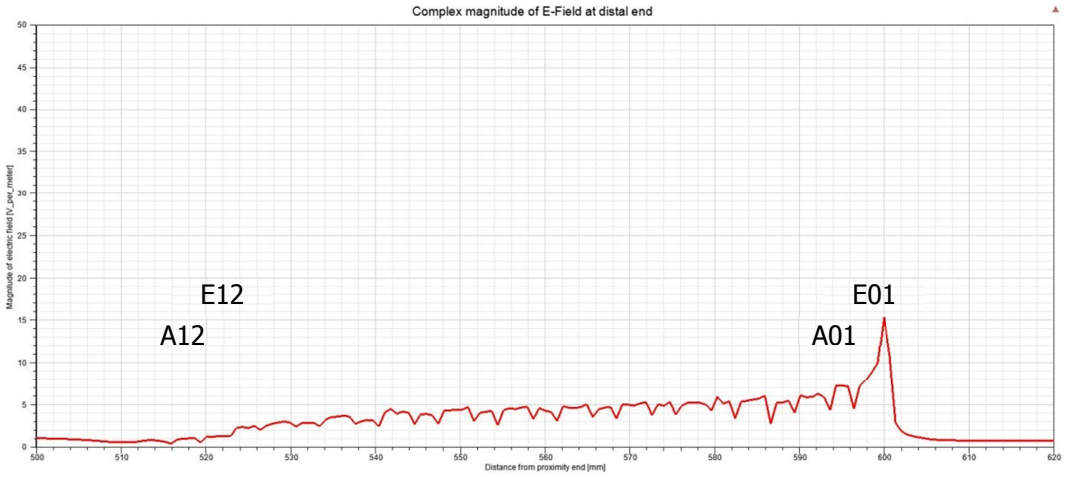

Figure 5-225 DV08C3 - 600 mm - complex magnitude of el. field at distal end

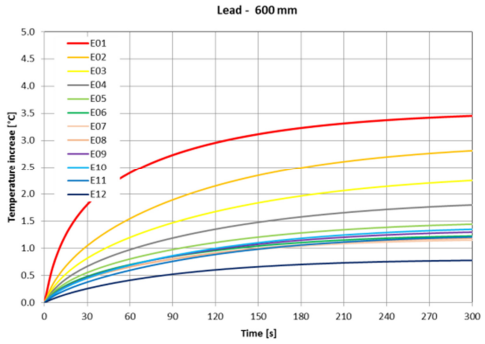

Figure 5-226 DV08C3 - 600 mm Simulation - Temp. Transient

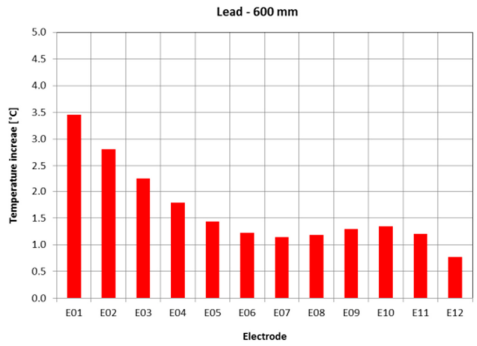

Figure 5-227 DV08C3 - 600 mm Simulation - Temp. after 300 s

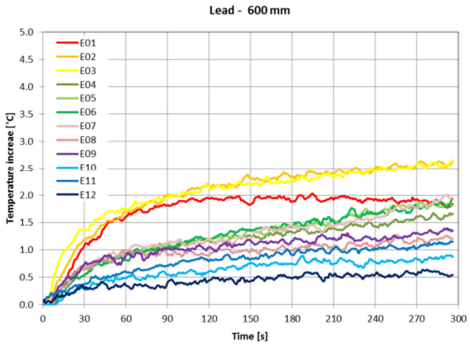

Figure 5-228 DV0C3 - 600 mm Measurement - Temp. Transient

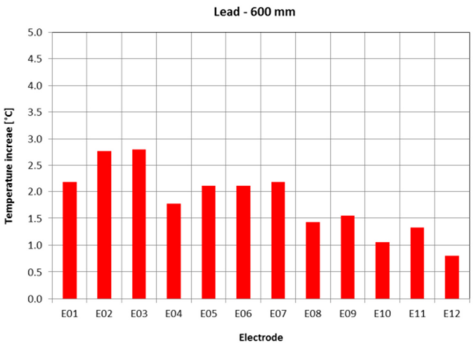

Figure 5-229 DV0C3 - 600 mm Measurement - Temp. after 300 s

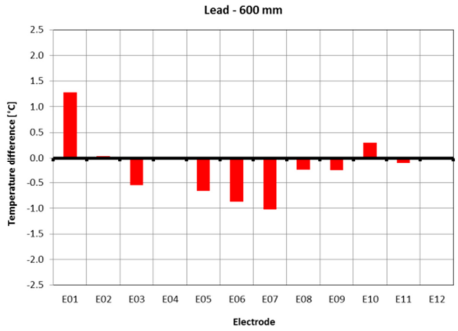

Figure 5-230 DV08C3 - 600 mm Difference - Temp. after 300 s

The comparison between design variations DV08C2 and DV08C3 shows that temperature increase patterns are very similar apart from a slightly higher temperature increase at Electrode E01 (Figure 5-231) for DV08C3. This confirms that capacitive coupled resistors integrated into the IPG header can replace capacitive coupled auxiliary electrodes at the proximity end. The impact of the termination resistance on voltage maxima along the Lead has been discussed in Section 5.1.9.9.

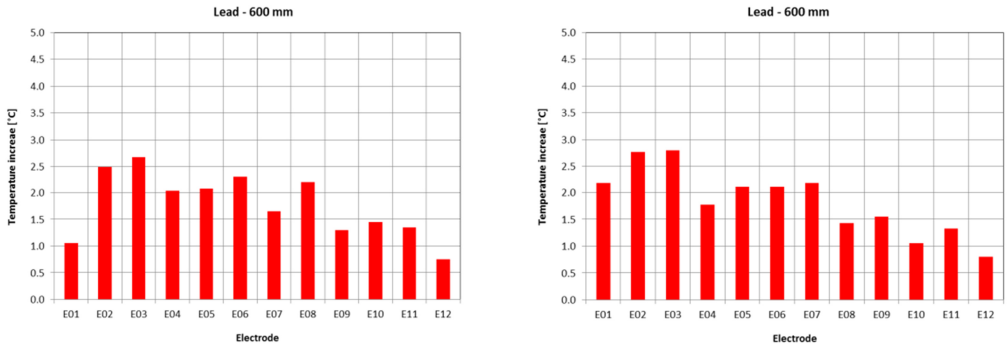

A) B)

Figure 5-231 Comparison between measured temperature increases after 300 s
A) DV08C2 for 600 mm (with 2.5 mm aux. electrodes at proximity end)
B) DV08C3 for 600 mm (with 100 Ohm resistor ring at proximity end)

5.1.11.6.4 DV08D1 - Lead 600 mm

Adding more capacitive coupled auxiliary electrodes between the proximity and distal end should result in further temperature decreases at the distal. But this is not the case. The settings for this test sequence are outlined in Figure 5-232 and Figure 5-233. Figure 5-234 shows the distal end of the assembled Lead. Twelve additional auxiliary electrodes labelled E13 to E24 have been added. The auxiliary electrodes are 2 mm long and the spacing between two adjacent auxiliary electrodes is 5 mm. The spacing between Electrode A12 and A13 is 9 mm.

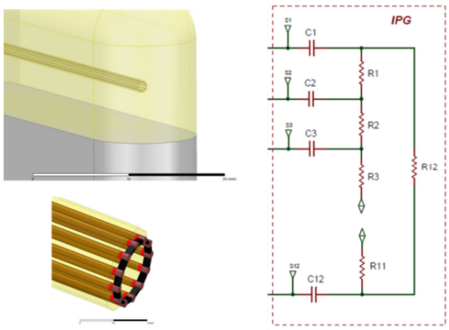

Figure 5-232 DV08D1 - Lead wires capacitive coupled to ring of resistors at IPG case

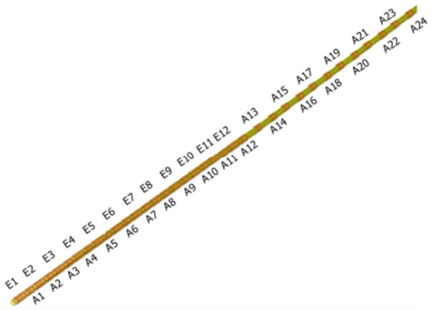

Figure 5-233 DV08D1 - outline - distal end

The total peak electric field at the distal end is shown in Figure 5-235 and the simulated transient responses in Figure 5-236 and Figure 5-237. Measured results are given in Figure 5-238 to Figure 5-241 and a comparison between simulated and measured results is shown in Figure 5-242.

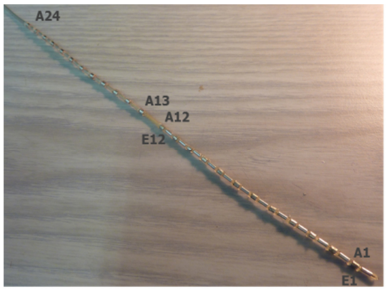

Figure 5-234 DV08D1 - Lead at distal end

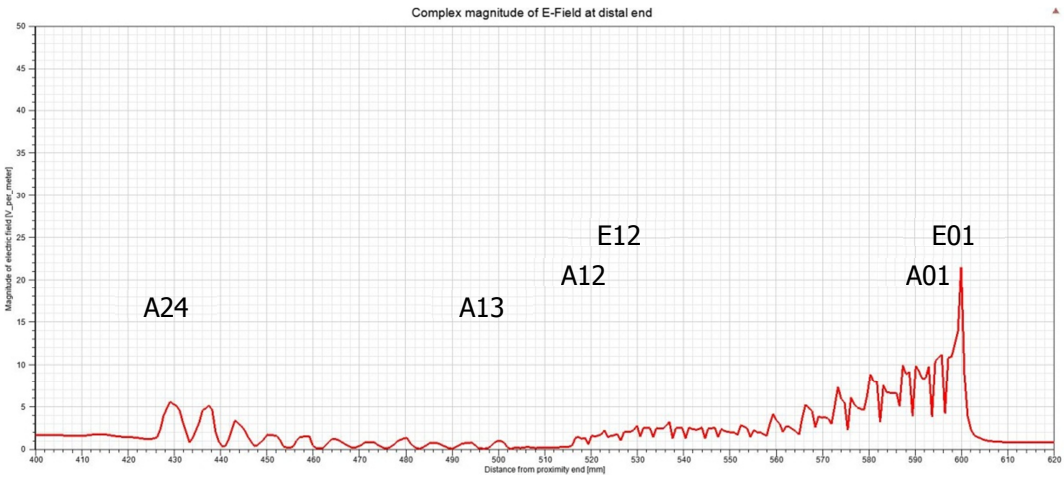

Figure 5-235 DV08D1 - 600 mm - complex magnitude of el. field at distal end

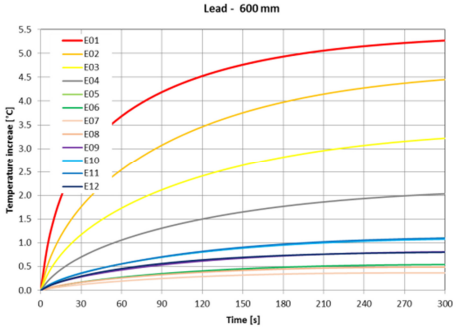

Figure 5-236 DV08D1 - 600 mm Simulation - Temp. Transient

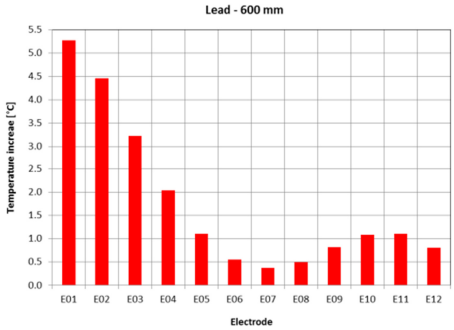

Figure 5-237 DV08D1 - 600 mm Simulation - Temp. after 300 s

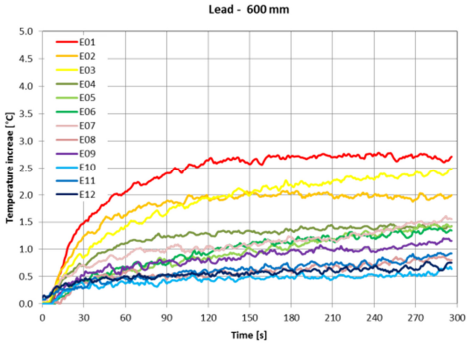

Figure 5-238 DV0D1 - 600 mm Measurement - Temp. Transient Therapeutic electrodes

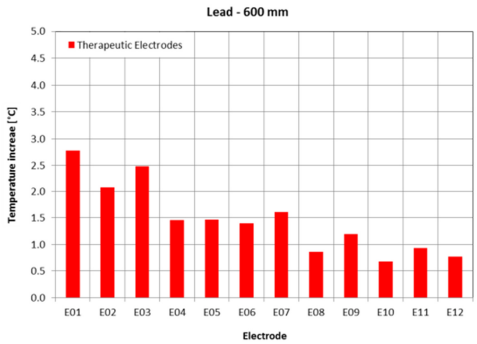

Figure 5-239 DV0D1 - 600 mm Measurement - Temp. Therapeutic Electrodes after 300 s

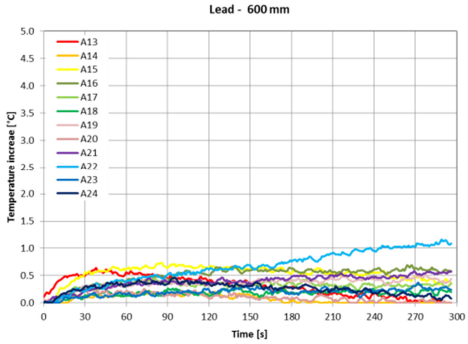

Figure 5-240 DV0D1 - 600 mm Measurement - Temp. Transient Auxiliary electrodes

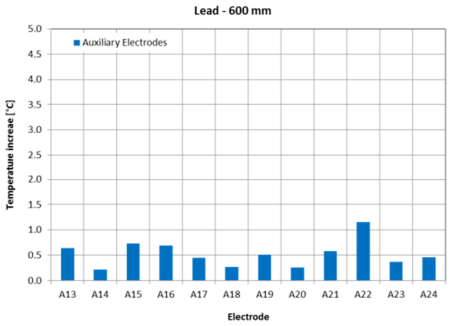

Figure 5-241 DV0D1 - 600 mm Measurement - Temp. Auxiliary Electrodes after 300 s

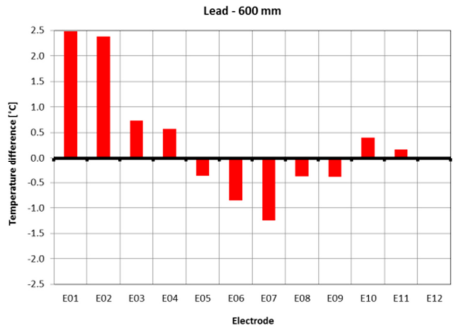

Figure 5-242 DV08D1 - 600 mm Difference - Temp. after 300 s

The twelve Auxiliary Electrodes A13 to A24 capture energy mainly from the common mode wave. This results in the temperature profile shown in Figure 5-241. In addition, the Auxiliary Electrodes A13 to A24 present short circuits for all differential modes. The distance between A13 and A01 is approximately 90 mm. Although this length does not present a resonance condition for common or differential modes ($\lambda_{com} \approx 400\,mm$, $\lambda_{diff} \approx 800\,mm$), nearly all energy captured by the electrodes at the distal end (due to the distal end excitation scheme) propagates towards the proximity end and is reflected back into the distal end from the array of Auxiliary Electrodes A13 to A24. Therefore, positioning of auxiliary electrodes along the MLC should be carefully considered. To avoid standing waves, multiples of $\frac{\lambda_{com}}{2}$ or $\frac{\lambda_{diff}}{2}$ between therapeutic and

auxiliary electrodes should be avoided. Figure 5-243 compares the two scenarios with and without Auxiliary Electrodes A13 to A24. Slight variations in the temperature increase profiles are visible but no significant temperature reduction is observed.

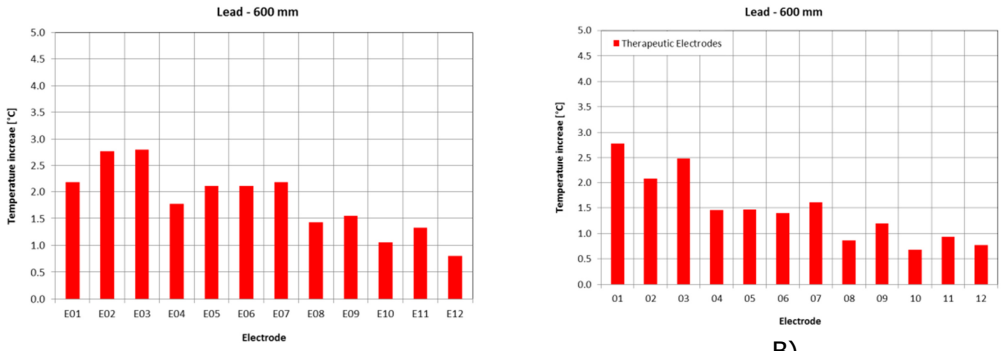

Figure 5-243 Comparison between measured temperature increases after 300 s
A) DV08C3 for 600 mm (100 Ohm)
B) DV08D1 for 600 mm (100 Ohm; 12 additional aux. electrodes)

5.1.11.6.5 Comparison of results DV08C and DV08D

The four measured and simulated temperature profiles are compared in Figure 5-244 and Figure 5-245. Both measurements and simulations show the influence of terminal impedances between Lead wires on temperature rise patterns at the distal end. The location of auxiliary electrodes between proximity and distal end has to be carefully chosen to avoid reflection points that lead to constructive interference of common and/or differential modes at distal end electrodes.

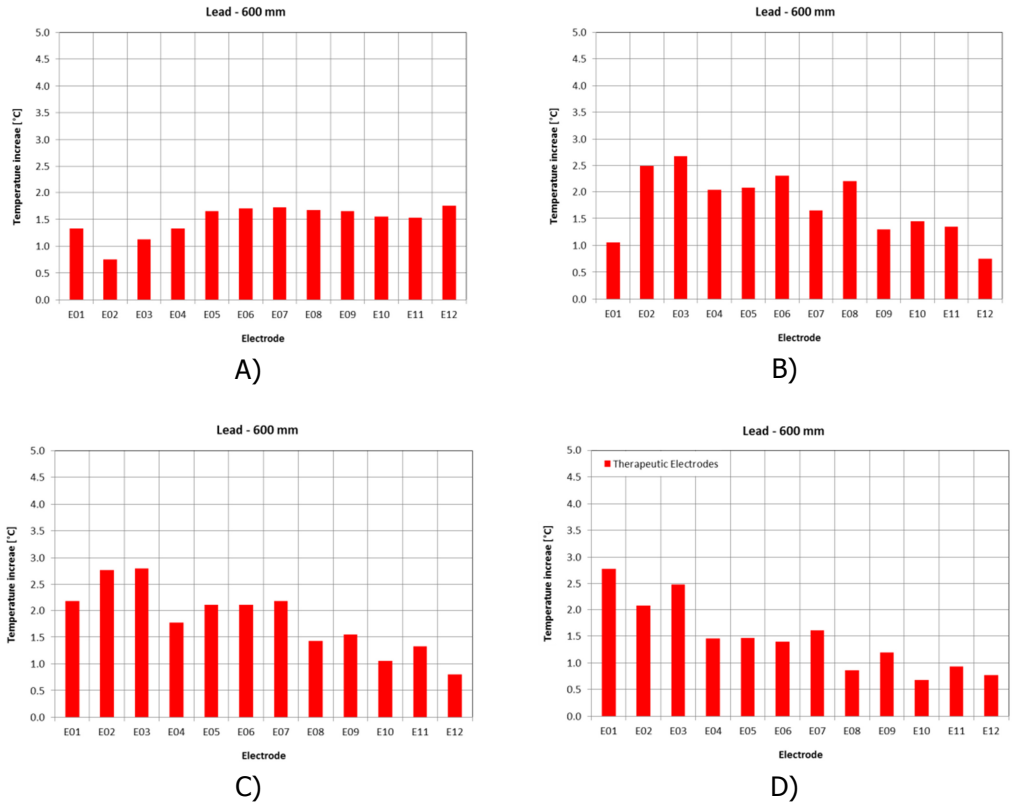

Figure 5-244 Comparison of measured temperature increases after 300 s
A) DV08C1 for 600 mm (with 5.0 mm aux. electrodes at proximity end)
B) DV08C2 for 600 mm (with 2.5 mm aux. electrodes at proximity end)
C) DV08C3 for 600 mm (with 100 Ohm resistor ring at proximity end)
D) DV08D1 for 600 mm (100 Ohm; 12 additional aux. electrodes)

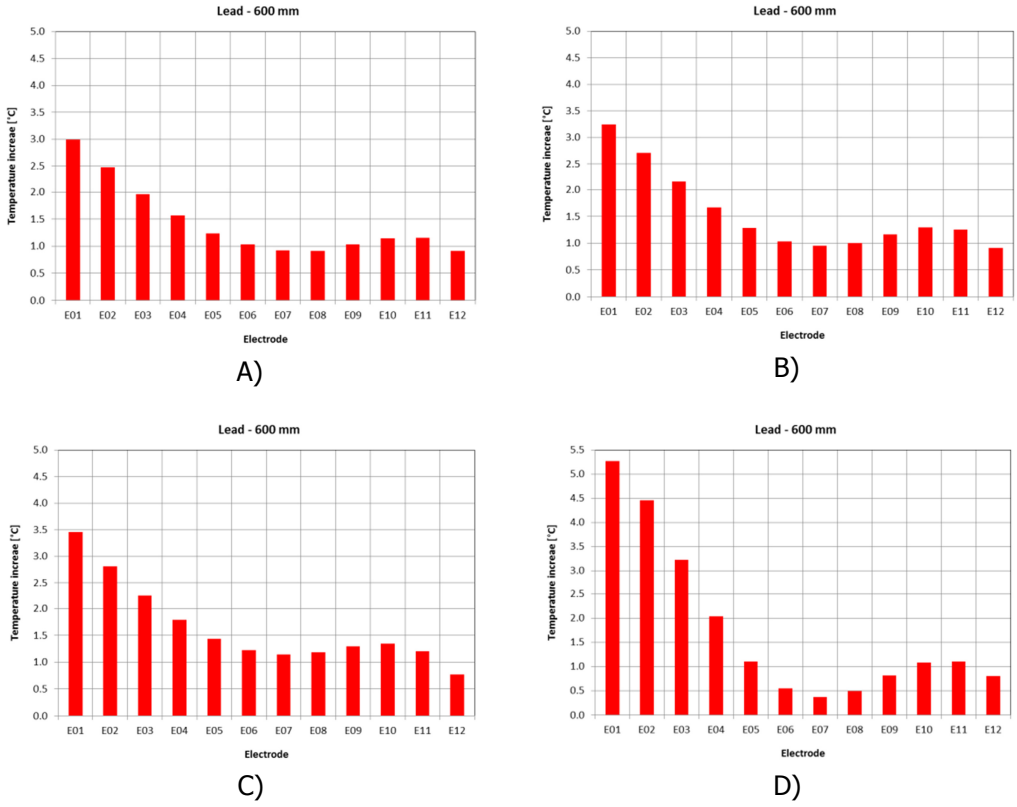

Figure 5-245 Comparison of simulated temperature increases after 300 s
A) DV08C1 for 600 mm (with 5.0 mm aux. electrodes at proximity end)
B) DV08C2 for 600 mm (with 2.5 mm aux. electrodes at proximity end)
C) DV08C3 for 600 mm (with 100 Ohm resistor ring at proximity end)
D) DV08D1 for 600 mm (100 Ohm; 12 additional aux. electrodes)

5.1.11.7 Therapeutic electrodes, resistors, DE extension

This section consolidates findings from previous sections and presents simulation and measurement results for a Lead and IPG that exhibit minimum RF induced temperature increase for three different excitation scenarios. The three excitation scenarios (distal, centre, and proximity end) are outlined in Figure 4-11 to Figure 4-13 for simulations and in Figure 5-143 to Figure 5-145 for RF induced temperature increase measurements.

Following simulation settings have been applied:

- EM model #3 (Table 4-2). The boundary layer has an isotropic permittivity of 3.5 and the double layer around the electrodes has the same characteristics as gelled saline.
- The peak electric field strength along the centre line of the dipole array is $300\ \frac{V}{m}$.

First, the most promising design variations and findings from simulations and measurements are summarised below.

Auxiliary electrodes

The impact of auxiliary electrodes has been investigated for four configurations:

- Auxiliary electrodes interleaved with therapeutic electrodes. This configuration has led to about 1 K temperature decrease (Section 5.1.11.5)

- Array of auxiliary electrodes located before therapeutic electrodes. This configuration has led to no significant improvement (Section 5.1.11.6.4).
- Auxiliary electrodes at the proximity end. This has led to 2.3 K temperature reduction (Sections 5.1.11.6.1 and 5.1.11.6.2).
- Single auxiliary electrode located half way between distal and proximity end (Section 5.1.6.7). This configuration has led to about 2 dB additional attenuation for the common mode.

The last configuration has been selected. For a 600 mm long Lead, two auxiliary electrodes have been placed at 250 mm and 350 mm from the proximity end. The spacing is a quarter wavelength of the common mode wave and hence reflections from both discontinuities cancel due to a 180 degree phase shift between the first and second reflection point. The impact of interleaved auxiliary and therapeutic electrodes has been demonstrated and this configuration can be applied to further reduce distal end temperature rises. The auxiliary electrodes at the proximity end will be replaced by a resistor ring encapsulated within the IPG header. Since the resistors are isolated from human tissue (gelled saline) they do not contribute to local tissue heating.

Ring of resistors

A 100 Ohm resistor ring has been selected although the characteristic impedance between two Lead wires is approximately 30 Ohm (Section 5.1.6.2.1). The simulations summarised in Section 5.1.9.9 show that the difference in differential voltages at the distal end is not significant when the resistor ring with 100 Ohm resistors is replaced by a resistor ring with 30 Ohm resistors.

Distal end extension

The transfer function measurements in Section 5.1.6.4 have shown that a deep null in the transfer function occurs about 20 mm from the distal end. Although the cause has not yet been fully understood, extending the distal end of the MLC and routing all Lead wires to the distal end can minimise the exposure for the distal end electrode. The impact of a distal end extension was simulated and the results were presented in Section 5.1.9.8.

Final configuration

The final configuration is outlined in Figure 5-246 to Figure 5-251. The Lead extension at the distal end is L = 10 mm.

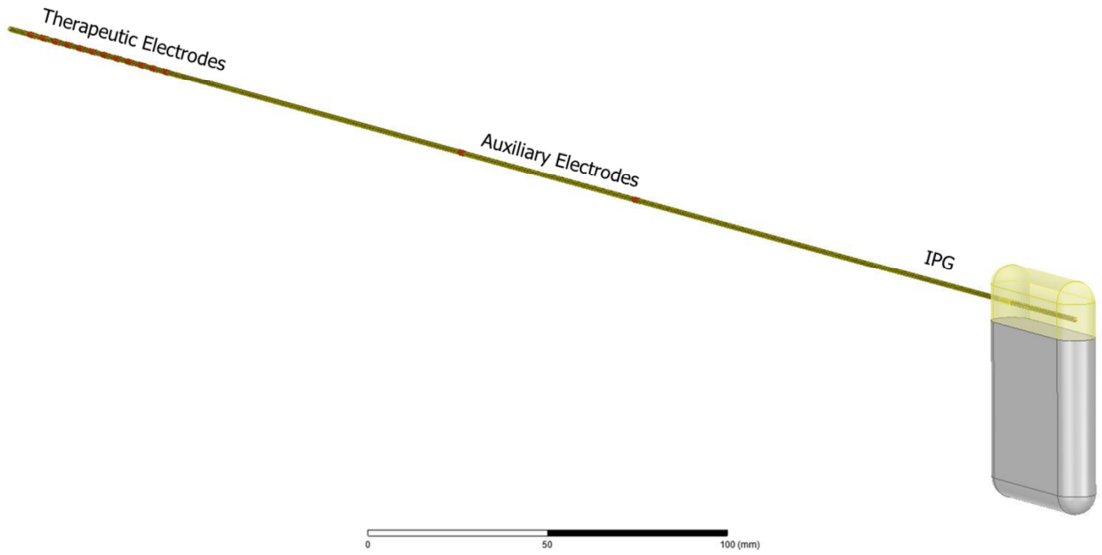

Figure 5-246 DV08LX - Outline - IPG and Lead

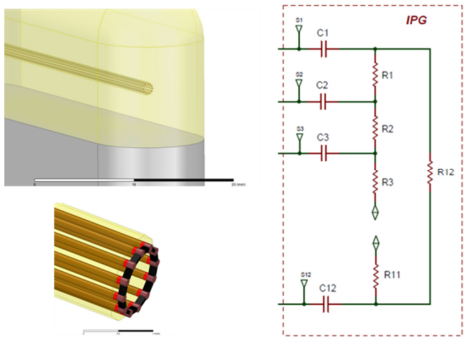

Figure 5-247 DV08LX - Lead wires capacitive coupled to ring of resistors in IPG header

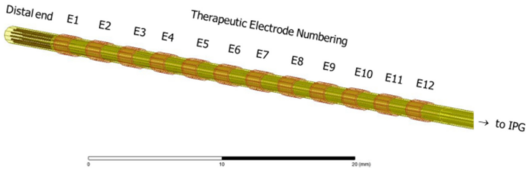

Figure 5-248 DV08LX - outline - distal end

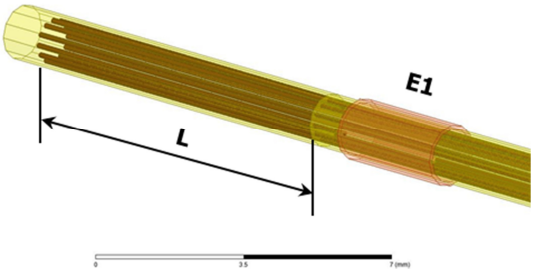

Figure 5-249 DV08LX - outline - length extension

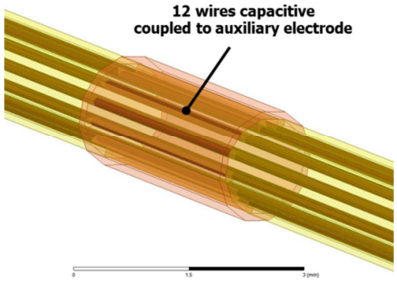

Figure 5-250 DV08LX - outline - auxiliary electrodes

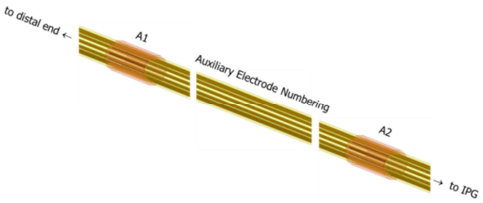

Figure 5-251 DV08LX - outline - auxiliary electrode numbering

The total peak electric field at the distal end is shown in Figure 5-252 and the simulated transient responses in Figure 5-253 and Figure 5-254. Measured results are given in Figure 5-255 and Figure 5-256 and a comparison between simulated and measured results is shown in Figure 5-257. These results are presented for the distal end excitation scheme.

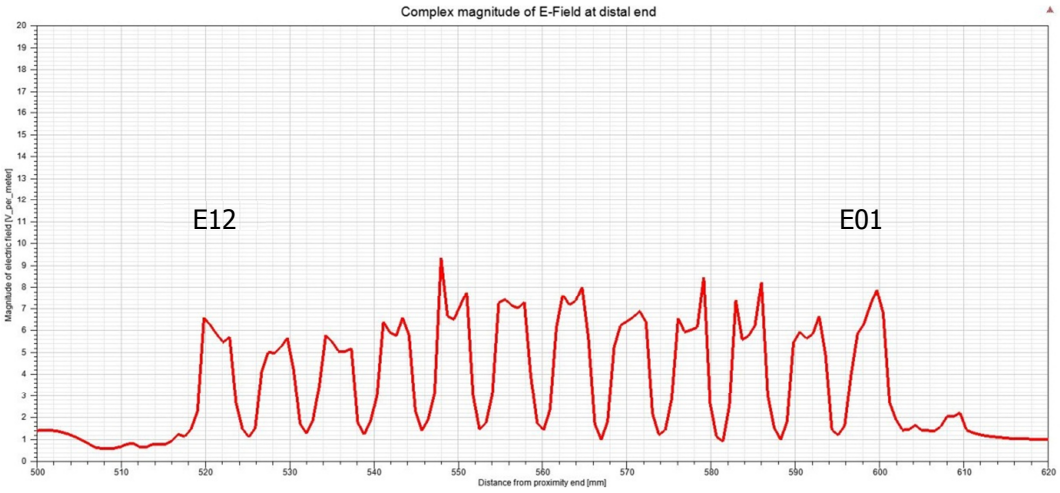

Figure 5-252 DV08L3_10_DEE - 600 mm - complex magnitude of el. field along Lead

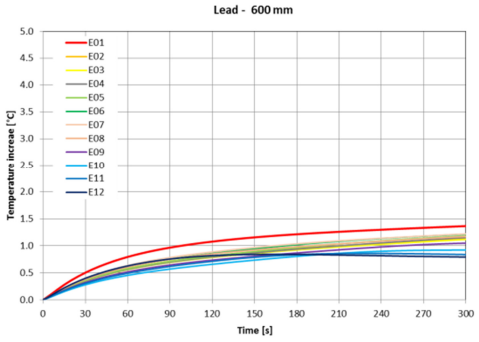

Figure 5-253 DV08L3_10_DEE - 600 mm Simulation - Temp. Transient

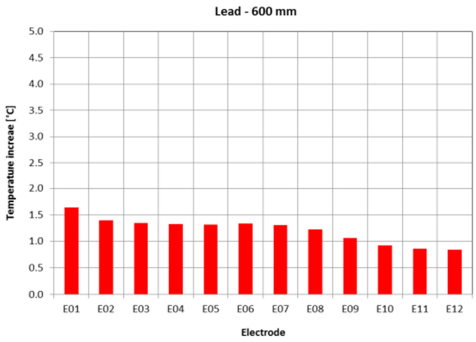

Figure 5-254 DV08L3_10_DEE - 600 mm Simulation - Temp. after 300 s

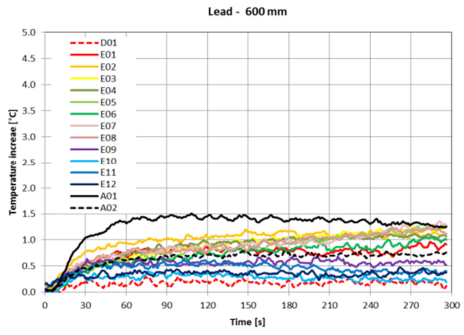

Figure 5-255 DV08L3_10_DEE Measurement - Temp. Transient

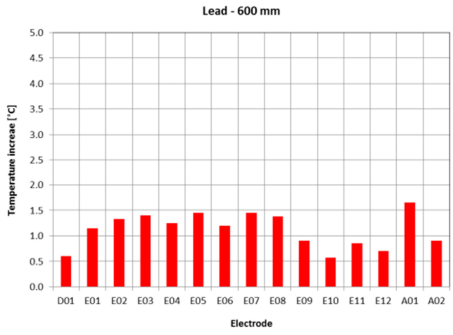

Figure 5-256 DV08L3_10_DEE Measurement - Temp. after 300 s

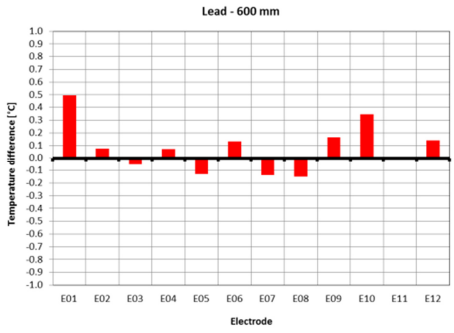

Figure 5-257 DV08L3_10_DEE Difference - Temp. after 300 s

In addition to the temperature rise at the therapeutic electrodes, the temperature rise at the tip of the distal end extension and the auxiliary electrodes has been measured. The maximum temperature rise is 1.6 K. Further, with a shift of the distal end reflection point and careful routing of Lead wires with minimum wire routing anomalies, the difference between measured and calculated temperature rises is significantly reduced (Figure 5-257).

The impact of distal end extension length on temperature rise profiles has been measured for distal end extensions between 50 mm and 10 mm (Figure 5-258). There are no significant variations in the temperature profile.

Finally, the impact of different excitation schemes is presented in Figure 5-259. The worst case temperature increase is 1.8 K for proximity excitation where the Auxiliary Electrodes A01 and A02 capture the bulk of the wave energy. This confirms that auxiliary electrodes placed between distal and proximity end can indeed reduce the temperature rise at distal end electrodes.

Comparison of Lead extension lengths

Lead length 600 mm

Extension: 50 mm

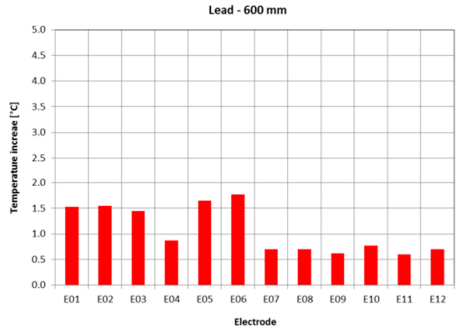

A)

Extension: 30 mm

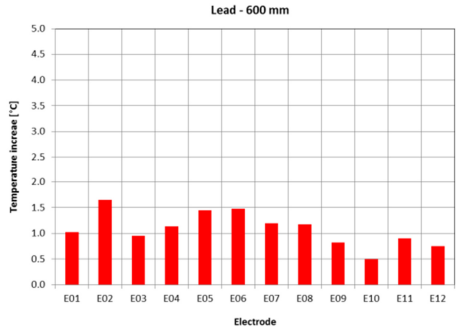

B)

Extension: 10 mm

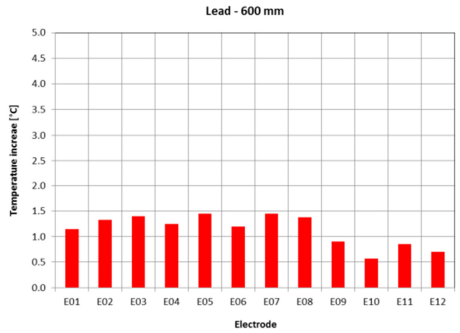

C)

Figure 5-258 Comparison of measured temperature increases after 300 s
A) DV08L3_50_DEE (50 mm Lead extension)
B) DV08L3_30_DEE (30 mm Lead extension)
C) DV08L3_10_DEE (10 mm Lead extension)

Comparison of excitation schemes

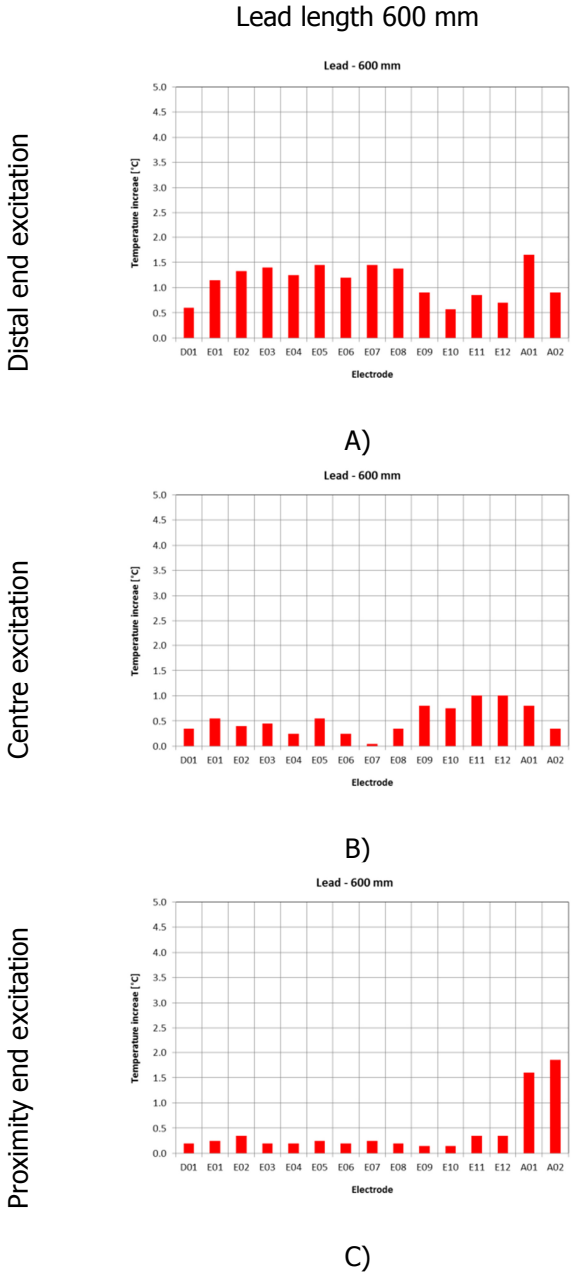

Figure 5-259 Comparison of measured temperature increases after 300 s
A) DV08L3_10_DEE (distal end excitation)
B) DV08L3_10_CEE (centre excitation)
C) DV08L3_10_PEE (proximity end excitation)

5.1.12 3T MRI scanner - RF induced temperature rise

To confirm the effectiveness of the design variations implemented in the final configuration presented in the previous section, Lead and IPG have been tested in a 3T MRI scanner. The test setup is shown in Figure 5-260 to Figure 5-262 and the test equipment is summarised in Table 5-10. Scanner settings are detailed in Appendix B.1. The position of IPG and Lead inside the phantom torso and the position of the phantom torso with respect to the scanner's iso-centre are shown in Figure 5-263.

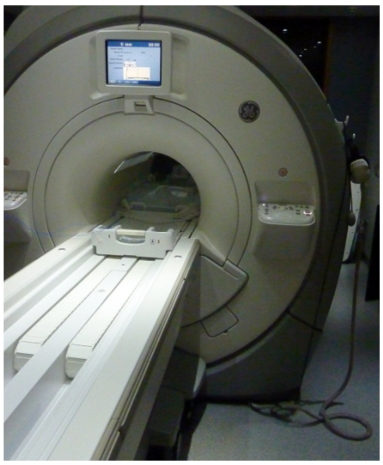

Figure 5-260 General Electric 3 Tesla Horizontal Field Scanner

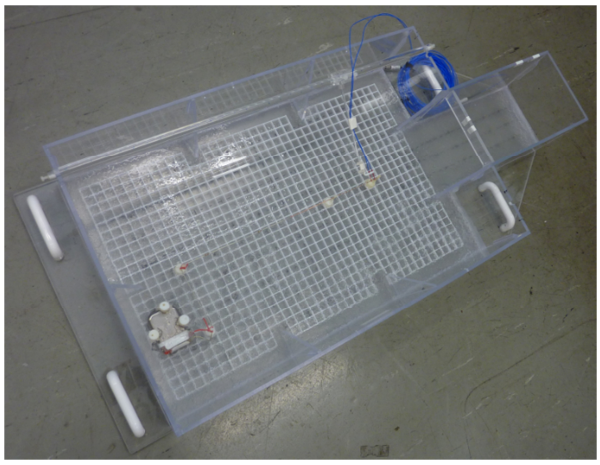

Figure 5-261 Phantom torso with IPG, Lead and temperature sensors

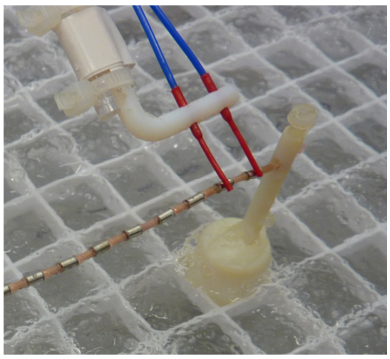

Figure 5-262 Position of temperature sensors on electrodes E01 and E02

The routing scenario is representative for a Lead positioned along the spinal cord and an IPG located next to the left buttock. The temperature rise has been recorded at the centre of each electrode over a 15 minutes (900 seconds) time interval for an average SAR of $2.4\ \frac{W}{kg}$ inside the phantom torso (PT).

Type	**Manufacturer**	**Model**
3 Tesla Horizontal Field Scanner	General Electric	Discovery™ MR750
Fibre-Optic Thermometer	OPTOCON	FOTEMP2
Fibre-Optic Temperature Probes	OPTOCON	TS2/10
Phantom torso	N/A	N/A
IPG and Lead	N/A	N/A

Table 5-10 MRI scanner and test and measurement equipment

The results of the temperature recordings are shown in Figure 5-264 and Figure 5-265. A maximum temperature rise of 0.8 K was recorded on Electrodes E01 and A01.

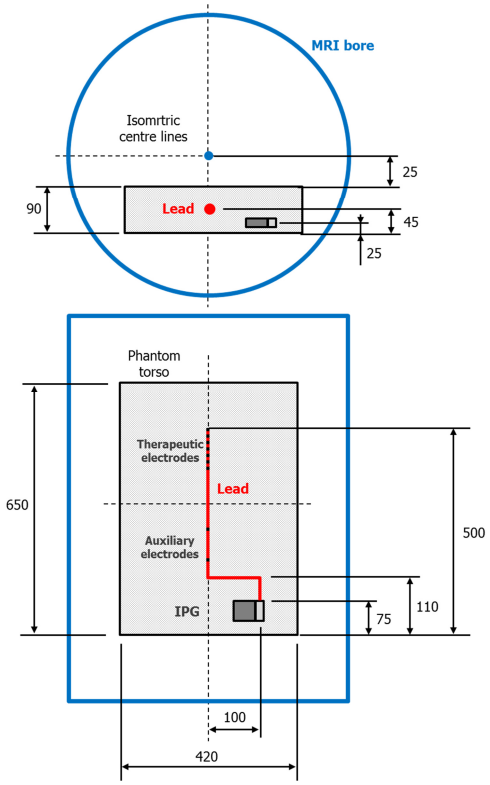

Figure 5-263 Position of IPG and Leads in PT and 3T MRI scanner

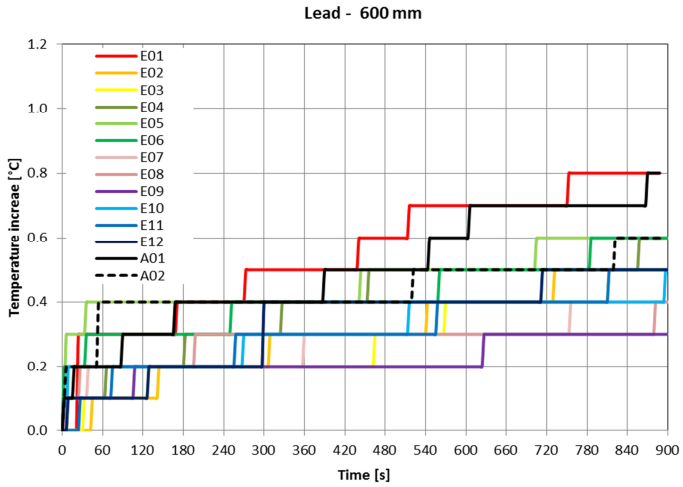

Figure 5-264 DV08L3_10_XXX - envelope of maximum recorded temperature increase

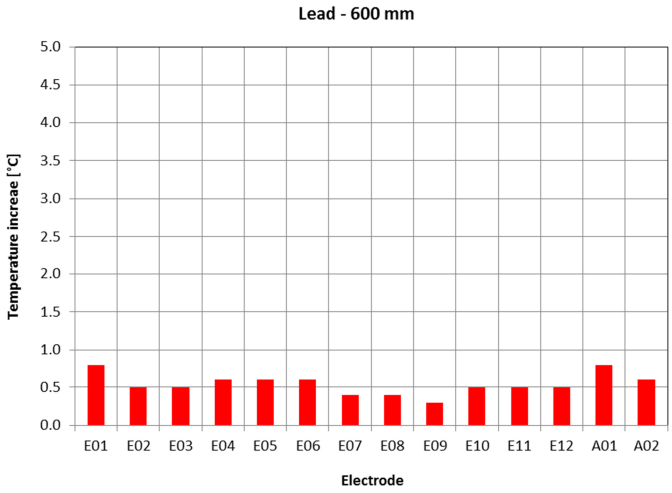

Figure 5-265 DV08L3_10_XXX - temperature increase after 900 s for all electrodes

For this routing scenario the equivalent peak electric field strength along the distal end is about $\sim 5\ \frac{V}{m}$ (Figure 4-108) and the equivalent peak electric field strength at the proximity end around the IPG is $\sim 180\ \frac{V}{m}$ along a $150\ mm$ section (Figure 4-109). The excitation scenario resembles the proximity end excitation scenario applied in the RF heating test bed (Figure 5-259). The differences are that the exposure length at the proximity end is about $300\ mm$ and that the peak tangential electric field strength is $300\ \frac{V}{m}$ (Figure 4-91).

The measured temperature rises show that the applied design variations are efficient and a step towards unconditional MRI safeness of Leads and IPGs for whole body exposure.

Finally, Lead and IPG have been superimposed on calculated electric field distributions for a male phantom body in a 3T MRI scanner (Hugo Human Body Model). The rms electric field strength along the routing path is $\sim 75\ \frac{V}{m}$ apart from a tiny section at the IPG where the rms electric field strengths is $\sim 125\ \frac{V}{m}$ (Figure 5-266). The peak electric field strength along the routing path is $\sim 106\ \frac{V}{m}$. For comparison, the equivalent averaged peak tangential electric field strength applied in the RF heating test bed and in EM and thermodynamic simulations is $\sim 210\ \frac{V}{m}$ (Figure 4-91). Assuming that the peak electric field strength in the Human Body Model is tangential to the routing path, the tangential electric field strength applied in the RF heating test bed is approximately twice the electric field strength along the routing path in the Human Body Model.

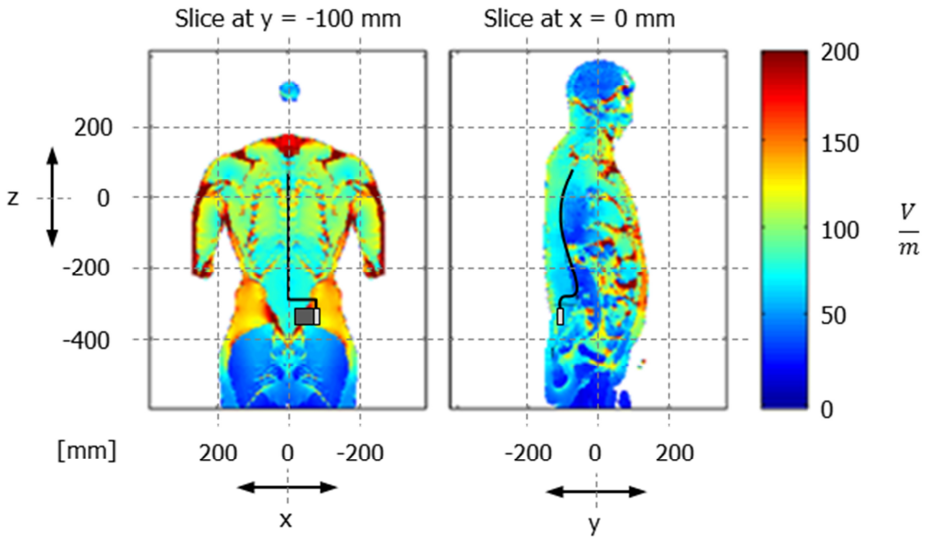

Figure 5-266 Superposition of IPG and Lead on Hugo Human Body Model at $f = 128\ MHz$ and $B_{RF,rms} = 2.1\ \mu T$; colour coding of the electric field is for rms electric field strengths

5.1.13 Simplified analytic models

5.1.13.1 Simple electrodynamic model

The maximum electric field at the distal end electrode can be estimated from (calculated or measured) attenuation, phase and reflection coefficients and a particular excitation scenario along the MLC. The algorithm and the Matlab source code are summarised in Appendix C.3.

The results presented here are for an incident electric field at 128 MHz. The characteristic line impedance of the MLC is given in Section 5.1.6.2.1 $\left(Z_{o,c} \approx (28 + j \cdot 7)\, Ohm\right)$ and the characteristic impedance of a surface wave travelling along the MLC is assumed to be equivalent to the plane wave impedance in gelled saline indicated in Appendix A.5 ($Z_{o,w} \approx (34 + j \cdot 13)\, Ohm$). For simplicity, the results are shown for a real characteristic impedance of $31\, Ohm$. The reflection coefficient at the proximity end is either $\Gamma_{min,open} \approx 0.9 \cdot e^{j \cdot 0}$ for open ended Lead wires or $\Gamma_{short} \approx 0.9 \cdot e^{-j \cdot \pi}$ for shorted Lead wires at the IPG. The reflection coefficient at the distal end Electrode E01 has been estimated from EM field simulations for the four base cases. There is only a single reflection coefficient that matches the electric field distribution at Electrode E01 in all four scenarios. This reflection coefficient is $\Gamma_{max} \approx 0.9 \cdot e^{-j \cdot 0.625 \cdot \pi}$. From the reflection coefficient the electrode capacitance and resistance can be deduced. The RF capacitance is $C_e \approx 21 \frac{pF}{mm}$ and the RF resistance is $R_e \approx 0.8 \frac{Ohm}{mm}$ for a typical cylinder electrode described in Section 3.1. The dominant (TEM Mode) propagation constant for long Lead lengths has been presented in Section 5.1.6.4. The dominant propagation constant for short Lead lengths is different since energy predominantly travels as slower surface wave along the MLC (see Appendix A.5). It is further assumed that the distal end electrode is connected to all Lead wires of the

MLC. Figure 5-267 and Figure 5-268 show the electric field distribution along a 200 mm and 600 mm long MLC terminated with a single distal end electrode, respectively (equivalent to UM03, UM04, open and short at IPG).

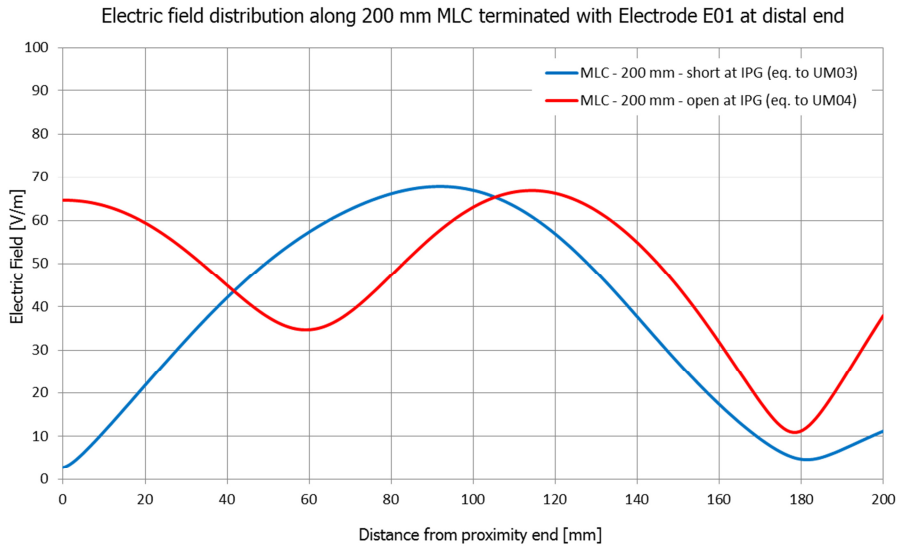

Figure 5-267 Electric field distribution at 128 MHz along a 200 mm MLC terminated with Electrode E01 for a normalised incident electric field according to Figure 4-93 (magnetic dipole; $\pm 100\ mm$)

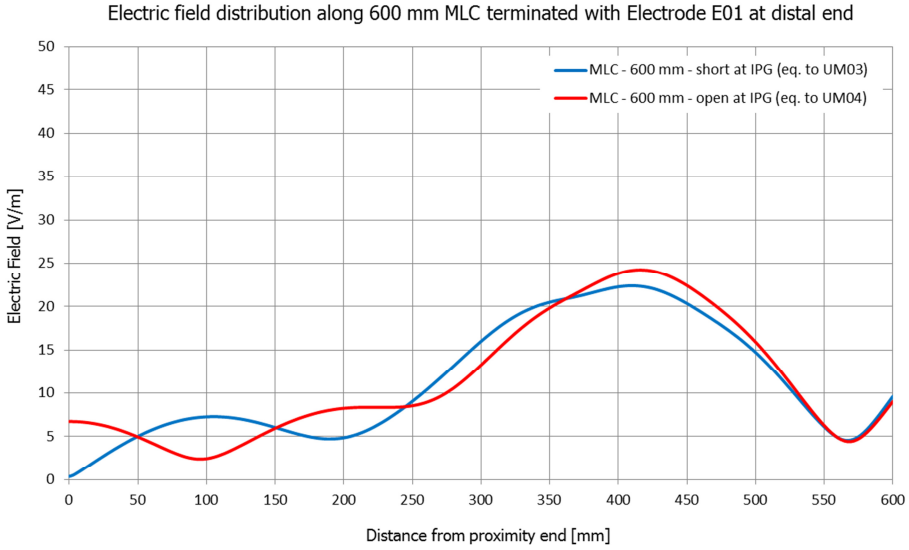

Figure 5-268 Electric field distribution at 128 MHz along a 600 mm MLC terminated with Electrode E01 for a normalised incident electric field according to Figure 4-93 (magnetic dipole; $^{+100\ mm}_{-200\ mm}$)

The distal end electric field strengths from the analytic and EM model are compared in Table 5-11.

	Magnitude of average radial electric field strength on Electrode E01 $\left[\frac{V}{m}\right]$	
Lead	EM model	Analytic model
$UM03 - MLC - 200\ mm - short$	9.0	11.2
$UM04 - MLC - 200\ mm - open$	37.0	38.0
$UM03 - MLC - 600\ mm - short$	15.0	9.6
$UM04 - MLC - 600\ mm - open$	12.0	9.0

Table 5-11 Comparison of electric field magnitudes at Electrode E01 for a normalised incident electric field according to Figure 4-93

The simple analytic model predicts the impact of proximity end terminations (open, short) on distal end electric fields for short and long MLC lengths. For short MLC lengths, the difference in electric field strength at the distal end is large whereas for long MLC lengths the difference in electric field strength at the distal end is small. The absolute electric field values vary slightly due to following reasons. The EM simulations have been carried out for a Lead with 12 electrodes at the distal end whereas the simple analytic model assumes a single electrode at the distal end. The 11 electrodes located before the most distal end electrode cause reflections, attenuations and phase shifts and therefore influence the electric field distribution at the distal end electrode.

In summary, the analytic model provides an order of magnitude of the electric field strength at the distal end electrode. The magnitude of the electric field strength can be used as input for the analytic thermodynamic model described in the next section. In addition, distal end electrode reflection coefficients can be optimised to minimise the electric field strength exposure for a given Lead length. For example, hydrogel coatings on electrodes have an impact on the resistive and capacitive behaviour at RF frequencies.

5.1.13.2 Simple thermodynamic model

An analytic solution for heat transfer caused by an incident EM wave penetrating into a one-dimensional absorptive infinite half space is outlined in Appendix D.1. The incident EM wave is represented by the radial electric and angular magnetic field of a single cylinder electrode. The unwrapped surface of a single cylinder electrode results in a rectangular aperture that is in contact with the one-dimensional absorptive infinite half space (electrolyte, gelled saline, or human tissue). Apart from the dimensions of the electrode (Section 3.1) and material properties of gelled saline (Appendix A.5), the model needs three input parameter:

- the power absorption coefficient
- the intensity of the incident EM wave
- the perfusion rate

The power absorption coefficient of the radial wave can be deduced from the $\frac{1}{e}$ penetration depths of the total electric field along a line radially pointing from the centre of the distal end electrode into saline solution (Figure 5-269).

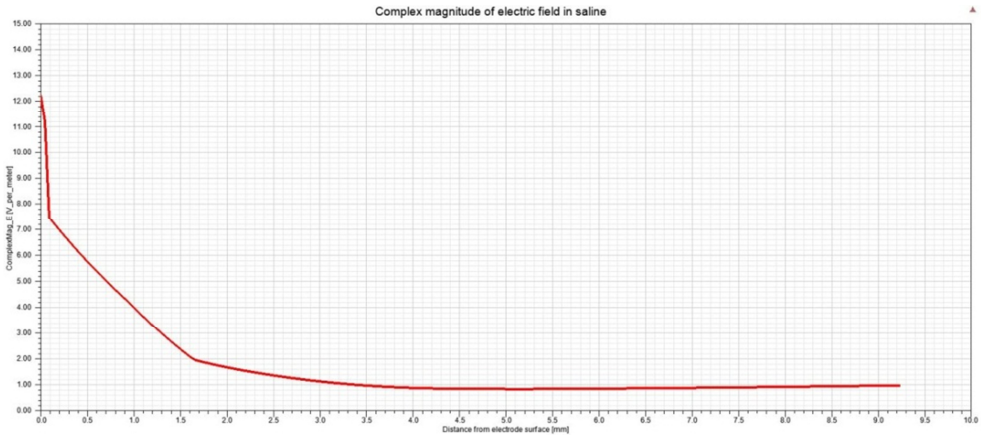

Figure 5-269 Total electric field along line radially pointing from the centre of the distal end electrode surface into saline solution for an incident axio-lateral electric field of $1\ \frac{V}{m}$

The initial steep slope occurs in the boundary layer around the electrode. The second slope up to about 1.6 mm from the electrode surface is quasi-linear. The curve decays to 1 V/m since the total electric field is presented. For the particular case of a 3 mm long cylinder electrode (see Section 3.1) in contact with gelled saline the power absorption coefficient is $\alpha_p \approx 2 \cdot \alpha_e \approx 2000 \frac{1}{m}$. The intensity of the EM wave has to be estimated from the calculated net power flow through the surface of an electrode for a given (driving) incident electric field. The resulting intensity is normalised with respect to $1 \frac{V}{m}$ of the averaged peak radial electric field on the electrode surface as follows.

$$I_0 \approx 3.974 \frac{W}{m^2} \cdot \left(\frac{E_{peak,average,radial,electrode}}{1 \frac{V}{m}} \right)^2 \tag{5–20}$$

The perfusion rate r' depends exponentially on the EM wave intensity I_0 and is connected to tracer particle velocities in gelled saline. Tracer particle velocities presented in Reference [P185] have been used to determine the viscosity of gelled saline (Section 5.1.4). Here, tracer particle velocities have been used to determine the perfusion rate r' in gelled saline as function of EM wave intensity (Figure 5-270).

For the four base cases (UM03, UM04, Lead lengths of 200 mm and 600 mm) the electric fields at the distal end Electrode E01 have been retrieved from EM simulations (see Section 5.1.11.4) and used as input parameter for the analytic model. The results are presented in Figure 5-271. Table 5-12 compares calculated temperature increases after 300 seconds exposure time for the EM / thermodynamic model and the analytic model.

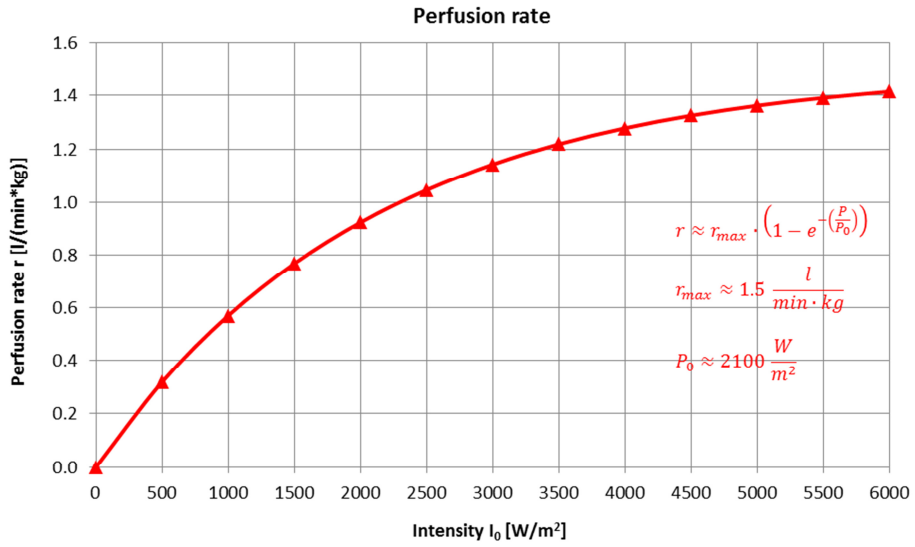

Figure 5-270 Perfusion rate in gelled saline as function of EM wave intensity

The steady state temperature increases predicted with the simple analytic model are in good agreement with the steady state temperature increases predicted with the EM/thermodynamic model.

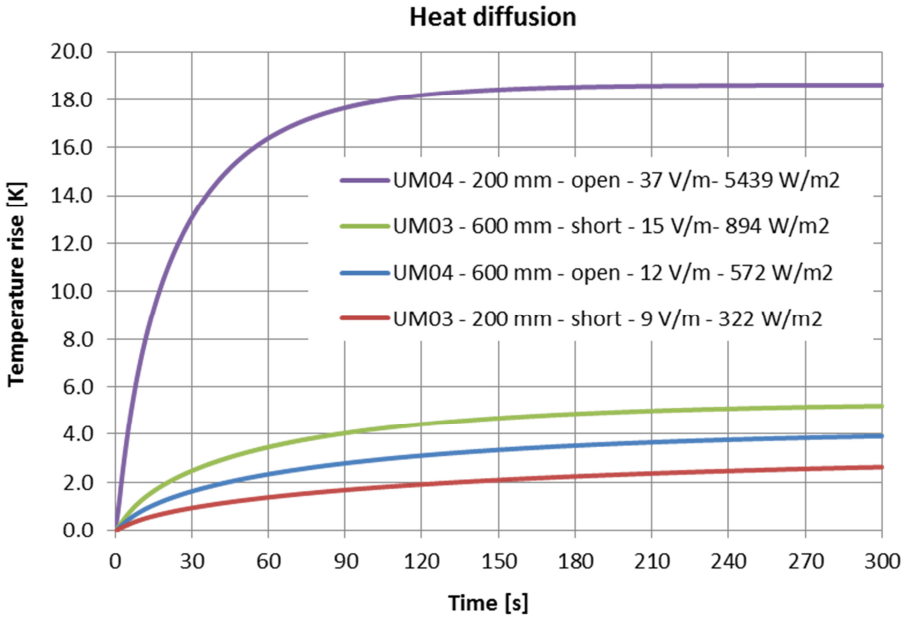

Figure 5-271 Calculated temperature rise at Electrode E01 for four base cases

Slight variations are observable in the transition region. The EM/thermodynamic model predicts steeper transition slopes than the

analytic model. The main reason is that the analytic model assumes a constant perfusion rate whereas the thermodynamic model assumes natural convection.

	Calc. temperature increase after 300 seconds $[K]$	
Normalised radial peak electric field strength on electrode $\left[\frac{V}{m}\right]$	EM/thermodynamic model	Analytic model
9.0	2.5	2.5
12.0	4.0	4.0
15.0	5.0	5.1
37.0	18.0	18.6

Table 5-12 Comparison of temperature increases after 300 seconds

Summing up, the simple analytic model provides first indications of the expected steady state temperature increase around cylindrical electrodes immersed in gelled saline. The same approach can be used for other electrode types provided that the surface of the electrode can be mapped onto an equivalent planar surface and that the electric field distribution surrounding the electrode is representative for the impinging EM wave.

5.2 Artefacts

5.2.1 Overview

This section explores whether the EM model is suitable to predict artefacts caused by charge displacements and relaxation processes around electrodes due to typical pulse patterns used in neural stimulations. The double layer parameters have been extracted from DC and step function measurements (Sections 5.2.2 and 5.2.3). The transient model is described in Section 4.1.5 and the test setup for transient measurements is shown in Figure 4-114. The pulse patterns were injected between Electrodes E01 and E02 and the artefacts have been measured between Electrodes E04 and E07 as function of terminal resistance RV2. First, the electric and magnetic field distributions around excited electrodes are shown (Section 5.2.4). Then, calculated and measured results for three different pulse patterns are presented; a positive and negative monophasic pulse pattern (Sections 5.2.5 and 5.2.6) and a biphasic pulse pattern (Section 5.2.7).

5.2.2 Voltages, currents and resistances

Electrostatic potentials caused by surface charge distributions on square and triangular conductive sheets have been analysed in References [P34] to [P37]. This section summarises the results of DC voltage and current measurements and equivalent DC and small signal RF resistances. The test setup has been described in Section 4.3.2. The extracted parameters are used in EM transient simulations to characterise the voltage dependent double layer resistance at electrode-electrolyte interfaces.

Figure 5-272 shows the I-V curve for positive voltages between 0 VDC and 8 VDC injected subsequently into E02 to E12. The return path is E01. All recordings have been made after 8 seconds.

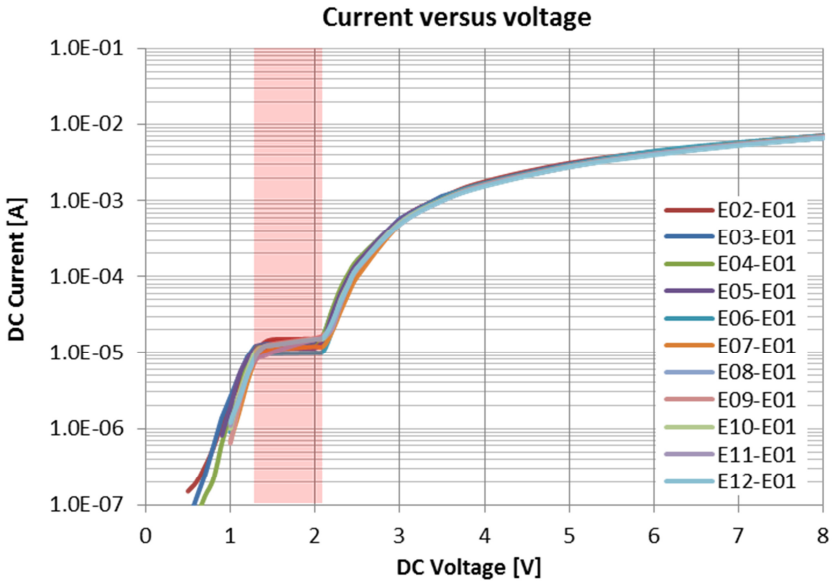

Figure 5-272 Current vs. voltage after 8 seconds

The resulting DC and small signal RF resistances after 8 seconds exposure are given in Figure 5-273 and Figure 5-274, respectively.

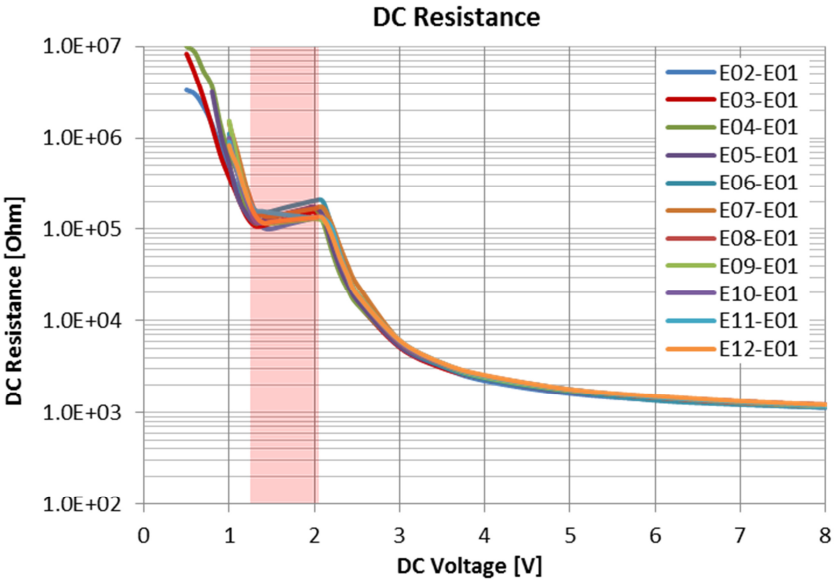

Figure 5-273 DC resistance after 8 seconds

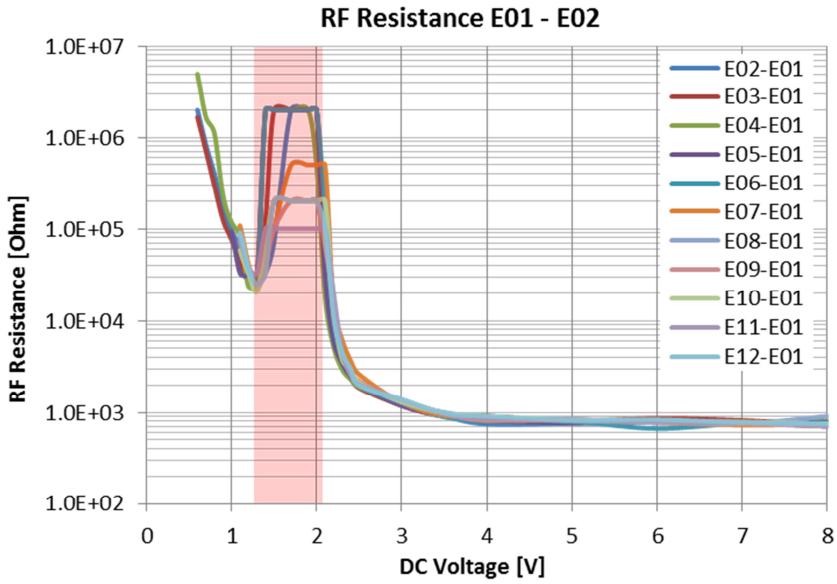

Figure 5-274 Small signal RF resistance after 8 seconds

The lower limit of the red shaded areas shown in the figures above indicates the onset of water electrolysis and and the upper limit the onset of sodium chloride electrolysis (Section 2.8). It seems that the DC resistance between electrodes is constant despite the increasing distance between them. Since the bulk resistance increases with distance between electrodes the constant DC resistance must have other roots. Charges are carried by ions in electrolytes and ions diffuse from electrode surfaces into the bulk solution or from the bulk solution towards electrode surfaces depending on ion and electrode polarity. Therefore, the current injected into the bulk depends mainly on electrode surface area and applied potential difference between electrodes and surrounding bulk solution and to a lesser degree on separation between electrodes. This leads to a quasi-constant DC resistance independent of electrode separation. The same reasoning can be applied for small signal RF resistances.

Figure 5-275 shows the time dependence of injected currents for three constant DC voltages between Electrodes E01 and E02. For voltages below the onset of sodium chloride electrolysis, the current is constant for about

100 ms and then starts to decrease. For voltages above the onset of sodium chloride electrolysis the current starts to decrease after ~20 μs.

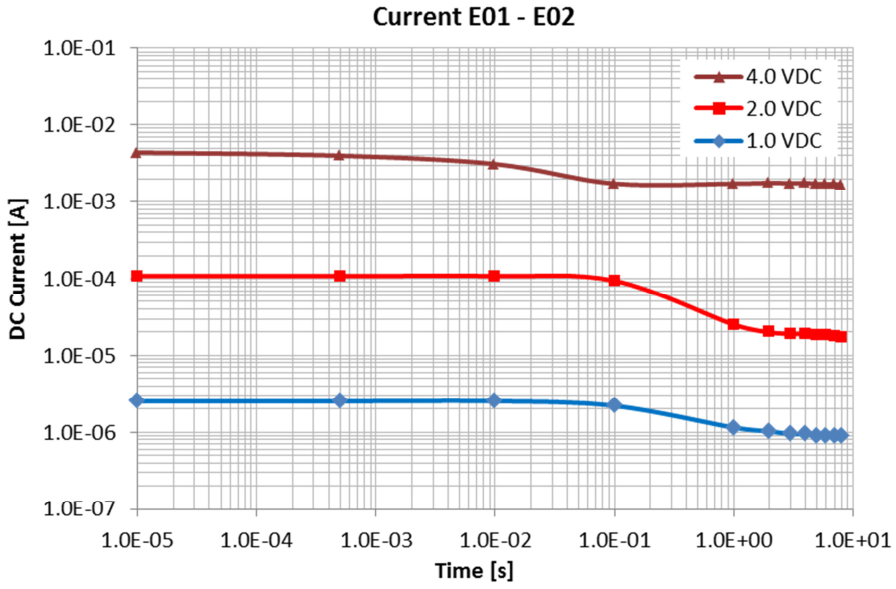

Figure 5-275 Current vs. time for constant voltage

5.2.3 Step function and transient response

This section summarises the results for transient response measurements. The test setup is described in Section 4.3.3. AC small signal double layer models are described in References [P8] and [P46]. The extracted parameters are used to characterise the resistance of the double layer around electrodes in EM transient simulations where the driving voltage is above the onset of sodium chloride electrolysis. A step function with $+4.0\ V$ was injected into Electrode E02 with Electrode E01 as return path and the transient response has been recorded over Resistor $RV1$ (Figure 5-276).

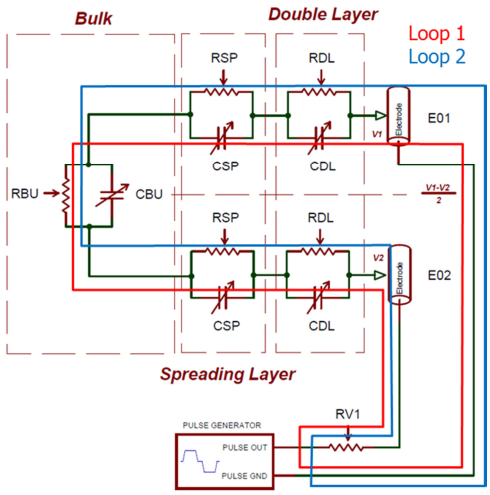

Figure 5-276 Simplified equivalent circuit diagram with three time constants

The transient response shows three time intervals over a time span of 40 ms (Figure 5-277). The first time interval $(t \leq 20\ \mu s)$ is associated with charging of all capacitances, i.e. double layer, spreading and bulk capacitance. The second time interval $(20\ \mu s < t \leq 4\ ms)$ is associated with the onset of electrolysis at the electrode-electrolyte interface, diffusion of chemical species and charge relocation around electrodes. The third time interval $(t > 4\ ms)$ is associated with diffusion and charge relocation in the bulk electrolyte.

In the following analysis it is assumed that the capacitances decrease from the electrode surface into the bulk electrolyte, i.e. $C_{dl} \gg C_{sp} > C_{bu}$.

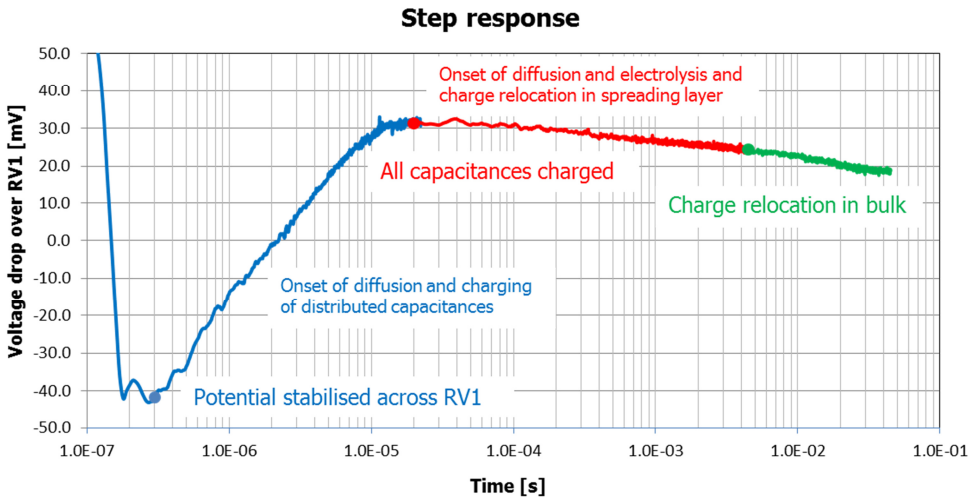

Figure 5-277 Voltage drop over resistance $RV1 = 7.2\ Ohm$ caused by step function of $+4V$ into Electrode E02 with return path via Electrode E01

At $t \approx 350\ ns$ the voltage drop over Resistor $RV1$ stabilised and the resistance R_{bu} can be determined from the current through Loop 1 in Figure 5-276.

$$R_{bu} = \frac{\left(U_{step} - U_{t=350ns}\right)}{\left|\frac{U_{t=350ns}}{RV1}\right|} = \frac{\left(4\ .0V - (-0.040\ V)\right)}{\left|\frac{-0.040V}{7.2\ Ohm}\right|} = 727\ Ohm$$

(5–21)

At $t \approx 20\ \mu s$ all charging processes have stopped and the resistance $2 \cdot R_{dl} + 2 \cdot R_{sp} + R_{bu}$ can be determined from the current through Loop 2 Figure 5-276.

$$2 \cdot R_{dl} + 2 \cdot R_{sp} + R_{bu} = \frac{\left(U_{step} - U_{t=20\mu s}\right)}{\left|\frac{U_{t=20\mu s}}{RV1}\right|} = \frac{\left(4\ .0V - (+0.031\ V)\right)}{\left|\frac{+0.031V}{7.2\ Ohm}\right|} = 922\ Ohm$$

(5–22)

The difference of the two equations above results in ...

$$R_{dl} + R_{sp} = \frac{1}{2}(922\ Ohm - 727\ Ohm) = 97\ Ohm$$

(5–23)

For comparison, the calculated bulk resistance without spreading and double layer resistances using the EM transient model is $R_{bu,calc} = 717\ Ohm$. A single resistance of $R_{dl} + R_{sp} = 105\ Ohm$ has been used in EM transient models to characterise the combinded effect of double layer and spreading resistance for pulse patterns with dwell voltages of $\pm 4.0\ V$.

5.2.4 Electric and magnetic fields

The magnitude of electric and magnetic field distributions for a voltage difference of 4 Volt between Electrodes E01 and E02 is shown in Figure 5-278 and Figure 5-279, respectively. The electric field is concentrated around the electrode-electrolyte boundary whereas the magnetic field is concentrated in the spacing between electrodes.

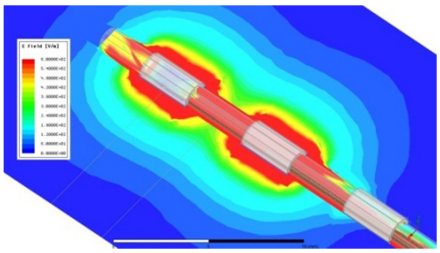

Figure 5-278 Electric field magnitude for bipolar stimulus of 4 VDC between E01 and E02

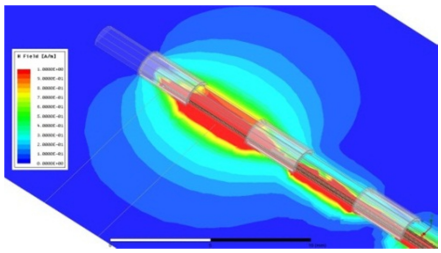

Figure 5-279 Magnetic field magnitude for bipolar stimulus of 4 VDC between E01 and E02

For the electric field along a path perpendicular to the surface at the centre of Electrode E01 a quasi-linear decrease is observed within the double layer followed by an exponential decrease into the bulk electrolyte.

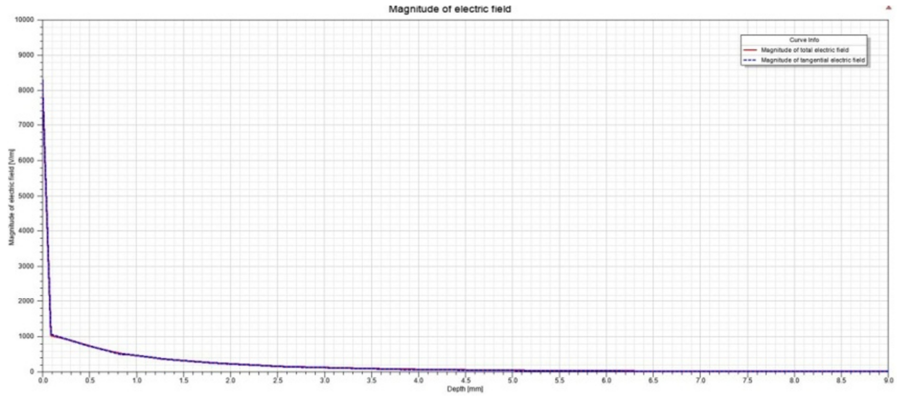

Figure 5-280 Decrease of electric field magnitude into gelled saline at E01 for bipolar stimulus of 4 VDC between E01 and E02

The magnetic field decreases exponentially from the surface. The evolution is shown for two paths; the first path is perpendicular to the surface at the centre of Electrode E01 and the second path is perpendicular to the surface at the centre between Electrodes E01 and E02.

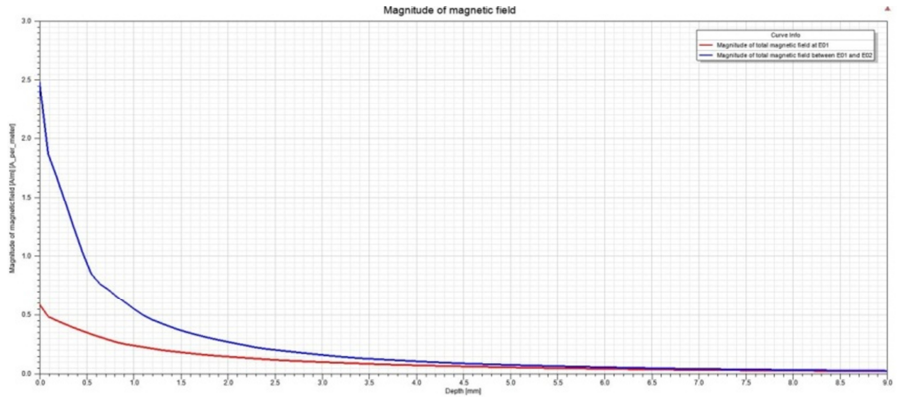

Figure 5-281 Decrease of magnetic field magnitude into gelled saline at E01 (red curve) and half way between E01 and E02 (blue curve) for bipolar stimulus of 4 VDC between E01 and E02

5.2.5 Monophasic positive pulse patterns

The monophasic positive pulse pattern is sketched in Figure 5-282. This pulse pattern is representative for long term artefact responses. The artefacts as function of terminal resistance RV2 are shown in Figure 5-283.

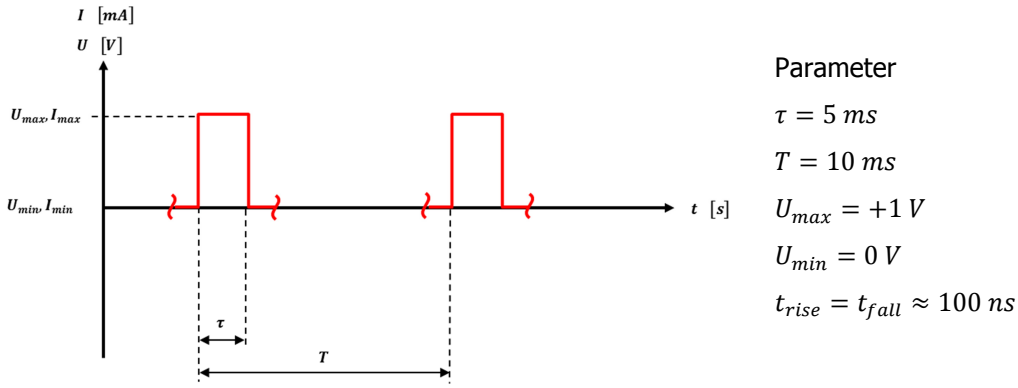

Figure 5-282 Monophasic positive pulse pattern for $\tau = 5\ ms$ and $T = 10\ ms$

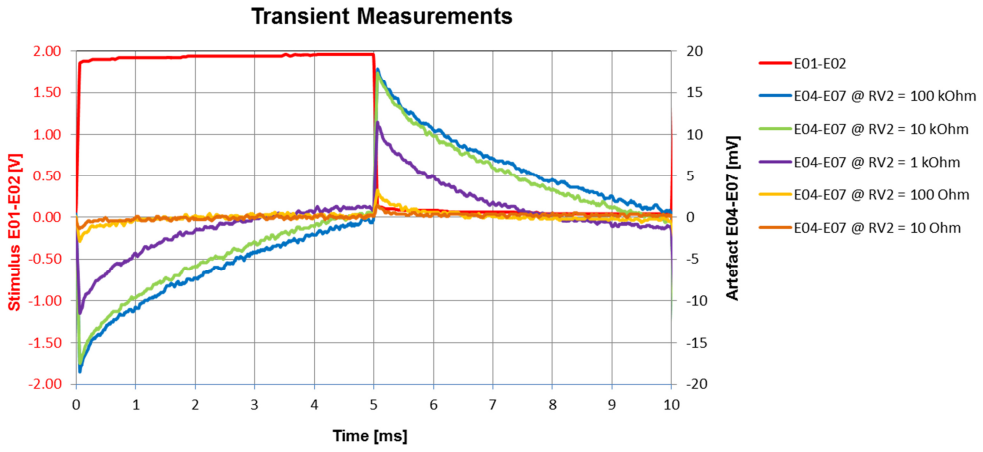

Figure 5-283 Measured artefacts between Electrodes E04 and E07 as function of resistance RV2 caused by a positive bipolar monophasic input pulse between Electrodes E01 and E02 (see Figure 4-114)

For comparison, the calculated transient responses are shown in Figure 5-284.

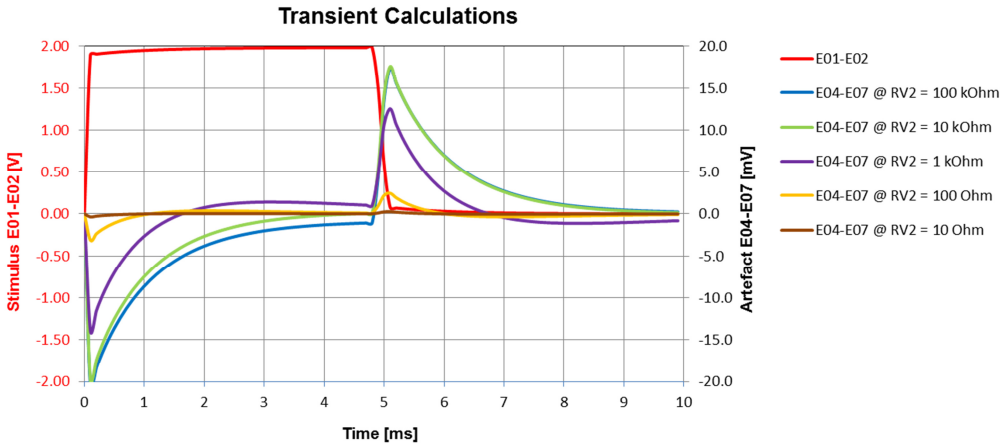

Figure 5-284 Calculated artefacts between Electrodes E04 and E07 as function of resistance RV2 caused by a positive bipolar monophasic input pulse between Electrodes E01 and E02 (see Figure 4-23 and Figure 4-24); Parameter: $R_{dl} = 10.1\ k\Omega\ and\ C_{dl} = 2.5\ \mu F$

The model takes polarity and change in polarity of the artefact responses into account and predicts the influence of terminal impedances on maximum artefact levels. The magnitudes of calculated and measured artefacts and the duration of artefacts are in good agreement. The calculated artefact slopes (following rising and falling stimulus slopes) are slightly steeper than the measured artefact slopes. The reasons for the differences in slopes have been outlined at the end of Section 4.1.5. Measured and calculated stimulus voltages between Electrodes E01 and E02 show both a steep linear positive slope followed by a positive exponential slope approaching the stimulus voltage.

5.2.6 Monophasic negative pulse pattern

The monophasic negative pulse pattern is of short duration and shown in Figure 5-285. Measured and calculated artefacts are presented in Figure 5-286 and Figure 5-287.

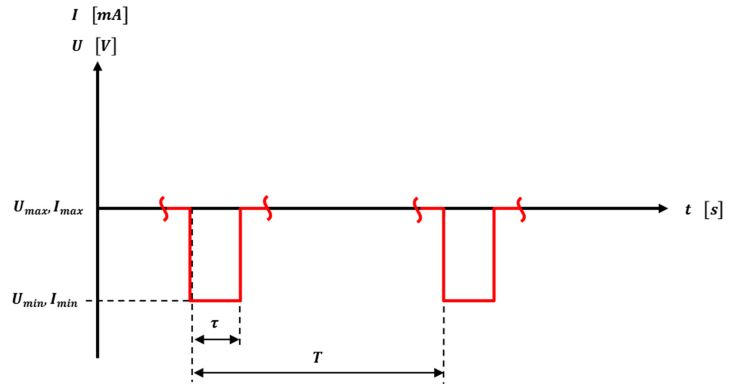

Parameter

$\tau = 250\ \mu s$

$T = 1\ ms$

$U_{max} = 0\ V$

$U_{min} = -1\ V$

$t_{rise} = t_{fall} \approx 100\ ns$

Figure 5-285 Monophasic negative pulse pattern for $\tau = 250\ \mu s$ and $T = 1\ ms$

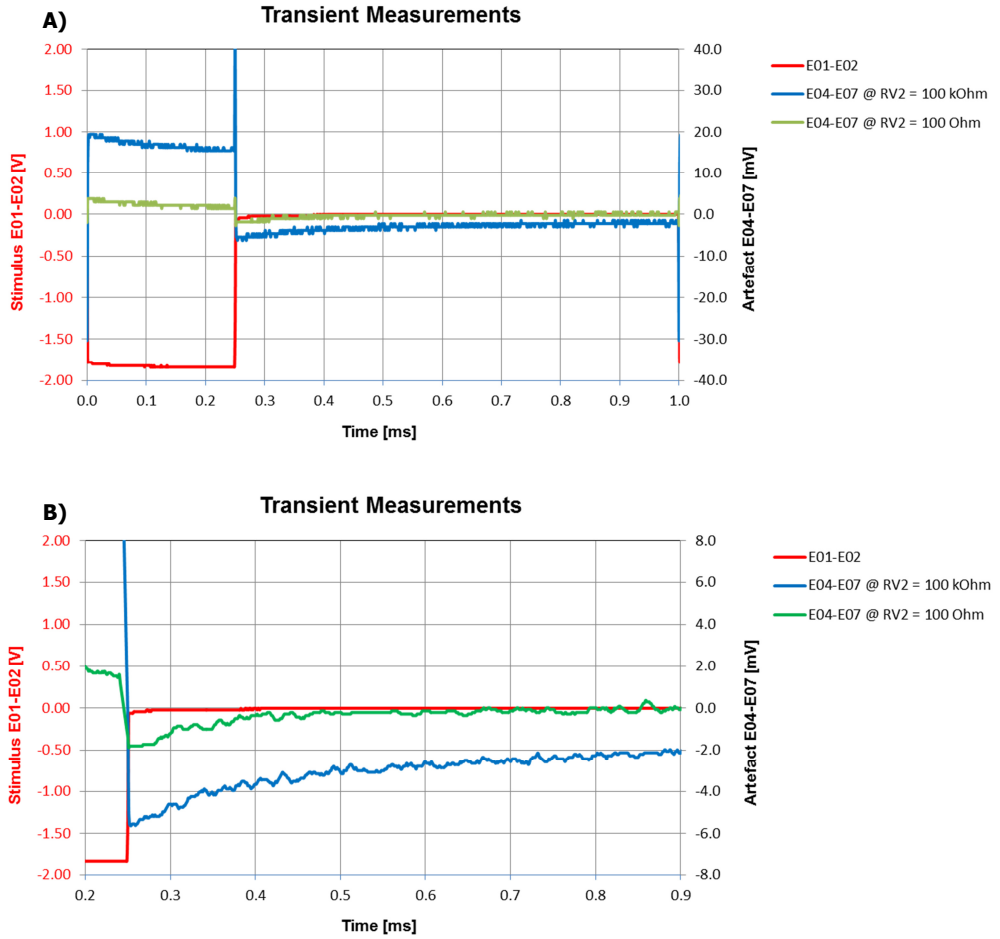

Figure 5-286 Artefacts between Electrodes E04 and E07 as function of resistance RV2 caused by a negative bipolar monophasic input pulse of 1 V between Electrodes E01 and E02
A) Full pulse
B) Zoom into tail of pulse

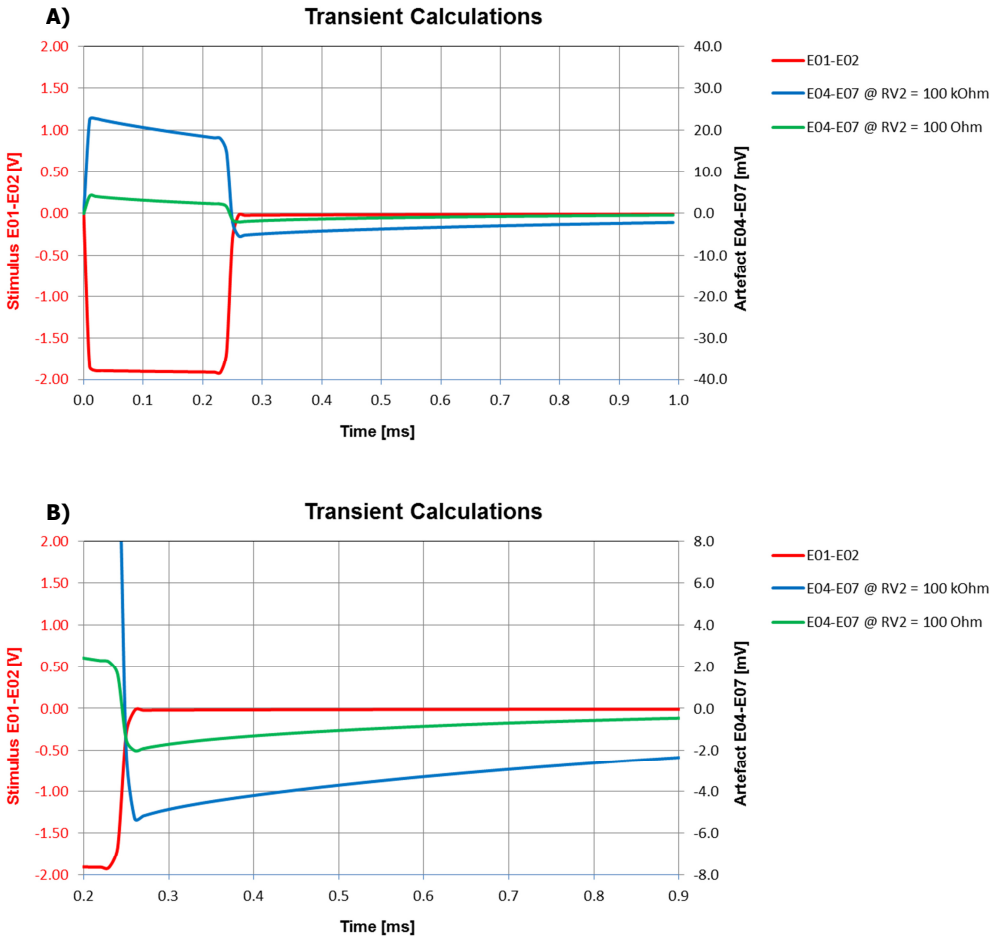

Figure 5-287 Calculated artefacts between Electrodes E04 and E07 as function of resistance RV2 caused by a negative bipolar monophasic input pulse of 1 V between Electrodes E01 and E02 (see Figure 4-23 and Figure 4-24); Parameter: $R_{dl} = 10.1\ k\Omega\ and\ C_{dl} = 2.5\ \mu F$
A) Full pulse
B) Zoom into tail of pulse

There is reasonable agreement between measured and calculated artefacts in terms of polarity, magnitude, duration and dependence on terminal resistance. As stated in the previous section, the initial artefact slopes differ slightly.

5.2.7 Bi-phasic pulse pattern

The last pulse pattern resembles a typical biphasic sequence that is applied in Spinal Cord Stimulation (SCS). The detrimental effects of artefacts during SCS have been outlined in Section 2.3. The pulse sequence is shown in Figure 5-288.

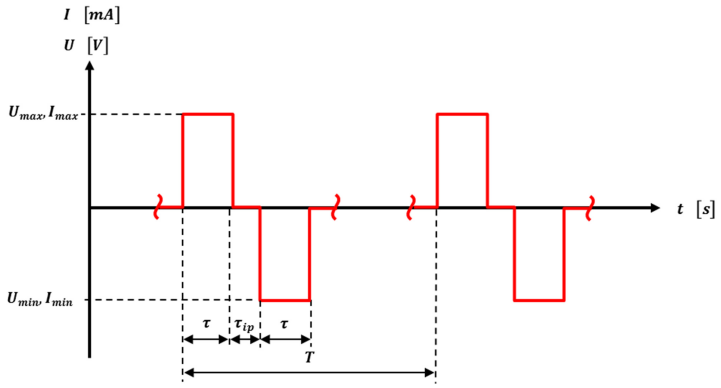

Parameter

$\tau = 250\ \mu s$

$\tau_{ip} = 200\ \mu s$

$T = 4\ ms$

$U_{max} = +2\ V$

$U_{min} = -2\ V$

$t_{rise} = t_{fall} \approx 1\ \mu s$

Figure 5-288 Biphasic pulse pattern for $\tau = 250\ \mu s$ and $T = 4\ ms$

The voltage drop over Resistor $RV1$ has been measured to determine the current through $RV1$. Figure 5-289 shows measured and calculated currents. The calculated peak voltage (current) is slightly lower than the measured peak voltage (current) whereas both calculated and measured values agree towards the end of the pulse. The reason for the difference is rooted in the time discretisation that dampens the transient response around the slopes of the stimulus voltage.

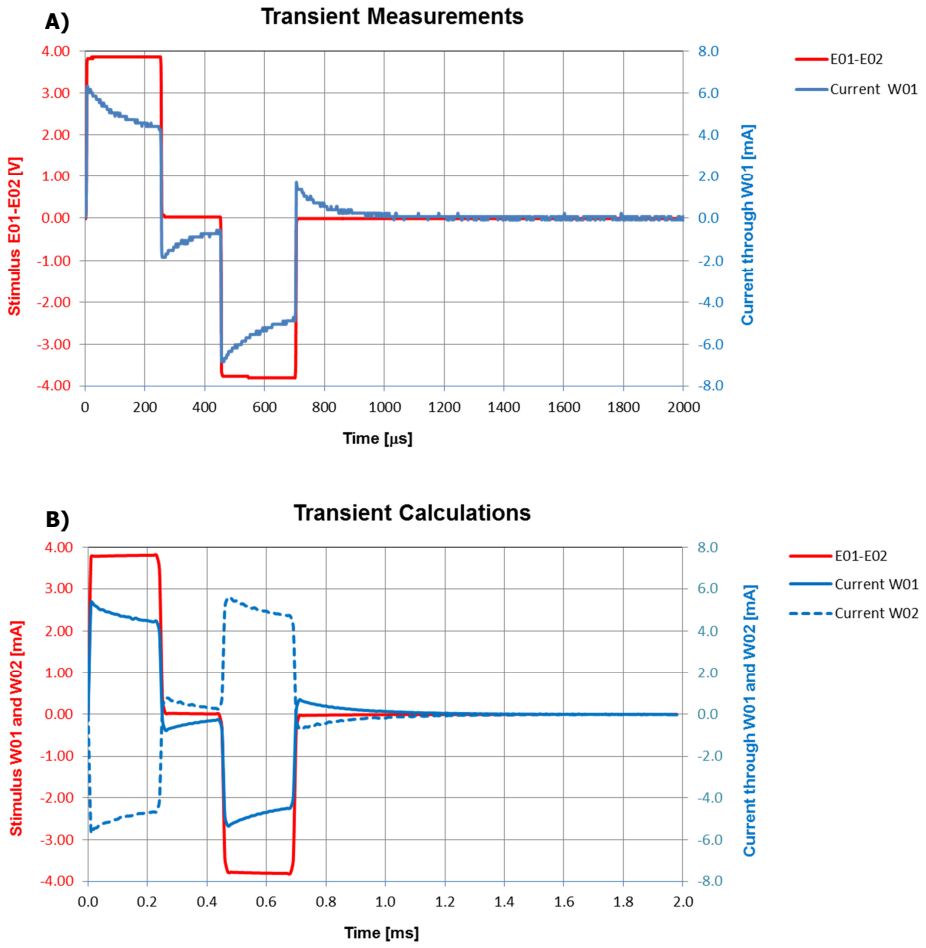

Figure 5-289 Currents caused by a bipolar biphasic pulse pattern of ±2 V between Electrodes E01 and E02
A) Measured current through resistance $RV1 = 5\ Ohm$
B) Calculated current through Wires W01 and W02;
Parameter: $R_{dl} = 105\ \Omega\ and\ C_{dl} = 2.5\ \mu F$

The measured and calculated artefacts between Electrodes E04 and E07 over a 2 ms time interval are shown in Figure 5-290. In addition, Figure 5-291 zooms into the artefact following the slope at $t = 700\ \mu s$. Polarity, magnitude, duration and slope tails are well captured by the EM transient model. A discrepancy is observed for the artefact slope following directly the stimulus slopes (see previous sections).

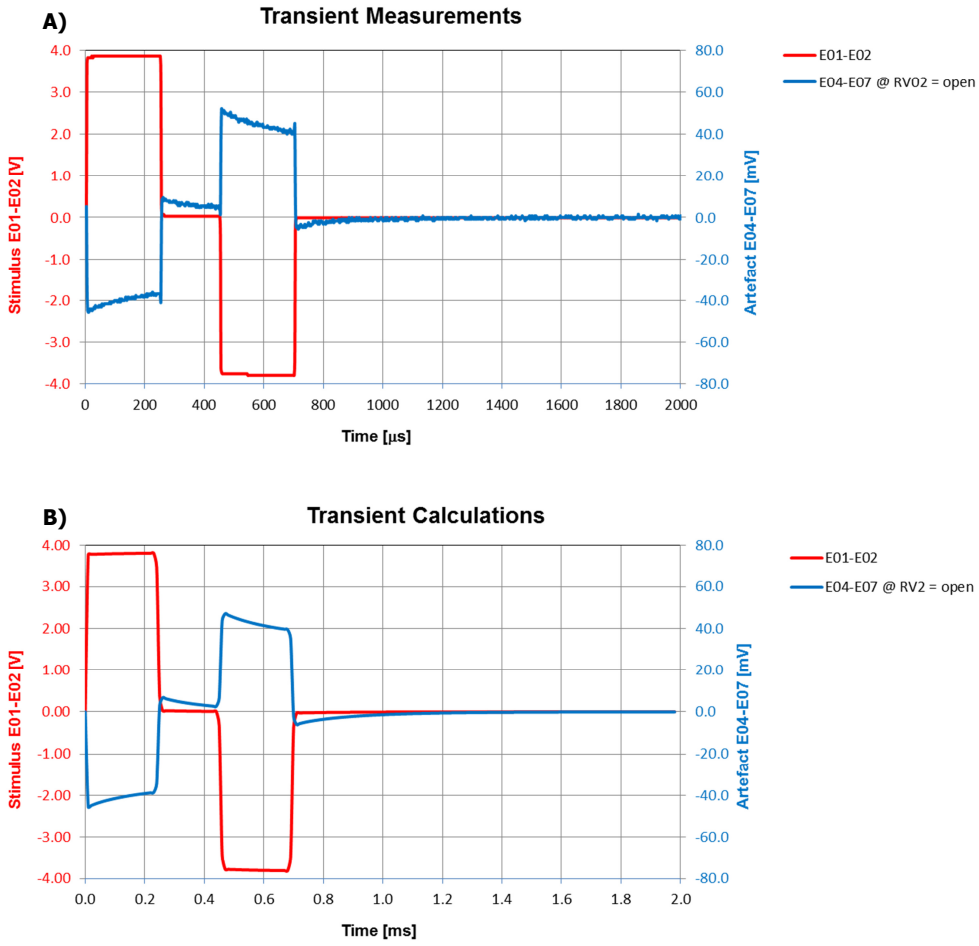

Figure 5-290 Artefacts between Electrodes E04 and E07 caused by a bipolar biphasic pulse pattern of ±2 V between Electrodes E01 and E02
A) Measured
B) Calculated; Parameter: $R_{dl} = 105\ \Omega\ and\ C_{dl} = 2.5\ \mu F$

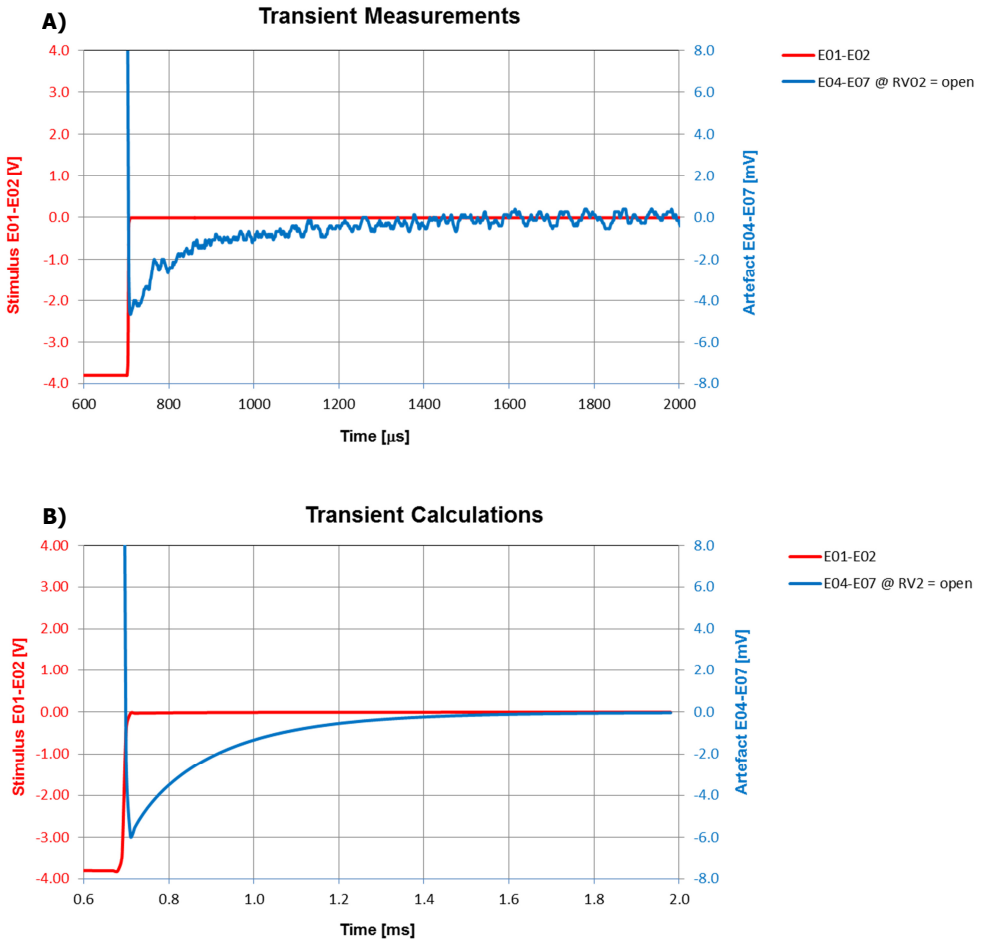

Figure 5-291 Zoom into artefacts between Electrodes E04 and E07 caused by a bipolar biphasic pulse pattern of ±2 V between Electrodes E01 and E02
A) Measured
B) Calculated; Parameter: $R_{dl} = 105\ \Omega\ and\ C_{dl} = 2.5\ \mu F$

5.2.8 Summary

Reasonable agreement in polarity, magnitude, duration and slope between transient simulations and measurements is observed and deviations have been tracked back to the limitations of the EM model. The most promising way to reduce artefact voltages captured by recording electrodes is to reduce the terminal impedances of recording electrodes during stimuli. Further, injecting a potential over recording electrodes that is reversed with respect to the potential that is driving the artefacts can further reduce detected artefact voltages. The reverse potential can easily be

picked up and scaled from the potential difference over two adjacent electrodes not involved in stimuli and neural response recordings. Artefact reduction circuits are not disclosed in this document.

6. Conclusions and outlook

Spinal cord stimulation is frequently applied in cases of chronic pain. Real time tracking of neural responses is essential to adjust stimuli after changes in body posture. Artefacts can camouflage neural responses and inhibit or alter the adjustment of stimuli. Therefore, artefact reduction is crucial for real time tracking of neural responses. The most promising way to reduce artefacts is to reduce the terminal impedance of the recording electrodes during stimuli and to inject a potential over the recording electrodes that is reversed with respect to the potential that is driving the artefacts. The reverse potential can easily be picked up and scaled from the potential difference over two adjacent electrodes not involved in stimuli and neural response recordings.

Patients with implanted SCS frequently undergo medical follow-up examinations including MRI assisted medical diagnosis. RF induced excess heating during MRI scans can lead to local tissue degeneration, accelerated cell death or flash burns in the spinal canal. Therefore, minimising RF induced heating is crucial for safe MRI scans. To mitigate heating in human tissue next to IMDs several proposals have been made, including auxiliary electrodes at distal and proximity ends of Leads, auxiliary electrodes mid-way between distal and proximity end of Leads, integrated resistor matrices, distal end extensions, revised wire routing schemes, and coiled electrodes. In addition, it has been shown that material parameters of MLCs can be adjusted to confine fields within and/or to attenuate waves propagating along MLCs. Finally, anisotropic hydrogel coatings can be applied to electrode surfaces blocking surface

currents that would otherwise continue as volume currents in human tissue.

Electromagnetic and thermodynamic models for Leads and IPGs have been created to facilitate the analysis of design variations. Available computing resources have put severe constraints on model sizes and simulation time and accuracy. Despite these hurdles, reasonable agreement between simulated and measured results could be achieved. Further, several RF test beds have been built to analyse wave propagation along MLCs and Leads and to measure RF induced heating at distal end electrodes. Finally, a prototype Lead and IPG has been realised and tested in a 3T MRI scanner. The results proofed the effectiveness of implemented design variations.

The EM models have been revised and extended to investigate the impact of electrode configurations, stimulation schemes and pulse sequences (magnitude, polarity, pulse patterns) on fibre recruitment areas along the dorsal column of the spinal cord. In addition, artefacts can be more accurately predicted. Further, the thermodynamic model has been revised and includes multi-phase fluids taking into account clothing of gelled saline. Results using revised and extended models are not presented in this document.

It appears that electromagnetic fields change material properties in interface layers along Leads embedded in electrolytes. For example, permittivities, conductivities and viscosities show anisotropic behaviour and depend on local field strengths as well as orientations of ionic electric and magnetic dipole moments. These field induced changes in material properties have to be further investigated using molecular dynamics simulations and molecular dynamics measurement techniques.

References

R.1 Books

Biomedical

[B1] Brahme, A., "Comprehensive biomedical physics", Newnes, 2014

[B2] Klabunde, R., "Cardiovascular physiology concepts", Lippincott Williams & Wilkins, 2011

[B3] Martinsen, O. G., & Grimnes, S., "Bioimpedance and bioelectricity basics", Academic press, 2008

[B4] Patterson, M., "Electrical stimulation research techniques", Vol. 3, Elsevier, 2013

[B5] Plonsey, R., & Barr, R. C., "Bioelectricity: a quantitative approach", Springer Science & Business Media, 1988

[B6] Rumble, J.R. (ed), "Handbook of Chemistry and Physics", 100th Edition, CRC Press, 2020

[B7] Schmidt, R.F., Willis, W.D., "Encyclopedia of pain", Springer-Verlag Berlin Heidelberg, 2007

[B8] Squire, L., Berg, D., Bloom, F.E., Du Lac, S., Ghosh, A., Spitzer, N.C. eds., "Fundamental neuroscience", Academic Press, 2012

Electrochemistry

[B9] Cussler, E. L., "Diffusion: Mass Transfer in Fluid Systems", Cambridge University Press, 2009

[B10] Lvovich, V.F., "Impedance spectroscopy: applications to electrochemical and dielectric phenomena", John Wiley & Sons, 2012

[B11] Orazem, M.E., Tribollet, B., "Electrochemical Impedance Spectroscopy", John Wiley & Sons, 2017

[B12] Paunovic, M. "Fundamentals of Electrochemical Deposition", Wiley, 2006

Electromagnetics

[B13] Collin, R.E., "Foundations for Microwave Engineering", Wiley, 2001

[B14] King, R. W. P. & Smith, G. S., "Antennas in matter: fundamentals, theory, and applications", The MIT Press, Cambridge, MA, 1981.

[B15] Lucht, P., "Transmission Lines and Maxwell's Equations", Rimrock Digital Technology, Salt Lake City, Utah 84103, 2014, DOI. 10.13140/RG.2.1.4774.0320

[B16] Marcuvitz, N., "Waveguide Handbook", Peregrinus, 1986

[B17] Mongia, R. K., Bahl, I. J., Bhartia, P., Hong, J., "RF and Microwave Coupled-Line Circuits", Artech House, 2007

[B18] Pozar, D. M., "Microwave Engineering", Wiley, 2012

[B19] Vasiliev, V.A., Romanovskii, Y.M., Chernavskii, D.S. and Yakhno, V.G., "Autowave Processes in Kinetic Systems: Spatial and Temporal Self-Organisation in Physics, Chemistry, Biology, and Medicine", Springer Science & Business Media, 2012

Material Science

[B20] Martienssen, W., Warlimont, H., "Springer Handbook of Condensed Matter and Materials Data", Springer Science & Business Media, 2006

[B21] Michaelides, A., Scheffler, M., "An Introduction to the Theory of Metal Surfaces", Textbook of Surface and Interface Science, Vol. I., Wiley, 2010

Mathematics

[B22] Gradshteyn, I. S., & Ryzhik, I. M., "Table of Integrals, Series, and Products", Elsevier Academic Press, 2007

[B23] Hazewinkel, M, "Galerkin method", Encyclopedia of Mathematics, Springer Science + Business Media, 2001

Measurement Techniques

[B24] Komarov, V., "Permittivity and Measurements", Encyclopedia of RF and Microwave Engineering, Wiley, 2005

[B25] Watts, J.F., Wolstenholme, J., "An introduction to surface analysis by XPS and AES", Wiley Online Library, 2003

NMR and MRI

[B26] Bernstein, M.A.; King, K.F.; Zhou, X.J., "Handbook of MRI Pulse Sequences", Elsevier Academic Press, 2004

[B27] Brown, R. W., et al., "Magnetic Resonance Imaging", Wiley, 2014

[B28] Buxton, R. B., "Introduction to Functional Magnetic Resonance Imaging" Cambridge University Press, 2009

[B29] Mamourian, A. C., "Practical MR Physics", Oxford University Press, 2010

Numerical Techniques

[B30] Cockburn, B., Karniadakis, G., Shu, C.W., "Discontinuous Galerkin Methods: Theory, Computation and Applications" Springer Science & Business Media, 2012

[B31] Hesthaven, J., Warburton, T., "Nodal Discontinuous Galerkin Methods: Algorithms, Analysis, and Applications", Springer Science & Business Media, 2007

[B32] Jin, J.M., "The Finite Element Method in Electromagnetics", John Wiley & Sons, 2002

[B33] Silvester, P. P., R. L. Ferrari, "Finite Elements for Electrical Engineers", 3rd Edition, New York: Cambridge University Press, 1996

Thermodynamics

[B34] Boussinesq, M. J., "L'écoulement tourbillonnant et tumulteux des liquides dans les lits rectilignes a grande section", Gauthier-Villars et fils, Imprimeurs-Libraires, 1897

[B35] deGroot, S.R., Mazur, P., "Non-equilibrium Thermodynamics", Dover Publications, 1984

R.2 Publications

Electrochemistry

[P1] Bryantsev, V.S., Diallo, M.S. and Goddard Iii, W.A., "Calculation of solvation free energies of charged solutes using mixed cluster/continuum models" The Journal of Physical Chemistry B, 2008, Vol. 112(32), pp. 9709-9719

[P2] Glueckauf, E, "The influence of ionic hydration on activity coefficients in concentrated electrolyte solutions", Transactions of the Faraday Society, 1955, Vol. 51, pp. 1235-1244

[P3] Hodgkin, A. L., Huxley, A. F., "A quantitative description of membrane current and its application to conduction and excitation in nerve", The Journal of Physiology, 1952, Vol. 117(4), pp. 500–544

[P4] Hodgkin, A. L., Huxley, A. F., "Currents carried by sodium and potassium ions through the membrane of the giant axon of Loligo", The Journal of Physiology, 1952, Vol. 116(4), pp. 449–472

[P5] Hummer, G., Pratt, L.R. and Garcia, A.E., "Free energy of ionic hydration", The Journal of Physical Chemistry, 1996, Vol. 100(4), pp. 1206-1215

[P6] Lyubartsev, A. P., & Laaksonen, A., "Concentration Effects in Aqueous NaCl Solutions. A Molecular Dynamics Simulation", The Journal of Physical Chemistry, 1996, Vol. 100(40), pp. 16410–16418

[P7] Macdonald, J. R. "Generalizations of universal dielectric response and a general distribution-of-activation-energies model for dielectric and conducting systems", Journal of Applied Physics, 1985, Vol. 58(5), pp. 1971–1978.

[P8] Macdonald, J. R., "Impedance spectroscopy and its use in analyzing the steady-state AC response of solid and liquid electrolytes", Journal of Electroanalytical Chemistry and Interfacial Electrochemistry, 1987, Vol. 223(1-2), pp. 25–50

[P9] Macdonald, J. R., "Static Space-Charge Effects in the Diffuse Double Layer", The Journal of Chemical Physics, 1954, Vol. 22(8), pp. 1317–1322.

[P10] Makino, K. and Ohshima, H., "Electrophoretic mobility of a colloidal particle with constant surface charge density" Langmuir, 2010, Vol. 26(23), pp. 18016-18019.

[P11] Mohanta, S., & Fahidy, T. Z., "The effect of a magnetic field on electrolyte conductivity", Electrochimica Acta, 1976, Vol. 21(1), pp. 25–27

[P12] Mouhat, F., Bonella, S., & Pierleoni, C., "Charge transport simulations of NaCl in an external magnetic field: the quest for the Hall effect", Molecular Physics, 2013, Vol. 111(22-23), pp. 3651–3661

[P13] Nörtemann, K., Hilland, J., & Kaatze, U., "Dielectric Properties of Aqueous NaCl Solutions at Microwave Frequencies", The Journal of Physical Chemistry A, 1997, Vol. 101(37), pp. 6864–6869

[P14] Schalenbach, M., Zeradjanin, A.R., Kasian, O., Cherevko, S., Mayrhofer, K.J., "A perspective on low-temperature water electrolysis – challenges in alkaline and acidic technology", International Journal of Electrochemical Science, 2018, Vol. 13(2), pp. 1173-1226

[P15] Shen, M., Bennett, N., Ding, Y. and Scott, K., "A concise model for evaluating water electrolysis", International Journal of Hydrogen Energy, 2011, Vol. 36(22), pp. 14335-14341

[P16] Shinagawa, T., Garcia-Esparza, A. T., Takanabe, K., "Insight on Tafel slopes from a microkinetic analysis of aqueous electrocatalysis for energy conversion", Nature, Scientific Reports, 2015, Vol. 5(1), pp. 1-21

[P17] Simoes, M. C., Hughes, K. J., Ingham, D. B., Ma, L., & Pourkashanian, M., "Estimation of the Thermochemical Radii and Ionic Volumes of Complex Ions" Inorganic Chemistry, 2017, Vol. 56(13), pp. 7566–7573

[P18] Skúlason, E., Tripkovic, V., Björketun, M. E., Gudmundsdóttir, S., Karlberg, G., Rossmeisl, J., Nørskov, J. K., "Modeling the Electrochemical Hydrogen Oxidation and Evolution Reactions on the Basis of Density Functional Theory Calculations", The Journal of Physical Chemistry C, 2010, Vol. 114(50), pp. 22374–22374

[P19] Vilekar, S. A., Fishtik, I., Datta, R., "Kinetics of the Hydrogen Electrode Reaction", Journal of The Electrochemical Society, 2010, Vol. 157(7), pp. B1040-B1050

[P20] Vincent, C.A., "The motion of ions in solution under the influence of an electric field", Journal of Chemical Education, 1976, Vol. 53(8), pp. 490-493

Electrodmagnetics

[P21] Bardakjian, B.L., Vigmond, E.J., "Effects of the propagation velocity of a surface depolarization wave on the extracellular potential of an excitable cell", IEEE Transactions on Biomedical Engineering, 1994, Vol. 41(5), pp. 432-439

[P22] Eisenstadt, W.R., Eo, Y., "S-parameter-based IC interconnect transmission line characterization", IEEE Transactions on Components, Hybrids, and Manufacturing Technology, 1992, Vol. 15(4), pp. 483–490

[P23] Harms, F., "Elektromagnetische Wellen an einem Draht mit isolierender zylindrischer Hülle", Annalen der Physik, 1907, Vol. 23, pp. 44 - 60

[P24] Marks, R.B., & Williams, D.F., "A general waveguide circuit theory", Journal of Research of the National Institute of Standards and Technology, 1992, Vol. 97(5), pp. 533-562

[P25] McNeal, D.R., "Analysis of a model for excitation of myelinated nerve", IEEE Transactions on Biomedical Engineering, 1976, Vol. 4, pp. 329-337

[P26] Molotkov, I. A., Vakulenko, S. A., "Autowave propagation for general reaction diffusion systems" Wave Motion, 1993, Vol. 17(3), pp. 255–266

[P27] Overfelt, P.L., "Review of Electromagnetic Surface Waves: 1960 through 1987", Naval Weapons Center, China Lake, USA (CA), 1988

[P28] Paoletti, U., Suga, T., & Osaka, H., "Equivalent circuit for Sommerfeld wave", IEICE Electronics Express, 2011, Vol. 8(19), pp. 1590-1595

[P29] Severin, H.; "The various types of transmission line", Philips Technical Review, 1965, Vol. 26, pp. 342-350

[P30] Siart, U., Adrian, S., Eibert, T., "Properties of axial surface waves along dielectrically coated conducting cylinders", Advances in Radio Science, Vol. 10, pp. 79-84.

[P31] Sommerfeld, A., "Ueber die Fortpflanzung elektrodynamischer Wellen längs eines Drahtes", Annalen der Physik und Chemie, 1899, Vol. 67(2), pp. 233-290

[P32] Whites, K.W., " Electromagnetic Wave Propagation Through Circular Waveguides Containing Radially Inhomogeneous Lossy Media", Final Report Army Construction Engineering Research Lab., Champaign, IL, USA, 1989

[P33] Zhabotinsky, A. M., Zaikin, A. N. "Autowave processes in a distributed chemical system", Journal of Theoretical Biology, 1973, Vol. 40(1), pp. 45–61

Electrostatics

[P34] Aghamohammadi, A., "Dimensional analysis and electric potential due to a uniformly charged sheet", European Journal of Physics, 2011, Vol. 32(3), pp. 633–643

[P35] Ciftja, O., "Coulomb self-energy and electrostatic potential of a uniformly charged square in two dimensions" Physics Letters A, 2010, Vol. 374(7), pp. 981–983

[P36] Ciftja, O., "Coulomb self-energy of a uniformly charged three-dimensional cube", Physics Letters A, 2011, Vol. 375(3), pp. 766–767

[P37] Ciftja, O., "Electric potential of a uniformly charged square on its plane", European Journal of Physics, 2011, Vol. 32(6), pp. 55–57

Fluiddynamics

[P38] Bonthuis, D.J., Netz, R.R., "Unraveling the combined effects of dielectric and viscosity profiles on surface capacitance, electro-osmotic mobility, and electric surface conductivity", Langmuir, 2012, Vol. 28(46), pp. 16049-16059

[P39] Lyklema, J., Overbeek, J. T., "On the interpretation of electrokinetic potentials", Journal of Colloid Science, 1961, Vol. 16(5), pp. 501–512

[P40] Lyklema, J., "On the slip process in electrokinetics", Colloids and Surfaces A: Physicochemical and Engineering Aspects, 1994, Vol. 92(1-2), pp. 41–49

[P41] Yao, G.F. , "A computational model for simulation of electroosmotic flow in microsystems", Technical Proceedings of the 2003 Nanotechnology Conference, 2003, Vol. 1, pp. 218-221

Interface Dynamics

[P42] Brummer, S. B., & Turner, M. J., "Electrical stimulation of the nervous system: The principle of safe charge injection with noble metal electrodes", Bioelectrochemistry and Bioenergetics, 1975, Vol. 2(1), pp. 13–25

[P43] Brummer, S. B., McHardy, J., & Turner, M. J., "Electrical Stimulation with Pt Electrodes: Trace Analysis for Dissolved Platinum and Other Dissolved Electrochemical Products. Brain", 1977, Behavior and Evolution, Vol. 14(1-2), pp. 10–22

[P44] Brummer, S.B., McHardy, J. and Turner, M.J., "Electrical stimulation with Pt electrodes: Trace analysis for dissolved platinum and other dissolved electrochemical products", Brain behavior and evolution, 14(1-2), pp. 10-22

[P45] Dobson, J.F., Rose, J.H., "Surface properties of simple metals via inhomogeneous linear electronic response: I. Theory", Journal of Physics C: Solid State Physics., 1982, Vol. 15, pp. 7429-7456

[P46] Fahrenberger, F., "Simulation of Electric Double Layers around Charged Colloids in Aqueous Solution of Variable Permittivity", The Journal of Chemical Physics, 2016, Vol. 141(6), pp. 064902

[P47] Gabovich, A. M. et al, "Screening of charges and Friedel oscillations of the electron density in metals having differently shaped Fermi surfaces", Sov. Phys. JETP, Vol. 48(1), 1978, pp. 124-131

[P48] Gongadze, E., van Rienen, U., Kralj-Iglič, V., Iglič, A., "Spatial variation of permittivity of an electrolyte solution in contact with a charged metal surface: a mini review", Computer Methods in Biomechanics and Biomedical Engineering, 2013, Vol. 16(5), pp. 463-80

[P49] Grahame, D.C., "The Electrical Double Layer and the Theory of Electrocapillarity", Chemical Reviews, 1947, 41 (3), pp. 441–501

[P50] Holze, R., "Table 5.1. Exchange current densities and rate constants in aqueous systems", Landolt-Börnstein, Group IV, Physical Chemistry, 2007, pp. 330–441

[P51] Inglesfield, J.E., "Surface electronic structure", Reports on Progress in Physics, 1982, Vol. 45(3), pp. 223-284

[P52] Keller, R.C., "Calculations of the barrier height and charge distribution of a metal–dielectric interface", Journal of Vacuum Science & Technology A, 1992, Vol. 10, pp. 775-780

[P53] Landstorfer, M. et al., "Theory and structure of the metal-electrolyte interface incorporating adsorption and solvation effects", Electrochimica Acta 201, 2016, pp. 187–219

[P54] Lang, N.D., Kohn, W., "Theory of Metal Surfaces: Charge Density and Surface Energy", Physical Review B, Vol. 1(12), pp. 4555-4568

[P55] McHardy, J., Robblee, L.S., Marston, J.M. and Brummer, S.B., "Electrical stimulation with Pt electrodes. IV. Factors influencing Pt dissolution in inorganic saline", Biomaterials, 1(3), pp. 129-134

[P56] Merrill, D.R., Bikson, M. and Jefferys, J.G.R., "Electrical stimulation of excitable tissue: design of efficacious and safe protocols", Journal of Neuroscience Methods, 2005, Vol. 141(2), pp. 171–198

[P57] Patil, R. S., Juvekar, V. A., & Naik, V. M., "Oxidation of Chloride Ion on Platinum Electrode: Dynamics of Electrode Passivation and its Effect on Oxidation Kinetics", Industrial & Engineering Chemistry Research, 2011, Vol. 50(23), pp. 12946–12959.

[P58] Priyantha, N. and Malavipathirana, S., "Effect of chloride irons on the electrochemical behaviour of platinum surfaces", Journal of the National Science Foundation of Sri Lanka, 1996, Vol. 24(3), pp. 237–246

[P59] Shannon, R. V., "A model of safe levels for electrical stimulation", IEEE Transactions on Biomedical Engineering 39.4 (1992), pp. 424-426

[P60] Singh, M. B., & Kant, R., "Debye-Falkenhagen dynamics of electric double layer in presence of electrode heterogeneities", Journal of Electroanalytical Chemistry, 2013, Vol. 704, pp. 197–207

[P61] Taylor, D.M., Macdonald, A.G., "AC admittance of the metal/insulator/electrolyte interface", Journal of Physics D: Applied Physics, 1987, Vol. 20, pp. 1277-1283

[P62] Tikhonov, A.M., "Water Density in the Electric Double Layer at the Insulator/Electrolyte Solution Interface", Journal of Physical Chemistry B, 2006, Vol. 110(6), pp. 2746-2750

[P63] Zhang, C., "Communication: Computing the Helmholtz capacitance of charged insulator-electrolyte interfaces from the supercell polarization", The Journal of Chemical Physics, 2018, Vol. 149, pp. 031103

[P64] Zhu, H., Ramprasad, R., "Effective work function of metals interfaced with dielectrics: A first-principles study of the Pt-HfO2 interface", Physical Review B, 2011, Vol. 83, pp. 081416-1

[P65] Zolotovitskii, Y.M. et al, "Electron work function from metals in a liquid dielectric", Bulletin of the Academy of Sciences of the USSR, Division of Chemical Science, 1972, Vol. 21(4), pp. 760–763

Measurement Techniques

[P66] Abbou, J., Demaille, C., Druet, M., Moiroux, J., "Fabrication of submicrometer-sized gold electrodes of controlled geometry for scanning electrochemical-atomic force microscopy", Analytical chemistry, 2002, Vol. 74(24), pp. 6355-6363

[P67] Asaki, M. L. T., Redondo, A., Zawodzinski, T. A., & Taylor, A. J., "Dielectric relaxation of electrolyte solutions using terahertz transmission spectroscopy", The Journal of Chemical Physics, 2002, Vol. 116(19), pp. 8469-8482

[P68] Chen, T., Hefter, G., Buchner, R., "Dielectric Spectroscopy of Aqueous Solutions of KCl and CsCl", The Journal of Physical Chemistry A, 2003, Vol. 107(20), pp. 4025–4031

[P69] Comstock, D.J., Elam, J.W., Pellin, M.J., Hersam, M.C., "Integrated ultramicroelectrode-nanopipet probe for concurrent scanning electrochemical microscopy and scanning ion conductance microscopy", Analytical chemistry, 2010, Vol. 82(4), pp. 1270-1276

[P70] Dhillon, S., & Kant, R., "Theory for electrochemical impedance spectroscopy of heterogeneous electrode with distributed capacitance and charge transfer resistance", Journal of Chemical Sciences, 2017, Vol. 129(8), pp. 1277–1292

[P71] Du Bois, D., Du Bois, E.F., "A formula to estimate the approximate surface area if height and weight be known", Archives of Internal Medicine, 1916, Vol. 17 (6), pp. 863-71

[P72] Favaro, M., Jeong, B., Ross, P. N., Yano, J., Hussain, Z., Liu, Z., & Crumlin, E. J., "Unravelling the electrochemical double layer by direct probing of the solid/liquid interface", Nature Communications, 2016, 7, 12695.

[P73] Fowkes, F.M., "Attractive forces at interfaces", Industrial & Engineering Chemistry, 1964, Vol. 56(12), pp. 40-52

[P74] Frederix, P.L., Gullo, M.R., Akiyama, T., Tonin, A., De Rooij, N.F., Staufer, U., Engel, A., "Assessment of insulated conductive cantilevers for biology and electrochemistry", Nanotechnology, 2005, Vol. 16(8), pp. 997-1005

[P75] Giovannetti, G., Frijia, F., Menichetti, L., Hartwig, V., Viti, V., Landini, L., "An efficient method for electrical conductivity measurement in the RF range", Concepts in Magnetic Resonance Part B: Magnetic Resonance Engineering, 2010, Vol. 37B(3), pp. 160–166

[P76] Gu, S., Lin, T., & Lasri, T., "Dielectric properties characterization of saline solutions by near-field microwave microscopy".

Measurement Science and Technology, 2016, Vol. 28(1), pp. 014014

[P77] Hansma, P.K., Drake, B., Marti, O., Gould, S.A.C., Prater, C.B., "The scanning ion-conductance microscope" Science, 1989, Vol. 243(4891), pp. 641-643

[P78] Kueng, A., Kranz, C., Lugstein, A., Bertagnolli, E., Mizaikoff, B., "Integrated AFM–SECM in tapping mode: simultaneous topographical and electrochemical imaging of enzyme activity", "Angewandte Chemie International Edition, 2003, Vol. 42(28), pp. 3238-3240

[P79] Kwak, J., Bard, A.J., "Scanning electrochemical microscopy. Theory of the feedback mode", Analytical Chemistry, 1989, Vol. 61(11), pp. 1221-1227

[P80] Macpherson, J.V. and Unwin, P.R., "Noncontact electrochemical imaging with combined scanning electrochemical atomic force microscopy", Analytical chemistry, 2001, Vol. 73(3), pp. 550-557

[P81] Macpherson, J.V., Jones, C.E., Barker, A.L., Unwin, P.R., "Electrochemical imaging of diffusion through single nanoscale pores", Analytical chemistry, 2002, Vol. 74(8), pp. 1841-1848.

[P82] Macpherson, J.V., Unwin, P.R., "Combined scanning electrochemical atomic force microscope", Analytical Chemistry, 2000, Vol. 72(2), pp. 276-285

[P83] Macpherson, J.V., Unwin, P.R., Hillier, A.C., Bard, A.J., "In-situ imaging of ionic crystal dissolution using an integrated electrochemical/AFM probe", Journal of the American Chemical Society, 1996, Vol. 118(27), pp. 6445-6652.

[P84] Morris, C. A., Chen, C.-C., Baker, L. A., "Transport of redox probes through single pores measured by scanning electrochemical-scanning ion conductance microscopy (SECM-SICM)", The Analyst, 2012, Vol. 137(13), pp. 2933-2938

[P85] Owens, D.K., Wendt, R.C., "Estimation of the surface free energy of polymers", Journal of Applied Polymer Science, 1969, Vol. 13(8), pp. 1741-1747

[P86] Rabi, I. I., Zacharias, J. R., Millman, S., Kusch, P., "A New Method of Measuring Nuclear Magnetic Moment", Physical Review, 1938, Vol. 53(4), pp. 318

[P87] Shanker, N., Bane, S. L., "Basic Aspects of Absorption and Fluorescence Spectroscopy and Resonance Energy Transfer Methods", Methods in Cell Biology, 2008, pp. 213-242

[P88] Shin, H., Hesketh, P.J., Mizaikoff, B., Kranz, C., "Batch fabrication of atomic force microscopy probes with recessed integrated ring microelectrodes at a wafer level", Analytical chemistry, 2007, Vol. 79(13), pp. 4769-4777

[P89] Stuchly, M. A., & Stuchly, S. S., "Coaxial Line Reflection Methods for Measuring Dielectric Properties of Biological Substances at Radio and Microwave Frequencies-A Review", IEEE Transactions on Instrumentation and Measurement, 1980, Vol. 29(3), pp. 176–183

[P90] Takahashi, Y., Shevchuk, A.I., Novak, P., Murakami, Y., Shiku, H., Korchev, Y.E., Matsue, T., "Simultaneous noncontact topography and electrochemical imaging by SECM/SICM featuring ion current feedback regulation", Journal of the American Chemical Society, 2010, Vol. 132(29), pp. 10118-10126

[P91] Takahashi, Y., Shevchuk, A.I., Novak, P., Zhang, Y., Ebejer, N., Macpherson, J.V., Unwin, P.R., Pollard, A.J., Roy, D., Clifford, C.A., Shiku, H., "Multifunctional nanoprobes for nanoscale chemical imaging and localized chemical delivery at surfaces and interfaces", Angewandte Chemie International Edition, 2011, Vol. 50(41), pp. 9638-9642

[P92] Tang, J. X., "Measurements of fluid viscosity using a miniature ball drop device", Review of Scientific Instruments, 2016, Vol. 87(5), pp. 054301

[P93] Van Oss, C.J., Good, R.J., Chaudhury, M.K., "The role of van der Waals forces and hydrogen bonds in hydrophobic interactions between biopolymers and low energy surfaces", Journal of Colloid and Interface Science, 1986, Vol. 111(2), pp. 378-390

[P94] Zhou, Y., Chen, C.C., Baker, L. A., "Heterogeneity of Multiple-Pore Membranes Investigated with Ion Conductance Microscopy", Analytical Chemistry, 2012, Vol. 84(6), pp. 3003–3009

[P95] Zisman, W.A., "Relation of the equilibrium contact angle to liquid and solid constitution", Advances in Chemistry Series, 1964, Vol. 43, pp. 1-51

[P96] Zoski, C.G., Mirkin, M.V., 2002, "Steady-state limiting currents at finite conical microelectrodes", Analytical chemistry, 2002, Vol. 74(9), pp. 1986-1992

Modelling - Leads, Wires, Electrodes, Membranes, Cells and Electrolytes

[P97] Barthel, J. M. G., & Buchner, R., "High frequency permittivity and its use in the investigation of solution properties", Pure and Applied Chemistry, 1991, Vol. 63(10), pp. 1473–1482

[P98] Barthel, J., Buchner, R., "Dielectric permittivity and relaxation of electrolyte solutions and their solvents", Chemical Society Reviews, 1992, Vol. 21(4), pp. 263-270

[P99] Buchner, R., Hefter, G. T., May, P. M., "Dielectric Relaxation of Aqueous NaCl Solutions", The Journal of Physical Chemistry A, 1999, Vol. 103(1), pp. 1–9

[P100] Chandra, A., & Bagchi, B., "Frequency dependence of ionic conductivity of electrolyte solutions", The Journal of Chemical Physics, 2000, Vol. 112(4), pp. 1876–1886

[P101] Debye, P., Hückel, E., "A Theory of Electrolytes", Physikalische Zeitschrift, 1923, Vol. 24(9), pp. 185-206

[P102] Holloway, C. L., Kuester, E.F., "Impedance-type boundary conditions for a periodic interface between a dielectric and a

highly conducting medium", IEEE Transactions on Antennas and Propagation, Vol. 48, No. 10, pp. 1660-1672

[P103] Jones, M. H. & Scott, J. B., "Scaling of Electrode-Electrolyte Interface Model Parameters In Phosphate Buffered Saline", IEEE Transactions on Biomedical Circuits and Systems, 2014 British Crown Copyright

[P104] Scott, J. B. & Single, P., "Compact Nonlinear Model of an Implantable Electrode Array for Spinal Cord Stimulation (SCS)", IEEE Transactions on Biomedical Circuits and Systems, Volume: 8, Issue: 3, June 2014, pp. 382 - 390

[P105] Struijk, J.J., "Passive models for excitable cells", Centre for Sensory-Motor Interaction, Aalborg University, Denmark

MRI Induced Heating

[P106] Goldstein, L.S., et al., "Summary, conclusions and recommendations: adverse temperature levels in the human body", Int. J. Hyperthermia, 2003, Vol. 19(3), pp. 373–384

[P107] Ho, H.S., "Safety of metallic implants in magnetic resonance imaging", Journal of Magnetic Resonance Imaging, 2001, Vol. 14(4), pp. 472–477

[P108] McCabe, S., Scott, J., "A Novel Implant Electrode Design Safe in the RF Field of MRI Scanners", IEEE Transactions on Microwave Theory and Techniques, 2017, Vol. 65(9), pp. 3541–3547

[P109] McCabe, S., Scott, J., "Cause and amelioration of MRI-induced heating through medical implant Lead wires", https://researchcommons.waikato.ac.nz

[P110] McCabe, S., Scott, J., "New MRI-safe Implant Electrode Design", https://researchcommons.waikato.ac.nz

[P111] McCabe, S., Scott, J., "Technique to Minimise RF Electrode Heating", https://researchcommons.waikato.ac.nz

[P112] Nyenhuis, J. A., et al., "MRI and implanted medical devices: basic interactions with an emphasis on heating", IEEE Transactions on

Device and Materials Reliability, Volume: 5, Issue: 3, Sept. 2005, pp. 467-480

[P113] Park, S.-M., Kamondetdacha, R., Nyenhuis, J. A., "Calculation of MRI-induced heating of an implanted medical Lead wire with an electric field transfer function", Journal of Magnetic Resonance Imaging, 2007, Vol. 26(5), pp. 1278–1285

[P114] van Rhoon, G.C., et al., "CEM43°C thermal dose thresholds: a potential guide for magnetic resonance radiofrequency exposure levels?", European Radiology, 2013, Vol. 23(8), pp. 2215–2227

Neural Stimulation

[P115] BeMent, S. L., Ranck, J. B., "A quantitative study of electrical stimulation of central myelinated fibers", Experimental Neurology, 1969, Vol. 24(2), pp. 147–170

[P116] Brown, E.A., Ross, J.D., Blum, R.A., DeWeerth, S.P., "Stimulation and recording of neural tissue, closing the loop on the artifact", Proceedings of the IEEE International Symposium on Circuits and Systems, 2008, pp. 356-359

[P117] Brown, E.A., Ross, J.D., Blum, R.A., Nam, Y., Wheeler, B.C., DeWeerth, S.P., "Stimulus-Artifact Elimination in a Multi-Electrode System", IEEE Transactions on Biomedical Circuits and Systems, 2008, Vol. 2(1), pp. 10–21

[P118] Chu, P., Muller, R., Koralek, A., Carmena, J. M., Rabaey, J. M., Gambini, S., Equalization for intracortical microstimulation artifact reduction", Proceddings of the 35th Annual International Conference of the IEEE Engineering in Medicine and Biology Society (EMBC), Osaka, Japan, 2013, pp. 245-248

[P119] Girsch, W. et al, "Histological assessment of nerve lesions caused by epineural electrode application in rat sciatic nerve" Journal of Neurosurgery, 1991, Vol. 74, pp. 636–642

[P120] Holsheimer, J., "Which Neuronal Elements are Activated Directly by Spinal Cord Stimulation", Neuromodulation: Technology at the Neural Interface, 2002, Vol. 5(1), pp. 25–31

[P121] Holsheimer, J., Struijk, J. J., "How Do Geometric Factors Influence Epidural Spinal Cord Stimulation?", Stereotactic and Functional Neurosurgery, 1991, Vol. 56(1-4), pp. 234–249

[P122] Holsheimer, J., Struijk, J.J., Wesselink, W.A., "Analysis of spinal cord stimulation and design of epidural electrodes by computer modeling", Neuromodulation: Technology at the Neural Interface, 1998, Vol. 1(1), pp. 14-18

[P123] Lapicque, L., "Recherches quantitatives sur l'excitation électrique des nerfs traitée comme une polarisation", Journal de physiologie et de pathologie générale, 1907, Vol. 9, pp. 620-635

[P124] Miller, J. P., Eldabe, S., Buchser, E., Johanek, L. M., Guan, Y. Linderoth, B., "Parameters of Spinal Cord Stimulation and Their Role in Electrical Charge Delivery: A Review", Neuromodulation: Technology at the Neural Interface, 2016, Vol. 19(4), pp. 373–384

[P125] Robbins, A.A., Fox, S.E., Holmes, G.L., Scott, R.C., Barry, J.M., "Short duration waveforms recorded extracellularly from freely moving rats are representative of axonal activity", Frontiers in Neural Circuits, 2013, Vol. 7, pp. 181-192

[P126] Roxin, A., Brunel, N., Hansel, D., Mongillo, G., van Vreeswijk, C., "On the distribution of firing rates in networks of cortical neurons", Journal of Neuroscience, 2011, Vol. 31(45), pp. 16217-16226

[P127] Shealy, C.N., Taslitz, N., Mortimer, J.T., Becker, D.P., "Electrical inhibition of pain: experimental evaluation" Anesthesia & Analgesia, 1967, Vol. 46(3), pp. 299-305

[P128] Shealy, C.N., Mortimer, J.T., Reswick, J.B., "Electrical inhibition of pain by stimulation of the dorsal columns: preliminary clinical report", Anesthesia & Analgesia, 1967, Vol. 46(4), pp. 489-491

[P129] Stecker, M. et al., "Factors Affecting Stimulus Artifact: Solution Factors", EC Neurology, 2017, Vol. 5.2, pp. 52-61

[P130] Wall, P.D. Sweet, W.H., "Temporary abolition of pain in man", Science, 1967, Vol. 155(3758), pp. 108-109

[P131] Wesselink, W. A., Holsheimer, J., Nuttin, B., Boom, H. B. K., King, G. W., Gybels, J. M., de Sutter, P., "Estimation of fiber diameters in the spinal dorsal columns from clinical data", IEEE Transactions on Biomedical Engineering, 1998, Vol. 45(11), pp. 1355–1362

[P132] Wesselink, W., "Analysis of Current Density and Related Parameters in Spinal Cord Stimulation", IEEE Transactions on Rehabilitation Engineering, 1998, Vol. 6(2), pp. 200-207

[P133] Zhou, A. et al, "Toward true closed-loop neuromodulation: artifact-free recording during stimulation", Current Opinion in Neurobiology, 2018, Vol. 50, pp. 119–127

NMR and MRI

[P134] Gibbs, E., Liu, Ch., " Feasibility of Imaging Tissue Electrical Conductivity by Switching Field Gradients with MRI", Tomography, 2015, Vol. 1, No. 2, pp. 125–135

[P135] Larmor, J., "LXIII. On the theory of the magnetic influence on spectra; and on the radiation from moving ions", The London, Edinburgh, and Dublin Philosophical Magazine and Journal of Science, 1897, Vol. 44(271), pp. 503–512

[P136] Smith, S. A., Edden, R. A. E., Farrell, J. A. D., Barker, P. B., Van Zijl, P. C. M., "Measurement of T1 and T2 in the cervical spinal cord at 3 Tesla", Magnetic Resonance in Medicine, 2008, Vol. 60(1), pp. 213–219

[P137] Stanisz, G.J., et al.; "T1, T2 Relaxation and Magnetization Transfer in Tissue at 3T"; Magnetic Resonance in Medicine; 2005, Vol. 54, Issue 3, pp. 507-512

Numerical Techniques

[P138] Arnold, D.N., "Differential complexes and numerical stability", International Congress of Mathematicians, China, Beijing, 24 August 2002

[P139] Baker, T. J., "Three Dimensional Mesh Generation By Triangulation of Arbitrary Point Sets", American Institute of Aeronautics and Astronautics, 1987,Technical Report AIAA-87-1124

[P140] Bardi, I., Peng, G., Cendes, Z.J, "Improvements in Adaptive Mesh Refinement and Multi-level methods in High Frequency Electromagnetics", ACES Symposium, 2002

[P141] Barth, T. J., "Three-Dimensional Unstructured Grid Generation via Incremental Insertion and Local Optimization In Software Systems for Surface Modelling and Grid Generation", Langley Research Center, Hampton, Virginia, April 1992, NASA Conference Publication. 3143

[P142] Bowyer, A., "Computing Dirichlet tessellations", The Computer Journal, 1981, Vol. 24, No. 2, pp. 162-166

[P143] Chorin. A. J., "Numerical solution of Navier-Stokes equations", Mathematics of Computation, 1968, Vol. 22, pp. 745–762

[P144] Hesthaven, J., Warburton, T., "Nodal high-order methods on unstructured grids", Journal of Computational Physics, September 2002, Vol. 181, No. 1, pp. 186-221

[P145] Hutchinson, B. R., Raithby, G. D., "A Multigrid Method Based on the Additive Correction Strategy", Numerical Heat Transfer, 1986, Vol. 9, pp. 511–537

[P146] Kallinderis, Y., "Hybrid Prismatic/Tetrahedral Grid Generation for Complex Geometries", American Institute of Aeronautics and Astronautics, 1995, Technical Report AIAA-95-0211

[P147] Liu, H., Jiao, D., "H-matrix-based fast direct finite element solver for large-scale electromagnetic analysis",. ECE Technical Reports, 2010, Paper 396

[P148] Löhner, R., "Generation of Three-Dimensional Unstructured Grids by the Advancing Front Method", American Institute of Aeronautics and Astronautics, 1988, Technical Report, AIAA-88-0515

[P149] Meijerink, J. A.; Vorst, Van Der; A, H., "An iterative solution method for linear systems of which the coefficient matrix is a symmetric M-matrix", Mathematics of Computation, 1977, Vol. 31 (137), pp. 148-162

[P150] Sun, D. K., Lee J. F., Cendes, Z. J., "Construction of nearly orthogonal Nedelec bases for rapid convergence with multilevel preconditioned solvers", SIAM Journal on Scientific Computing, 2001, Vol. 23, No. 4, pp. 1053-1076

Pain Mechanisms

[P151] Melzack, R., Wall, P.D., "Pain Mechnisms: A New Theory", Science, 1965, Vol. 150(3699), pp. 971-979

[P152] Moayedi, M., Davis, K.D., "Theories of pain: from specificity to gate control", Neurophysiol Journal, 2013, Vol. 109, pp. 5–12

Properties of Matter

[P153] Adamczyk, Z., Bratek, A., Jachimska, B., Jasiński, T., & Warszyński, P., "Structure of Poly(acrylic acid) in Electrolyte Solutions Determined from Simulations and Viscosity Measurements", The Journal of Physical Chemistry B, 2006, Vol. 110(45), pp. 22426–22435

[P154] Baker-Jarvis, J., Kim, S., "The Interaction of Radio-Frequency Fields with Dielectric Materials at Macroscopic to Mesoscopic Scales", Journal of Research of the National Institute of Standards and Technology, 2012, Volume 117, pp. 1-60

[P155] Biotectix, "Amplicoat: Conductive medical electrode coating with proven clinical performance for enhanced sensing and stimulation" www.biotectix.com

[P156] Bondy, G.P., "Cerebrospinal Fluid", Department of Pathology and Laboratory Medicine at the University of British Columbia, November 2011

[P157] Flory, P. J., & Osterheld, J. E., "Intrinsic Viscosities of Polyelectrolytes. Poly-(acrylic Acid)", The Journal of Physical Chemistry, 1954, Vol. 58(8), pp. 653–661

[P158] Gabriel, C., "Compilation of the dielectric properties of body tissues at RF and microwave frequencies", Physics Department King's College London, WC2R 2LS, UK, 1996

[P159] Green, R. A., Baek, S., Poole-Warren, L. A., Martens, P. J., "Conducting polymer-hydrogels for medical electrode applications", Science and Technology of Advanced Materials, 2010, Vol. 11(1), pp. 014107

[P160] Gubskaya, A. V., & Kusalik, P. G, "The total molecular dipole moment for liquid water", The Journal of Chemical Physics, 2002, Vol. 117(11), pp. 5290–5302

[P161] Neusel, C., & Schneider, G. A., "Size-dependence of the dielectric breakdown strength from nano- to millimeter scale", Journal of the Mechanics and Physics of Solids, 2014, Vol. 63, pp. 201–213

[P162] Park, S. M., Nyenhuis, J. A., Smith, C. D., Lim, E. J., Foster, K. S., Baker, K. B., Tkach, J., "Gelled versus nongelled phantom material for measurement of MRI-induced temperature increases with bioimplants", IEEE Transactions on Magnetics, 2003, Vol. 39(5), pp. 3367–3371

[P163] Ravichandran, R., Sundarrajan, S., Venugopal, J. R., Mukherjee, S., Ramakrishna, S., "Applications of conducting polymers and their issues in biomedical engineering", Journal of The Royal Society Interface, 2010, Vol. 7 (Supplement 5), pp. 559–579

[P164] Schroeder, M.J., Sadasiva, A., Nelson, R.M., "An analysis on the role of water content and state on effective permittivity using mixing formulas", Journal of Biomechanics, Biomedical, and Biophysical Engineering, 2008, Vol. 2(1), pp. 1-11

[P165] Schwan, H. P., "Electrical Properties of Bound Water", Annals of the New York Academy of Sciences, 1965, Vol. 125, pp. 344-354

[P166] Scipioni, R., Schmidt, D. A., Boero, M., "A first principles investigation of water dipole moment in a defective continuous hydrogen bond network", The Journal of Chemical Physics, 2009, Vol. 130(2), pp. 024502

[P167] Teschke, O., Ceotto, G., de Souza, E. F., "Interfacial water dielectric-permittivity-profile measurements using atomic force microscopy", Physical Review E, 2001, Vol. 64, pp. 1-10

Spinal Cord

[P168] Ellis, H., "The anatomy of the epidural space", Anaesthesia & Intensive Care Medicine, 2006, Vol. 7(11), pp. 402-404

[P169] Elsharkawy, H., Sonny A., Chin K.J., "Localization of epidural space: A review of available technologies", Journal of Anaesthesiology Clinical Pharmacology, 2017, Vol. 33(1), pp. 16-27

[P170] Feirabend, H.K.P., Choufoer, H., Ploeger, S., Holsheimer, J., Van Gool, J.D., "Morphometry of human superficial dorsal and dorsolateral column fibres: significance to spinal cord stimulation", Brain, 2002, Vol. 125(5), pp. 137-1149

[P171] Fradet, L., Arnoux, P.-J., Ranjeva, J.-P., Petit, Y., Callot, V., "Morphometrics of the Entire Human Spinal Cord and Spinal Canal Measured From In Vivo High-Resolution Anatomical Magnetic Resonance Imaging", Spine, 2014, Vol. 39(4), pp. E262–E269

[P172] Liu, Y., Zhou, X., Ma, J., Ge, Y., Cao, X., "The diameters and number of nerve fibers in spinal nerve roots" The Journal of Spinal Cord Medicine, 2015, Vol. 38(4), pp. 532-537

[P173] Ravi, K.K., Kaul, T.K., Kathuria, S., Gupta, S., Khurana, S., "Distance from Skin to Epidural Space: Correlation with Body Mass Index (BMI)", Journal of Anaesthesiology Clinical Pharmacology, 2011, Vol. 27(1), pp. 39-42

[P174] Tan, S.H., Teo, E.C., Chua, H.C., "Quantitative three-dimensional anatomy of cervical, thoracic and lumbar vertebrae of Chinese Singaporeans", European Spine Journal, 2004, Vol. 13(2), pp. 137-146

Surface Roughness

[P175] Hall, S., et al., "Multigigahertz Causal Transmission Line Modeling Methodology Using a 3-D Hemispherical Surface Roughness Approach", IEEE Transactions on Microwave Theory and Techniques, Dec. 2007, Vol. 55, No. 12, pp. 2614-2624

[P176] Hammerstad, E., & Jensen, O., "Accurate Models for Microstrip Computer-Aided Design," IEEE MTT-S International Microwave Symposium Digest, Washington, DC, USA, 1980, pp. 407-409

[P177] Huray, P.G., et al., "Impact of Copper Surface Texture on Loss: A Model that Works", DesignCon 2010, Vol. 1, pp. 462-483.

[P178] Lukic, M. V., Filipovic, D.S., "Modeling of 3-D Surface Roughness Effects With Application to Coaxial Lines", IEEE Transactions on Microwave Theory and Techniques, 2007, Vol. 55, No. 3, pp. 518-525

[P179] Morgan, S.P., "Effect of Surface Roughness on Eddy Current Losses at Microwave Frequencies", Journal of Applied Physics, 1949, Vol. 20, pp. 352-362

[P180] Sanderson, A. E., "Effect of surface roughness on propagation of the TEM mode", Advances in Microwaves, 1971, Vol. 1, pp. 1-57

[P181] Shlepnev, Y., Nwachukwu, Ch., "Roughness characterization for interconnect analysis", IEEE International Symposium on Electromagnetic Compatibility (EMC), 2011, pp. 518-523

[P182] Simonovich, B., "Practical Method for Modelling Conductor Surface Roughness Using Close Packing of Equal Spheres", DesignCon 2015

[P183] Tsang, L., Gu, X., Braunisch, H., "Effects of random rough surfaces on absorption by conductors at microwave frequencies", IEEE Microwave and Wireless Components Letters, April 2006, Vol. 16, No. 4, pp. 221- 223

Thermodynamics

[P184] Cundin, L.X., Roach, W.P. and Millenbaugh, N., "Empirical comparison of Pennes' bio-heat equation", Optical Interactions with Tissue and Cells XX, International Society for Optics and Photonics, 2009, Vol. 7175, pp. 16-1 - 16-9

[P185] Liu, Y., Hopkins, C. C., Handler, W. B., Chronik, B. A., de Bruyn, J. R., "Rheology and heat transport properties of a hydroxyethyl cellulose-based MRI tissue phantom", Biomedical Physics & Engineering Express", 2017,. Vol. 3(4), pp. 045008

[P186] Pennes, H.H., "Analysis of tissue and arterial blood temperatures in the resting human forearm", Journal of Applied Physiology, 1948, Vol. 1(2), pp. 93-122

R.3 Specifications and standards

[SPE1] ASTM Int'l F2052 "Standard Test Method for Measurement of Magnetically Induced Displacement Force on Medical Devices in the Magnetic Resonance Environment", www.astm.org

[SPE2] ASTM Int'l F2182(11a), "Standard Test Method for Measurement of Radio Frequency Induced Heating On or Near Passive Implants During Magnetic Resonance imaging", www.astm.org

[SPE3] ASTM Int'l F2213, "Standard Test Method for Measurement of Magnetically Induced Torque on Medical Devices in the Magnetic Resonance Environment", www.astm.org

[SPE4] U.S. Department of Health and Human Services Food and Drug Administration, Centre for Devices and Radiological Health, "Criteria for Significant Risk Investigations of Magnetic Resonance Diagnostic Devices", June 2014

R.4 Software

[SW1] ANSYS Electromagnetics Suite, Manual, Release 18.2, July 2017

[SW2] ANSYS Fluent, User's Guide, Release 17.0, January 2016

[SW3] ANSYS Fluent, Theory Guide, Release 17.0, January 2016

[SW4] ANSYS Meshing, User's Guide, Release 18.2, August 2017

R.5 Databases

[DB1] "Biological tissues and fluids database", Foundation for Research on Information Technologies in Society, Date 12.10.2016 (release 3.1)

[DB2] National Standard Reference Data System, "Bond Dissociation Energies in Simple Molecules", Nat. Stand. Ref. Data Ser., Nat. Bur. Stand. (U.S.), 31, 52 pages (Jan. 1970)

[DB3] Zakarian, A., "Bond Dissociation Energies", University of California Santa Barbara, https://labs.chem.ucsb.edu/zakarian/armen/11---bonddissociationenergy.pdf

R.6 Internet

[IN1] Types of pain
https://nba.uth.tmc.edu/neuroscience/s2/chapter07.html
Date: October 2018

Appendices

A Properties of matter

A.1 Human tissue

The table below summarises electro-dynamic and thermodynamic characteristics of human tissue and bones along the spinal canal.

Human tissue	**Energy storage per cycle ε_s**	**Loss per cycle ε_l**	**Conductivity σ $\left[\frac{S}{m}\right]$**
Epidural space (cerebrospinal fluid)	84	301	2.1
White matter	53	48	0.3
Grey matter	74	82	0.6
Hard bones	6 ... 26	3 ... 25	0.02 ... 0.2

Table A-1 Electrical characteristics for selected human tissues at 128 MHz [P158]

Cerebrospinal fluid (CSF)

Part	**Symbol**	**Value**	**Unit**
Water	H_2O	99.0	%
Sodium	Na	135 ... 150	$\frac{mmol}{litre}$
Potassium	K	2.6 ... 3.0	$\frac{mmol}{litre}$
Chlorine	Cl	115 ... 130	$\frac{mmol}{litre}$
Calcium	Ca	1.0 ... 1.4	$\frac{mmol}{litre}$
Magnesium	Mg	1.2 ... 1.5	$\frac{mmol}{litre}$
Iron	Fe	0.2 ... 0.4	$\frac{\mu mol}{litre}$

Table A-2 Constituent chemical species of CSF [P156]

Parameter	Symbol	Value	Unit
Total amount of fluid (absorbed and free)	$V_{cfs,t}$	~ 0.500	$liter$
Amount of free fluid	$V_{cfs,f}$	$0.100 \ldots 0.160$	$liter$
Rate of production	r_{prod}	$5.8 \cdot 10^{-6}$	$\frac{liter}{s}$
Rate of production	r_{prod}	$11.6 \cdot 10^{-6}$	$\frac{1}{s}$
Rate of perfusion	$r_{perf} = r_{prod}$	$11.6 \cdot 10^{-6}$	$\frac{1}{s}$
Mass density	ρ	1007	$\frac{kg}{m^3}$
Mass specific heat capacity	c	4096	$\frac{J}{kg \cdot K}$
Thermal conductivity	k	0.57	$\frac{W}{m \cdot K}$
Rate of metabolic heat generation	q	0.0	$\frac{W}{m^3}$

Table A-3 Thermodynamic parameter of CSF [DB1]

A.2 Platinum

Typical platinum Lead wires and electrodes (without coatings) have following characteristics:

Characteristic	Value	Unit
Conductivity	$9.4 \cdot 10^{6}$	$\frac{S}{m}$
Electron density	$6.6 \cdot 10^{28}$	$\left[\frac{electrons}{m^3}\right]$
Mean free flight time of electrons between collisions for $E = 1\frac{V}{m}$	$5.0 \cdot 10^{-15}$	s
Mean free path length of electrons between collisions for $E = 1\frac{V}{m}$	$4.5 \cdot 10^{-18}$	m
Relaxation time of electrons	$9.4 \cdot 10^{-19}$	s
Drift velocity of electrons for $E = 1\frac{V}{m}$	$8.9 \cdot 10^{-4}$	$\frac{m}{s}$
Mass density	$\sim 21'460$	$\frac{kg}{m^3}$
Thermal capacity	~ 133	$\frac{J}{kg \cdot K}$
Thermal conductivity	~ 72	$\frac{W}{m \cdot K}$
Thermal expansion	$\sim 8.8 \cdot 10^{-6}$	$\frac{1}{K}$

Table A-4 Typical characteristics of platinum Lead wires and electrodes [B20]

Magnitudes of fields are normalised to the values of the transmitted components at $z = 0$.

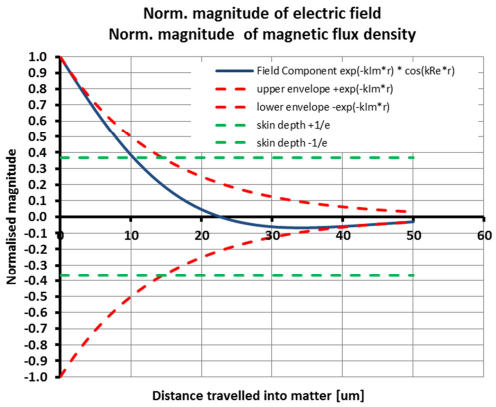

Figure A-1 Normalised dampened field magnitude (platinum)

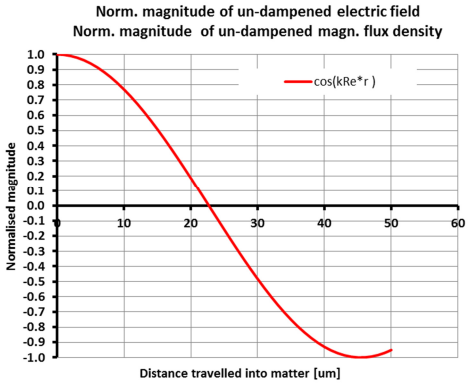

Figure A-2 Normalised un-dampened field magnitude (platinum)

Characteristic	**Symbol**	**Value**	**Unit**
Propagation velocity	$\lvert\vec{v}_{wave}\rvert$	$\approx 8.3 \cdot 10^3$	$\frac{m}{s}$
Wavelength	$\lambda_{wave,platinum}$	≈ 91	μm
Attenuation constant	k_{Im}	≈ 55	$\frac{dB}{\lambda_{wave,platinum}}$
Phase constant	k_{Re}	≈ 6.283	$\frac{rad}{\lambda_{wave,platinum}}$
Skin depth	$\delta_{wave,platinum}$	≈ 14.5	μm

Table A-5 Characteristics of electromagnetic waves in platinum

Velocity	**Symbol**	**Value**	**Unit**
Electromagnetic wave	$\lvert\vec{v}_{wave}\rvert$	$\sim 8.3 \cdot 10^3$	$\frac{m}{s}$
Fermi velocity of particle (electron)	$\lvert\vec{v}_{F,3D,particle}\rvert$	$\sim 1.4 \cdot 10^6$	$\frac{m}{s}$
Fermi velocity of wave (electron)	$\lvert\vec{v}_{F,3D,wave}\rvert$	$\sim 7.2 \cdot 10^5$	$\frac{m}{s}$
Orbital velocity of particle (electron)	$\lvert\vec{v}_{orbit,\,mass}\rvert$	$\sim 2.8 \cdot 10^4$	$\frac{m}{s}$
Orbital velocity of wave (electron)	$\lvert\vec{v}_{orbit,\,wave}\rvert$	$\sim 1.4 \cdot 10^4$	$\frac{m}{s}$
Thermal velocity of particle (electron)	$\lvert\vec{v}_{thermal,\,mass}\rvert$	$\sim 1.1 \cdot 10^5$	$\frac{m}{s}$

Table A-6 Comparison of wave and particle (electron) velocities in platinum

A.3 Pellethane

Pellethane has following characteristics:

Characteristic	Value	Unit
Material	Pellethane® 2363-55D TPU	
Permittivity	~ 6.5	N/A
Dielectric loss tangent	~ 0.03	N/A
Dielectric strength	~ 45	$\frac{kV}{mm}$
Coefficient of Linear Thermal Expansion	$\sim 150 \cdot 10^{-6}$	$\frac{mm}{mm \cdot K}$
Mass density	$\sim 1'175$	$\frac{kg}{m^3}$
Surface resistivity	$\sim 10^{11}$	$\Omega \cdot$ □
Thermal heat capacity	~ 500	$\frac{J}{kg \cdot K}$
Thermal conductivity	~ 1.7	$\frac{W}{m \cdot K}$
Thermal expansion	$\sim 8.8 \cdot 10^{-6}$	$\frac{1}{K}$

Table A-7 Characteristics of Pellethane [B20]

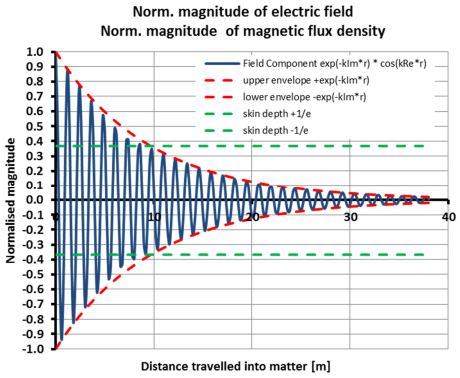

Figure A-3 Normalised field magnitude (Pellethane, period not to scale)

Characteristic	Symbol	Value	Unit
Propagation velocity	$\lvert\vec{v}_{wave}\rvert$	$\approx 1.6 \cdot 10^8$	$\frac{m}{s}$
Wavelength	$\lambda_{wave,Pellethane}$	≈ 1217	mm
Attenuation constant	k_{Im}	≈ 1.1	$\frac{dB}{\lambda_{wave,Pellethane}}$
Phase constant	k_{Re}	≈ 6.283	$\frac{rad}{\lambda_{wave,Pellethane}}$
Skin depth	$\delta_{wave,Pellethane}$	≈ 9.7	m

Table A-8 Characteristics of electromagnetic waves in Pellethane

A.4 Saline solution

The saline solution referenced in the table below has been used for transient and artefact measurements on spinal cord stimulator Leads.

Type	Characteristics
Saline	Deionised water with 0.94 g/litre NaCl Molarity ~ 0.011 mol/litre Conductivity ~ 0.188 S/m

Table A-9 Characteristics of saline solution

A.5 Gelled saline solution

The table below summarises electrical characteristics of gelled NaCl solution used for testing of spinal cord stimulators (Leads and IPGs) in phantom torsos (PT). The gelled saline solution is electrically and thermally equivalent to the composite matter encountered in humans but without taking into account heat convection through perfusion.

Characteristic	Value	Unit
Energy storage per cycle ε_s at 128 MHz (relative permittivity)	~ 80	-
Loss per cycle ε_l at 128 MHz	~ 4	-
Conductivity (DC ... 200 MHz)	~ 0.47	$\frac{S}{m}$
Mass density	~ 993	$\frac{kg}{m^3}$
Thermal capacity	~ 4200	$\frac{J}{kg \cdot K}$
Thermal conductivity	~ 0.62	$\frac{W}{m \cdot K}$
Thermal diffusion coefficient (thermal diffusivity)	$\sim 130 \cdot 10^{-9}$	$\frac{m^2}{s}$
Thermal expansion coefficient at 1 bar	$\sim 215 \cdot 10^{-6}$	$\frac{1}{K}$
Dynamic viscosity	~ 0.1	$Pa \cdot s$

Table A-10 Characteristics of gelled saline at 20 °C

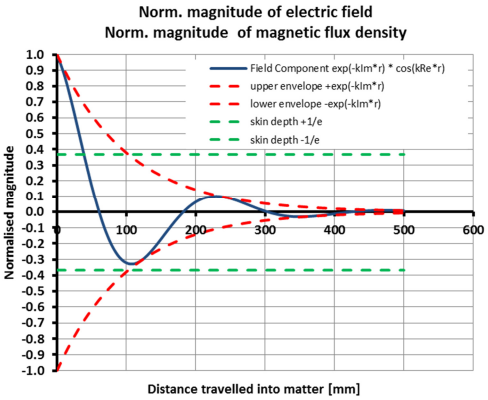

Figure A-4 Normalised field magnitude (gelled saline)

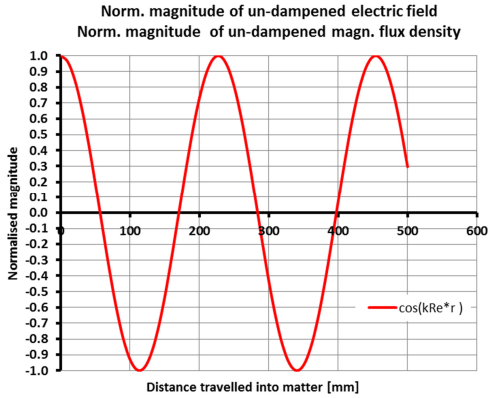

Figure A-5 Normalised un-dampened field magnitude (gelled saline)

Characteristic	Symbol	Value	Unit
Planar wave impedance	$\tilde{Z}_{wave}$	$\approx 34.2 + j \cdot 12.8$	Ohm
Propagation velocity	$\lvert\vec{v}_{wave}\rvert$	$\approx 2.6 \cdot 10^7$	$\frac{m}{s}$
Wavelength	$\lambda_{wave,saline}$	≈ 243	mm
Attenuation constant	k_{Im}	≈ 20.5	$\frac{dB}{\lambda_{wave,saline}}$
Phase constant	k_{Re}	≈ 6.283	$\frac{rad}{\lambda_{wave,saline}}$
Skin depth	$\delta_{wave,saline}$	≈ 105	mm

Table A-11 Characteristics of electromagnetic waves in saline

The recipe for the gelled saline solution is indicated below [SPE2]:

Deionized or distilled water (conductivity less than $1.0\ \frac{mS}{m}$)

Saline (NaCl, reagent grade, >99 % pure): $1.4\ \frac{g}{litre}$

Polyacrylic acid (PAA): $9.0\ \frac{g}{litre}$ (Sigma Aldrich #43636)

B MRI scanner parameter

B.1 MRI scanner - GE - 3.0 T

The sequence and parameter used for test runs in a 3-Tesla General Electric Horizontal Field Scanner (Discovery™ MR750 3.0T - 60cm) are summarised in Table B-1.

Parameter	Values
Fast spin echo sequence	N/A
Lumbar region	N/A
First level controlled operating mode	N/A
TR	425 ms
TE	14 ms
Transmit pulses	20 pulses in 425 ms
Echo train length	4
Plane	axial
Flip angle	90°
Bandwidth	16 kHz
Field of view	40 cm
Matrix	256x256
Section thickness	10 mm
Total slices	40
Transmit gain	175
SAR - 10 second gliding average over total scan time	2.4 W/kg
Scan time	15 minutes per electrode

Table B-1 MRI parameter

B.2 MRI gradient pulse pattern parameter

Parameter	Symbol	Values
Maximum magnetic flux density at iso-centre	$B_{G,max}$	$0.5, 1, 2.5, 5, 10, 15, 20\ \mu T$
Pulse shape	N/A	$trapezoidal$
Pulse width	T	$T = 2 \cdot t_d + 2 \cdot t_f$
Burst width	$N \cdot T$	$N = 1, 2, 5, 10, 20$
Dwell time	$t_d = t_2 - t_1$	$0.0, 0.5, 5.0, 20.0\ ms$
Fall time (peak - peak)	$t_f = t_4 - t_2$	$0.2, 0.4, 1.0, 2.0\ ms$
Off time	$t_{off} = t_S - t_N$	$0.2, 0.5, 1.0, 2.0, 5.0, 10.0, 20.0, 50.0, 100.0\ ms$ $200.0, 500.0, 1000.0, 2000.0\ ms$
Exposure time (number of bursts)	t_e	$min. 15\ s$

Table B-2 Typical gradient pulse parameter for MRI scanner - GE - 3.0 T

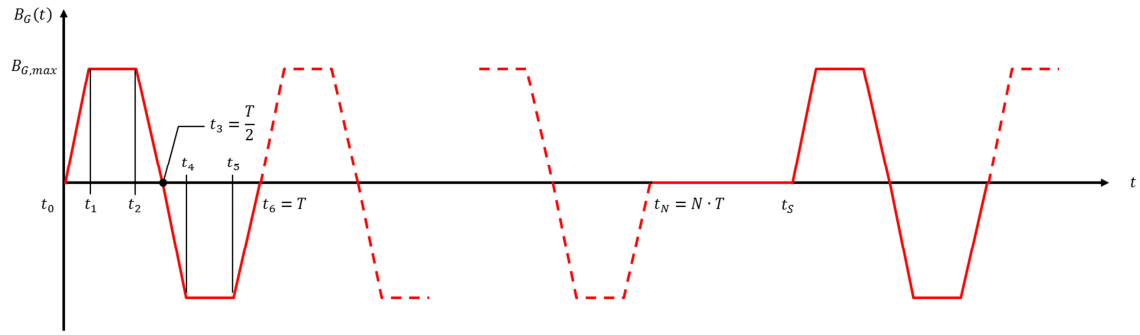

Figure B-1 Typical gradient field pulse pattern for MRI scanner - GE - 3.0 T

B.3 MRI RF pulse pattern parameter

Parameter	Values
Peak magnetic flux density at pulse centre	$B_{1,max} = 1, 2, 5, 10, 20, 30\ \mu T$
Pulse shape	$square$
Frequency	$128 \pm 0.5\ MHz\ (at\ 3\ Tesla)$
Polarisation	$circular$
Rise/fall time of pulse shape	$max. 500\ ns$
Exposure time per sequence	$min. 15\ s$

Table B-3 Typical RF pulse parameter for MRI scanner - GE - 3.0 T

	Pulse width τ							
Pulse period T	50 µs	100 µs	200 µs	500 µs	1 ms	2 ms	5 ms	10 ms
1 ms	test	test	test	---	---	---	---	---
2 ms	test	test	test	---	---	---	---	---
5 ms	test	test	test	test	test	---	---	---
10 ms	test	test	test	test	test	test	---	---
20 ms	test	test	test	test	test	test	---	---
50 ms	test	test	test	test	test	test	test	test
100 ms	test	test	test	test	test	test	test	test
200 ms	test	test	test	test	test	test	test	test
500 ms	test	test	test	test	test	test	test	test
1000 ms	test	test	test	test	test	test	test	test

Table B-4 Typical pulse widths and pulse periods MRI scanner - GE - 3.0 T

C Electromagnetic modelling

C.1. Surface currents on electrodes

A simple model for determining the order of magnitude of surface currents on electrodes is indicated in Figure C-1 and Figure C-2 below.

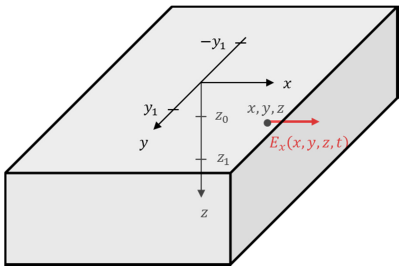

Figure C-1 Coordinate system

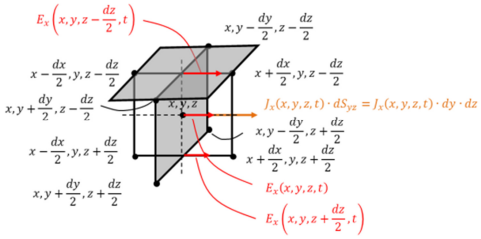

Figure C-2 Field components

Current I_x as sum of current density J_x through surface in y,z plane

$$I_x = \int_S \vec{J}(y,z)\cdot d\vec{S} = \int_S J_x(y,z)\cdot dS_{yz} = \sigma \cdot \int_{y=-y_1}^{y_1}\left(\int_{z=z_0}^{z_1} E_x(y,z)\cdot dz\right)\cdot dy \tag{C-1}$$

... with ...

$$E_x(y,z) = E_{x,max}\cdot e^{j\tilde{k}_y\cdot y}\cdot e^{j\tilde{k}_z\cdot z} \tag{C-2}$$

... follows ...

$$I_x = \int_S \vec{J}(y,z,t)\cdot d\vec{S} = \sigma\cdot E_{x,max}\cdot \int_{y=-y_1}^{y_1} e^{j\tilde{k}_y\cdot y}\cdot\left(\int_{z=z_0}^{z_1} e^{j\tilde{k}_z\cdot z}\cdot dz\right)\cdot dy \tag{C-3}$$

... and solving the integral for the real part and the imaginary part ([B22]) results in ...

$$Re\{I_x\} = \sigma \cdot E_{x,max} \cdot \left(\frac{1}{\left(-k_{Im,z}\right)^2 + \left(k_{Re,z}\right)^2} \cdot \left[\left(-k_{Im,z} \cdot cos\left(k_{Re,z} \cdot z\right) + k_{Re,z} \cdot sin\left(k_{Re,z} \cdot z\right) \right) \cdot e^{-k_{Im,z} \cdot z} \right]_{z_0}^{z_1} \right) \cdot \Delta y \quad \text{(C-4)}$$

$$Im\{I_x\} = \sigma \cdot E_{x,max} \cdot \left(\frac{1}{\left(-k_{Im,z}\right)^2 + \left(k_{Re,z}\right)^2} \cdot \left[\left(-k_{Im,z} \cdot sin\left(k_{Re,z} \cdot z\right) - k_{Re,z} \cdot cos\left(k_{Re,z} \cdot z\right) \right) \cdot e^{-k_{Im,z} \cdot z} \right]_{z_0}^{z_1} \right) \cdot \Delta y \quad \text{(C-5)}$$

C.2. RF permittivity and conductivity extraction

Material parameter of matter can be extracted from s-parameter measurements of coaxial cavities (CC) embedded in coaxial transmission lines with known characteristic impedance ([B24], [P21], [P89]). This approach is used to determine RF permittivities and conductivities of electrolytes (Figure C-3). Other approaches for material parameter extractions from s-parameter measurements are outlined in References [P75] and [P76]. A theory for the frequency dependence of ionic conductivity of electrolyte solutions is outlined in Reference [P100]. The dimensions of the coaxial cavity are given in Figure C-4 and an equivalent transmission line circuit is shown in Figure C-5.

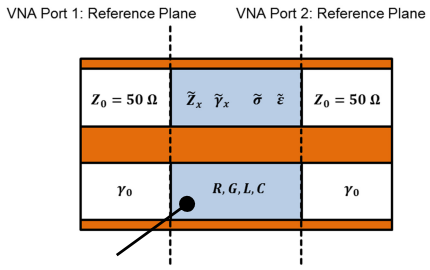

Coaxial Cavity (CC)

Figure C-3 Schematic of coaxial test fixture

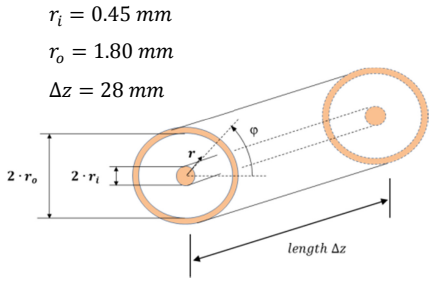

Figure C-4 Dimensions of coaxial cavity

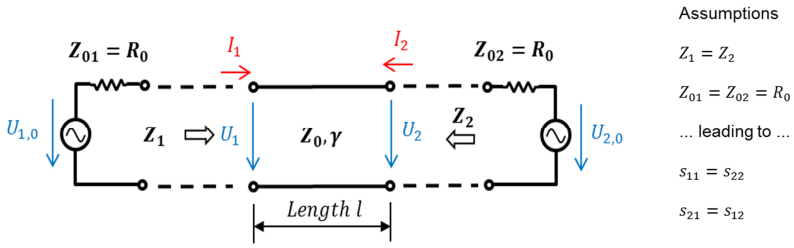

Figure C-5 Equivalent transmission line circuit of coaxial test fixture

Voltages and currents of incident and reflected waves at Port 1 and 2 as well as corresponding port impedances are summarised in Equations (C-6) to (C-9).

Voltages

$$U_1 = U_{1,in} + U_{1,out}$$
$$U_2 = U_{2,in} + U_{2,out}$$

(C-6)

Currents

$$I_1 = I_{1,in} + I_{1,out}$$
$$I_2 = I_{2,in} + I_{2,out}$$

(C-7)

Input Impedances

$$Z_1 = \frac{U_1}{I_1} = \frac{U_{1,in}}{I_{1,in}} = \frac{U_{1,out}}{I_{1,out}} = \frac{U_{1,in} + U_{1,out}}{U_{1,in} - U_{1,out}} \cdot Z_{01} = Z_0 \cdot \frac{R_0 + Z_0 \cdot tanh(\gamma \cdot l)}{Z_0 + R_0 \cdot tanh(\gamma \cdot l)}$$

(C-8)

$$Z_2 = \frac{U_2}{I_2} = \frac{U_{2,in}}{I_{2,in}} = \frac{U_{2,out}}{I_{2,out}} = \frac{U_{2,in} + U_{2,out}}{U_{2,in} - U_{2,out}} \cdot Z_{02} = Z_0 \cdot \frac{R_0 + Z_0 \cdot tanh(\gamma \cdot l)}{Z_0 + R_0 \cdot tanh(\gamma \cdot l)}$$

(C-9)

The voltage gain between Port 2 and Port 1 is given in Equations (C-10) to (C-12) using the s-parameter definitions in Equations (C-13) to (C-15).

Voltage Gain

$$\frac{U_2}{U_1} = \frac{U_{2,in} + U_{2,out}}{U_{1,in} + U_{1,out}}$$

(C-10)

... for $U_{2,in} = 0$ follows ...

$$\frac{U_2}{U_1} = \frac{U_{2,out}}{U_{1,in} + U_{1,out}} = \frac{\frac{U_{2,out}}{U_{1,in}}}{\frac{U_{1,in}}{U_{1,in}} + \frac{U_{1,out}}{U_{1,in}}}$$

(C-11)

$$\frac{U_2}{U_1} = \frac{s_{21}}{1 + s_{11}}$$

(C-12)

S-Parameter

$$s_{11} = \frac{b_1}{a_1}\Big|_{a_2=0} = \frac{U_{1,out}}{U_{1,in}} = \frac{Z_1 - {Z_{01}}^*}{Z_1 + Z_{01}} = \frac{Z_1 - R_0}{Z_1 + R_0} = \frac{1}{D_s} \cdot \left({Z_0}^2 - {R_0}^2\right) \cdot sinh(\gamma \cdot l)$$

$$s_{22} = \frac{b_2}{a_2}\Big|_{a_1=0} = \frac{U_{2,out}}{U_{2,in}} = \frac{Z_2 - {Z_{02}}^*}{Z_2 + Z_{02}} = \frac{Z_2 - R_0}{Z_2 + R_0} = \frac{1}{D_s} \cdot \left({Z_0}^2 - {R_0}^2\right) \cdot sinh(\gamma \cdot l)$$

(C-13)

$$D_s = 2 \cdot Z_0 \cdot R_0 \cdot cosh(\gamma \cdot l) + \left({Z_0}^2 + {R_0}^2\right) \cdot sinh(\gamma \cdot l)$$

(C-14)

$$s_{21} = \frac{b_2}{a_1}\Big|_{a_2=0} = \frac{U_{2,out}}{U_{1,in}} = 2 \cdot Z_0 \cdot R_0$$

$$s_{12} = \frac{b_1}{a_2}\Big|_{a_1=0} = \frac{U_{1,out}}{U_{2,in}} = 2 \cdot Z_0 \cdot R_0$$

(C-15)

With $s_{11} = s_{22}$ and $s_{21} = s_{12}$ and Equations (C-12) to (C-15) expressions for the line impedance Z_0 (Equation (C-16)) and the propagation constant γ (Equation (C-17)) are found.

Line impedance Z_0 and propagation constant γ

$$Z_0 = R_0 \cdot \sqrt{\frac{(1+s_{11}+s_{21})\cdot(1+s_{11}-s_{21})}{(1-s_{11}-s_{21})\cdot(1-s_{11}+s_{21})}} \tag{C-16}$$

$$\gamma = \frac{2}{l} \cdot arctanh\left[\sqrt{\frac{(1+s_{11}-s_{21})\cdot(1-s_{11}-s_{21})}{(1-s_{11}+s_{21})\cdot(1+s_{11}+s_{21})}}\right] \tag{C-17}$$

From line impedance and propagation constant the corresponding $\boldsymbol{R'G'L'C'}$ parameter can be derived (Equation (C-18)) and from the primed parameter the absolute values (Equation (C-19)).

$\boldsymbol{R'G'L'C'}$ parameter

$$\begin{aligned} R' &= Re\{\gamma \cdot Z_0\} && \left[\frac{Ohm}{m}\right] \\ L' &= \frac{1}{\omega} \cdot Im\{\gamma \cdot Z_0\} && \left[\frac{H}{m}\right] \\ G' &= Re\left\{\frac{\gamma}{Z_0}\right\} && \left[\frac{S}{m}\right] \\ C' &= \frac{1}{\omega} \cdot Im\left\{\frac{\gamma}{Z_0}\right\} && \left[\frac{F}{m}\right] \end{aligned} \tag{C-18}$$

$\boldsymbol{RGLC}$ parameter

$$\begin{aligned} R &= R' \cdot l && [Ohm] \\ L &= L' \cdot l && [H] \\ G &= G' \cdot l && [S] \\ C &= C' \cdot l && [F] \end{aligned} \tag{C-19}$$

In a last step the transversal permittivity and conductivity can be calculated using the relationships for capacitance and conductance of coaxial transmission line sections.

Permittivity and conductivity

$$C = \varepsilon_0 \cdot \varepsilon_s \cdot \frac{2 \cdot \pi \cdot \Delta z}{ln\left(\frac{r_o}{r_i}\right)} \tag{C-20}$$

$$\varepsilon_s = \varepsilon_r = C \cdot \frac{1}{\varepsilon_0} \cdot \frac{ln\left(\frac{r_o}{r_i}\right)}{2 \cdot \pi \cdot \Delta z} \tag{C-21}$$

$$G = \sigma_{eff} \cdot \frac{2 \cdot \pi \cdot \Delta z}{ln\left(\frac{r_o}{r_i}\right)} \tag{C-22}$$

$$\sigma_{eff} = G \cdot \frac{ln\left(\frac{r_o}{r_i}\right)}{2 \cdot \pi \cdot \Delta z} \tag{C-23}$$

C.3. EM wave excitation scenarios

An incident electromagnetic wave impinging onto an unshielded transmission line generates guided (source) waves along the transmission line propagating into both directions. The guided waves are reflected at the distal ends of the transmission line and after multiple reflections eventually dissipate all their energy. The resulting amplitude and phase distribution along the transmission line is the superposition of all source waves and all reflected waves. The impinging wave can be represented as distributed line source with given magnitude and phase (Figure C-6). In the following only the steady state condition $(t \to \infty)$ is considered.

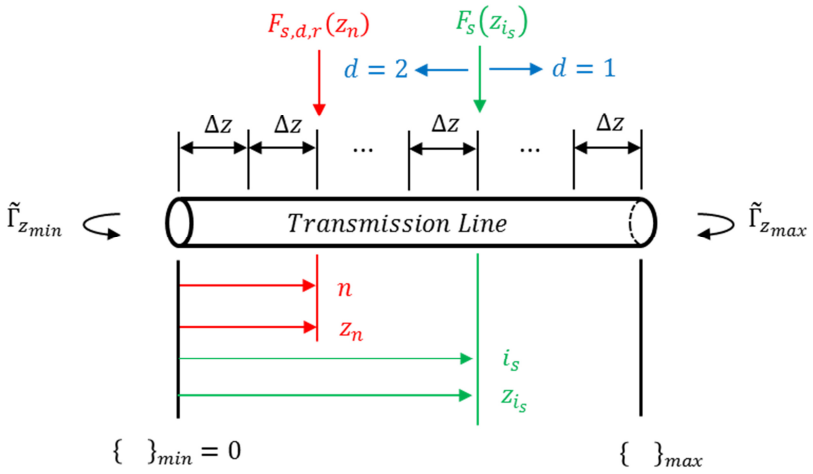

Figure C-6 Transmission line with reflections at both ends

s $source\ number$ $s = 1,2,3 \dots s_{max}$

d $propagation\ direction$ $d = 1,2,3,4,5, \dots d_{max}$ $d = 1 \to right$; $d = 2 \to left$

r $reflection\ number\ at\ boundary$ $r = 0,1,2,3 \dots r_{max}$

$r = 0 \to source\ wave$

$r = 1 \to wave\ from\ first\ reflection$

$r = 2 \to wave\ from\ second\ second\ reflection$

n $field\ location\ increment\ along\ z - direction$ $n = 0,1,2,3 \dots n_{max}$ $with\ n_{min} = 0$

i_s $source\ location\ along\ z - direction$ $i_s = 0,1,2,3 \dots i_{s,max}$

$with\ i_{s,max} = n_{max}\ and\ i_{s,min} = n_{min}$

$z_n = n \cdot \Delta z \quad with\ z_{min} = n_{min} \cdot \Delta z = 0 \ \ and\ z_{max} = n_{max} \cdot \Delta z$

$z_{i_s} = i_s \cdot \Delta z$

$\tilde{\Gamma}_{z_{min}} \quad complex\ reflection\ coefficient\ at\ z_{min}$

$\tilde{\Gamma}_{z_{max}} \quad complex\ reflection\ coefficient\ at\ z_{max}$

$F_s(z_{i_s}) \quad source\ at\ location\ z_{i_s}$

$F_{s,d,r}(z_n) \quad field\ at\ location\ z_n\ from\ source\ s, propagation\ direction\ d\ and\ r^{th}\ reflection$

$$\Delta z = \frac{z_{max}}{n_{max}} \tag{C-24}$$

The first source $(s = 1)$ generates guided source waves travelling into initial direction $d = 1$ and $d = 2$. At the distal end z_{max} the source wave $d = 1$ is reflected. At the distal end z_{min} the source wave $d = 2$ is reflected. The two guided waves travel between the distal ends until they have dissipated all their energy.

The contributions of source wave $(s = 1)$ travelling into initial direction $d = 1$ and all its reflected waves are given below.

Source $s = 1$

Propagation direction $d = 1$

Source wave

$$F_{1,1,0}(z_n) = F_{1,1,0}(z_{i_1}) \cdot e^{-j \cdot \tilde{k}_z \cdot |z_n - z_{i_1}|} = F_{1,1,0}(z_{i_1}) \cdot e^{-j \cdot \tilde{k}_z \cdot |n - i_1| \cdot \Delta z} \quad \text{with } n \geq i_1 \tag{C-25}$$

First reflected wave (right side)

$$F_{1,1,1}(z_n) = F_{1,1,0}(z_{i_1}) \cdot e^{-j \cdot \tilde{k}_z \cdot |n_{max} - i_1| \cdot \Delta z} \cdot \tilde{\Gamma}_{z_{max}} \cdot e^{-j \cdot \tilde{k}_z \cdot |n_{max} - n| \cdot \Delta z} \tag{C-26}$$

Second reflected wave (left side)

$$F_{1,1,2}(z_n) = F_{1,1,0}(z_{i_1}) \cdot e^{-j \cdot \tilde{k}_z \cdot |n_{max} - i_1| \cdot \Delta z} \cdot \tilde{\Gamma}_{z_{max}} \cdot e^{-j \cdot \tilde{k}_z \cdot n_{max} \cdot \Delta z} \cdot \tilde{\Gamma}_{z_{min}} \cdot e^{-j \cdot \tilde{k}_z \cdot n \cdot \Delta z} \tag{C-27}$$

Third reflected wave (right side)

$$F_{1,1,3}(z_n) = F_{1,1,0}\left(z_{i_1}\right) \cdot e^{-j\cdot\tilde{k}_z\cdot|n_{max}-i_1|\cdot\Delta z} \cdot \tilde{\Gamma}_{z_{max}} \cdot e^{-j\cdot\tilde{k}_z\cdot n_{max}\cdot\Delta z} \cdot \tilde{\Gamma}_{z_{min}} \cdot e^{-j\cdot\tilde{k}_z\cdot n_{max}\cdot\Delta z} \cdot \tilde{\Gamma}_{z_{max}} \cdot e^{-j\cdot\tilde{k}_z\cdot|n_{max}-n|\cdot\Delta z} \tag{C-28}$$

Fourth reflected wave (left side)

$$F_{1,1,4}(z_n) = F_{1,1,0}\left(z_{i_1}\right) \cdot e^{-j\cdot\tilde{k}_z\cdot|n_{max}-i_1|\cdot\Delta z} \cdot \tilde{\Gamma}_{z_{max}} \cdot e^{-j\cdot\tilde{k}_z\cdot n_{max}\cdot\Delta z} \cdot \tilde{\Gamma}_{z_{min}} \cdot e^{-j\cdot\tilde{k}_z\cdot n_{max}\cdot\Delta z} \cdot \tilde{\Gamma}_{z_{max}} \cdot e^{-j\cdot\tilde{k}_z\cdot n_{max}\cdot\Delta z} \cdot \tilde{\Gamma}_{z_{min}} \cdot e^{-j\cdot\tilde{k}_z\cdot n\cdot\Delta z} \tag{C-29}$$

Fifth reflected wave (right side)

$$F_{1,1,5}(z_n) = F_{1,1,0}\left(z_{i_1}\right) \cdot e^{-j\cdot\tilde{k}_z\cdot|n_{max}-i_1|\cdot\Delta z} \cdot \tilde{\Gamma}_{z_{max}} \cdot e^{-j\cdot\tilde{k}_z\cdot n_{max}\cdot\Delta z} \cdot \tilde{\Gamma}_{z_{min}} \cdot e^{-j\cdot\tilde{k}_z\cdot n_{max}\cdot\Delta z} \cdot \tilde{\Gamma}_{z_{max}} \cdot e^{-j\cdot\tilde{k}_z\cdot n_{max}\cdot\Delta z} \cdot \tilde{\Gamma}_{z_{min}} \cdot e^{-j\cdot\tilde{k}_z\cdot n_{max}\cdot\Delta z} \cdot \tilde{\Gamma}_{z_{max}} \cdot e^{-j\cdot\tilde{k}_z\cdot|n_{max}-n|\cdot\Delta z} \tag{C-30}$$

The superposition of source wave $s = 1$ travelling in propagation direction $d = 1$ and all its reflected waves results in ...

$$F_{1,1,r_{max}}(z_n) = F_{1,1,0}\left(z_{i_1}\right) \cdot \left[\begin{matrix} e^{-j\cdot\tilde{k}_z\cdot|n-i_1|\cdot\Delta z} & for\ n \geq i_1 \\ 0 & for\ n < i_1 \end{matrix}\right] + e^{-j\cdot\tilde{k}_z\cdot|n_{max}-i_1|\cdot\Delta z} \cdot \left[\begin{matrix} \tilde{\Gamma}_{z_{max}} \cdot e^{-j\cdot\tilde{k}_z\cdot|n_{max}-n|\cdot\Delta z} & for\ r \geq 1 \\ 0 & for\ r = 0 \end{matrix}\right] + \left[\begin{matrix} \left[\sum_{r=2}^{r_{max}} \left(\tilde{\Gamma}_{z_{max}}\right)^{\left(1+floor\left(\frac{r-1}{2}\right)\right)} \cdot \left(\tilde{\Gamma}_{z_{min}}\right)^{\left(floor\left(\frac{r}{2}\right)\right)} \cdot e^{-j\cdot\tilde{k}_z\cdot\Delta z\cdot[(r-1)\cdot n_{max}+|mod[r,2]\cdot n_{max}-n|]}\right] & for\ r \geq 2 \\ 0 & for\ r \leq 1 \end{matrix}\right] \tag{C-31}$$

$$f_1(r) = 1 + floor\left(\frac{r-1}{2}\right) \rightarrow f(\{r = 1,2,3,4,5, \dots\}) = 1,1,2,2,3,3,4,4,5,5, \dots$$
$$\rightarrow A008619\ Positive\ integers\ repeated$$
$$f_2(r) = floor\left(\frac{r}{2}\right) \rightarrow f(\{r = 1,2,3,4,5, \dots\}) = 0,1,1,2,2,3,3,4,4,5,5, \dots$$
$$f_3(r) = mod[r,2] \rightarrow f(\{r = 1,2,3,4,5, \dots\}) = 1,0,1,0,1,0,1,0 \dots$$
$$\rightarrow A059841$$
$$mod[r,a] = r - a \cdot floor\left(\frac{r}{a}\right) \tag{C-32}$$

Now, the contributions of source wave $(s = 1)$ travelling into initial direction $d = 2$ and all its reflected waves are derived ...

Propagation direction $d = 2$

Source wave

$$F_{1,2,0}(z_n) = F_{1,2,0}\left(z_{i_1}\right) \cdot e^{-j\cdot\tilde{k}_z\cdot|z_n - z_{i_1}|} = F_{1,2,0}\left(z_{i_1}\right) \cdot e^{-j\cdot\tilde{k}_z\cdot|n-i_1|\cdot\Delta z} \quad \text{with } n \le i_1 \tag{C-33}$$

First reflected wave (left side)

$$F_{1,2,1}(z_n) = F_{1,2,0}\left(z_{i_1}\right) \cdot e^{-j\cdot\tilde{k}_z\cdot|n_{min}-i_1|\cdot\Delta z} \cdot \tilde{\Gamma}_{z_{min}} \cdot e^{-j\cdot\tilde{k}_z\cdot n\cdot\Delta z} \tag{C-34}$$

Second reflected wave (right side)

$$F_{1,2,2}(z_n) = F_{1,2,0}\left(z_{i_1}\right) \cdot e^{-j\cdot\tilde{k}_z\cdot|n_{min}-i_1|\cdot\Delta z} \cdot \tilde{\Gamma}_{z_{min}} \cdot e^{-j\cdot\tilde{k}_z\cdot n_{max}\cdot\Delta z} \cdot \tilde{\Gamma}_{z_{max}} \cdot e^{-j\cdot\tilde{k}_z\cdot|n_{max}-n|\cdot\Delta z} \tag{C-35}$$

Third reflected wave (left side)

$$F_{1,2,3}(z_n) = F_{1,2,0}\left(z_{i_1}\right) \cdot e^{-j\cdot\tilde{k}_z\cdot|n_{min}-i_1|\cdot\Delta z} \cdot \tilde{\Gamma}_{z_{min}} \cdot e^{-j\cdot\tilde{k}_z\cdot n_{max}\cdot\Delta z} \cdot \tilde{\Gamma}_{z_{max}} \cdot e^{-j\cdot\tilde{k}_z\cdot n_{max}\cdot\Delta z} \cdot \tilde{\Gamma}_{z_{min}} \cdot e^{-j\cdot\tilde{k}_z\cdot n\cdot\Delta z} \tag{C-36}$$

Fourth reflected wave (right side)

$$F_{1,2,4}(z_n) = F_{1,2,0}\left(z_{i_1}\right) \cdot e^{-j\cdot\tilde{k}_z\cdot|n_{min}-i_1|\cdot\Delta z} \cdot \tilde{\Gamma}_{z_{min}} \cdot e^{-j\cdot\tilde{k}_z\cdot n_{max}\cdot\Delta z} \cdot \tilde{\Gamma}_{z_{max}} \cdot e^{-j\cdot\tilde{k}_z\cdot n_{max}\cdot\Delta z} \cdot \tilde{\Gamma}_{z_{min}} \cdot e^{-j\cdot\tilde{k}_z\cdot n_{max}\cdot\Delta z} \cdot \tilde{\Gamma}_{z_{max}} \cdot e^{-j\cdot\tilde{k}_z\cdot|n_{max}-n|\cdot\Delta z} \tag{C-37}$$

Fifth reflected wave (left side)

$$F_{1,2,5}(z_n) = F_{1,2,0}\left(z_{i_1}\right) \cdot e^{-j\cdot\tilde{k}_z\cdot|n_{min}-i_1|\cdot\Delta z} \cdot \tilde{\Gamma}_{z_{min}} \cdot e^{-j\cdot\tilde{k}_z\cdot n_{max}\cdot\Delta z} \cdot \tilde{\Gamma}_{z_{max}} \cdot e^{-j\cdot\tilde{k}_z\cdot n_{max}\cdot\Delta z} \cdot \tilde{\Gamma}_{z_{min}} \cdot e^{-j\cdot\tilde{k}_z\cdot n_{max}\cdot\Delta z} \cdot \tilde{\Gamma}_{z_{max}} \cdot e^{-j\cdot\tilde{k}_z\cdot n_{max}\cdot\Delta z} \cdot \tilde{\Gamma}_{z_{min}} \cdot e^{-j\cdot\tilde{k}_z\cdot n\cdot\Delta z} \tag{C-38}$$

The superposition of source wave $s = 1$ travelling in propagation direction $d = 2$ and all its reflected waves results in ...

$$F_{1,2,r_{max}}(z_n) = F_{1,2,0}(z_{i_1}) \cdot \left[\begin{bmatrix} e^{-j\cdot\tilde{k}_z\cdot|n-i_1|\cdot\Delta z} & for\ n \le i_1 \\ 0 & for\ n > i_1 \end{bmatrix} + e^{-j\cdot\tilde{k}_z\cdot|n_{min}-i_1|\cdot\Delta z} \right] \cdot \left[\begin{bmatrix} \tilde{\Gamma}_{z_{min}} \cdot e^{-j\cdot\tilde{k}_z\cdot n\cdot\Delta z} & for\ r \ge 1 \\ 0 & for\ r = 0 \end{bmatrix} + \left[\begin{bmatrix} \sum_{r=2}^{r_{max}} \left(\tilde{\Gamma}_{z_{min}}\right)^{\left(1+floor\left(\frac{r-1}{2}\right)\right)} \cdot \left(\tilde{\Gamma}_{z_{max}}\right)^{\left(floor\left(\frac{r}{2}\right)\right)} \cdot e^{-j\cdot\tilde{k}_z\cdot\Delta z\cdot[(r-1)\cdot n_{max}+|mod[(r-1),2]\cdot n_{max}-n|]} & for\ r \ge 2 \\ 0 & for\ r \le 1 \end{bmatrix} \right] \right] \quad \text{(C-39)}$$

$$f_4(r) = mod[(r-1), 2] \rightarrow f(\{r = 1,2,3,4,5, \dots\}) = 0,1,0,1,0,1,0,1 \dots \quad \text{(C-40)}$$

Finally all source and all reflected waves from both propagation directions have to be superimposed.

$$F_{s_{all},d,r_{max}}(z_n) = \sum_{s=1}^{s_{max}} \left[\sum_{d=1}^{d=2} F_{s,d,r_{max}}(z_n) \right] \quad \text{(C-41)}$$

In many cases the source waves travelling from the source location z_{i_s} into direction $d = 1$ and $d = 2$ are equal.

$$F_{s,1,0}(z_{i_s}) = F_{s,2,0}(z_{i_s}) \quad \text{(C-42)}$$

The Matlab source code for the electromagnetic wave excitation scenario is given below. The results have been presented in Section 5.1.13.1.

```
% AUTHOR:        Dirk Hartung
% DATE:          17.07.2017
% DESCRIPTION:  Colinear Array - Spinal Cord Stimulator - Lead

% Data files
% Source data file : Cola_Sources_01.xlsx
% Output data file : Cola_Results_01.xlsx

% INPUT PARMAETERS:
lamda_mm = 400;          % lambda [mm] ; for 200 mm Lead: 243 mm ; for 600 mm Lead: 400 mm
alpha_dB_mm = -2.65;    % alpha [dB/100 mm]  for 200 mm: -2.05;  for 400 mm: -2.65
n_min = 1;               % Min. field sample number along colinear array
n_max = 256;             % Max. field sample number along colinear array
is_min = n_min;          % First source location along colinear array
is_max = n_max;          % Last source location along colinear array
z_min = 0.0;             % Start of colinear array length [m]
z_max = 0.600;           % End of colinear array length [m]
d_min = 1;               % propagation direction (d = 1 ---> right; d = 2 ---> left)
d_max = 2;               % propagation direction (d = 1 ---> right; d = 2 ---> left)
r_rfl_min = 0.9 * exp(1i*0/4*pi);              % Complex reflection coefficient at z_min
r_rfl_max = 0.9 * exp(-1i*0.625*pi);          % Complex reflection coefficient at z_max
r_min = 0;               % Minimum number of reflections at boundary
r_max = 5;               % Maximum number of reflections at boundary

% Variables:
n_act = 0;                    % Actual (current) field number n_act = n_min ... n_max
r_act = 1;                    % Actual (current) reflection number r_act = r_min ... r_max
z_del = (z_max-z_min)/(n_max-1);  %Length increment along colinear array
d_act = 1;                    % propagation direction (d = 1 ---> right; d = 2 ---> left)
is_act = 0;                   % Actual (current) source number is_act = is_min ... is_max
z_fld = n_act * z_del;          % Actual (current) field location z_fld = z_min ... z_max
z_src = is_act * z_del;         % Actual (current) source location z_src = is_min ... is_max

% CONSTANTS:
alpha = log(10^((alpha_dB_mm*10)/20));      % Attenuation constant [1/m]]
beta = (2*pi)/(lamda_mm/1000);              % Phase constant [rad/m]
kz = alpha - 1i*beta;                       % complex propagation constant [1/m]]

% FIELDS (Arrays):
F_s_amp = zeros(is_max,1);          % Input array containing amplitude terms
F_s_pha = zeros(is_max,1);          % Input array containing phase terms
F_s_cmplx = zeros(is_max,1);        % Input array containing complex source terms
F_s = zeros(is_max,1);              % Array for source contribution
F_d = zeros(d_max,1);               % Array for propagation direction
F_n = zeros(n_max,1);                    % Array for field points
F_nsdr = zeros(n_max,is_max,d_max,r_max);  % Contribution at n_act from r_act, d_act, is_act
F_nsdr_sum = zeros(n_max,2);               % Sum of all contribution F_nsdr

% Start main program

% Open source data file
source_data = xlsread('Cola_Sources_01.xlsx','Source_600mm','B5:D260');

% Select datasets
dataset_size = is_max;
dataset_increment = 1;
```

```
% Assign source data to array
for is_act = (1:dataset_increment:dataset_size)
      F_s_amp(is_act) = source_data(is_act,2);
      F_s_pha(is_act) = source_data(is_act,3);
end

% Normalisation of input data
F_s_amp_norm = 1.0;              % normaisation to single source amplitude

% Propagation direction
for is_act = (1:dataset_increment:dataset_size)
      F_s_amp(is_act) = F_s_amp(is_act)/F_s_amp_norm;
      if (d_min == d_max)
         F_s_cmplx(is_act) =  F_s_amp(is_act)*exp(-1i*F_s_pha(is_act)*pi/180);
      else
         F_s_cmplx(is_act) =  0.5 * F_s_amp(is_act)*exp(-1i*F_s_pha(is_act)*pi/180);
      end
end

% Field calculation
for n_act = (n_min:n_max)
   for is_act = (is_min:is_max)
      for d_act = (d_min:d_max)
          % Calculate contribution at n_act from r_act reflection in propagation direction d_act from source is_act
          for r_act = (r_min:r_max)
             r_index=r_act+1;
             if (d_act == 1)
                if (r_act == 0)
                    if (n_act == is_act)
                          F_nsdr(n_act,is_act,d_act,r_index)= 0.5 * F_s_cmplx(is_act);
                    elseif (n_act > is_act)
                          F_nsdr(n_act,is_act,d_act,r_index)= F_s_cmplx(is_act) * exp(kz* abs((n_act-1)-(is_act-1))*z_del);
                    elseif (n_act < is_act)
                          F_nsdr(n_act,is_act,d_act,r_index)= 0;
                    end
                elseif  (r_act == 1)
                    F_r=r_rfl_max*exp(kz* abs((n_max-1)-(n_act-1))*z_del);
                    F_nsdr(n_act,is_act,d_act,r_index)= F_s_cmplx(is_act) * exp(kz* abs((n_max-1)-(is_act-1))*z_del) * F_r;
                elseif  (r_act >= 2)
                    F_r= r_rfl_max^(1+floor((r_act-1)/2)) * r_rfl_min^(floor(r_act/2)) * exp(  kz*z_del*  ( (r_act-1)*(n_max-1) +
                         abs(mod(r_act,2)*(n_max-1)-(n_act-1) ) ) ) ;
                    F_nsdr(n_act,is_act,d_act,r_index)= F_s_cmplx(is_act) * exp(kz* abs((n_max-1)-(is_act-1))*z_del) * F_r;
                end
             elseif (d_act == 2)
                if (r_act == 0)
                    if (n_act == is_act)
                          F_nsdr(n_act,is_act,d_act,r_index)= 0.5 * F_s_cmplx(is_act);
                    elseif (n_act < is_act)
                          F_nsdr(n_act,is_act,d_act,r_index)= F_s_cmplx(is_act) * exp(kz* abs((n_act-1)-(is_act-1))*z_del);
                    elseif (n_act > is_act)
                          F_nsdr(n_act,is_act,d_act,r_index)= 0;
                    end
                elseif  (r_act == 1)
                    F_r=r_rfl_min*exp(kz* abs((n_act-1))*z_del);
                    F_nsdr(n_act,is_act,d_act,r_index)= F_s_cmplx(is_act) * exp(kz* abs((n_min-1)-(is_act-1))*z_del) * F_r;
                elseif  (r_act >= 2)
                    F_r= r_rfl_min^(1+floor((r_act-1)/2) ) *  r_rfl_max^(floor(r_act/2)) * exp(  kz*z_del*( (r_act-1)*(n_max-1) + abs(mod((r_act-
                         1),2)*(n_max-1)-(n_act-1) ) ) ) ;
                    F_nsdr(n_act,is_act,d_act,r_index)= F_s_cmplx(is_act) * exp(kz* abs((n_min-1)-(is_act-1))*z_del) * F_r;
                end
             end
          end % r_act
      end % d_act
```

```
    end % is_act
end % n_act

for n_act = (n_min:n_max)
    F_nsdr_sum(n_act,1)= (n_act-1)*z_del*1000;
    for is_act = (is_min:is_max)
        for d_act = (d_min:d_max)
            % Calculate contribution at n_act from r_act reflection in propagation direction d_act from source s_act
            for r_act = (r_min:r_max)
                r_index=r_act+1;
                F_nsdr_sum(n_act,2)= F_nsdr_sum(n_act,2) + F_nsdr(n_act,is_act,d_act,r_index);
            end
        end
    end
end

% Normalisation of output data
F_nsdr_sum_max = max(abs(F_nsdr_sum(:,2)));

% Write data into output data file
xlswrite('Cola_Results_01.xlsx', abs(F_nsdr_sum(:,1)) ,'Results_01','B3');
xlswrite('Cola_Results_01.xlsx', abs(F_nsdr_sum(:,2)) ,'Results_01','C3');
xlswrite('Cola_Results_01.xlsx', angle(F_nsdr_sum(:,2)) ,'Results_01','D3');

% Plot field magnitude
figure('Name','Magnitude')
% plot(abs(F_nsdr(:,:,:,1)));
plot(  (F_nsdr_sum(:,1)) , abs(F_nsdr_sum(:,2)) );
xlim([0 (z_max*1000)]);
ylim([0 100]);

% Plot field phase
figure('Name','Phase')
% plot(angle(F_nsdr(:,:,:,1)));
plot(  (F_nsdr_sum(:,1)) , angle(F_nsdr_sum(:,2)) );
xlim([0 (z_max*1000)]);
% ylim([-pi pi]);

% End main program
```

D Thermodynamic modelling

D.1 Heat dissipation in perfused tissue

The partial differential equation describing heat transfer in human tissue is given in Equation (D-1).

$$\underbrace{\rho_{ti} \cdot c_{ti} \cdot \frac{\delta T_{ti}}{\delta t}}_{\text{Term 1}} = \Big[\underbrace{k_{ti} \cdot \frac{\delta^2 T_{ti}}{\delta x^2}}_{\text{Term 2}} + \underbrace{\rho_{fl} \cdot c_{fl} \cdot r_{fl} \cdot (T_{fl} - T_{ti})}_{\text{Term 3}} + \underbrace{q_{me}}_{\text{Term 4}} + \underbrace{p_{em}}_{\text{Term 5}}\Big] \quad \left[\frac{W}{m^3}\right] \tag{D-1}$$

T	*temperature*	$[K]$	k	*thermal conductivity*	$\left[\frac{W}{m \cdot K}\right]$
r	*rate of perfusion*	$\left[\frac{1}{s}\right]$	q	*metabolic rate of heat generation*	$\left[\frac{W}{m^3}\right]$
c	*mass specific heat capacity*	$\left[\frac{J}{kg \cdot K}\right]$	p	*dissipated power density*	$\left[\frac{W}{m^3}\right]$
ρ	*mass density*	$\left[\frac{kg}{m^3}\right]$	x	*distance*	$[m]$
t	*time*	$[s]$			

ti	*tissue*	me	*metabolic*
fl	*fluid (in most cases blood or cerebrospinal fluid)*	em	*electromagnetic*

Five terms are taken into account for heat generation and heat transfer ...

Term 1 accounts for internal energy storage, i.e. temperature increase over time.

Term 2 accounts for conduction of heat from regions of higher temperature to regions of lower temperature.

Term 3 accounts for convection of heat (perfusion).

Term 4 accounts for metabolic heat generation.

Term 5 accounts for RF induced heat generation (exposure to electromagnetic fields).

The differential equation is a simplistic representation of human tissue not taking into account multi-layered structures of tissue and time dependent temperature increases of perfusion liquids. In addition, heat capacities and thermal conductivities of IMDs in contact with human tissue are neglected. One particular scenario is depicted in Figure D-1 and described below.

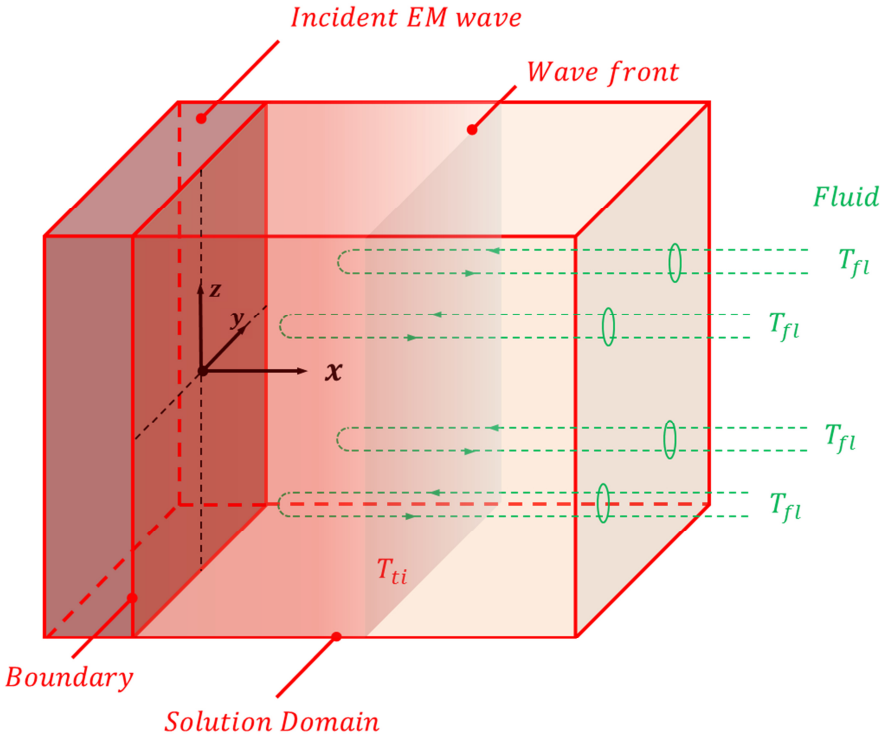

Figure D-1 Outline of solution domain

The assumptions are summarised below:

- For $x \geq 0$, the solution domain is a one-dimensional absorptive infinite half space.
- The domain for $x < 0$ has no impact on the solution domain $x \geq 0$ apart from being the region for an incident wave or the location of an external heat source.
- The incident wave hits the boundary a $t = 0$ and continues for all times $t \geq 0$ (Heaviside step function)

- The perfusion liquid (e.g. blood) flowing through the solution domain has a constant temperature T_{fl} equal to the core temperature T_{core} of the human body.
- Metabolic heat generation is neglected.
- At $x = 0$ and $t = 0$, the temperature of the tissue $T_{ti}(x = 0, t = 0)$ along the boundary in the $yz\ plane$ is known (initial condition).
- At $t = 0$, the temperature of the tissue T_{ti} is the same for all locations x.
- For all locations $x \geq 0$ and all times $t \geq 0$, the perfusion rate r determines cooling or heating of the tissue (T_{ti}). A perfusion rate of zero means that tissue temperature T_{ti} is not influenced by fluid temperature T_{fl}.
- For all locations $x \geq 0$ and all times $t \geq 0$, the incident heat intensity (incident planar wave or external heat source) determines heating of the tissue (T_{ti}).
- The power absorption coefficient α_p determines the profile (envelope) of the absorbed (deposited) power in human tissue caused by incident planar wave intensity I_0. The power transfer efficiency factor τ determines the fraction of the incident wave intensity that is absorbed.

$$I_x = \tau \cdot I_0 \cdot e^{-\alpha_p \cdot x} \qquad \left[\frac{W}{m^2}\right]$$

(D-2)

With these assumptions an analytic expression for the tissue temperature $T_{ti}(x,t)$ for $x \geq 0$ and $t \geq 0$ can be derived [P184].

$$T_{ti}(x,t) = T_{fl}$$
$$+ \tau \cdot I_0 \cdot \frac{1}{k_{ti}} \cdot \frac{\alpha_p \cdot {l_c}^3}{\left((\alpha_p \cdot l_c)^2 - 1\right)} \cdot \left[\left(\alpha_p \cdot e^{-\frac{x}{l_c}} - \frac{1}{l_c} \cdot e^{-\alpha_p \cdot x}\right) - \left(\alpha_p \cdot g\left(x, \frac{1}{l_c}, t\right) - \frac{1}{l_c} \cdot g(x, \alpha_p, t)\right)\right]$$
$$+ \frac{1}{2} \cdot \left|T_{ti}(x = 0, t = 0) - T_{fl}\right|_{I_0 = 0} \cdot e^{-\frac{x}{l_c}} \cdot e^{-\frac{1}{{l_c}^2} \alpha \cdot t} \cdot \left[1 + erf\left(\frac{1}{\sqrt{4 \cdot \alpha \cdot t}} \cdot x - \sqrt{\alpha \cdot t} \cdot \frac{1}{l_c}\right)\right] \qquad [K]$$

(D-3)

The function $g(x,m,t)$ takes into account conductive and convective heat transfer between the tissue and the fluid (modified Green's heat kernel).

$$g(x,m,t) = \frac{1}{2} \cdot e^{m^2 \cdot \alpha \cdot t} \cdot \left[2 \cdot e^{-m \cdot x} + e^{+m \cdot x} \cdot erfc\left(\frac{x + 2 \cdot \alpha \cdot t \cdot m}{\sqrt{4 \cdot \alpha \cdot t}} \right) - e^{-m \cdot x} \cdot erfc\left(\frac{x - 2 \cdot \alpha \cdot t \cdot m}{\sqrt{4 \cdot \alpha \cdot t}} \right) \right] \cdot e^{-\frac{1}{l_c^2} \cdot \alpha \cdot t}$$

$$with \quad m \rightarrow \frac{1}{l_c} \quad or \quad \alpha_p$$

(D-4)

Characteristic length

$$l_c = \sqrt{\frac{k_{ti}}{f_{fl}}} \qquad [m]$$

Power absorption coefficient

$$\alpha_p \qquad \left[\frac{1}{m}\right]$$

Flow constant (power density per Kelvin)

$$f_{fl} = \rho_{fl} \cdot c_{fl} \cdot r_{fl} \qquad \left[\frac{W}{m^3 \cdot K}\right]$$

Diffusivity

$$\alpha = \frac{k_{ti}}{\rho_{ti} \cdot c_{ti}} = \frac{k_{ti}}{t_c \cdot f_{bl}} \qquad \left[\frac{m^2}{s}\right]$$

(D-5)

Blank Page

Blank Page